

Université Paris Diderot (Paris 7) - Sorbonne Paris Cité

École Doctorale “Physique en Île-de-France”



THÈSE DE DOCTORAT

Discipline : Physique théorique



présentée par

Étienne Fodor

**Signatures hors de l'équilibre
dans les systèmes vivants et actifs**

**Tracking nonequilibrium in living matter
and self-propelled systems**

dirigée par Paolo VISCO et Frédéric VAN WIJLAND

Soutenue le 4 juillet 2016 devant le jury composé de

Eric BERTIN	examinateur
Chase P. BROEDERSZ	rapporiteur
David S. DEAN	rapporiteur
Jean-François JOANNY	président
Paolo VISCO	co-directeur de thèse
Frédéric VAN WIJLAND	directeur de thèse

Acknowledgments

I would like to warmly thank my Ph.D. advisors, Paolo Visco and Frédéric van Wijland, for their support, guidance and encouragement all along the three years of my Ph.D. thesis. I have highly benefited from all the enthusiasm, clarity and rigor that characterize their supervision. I am indebted to Nir S. Gov for the recurrent discussions which have largely contributed to shape my conception of active fluctuations in living matter. I am very grateful to Julien Tailleur for sharing his vision of active matter which has motivated the second part of my thesis, and I sincerely thank Julien for his overall support. I am also thankful to Cesare Nardini and Michael E. Cates for their collaboration in the study of self-propelled particles as an active matter system. Besides, I would like to thank the members of my thesis committee: Eric Bertin, Chase P. Broedersz, David S. Dean and Jean-François Joanny, for accepting to evaluate my Ph.D. work. In particular, I am grateful to the referees, Chase P. Broedersz and David S. Dean, for their comments which enabled me to improve this manuscript.

Moreover, I would like to express my sincere gratitude to the three different experimental groups with whom I had the opportunity to collaborate. I am grateful to David A. Weitz and Ming Guo for sharing their results on tracer dynamics inside living melanoma cells, as a first insight into the captivating issues raised by the intracellular dynamics. I thank Timo Betz and Wylye W. Ahmed for the fruitful collaboration that we had all along my Ph.D. thesis. I really enjoyed our collaborative effort to analyze the dynamics within living mouse oocytes as a fascinating nonequilibrium material. I am thankful to Marie-Hélène Verlhac and Maria Almonacid who provided us with the oocytes. My sincere thanks also go to Daniel Riveline, Vishu Mehandia, Jordi Comelles and Raghavan Thiagarajan. Our collaboration has been a stunning opportunity to complement our study of active fluctuations in living matter with epithelial tissues.

Furthermore, I am obliged to Hisao Hayakawa for providing me with the opportunity to visit the Yukawa Institute of Theoretical Physics at Kyoto University.

The two visits during the second and third year of my Ph.D. were exciting experiences to discover the academic research conducted at the YITP and in the Physics Department of Kyoto University. I have largely benefited from Hisao's experience to gain a deeper view into the intriguing phenomena which feature non-Gaussian fluctuations. I thank the Ph.D. students of the Advanced Statistical Mechanics group for the many interesting discussions that we had, notably Kiyoshi Kanazawa and Tomohiko Sano. Besides, I am very grateful to Shinichi Sasa, Takahiro Nemoto and Andreas Dechant for sharing their insight into nonequilibrium statistical mechanics.

Eventually, I would like to thank the various members of the laboratory Matière et Systèmes Complexes for the very nice working atmosphere in which I enjoyed studying during the past three years. In particular, I am grateful to François Graner, François Gallet, Atef Asnacios, Sylvie Hénon, Fabien Montel, Jean-François Berret and Jean-Baptiste Fournier for insightful discussions. Besides, I also thank the many Ph.D. students who made the everyday life in the laboratory so animated: Thomas, Gwen, Tanguy, Simon, Mourtaza, Agnese, Alex, Sham, David, François, Iris and others.

Contents

Introduction	1
1 Modeling the fluctuations of passive tracers	7
1.1 Tracer in a thermal bath	8
1.2 Nonequilibrium dynamics driven by active fluctuations	12
2 Living matter: a paradigm of nonequilibrium systems	17
2.1 Structure and dynamics of the intracellular environment	18
2.2 Measuring fluctuations and response	20
2.2.1 Statistics of tracer displacement	21
2.2.2 Mechanical properties at the subcellular scale	24
2.3 Models for the intracellular mechanics and dynamics	27
3 Active cage model of fluctuations in living cells	31
3.1 Caging dynamics	32
3.2 Model predictions	36
3.2.1 Statistics of tracer displacement	36
3.2.2 Energetics of active fluctuations	39
Paper A: Energetics of active fluctuations in living cells	43
4 Colloidal tracers in living melanoma cells	55
Paper B: Activity-driven fluctuations in living cells	59
5 Vesicle dynamics in living mouse oocytes	67
Paper C: Active mechanics reveal molecular-scale force kinetics in living oocyte	75
Paper D: Nonequilibrium dissipation in living oocytes	107

6 Vertex fluctuations in epithelial layers	119
Paper E: Active fluctuations are controlled by molecular motor regulations in cell monolayer	123
7 Nonequilibrium properties of persistent self-propelled particles	137
7.1 Self-propelled particles as an active matter system	138
7.2 Interacting particles under persistent fluctuations	140
7.3 Effective equilibrium regime	146
Paper F: How far from equilibrium is active matter?	149
7.4 Collective modes	156
Main results and outlook	163
A Persistent self-propelled particles: approximate dynamics	167
B Persistent self-propelled particles: Dean-Kawasaki equation	173
Paper G: Generalized Langevin equation with hydrodynamic backflow: Equilibrium properties	177
Paper H: Active cell mechanics: Measurement and theory	183
Paper I: Modeling the dynamics of a tracer particle in an elastic active gel	195
Paper J: Active cage model of glassy dynamics	204
Bibliography	212
Papers	231

Introduction

The aim of statistical mechanics is to describe the properties of macroscopic systems from the sole knowledge of their microscopic constituents and of their interactions. The predictions of statistical mechanics offer the opportunity to compare a wide range of systems by using a reduced number of macroscopic quantities. Equilibrium systems are characterized by very specific properties both at the dynamical and stationary levels. An important feature of equilibrium systems is the time reversibility of their dynamics. It constrains the relaxation after a (small) perturbation to be fully encoded in the spontaneous stationary fluctuations. Moreover, fluctuations in equilibrium are entirely controlled by only two parameters: the temperature and the friction coefficient with the surrounding thermostat, which endow these fluctuations with a strong sense of universality. No further details from the thermostat are at play.

Waiving the constraints of equilibrium opens the door to a wide variety of nonequilibrium dynamics. The first nonequilibrium systems that come to mind are systems caught during their relaxation towards equilibrium. Others can be maintained out-of-equilibrium by applying an external field enforcing a steady flux, such as a particle or charge current, or an energy flux. Yet another class of nonequilibrium systems comprises systems in which energy is injected and dissipated at the microscopic level of their individual components [1]. These are called active systems, and they are the main focus of the present study. The energy stored in the environment, most often in a chemical form, is converted into mechanical work to produce directed forces and thus directed motion.

By contrast to equilibrium settings, the breakdown of equilibrium laws in active systems can be used to extract quantitative information about the microscopic active processes making up the energy reservoir. One can access the kinetic details of the fluctuations, to be characterized in terms of time, length and energy scales. In equilibrium, the reversibility of the dynamics is enforced by the detailed balance principle: the forward and reverse transitions between microstates are equally probable in a steady state. The existence of an arrow of time only emerges

at the macroscopic level as a result of a coarse graining of the dynamics [2]. By contrast, the arrow of time is already defined at the microscopic level in active systems because of the irreversibility of the dynamics. Recent methods of stochastic thermodynamics have been proposed to extend thermodynamic concepts when fluctuations are of paramount importance [3]. They provide a powerful framework to relate the breakdown of time reversal to the microscopic energy conversion at the basis of the nonequilibrium dynamics. We will discuss some of the most fruitful ideas of this developing field in Chapter 1.

From individual tracers in living systems ...

A paradigm of active systems are living systems. In living cells, it is the continuous injection of energy provided by adenosine triphosphate (ATP) which initially triggers the activity of intracellular nonequilibrium processes. For instance, the molecular motors can convert the chemical energy provided by ATP hydrolysis into a mechanical work to exert forces within the cell. The ensuing fluctuations are referred to as active fluctuations, distinct from the thermal fluctuations already present in the absence of nonequilibrium activity. The effect of these fluctuations is apparent in a large variety of living systems, from individual crawling cells to cell aggregates and epithelial tissues. They drive the dynamics of intracellular components, such as proteins, organelles and cytoskeletal filaments [4, 5]. Tracer particles are injected in living cells to probe these fluctuations. Alternatively, the intracellular environment is reconstituted *in vitro* as minimal model systems. Recent progress in tracking methods allow one to gather a large amount of statistics to analyze the tracer displacement. Moreover, the tracer can be manipulated to measure the response of the system: it reveals the viscoelastic properties of the intracellular medium [6–8]. These techniques, known as microrheology, are presented in our overview in Chapter 2. Combining measurements of the spontaneous fluctuations and of the response, the departure from equilibrium is generally quantified by a frequency dependent effective temperature [9]. Yet, its physical interpretation is at best limited. Not only does it lack any microscopic interpretation, unlike the kinetic energy of thermal agitation, but it also depends on the measured observables.

To go beyond this characterization of the intracellular nonequilibrium properties, one has to rely on a modeling of the tracer dynamics. Based on experimental observations, we propose a phenomenological picture for the constant remodeling of the intracellular environment in terms of an active cage subjected to random hops. Our minimal model, which we present in Chapter 3, reproduces qualitatively and quantitatively the fluctuations and the departure from equilibrium reported experimentally. It provides a useful framework to analyze fluctuations and response in actual living systems, allowing one to extract information about the

intracellular activity. These applied quantitative aspects come in the subsequent Chapters 4, 5 and 6.

To test our predictions with experimental data, we consider three different living systems. First, we treat the dynamics of tracers injected in living melanoma cells under three conditions: motor inhibited cells, ATP depleted cells, and untreated cells as a control. We demonstrate that our predictions are consistent with a series of measurements, supporting the validity of our phenomenological picture. We provide a quantitative characterization of active fluctuations in terms of time, length and energy scales (Chapter 4). Second, we propose a detailed analysis of fluctuations in living oocytes as probed by intracellular vesicles. We estimate the energy fluxes between the active processes, the tracer and the thermostat. In particular, we reveal that the efficiency of energy transduction from the cytoskeleton remodeling to the tracer motion is very low (Chapter 5). Eventually, we investigate the dynamics of epithelial tissues through the fluctuations of tricellular junctions, named as vertices. The analysis of vertex fluctuations provides a synthetic read-out of the effect of inhibitors acting on the molecular pathway regulating motor activity (Chapter 6).

... to interacting self-propelled particles

Another canonical example of active systems are the ones made of interacting self-propelled constituents. The first experimental studies of such systems were concerned with biological systems in which the emerging phenomenology results from various complex ingredients. As an example, the interplay of the self-propulsion, of the alignment interaction, and of the hydrodynamics interaction drive the dynamics in dense swarms of bacteria [10]. To create minimal biomimetic systems, motile colloids with well-controlled properties have been synthesized in the past decades. As an example, Janus particles have two different sides with distinct physical and/or chemical properties [11]. Such a symmetry breaking induces a local gradient in the surrounding environment, of either thermal, electric or chemical origin, which results in a self-propelled motion. Inspired by such experimental systems, recent theoretical works have focused on simple models of interacting active particles. These have shed light on the mechanism of the transition to collective motion in the presence of aligning interactions [12], and shown the possibility of a motility-induced phase separation (MIPS) even when the pair interaction between particles is purely repulsive [13, 14].

Despite the nonequilibrium nature of active particles, it is often difficult to precisely pinpoint the truly nonequilibrium signature in their emerging properties. For instance, MIPS is not associated with the emergence of steady-state mass currents. Even for systems with steady currents, the connection to equilibrium physics can sometime be maintained – the transition to collective motion amounts in some

cases to a liquid-gas phase transition [15, 16]. It is an open question whether, and to what extent, the concepts of equilibrium physics are useful to describe active matter. Building a thermodynamic approach for active matter first requires understanding how active systems depart from equilibrium. We investigate in Chapter 7 the nonequilibrium properties of a specific dynamics for which the self-propulsion is embodied by a persistent noise. We report on existing approximated treatments of such dynamics, and we determine the steady state distribution within a systematic approximation scheme. It allows us to quantify the time reversal breakdown of the dynamics and to delineate a bona fide effective equilibrium regime.

Outline

- Chapter 1 – Review of nonequilibrium statistical mechanics: Langevin equation, fluctuation-dissipation relation, entropy production, Harada-Sasa relation, stochastic thermodynamics.
- Chapter 2 – Review of the biological framework: mechanics and dynamics at the subcellular scale, microrheology techniques, previous modeling of the intracellular environment.
- Chapter 3 – Minimal model of tracer dynamics in living cells: phenomenological motivations, analytic and numerical predictions for the tracer statistics, departure from equilibrium, energetics of nonequilibrium fluctuations (paper A).
- Chapter 4 – Insight into the dynamics within living melanoma cells: analysis of tracer fluctuations, extracting an active temperature three orders of magnitude smaller than the bath temperature, quantifying the amplitude of active forces and their time scales (paper B).
- Chapter 5 – Analyzing fluctuations inside living mouse oocytes: including memory effects in the modeling, extracting force and time scales in line with estimations from single motor experiments, quantifying dissipation of energy, estimating the very low efficiency of power transmission from the intracellular network rearrangement to the tracer dynamics (papers C and D).
- Chapter 6 – Understanding the regulation of fluctuations in epithelial tissues by molecular motors: extracting active parameters from the statistics of vertex fluctuations (energy, time, and length scales), establishing a correlation between the hierarchy in the molecular pathway controlling motor activity and the mesoscopic fluctuations of the tissue (paper E).
- Chapter 7 – Collective dynamics of interacting self-propelled particles: review of the phenomenology and existing approximate treatments of the dynamics, derivation of the steady state based on a systematic perturbation scheme, existence of an effective equilibrium regime and the associated fluctuation-dissipation relation, hydrodynamic equations and collective modes (paper F).

Chapter 1

Modeling the fluctuations of passive tracers

In this introductory Chapter, we first present the modeling of the dynamics of a passive particle subjected to equilibrium fluctuations. We introduce the phenomenological description proposed by Paul Langevin after the seminal experiment by Jean Perrin. We highlight the importance of the fluctuation-dissipation theorem (FDT), as well as its practical consequences for the characterization of a thermal bath. Second, we discuss the case of a nonequilibrium dynamics driven by active fluctuations. We report on methods used to extract qualitative and quantitative information from the violation of the FDT, with a view to analyzing the nonequilibrium source of the dynamics.

1.1 Tracer in a thermal bath

The seminal experiment performed by the Jean Perrin in the early twentieth century was one of the first attempts to extract quantitative information from the dynamics of tracers immersed in a thermal bath [17]. Thanks to the development of optical tools, he could resolve the trajectories of colloidal grains suspended in water with unprecedented accuracy, yielding the picture reported in Fig. 1.1. In his observations, Perrin noticed that the trajectories were so erratic that one could not quantify properly the velocity of the grains. The discontinuity in the trajectory between two successive measurements led to wrong estimates. Both the direction and the norm of velocities did not converge to any limit as the accuracy of measurement was increased. Indeed, the individual collisions between the colloidal grains and the solvent molecules were by far beyond experimental resolution, so that the variations of velocity observed by Perrin already resulted from a large number of such collisions.

Langevin dynamics

These experiments motivated the theoretical description developed by Paul Langevin at the same period [18]. In his approach, Langevin deliberately avoids a kinetic description of the collisions between the tracer particle and the bath particles. He postulated that the effect of these collisions could be rationalized by two forces. A viscous friction force $-\gamma\mathbf{v}$ opposed to the displacement of the tracer, where \mathbf{v} and γ respectively denote the tracer velocity and the friction coefficient, and a stochastic force ξ . According to the second Newton law, the dynamics follows as

$$m\dot{\mathbf{v}} = -\nabla U - \gamma\mathbf{v} + \xi, \quad (1.1)$$

where m is the particle's mass, and $-\nabla U$ is the force deriving from an arbitrary potential U . When inertial effects can be neglected, the dynamics is simplified as

$$\gamma\dot{\mathbf{r}} = -\nabla U + \xi. \quad (1.2)$$

This is the Langevin dynamics in its overdamped formulation. Stokes law states that the friction coefficient reads $\gamma = 6\pi\eta a$ for spherical tracers of radius a , where η denotes the fluid's viscosity. The stochastic force ξ is a Gaussian white noise with correlations $\langle \xi_\alpha(t)\xi_\beta(0) \rangle = 2\gamma T\delta_{\alpha\beta}\delta(t)$, where T is the temperature of the surrounding bath, and the Greek indices refer to the spatial components.

Based on this phenomenological approach, one can predict the time evolution of a number of observables. Perhaps the most intuitive observable to consider is the mean-square displacement (MSD) defined as $\langle \Delta\mathbf{r}^2(t,s) \rangle = \langle [\mathbf{r}(t) - \mathbf{r}(s)]^2 \rangle$, which only depends on the time difference $t - s$ at large times. From the dynamics (1.1), one can deduce that, for a free particle, the MSD behaves at large times

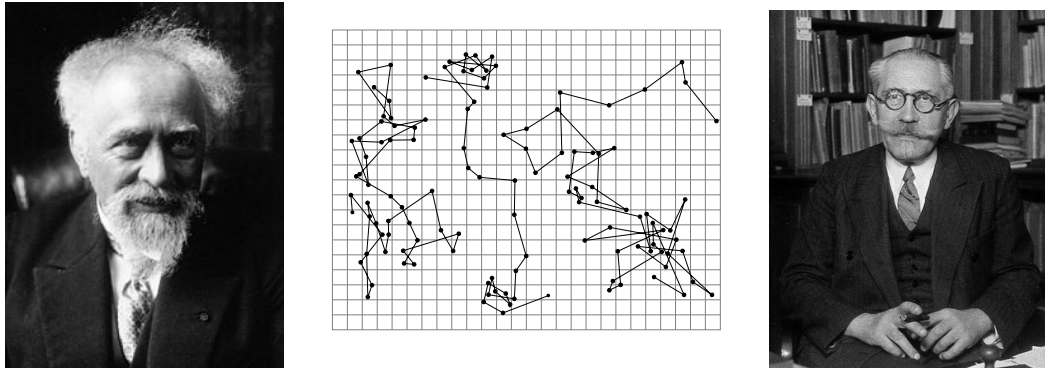


Figure 1.1 – Pictures of Jean Perrin (left), and Paul Langevin (right). Middle: Three trajectories of colloidal particles of radius $0.53 \mu\text{m}$ where measurements are taken every 30 s. Reproduced from the book *Les Atomes* of Jean Perrin. Mesh size $3.2 \mu\text{m}$.

as $\langle \Delta \mathbf{r}^2(t) \rangle \sim 2dDt$, where we have introduced the diffusion coefficient $D = T/\gamma$, and d refers to the space dimension. Another observable of interest is the autocorrelation function of velocity $\langle \mathbf{v}(t) \cdot \mathbf{v}(s) \rangle$. It only depends on the time difference $t - s$ at large times, and it is related to the diffusion coefficient as

$$D = \frac{1}{d} \int_0^\infty \langle \mathbf{v}(t) \cdot \mathbf{v}(0) \rangle dt. \quad (1.3)$$

This definition connects the amplitude of the thermal fluctuations to the relaxation of the velocity, which is driven by the dissipation of energy from the tracer to the thermostat.

Fokker-Planck equation

Beyond the relaxation of the dynamics, some specific features of equilibrium can also be found in the stationary properties of the tracer. These properties are encoded in the steady state distribution of velocity and position. To obtain such a distribution from the underdamped dynamics (1.1), we first express the time evolution for the probability $P(\mathbf{v}, \mathbf{r}, t)$ of finding the tracer at position \mathbf{r} with velocity \mathbf{v} at time t . It is given by the following Fokker-Planck equation [19]:

$$\frac{\partial P}{\partial t} = -v_\alpha \frac{\partial P}{\partial r_\alpha} + \frac{1}{m} \frac{\partial U}{\partial r_\alpha} \frac{\partial P}{\partial v_\alpha} + \frac{\gamma}{m} \frac{\partial}{\partial v_\alpha} \left[\left(v_\alpha + \frac{T}{m} \frac{\partial}{\partial v_\alpha} \right) P \right], \quad (1.4)$$

where we have used the convention of summation over repeated indices, as for the following Chapters. The stationary distribution, known as the Maxwell-Boltzmann

distribution, follows as

$$P_s(\mathbf{v}, \mathbf{r}) \sim \exp \left[-\frac{U(\mathbf{r})}{T} - \frac{m\mathbf{v}^2}{2T} \right]. \quad (1.5)$$

It can be split into a potential and a kinetic part as a property of equilibrium. In particular, we deduce that $\langle \mathbf{v}^2 \rangle = dT/m$, which is known as the equipartition theorem for the velocities. Integrating over the velocities yields the Boltzmann distribution $P_s(\mathbf{r}) \sim e^{-U(\mathbf{r})/T}$. Alternatively, the Fokker-Planck equation associated with the overdamped dynamics (1.2) reads

$$\frac{\partial P}{\partial t} = \frac{1}{\gamma} \frac{\partial}{\partial r_\alpha} \left[\left(\frac{\partial U}{\partial r_\alpha} + T \frac{\partial}{\partial r_\alpha} \right) P \right]. \quad (1.6)$$

The stationary distribution directly follows, and coincides with the Boltzmann distribution, as it should.

Fluctuation-dissipation theorem

To probe the equilibrium properties of the dynamics, an external operator can perturb the dynamics and measure the relaxation of the system. We consider that the underdamped dynamics (1.1) is perturbed by applying a force $\mathbf{f}(t)$ of small amplitude to the tracer:

$$m\dot{\mathbf{v}} = -\nabla U + \mathbf{f} - \gamma\mathbf{v} + \boldsymbol{\xi}. \quad (1.7)$$

The response function R quantifies how the average position is affected by the perturbation:

$$R_{\alpha\beta}(t, s) = \frac{\delta \langle r_\alpha(t) \rangle}{\delta f_\beta(s)} \Big|_{f=0}. \quad (1.8)$$

Causality enforces that it vanishes when $t \leq s$, and it only depends on the time difference $t - s$ provided that the dynamics has reached a steady state. For an equilibrium dynamics, the response function can be related to correlations in the absence of the perturbation $C_{\alpha\beta}(t) = \langle r_\alpha(t)r_\beta(0) \rangle$ as

$$R_{\alpha\beta}(t) = -\frac{1}{T} \frac{dC_{\alpha\beta}}{dt}. \quad (1.9)$$

This is the dynamic version of the FDT. It formally expresses the fact that the thermal fluctuations and the damping force originate from the same microscopic process, namely the collision between the tracer and the bath particles. Introducing the Fourier transform of an arbitrary function $\mathcal{F}(t)$ as $\mathcal{F}(\omega) = \int e^{i\omega t} \mathcal{F}(t) dt =$

$\mathcal{F}'(\omega) + i\mathcal{F}''(\omega)$, where $\mathcal{F}'(\omega)$ and $\mathcal{F}''(\omega)$ denote its real and imaginary parts, respectively, the FDT can be expressed in the Fourier domain as

$$T = \frac{\omega C_{\alpha\beta}(\omega)}{2R''_{\alpha\beta}(\omega)}. \quad (1.10)$$

A major consequence of the FDT is that one can independently measure the response function and the position autocorrelation, by perturbing the dynamics and tracking the spontaneous fluctuations of the tracer, respectively, to evaluate the temperature of an equilibrium bath. Such a method can be extended to an arbitrary perturbation defined by $U \rightarrow U - h(t)B(\mathbf{r}, \mathbf{v})$, where h is the strength of the perturbation. Introducing the generalized response for an arbitrary observable A as

$$R_G(t) = \left. \frac{\delta \langle A(t) \rangle}{\delta h(0)} \right|_{h=0}, \quad (1.11)$$

the FDT states that [20]

$$R_G(t) = -\frac{1}{T} \frac{d}{dt} \langle A(t)B(0) \rangle. \quad (1.12)$$

It is an important property of equilibrium that the only information that one can extract from the comparison between response and correlations is the bath temperature.

Generalized dynamics: memory effects

When considering short enough time scales to probe the collisions at the origin of the thermal forces [21], the details of the interactions between the tracer and the bath affect the Langevin dynamics. When integrating out these interactions, some memory effect appear in the dynamics [22]. Such effects are accounted for by including a memory kernel γ in the damping force:

$$m\dot{\mathbf{v}} = -\nabla U - \int_0^t \gamma(t-s)\mathbf{v}(s)ds + \boldsymbol{\xi}. \quad (1.13)$$

The correlations of the stochastic force are also modified as

$$\langle \xi_\alpha(t)\xi_\beta(0) \rangle = T\delta_{\alpha\beta}\gamma(|t|). \quad (1.14)$$

The FDT (1.12) is still valid, as a property of an equilibrium bath. The relation between the damping kernel and the noise correlations is a direct consequence of the FDT [23]. Some hydrodynamic effects may also yield a memory kernel [24]. Moreover, memory effect can arise when considering a complex bath beyond the simple case of water, such as a gel of polymers [25, 26]. As an example, power-law

kernels are reported in gels of cytoskeletal filaments, thus affecting the dynamics at every time scale [6]. In general, the memory effects lead to anomalous diffusion of the tracers, either superdiffusive or subdiffusive behavior depending on the properties of the kernel.

1.2 Nonequilibrium dynamics driven by active fluctuations

We now consider the dynamics of a tracer subjected to thermal and active fluctuations. We take the equilibrium Langevin dynamics in its overdamped formulation as a passive reference:

$$\gamma \dot{\mathbf{r}} = -\nabla U + \boldsymbol{\xi} + \mathbf{f}_A, \quad (1.15)$$

where we have introduced the active force \mathbf{f}_A . We want to investigate the effect of this force on the dynamics of the tracer. To this aim, we report on methods used to reveal the nonequilibrium properties of the dynamics from the violation of equilibrium laws, and to relate such violations to the microscopic features of the active force.

Effective temperature and extended fluctuation-dissipation relation

Though one can always define correlations and response in the presence of an active force, there is no reason for the specific relation given by the FDT to hold anymore. As a consequence, any method based on comparing response and correlations at every time scale to measure the bath temperature is no longer valid. Then, one can wonder if such a method can be extended far from equilibrium to assess asymptotic regimes where temperatures can be defined. These may a priori differ from the bath temperature, and are to be related to the energy scales involved in the active force. An early attempt to get an insight these issues has been to define a frequency-dependent effective temperature, by analogy with the FDT (1.10), as [9]

$$T_{\text{eff}}(\omega) = \frac{\omega C_{\alpha\beta}(\omega)}{2R''_{\alpha\beta}(\omega)}. \quad (1.16)$$

It reduces to the bath temperature at large frequencies provided that the collisions at the origin of thermal fluctuations occur on time scales shorter than any of the microscopic processes powering active fluctuations. In that respect, the typical frequency at which the effective temperature departs from the equilibrium prediction provides information about the shortest time scale involved in these fluctuations. Alternatively, the definition of a time-dependent effective temperature can also provide some insight into the nonequilibrium dynamics. It has been

used in sheared fluids to propose the existence of two distinct temperatures associated with different time scales [27, 28]. However, the physical interpretation of the effective temperature is at best limited. It does not contain the universal meaning of a temperature, since the violation of the FDT is different for each type of perturbation. Besides, there is no clear connection with any underlying microscopic processes driving the dynamics far from equilibrium.

Though the FDT is violated out-of-equilibrium, the response can still be related to additional correlations which involves the potential and the active force [29, 30]:

$$R_{\alpha\beta}(t) = -\frac{1}{2T} \frac{dC_{\alpha\beta}}{dt} + \frac{1}{2\gamma T} \langle r_\alpha(t) (\mathbf{f}_A - \nabla U)_\beta(0) \rangle, \quad (1.17)$$

Measuring the temperature from response and correlations now requires the knowledge of the potential and the active force by contrast to equilibrium. Moreover, the additional correlations of the extended fluctuation-dissipation relation (FDR) in Eq. (1.17) depend on the type of perturbation, thereby breaking the universal formulation of the FDT in Eq. (1.12). From a practical perspective, the FDR can be used to deduce the correlation between tracer position and non-thermal forces [31, 32]. The FDR can be cast in the following form:

$$R_{\alpha\beta}(t) = -\frac{1}{T} \frac{dC_{\alpha\beta}}{dt} + \frac{1}{2\gamma T} [\langle r_\alpha(t) (\mathbf{f}_A - \nabla U)_\beta(0) \rangle - \langle r_\alpha(0) (\mathbf{f}_A - \nabla U)_\beta(t) \rangle]. \quad (1.18)$$

In the equilibrium case for which the dynamics is invariant under a time reversal, the second term in Eq. (1.18) vanishes at all times, and the FDR reduces to the FDT as it should. This writing explicitly connects the violation of the FDT with the time reversal breakdown.

Entropy production

It has been shown in the last decades that the breakdown of time reversibility, as a hallmark of nonequilibrium, can be quantified by the rate of entropy production. It is defined in terms of the weights for a given time realization of the forward and backward processes, provided that the backward one exists, respectively denoted by \mathcal{P} and \mathcal{P}^R , as [33]

$$\sigma = \lim_{t \rightarrow \infty} \frac{1}{t} \ln \frac{\mathcal{P}}{\mathcal{P}^R}. \quad (1.19)$$

It characterizes the irreversible properties of the dynamics, and it satisfies a fluctuation theorem. Given that the thermal noise term in the dynamics (7.1) is Gaussian, the probability weight can be written as $\mathcal{P} \sim e^{-\mathcal{A}}$, where the dynamic action \mathcal{A} reads [34]

$$\mathcal{A} = \frac{1}{4\gamma T} \int_0^t (\gamma \dot{\mathbf{r}} + \nabla U - \mathbf{f}_A)^2 ds. \quad (1.20)$$

The reversed dynamics is defined in terms of the forward one as $\mathbf{r}^R(t) = \mathbf{r}(-t)$ and $\dot{\mathbf{r}}^R(t) = -\dot{\mathbf{r}}(-t)$, so that \mathcal{P}^R is simply obtained by substituting these expressions into Eq. (1.20). The entropy production rate follows as

$$\sigma = \frac{1}{T} \lim_{t \rightarrow \infty} \frac{1}{t} \int_0^t \dot{\mathbf{r}} \cdot (\mathbf{f}_A - \nabla U) ds. \quad (1.21)$$

We identify the time and ensemble averages under the ergodic assumption. The contribution from the potential $\langle \dot{\mathbf{r}} \cdot \nabla U \rangle = d \langle U \rangle / dt$ vanishes in the steady state, yielding

$$\sigma = \frac{1}{T} \langle \dot{\mathbf{r}} \cdot \mathbf{f}_A \rangle. \quad (1.22)$$

As a result, the entropy production rate coincides with the power of the active force divided by the bath temperature. One can use the violation of the FDT to evaluate the entropy production rate. An important result is that σ can explicitly be written in terms of such a violation as [35, 36]

$$\sigma = \frac{\gamma}{T} \lim_{t \rightarrow 0} \frac{d}{dt} \left[T R_{\alpha\alpha}(t) + \frac{d C_{\alpha\alpha}}{dt} \right]. \quad (1.23)$$

It is written in the Fourier domain as

$$\sigma = \frac{\gamma}{T} \int \frac{d\omega}{2\pi} \omega [\omega C_{\alpha\alpha}(\omega) - 2TR''_{\alpha\alpha}(\omega)]. \quad (1.24)$$

This is the Harada-Sasa relation. It provides a simple way to estimate the entropy production rate by independently measuring response and correlations. In that respect, it does not require any information about the details of the potential and the active force. Moreover, it shows that the violation of the FDT can be related to the microscopic active processes. Considering a generalized overdamped dynamics with memory effects as

$$\int_0^t \gamma(t-s) \dot{\mathbf{r}}(s) ds = -\nabla U + \boldsymbol{\xi} + \mathbf{f}_A, \quad (1.25)$$

where $\langle \xi_\alpha(t) \xi_\beta(0) \rangle = T \delta_{\alpha\beta} \gamma(|t|)$, the Harada-Sasa relation is extended as [37]

$$\sigma = \frac{1}{T} \int \frac{d\omega}{2\pi} \omega \gamma'(\omega) [\omega C_{\alpha\alpha}(\omega) - 2TR''_{\alpha\alpha}(\omega)], \quad (1.26)$$

where $\gamma'(\omega)$ denotes the real part of the damping kernel in the Fourier domain.

Energy exchanges with the thermostat

A more physical interpretation of the entropy production rate is based on energy exchanges between the tracer and the surrounding thermostat. According

to the action-reaction principle, the force exerted by the tracer on the heat bath is opposed to the thermal forces. As a result, the work done by the tracer on the heat bath per unit time is given by $\dot{\mathbf{r}} \cdot (\gamma\dot{\mathbf{r}} - \boldsymbol{\xi})$. This is also the power transferred from the tracer to the thermostat, as introduced by Sekimoto [38, 39]. These energetic observables are fluctuating quantities, by contrast to the ones defined in standard thermodynamics. They are at the basis of stochastic thermodynamics [3, 40], which aims at extending thermodynamic concepts to small systems, for which fluctuations are of paramount importance.

In equilibrium, the average power transferred to the thermostat is zero. This is because, on average, the power injected by the thermal fluctuations, which drives the tracer's motion, is balanced by the power dissipated through the drag force. For a nonequilibrium dynamics, there is an extra source of energy due to the active force. More energy is released into the bath through the drag force compared with the one injected by the thermal fluctuations only. As a result, the power transferred to the thermostat is positive. From the expression in Eq. (1.22), it follows that the entropy production rate is simply related to the average power as $\sigma = \langle \dot{\mathbf{r}} \cdot (\gamma\dot{\mathbf{r}} - \boldsymbol{\xi}) \rangle / T$. Hence, the entropy production rate is of direct physical relevance to quantify energy exchanges with the heat bath.

Chapter 2

Living matter: a paradigm of nonequilibrium systems

In this Chapter, we review the biological framework which controls the dynamics and mechanics in living systems. Then, we present the experimental techniques used to investigate the fluctuations of the intracellular components as well as the mechanical properties at the subcellular scale, known as microrheology methods. We present typical microrheology data, leading us to discuss the complex rheological properties of the intracellular environment, and to highlight the nonequilibrium features apparent in the tracer statistics. For completeness, we present previous models of the intracellular fluctuations and mechanics.

2.1 Structure and dynamics of the intracellular environment

Cytoskeleton: architecture of the cell

The structure of the cell is supported by a network of polymer filaments named the cytoskeleton [41]. This network is a dynamic entity in constant remodelling. There are three types of filaments: two of them are polar, namely the actin filaments and the microtubules, and the third ones, known as the intermediate filaments, are apolar. Each kind of filament has different mechanical properties and is made of different subunits. Thousands of these subunits agglomerate to form a strand of protein that can extend all along the cell. Intermediate filaments are fibers with a diameter of approximately 10 nm which are able to deform under a mechanical stress. The main function of intermediate filaments is to enable the cells to bear external stress. Microtubules are empty tubes with a diameter of about 25 nm. They are stiffer than both intermediate and actin filaments, and they can rupture when stretched. They are crucial in the regulation of the intracellular transport. Actin filaments are helical polymers with a diameter of about 7 nm which are more flexible than the microtubules. They are more abundant in the cell than both intermediate filaments and microtubules. They can be found generally in bundles or entangled networks, with connectivity controlled by binding proteins such as cross-linkers. The assembly and disassembly of actin filaments is controlled by the hydrolysis of ATP through treadmilling. The properties of actin networks have received a lot of attention, since they are believed to be the main filaments controlling the mechanical properties and the motility of the cell.

Molecular motors

Some proteins known as the molecular motors can exert forces on these filaments. These forces result from the conversion of the chemical energy provided by ATP hydrolysis, which provides around $50 k_B T/\text{mol}$ in normal physiologic conditions, into mechanical work. Each type of motors is associated with specific filaments. The intermediate filaments being apolar, there is no corresponding motor. The kinesin and dynein motors are moving along the microtubules in opposite directions. They carry organelles and vesicles throughout the cell, thereby regulating the intracellular transport at large scales. Similarly, the myosin-I motors can transport various kinds of cargos along the actin filaments. These motors can also bind separately to an actin filament and the cell membrane to pull the membrane into a new shape. Another important type of motors acting on actin filaments are the myosin-II motors, whose power stroke time is about 10 s. Many of these motors can bind together to form a myosin filament: a double-headed

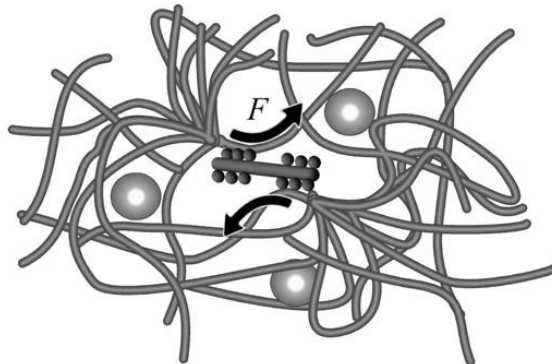


Figure 2.1 – Schematic picture of a myosin filament pulling two actin filament past each other. The resulting modification of the actin network affects the dynamics of intracellular components, represented in grey circles. Taken from [42].

strand with the two heads pointing in opposite directions. Such filaments can attach to different actin filaments to slide them past each other, as shown in Fig. 2.2. The forces produced by these filaments lead to constantly modify the structure of the actin network. Therefore, motor activity affects the dynamics of intracellular components not only through directed transport, but also via the remodeling of the surrounding cytoskeletal network.

Reconstituted in vitro systems

Understanding the mechanical properties of the complex intracellular structure and predicting the effect of active forces in the cell is largely a challenge to physical interpretation. As a result, the cytoskeleton is reconstituted *in vitro* to investigate its properties in simplified model systems. First experiments have been carried out in the absence of molecular motors, specifically to study actin filaments [43–45]: the corresponding network is referred to as a passive gel. These experiments aimed at characterizing the mechanics and the dynamics of passive gels under strictly thermal fluctuations. The effect of motor activity was then investigated by adding myosin filaments in the actin network. Recent studies have studied the coarsening of the network driven by the motors [46, 47]. In particular, they have shown that such a collapse into a reduced number of points in the gel can provide insight into the connectivity of the network, as controlled by cross-linkers [48, 49].

Control parameters

To investigate the role of the different intracellular components in the mechanics and dynamics within the cell, the system can be subjected to various treat-

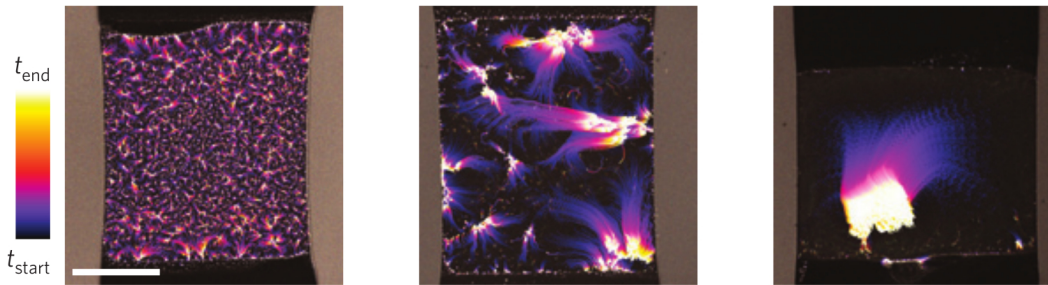


Figure 2.2 – Time evolution of acto-myosin networks with different concentration of cross-linkers. From left to right, the molar ratio of cross-linker over actin concentration varies as 0.01, 0.05, and 0.1. The system collapses into a reduced number of points as this ratio increases. Scalebar 1 mm. Taken from [48].

ments. For living cells, polyethylene glycol can be added to modify the mechanics by inducing an osmotic compression [50]. The addition of blebbistatin is largely used to inhibit the activity of myosin-II motors. Besides, the whole cell can also be depleted in ATP, thus providing an equilibrium-like reference [51]. The effects of the drugs depend on both the cell conditions and the concentration added to it, and it may affect different components of the cells beyond the targeted one. Alternatively, mutant cells provide efficient ways to act precisely on specific components. Yet, inhibiting one component, such as one type of molecular motors or cytoskeletal filaments, alters both the mechanics and the dynamics in general, as discussed below. In contrast, the properties of the reconstituted actin gels are better controlled, thus providing the opportunity to decipher the role of the different constituents of the gels. The concentration of motors, filaments, cross-linkers, and ATP can be varied independently to study the dynamical and mechanical properties of these model systems.

2.2 Measuring fluctuations and response

Fluctuations and mechanical properties of the intracellular environment are measured with microrheology techniques [7]. They rely on tracking and manipulating tracer particles, known respectively as passive and active microrheology methods. These tracers can be either injected in the system [42, 51], or attached to the cell cortex [31, 52–54]. Alternatively, components already present in the system, such as vesicles in living cells, can also serve as such probes [51]. Acto-myosin gels represent controlled systems for which the motor activity can be regulated externally through the concentration of ATP. It provides a useful tool to investi-

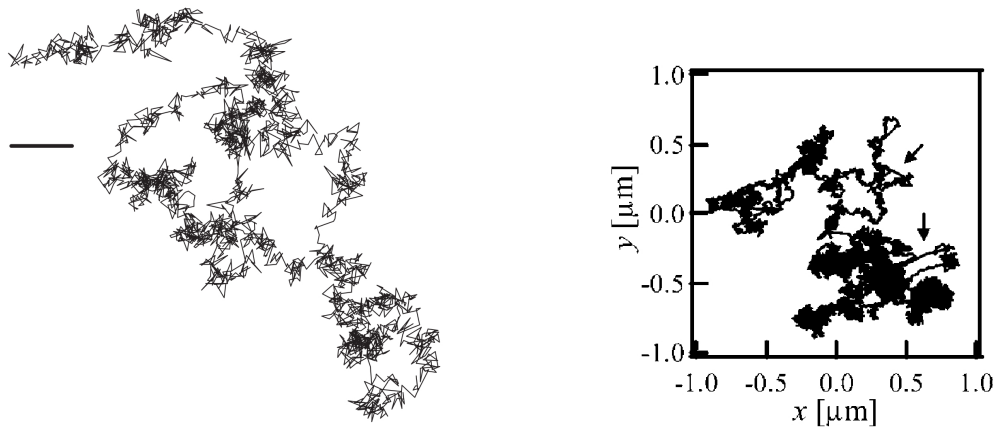


Figure 2.3 – Typical trajectories of micro-size tracers in living systems. Left: Beads attached to the cell cortex. Scalebar 10 nm. Taken from [53]. Right: Beads injected in an acto-myosin gel. Arrows indicate displacements of large amplitude. Taken from [42].

gate the effect of such an activity in both the fluctuations and the mechanics. In living cells, the system can also be depleted in ATP, though the properties of the whole cell get significantly altered by such a treatment. Alternatively, the activity of some motors can be inhibited via specific drugs, or by considering mutant cells. Finally, when considering tracers bound to the cell cortex, some tracers are generally glued to the cortex to provide an equilibrium-like reference sensitive to thermal fluctuations only.

2.2.1 Statistics of tracer displacement

The trajectories of the tracers probing the dynamics of either the intracellular environment or reconstituted acto-myosin gels show a similar behavior [42, 53]. Typically, one tracer exhibits locally confined fluctuations, and also experiences rapid directed motions until it reaches a new position around which it fluctuates again [Fig. 2.3]. This suggests that the dynamics are made of intermittent transitions between locally stable positions.

Mean-square displacement

The statistics of spontaneous displacement is extracted from the particle tracking. The time evolution of the MSD provides an intuitive characterization of the typical excursion of the tracer as a function of time [8]. The large time diffusion of the tracer is controlled by active fluctuations, since thermal diffusion alone is not efficient enough to regulate the large scale transport across the cell. By contrast

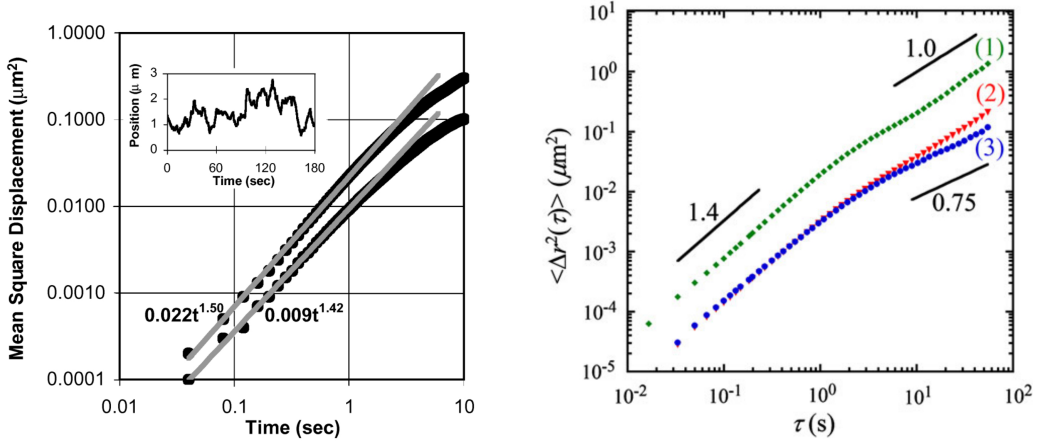


Figure 2.4 – Typical measurements of the mean-square displacement for tracers injected in living cells showing transient superdiffusive behavior. Taken from [55] and [57] in left and right, respectively.

with the dynamics of a tracer immersed in water, it can also exhibit subdiffusive behavior because of crowding effects in the intracellular environment and interactions with the surrounding cytoskeletal network. Moreover, transient superdiffusive behaviors are also assessed and associated with motor activity [55–57], as shown in Fig. 2.4. Overall, a large variety of exponents for the anomalous diffusion have been assessed. Such a variability has two main origins. First, the different types of tracers used as probes, either attached to the cortex or injected in the cell, without various protocols of injection, lead to different interactions with the intracellular environment. Second, the mechanical properties are modified across cell types, thus modifying the dynamics even in regimes where thermal fluctuations are predominant. In that respect, a crucial issue is to consider observables independent of the mechanical properties with a view to analyzing and comparing fluctuations in different living systems.

Distribution of displacement

Recent improvements in tracking methods also allow one to gather sufficient statistics to study the time evolution of the whole distribution of displacement. In a large variety of living systems, ranging from crawling cells to reconstituted acto-myosin gels [8, 42, 53, 58], it typically exhibits a central Gaussian part with exponential tails [Fig. 2.5]. As for the MSD, the variance of the central Gaussian and the extension of the tails are system dependent. In acto-myosin gels, the comparison between results of active and passive gels provides an insight into effects of the motors. The passive distribution is always Gaussian, as expected for an equi-

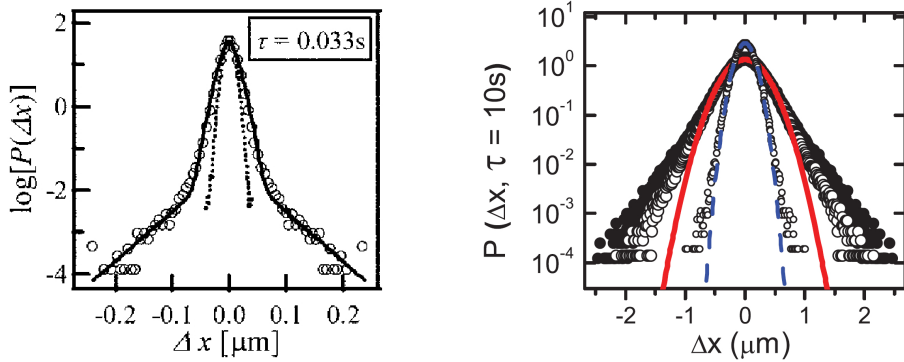


Figure 2.5 – Typical measurements of the displacement distribution for tracers injected in acto-myosin gels. It is Gaussian for passive gels, and exponential tails are present in active gels for which molecular motors are added. Left: Passive and active gels in dotted lines and open circles, respectively, at same lag time. Taken from [42]. Right: Passive and active gels in small and large symbols, respectively, at same lag time. Taken from [58].

librium system. It is reported that the variance of the central Gaussian is enhanced in the active case compared with its passive counterpart [58, 59]. Therefore, motor activity also affects the fluctuations of small amplitude. Besides, the mechanical properties of the surrounding environment controls these fluctuations: motor activity also modifies the mechanical properties, as discussed below. The tails get more pronounced as time increases. Note that the exponential tails are usually measured within a decade or less, thereby being indistinguishable from power-law tails. A striking feature of the distribution is the scale invariance reported in some systems. When scaling the displacement by the variance of either the central Gaussian part or the whole distribution, which are hardly different provided that the tails are not so pronounced, both the central part and the tails fall onto a master curve [8, 53]. Note that such a scale invariance is also reported in a different context of tracers immersed in bath made of bacteria [60]. This is of particular interest since it provides the opportunity to compare observables insensitive of the dynamics, independently of the exponents characterizing the time evolution of the MSD. In that respect, the deviation from the central scaled Gaussian is perhaps the simplest feature to be analyzed through different cell types.

Non-Gaussian parameter

To capture the non-Gaussian features with a single observable, the non-Gaussian parameter is commonly introduced as the scaled kurtosis of the distribution [61]:

$$\text{NGP} = \frac{\langle \Delta x^4 \rangle}{3 \langle \Delta x^2 \rangle^2} - 1, \quad (2.1)$$

where Δx is the one-dimensional projection of the displacement. The NGP vanishes when the distribution is Gaussian. It takes positive and negative values when the distribution is respectively smaller and broader than Gaussian. The main drawback of measuring the NGP experimentally is that the noise is enhanced with respect to measurements of the MSD. The NGP reported experimentally usually exhibits a transient regime of positive values [8, 42, 53], as shown in Fig. 2.6. It corresponds to the time scales at which exponential tails are reported aside the central Gaussian part of the displacement distribution. At short and large times, the NGP vanishes, showing that the tracer statistics is asymptotically Gaussian in these regimes. Note that the NGP shrinks towards negative values at very large times. This is not due to motor activity, since it is also observed in passive gels without motors.

2.2.2 Mechanical properties at the subcellular scale

Measurements in living cells

The mechanical properties of the intracellular environment are probed by measuring the response of the tracer to an external perturbation. By contrast to experiments which investigate the cellular rheology by applying a stress to the whole cell [62], the aim of active microrheology is to characterize the mechanics at the subcellular scale. Perhaps the main drawback of such methods is the high variability of the measurements. First, the intracellular environment is a non-homogeneous medium, so that tracers can experience very different interactions with the surrounding environment when evolving in various locations in the cell. Second, the cytoskeleton being a dynamic structure, the local mechanical properties also vary in time. When comparing response and fluctuations, it is then crucial to consider active and passive microrheology measurements performed on the same tracer and with a reduced delay between the two measurements.

The perturbation is commonly applied by means of either optical [63, 64] or magnetic tweezers [52, 65, 66]. A simple protocol consists in applying a step-like force, in which case the response is quantified by the relaxation of the tracer position. Another type of perturbation relies on applying a time-oscillating force. As a result, the tracer position oscillates with an amplitude and a phase delay with respect to the perturbation which are characteristic of the mechanics of the

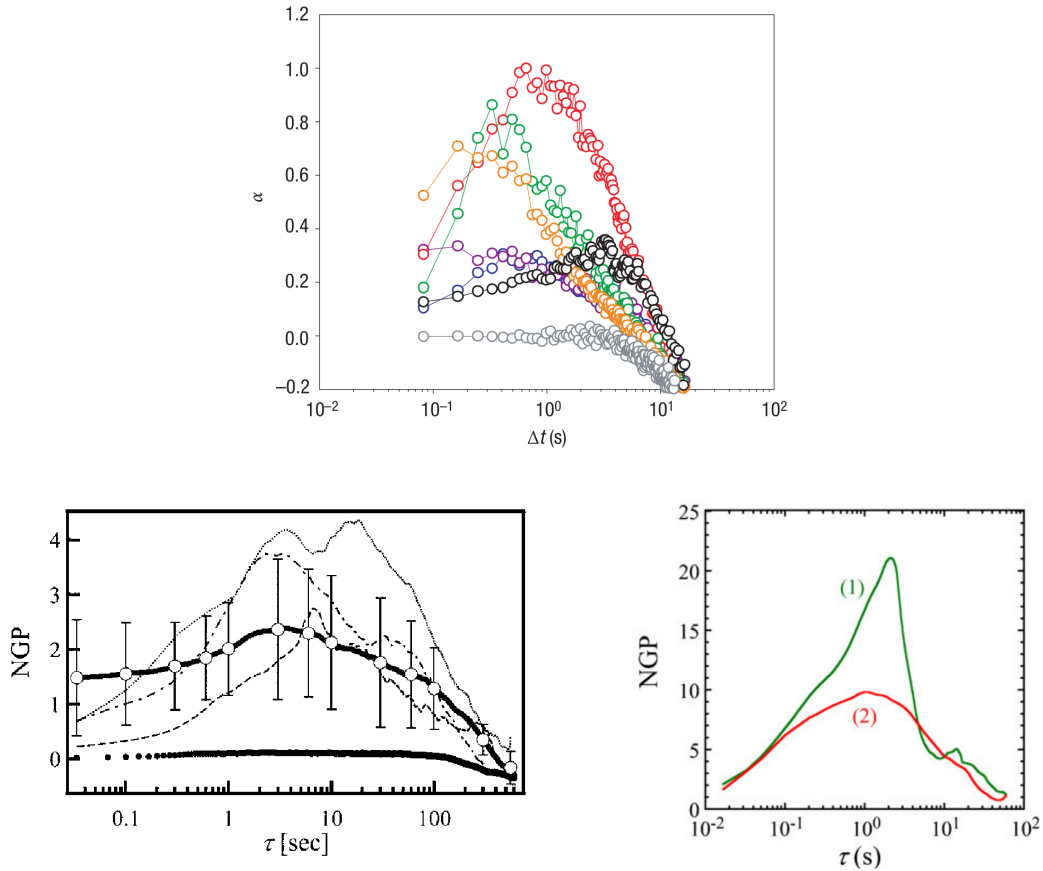


Figure 2.6 – Typical measurements of the non-Gaussian parameters defined in Eq. (2.1). Up: Beads attached to the cell cortex. Taken from [53]. Bottom left: Beads injected in an acto-myosin gel. Taken from [42]. Bottom right: Beads injected in living cells. Taken from [8].

surrounding medium. The corresponding average displacement of the tracer $\langle \delta x \rangle$ is related to the perturbation force f through the response R as

$$\langle \delta x(t) \rangle = \int_{-\infty}^t R(t-s) f(s) ds. \quad (2.2)$$

The average is taken over realizations of the perturbation, so that the intracellular fluctuations, both thermal and active, do not affect measurements of the response. It follows that the response can be extracted by comparing the time series of the tracer displacement and the perturbation for different frequencies of the perturbation oscillations.

Viscoelastic behavior

Measurements of the response are generally reported through the complex modulus G^* . Considering spherical particles of radius a , it is related to the Fourier response as $G^*(\omega) = [6\pi a R(\omega)]^{-1}$. Its real part G' is named the storage or elastic modulus, the imaginary part G'' is referred to as the loss or viscous modulus. The origin of this naming can be understood by considering two simple cases of rheology. For a purely elastic material associated with a Young modulus E , the complex modulus is real and equal to E . It follows that the tracer displacement is in phase with the perturbation when applying a oscillatory force. The Young modulus is deduced by comparing the amplitude of oscillations between displacement and forcing. For a purely viscous material with a viscosity η , the complex modulus has only a non-vanishing imaginary part equal to $i\omega\eta$. In such a case, there is a phase delay between displacement and forcing.

The intracellular environment is a viscoelastic material [65, 67, 68]. Its mechanical properties can not simply be described in terms of a purely elastic or viscous behavior, but rather as an interplay between these two. An important feature of such materials is that the response depends on the time scale of the applied force, namely on the frequency of oscillations for an oscillatory perturbation. As a result, one can distinguish several regimes in the frequency dependence of the complex modulus. In particular, some viscoelastic materials can be regarded as elastic or viscous asymptotically. In living cells, a large variety of power law behaviors for the complex modulus is reported depending both on the cell type and the probing methods [6, 69, 70]. By contrast, the measurements in reconstituted systems are more reproducible, since these synthetic systems are much more controlled than the *in vivo* cytoskeleton [44, 45, 71, 72]. In particular, recent studies have investigated the role of motor activity in the mechanics of reconstituted network [58]. They show that the motors not only add an extra source of the fluctuations in the system, they also change its rheological properties. As a result, motor activity affects the properties of thermal forces applied on the tracers, since these forces

depend on the details of the mechanics of the cytoskeletal network. For instance, some studies have shed light on the ability of myosin motors to “fluidize” the cytoskeletal network [73]. Others have shown that motor activity can also lead to a stiffening of the network [74, 75].

Departure from equilibrium

When motor activity modifies the structure of the cytoskeletal network, by adding an extra source of fluctuations and affecting the network mechanics, the FDT is no longer valid. To quantify the departure from equilibrium, the measurements from passive and active microrheology are gathered in a frequency dependent effective temperature, which has already been defined in Eq. (1.16) of Chapter 1. This observable is of particular interest since it provides the opportunity to compare a large variety of living systems with different rheological properties. At large frequencies, experiments in different cell types report that the effective temperature converges towards a constant value close to the bath temperature [54, 63, 64, 74, 76], expressing that the thermal fluctuations are predominant in this regime, as expected. Moreover, some works have brought forth a power-law behavior of the effective temperature [77]. The authors relate this power-law to the exponent characterizing the mechanics and to the one describing the anomalous diffusion of the tracers.

2.3 Models for the intracellular mechanics and dynamics

While the mechanisms of force generation are well understood at the level of individual motors, understanding the details of the ensuing fluctuations at the subcellular scale is still a challenge to physical interpretation. Therefore, studying the role of active fluctuations in the intracellular dynamics requires to develop specific models.

Modeling motor-induced deformations of the cytoskeleton

A first type of approach has consisted in investigating the effect of the motors on the mechanical properties and the fluctuations of the cytoskeletal network [78, 79]. The corresponding studies are based on regarding the myosin filaments as force dipoles able to generate contractile stresses. Through a continuum description of the network, it is possible to predict the mechanical deformation induced by the motors and its effect on both mechanics and fluctuations. A related set of works has described the active deformation of the cytoskeletal network via a random force [80–83]. They are based on taking the active force as a fluctuat-

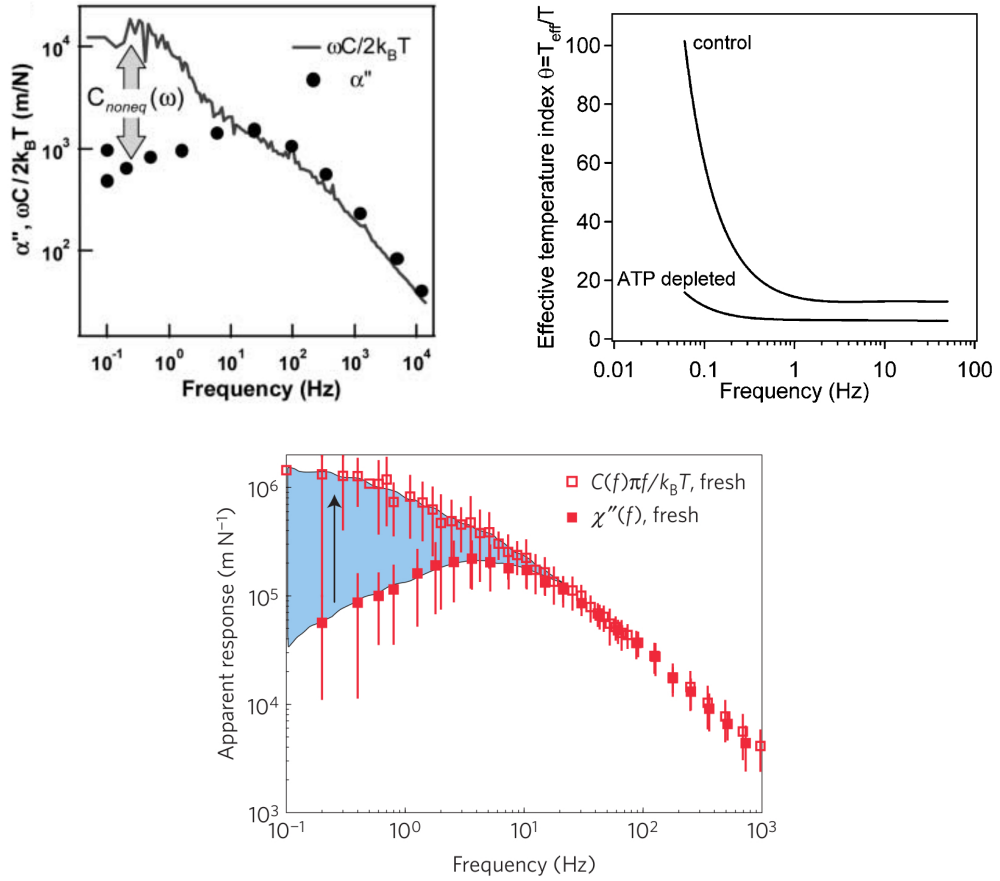


Figure 2.7 – Experimental measurements of the FDT violation. Upper left: Comparison between spontaneous fluctuations and response for beads injected in acto-myosin gel. Taken from [74]. Upper right: Effective temperature extracted from response and fluctuations of tracers attached to the membrane of living cells. Taken from [54]. Bottom: Comparison between spontaneous fluctuations and response for the membrane of red blood cells. Taken from [64].

ing term with exponentially decaying correlations. Such a specific form emerges when considering that the motors exert forces on the filaments over random times drawn from a Poisson process. In particular, these works provide predictions for the frequency behavior of the effective temperature in line with experimental measurements. Other studies have investigated the dependence of the mechanics on the structural organization of the cytoskeletal network, such as the concentration of filaments and cross-linkers. Using the tools of polymer physics, they aim at understanding the properties of entangled solutions and disordered networks starting from the mechanics of individual components [84]. Force propagation in these structures is a crucial issue to understand their stability when motors are added [85, 86].

A coarse-grained description of the intracellular environment

A second type of approach is based on a coarse-grained treatment of the continuous remodeling of the cytoskeleton induced by motor activity. They do not rely on the specific modes of deformation of the filaments. Following this approach, a set of works has described the active behavior of the cytoskeleton by considering gel-like constitutive relations [87–89]. They have led to predict instabilities and transitions in the spontaneous flow of actin [90, 91], and they have provided a new insight into the kinetics of cell division [92]. When considering the dynamics of a tracer, the validity of the continuum description is supported by a separation of scales between the network mesh size and the tracer radius, despite the heterogeneous nature of the intracellular environment. The effect of the network remodelling on the tracers is taken into account via a noise term. Therefore, a Langevin description is generally used, for which the details of the network structure and dynamics are gathered into thermal and active forces. As an example, such an approach has led to predict the power-law behavior of the fluctuating force spectrum, in agreement with measurements extracted from tracers attached to the cell cortex [93]. As another example, a minimal model has described the interactions between such tracers and the underlying cytoskeletal network [94–96]. The transmembrane interactions are regarded as an effective caging of the tracer. The location of the cage is fluctuating as a result of the network rearrangement. The transition from anti-persistent to persistent motion observed experimentally is captured by using a specific form of the forces driving the cage center. In the Langevin framework, the viscoelastic properties of the material are accounted for by including memory effects in the dynamics. The expression of the memory kernel is enforced by the generalized Stokes-Einstein relation: $\gamma(\omega) = 6\pi a G(\omega)/(i\omega)$ [97, 98]. The correlations of the thermal noise term are related to γ , as given by Eq. (1.14) in Chapter 1.

Chapter 3

Active cage model of fluctuations in living cells

In this Chapter, we propose a minimal model to describe the fluctuations of tracers in living cells. On the basis of experimental observations, we propose that such dynamics can be viewed as made of intermittent transitions between locally stable positions. After discussing the details of our modeling, we bring forth predictions for the tracer statistics and the departure from equilibrium dynamics to be tested against experimental results. Eventually, we offer specific protocols of ours, based on the external manipulation of the tracers, that aim at characterizing the intracellular activity.

3.1 Caging dynamics

Previous modeling has described the fluctuations of tracer in living cells in line with experimental observations. Yet, a unified picture able to capture the statistics of both the tracer displacement and the active force for a large variety of mechanics is still lacking. As discussed in Chapter 2, the fluctuations of the stochastic forces can be measured from a combination of response and fluctuations of the tracers. Extracting the active component of this spectrum requires to disentangle the equilibrium and nonequilibrium contributions of the stochastic forces acting on the tracer. In that respect, our model is built on a passive reference, corresponding to the dynamics in absence of active forces, on top which we add a specific source of nonequilibrium fluctuations: the thermal and active forces are clearly separated. This allows us to relate the departure from equilibrium to the features of the active forces. Overall, our aim is to provide a consistent framework able to reproduce existing experimental data, with a view to characterizing the active component of the fluctuations independently of their passive counterpart.

Tracer dynamics

We regard the dynamics of tracers in living systems, either living cells or reconstituted gels, as made of intermittent transitions between locally stable positions. Our phenomenological model is based on a common picture which has emerged to describe the tracer dynamics [99]. The tracers experience fluctuations of small amplitude in a cage formed by the cytoskeletal filaments. The effect of motor activity is to “open” the cage as a result of the remodeling of the surrounding cytoskeletal network. Based on this picture, we assume that each tracer is confined in a cage, taken as a harmonic potential in first approximation, corresponding to the local minimum of the complex energy landscape imposed by the network. As a result, a spring force drives the tracer position \mathbf{r} towards the center of the cage \mathbf{r}_0 . The fluctuations around the cage position \mathbf{r}_0 are powered by thermal noise. We first consider the case where memory effects are irrelevant in the dynamics. Given that inertial effects can be neglected, the dynamics is then simply given by a force balance:

$$\gamma \dot{\mathbf{r}} = -k(\mathbf{r} - \mathbf{r}_0) + \boldsymbol{\xi}. \quad (3.1)$$

The forces generated by the motors rearrange the network structure. Therefore, the form of the potential in which the tracer evolves gets modified, and the position of the resulting local minimum may be translated. It leads us to assume that the only effect of motor activity is to shift the cage center by a random amount. This is implemented by endowing the cage center with a dynamics of its own independent of the tracer position. We express it in terms of a stochastic process \mathbf{v}_A , referred

to as an active burst, as

$$\dot{\mathbf{r}}_0 = \mathbf{v}_A. \quad (3.2)$$

Since the thermal and active fluctuations originate from two separated sources, we assume that the thermal noise term and the active burst are uncorrelated processes. Comparing our phenomenological picture with the framework presented in Chapter 1, the active force $\mathbf{f}_A = k\mathbf{r}_0$ which is applied on the tracers results from the random hops of the cage. In that respect, we assume that the forces induced by the motors are not directly applied to the tracers, they are mediated by the network remodeling. In actual living systems, the tracer motion is driven by both direct interactions with neighbouring motors and indirect interactions which can propagate over large distances via the surrounding network.

Active burst statistics

To mimic the experimental trajectories, the dynamics of the cage center should be made of transitions between a quiescent state, during which the tracer fluctuates in a confined volume of the system, and an active state, when the cage gets translated. This is achieved by enforcing that \mathbf{v}_A alternates between a zero value during a random quiescence time, and a value $v\hat{\mathbf{n}}$ during a random persistence time, where $\hat{\mathbf{n}}$ is a random direction [Fig. 3.1]. We assume that both the persistence and waiting times are Poisson processes with mean values τ and τ_0 , respectively. We take the burst amplitude v as a constant value, and we consider that $\hat{\mathbf{n}}$ is uniformly distributed in space. To compute the correlations of the active burst one-dimensional projection v_A , we introduce P_{on} and P_{off} as the transition probabilities to the state where v_A is zero, and the one to the state where $v_A = pv$. We denote by p the projection of $\hat{\mathbf{n}}$, defined in $[-1, 1]^d$, whose distribution P_d depends on the spatial dimension d :

$$P_d(p) = \begin{cases} \frac{\delta(p-1) + \delta(p+1)}{2} & \text{for } d = 1, \\ \frac{1}{\pi\sqrt{1-p^2}} & \text{for } d = 2, \\ \frac{1}{2} & \text{for } d = 3. \end{cases} \quad (3.3)$$

The equations ruling the time evolution of the transition probabilities read

$$\begin{aligned} \dot{P}_{\text{off}} &= \frac{1}{\tau} - P_{\text{off}} \left(\frac{1}{\tau} + \frac{1}{\tau_0} \right), \\ \dot{P}_{\text{on}} &= \frac{P_d P_{\text{off}}}{\tau_0} - \frac{P_{\text{on}}}{\tau}. \end{aligned} \quad (3.4)$$

We derive the explicit form of P_{on} and P_{off} from these equations. For symmetry reasons, only the even-time correlation functions of v_A are non-zero. They can be

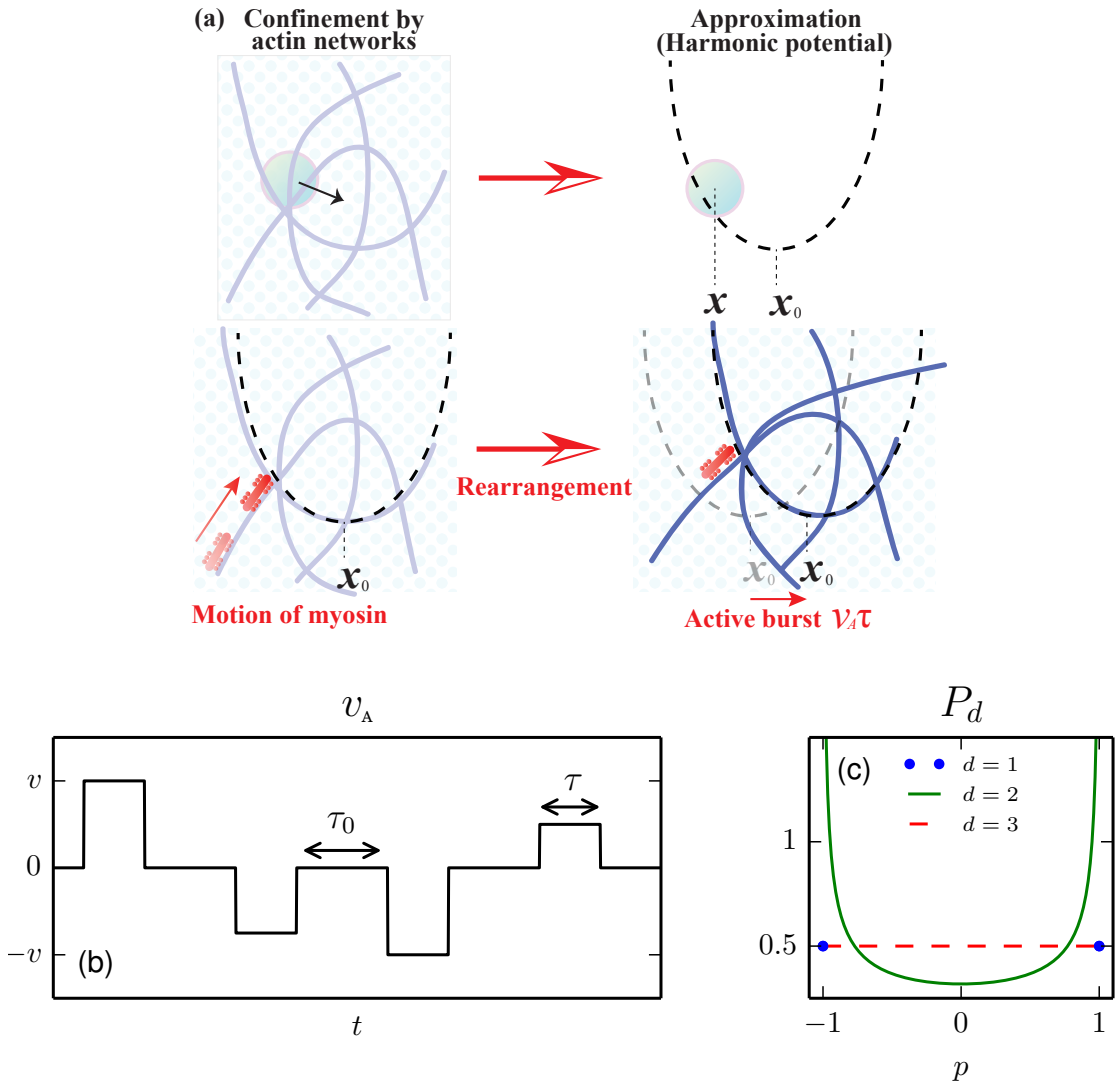


Figure 3.1 – (a) Schematic representation of the network remodelling induced by motor activity. (b) Typical realization of the active burst. (c) Distribution P_d of the one-dimensional projection p of a random direction in d dimensions for $d = \{1, 2, 3\}$ in dot blue, green solid, and red dashed line, respectively. Taken from paper A.

expressed in terms of the transition probabilities in the steady state as

$$\langle v_A(t_1) \cdots v_A(t_{2n}) \rangle = \int p_1 P_{\text{on},S}(p_1) \prod_{i=2}^{2n} p_i P_{\text{on}}(t_i - t_{i-1}, p_i | p_{i-1}) dp_1 \cdots dp_{2n}, \quad (3.5)$$

where $P_{\text{on}}(t, p_1 | p_0)$ denotes the transition probability from p_0 to p_1 within a time t , and $P_{\text{on},S}$ is the stationary probability. It can be written explicitly as

$$\langle v_A(t_1) \cdots v_A(t_{2n}) \rangle = \phi(t_1 - t_2) \prod_{i=1}^{n-2} \psi(t_{2i} - t_{2i+1}) \phi(t_{2i+1} - t_{2i+2}). \quad (3.6)$$

The functions ϕ and ψ are defined in terms of the active diffusion coefficient $D_A = (v\tau)^2/d/(\tau + \tau_0)$ and the time scales $\{\tau, \tau_0\}$ as

$$\begin{aligned} \phi(t) &= D_A e^{-|t|/\tau}/\tau, \\ \psi(t) &= 1 + e^{-|t|/\tau} \left[c_d \left(1 + \frac{\tau_0}{\tau} \right) + \frac{\tau_0}{\tau} e^{-|t|/\tau_0} \right]. \end{aligned} \quad (3.7)$$

The two-time correlation function is given by ϕ . The active burst is both a colored and non-Gaussian noise. In the limit of vanishing τ , it reduces to a white noise, yet it remains non-Gaussian. The coefficient c_d depends on spatial dimension d : it equals $\{0, 1/2, 4/5\}$ for $d = \{1, 2, 3\}$, respectively.

This specific form of the active burst statistics may appear artificial as it relies on the phenomenological picture that we use to describe the cage dynamics. The detachment of the myosin heads from the actin filaments, which controls the network remodelling, is often modelled as a Poisson process [42]. In that respect, assuming that the persistence and waiting times are Poisson distributed amounts to considering that only a few nearby motors control the local rearrangement of the network surrounding the tracer. To support the validity of our approach, we will show in what follows that our picture is sufficient to quantitatively capture the observed tracer statistics in living systems. One can consider extended forms of the active burst process. For instance, considering that the active bursts result from the cooperative action of several motors, the active times scales could be taken as the sum of Poisson variables to model the net effect of a few myosin detachment and attachment on the network. As a result, the distribution of these time scales would be given by a Gamma law with power-law tails. Another possible extension would rely on considering a distributed burst amplitude. Such extensions would lead to introducing additional parameters as a more complex description of the underlying processes. Our aim is to propose a minimal model for the dynamics with a reduced number of parameters. In that respect, the active burst statistics only depend on three independent parameters: the active burst amplitude, the mean persistence time, and the mean waiting time. Note that the second moment of

the statistics is controlled by only two parameters: the active diffusion coefficient and the persistence time. Considering the three additional passive parameters, the spring constant, the friction coefficient, and the bath temperature, our modeling is finally made of five independent parameters in total. In what follows, we will show that the two passive parameters γ and k can be independently characterized, through measurements of the mechanics for instance, so that the analysis of the tracer fluctuations is used to extract only the active burst features.

3.2 Model predictions

3.2.1 Statistics of tracer displacement

We compute the statistics of the tracer displacement projected onto one spatial direction. Given that the dynamics is linear, we can express the projected tracer position at a time t as

$$x(t) = \int_0^\infty R(t-s) (\xi + f_A)(s) ds. \quad (3.8)$$

where the active force is given by $f_A = kx_0$. The contribution from the initial position is irrelevant at large times, so that we take $x(0) = 0$ to facilitate the analytic derivations. The response reads $R(t) = \gamma^{-1} e^{-t/\tau_R} \Theta(t)$, where Θ denotes the Heaviside step function, and we have introduced a relaxation time τ_R associated with the caging harmonic potential.

Mean square displacement

The first observable that we consider is the one-dimensional MSD. The thermal noise term and the active burst are uncorrelated, so that we can separate the MSD into two terms: $\langle \Delta x^2 \rangle = \langle \Delta x^2 \rangle_T + \langle \Delta x^2 \rangle_A$, where the subscripts T and A respectively refer to the thermal and active contributions. From the dynamics (3.1) and the specific form of the active burst, we obtain

$$\begin{aligned} \langle \Delta x^2(t) \rangle_T &= 2D\tau_R \left(1 - e^{-t/\tau_R} \right), \\ \langle \Delta x^2(t) \rangle_A &= \frac{2D_A\tau_R}{1 - (\tau/\tau_R)^2} \left[\left(\frac{\tau}{\tau_R} \right)^2 \left(1 - e^{-t/\tau} - \frac{t}{\tau} \right) + e^{-t/\tau_R} + \frac{t}{\tau_R} - 1 \right]. \end{aligned} \quad (3.9)$$

In the absence of active forces, the MSD saturates to the equilibrium value $2T/k$ within a time τ_R , showing that the tracer is confined in a volume of the system. In the presence of active forces, the tracers can escape from the local confinement to visit a larger volume in the system, as a result of the cage activity. The large time behavior is diffusive with diffusion coefficient D_A . It reflects the free diffusion

of the cage with the same coefficient. At short times, the dynamics is similar to the one in the passive case: the tracer diffuses with diffusion coefficient D . In the intermediate regime, there are different types of behavior depending on the ratios of diffusion coefficients D_A/D and of time scales τ/τ_R . When $\tau \gg \tau_R$ and $D_A \ll D$, the MSD exhibits a transient plateau regime to the equilibrium value, and it departs from the plateau at a time τ . When D_A/D increases, a superdiffusive regime with exponent between one and two sets in between the two diffusions, as a signature of the ballistic motion of the cage, as shown in Fig. 3.2.

Non-Gaussian parameter

As a first insight into the non-Gaussian properties of the tracer statistics, we compute analytically the time evolution of the non-Gaussian parameter. To this aim, we derive the one-dimensional mean-quartic displacement (MQD) defined as $\langle \Delta x^4(t, s) \rangle = \langle [x(t) - x(s)]^4 \rangle$, which only depends on the time difference $t - s$ at large times. It can be separated into three contributions:

$$\langle \Delta x^4 \rangle = \langle \Delta x^4 \rangle_T + \langle \Delta x^4 \rangle_A + 6\langle \Delta x^2 \rangle_T \langle \Delta x^2 \rangle_A. \quad (3.10)$$

The thermal MQD is related to the thermal MSD as $\langle \Delta x^4 \rangle_T = 3 \langle \Delta x^2 \rangle_T^2$, since the statistics is Gaussian in the absence of active force. To obtain the active MQD, we express the displacement in the absence of thermal noise as $\Delta x = \Delta x_a + \Delta x_b$, where

$$\begin{aligned} \Delta x_a(t, s) &= \left[e^{-(t-s)/\tau_R} - 1 \right] \int_0^\infty e^{-(s-u)/\tau_R} v_A(u) du, \\ \Delta x_b(t, s) &= \int_s^\infty \left[1 - e^{-(t-u)/\tau_R} \right] v_A(u) du, \end{aligned} \quad (3.11)$$

so that

$$\langle \Delta x^4 \rangle_A = \langle \Delta x_a^4 \rangle + 3\langle \Delta x_a^3 \Delta x_b \rangle + 6\langle \Delta x_a^2 \Delta x_b^2 \rangle + 3\langle \Delta x_a \Delta x_b^3 \rangle + \langle \Delta x_b^4 \rangle. \quad (3.12)$$

We explicitly compute each term of the active MQD, and we take the limit of large s at fixed $t - s$, corresponding to the regime invariant under a time translation. The advantage of the separation into the two terms (3.11) is that every contribution to $\langle \Delta x^4 \rangle_A$ converges in this limit. Eventually, substituting this result in Eq. (3.10), and by using the expression of the MSD, we deduce the time evolution of the MQD. The NGP directly follows.

The NGP vanishes at short and large times, and it takes positive values in the intermediate regime, as shown in Fig. 3.2. This is in qualitative agreement with the experiments. As a result, the short and large time diffusions are Gaussian regimes. Besides, the intermediate regime, be it either superdiffusive or subdiffusive, contains all the interesting physics: the tails of the distribution should be

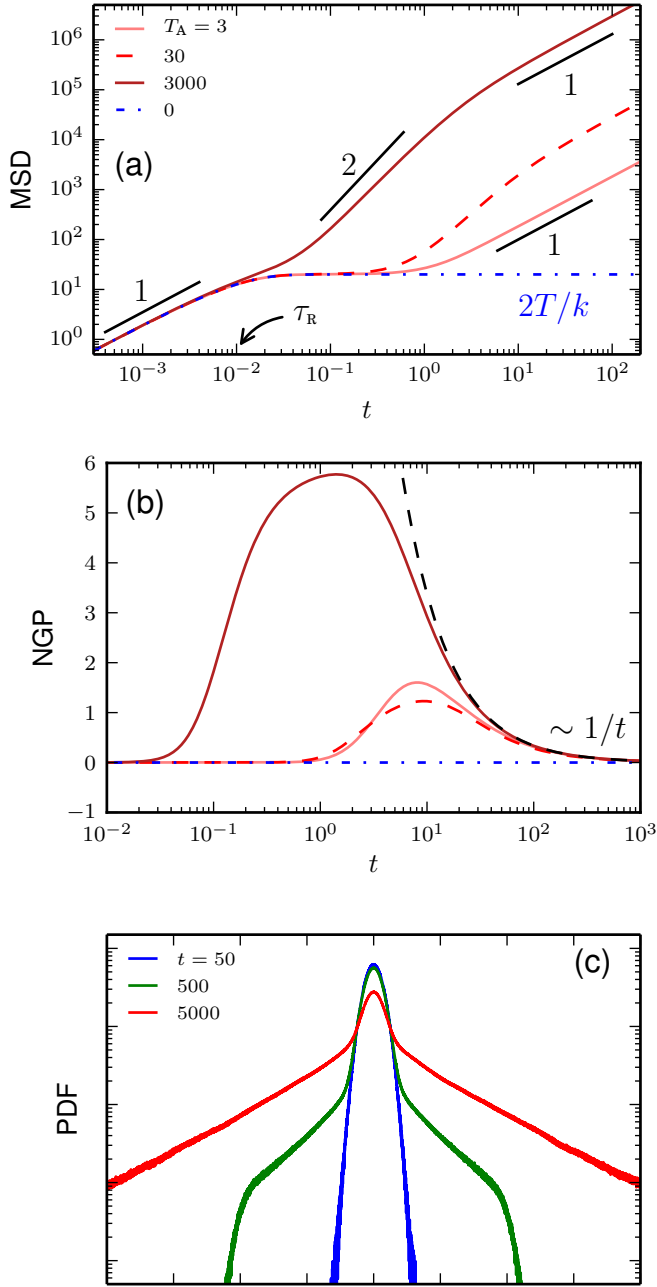


Figure 3.2 – Statistics of tracer displacement in the active cage model. Time evolution of the mean-square displacement (a) and the non-Gaussian parameter (b). Parameters $\{\tau_0, k, \gamma, T\} = \{10, 100, 1, 1000\}$. (c) Distribution of displacement for at three different times. Same parameter values as for the brown curves in (a-b).

mostly apparent in this regime. The large time NGP is entirely under the control of the active burst parameters:

$$\text{NGP}(t) \underset{t \rightarrow \infty}{\sim} \frac{2}{t} \left[(1 + c_d)(\tau + \tau_0) + \tau \left(\frac{\tau}{\tau + \tau_0} - 3 \right) \right]. \quad (3.13)$$

Given that the full expression of the NGP is rather complicated, this asymptotic regime provides a simplified form to fit experimental data. In that respect, measurements of the large time behavior of the NGP can be combined with measurements of the MSD to fully characterize the active burst statistics, namely to quantify τ , τ_0 and v .

Distribution of displacement

To provide a complete characterization of the tracer statistics, we investigate the time evolution of the whole distribution of displacement via numerical simulations. The central part is Gaussian, and some tails develop in the intermediate regime as reported experimentally. When the MSD exhibits a transient plateau regime, the distribution evolves in time as follows. The short time distribution is Gaussian with variance given by the thermal MSD, which saturates to the equilibrium value. After the saturation, the tails start to develop next to the central Gaussian, and another Gaussian distribution sets in at large displacement. The variance of the large scale Gaussian increases with time, and is given by the MSD at long times, while the relative proportion of the central Gaussian shrinks, as shown in Fig. 3.2. In experiments, the presence of active fluctuations is assessed by exponential tails, yet the large scale Gaussian is generally not reported. One may suggest that the experimental window of measured displacement is not extended enough to observe the large Gaussian. We will show in what follows that our model is able to capture the existence of transient exponential tails as a cross over between the central and large Gaussian parts, provided that they are well separated. Within our model, the central part accounts for fluctuations of small amplitude, whereas the exponential tails are a signature of directed motion events in the trajectories, namely excursions of the tracer with a larger amplitude.

3.2.2 Energetics of active fluctuations

Departure from equilibrium

To provide a further insight into the departure from equilibrium induced by the active fluctuations, we compute the effective temperature as

$$T_{\text{eff}}(\omega) = T + \frac{1}{(\omega\tau_R)^2} \frac{T_A}{1 + (\omega\tau)^2}, \quad (3.14)$$

where we have introduced the active temperature $T_A = \gamma D_A$. The effective temperature converges towards the bath temperature at large frequency, in agreement with experiments. The divergence at small frequency can be understood as follows. The behavior of the thermal MSD is encoded in the response function. Therefore, the effective temperature can be regarded as a comparison between the thermal and the actual MSDs in the Fourier domain. In that respect, the divergence of T_{eff} stems from the thermal MSD saturating at large times whereas the actual MSD diffuses.

The additional correlation function appearing in the extended fluctuation-dissipation relation (1.17) involves the spring force $-k(x - x_0) = -kx + f_A$, and the tracer position:

$$R(t) = -\frac{1}{2T} \frac{dC}{dt} - \frac{k}{2\gamma T} \langle x(t)k(x - x_0)(0) \rangle. \quad (3.15)$$

We compute it explicitly as

$$-\langle x(t)k(x - x_0)(0) \rangle = -Te^{-t/\tau_R} + \frac{T_A}{1 - (\tau/\tau_R)^2} \left[1 - e^{-t/\tau_R} - \left(\frac{\tau}{\tau_R} \right)^2 (1 - e^{-t/\tau}) \right]. \quad (3.16)$$

It is negative at short times and saturates at large times towards T_A . The short time regime corresponds to anticorrelation between the spring force and the tracer position, as an evidence of the tracer transient confinement. The transition to positive values is a signature of the tracer escaping from the local confinement. It agrees with experimental evidence [31], yet the large time saturation has not been observed yet. Observing this saturation experimentally would provide an interesting test for our minimal model, since the extracted value for T_A could be compared to the one deduced from the large time diffusion.

Using the Harada-Sasa relation recalled in Chapter 1, the average power transferred from the tracer to the thermostat, defined as $\langle \dot{x}(\gamma \dot{x} - \xi) \rangle$, can be computed from the violation of the FDT. We determine the explicit expression of its spectral density $I(\omega)$ as

$$I(\omega) = \frac{1}{1 + (\omega\tau_R)^2} \frac{2T_A}{1 + (\omega\tau)^2}. \quad (3.17)$$

Integrating over all frequencies, we deduce

$$\langle \dot{x}(\gamma \dot{x} - \xi) \rangle = \int I(\omega) \frac{d\omega}{2\pi} = \frac{T_A}{\tau + \tau_R}. \quad (3.18)$$

The overall power transmitted to the thermostat depends on both active and passive parameters. In our phenomenological picture, the energy injected by motor activity into the tracer is mediated by the network remodeling. The forces generated by the motors do not act directly on the tracers, they serve to randomly shift

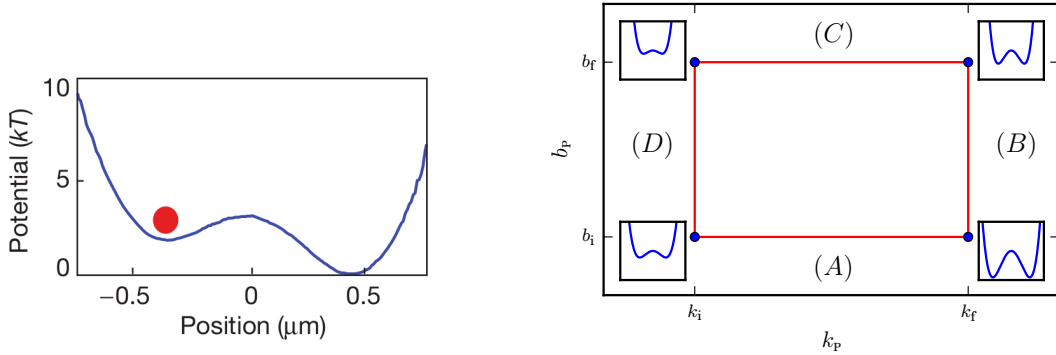


Figure 3.3 – Experimental realization of a quartic potential with two optical tweezers. Taken from [100]. Right: Schematic representation of a circular protocol in parameter space for an external potential of the form $U = k_p x^2/2 + b_p x^4/4$. Taken from paper A.

the cage in which each tracer is confined. As a result, the power of the active force $f_A = kx_0$, which coincides with the power transferred to the thermostat, depends on parameters of the thermostat, namely the relaxation time τ_R in the present case.

Alternative protocols: extracting work from an external potential

We want to propose alternative protocols based on extracting work from an external potential with a view to characterizing the active fluctuations. The use of optical and magnetic tweezers has become increasingly standard with the development of microrheology methods. They enable one to confine and manipulate the tracers. The effect of an optical tweezer is well approximated by a harmonic potential. Combining two of them can lead to design a more complex energetic landscape such as double-well potentials [100], as shown in Fig. 3.3. The parameters of the potential can be varied in time. We first consider the case of a harmonic potential whose spring constant is changed in a quasistatic way, and derive the corresponding extracted work. In particular, we show that no work can be extracted from a cyclic protocol in such a case, in line with previous studies [101]. Second, we build a cyclic protocol with a double-well potential for which a non-vanishing work can be extracted. Since work can not be extracted from such a cyclic protocol in equilibrium, the extracted work only characterizes the active component of the fluctuations independently of its thermal counterpart.

In the present formulation of the model, the active force always leads to overcome the transient confinement, no matter if it stems from the cage potential or from an external potential. This is because we have not taken into account the effect of the tracer in the cage dynamics, resulting from the action-reaction principle.

To reproduce the confinement by an external potential, we propose an extended version of the active cage model which accounts for the force exerted by the tracer on the cage, referred to as the back action force. Given that the length scale of the cage and the tracers are well separated, the effect of the back action force in absence of external potential is of second order. Yet, an important consequence of this new ingredient is that the tracer eventually escapes the confinement at large time even in the absence of active force: this can be related to the spontaneous flow of reconstituted actin gels in the absence of motors, as a result of the slow structural relaxation of the network. Finally, we demonstrate that this additional coupling between cage and tracer is sufficient to result in an effective tracer confinement in the presence of an external potential. The cage can no longer freely diffuse in the medium since it is now bound to the tracer.

The results presented in this section are derived and discussed in details in paper [A](#) reproduced below.

Energetics of active fluctuations in living cells

É. Fodor,^{1,*} K. Kanazawa,² H. Hayakawa,² P. Visco,¹ and F. van Wijland¹

¹Laboratoire Matière et Systèmes Complexes, UMR 7057 CNRS/P7, Université Paris Diderot,

10 rue Alice Domon et Léonie Duquet, 75205 Paris cedex 13, France

²Yukawa Institute for Theoretical Physics, Kyoto University, Kitashirakawa-oiwake cho, Sakyo-ku, Kyoto 606-8502, Japan

(Received 10 June 2014; published 29 October 2014)

The nonequilibrium activity taking place in a living cell can be monitored with a tracer embedded in the medium. While microrheology experiments based on optical manipulation of such probes have become increasingly standard, we put forward a number of experiments with alternative protocols that, we claim, will provide insight into the energetics of active fluctuations. These are based on either performing thermodynamiclike cycles in control-parameter space or determining response to external perturbations of the confining trap beyond simple translation. We illustrate our proposals on an active itinerant Brownian oscillator modeling the dynamics of a probe embedded in a living medium.

DOI: 10.1103/PhysRevE.90.042724

PACS number(s): 87.10.Mn, 87.15.A-, 05.40.-a

I. INTRODUCTION

A living cell is a nonequilibrium system which needs to constantly maintain its activity to preserve an organized structure. Major contributors to this activity are the molecular motors which generate forces of the order of a piconewton within the cell. This force generation is an essential process for life as it is the basis of cell motility, wound healing, and cell division. It is fueled by adenosine triphosphate hydrolysis, thus being a nonequilibrium process commonly named an *active* process. The force is applied by the motors on some polar self-assembled filaments, such as the actin filaments for myosin motors. The polarity of these filaments added to the force generation enable the motors to perform a stochastic directed motion. These phenomena have been experimentally explored *in vivo* with living cells [1,2] and *in vitro*, with reconstituted actin gels in which molecular motors density can be externally controlled [3,4].

One of the major experimental techniques which has uncovered the nonequilibrium behavior of living cells and active gels is microrheology [2–6]. Thanks to the progress of high resolution microscopy, it is now possible to track micron sized probes injected into complex fluids, including living organisms. In addition, by means of optical or magnetic tweezers, one can apply a controlled force on these probes and measure rheological properties such as complex shear modulus [7–9] or creep function [10]. By combining these two measurements, it has been possible to quantify the extent to which the fluctuation-dissipation theorem (FDT) is violated these systems [5,11]. So far, the central quantity that has been investigated is a frequency-dependent effective temperature [12–16], which serves as an all-purpose measurement of the distance from thermal equilibrium.

Our aim in this paper is to put forward other quantities that can reveal interesting properties of nonequilibrium activity and that can be measured with the same experimental toolbox of microrheology. In order to render the presentation of these methods more concrete, their predictions are illustrated on a

recent theoretical model [1] describing the dynamics of a probe in an active medium.

We begin with giving the basic physical ingredients of our model in Sec. II. We then discuss the simplest protocols in which the spring constant of a harmonic external potential is changed with time in Sec. III. In Sec. IV, we use a quartic potential for which two parameters are changed in time to mimic a thermodynamic cycle [17]. In Sec. V, we review an already proposed method of extracting correlations between active force and position [18] by exploiting the extended fluctuation-dissipation relations [19]. In Sec. VI, we apply the Harada-Sasa relation to quantify the dissipation rate arising from the nonequilibrium behavior of the probe [20].

II. MODEL

We model the dynamics of the tracer's position \mathbf{r} by means of an overdamped Langevin equation as described in [1]. From a physical viewpoint, the active medium has a complex polymer cross-linked reticulated structure, surrounded by a viscous Newtonian fluid. The complex structure of the network confines the particle, and we model this as a harmonic potential acting on the probe, centered at position \mathbf{r}_0 . Active forces which originate from surrounding molecular motors continuously modify the network structure, thus spatially translating the minimum of this potential. However, the bead itself modifies the internal network dynamics: Arbitrarily large local deformations are unlikely. To account for this feedback mechanism, we introduce a small backaction force on the potential location. Since the harmonic trap models the confinement by the network, the characteristic size of the trap is much larger than the particle size to avoid any escape of the particle as shown in Fig. 1(a). The backaction force is then necessarily small compared to the force applied on the particle, a feature which we will have to verify in actual experiments. In other words, the tracer dynamics has only a small effect on the \mathbf{r}_0 dynamics, and was, in fact, neglected in [1]. Moreover, the thermal fluctuations applied on the potential center position \mathbf{r}_0 must be taken into account, and the corresponding fluctuation amplitude should be negligible compared with the ones of thermal force applied on the tracers. Introducing a dimensionless parameter $\varepsilon \ll 1$, which,

*Corresponding author: etienne.fodor@univ-paris-diderot.fr

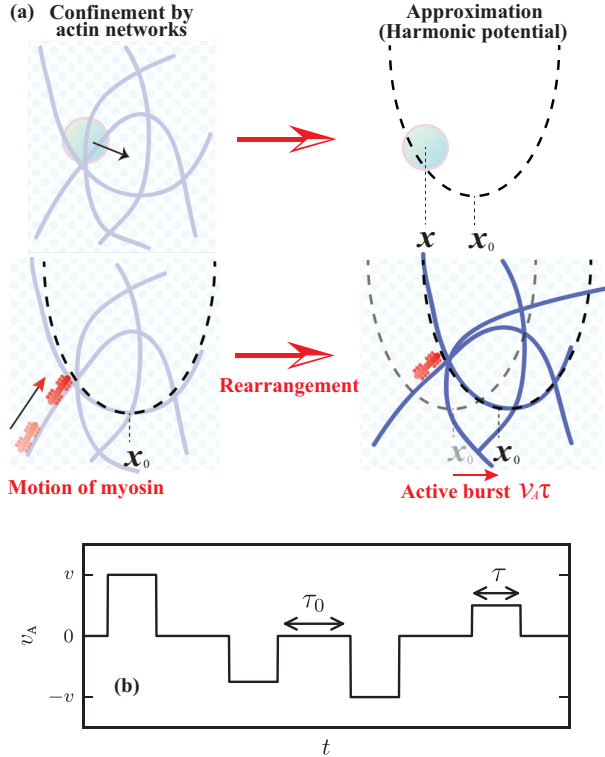


FIG. 1. (Color online) (a) Schematic representation of the energetic landscape rearrangement due to motor activity and its modeling using the active burst applied on the local minimum. In the passive case without motors, the tracer is confined within a harmonic potential. When motors are introduced, their activity modifies the network structure, thus leading to a displacement $v_A\tau$ of the potential local minimum x_0 . (b) Example trajectory of the active burst projection v_A . It equals zero over a random duration of average τ_0 and is a random value between $-v$ and v during a random time of order τ .

we anticipate, will be small, we arrive at the coupled set of equations

$$\frac{d\mathbf{r}}{dt} = -\frac{1}{\tau_d}(\mathbf{r} - \mathbf{r}_0) + \sqrt{2D_T}\xi, \quad (1a)$$

$$\frac{d\mathbf{r}_0}{dt} = -\frac{\varepsilon}{\tau_d}(\mathbf{r}_0 - \mathbf{r}) + \mathbf{v}_A + \sqrt{2\varepsilon D_T}\xi_0, \quad (1b)$$

where T is the bath temperature, γ is the friction coefficient of the tracer particle with the surrounding environment, k is the spring constant of the harmonic trap, $D_T = T/\gamma$ is a thermal diffusion coefficient, and $\tau_d = \gamma/k$ is a microscopic time scale. The Gaussian white noises ξ and ξ_0 accounting for thermal fluctuations are uncorrelated, and \mathbf{v}_A is another noise term, referred to as an *active burst*, describing the effect of molecular motors on the network structure. It denotes the velocity at which the potential is moving, and we model it as a stochastic process inspired from the dynamics of individual motors: There are quiescent periods of random duration of average time τ_0 alternating with active bursts of typical velocity v in a random direction and for a random time of average τ . In the absence of active forces, this is the itinerant oscillator model

introduced by Hill [21] and Sears [22] within the framework of simple liquids dynamics (see [23] for a review) which has equilibrium dynamics. Such dynamics for the tracer particles is associated with a complex modulus of the form [24,25]

$$G^*(\omega) = i\omega\eta \frac{1 + \varepsilon + i\omega\tau_d}{\varepsilon + i\omega\tau_d}. \quad (2)$$

The viscosity η is related to the friction coefficient γ via Stokes' law: $\gamma = 6\pi a\eta$, where a is the tracers' radius. Within this minimal rheology, we assume the material behaves like a fluid at short and large time scales, with associated viscosity η and η/ε , respectively, to leading order in ε . Thus, this material behaves like a much more viscous fluid at large time scale compared with the short time scale behavior. In experimental measurements, one has direct access to one dimensional projections of the position. We shall thus look at the one dimensional projection of Eq. (1) on the scalar position x ,

$$\frac{dx}{dt} = -\frac{1}{\tau_d}(x - x_0) + \sqrt{2D_T}\xi, \quad (3a)$$

$$\frac{dx_0}{dt} = -\frac{\varepsilon}{\tau_d}(x_0 - x) + v_A + \sqrt{2\varepsilon D_T}\xi_0, \quad (3b)$$

where $\langle \xi(t)\xi(t') \rangle = \delta(t - t') = \langle \xi_0(t)\xi_0(t') \rangle$ are still Gaussian noises, and v_A equals 0 over a random duration of order τ_0 and is a uniform random value between $-v$ and v over the duration of average τ , as depicted in Fig. 1(b). The active burst projection v_A is a non-Gaussian process [26,27], and the two-time correlation function reads $\langle v_A(t)v_A(0) \rangle = T_A e^{-|t|/\tau}/(\tau\gamma)$. The energy scale T_A defines an effective active temperature in terms of the duty ratio $p_{on} = \tau/(\tau + \tau_0)$:

$$T_A = \frac{\gamma v^2 \tau p_{on}}{3}. \quad (4)$$

This temperature is frequency independent, and we describe in this paper several methods to measure this quantity. It quantifies the amplitude of the active fluctuations, as defined by the active force correlations, and we will see later that it characterizes the tracer's statistics at large time scale. We postpone to Appendix A the derivation of the n -time correlation function of the active burst v_A . We derive the analytic expressions of the physical observables to leading order in ε .

To describe the phenomenology of this model, we focus on the mean square displacement (MSD) $\langle \Delta x^2 \rangle(t_i, t_f) = \langle (x(t_i) - x(t_f))^2 \rangle$. Even though the MSD depends on two time variables, in the limit where the initial time t_i is large enough compared to the microscopic relaxation time scale τ_d it becomes effectively a function of the only time lag $t = t_f - t_i$. This is the case we consider in this paper, as we only consider quasistatic transformations. Using the Fourier transform of Eq. (3), we compute the position autocorrelation function $C(t) = \langle x(t)x(0) \rangle$, from which we deduce the MSD as $\langle \Delta x^2 \rangle(t) = 2[C(0) - C(t)]$. We denote the thermal contribution to the MSD by $\langle \Delta x_T^2 \rangle$ and the MSD when the particle is only subjected to motor activity by $\langle \Delta x_A^2 \rangle$. We compute these

two contributions to leading order in ε :

$$\langle \Delta x_T^2 \rangle(t) = \frac{2T}{k} \left(1 - e^{-t/\tau_d} + \varepsilon \frac{t}{\tau_d} \right), \quad (5a)$$

$$\begin{aligned} \langle \Delta x_A^2 \rangle(t) &= \frac{2T_A/k}{1 - (\tau/\tau_d)^2} \left[e^{-t/\tau_d} + \frac{t}{\tau_d} - 1 \right. \\ &\quad \left. + \left(\frac{\tau}{\tau_d} \right)^3 \left(1 - e^{-t/\tau} - \frac{t}{\tau} \right) \right]. \end{aligned} \quad (5b)$$

The expression without any assumption made on ε is presented in Appendix B 1. In the active case, the time evolution of the MSD exhibits a two step growth with an intermediate plateau. The first growth and saturation correspond to the equilibriumlike behavior of a probe caged in a fixed trap. The initial growth is diffusive with a standard diffusion coefficient D_T , and the plateau value is given by $2T/k$. The evolution of the MSD at larger time scales, reflecting the nonequilibrium features of the system, is a diffusive growth with a diffusion coefficient $\varepsilon D_T + D_A$, where $D_A = T_A/\gamma$ is an “active” diffusion coefficient. In the passive case, the tracer particle can also escape the confinement at time scales larger τ_d/ε , and the large time scale diffusion coefficient εD_T is small compared to the short time scale one, as shown in Fig. 2(a).

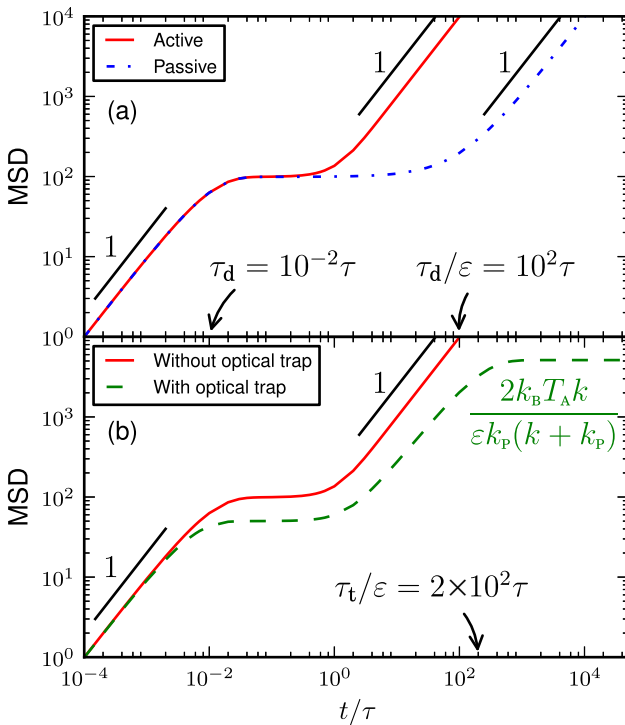


FIG. 2. (Color online) (a) Mean square displacement as a function of the scaled time t/τ for active (red solid line) and passive (blue dot-dashed line) systems. (b) Mean square displacement as a function of the scaled time t/τ with (green dashed line) and without (red solid line) an external potential, in this case a harmonic optical trap. The evolution is qualitatively similar for time scale smaller than τ_t/ε . At large time scale, there is a plateau due to the confinement within the optical trap, which value diverges with ε . $\{T, \varepsilon, k, \tau_d, \tau_t, T_A, \tau\} = \{10^2, 10^{-4}, 2, 10^{-2}, 2 \times 10^2, 1, 1\}$.

The expression of the thermal diffusion coefficient at large time scale agrees with the fluidlike behavior of the material with the associated viscosity η/ε . The backaction reflects the ability of the particle to modify its environment. The local minimum motion is not only affected by activity within the network, but also by the interaction of the bead with the network. The large time scale diffusion in the passive case is in agreement with experimental observations of tracers embedded in living cells [1,3]. Assuming $\tau_d \simeq 1$ ms and given that a large time scale diffusion appears for $t > 10$ s in [1], we deduce $\varepsilon \simeq 10^{-4}$ in agreement with $\varepsilon \ll 1$.

III. VARYING THE SPRING CONSTANT

One of the most fruitful approaches to gather information in living cells has been achieved by applying external forces to probe particles. This has been carried out by different methods, such as optical or magnetic tweezers [5,28], resulting in an effective external potential U_P acting on the probe. To our knowledge, the general protocol has always been to apply the potential and then to execute a space translation, typically with an oscillation, to measure quantities such as the complex shear modulus. Here we would like to pursue a different route, where, instead of translating the potential well, we consider a time-dependent change in other parameters of the external potential. Our main goal is to design a protocol with time-dependent parameters and to estimate the work extracted over the whole protocol. Optical tweezers effects are well approximated by a harmonic potential, though more complex energy landscape can be crafted [29].

The simplest protocol is thus to slowly vary the spring constant k_P in time (this is sometimes called a “capture experiment” [30]). We consider that an external potential $U_P = k_P x^2/2$ is applied to the tracer as presented in Fig. 3, so that an additional term $-k_P x/\gamma$ is to be inserted in the x dynamics in Eq. (3a). We postpone the derivation of the MSD to Appendix B 2. Within our model, when we apply this external force, the evolution of the MSD for time scales smaller than τ_t/ε , where $\tau_t = \gamma(k + k_P)/(kk_P)$ to leading order in ε , is qualitatively similar to the case without optical trap. At large time scale, the MSD saturates, meaning the tracer is confined within the optical trap. After a relaxation time τ_t/ε , the system reaches a steady state characterized by active fluctuations, the optical trap stiffness, and the properties of the network via k as presented in Fig. 2(b). Note that the plateau value

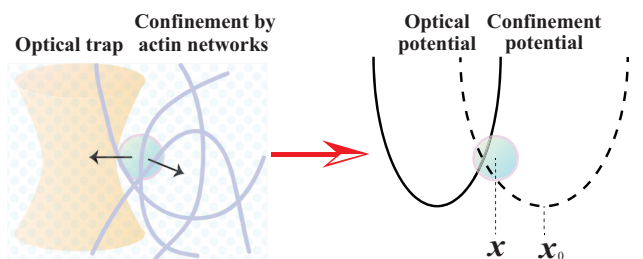


FIG. 3. (Color online) Schematic representation of the energetic landscape when a quadratic optical trap is applied on the tracers, in addition to the harmonic confinement potential.

$2T_A k / [\varepsilon k_p(k + k_p)]$ does not depend on the bath temperature T to leading order in ε , and it diverges with ε so that the backaction is necessary to model the confinement of the bead by the optical trap. We show that the stationary displacement probability density function is a Gaussian distribution to leading order in ε , so that the non-Gaussian nature of the active process v_A does not affect the steady-state tracer's distribution to that order of the calculation. Likewise, the leading term in ε of the tracer's stationary distribution is unchanged when considering a white noise for v_A , be it Gaussian or not. The time scales τ and τ_0 do appear to the next orders in ε of the steady-state distribution, though. To quantify the deviation of the stationary distribution from a Gaussian distribution, we determine the non-Gaussian parameter (NGP),

$$\kappa = \frac{\langle x^4 \rangle_{\text{ss}}}{3\langle x^2 \rangle_{\text{ss}}^2} - 1, \quad (6)$$

where $\langle \cdot \rangle_{\text{ss}}$ denotes the steady-state average. The NGP is zero for a Gaussian distribution and is often used to quantify deviations to the Gaussian distribution [31]. We compute this quantity to leading order in ε , as presented in Appendix B 2:

$$\kappa = \frac{2\varepsilon}{5(1+k/k_p)} \frac{9\tau_0^2 + 3\tau\tau_0 - \tau^2}{(\tau + \tau_0)\tau_d}. \quad (7)$$

The NGP is proportional to ε , as another evidence that the tracer's statistics is Gaussian to leading order in ε . As far as the active temperature T_A is concerned, it can be determined independently of the active time scales by applying a quadratic external potential on the tracer and by measuring its stationary distribution of displacement. It can also be measured from the large time scale diffusion in the absence of external potential. The method we propose is more convenient because the tracer does not experience large excursions, which would otherwise make it hard to keep in focus, as it remains confined within the optical trap.

The backaction reflects the ability of the tracer to act on the surrounding network, thus affecting the dynamics of the local minimum. In the present case, it exerts a force on the network which compensates the driving force due to the active burst, so that a work is applied by the tracer on the network. We see that the measurement of this work enables one to characterize activity within the system. We consider a protocol where k_p is slowly varied from k_i to k_f ; that is, the time evolution of the protocol is much longer than τ_i/ε and the time variation of k_p is negligible compared to the inverse duration of the protocol in terms of ε . The average quasistatic work W_H done by applying the external potential to the probe is [32,33]

$$W_H = \frac{1}{2} \int dk_p \langle x^2 \rangle_{\text{ss}}, \quad (8)$$

where the $\langle \cdot \rangle_{\text{ss}}$ means that the average is taken in the steady state with a *fixed* optical trap, in the present case a harmonic trap of constant k_p . We determine the expression of this quasistatic work in Appendix B 2. It takes the form

$W_H = E_H(k_f) - E_H(k_i)$, where E_H reads

$$E_H(k_p) = \frac{T_A}{2\varepsilon} \ln \left[\frac{k_p}{k + k_p} \right] - \frac{k T_A}{2(k + k_p)} + \frac{T}{2} \ln [k_p] \\ + \frac{T_A}{2} \left(\frac{\tau}{\tau_d} \right)^2 \ln \left[\frac{k_p \tau + k(\tau + \tau_d)}{k + k_p} \right] \\ - \frac{T_A}{2} \ln \left[\frac{k_p}{k + k_p} \right] + O(\varepsilon). \quad (9)$$

This energy scale is defined up to a constant which should render the argument of the logarithms dimensionless. It diverges with ε , meaning that if the backaction mechanism were neglected it would take an infinite work to confine the tracer in a harmonic well. This result does not depend on the non-Gaussian nature of the active noise, since W_H is only affected by the second moment of the tracers' statistics, and the dynamics of the tracer's position x is linear in x . We have run numerical simulations to determine the accuracy of the above formula. There is perfect agreement with our prediction for small values of ε . When $\varepsilon \simeq 0.15$, the term of order ε in Eq. (9) is no longer negligible. We compute the expression of the $O(\varepsilon)$ correction term, and we show it indeed explains for the deviation of numerical results with Eq. (9), as presented in Fig. 4. Note that in the passive case, without active bursts, the work does not vanish but reduces to the difference of the Helmholtz free energies, as it should for an isothermal transformation. This contribution enters in the $O(1)$ term of the above formula. An interesting feature of formula (9) is that the work is independent of T to leading order in ε , meaning that it should be possible to directly access T_A with a rather simple protocol. For example, one could measure the average

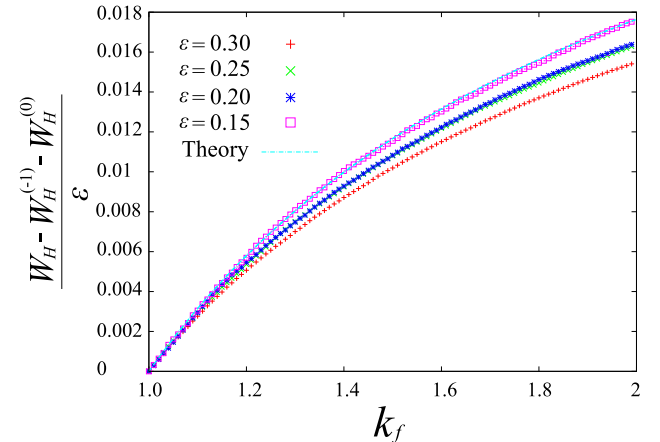


FIG. 4. (Color online) Study of the influence of the $O(\varepsilon)$ correction term in Eq. (9). The quasistatic work W_H is obtained numerically from simulations of the dynamics in Eq. (3), where $\varepsilon = \{0.3, 0.25, 0.2, 0.15\}$. We extract the correction term as $W_H - W_H^{(-1)} - W_H^{(0)}$, where the expression of $W_H^{(n)} = O(\varepsilon^n)$ is given by Eq. (9). The analytic expression of the $O(\varepsilon)$ correction term is plotted in a cyan dotted line as a function of k_f , and it agrees with numerical simulations for $\varepsilon = 0.15$. For larger values of ε , the next order terms should be taken into account to explain the deviation of the simulated quasistatic work from the prediction in Eq. (9). $\{T, k, k_i, \gamma, \tau_0, \tau, v\} = \{0, 1, 1, 1, 5, 0.6, 4\}$.

work with different values of k_i and k_f to deduce values for k , ε , and T_A . However, one should be aware that the protocol has to be operated over large time scales to remain quasistatic. If the operator reduces the volume accessible by the bead by setting $k_f > k_i$, the work is positive, in agreement with the fact that the probe “cools down” when k_p increases. Considering a circular protocol for which $k_f = k_i$, the extracted work is zero as for an equilibrium process. The nonequilibrium properties remain hidden for a circular protocol when a harmonic trap is applied to a tracer.

IV. THERMODYNAMIC CYCLES WITH QUARTIC POTENTIALS

By combining multiple optical tweezers it is possible to confine the tracer in a more complex potential such as a double well [29]. The corresponding quartic optical trap $U_p = k_p x^2/2 + b_p x^4/4$ depends on two parameters that are both tunable by the operator. In particular, the parameter k_p can take negative values, as long as the condition $k + k_p > 0$ is fulfilled. We regard the potential anharmonicity as a small perturbation with respect to the harmonic case: $b_p = O(\varepsilon^n)$. Our picture is that ε is a material-dependent quantity, but the shape of the trap, namely the parameter n , is fully controlled by the operator. We consider a quasistatic protocol where k_p varies as before and b_p is set constant. The associated work is expressed as $W_Q = \int dk_p \langle x^2 \rangle_{SS}/2$. The steady-state average is different from the value presented before due to the quartic term in the optical trap. By using a perturbation method with respect to b_p , we derive the expression of this steady-state average to order b_p . It follows that the average quasistatic work from an initial value k_i to a final one k_f is expressed as $W_Q = W_H + E_{Q1}(k_f, b_p) - E_{Q1}(k_i, b_p) + O(b_p^2)$, where E_{Q1} is linear in b_p . We compute the expression of E_{Q1} to leading order in ε , as presented in Appendix B 3:

$$\frac{E_{Q1}(k_p, b_p)}{b_p} = \left(\frac{T_A}{2k\varepsilon} \right)^2 \left\{ \frac{2k^4}{k_p^2(k+k_p)^2} + \frac{3k^2\tau}{k_p^2(\tau+\tau_d)} \right. \\ - 6k\tau \left[\frac{3\tau+2\tau_d}{k_p(\tau+\tau_d)^2} + \frac{1}{\tau_d(k+k_p)} \right] \\ + \frac{6\tau^5}{\tau_d^2(\tau+\tau_d)^3} \ln[k(\tau+\tau_d)+k_p\tau] \\ - \frac{6\tau(6\tau^2+8\tau\tau_d+3\tau_d^2)}{(\tau+\tau_d)^3} \ln[k+k_p] \\ \left. - \frac{6\tau(\tau-3\tau_d)}{\tau_d^2} \ln[k+k_p] \right\} + O(1/\varepsilon). \quad (10)$$

As for E_H , it is defined up to constant. The contribution E_{Q1} of the quartic term in the quasistatic work is of order ε^{n-2} to leading order in ε . Given that this contribution should be negligible with respect to W_H , we deduce that n should fulfill the condition $n > 1$. The energy scale E_{Q1} is affected by the non-Gaussian statistics of the active noise. Given that the tracers’ dynamics is nonlinear in x , the second moment of the tracers’ statistics now depends on higher moments of the active noise which reveal the non-Gaussian nature of the dynamics.

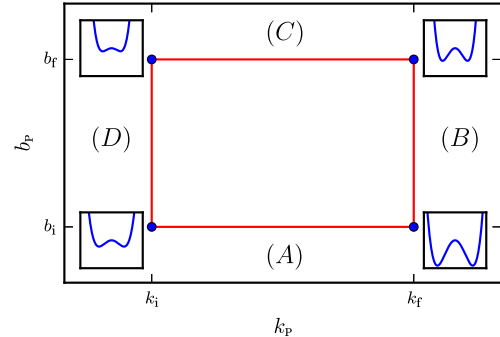


FIG. 5. (Color online) Schematic representation of cycle \mathcal{C} . The optical trap parameters undergo the transformations (A) to (D): $\{b_i, k_i\} \xrightarrow{(A)} \{b_i, k_f\} \xrightarrow{(B)} \{b_f, k_f\} \xrightarrow{(C)} \{\beta_f, k_f\} \xrightarrow{(D)} \{b_i, k_i\}$. The shape of the external potential tuned by the operator is depicted as a function of the position for the four parameter sets, where $k_f = 2k_i < 0$ and $b_f = 2b_i$.

We consider a circular protocol \mathcal{C} where both k_p and b_p are modified in time. The simplest protocol is then given by four elementary transformations during which a single parameter is varied, the other one remaining constant. The cycle is illustrated in Fig. 5. It connects four points in the $\{k_p, b_p\}$ plane:

$$\{b_i, k_i\} \xrightarrow{(A)} \{b_i, k_f\} \xrightarrow{(B)} \{b_f, k_f\} \xrightarrow{(C)} \{b_f, k_i\} \xrightarrow{(D)} \{b_i, k_i\}. \quad (11)$$

The associated average quasistatic work is defined as

$$W_C = \frac{1}{2} \oint_C dk_p \langle x^2 \rangle_{SS} + \frac{1}{4} \oint_C db_p \langle x^4 \rangle_{SS}. \quad (12)$$

To leading order in b_p , the steady-state average $\langle x^4 \rangle_{SS}$ in the above formula is evaluated for a quadratic optical trap, as we compute it in Appendix B 2. It follows the quasistatic work associated with the protocol \mathcal{C} is expressed to leading order in b_i and b_f as

$$W_C = E_{Q1}(k_f, b_i) - E_{Q1}(k_i, b_i) + E_{Q2}(k_f, b_f) - E_{Q2}(k_f, b_i) \\ + E_{Q1}(k_i, b_f) - E_{Q1}(k_f, b_f) \\ + E_{Q2}(k_i, b_i) - E_{Q2}(k_i, b_f), \quad (13)$$

where E_{Q2} is linear in b_p :

$$\frac{E_{Q2}(k_p, b_p)}{b_p} = 3 \left[\frac{kT_A}{2k_p(k+k_p)\varepsilon} \right]^2 + O(1/\varepsilon). \quad (14)$$

The formula (13) reveals that one can measure some work for a circular protocol if the external potential applied on the tracer contains an anharmonic component [17]. The equilibrium counterpart of this work vanishes, namely, for the itinerant oscillator case when $T_A = 0$, and a nonzero work can thus be regarded as a signature of nonequilibrium activity within the system. The work applied during such a protocol is of order ε^{n-2} to leading order in ε . Being n necessarily greater than 1, we deduce this work is negligible compared with the work associated to the protocol presented in Sec. III. Thus, the anharmonicity of the external potential leads to a nonzero quasistatic work for a circular protocol, but its small value may be hard to measure experimentally.

Assuming an experimental apparatus can actually detect such a work, the active temperature can then be extracted from this measurement, given that the backaction strength ε has been estimated by another method and the parameter n is controlled by the operator. A simple method to fix n is to tune the anharmonicity so that it gives a nonzero contribution to $W_Q - T_A \ln [k_f(k + k_i)/k_i(k + k_f)]/(2\varepsilon)$ by detecting when the value of this work differs from the order ε^0 in W_H . In such a case, the contribution of E_{Q1} is to be taken into account, so that it corresponds to the case $n = 2$. Note that neither E_{Q1} nor E_{Q2} depends on τ_0 to leading order in ε . Then, the expressions we present would remain unchanged in the limit $\tau_0 \rightarrow 0$, where the active noise is a symmetric two-state process usually referred to as a random telegraphic noise [34]. The waiting time scale τ_0 affects the next order in ε of the work associated with the cycle \mathcal{C} . Moreover, the work applied during such a protocol does not vanish in the limit where the active process v_A becomes a white noise, namely when $\{\tau, \tau_0, v\} \rightarrow \{0, 0, \infty\}$ with fixed T_A . In such a limit and assuming $T = 0$, the dynamics presented in Eq. (3) describes the evolution of a particle subjected to a white non-Gaussian noise, so that one can indeed extract work from a cycle as already noticed in [17].

V. EFFECTIVE TEMPERATURE AND FORCE-POSITION CORRELATIONS

Active microrheology experiments on living cells measure the response χ to an external stress, and its temporal Fourier transform $\tilde{\chi}(\omega) = \int dt e^{-i\omega t} \chi(t)$. The latter is, up to a constant, the inverse of the complex modulus G^* [35]: $G^* = 1/[6\pi a \tilde{\chi}]$, where $\tilde{\chi}$ is the response function in the Fourier domain. We assume that motor activity does not affect the rheological properties of the network, so that we deduce the response function from the expression of the complex modulus in a passive system as presented in Eq. (2). Following Lau *et al.* [36], the tracer's evolution in a viscous fluid is modeled as

$$\gamma \frac{dx}{dt} = F_{\text{cell}}(t), \quad (15)$$

where F_{cell} describes all the forces arising from the medium. Within this minimal assumption several works have measured the nonequilibrium properties of the force F_{cell} [11,16]. These were quantified by looking at the deviation from such equilibrium relations as the FDT. For example, the correlation-to-response ratio leads to a frequency-dependent “effective temperature” as [12–14] $T_{\text{eff}}(\omega) = -\omega \tilde{C}(\omega)/[2\tilde{\chi}''(\omega)]$, where $\tilde{\chi}''$ is the imaginary part of the response Fourier transform and \tilde{C} is the position autocorrelation function in the Fourier domain. Of course, this effective temperature is not a *bona fide* temperature, in the sense that even in a stationary regime it is generally observable-dependent, but the fact that its high frequency value collapses to the bath temperature in the absence of nonequilibrium processes constitutes a useful benchmark. This is the simplest manner to evaluate the distance from equilibrium. In the absence of external potential as described in Eq. (3), we compute analytically this temperature to leading order in ε :

$$T_{\text{eff}}(\omega) = T + \frac{1}{\varepsilon + (\omega\tau_d)^2} \frac{T_A}{1 + (\omega\tau)^2}. \quad (16)$$

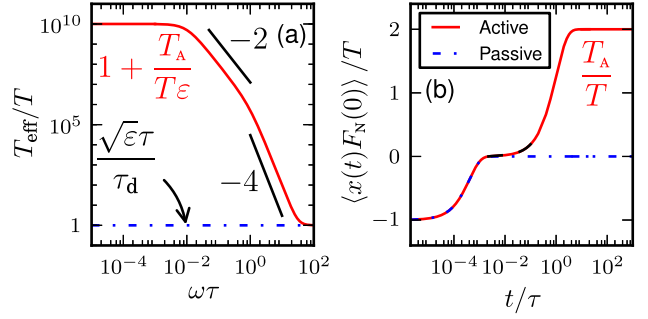


FIG. 6. (Color online) (a) Effective temperature as a function of the scaled frequency $\omega\tau$. The plateau value at low frequency equals $T + T_A/\varepsilon$ (red solid line), and it equals T at high frequency as for the passive case (blue dot-dashed line). Between the two saturations, it scales successively like $1/\omega^2$ and $1/\omega^4$, provided the time scales τ and $\tau_d/\sqrt{\varepsilon}$ are well separated. (b) Evolution of the force-position correlation function with the scaled time t/τ in the passive (blue dot-dashed line) and active (red solid line) cases. The correlation function is negative at short time scale with an initial value $-T$. It remains negative in the passive case. There is a linear growth regime in the active case (black dashed line), and the correlation function saturates to a plateau value T_A . (a) $\{T, \varepsilon, \tau_d, T_A, \tau\} = \{1, 10^{-8}, 1, 10^2, 10^2\}$. (b) $\{T, \tau_d, T_A, \tau\} = \{5, 0.2, 10, 5 \times 10^2\}$.

At high frequencies, the effective temperature coincides with the bath temperature T , meaning thermal fluctuations are predominant with respect to motor activity in this regime, in agreement with the MSD short time behavior. The plateau value $T + T_A/\varepsilon$ at low frequency represents an alternative measurement of the active fluctuation amplitude. Between the two plateaus, the effective temperature successively scales like $1/\omega^4$ and $1/\omega^2$ given that the two time scales τ and $\tau_d/\sqrt{\varepsilon}$ are well separated as shown in Fig. 6(a), thus providing a way to determine these time scale values from the slope variation. When we neglect the backaction effect, the effective temperature diverges at low frequencies. It results from the fact that the active MSD diffuses at large time scale, whereas it saturates to the equilibrium value for a passive system. The introduction of the backaction changes the rheology of the material, so that the passive MSD also diffuses at a large time scale, from which we deduce the effective temperature saturates at low frequency.

A generalization of usual microrheology measurements relies on applying an arbitrary perturbation on the tracers and measuring their response function. The external stimulus is generally a homogeneous force. We address here the case where an arbitrary potential $V_p = -a_p(t)V(x(t))$ is applied on the tracers. The generalized tracers' response χ_G quantifies the effect of the perturbation on an arbitrary observable A :

$$\chi_G(s, u) = \left. \frac{\delta \langle A(s) \rangle}{\delta a_p(u)} \right|_{a_p=0}. \quad (17)$$

Causality ensures that the response function is zero when the measurement is performed before the perturbation, at $u < s$. Since the thermal noise has Gaussian statistics, the probability weight \mathcal{P} associated with a given realization of the thermal noise is defined as $\mathcal{P}[\xi] \propto e^{-S[\xi]}$, where $S[\xi] = \int dt' \xi^2(t')/2$ is the Onsager-Machlup (or action) functional, in which ξ

determines the dynamics of the probe [18,19]. The application of the external potential V_p results in a variation δS of the action functional, so that the response function is expressed as

$$\chi_G(s,u) = - \left\langle A(s) \frac{\delta S}{\delta a_p(u)} \Big|_{a_p=0} \right\rangle. \quad (18)$$

To determine the response function, we only need to compute the action functional to leading order in a_p ,

$$S = - \int dt' \frac{a_p(t')}{2\gamma T} \left[\gamma \frac{dx}{dt'} - F_N(t') \right] \frac{dV(x(t'))}{dx} + O(a_p^2), \quad (19)$$

where $F_N = -k(x - x_0)$ is the force reflecting the interaction of the tracer with the surrounding actin network. We deduce the response function in terms of the probe's statistics and the network force,

$$\chi_G(s,u) = \frac{1}{2\gamma T} \left[\gamma \frac{\partial C_{AV}(s,u)}{\partial u} - \left\langle A(s) \frac{dV(x(u))}{dx} F_N(u) \right\rangle \right], \quad (20)$$

where $C_{AV}(s,u) = \langle A(s)V(u) \rangle$. This expression reveals that one can gain information about the correlation between the network force and the tracers' statistics by independently measuring χ_G and C_{AV} .

In the case where a_p is a homogeneous force, when $V_p = -a_p x$, the response function is measured by usual microrheology methods. If we choose the observable A to be the tracers' position x , it is possible to access the force-position correlation $\langle x(s)F_N(u) \rangle$ [18]. After an exponentially fast initial transient regime which we neglect, this correlation function depends only on the lag time $t = s - u$. The expression for this correlation is not invariant under time reversal, and we compute it for the case $t > 0$ to leading order in ε :

$$\begin{aligned} \langle x(t)F_N(0) \rangle &= -Te^{-t/\tau_d} + \frac{T_A}{1 - (\tau/\tau_d)^2} \\ &\times \left[1 - e^{-t/\tau_d} - \left(\frac{\tau}{\tau_d} \right)^2 (1 - e^{-t/\tau}) \right]. \end{aligned} \quad (21)$$

The initial value $-T$ is negative and equals the thermal fluctuation amplitude in agreement with [18]. This anticorrelation between the network force and the tracers' displacement is another evidence of the short time scale confinement. In the active case, the correlation function can take positive values, showing that the active burst allows the tracer to overcome the short time scale confinement. When $\tau \gg \tau_d$, there is a linear growth with coefficient $T_A/\tau/[1 - (\tau_d/\tau)^2]$, and then it reaches a plateau value T_A as presented in Fig. 6(b). The linear regime is observed in [18], but the plateau is not present. We speculate that a larger time window would allow one to observe the saturation of the correlation function. The existence of the plateau calls for new experiments as it would provide yet another way of measuring the amplitude of active fluctuations. Note that this amplitude is also accessible via the linear growth coefficient if τ and τ_d are already known. Moreover, a positive value of the force-position correlation function is a signature of nonequilibrium activity within the system as it would remain negative for an equilibrium process.

VI. ENERGY DISSIPATION AND HARADA-SASA RELATIONS

The dissipation within the system is the work applied by the tracer on the surrounding environment regarded as a heat bath [33]. It has already been measured in colloidal systems [37,38] and should be a good criterion to characterize nonequilibrium activity in biological systems. We adopt a natural definition for the mean rate of energy dissipation [32,33]: $J = \langle \dot{x}(\gamma \dot{x} - \xi) \rangle$, where \dot{x} is the velocity of the tracer. It is the difference between the mean power given by the particle to the heat bath via the drag force $\gamma \dot{x}$ and the one provided in average by the thermostat to the particle via the thermal force ξ . It has been demonstrated by Harada and Sasa that this quantity is related to the correlation and response functions defined previously [20]: $J = \gamma \int d\omega [\omega \tilde{C}(\omega) + 2T \tilde{\chi}''(\omega)]\omega/(2\pi)$. This relation presents the heat current J as a quantification of the deviation from the FDT valid for an equilibrium process. Within our model, the energy dissipation rate equals the average power of the network force: $J = \langle \dot{x} F_N \rangle$. We compute it in terms of the microscopic ingredients:

$$J = \frac{T_A}{\tau + \tau_d}. \quad (22)$$

It is not affected by the backaction to leading order in ε . The energy dissipation rate is zero when no activity occurs in the medium for an arbitrary value of ε , as expected for an equilibrium process. The dissipation rate depends on the coupling between the probe and its environment via τ_d . To minimize the dissipation rate, the time scale of the quiescent periods τ_0 should be as large as possible, whereas the time scale of the ballistic jumps τ should be very small, in agreement with observations in biological systems for which $\tau_0 > \tau$ [3,11]. As in the previous section, the definition and the expression of J show that one can access the microscopic features of motor activity via independent measurements of the correlation and response functions.

The main drawback of this approach is that one should measure \tilde{C} and $\tilde{\chi}$ over a large range of frequencies to access the energy dissipation rate. Thus, it is interesting to focus on the spectral density of the energy dissipation rate, $\tilde{I}(\omega) = \gamma \omega [\omega \tilde{C}(\omega) + 2T \tilde{\chi}''(\omega)]$, which, when integrated over the whole frequency range, equals the energy dissipation rate [20,37]: $J = \int d\omega \tilde{I}(\omega)/(2\pi)$. To give a physical interpretation of this quantity, we introduce the operators θ_{\pm} the effect of which on an arbitrary function $f(t)$ is to extract its even/odd component: $\theta_{\pm}[f(t)] = [f(t) \pm f(-t)]/2$. The Fourier transform of the symmetrized force-velocity correlation function is \tilde{I} [20,39], so that $I(t) = \theta_+[\langle \dot{x}(t)F_N(0) \rangle]$. This relation is a reformulation of Eq. (21) when $V = x = A$, and we see in which sense it enables one to easily access the characteristics of motor activity. Note that the antisymmetrized force-position correlation function defined previously is also related to this quantity: $I(t) = d\theta_-[\langle x(t)F_N(0) \rangle]/dt$. We compute the dissipation rate spectrum analytically to leading order in ε :

$$\tilde{I}(\omega) = \frac{1}{1 + (\omega\tau_d)^2} \frac{2T_A}{1 + (\omega\tau)^2}. \quad (23)$$

The low frequency plateau provides a direct measurement of the active fluctuation amplitude T_A . At high frequency, it scales

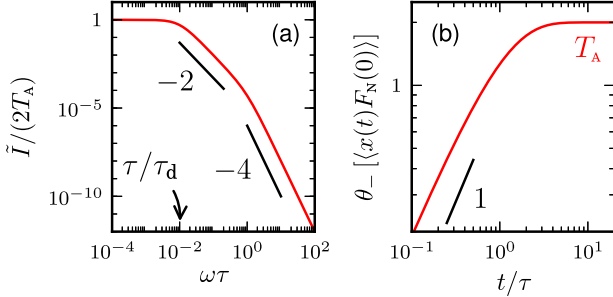


FIG. 7. (Color online) (a) Evolution of the Fourier transform of the spectral density of the energy dissipation rate with the scaled frequency $\omega\tau$ when $\tau \gg \tau_d$. The plateau value at low frequency equals $2T_A$. It scales like $1/\omega^4$ at high frequency, and there is a crossover regime $1/\tau_d \ll \omega \ll 1/\tau$ with another power law $1/\omega^2$. (b) Antisymmetric force-position correlation function as a function of the scaled time t/τ . It is linear in time at short time scale with a growth coefficient J and saturates to the value T_A at large time scale. $\{T_A, \tau, \tau_d\} = \{2, 10, 0.1\}$.

like $1/\omega^4$, and there is a crossover regime $\omega_1 \ll \omega \ll \omega_2$, where $\omega_1, \omega_2 \in \{1/\tau, 1/\tau_d\}$, with a power law behavior $1/\omega^2$. Thus, one can determine τ and τ_d from the variation of the slope, provided the two time scales are well separated, as presented in Fig. 7(a). We derive the antisymmetric force-position correlation function from \tilde{I} to leading order in ε :

$$\theta_- [\langle x(t)F_N(0) \rangle] = \frac{T_A}{1 - (\tau/\tau_d)^2} \left[1 - e^{-t/\tau_d} - \left(\frac{\tau}{\tau_d} \right)^2 (1 - e^{-t/\tau}) \right]. \quad (24)$$

It equals the force-position correlation function in Eq. (21) when $T = 0$. At short time scale, growth is linear with a coefficient J . Hence, it is possible to estimate the energy dissipation rate by measuring its spectral density only in the high frequency domain, which mostly facilitates the experimental task with respect to the procedure proposed in [20]. The correlation function saturates to a plateau value T_A at large time scale as presented in Fig. 7(b), showing that it provides an alternative to directly measuring both the energy dissipation rate and the amplitude of the tracer's active fluctuations.

VII. CONCLUSION

We offer theoretical predictions for energetic observables of a system where both thermal fluctuations and nonequilibrium activity coexist. We also propose a set of concrete experimental methods and protocols so that our predictions may be tested with existing experimental techniques. These new methods end up in more stringent constraints on the theoretical modeling which is employed in the studies of tracer dynamics, and thus they should also be a crucial test for the robustness of our own model. By applying such methods, we find that one can access the microscopic features of motor activity and fully characterize the nonequilibrium process arising in the medium. The most natural step forward is to address the analytic computation of the finite time extracted work, for which one should find an optimal protocol maximizing the

extracted power [40]. Another interesting issue is the excess heat and housekeeping heat produced by such a protocol, the computation of which requires the determination of the steady-state distribution of the process [41]. The bath temperature could be regarded as another tunable parameter provided its variation does not modify the microscopic features of the system [42], which is not the case in biological systems but could be conceivable in colloidal systems. Finally, the rheology of living matter can be more complex than we propose in this paper [43,44]. Memory effects arise from the interaction of the particle with the environment, due to the integration of some additional degrees of freedom, leading to a power law behavior for the complex modulus. Dressing the tracers' dynamics with a more realistic rheology should be included in a future elaboration of the model.

ACKNOWLEDGMENTS

Part of the numerical calculations was carried out on SR16000 at YITP in Kyoto University. This work was supported by the JSPS Core-to-Core Program Non-equilibrium Dynamics of Soft Matter and Information, the Grants-in-Aid for Japan Society for Promotion of Science (JSPS) Fellows (Grant No. 24.3751), and JSPS KAKENHI Grant No. 22340114.

APPENDIX A: ACTIVE BURST STATISTICS

We denote P_{off} the transition probability to the state in which v_A is zero, and P_{on} the transition probability to the state $v_A = pv$, where p is a uniform random value between -1 and 1 . The set of master equations describing the evolution of the active burst one dimensional projection is

$$d_t P_{\text{off}}(t) = \frac{1}{\tau} - P_{\text{off}}(t) \left(\frac{1}{\tau} + \frac{1}{\tau_0} \right), \quad (\text{A1a})$$

$$\partial_t P_{\text{on}}(t, p) = \frac{P_{\text{off}}(t)}{2\tau_0} - \frac{P_{\text{on}}(t, p)}{\tau}. \quad (\text{A1b})$$

We derive the expression of the transition probability P_{on} from these equations. For symmetry reasons, only the $2n$ -time correlation functions of the active burst are nonzero. Given that the active burst is in the steady state at the initial time, the $2n$ -time correlation function $K_A(\{t_i\}) = \langle v_A(t_{2n})v_A(t_{2n-1}) \dots v_A(t_1) \rangle$ reads

$$\frac{K_A(\{t_i\})}{v^{2n}} = \int d^{2n}p P_{\text{on}}^{\text{ss}}(p_1)p_1 \prod_{i=2}^{2n} P_{\text{on}}(t_i - t_{i-1}, p_i | p_{i-1})p_i, \quad (\text{A2})$$

where $P_{\text{on}}(t, p_b | p_a)$ is the transition probability from p_a to p_b , and $P_{\text{on}}^{\text{ss}}$ is the steady-state transition probability. We deduce the explicit expression of K_A ,

$$K_A(\{t_i\}) = \phi(t_2 - t_1) \prod_{i=1}^{n-2} \phi(t_{2i+2} - t_{2i+1}) \psi(t_{2i+1} - t_{2i}), \quad (\text{A3})$$

where $t_{2n} \geq t_{2n-1} \geq \dots \geq t_1$. The functions ϕ and ψ are defined as

$$\phi(t) = \frac{v^2 p_{\text{on}}}{3} e^{-|t|/\tau}, \quad (\text{A4a})$$

$$\psi(t) = 1 + \frac{4}{5} \left(1 + \frac{\tau_0}{\tau} \right) e^{-|t|/\tau} + \frac{\tau_0}{\tau} e^{-|t|(1/\tau+1/\tau_0)}. \quad (\text{A4b})$$

APPENDIX B: TRACER STATISTICS

1. Without optical trap

We compute the expression of the MSD for the dynamics without optical trap in Eq. (3) for an arbitrary value of ε ,

$$\langle \Delta x_T^2 \rangle(t) = \frac{2T/k}{(1+\varepsilon)^2} \left(1 - e^{-t/\tau_\varepsilon} + \varepsilon \frac{t}{\tau_\varepsilon} \right), \quad (\text{B1a})$$

$$\begin{aligned} \langle \Delta x_A^2 \rangle(t) &= \frac{2T_A/[k(1+\varepsilon)^3]}{1-(\tau/\tau_\varepsilon)^2} \left[e^{-t/\tau_\varepsilon} + \frac{t}{\tau_\varepsilon} - 1 \right. \\ &\quad \left. + \left(\frac{\tau}{\tau_\varepsilon} \right)^3 \left(1 - e^{-t/\tau} - \frac{t}{\tau} \right) \right], \end{aligned} \quad (\text{B1b})$$

where $\tau_\varepsilon = \tau_d/(1+\varepsilon)$.

2. Quadratic optical trap

The dynamics of x and x_0 is given by the set of equations

$$\frac{dx}{dt} = -\frac{1}{\tau_d}(x - x_0) - \frac{1}{\tau_p}x + \sqrt{2D_T}\xi, \quad (\text{B2a})$$

$$\frac{dx_0}{dt} = -\frac{\varepsilon}{\tau_d}(x_0 - x) + v_A + \sqrt{2\varepsilon D_T}\xi_0, \quad (\text{B2b})$$

where $\tau_p = \gamma/k_p$. Given that we are interested in the regime where the dynamics is time translational invariant, it should not depend on initial condition, so that we can choose $x(0) = 0 = x_0(0)$. Using the Fourier transform of Eq. (B2), we express the tracer's position in terms of the stochastic noises in the Fourier domain as

$$\tilde{x} = \gamma[\tilde{\chi}\sqrt{2D_T}\tilde{\xi} + \tilde{\chi}_A(\tilde{v}_A + \sqrt{2\varepsilon D_T}\tilde{\xi}_0)], \quad (\text{B3})$$

where the functions $\tilde{\chi}$ and $\tilde{\chi}_A$ are defined as

$$\tilde{\chi}(\omega) = \frac{(\varepsilon + i\omega\tau_d)/k}{i\omega\tau_d(1+\varepsilon+i\omega\tau_d) + k_p(\varepsilon+i\omega\tau_d)/k}, \quad (\text{B4a})$$

$$\tilde{\chi}_A(\omega) = \frac{1/k}{i\omega\tau_d(1+\varepsilon+i\omega\tau_d) + k_p(\varepsilon+i\omega\tau_d)/k}. \quad (\text{B4b})$$

Alternatively, the tracer's position is expressed in the time domain as

$$\begin{aligned} x(t) &= \gamma \int^t dt' \{ \chi(t-t') \sqrt{2D_T} \xi(t') \\ &\quad + \chi_A(t-t')[v_A(t') + \sqrt{2\varepsilon D_T} \xi_0(t')] \}. \end{aligned} \quad (\text{B5})$$

By using the residue theorem, we compute from Eq. (B4) the expression of χ and χ_A in the time domain,

$$\chi(t) = \frac{1}{\gamma(c_+ - c_-)} (c_+ e^{-t/\tau_+} - c_- e^{-t/\tau_-}), \quad (\text{B6a})$$

$$\chi_A(t) = \frac{1}{\gamma(c_+ - c_-)} (e^{-t/\tau_+} - e^{-t/\tau_-}), \quad (\text{B6b})$$

where $\tau_\pm = \tau_d/(\varepsilon - c_\pm)$, and the coefficients c_\pm read

$$c_\pm = \frac{\varepsilon - 1 - k_p/k}{2} \left[1 \pm \sqrt{1 + \frac{4\varepsilon}{(\varepsilon - 1 - k_p/k)^2}} \right]. \quad (\text{B7})$$

We determine the position autocorrelation function in the Fourier domain for an arbitrary ε :

$$\begin{aligned} \tilde{C}(\omega) &= \frac{2(\tau_+\tau_-)^2/(k\tau_d^3)}{[1+(\tau_+\omega)^2][1+(\tau_-\omega)^2]} \\ &\quad \times \left\{ [\varepsilon + \varepsilon^2 + (\omega\tau_d)^2]T + \frac{T_A}{1+(\omega\tau)^2} \right\}. \end{aligned} \quad (\text{B8})$$

We then deduce the expression of the MSD, without any assumption made on ε ,

$$\begin{aligned} \langle \Delta x_T^2 \rangle(t) &= \frac{2T/k}{(c_+ - c_-)(c_- + c_+ - 2\varepsilon)} \\ &\quad \times \left[\frac{c_-^2 - \varepsilon(1 + 2c_-)}{c_- - \varepsilon} (1 - e^{-t/\tau_-}) \right. \\ &\quad \left. - \frac{c_+^2 - \varepsilon(1 + 2c_+)}{c_+ - \varepsilon} (1 - e^{-t/\tau_+}) \right], \end{aligned} \quad (\text{B9a})$$

$$\begin{aligned} \langle \Delta x_A^2 \rangle(t) &= \frac{2T_A/k}{[(\tau/\tau_-)^2 - 1][(\tau/\tau_+)^2 - 1](c_+ - c_-)} \\ &\quad \times \left[(c_+ - c_-)(1 - e^{-t/\tau}) \left(\frac{\tau}{\tau_d} \right)^3 \right. \\ &\quad \left. + \frac{(\tau/\tau_+)^2 - 1}{c_+ + c_- - 2\varepsilon} (1 - e^{-t/\tau_-}) \right. \\ &\quad \left. - \frac{(\tau/\tau_-)^2 - 1}{c_- + c_+ - 2\varepsilon} (1 - e^{-t/\tau_+}) \right]. \end{aligned} \quad (\text{B9b})$$

From the saturation value of the MSD at large time scale, we deduce the expression of the steady-state average:

$$\begin{aligned} \langle x^2 \rangle_{\text{SS}} &= \frac{T_A k}{\varepsilon k_p(k+k_p)} \\ &\quad + \frac{T}{k_p} - \frac{T_A k}{(k+k_p)^2} \left[\frac{\tau}{\tau_d} + \frac{k^2(\tau + \tau_d)}{k_p(k+k_p)\tau + kk_p\tau_d} \right] \\ &\quad + O(\varepsilon). \end{aligned} \quad (\text{B10})$$

The expression of E_H is given by the primitive of the above formula with respect to k_p , thus being defined up to a constant. To determine the non-Gaussian parameter, we compute the steady-state average $\langle x^4 \rangle_{\text{SS}}$. Given that the tracer's statistics is Gaussian to leading order in ε , we can easily deduce $\langle x^4 \rangle_{\text{SS}}$ to first order in ε from the above formula:

$$\langle x^4 \rangle_{\text{SS}} = 3 \left[\frac{k T_A}{\varepsilon k_p(k+k_p)} \right]^2 + O(1/\varepsilon). \quad (\text{B11})$$

The computation of the next order requires to develop the expression of x^4 in terms of χ and χ_A . From Eq. (B5), we split the steady-state average in two contributions:

$$\langle x^4 \rangle_{\text{SS}} = \lim_{t \rightarrow \infty} (\kappa_1 + 6\kappa_2)(t). \quad (\text{B12})$$

The functions κ_1 and κ_2 read

$$\begin{aligned} \kappa_1(u) &= \int^u \iiint du_1 du_2 du_3 du_4 [\chi_{A1} \chi_{A2} \chi_{A3} \chi_{A4} \langle v_A(u_1) v_A(u_2) v_A(u_3) v_A(u_4) \rangle \\ &\quad + 4(\varepsilon D_T)^2 \chi_{A1} \chi_{A2} \chi_{A3} \chi_{A4} \langle \xi_0(u_1) \xi_0(u_2) \xi_0(u_3) \xi_0(u_4) \rangle + 4D_T^2 \chi_{A1} \chi_{A2} \chi_{A3} \chi_{A4} \langle \xi(u_1) \xi(u_2) \xi(u_3) \xi(u_4) \rangle], \end{aligned} \quad (\text{B13a})$$

$$\begin{aligned} \kappa_2(u) &= \int^u \iiint du_1 du_2 du_3 du_4 [2\varepsilon D_T \chi_{A1} \chi_{A2} \chi_{A3} \chi_{A4} \langle v_A(u_1) v_A(u_2) \rangle \langle \xi_0(u_3) \xi_0(u_4) \rangle \\ &\quad + 2D_T \chi_{A1} \chi_{A2} \chi_{A3} \chi_{A4} \langle v_A(u_1) v_A(u_2) \rangle \langle \xi(u_3) \xi(u_4) \rangle + 4\varepsilon D_T^2 \chi_{A1} \chi_{A2} \chi_{A3} \chi_{A4} \langle \xi_0(u_1) \xi_0(u_2) \rangle \langle \xi(u_3) \xi(u_4) \rangle], \end{aligned} \quad (\text{B13b})$$

where $\chi_i = \chi(u - u_i)$, $\chi_{Ai} = \chi_A(u - u_i)$, and $i \in \{1, 2, 3, 4\}$. The non-Gaussianity of the active bursts plays a role in the first term in the bracket of Eq. (B13a). Being ξ and ξ_0 thermal noises, their four-time correlation function is expressed in terms of their two-time correlation function as

$$\begin{aligned} \langle \xi(t_a) \xi(t_b) \xi(t_c) \xi(t_d) \rangle &= \langle \xi(t_a) \xi(t_b) \rangle \langle \xi(t_c) \xi(t_d) \rangle \\ &\quad + \langle \xi(t_a) \xi(t_c) \rangle \langle \xi(t_d) \xi(t_b) \rangle \\ &\quad + \langle \xi(t_a) \xi(t_d) \rangle \langle \xi(t_c) \xi(t_b) \rangle, \end{aligned} \quad (\text{B14})$$

and the same property holds for the correlations of ξ_0 . By using Eqs. (A3) and (B14), we finally deduce the next orders in the expression of $\langle x^4 \rangle_{\text{SS}}$.

3. Quartic optical trap

To compute the steady-state average $\langle x^2 \rangle_{\text{SS}}$, we expand the positions x and x_0 in terms of b_P as $x = x^{(0)} + x^{(1)} + O(b_P^2)$ and $x_0 = x_0^{(0)} + x_0^{(1)} + O(b_P^2)$, where $x^{(1)}$ and $x_0^{(1)}$ are of order b_P . The steady-state average is expressed as

$$\langle x^2 \rangle_{\text{SS}} = \langle (x^{(0)})^2 \rangle_{\text{SS}} + 2\langle x^{(0)} x^{(1)} \rangle_{\text{SS}} + O(b_P^2). \quad (\text{B15})$$

The leading order in b_P equals the steady-state average without quartic term in the optical trap, as we compute it in Sec. III. Thus, we write the work associated with the quasistatic protocol as $W_Q = W_H + W_P + O(b_P^2)$, where $W_P = \int dk_P \langle x^{(0)} x^{(1)} \rangle_{\text{SS}}$. The positions $x^{(0)}$ and $x_0^{(0)}$ follow the dynamics in Eq. (B2), so that the expression of $x^{(0)}$ is given by Eq. (B5). The positions $x^{(1)}$ and $x_0^{(1)}$ follow the coupled set of equations

$$\frac{dx^{(1)}}{dt} = -\frac{1}{\tau_d} (x^{(1)} - x_0^{(1)}) - \frac{1}{\tau_p} x^{(1)} - \frac{b_p}{\gamma} (x^{(0)})^3, \quad (\text{B16a})$$

$$\frac{dx_0^{(1)}}{dt} = -\frac{\varepsilon}{\tau_d} (x_0^{(1)} - x^{(1)}), \quad (\text{B16b})$$

from which we deduce

$$x^{(1)}(t) = -b_p \int^t dt' \chi(t - t') (x^{(0)})^3(t'). \quad (\text{B17})$$

We split the correlation function in the definition of W_P in three contributions,

$$\langle x^{(0)} x^{(1)} \rangle_{\text{SS}} = -\gamma b_P \lim_{t \rightarrow \infty} (C_1 + C_2 + C_3)(t), \quad (\text{B18})$$

where the functions C_1 , C_2 , and C_3 read

$$C_1(t) = \int \int du ds \chi(t - u) \chi_A(t - s) \langle v_A(s) (x^{(0)})^3(u) \rangle, \quad (\text{B19a})$$

$$C_2(t) = \int \int du ds \chi(t - u) \chi_A(t - s) \sqrt{2\varepsilon D_T} \langle \xi_0(s) (x^{(0)})^3(u) \rangle, \quad (\text{B19b})$$

$$C_3(t) = \int \int du ds \chi(t - u) \chi(t - s) \sqrt{2D_T} \langle \xi(s) (x^{(0)})^3(u) \rangle. \quad (\text{B19c})$$

By using Eq. (B5), we deduce

$$\begin{aligned} C_1(t) &= \gamma^3 \int \int du ds \int^u \iiint du_1 du_2 du_3 \chi(t - u) \chi_A(t - s) \\ &\quad \times [\chi_{A1} \chi_{A2} \chi_{A3} \langle v_A(s) v_A(u_1) v_A(u_2) v_A(u_3) \rangle \\ &\quad + 6\varepsilon D_T \chi_{A1} \chi_{A2} \chi_{A3} \langle v_A(s) v_A(u_1) \rangle \langle \xi_0(u_2) \xi_0(u_3) \rangle \\ &\quad + 6D_T \chi_{A1} \chi_{A2} \chi_{A3} \langle v_A(s) v_A(u_1) \rangle \langle \xi(u_2) \xi(u_3) \rangle], \end{aligned} \quad (\text{B20a})$$

$$\begin{aligned} C_2(t) &= \gamma^3 \int \int du ds \int^u \iiint du_1 du_2 du_3 \chi(t - u) \chi_A(t - s) \\ &\quad \times [4(\varepsilon D_T)^2 \chi_{A1} \chi_{A2} \chi_{A3} \langle \xi_0(s) \xi_0(u_1) \xi_0(u_2) \xi_0(u_3) \rangle \\ &\quad + 6\varepsilon D_T \chi_{A1} \chi_{A2} \chi_{A3} \langle \xi_0(s) \xi_0(u_1) \rangle \langle v_A(u_2) v_A(u_3) \rangle \\ &\quad + 12\varepsilon D_T^2 \chi_{A1} \chi_{A2} \chi_{A3} \langle \xi_0(s) \xi_0(u_1) \rangle \langle \xi(u_2) \xi(u_3) \rangle], \end{aligned} \quad (\text{B20b})$$

$$\begin{aligned} C_3(t) = & \gamma^3 \int \int du ds \int \int du_1 du_2 du_3 \chi(t-u) \chi(t-s) \\ & \times [4D_T^2 \chi_1 \chi_2 \chi_3 \langle \xi(s) \xi(u_1) \xi(u_2) \xi(u_3) \rangle \\ & + 6D_T \chi_1 \chi_{A2} \chi_{A3} \langle \xi(s) \xi(u_1) \rangle \langle v_A(u_2) v_A(u_3) \rangle \\ & + 12\epsilon D_T^2 \chi_1 \chi_{A2} \chi_3 \langle \xi(s) \xi(u_1) \rangle \langle \xi_0(u_2) \xi_0(u_3) \rangle]. \end{aligned} \quad (\text{B20c})$$

The non-Gaussianity of the active bursts plays a role in the first term in the bracket of Eq. (B20a). From Eqs. (A3) and (B14), we compute the three contributions of $\langle x^{(0)} x^{(1)} \rangle_{\text{SS}}$,

and we deduce the expression of this steady-state average to leading order in ϵ :

$$\begin{aligned} \langle x^{(0)} x^{(1)} \rangle_{\text{SS}} = & - \left(\frac{T_A}{\epsilon} \right)^2 \frac{b p k^2 \tau}{k_p (k + k_p)^3 [k_p \tau + k(\tau + \tau_d)]} \\ & \times \left[2 + \left(\frac{k}{k_p} \right)^2 \frac{5\tau + 2\tau_d}{2\tau} + \frac{k}{k_p} \frac{9\tau + 4\tau_d}{2\tau} \right]. \end{aligned} \quad (\text{B21})$$

Finally, the expression of E_{Q1} is given by the primitive of the above formula with respect to k_p , thus being defined up to a constant.

-
- [1] É. Fodor, M. Guo, N. S. Gov, P. Visco, D. A. Weitz, and F. van Wijland (unpublished).
 - [2] P. Bursac, G. Lenormand, B. F. M. Oliver, D. A. Weitz, V. Viasnoff, J. P. Butler, and J. J. Fredberg, *Nat. Mater.* **4**, 557 (2005).
 - [3] T. Toyota, D. A. Head, C. F. Schmidt, and D. Mizuno, *Soft Matter* **7**, 3234 (2011).
 - [4] B. Stuhrmann, M. Soares e Silva, M. Depken, F. C. MacKintosh, and G. H. Koenderink, *Phys. Rev. E* **86**, 020901 (2012).
 - [5] C. Wilhelm, *Phys. Rev. Lett.* **101**, 028101 (2008).
 - [6] D. Robert, T.-H. Nguyen, F. Gallet, and C. Wilhelm, *PLoS ONE* **5**, e10046 (2010).
 - [7] T. Gisler and D. A. Weitz, *Phys. Rev. Lett.* **82**, 1606 (1999).
 - [8] M. Yanai, J. P. Butler, T. Suzuki, H. Sasaki, and H. Higuchi, *Am. J. Physiol. Cell Physiol.* **287**, C603 (2004).
 - [9] N. Desprat, A. Richert, J. Simeon, and A. Asnacios, *Biophys. J.* **88**, 2224 (2005).
 - [10] M. Balland, N. Desprat, D. Icard, S. Féreol, A. Asnacios, J. Browaeys, S. Hénon, and F. Gallet, *Phys. Rev. E* **74**, 021911 (2006).
 - [11] D. Mizuno, C. Tardin, C. F. Schmidt, and F. C. MacKintosh, *Science* **315**, 370 (2007).
 - [12] L. F. Cugliandolo, J. Kurchan, and G. Parisi, *J. Phys. I* **4**, 1641 (1994).
 - [13] E. Ben-Isaac, Y. K. Park, G. Popescu, F. L. H. Brown, N. S. Gov, and Y. Shokef, *Phys. Rev. Lett.* **106**, 238103 (2011).
 - [14] J. Prost, J.-F. Joanny, and J. M. R. Parrondo, *Phys. Rev. Lett.* **103**, 090601 (2009).
 - [15] T. Betz, M. Lenz, J.-F. Joanny, and C. Sykes, *Proc. Natl. Acad. Sci. USA* **106**, 15320 (2009).
 - [16] F. Gallet, D. Arcizet, P. Bohec, and A. Richert, *Soft Matter* **5**, 2947 (2009).
 - [17] K. Kanazawa, T. Sagawa, and H. Hayakawa, *Phys. Rev. E* **90**, 012115 (2014).
 - [18] P. Bohec, F. Gallet, C. Maes, S. Safaverdi, P. Visco, and F. van Wijland, *Europhys. Lett.* **102**, 50005 (2013).
 - [19] C. Maes, S. Safaverdi, P. Visco, and F. van Wijland, *Phys. Rev. E* **87**, 022125 (2013).
 - [20] T. Harada and S.-i. Sasa, *Phys. Rev. Lett.* **95**, 130602 (2005).
 - [21] N. E. Hill, *Proc. Phys. Soc.* **82**, 723 (1963).
 - [22] V. F. Sears, *Proc. Phys. Soc.* **86**, 953 (1965).
 - [23] W. T. Coffey and Y. P. Kalmykov, *The Langevin Equation: With Applications to Stochastic Problems in Physics, Chemistry and Electrical Engineering*, 3rd ed. (World Scientific, Singapore, 2012).
 - [24] T. G. Mason, *Rheol. Acta* **39**, 371 (2000).
 - [25] T. G. Mason and D. A. Weitz, *Phys. Rev. Lett.* **74**, 1250 (1995).
 - [26] K. Kanazawa, T. Sagawa, and H. Hayakawa, *Phys. Rev. Lett.* **108**, 210601 (2012).
 - [27] K. Kanazawa, T. Sagawa, and H. Hayakawa, *Phys. Rev. E* **87**, 052124 (2013).
 - [28] M. Guo, A. J. Ehrlicher, M. H. Jensen, M. Renz, J. R. Moore, R. D. Goldman, J. Lippincott-Schwartz, F. C. Mackintosh, and D. A. Weitz, *Biophys. J.* **105**, 1562 (2013).
 - [29] A. Brut, A. Arakelyan, A. Petrosyan, S. Ciliberto, R. Dillenschneider, and E. Lutz, *Nature (London)* **483**, 187 (2012).
 - [30] E. Sevick, R. Prabhakar, S. R. Williams, and D. J. Searles, *Annu. Rev. Phys. Chem.* **59**, 603 (2008).
 - [31] A. Rahman, *Phys. Rev.* **136**, A405 (1964).
 - [32] K. Sekimoto and S.-i. Sasa, *J. Phys. Soc. Jpn.* **66**, 3326 (1997).
 - [33] K. Sekimoto, *J. Phys. Soc. Jpn.* **66**, 1234 (1997).
 - [34] C. W. Gardiner, *Handbook of Stochastic Methods* (Springer, Berlin, 2004).
 - [35] F. Gittes, B. Schnurr, P. D. Olmsted, F. C. MacKintosh, and C. F. Schmidt, *Phys. Rev. Lett.* **79**, 3286 (1997).
 - [36] A. W. C. Lau, B. D. Hoffmann, A. Davies, J. C. Crocker, and T. C. Lubensky, *Phys. Rev. Lett.* **91**, 198101 (2003).
 - [37] S. Toyabe, H.-R. Jiang, T. Nakamura, Y. Murayama, and M. Sano, *Phys. Rev. E* **75**, 011122 (2007).
 - [38] B. Lander, J. Mehl, V. Bickle, C. Bechinger, and U. Seifert, *Phys. Rev. E* **86**, 030401 (2012).
 - [39] M. Baiesi and C. Maes, *New J. Phys.* **15**, 013004 (2013).
 - [40] D. A. Sivak and G. E. Crooks, *Phys. Rev. Lett.* **108**, 190602 (2012).
 - [41] T. Hatano and S.-i. Sasa, *Phys. Rev. Lett.* **86**, 3463 (2001).
 - [42] P. R. Zulkowski, D. A. Sivak, G. E. Crooks, and M. R. DeWeese, *Phys. Rev. E* **86**, 041148 (2012).
 - [43] E. Barkai, Y. Garini, and R. Metzler, *Phys. Today* **65**, 29 (2012).
 - [44] F. Hfling and T. Franosch, *Rep. Prog. Phys.* **76**, 046602 (2013).

Chapter 4

Colloidal tracers in living melanoma cells

We present in this Chapter measurements of the spontaneous fluctuations and response of sub-micron colloidal tracers injected in living melanoma cells. On the basis of the minimal model presented in Chapter 3, we are able to recapitulate the observed fluctuations at the level of the whole distribution of displacement. Besides, we demonstrate that our model is consistent with the measured spectrum of the active forces stemming from the intracellular nonequilibrium processes. It allows us to characterize the ensuing nonequilibrium fluctuations in terms of time and energy scales, and to assess quantitatively the effect of various cell treatments on these fluctuations.

Activity-driven fluctuations in living cells

We investigate the regulation of nonequilibrium fluctuations by active intracellular components by considering cells in three different conditions. First, we use untreated cells as a control. Second, a specific type of motor, the myosin-II motors which gather into double headed myosin filaments, is inhibited by the addition of blebbistatin. Third, the whole cell is depleted in ATP, thereby depleting the main fuel of nonequilibrium fluctuations in the system. We present in Fig. 4.1 typical trajectories of colloidal tracers injected in the cells for the three conditions. The tracer trajectories in control and blebbistatin treated cells exhibit large displacements on top of the fluctuations of small amplitude. Yet, the amplitude of the directed events is reduced in blebbistatin treated cells with respect to control. By contrast, the tracers remain confined in a local volume of the cell in the ATP depleted case. To provide a clear relation between the existence of large displacement and the nonequilibrium nature of the dynamics, we compute the effective temperature in each condition. It coincides with the bath temperature at large frequencies in the three cases, as expected. It diverges at small frequencies for control and blebbistatin treated cells, showing that the nonequilibrium fluctuations drive the dynamics far from equilibrium in this regime. By contrast, it stays approximately constant at every frequency in the ATP depleted case, showing that the cell can not be distinguished from an equilibrium system for this condition. As a result, it leads us to regard the ATP depleted case as an equilibrium reference.

The response function is measured at the subcellular scale by using optical tweezers. In the three cases, the elastic modulus exhibits a weak dependence on frequency, and it has a higher value compared with the viscous modulus at every frequency. It follows that we approximate the cell as a purely elastic material in the frequency window of measurement. In that respect, the active cage model presented in Chapter 3, for which memory effects are neglected, can be used to recapitulate the measured fluctuations. The MSD is constant at short times for the three conditions, as a signature of the short time confinement. A diffusive regime sets in at large times for control and blebbistatin treated cells, with a reduced diffusion coefficient in the blebbistatin treated case, whereas it stays approximately constant in the ATP depleted case. When comparing this result with the prediction of our model, as presented in Chapter 3, it appears that the short time thermal diffusion is out of the measurement window. We use the analytic MSD to extract two active parameters: the mean persistence time, and the active temperature. Both in the control and blebbistatin treated case, the active temperature is lower than bath temperature. This result may appear contradictory with the active fluctuations powering displacement over larger distances compared with the motion under purely thermal fluctuations. Yet, the active and bath temperature control two distinct processes: the former quantifies the free diffusion at large times, the

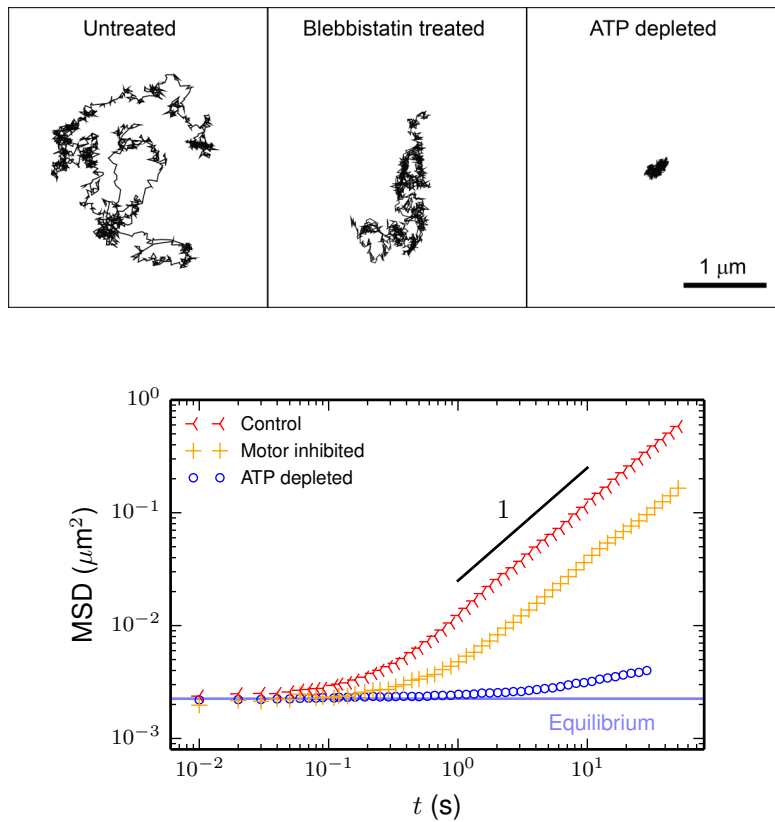


Figure 4.1 – Top: Typical trajectories of colloidal tracers in living melanoma cells under three conditions: ATP depleted cells, blebbistatin treated cells for which the activity of myosin-II motors is inhibited, and untreated cells as a control. Bottom: Mean square displacement as a function of time for the three conditions. Taken from paper [B](#).

latter is associated with the confined motion at short times. In that respect, a nonzero value of the active temperature, even small compared with the bath temperature, is sufficient to overcome the local confinement.

With the same parameters as the one extracted from the MSD, we reproduce theoretically the measured spectrum of the active force. This spectrum is extracted from the combination of spontaneous fluctuations and response measurements. As a result, the agreement with our prediction without any free parameters supports the validity of the simplified intracellular mechanics. Besides, it demonstrates that the main contribution of the active force is indeed mediated by the network, as accounted for by the active cage motion in our model. This in contrast with previous works which considered that the active force was acting directly on the tracer, for which the predicted active force spectrum did not exhibit any divergence at low frequency [51, 83]. Overall, the good agreement of the MSD and active spectrum data with our prediction corroborates the consistency of the underlying phenomenological picture, in which the active temperature not only characterizes tracer statistics at large times, it also quantifies the typical amplitude of fluctuations ensuing from the intracellular activity. Eventually, we demonstrate that our model is sufficient to reproduce the time evolution of the whole distribution of displacement. It leads us to quantify the mean waiting time between active bursts, thus providing a complete characterization of these fluctuations in control and blebbistatin treated cells within our model.

The data analysis is presented in details and discussed in paper B reproduced below.

Activity-driven fluctuations in living cells

É. FODOR^{1(a)}, M. GUO^{2(a)}, N. S. GOV³, P. VISCO^{1(b)}, D. A. WEITZ² and F. VAN WIJLAND¹

¹ Laboratoire Matière et Systèmes Complexes, UMR 7057 CNRS/P7, Université Paris Diderot
10 rue Alice Domon et Léonie Duquet, 75205 Paris cedex 13, France

² School of Engineering and Applied Sciences, Harvard University - Cambridge, MA 02138, USA

³ Department of Chemical Physics, Weizmann Institute of Science - 76100 Rehovot, Israel

received 7 April 2015; accepted in final form 22 May 2015

published online 11 June 2015

PACS 87.16.dj – Dynamics and fluctuations

PACS 87.16.ad – Analytical theories

PACS 87.16.Uv – Active transport processes

Abstract – We propose a model for the dynamics of a probe embedded in a living cell, where both thermal fluctuations and nonequilibrium activity coexist. The model is based on a confining harmonic potential describing the elastic cytoskeletal matrix, which undergoes random active hops as a result of the nonequilibrium rearrangements within the cell. We describe the probe's statistics and we bring forth quantities affected by the nonequilibrium activity. We find an excellent agreement between the predictions of our model and experimental results for tracers inside living cells. Finally, we exploit our model to arrive at quantitative predictions for the parameters characterizing nonequilibrium activity, such as the typical time scale of the activity and the amplitude of the active fluctuations.



Copyright © EPLA, 2015

Actin filaments are involved in a number of functions including cell motility, adhesion, gene expression, and signalling. When fueled by ATP supply, myosin motors advance along these filaments by performing a directed stochastic motion. By tracking the trajectory of a micron-size probe embedded within the cytoskeletal network, and by subjecting it to microrheology experiments, one can hope to access and understand some of the properties of the nonequilibrium activity inside the cytoskeletal network. Experiments were first carried out in actin gels without molecular motors, known as *passive gels* [1–5]. Some progress in the experimental field has provided new results for tracers attached to the cortex of living cells [6], and also for *in vitro* actin gels [7,8]. In such gels, called *active gels*, the tracer dynamics exhibits large excursions corresponding to directed motion events, in addition to the thermal fluctuations already observed in passive gels. Due to the active processes, the actin network fluctuations comprise a strongly nonequilibrium component. Experimentally, the out-of-equilibrium nature of such activity has been evidenced by the violation of the fluctuation dissipation theorem (FDT) [9–11]. To account

for nonequilibrium activity, a generalization of the FDT has been developed introducing a frequency-dependent effective temperature [12–14]. This generalization is based on a description of tracers dynamics at a mesoscopic scale, which can be described using a generalized Langevin equation [15–17]. At a macroscopic scale, the dynamics of actomyosin networks have been described via hydrodynamic treatments [18] or polymer theory [19,20].

In what follows, we present results of microrheology experiments in the cytoplasm of living cells, which are characterized by a highly nonequilibrium activity. Along with experiments, we propose a model which mixes simple but nontrivial rheology with random fluctuations due to active processes inside the cell. We carry out a comparison with experimental data, which allows us to directly determine some microscopic mechanisms that drive active fluctuations inside the cell. We demonstrate that our quantitative estimation of the nonequilibrium active features is consistent with different kinds of experimental measurements, thus supporting the overall consistency of our model.

We inject sub-micron colloidal tracers in the cytoplasm of living A7 cells, and track a two-dimensional projection of their fluctuating (3-D) motion with confocal microscopy [21]. We observe some directed motion events in the tracers' trajectories in addition to the thermal

(a)These authors contributed equally to this work.

(b)E-mail: pao.lo.visco@univ-paris-diderot.fr (corresponding author)

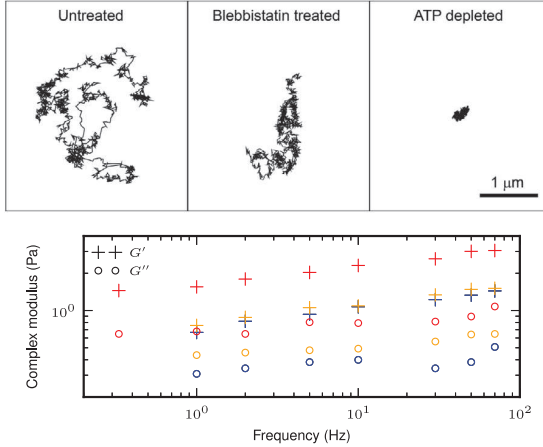


Fig. 1: (Color online) Top: typical trajectories of 200 nm PEG coated beads in A7 cells under three conditions: control, 10 μM blebbistatin treatment, ATP depletion. The trajectory length is about 2 min. Bottom: elastic storage modulus G' (+) and loss modulus G'' (o) from active microrheology experiments in untreated (red), blebbistatin treated (orange), and ATP depleted (blue) A7 cells.

fluctuations of small amplitudes (fig. 1), as already reported in synthetic active gels [7]. To investigate the role of biological activity in the intracellular mechanics, we subject cells to two treatments. We inhibit myosin II motors by adding 10 μM of blebbistatin to the culture medium, and we deplete cells of ATP through addition of 2 mM sodium azide and 10 mM of 2-deoxyglucose. We extract the one-dimensional mean square displacement (MSD) from the spontaneous motion of tracers for different radius sizes $a = \{50, 100, 250\}$ nm. We present the MSD multiplied by a for the control, blebbistatin and ATP depleted conditions in fig. 2(a), showing that the MSD scales like $1/a$. The small time MSD is constant in the three conditions, while the large time behavior is diffusive, apart for ATP depleted cells, where it remains almost constant. Since the time evolution of the MSD is qualitatively similar for tracers of different sizes, we deduce that the tracers are bigger than the mesh size of the cytoskeletal network, thus allowing us to consider that they evolve in a continuous medium in the first approximation.

We measure the mechanical properties of the cytoplasm *via* active microrheology method by using optical tweezers [22]. We impose a sinusoidal oscillation on a particle with diameter 0.5 μm within the cytoplasm. From the resultant displacement of the bead, we extract the complex modulus $G^* = 1/(6\pi a\chi)$, where χ is the Fourier response function. It reveals that it weakly depends on frequency, and that the elastic contribution is significantly larger than the dissipative one (fig. 1), in agreement with previous results [22,23]. Moreover, we do not observe a significant change in the cytoplasmic mechanical property according to active processes. The cytoplasm is still

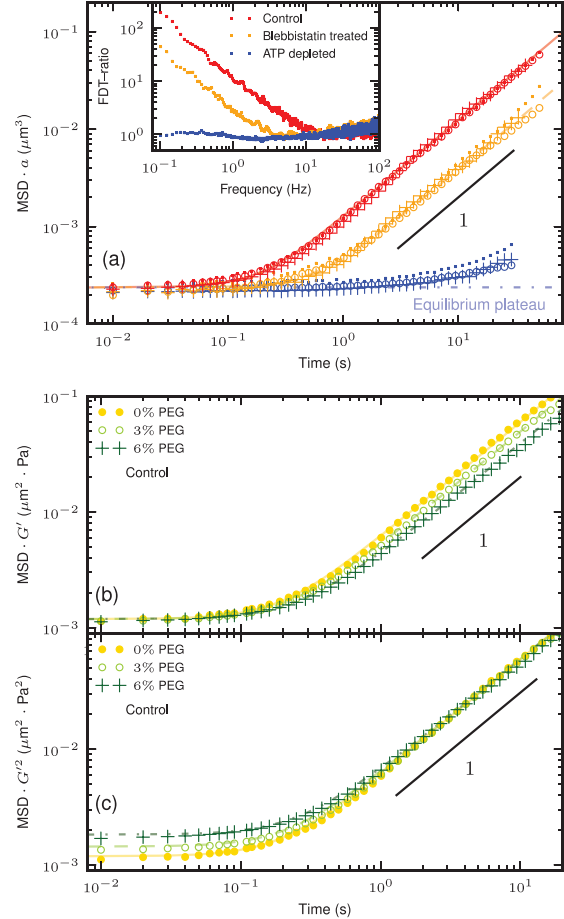


Fig. 2: (Color online) (a) Time evolution of the one-dimensional mean square displacement scaled with the tracer radius $a = 50$ (+), 100 (o) and 250 nm (small dots) for control (red), blebbistatin treated (orange), and ATP depleted (blue) cells, and the corresponding best-fitting curves (eq. (2)): solid, dashed, and dot-dashed line, respectively. Inset: FDT-ratio as a function of frequency. It equals 1 in ATP depleted cells as for an equilibrium system, and it deviates from it in the two other conditions at small frequency showing that nonequilibrium processes drive the dynamics in this regime. (b) Time evolution of the MSD scaled with G' measured with tracers of radius $a = 100$ nm in control cells. The G' value increases with the percentage of PEG introduced in the cell: 0% (yellow ●), 3% (light green ○), and 6% (dark green +). The best-fit curves are shown as solid, dashed, and dot-dashed lines, respectively. The short-time scale plateau scales like $1/G'$. (c) Time evolution of the MSD times G'^2 . The large-time diffusive part scales as $1/G'^2$.

mainly elastic in blebbistatin treated and ATP depleted cells, with a storage modulus being twice as small as in untreated cells where it equals approximately 2 Pa.

To quantify the departure from equilibrium, we extract the FDT-ratio which compares the active microrheology measurement with the random intracellular motion visualized by tracer particles [9–11]. It is defined in terms of the position power spectrum \tilde{C} and the imaginary part

of the Fourier response function χ'' as FDT-ratio(ω) = $-\omega\tilde{C}(\omega)/[2\chi''(\omega)k_B T]$, where T is the bath temperature. It equals 1 for an equilibrium system, and deviates from it otherwise. The control and blebbistatin treated cells are out-of-equilibrium, whereas the effect of the nonequilibrium processes are negligible in ATP depleted cells (inset in fig. 2(a)). This supports that the nonequilibrium processes hibernate in the latter as long as no ATP supply is provided, suggesting that there is an equilibrium reference state where the tracer particle is trapped in an elastic cytoskeletal network. Given that we cannot rely on equilibrium physics to describe the tracer's dynamics in the two other conditions, we offer a new model to characterize its nonequilibrium properties.

We vary experimentally the elastic modulus G' by adding various amount of 300 dalton polyethylene glycol (PEG) into the cell culture medium¹. This results in an osmotic compression on the cell, so that G' increases with the amount of PEG applied [24]. We report in figs. 2(b), (c) the MSD data multiplied by G' and G'^2 for different values of G' . It appears the value of the small time plateau scales as $1/G'$ while the long-time diffusion constant scales as $1/G'^2$.

The cytoskeleton acts as a thermostat for the tracer particle. Provided that inertial effects are negligible in the intracellular environment, we model the dynamics of the tracer's position \mathbf{r} by means of an overdamped Langevin equation. We use a harmonic approximation to account for the interaction of the tracer with the surrounding network. The main new ingredient of our model lies in expressing the effect of nonequilibrium activity. We postulate that the underlying action of the active processes induces local rearrangements of the network, resulting in an active force applied on the tracers. As an example of such nonequilibrium processes, the activity of myosin II motors can slide cytoskeletal filaments past each other leading to a local deformation of the network [7]. To account for the directed motion events observed in our experimental trajectories, we consider that the active force proceeds by a sequence of rapid ballistic jumps followed by quiescent periods. It remains constant during intervals of average quiescence time τ_0 , when the tracer is only subjected to thermal fluctuations, and it varies during a persistence time of order τ by a quantity $f_A = f\hat{\mathbf{n}}$, where $\hat{\mathbf{n}}$ is a random direction in the three-dimensional space. We assume that the persistence and quiescence times are exponentially distributed variables as observed in synthetic active gels [7,8,25], and that they do not depend on the network and tracer properties. Putting these ingredients together, we arrive at the equation for x , the one-dimensional projection of \mathbf{r} ,

$$\gamma \frac{dx}{dt} = -kx + \xi + f_A, \quad (1)$$

¹After the stress, cells are allowed to equilibrate for 10 min at 37 °C and 5% CO₂, before we perform the imaging or optical-tweezer measurement. The cell size and mechanics equilibrate in 2 min after adding PEG based on our imaging and previous studies [24].

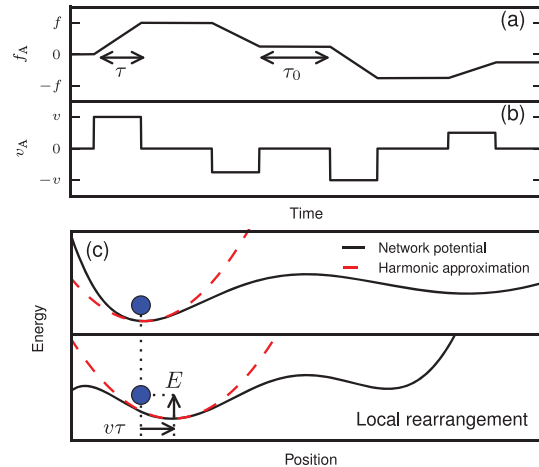


Fig. 3: (Color online) Typical realization of (a) the active force f_A , and (b) the corresponding active bursts v_A . f_A is constant over a quiescence time of typical value τ_0 , and varies linearly with a slope uniformly distributed in $[-f, f]$ during a persistence time of order τ . v_A is proportional to the time derivative of f_A . (c) Schematic representation of the energetic landscape rearrangement due to nonequilibrium activity and its modeling using the active burst applied on the local minimum. We depict the network potential with a black solid line, the harmonic approximation with a dashed red line, and the tracer particle with a filled blue circle. Nonequilibrium activity leads to a displacement $v\tau$ of the potential, resulting in an energy gain $E \simeq k(v\tau)^2$ for the tracer.

where ξ is a zero mean Gaussian white noise with correlations $\langle \xi(t)\xi(t') \rangle = 2\gamma k_B T \delta(t-t')$, and f_A is a random force with typical realization described in fig. 3(a). The spring constant of the surrounding network is k , and γ is the friction coefficient of the environment. Our model is associated with a Fourier response function $\chi = 1/(k + i\omega\gamma)$, from which we deduce that the complex modulus is of the form $G^* = 1/(6\pi a\chi) = k/(6\pi a) + i\omega\eta$, where η is the viscosity of the fluid surrounding the tracer [17,26]. We neglect the weak frequency dependence of the real part G' as determined from active microrheology measurements, so that the spring constant is directly given by $k = 6\pi a G'$, as already reported in other complex fluids with similar elastic behavior [26]. Stokes' law ensures that γ is independent of G' , and $\gamma \propto a$.

To illustrate our model with an immediate physical picture, we introduce the variable $\mathbf{r}_0 = \mathbf{f}_A/k$ which we regard as the position of the local minimum of the potential in which the tracer is trapped. The local rearrangements of the network due to nonequilibrium activity result in a shift of the local minimum the tracer sits in. Thus, this position has a dynamics of its own given by a random active burst \mathbf{v}_A in which a burst $v\hat{\mathbf{n}}$ is felt during the persistence time, while it equals zero during the quiescence time (fig. 3(b)). The active force projection is simply related to the active burst projection as $d\mathbf{f}_A/dt = kv_A$. We assume that the typical variation f of the active force is independent of the network properties, whereas the active

burst amplitude $v = f/(k\tau)$ depends on the properties of the cytoskeletal network *via* k .

From the Fourier transform of eq. (1), we compute the position autocorrelation function $C(t) = \langle x(t)x(0) \rangle$, and then deduce the one-dimensional MSD as $\langle \Delta x^2 \rangle(t) = 2(C(0) - C(t))$. We denote the thermal contribution to the MSD by $\langle \Delta x_T^2 \rangle$, and the MSD when the particle is only subjected to motor activity by $\langle \Delta x_A^2 \rangle$, so that: $\langle \Delta x^2 \rangle = \langle \Delta x_T^2 \rangle + \langle \Delta x_A^2 \rangle$. The thermal MSD is the same as for the Ornstein-Uhlenbeck process, and we compute the active contribution in terms of the parameters characterizing the active force:

$$\langle \Delta x_T^2 \rangle(t) = \frac{2k_B T}{k} \left(1 - e^{-t/\tau_r} \right), \quad (2a)$$

$$\begin{aligned} \langle \Delta x_A^2 \rangle(t) &= \frac{2k_B T_A/k}{1 - (\tau/\tau_r)^2} \left[\left(\frac{\tau}{\tau_r} \right)^3 \left(1 - e^{-t/\tau} - \frac{t}{\tau} \right) \right. \\ &\quad \left. + e^{-t/\tau_r} + \frac{t}{\tau_r} - 1 \right], \end{aligned} \quad (2b)$$

where $\tau_r = \gamma/k$ is a microscopic relaxation time scale. In the passive case, *i.e.* when $T_A = 0$, it saturates to the value $2k_B T/k$ within a time τ_r as predicted by the equipartition theorem, meaning that the tracer is confined in the cytoskeleton. The active force represents the random fluctuations of the cytoskeletal network induced by the nonequilibrium activity. With such a force, the MSD exhibits a plateau at the equilibrium value corresponding to a transient elastic confinement at times $\tau_r \ll t \ll \tau$, and then has a diffusion-like growth on longer times with coefficient $2k_B T_A/\gamma$. Provided that $k \propto G'$, it follows that the equilibrium plateau scales like $1/G'$, as we observe experimentally (fig. 2(b)). The energy scale $k_B T_A = \gamma(v\tau)^2/[3(\tau + \tau_0)]$ defines an active temperature, which is related to the amplitude of the active fluctuations as defined by the active burst correlations $\langle v_A(t)v_A(0) \rangle = k_B T_A e^{-|t|/\tau}/(\tau\gamma)$. The independence of f and τ with respect to G' yields $v \propto 1/G'$, from which we deduce that the long-time diffusion coefficient scales as $1/G'^2$, in agreement with our measurements (fig. 2(c)).

On the basis of our phenomenological picture where the nonequilibrium dynamics is driven by an active remodelling of the cytoskeletal network, we propose a physical argument for the scaling of the MSD with the tracers' size a presented in fig. 2(a). As presented above, we first assume that k and γ scale like a . Within our model, the active burst represents the activity-driven network deformation and reorganization, which result in a change of the tracer's local energetic landscape. During a burst event, the local minimum is shifted by a random amount. Regarding this event as instantaneous, the tracer finds itself at a distance of order $v\tau$ from the new local minimum position after each burst. It follows that the typical energy provided by nonequilibrium activity to the particle is $E \simeq k(v\tau)^2$, as depicted in fig. 3(c). We assume that it does not depend on the particle properties, just as τ and τ_0 , thus being independent of the tracer's typical size a .

Since $k \propto a$, we deduce $v \propto 1/\sqrt{a}$, implying that T_A is independent of a . Finally, the relaxation time τ_r is also independent of a , leading to a scaling of the MSD like $1/a$ which agrees with our observation.

We use our analytic expression to fit the MSD data multiplied by a for the three conditions described above. We assume the viscosity of the fluid surrounding the tracer is the cytoplasm viscosity $\eta \sim 10^{-3}$ Pa · s [27], and we deduce the damping coefficient from Stokes' law: $\gamma = 6\pi a\eta$. We estimate the k value from the small time plateau. The only remaining parameters are the ones characterizing nonequilibrium activity: $T_A/T = \{2.8, 0.9\} \times 10^{-3}$, $\tau = \{0.16 \pm 0.03, 0.39 \pm 0.09\}$ s, in control and blebbistatin treated cells, respectively. The estimation error made on T_A/T is of the order of 1% in control, and 0.1% in blebbistatin treated cells.

The amplitude of the active fluctuations is smaller in blebbistatin treated cells, meaning that the inhibition of myosin II motors reduces the proportion of nonequilibrium fluctuations with respect to the thermal ones as expected. Other nonequilibrium processes drive the out-of-equilibrium dynamics in this condition. The typical time scale τ of the persistent motion events is enhanced in blebbistatin treated cells. Assuming that each active burst persists until the stress that accumulates in the network causes the network to locally fail, weaker motors due to the addition of blebbistatin will contract for a longer duration until such a critical stress builds up. Provided that $1/\tau$ is the typical frequency below which the nonequilibrium processes affect the dynamics, this supports that the active fluctuations take over the thermal ones at larger frequencies in the control cells compared with the blebbistatin treated ones. Notice that T_A represents the ability of the tracer to diffuse on long times, and T quantifies here only the motion of the bead at short times when it is trapped within the elastic cytoskeletal network. The fact that we find T_A small compared to T does not mean that the active processes are negligible, as they control entirely the long-time and long-distance diffusion of the tracer. In the absence of activity, the tracer does not diffuse at all and remains trapped in the elastic network.

To characterize the properties of the active force, we focus on the power spectrum of the stress fluctuations, *i.e.* the Fourier transform of the time correlation function $\langle f_A(0)f_A(t) \rangle$ [9,11,15]. We extract the power spectrum of the overall force $f_A + \xi$ as the power spectrum of the position times $(6\pi a|G^*|)^2$ [15]. Provided that the ATP depleted condition is in an equilibrium state, the active force f_A is negligible in these cells and the overall force reduces to the ξ , thus providing a direct measurement of the thermal force spectrum. We remove this equilibrium contribution to the overall spectrum to deduce the active force spectrum in the two other conditions. We observe a $1/\omega^2$ behavior at low frequency as already accounted for on general grounds [9,14,15,28], and the large-frequency curvature hints a crossover to another power law (figs. 4(a), (b)). Our analytic prediction for the active

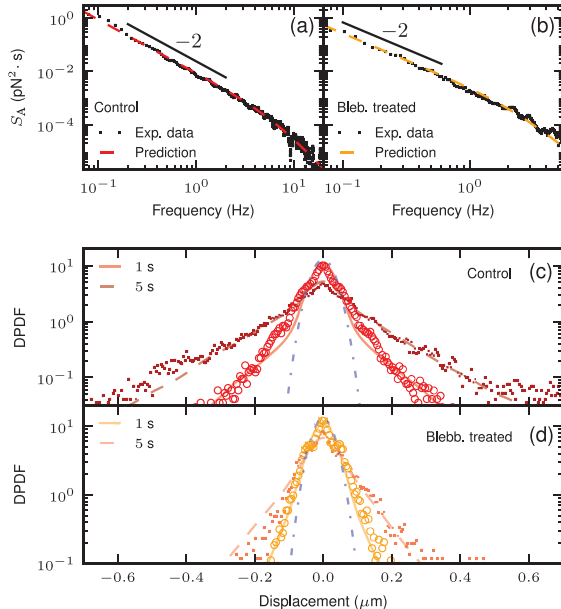


Fig. 4: (Color online) Top: active force spectrum S_A as a function of frequency measured with tracers of radius $a = 250 \text{ nm}$ in (a) control, and (b) blebbistatin treated cells. The experimental data are in black small dots, and the dashed lines correspond to eq. (3) with the parameter values deduced from the best fit of the MSD data. Bottom: probability distribution function of the tracer displacement (DPDF) at two different times: 1 s (○), and 5 s (small dots). The DPDF is measured with tracers of radius $a = 250 \text{ nm}$ in (c) control, and (b) blebbistatin treated cells. We present the corresponding results from numerical simulations of eq. (1) in solid and dashed lines, respectively. The blue dot-dashed line is the corresponding equilibrium Gaussian. The parameter values are the same for the two lag times: (b) $\{T_A/T, \tau, \tau_0, k, \gamma\} = \{2.8 \times 10^{-3}, 0.16 \text{ s}, 2.5 \text{ s}, 8.5 \text{ pN}/\mu\text{m}, 4.7 \times 10^{-3} \text{ pN} \cdot \text{s}/\mu\text{m}\}$, (c) $\{T_A/T, \tau, \tau_0, k, \gamma\} = \{9 \times 10^{-4}, 0.39 \text{ s}, 2.8 \text{ s}, 8.2 \text{ pN}/\mu\text{m}, 4.7 \times 10^{-3} \text{ pN} \cdot \text{s}/\mu\text{m}\}$.

force spectrum reads

$$S_A(\omega) = \frac{1}{(\omega\tau_r)^2} \frac{2\gamma k_B T_A}{1 + (\omega\tau)^2}. \quad (3)$$

It combines properties of the network and parameters characterizing the active force, since the effect of nonequilibrium activity on the tracer is mediated by the network within our model. We recover the divergence as $1/\omega^2$ at low frequency, and we predict a power law behavior $1/\omega^4$ at high frequency, the crossover between the two regimes appearing at $1/\tau$. We compare our prediction with the experimental data by using the best-fit parameters estimated from the MSD data. Without any free parameter, we reproduce the measured spectra (figs. 4(a), (b)). This result is a strong support for our model, in which T_A not only quantifies the long-time diffusion coefficient of the tracers, it is also related to the typical amplitude of the fluctuations generated by the nonequilibrium active force. The study of the high-frequency spectrum calls for new

experiments as it would confirm the validity of our phenomenological picture.

To study in more detail the properties of the active force, we analyze the probability distribution function of the tracer displacement (DPDF). It exhibits a Gaussian behavior at short and long times. In the intermediate regime, we observe a central Gaussian part which matches our equilibrium prediction in the absence of activity, and exponential tails accounting for directed motion events consistent with previous observations in synthetic active gels [7]. Within our model, the non-Gaussian behavior of the DPDF is a direct and unique consequence of the non-Gaussianity of the active force. We ran numerical simulations of the dynamics in eq. (1) to reproduce the time evolution of the DPDF. We set the different parameter values to the one estimated previously, letting us with only one free parameter: the average quiescence time τ_0 . It quantifies the average time between two successive directed motion events, thus controlling the relative importance of the exponential tails with respect to the Gaussian central part. We adjust this parameter by matching the exponential tails observed at different times.

With a fixed τ_0 value, we manage to reproduce the evolution in time of the whole experimental DPDF. This shows that the specific form we choose for the active process is sufficient to reproduce not only the MSD and force spectrum data, but also to account quantitatively for the dynamic non-Gaussian properties of the distribution (figs. 4(c), (d)). We estimate $\tau_0 = \{2.5, 2.8\} \text{ s}$ in control and blebbistatin treated cells, respectively. The extracted values are very similar for the two conditions, showing that the addition of blebbistatin does not affect the typical time over which the tracers are only subjected to thermal fluctuations. It suggests that this time scale is related to the recovery of the network following a large reorganization, thus being barely independent of the activity of the nonequilibrium processes. Notice that the corresponding duty ratio $p_{\text{on}} = \tau/(\tau + \tau_0)$ is smaller in control than in the blebbistatin treated cells: $p_{\text{on}} = \{6, 15\}\%$, respectively. It is a quantitative evidence that the exponential tails are more pronounced in the control condition, namely the proportion of directed motion events is increased. We deduce the value of the typical active burst amplitude: $v = \{0.86, 0.22\} \mu\text{m/s}$ in control and blebbistatin treated cells for $a = 250 \text{ nm}$, which are compatible with velocity scales observed in [29].

Microrheology methods have become a standard technique to explore cellular activity in living organisms [30]. In this work, we introduce a new model for characterizing the motion of a tracer in a living cell. This model explicitly accounts for the elastic behavior of the cytoskeletal network and successfully combines it with a description of the cellular *active force* — a well-defined non-Gaussian colored process. By analyzing the MSD data, we quantify two essential features of this force: its strength, and the typical time scale over which it is felt. Our model goes beyond previous modeling which treated the nonequilibrium activity

as a random noise with unprescribed characteristics [15]. In a previous work, activity was modeled as a trichotomous noise acting directly on the particle [12], whereas such activity is mediated by the surrounding network within our new proposal. The present model combines the short-time confined behavior with a long-time free diffusion which is driven by the active force, and recovers all the main experimental results. The model applies as long as we are in the regime of simple viscoelastic behavior. Dressing our model with a more realistic rheology, *e.g.*, with a power law behavior for the complex modulus, usually observed in cell rheology [31], is conceptually straightforward as a future elaboration of the model. Further generalization of our model could be used to describe active fluctuations in other nonequilibrium (living or mechanically driven) systems that exhibit similar behavior [7,32,33].

We acknowledge several useful discussions with JULIEN TAILLEUR and FRANÇOIS GALLET. NSG gratefully acknowledges funding from the Israel Science Foundation (grant No. 580/12).

REFERENCES

- [1] HOU L., LUBY-PHELPS K. and LANNI F., *J. Cell Biol.*, **110** (1990) 1645.
- [2] JONES J. D. and LUBY-PHELPS K., *Biophys. J.*, **71** (1996) 2742.
- [3] SANABRIA H. and WAXHAM M. N., *J. Phys. Chem. B*, **114** (2010) 959.
- [4] APGAR J., TSENG Y., FEDOROV E., HERWIG M. B., ALMO S. C. and WIRTZ D., *Biophys. J.*, **79** (2000) 1095.
- [5] TSENG Y., KOLE T. P., LEE S.-H. J. and WIRTZ D., *Curr. Opin. Colloid Interface Sci.*, **7** (2002) 210.
- [6] BURSAC P., LENORMAND G., OLIVER B. F. M., WEITZ D. A., VIASNOFF V., BUTLER J. P. and FREDBERG J. J., *Nat. Mater.*, **4** (2005) 557.
- [7] TOYOTA T., HEAD D. A., SCHMIDT C. F. and MIZUNO D., *Soft Matter*, **7** (2011) 3234.
- [8] STUHRMANN B., SOARES E SILVA M., DEPKEN M., MACINTOSH F. C. and KOENDERINK G. H., *Phys. Rev. E*, **86** (2012) 020901.
- [9] MIZUNO D., TARDIN C., SCHMIDT C. F. and MACINTOSH F. C., *Science*, **315** (2007) 370.
- [10] BETZ T., LENZ M., JOANNY J.-F. and SYKES C., *Proc. Natl. Acad. Sci. U.S.A.*, **106** (2009) 15320.
- [11] GALLET F., ARCIZET D., BOHEC P. and RICHERT A., *Soft Matter*, **5** (2009) 2947.
- [12] BEN-ISAAC E., PARK Y. K., POPESCU G., BROWN F. L. H., GOV N. S. and SHOKEF Y., *Phys. Rev. Lett.*, **106** (2011) 238103.
- [13] PROST J., JOANNY J.-F. and PARRONDO J. M. R., *Phys. Rev. Lett.*, **103** (2009) 090601.
- [14] LOI D., MOSSA S. and CUGLIANDOLO L. F., *Soft Matter*, **7** (2011) 3726.
- [15] LAU A. W. C., HOFFMANN B. D., DAVIES A., CROCKER J. C. and LUBENSKY T. C., *Phys. Rev. Lett.*, **91** (2003) 198101.
- [16] BOHEC P., GALLET F., MAES C., SAFAVERDI S., VISCO P. and VAN WIJLAND F., *EPL*, **102** (2013) 50005.
- [17] MASON T. G. and WEITZ D. A., *Phys. Rev. Lett.*, **74** (1995) 1250.
- [18] JOANNY J.-F. and PROST J., *HFSP J.*, **3** (2009) 94104.
- [19] MACKINTOSH F. C. and LEVINE A. J., *Phys. Rev. Lett.*, **100** (2008) 018104.
- [20] LEVINE A. J. and MACKINTOSH F. C., *J. Phys. Chem. B*, **113** (2009) 3820.
- [21] CUNNINGHAM C., GORLIN J., KWIATKOWSKI D., HARTWIG J., JANMEY P., BYERS H. and STOSSEL T., *Science*, **255** (1992) 325.
- [22] GUO M., EHRLICHER A. J., JENSEN M. H., RENZ M., MOORE J. R., GOLDMAN R. D., LIPPINCOTT-SCHWARTZ J., MACINTOSH F. C. and WEITZ D. A., *Biophys. J.*, **105** (2013) 1562.
- [23] FABRY B., MAKSYM G. N., BUTLER J. P., GLOGAUER M., NAVAJAS D. and FREDBERG J. J., *Phys. Rev. Lett.*, **87** (2001) 148102.
- [24] ZHOU E. H., TREPAT X., PARK C. Y., LENORMAND G., OLIVER M. N., MIJAILOVICH S. M., HARDIN C., WEITZ D. A., BUTLER J. P. and FREDBERG J. J., *Proc. Natl. Acad. Sci. U.S.A.*, **106** (2009) 10632.
- [25] SILVA M. S., STUHRMANN B., BETZ T. and KOENDERINK G. H., *New J. Phys.*, **16** (2014) 075010.
- [26] MASON T. G., *Rheol. Acta*, **39** (2000) 371.
- [27] MASTRO A. M., BABICH M. A., TAYLOR W. D. and KEITH A. D., *Proc. Natl. Acad. Sci. U.S.A.*, **81** (1984) 3414.
- [28] FAKHRI N., WESSEL A., WILLMS C., PASQUALI M., KLOPFENSTEIN D., MACINTOSH F. and SCHMIDT C., *Science*, **344** (2014) 1031.
- [29] RÖDING M., GUO M., WEITZ D. A., RUDEMO M. and SÄRKÄÄ A., *Math. Biosci.*, **248** (2014) 140.
- [30] GUO M., EHRLICHER A., JENSEN M., RENZ M., MOORE J., GOLDMAN R., LIPPINCOTT-SCHWARTZ J., MACINTOSH F. and WEITZ D., *Cell*, **158** (2014) 822.
- [31] KOENDERINK G. H., DOGIC Z., NAKAMURA F., BENDIX P. M., MACINTOSH F. C., HARTWIG J. H., STOSSEL T. P. and WEITZ D. A., *Proc. Natl. Acad. Sci. U.S.A.*, **106** (2009) 15192.
- [32] WEEKS E. R. and WEITZ D. A., *Chem. Phys.*, **284** (2001) 361.
- [33] FODOR E., KANAZAWA K., HAYAKAWA H., VISCO P. and VAN WIJLAND F., *Phys. Rev. E*, **90** (2014) 042724.

Future directions

Recent methods have been developed to investigate the nonequilibrium fluctuations in living cells by injecting micro-size wires. As for spherical tracers, they can serve as probes of the intracellular mechanical properties, and their spontaneous fluctuations reflects the intracellular dynamics. The ability to measure the response by applying a magnetic torque has been proven both in model systems [102, 103] and living cells [66, 70, 104]. Typical realizations of the angular position in living cells exhibit small fluctuations around a preferred orientation, followed by a larger rotation towards a new locally stable orientation, as shown in Fig. 4.2. Overall, such dynamics leads to angular diffusion, as assessed by the mean angular displacement. In that respect, the angular dynamics is reminiscent of the intermittent dynamics already reported at the translational level. To reproduce these observations, one could consider an extended version of the active cage model which would account for the transitions between different orientations of the wire. Such transitions seem to result from the local reorganizations of the surrounding network triggered by motor activity. Moreover, it would be interesting to investigate the coupling between the translational and rotational dynamics of wires injected in living cells on the basis of such a model.

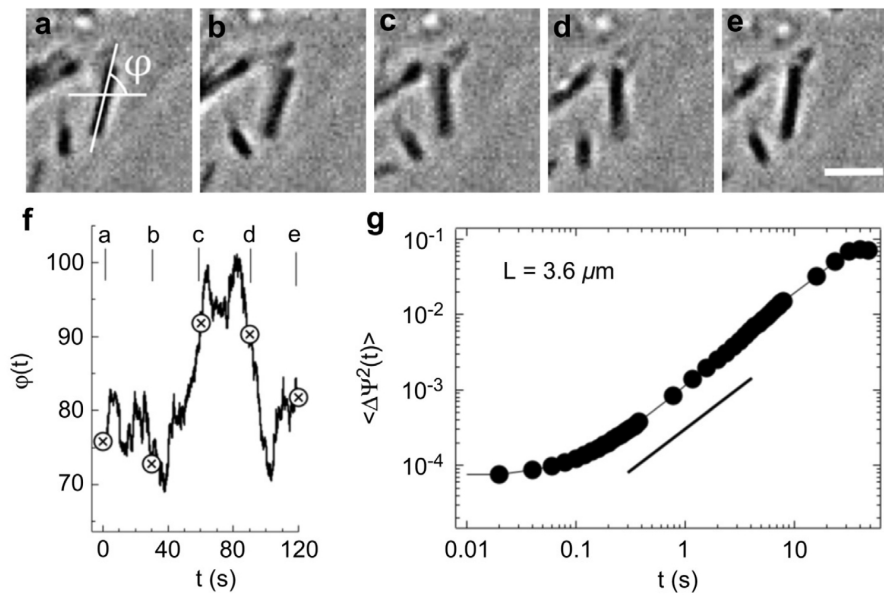


Figure 4.2 – (a-e) Snapshots of wires of size $3.6 \mu\text{m}$ in living cell. Time delay between each picture 30 s. (f) Typical realization of the angular dynamics. (g) Mean-square angular displacement as a function of time. Taken from [104].

Chapter 5

Vesicle dynamics in living mouse oocytes

In this Chapter, we present a detailed analysis of fluctuations inside living mouse oocytes. Vesicles that are already present in the cytoplasm serve as probes of the intracellular dynamics. By contrast to the case of living melanoma cells reported in Chapter 4, the viscoelastic behavior of the mechanics is now crucial to describe the intracellular fluctuations. We now include strong memory effects in the dynamics. We first calibrate the passive parameters of our modeling from active microrheology measurements. Then, we analyze the tracer statistics to extract the features of active fluctuations, to be compared with the kinetics of forces exerted by the molecular motors. Finally, using stochastic thermodynamics, we provide a quantitative insight into the energy fluxes between the nonequilibrium intracellular processes, the vesicles, and the thermostat.

Living mouse oocytes

Oocytes are immature female gametes. They are meant to be fertilized and to grow into a fully functioning state. A number of recent studies have investigated the active transport of the meiotic spindle during cell division [105–108]. They have shed light on the coordination between the cytoskeleton and the motor dynamics during such a process. In that respect, a specific type of motors, the myosin-V motors, have been identified to play a crucial role in the intracellular activity of mouse oocytes. Mouse oocytes are spherical in shape and of typical size a hundred of microns, as shown in Fig. 5.1. They are much bigger than many of the usual cell types which are commonly used for microrheology experiments, such as the living melanoma cells presented in Chapter 4. This represents an advantage with respect to previous studies in several ways. First, one can perform measurements in a region where the interaction between the tracers and the nucleus or the cortex is negligible. This is in contrast with usual cell types for which such interactions, which are both uncontrolled and not characterized, can explain for the high variability of measurements. Second, it allows one to investigate the variability of both the mechanics and the fluctuations across the oocytes. Moreover, oocytes are a rare example of living cells that remain steady up to hours, thus allowing for a large number of repeated measurements in the same system. Furthermore, the use of vesicles already present in the cytoplasm as tracer particles is another asset, since it enables one to probe the intracellular dynamics and mechanics without any invasive treatment which may modify the local environment.

Intracellular mechanics: the role of molecular motors

To explore the regulation of the mechanics and the dynamics by the intracellular components, we consider two types of mutants: oocytes for which the actin filaments nucleated by formin-2 are lacking, and oocytes for which myosin-V motors are de-activated, respectively referred to as Fmn -/- and MyoV(-). Measurements of the mechanics exhibit a strong frequency dependence in contrast with the rheological properties of living melanoma cells discussed in Chapter 4. The viscous modulus behaves as a power-law with an exponent 0.6 which is approximately constant in the frequency window of measurement. The elastic modulus has a similar power-law dependence at large frequencies, and it levels off at small frequencies, as shown in Fig. 5.2. Surprisingly, the mechanics is barely changed in Fmn -/- with respect to control. Likewise, the inhibition of microtubules by nocodazole treatment does not significantly affect rheological properties. By contrast, the viscous and elastic moduli are systematically higher when myosin-V motors are not activated, yet the frequency behavior remains the same. This illustrates the crucial role of molecular motors in the mechanical properties.

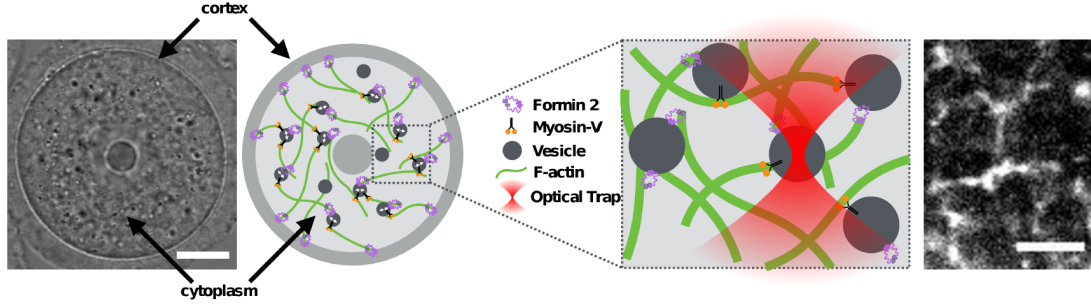


Figure 5.1 – Left: Snapshot of living mouse oocytes. Scalebar 20 μm . Middle: Schematic representation of the intracellular environment and the manipulation of vesicles using optical tweezers. Right: Vizualisation of the intracellular actin network. Scalebar 5 μm . Taken from paper C.

Generalized active cage model: memory effects

The nontrivial frequency dependence of the mechanics suggests that memory effects can not be neglected when describing the intracellular dynamics of living oocytes. To account for such effects, the tracer dynamics is modified following the generalized Langevin approach presented in Chapter 1. The drag force now contains a memory kernel, and the correlations of the thermal fluctuating terms are modified accordingly, as enforced by the FDT. The memory effects arise from the interaction between the tracer and its complex surrounding environment, the cytoskeletal network in the present case. Given that the cage also interacts with the surrounding network, memory effects should also appear in the cage dynamics. Provided that the tracer and the cage interact with the same local environment, we assume that the memory kernel in the cage dynamics is also the one appearing in the tracer dynamics:

$$\begin{aligned} \int_0^t \gamma(t-s) \dot{\mathbf{r}}(s) ds &= -k(\mathbf{r} - \mathbf{r}_0) + \boldsymbol{\xi}, \\ \int_0^t \gamma(t-s) \dot{\mathbf{r}}_0(s) ds &= k\tau_\alpha \mathbf{v}_A. \end{aligned} \quad (5.1)$$

The spectrum of the fluctuating thermal force is entirely determined by the mechanical properties of the system:

$$\langle \xi_\alpha(\omega) \xi_\beta(-\omega) \rangle = 2T\delta_{\alpha\beta} \frac{6\pi a G''(\omega)}{\omega}, \quad (5.2)$$

where we have used the generalized Stokes-Einstein relation: $\gamma(\omega) = 6\pi a G(\omega)/(i\omega)$. On the basis of the mechanical measurements in Fig. 5.2, we choose the memory kernel to take a power-law form as $\gamma(t) = k(\tau_\alpha/t)^\alpha/\Gamma(1-\alpha)$, where Γ is the Gamma

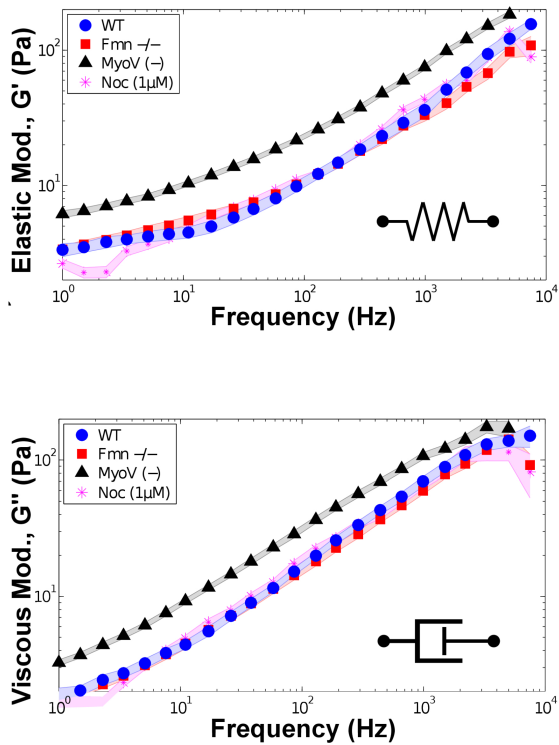


Figure 5.2 – Intracellular rheological properties of living mouse oocytes when microtubules are depolymerized (Noc), when myosin-V motors are de-activated (MyoV $(-)$), when actin filaments are lacking (Fmn $-/-$), and wild type as a control. Elastic (left) and viscous (right) modulus as functions of frequency. Taken from paper C.

function and $\alpha < 1$. We have introduced the passive time scale τ_α that characterizes the dynamics in the absence of active forces. The corresponding complex modulus reads $G^*(\omega) = G_0 [1 + (i\omega\tau_\alpha)^\alpha]$, where $G_0 = k/(6\pi a)$ for spherical tracers of radius a . We recover the case of a simple viscous fluid in the limit $\alpha \rightarrow 1$. Such an expression for the complex modulus is sufficient to reproduce the measured mechanics. One could consider more complex forms, by including several power-law dependence for instance, to propose a more precise description of the rheology. Yet, it would lead to introducing additional parameters, as opposed to our will to retaining a minimal description of the intracellular dynamics. We argue that three independent parameters, namely $\{k, \alpha, \tau_\alpha\}$, already provide us with a good agreement with experimental data. The generalization to other type of mechanics beyond power law behavior is straightforward, as the rheological properties are an input in the dynamics (5.1).

We derive the corresponding evolution in time of the MSD. The thermal MSD can be computed as

$$\langle \Delta x^2(t) \rangle_T = \frac{2T}{k} \left\{ 1 - E_\alpha \left[- \left(\frac{t}{\tau_\alpha} \right)^\alpha \right] \right\}, \quad (5.3)$$

where we have introduced the Mittag Leffler function defined as

$$E_\alpha(z) = \sum_{n=0}^{\infty} \frac{z^n}{\Gamma(1+n\alpha)}. \quad (5.4)$$

The thermal MSD relaxes within a time τ_α to the equilibrium value $2T/k$, and it has a subdiffusive behavior at short times with exponent α . We obtain the active component of the position autocorrelation $C_A(t) = \langle x(t)x(0) \rangle_A$ in the Fourier domain as

$$C_A(\omega) = \frac{\tau_\alpha k^{-1} (\omega\tau_\alpha)^{-2\alpha}}{1 + 2(\omega\tau_\alpha)^\alpha \cos(\pi\alpha/2) + (\omega\tau_\alpha)^{2\alpha}} \frac{2T_A}{1 + (\omega\tau)^2}. \quad (5.5)$$

We deduce that the large time MSD behaves as $t^{2\alpha-1}$: it can be either a superdiffusive or a subdiffusive regime depending on the value of α . Provided that τ and τ_R are well separated, a transient regime with exponent 2α appears between the two anomalous diffusions, as shown in Fig. 5.3. To quantify the departure from equilibrium, we compute the effective temperature as

$$T_{\text{eff}}(\omega) = T + \frac{(\omega\tau_\alpha)^{1-3\alpha}}{\sin(\pi\alpha/2)} \frac{T_A}{1 + (\omega\tau)^2}. \quad (5.6)$$

To recover the bath temperature at large frequencies, as observed experimentally, the condition $\alpha > 1/3$ is to be satisfied. It follows that the effective temperature

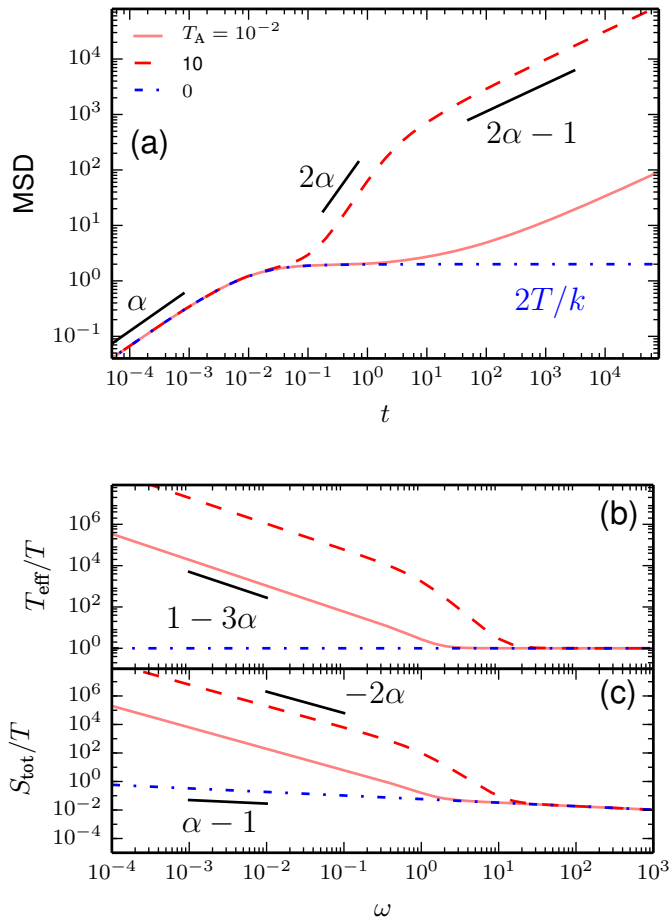


Figure 5.3 – Statistics of tracer displacement in the generalized active cage model with memory effects. (a) Mean-square displacement as a function of time. (b) Effective temperature and (c) total force spectrum as functions of frequencies. Parameters: $\{T, \alpha, \tau_\alpha, k, \tau\} = \{1, 3/4, 10^{-2}, 1, 1\}$.

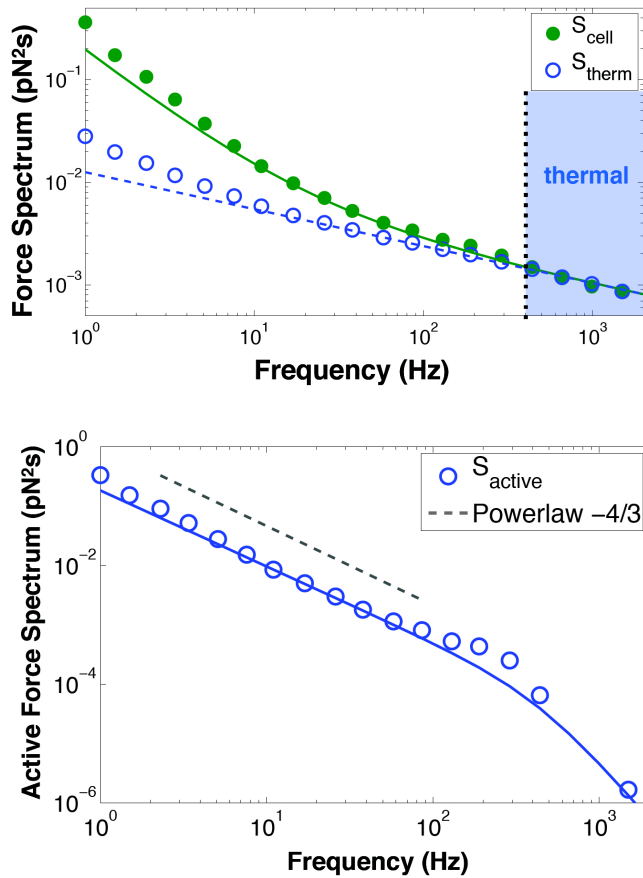


Figure 5.4 – Total and thermal force spectrum (top), and active force spectrum (bottom) extracted from the dynamics of vesicles inside living mouse oocytes. Taken from paper C.

diverges at small frequencies with a negative exponent $1 - 3\alpha$. In the case of the oocytes, the experimental data does not allow us to access this power-law regime. We only obtain measurements in a cross-over regime. To assess experimentally the existence of power-law regimes related to the exponent α of the mechanics, we turn to the power spectrum of the stochastic force applied to the vesicles. It can be split into thermal and active contributions. The thermal spectrum is entirely determined by the mechanical properties, as apparent in Eq. 5.2, yielding

$$S_T(\omega) = 2k\tau_\alpha(\omega\tau_\alpha)^{\alpha-1} \sin\left(\frac{\pi\alpha}{2}\right). \quad (5.7)$$

The active spectrum depends on both the mechanics and the active burst statistics. This is because, in our phenomenological picture, the forces stemming from the nonequilibrium processes are not directly applied to the tracers, they are mediated by the motion of the cage. Given that the cage dynamics is affected by the local rheological properties, as embodied by the memory kernel, the active force $\mathbf{f}_A = k\mathbf{r}_0$ acting on the tracers also depends on these properties. The active spectrum follows as

$$S_A(\omega) = \frac{2k\tau_\alpha}{(\omega\tau_\alpha)^{2\alpha}} \frac{T_A}{1 + (\omega\tau)^2}. \quad (5.8)$$

It diverges faster than the thermal spectrum at low frequencies with exponent -2α . By contrast to the case of the effective temperature, the power law behavior of the active force spectrum is measured over two decades, as shown in Fig. 5.4. It provides a stringent test of our phenomenological picture. We demonstrate that our predictions for the effective temperature and the force spectra reproduce the experimental data. We use the rheological measurements to calibrate the three independent parameters of the complex modulus. It leaves us with only two free parameters to fit the effective temperature and active force spectrum: the mean persistence time and the active temperature. Moreover, we show that we also reproduce the experimental distribution of displacement, thus allowing us to estimate the mean waiting time of active fluctuations. The extracted parameters for the active burst statistics are in close agreement with the one deduced from single motor experiments. It supports the major role of myosin-V motors in the force generation at the basis of active fluctuations in living mouse oocytes.

The data analysis and the interpretation of the extracted parameters is presented in details in paper C reproduced below.

Active mechanics reveal molecular-scale force kinetics in living oocytes

Wylie W. Ahmed^{1,*}, Etienne Fodor^{2,*}, Maria Almonacid^{3,*}, Matthias Bussonnier¹, Marie-Helene Verlhac³, Nir S. Gov⁴, Paolo Visco², Frederic van Wijland², and Timo Betz¹

¹*Institut Curie, Centre de recherche, 11, rue Pierre et Marie Curie, 75005 Paris, France; Sorbonne Universites, Universite Pierre et Marie Curie, Paris, France; Centre National de la Recherche Scientifique, UMR168, Paris, France.*

²*Laboratoire Matiere et Systemes Complexes, UMR 7057, Universite Paris Diderot, 75013 Paris, France*

³*CIRB, College de France, and CNRS-UMR7241 and INSERM-U1050, Equipe Labellisee Ligue Contre le Cancer, Paris F-75005, France.*

⁴*Department of Chemical Physics, Weizmann Institute of Science, 76100 Rehovot, Israel
equally contributing authors

October 29, 2015

Abstract

Unlike traditional materials, living cells actively generate forces at the molecular scale that change their structure and mechanical properties. This nonequilibrium activity is essential for cellular function, and drives processes such as cell division. Single molecule studies have uncovered the detailed force kinetics of isolated motor proteins in-vitro, however their behavior in-vivo has been elusive due to the complex environment inside the cell. Here, we quantify active force generation in living oocytes using in-vivo optical trapping and laser interferometry of endogenous vesicles. We integrate an experimental and theoretical framework to connect mesoscopic measurements of nonequilibrium properties to the underlying molecular-scale force kinetics. Our results show that force generation by myosin-V drives the cytoplasmic-skeleton out-of-equilibrium (at frequencies below 300 Hz) and actively softens the environment. In vivo myosin-V activity generates a force of $F \sim 0.4$ pN, with a power-stroke of length $\Delta x \sim 20$ nm and duration $\tau \sim 300 \mu s$, that drives vesicle motion at $v_v \sim 320$ nm/s. This framework is widely applicable to quantify nonequilibrium properties of living cells and other soft active materials.

1 Introduction

Living cells utilize motor proteins to actively generate force at the molecular scale to drive motion and organization in the crowded intracellular environment [1, 2, 3, 4]. For example, force generation is critical to facilitate the basic tasks of living cells such as spatial organization, motility, division, and vesicle transport. Non-living systems in thermal equilibrium also self-organize, which can often be explained by minimization of energy [5]. However, self-organization is also observed in far-from-equilibrium systems such as driven colloids [6], molecular motors [7], and living cells [8], but the underlying physics is not well understood. Biology is full of many striking examples of far-from-equilibrium self-organization [9, 10].

An interesting example occurs during early vertebrate development, namely oocyte meiosis. Oocytes are immature female gametes that are destined to be fertilized and grow into a fully functioning organism. They are very large cells ($80 \mu m$ in diameter) of spherical geometry with a thick cortex and a well separated cytoplasmic-skeleton (Fig. 1A). The cytoplasmic-skeleton of a mouse oocyte is a composite material that includes actin filaments, microtubules, and intermediate filaments. The actin network is composed of long unbranched filaments polymerized from the surface of vesicles that harbor actin nucleating factors [11]. These vesicles act as nodes to create an inter-connected actin network that is uniform in density throughout the cytoplasm and not polarized [12]; Microtubules are organized in small seeds and do not form long filaments during prophase I [13]; And while it is probable that intermediate filaments are present [14], little is known about their structure or function in mouse oocytes.

The interior of the oocyte is highly dynamic due mainly to an active F-actin network, nucleated by Formin-2 [15, 12]. During their development, oocytes must move large intracellular structures such as the meiotic spindle in preparation for fertilization [16, 17]. When oocytes undergo asymmetric division they actively transport their meiotic spindle to one side of the cell to facilitate splitting of chromosomes while retaining sufficient storage material for development [18]. This requires precise spatial and temporal coordination of the cytoskeleton and molecular motors [19, 12]. Recent work has shown the importance of mechanical processes in oocyte development [19, 12, 20]. Proper spindle positioning requires the oocyte cortex to soften and exhibit plastic deformation [19], and motion of the cytoplasmic actin network is closely regulated by myosin-V motors [12]. Motion of large objects, such as positioning of the spindle[19] or nucleus [20], must be driven by a physical force. In this study, we directly quantify the nonequilibrium activity and extract the molecular-scale forces generated by the actin-myosin-V network that drive cytoplasmic vesicle motion.

From the material science point-of-view, oocytes are an encapsulated polymer droplet filled with colloidal particles actively driven by their surrounding medium. This forms an active soft material that is maintained in a far-from-equilibrium state, providing a well-suited system to study nonequilibrium physics. From the biological point-of-view, oocytes are the precursor for development of all complex organisms, but much of their inner-workings remain a mystery due to lack of quantitative measurements of activity and behavior.

To investigate the nonequilibrium mechanical activity in living cells, it is necessary to independently measure the active molecular force generation and the mechanical properties of the local area to understand how objects navigate the complex intracellular environment. This methodology was introduced to study active processes in hair bundles [21] and stress fluctuations in cells [22]. Subsequent studies utilized this concept to

investigate cross-linked actin-myosin-II networks in reconstituted systems [23] and beads embedded in living cells [24, 25, 26, 27].

We measure the out-of-equilibrium motion (activity) of endogenous vesicles in the largely unexplored cytoplasmic-skeleton of in-vivo mouse oocytes and develop a theoretical model to account for strong viscoelastic effects that quantifies the driving forces. We combine optical tweezer based active microrheology (AMR) and laser-tracking interferometry with our theoretical framework to quantify the in-vivo active mechanics and relate them to the underlying force kinetics. To study the activity of the actin-myosin-V network, we examine the cytoplasmic-skeleton of mouse oocytes in prophase-I. While this network is the key element in nuclear positioning [20], the underlying physical processes are not well understood. By using statistical mesoscopic measurements on in-situ vesicles, and theoretical modeling, we are able to extract the molecular-scale force kinetics (power-stroke duration and length, force, and velocity) of myosin-V. Our results demonstrate that nonequilibrium activity of the actin-myosin-V network is the dominant mechanism that drives active motion and determines the mechanical properties in the oocyte.

2 Results

2.1 Intracellular mechanics of the cytoplasmic-skeleton

To measure the local mechanical properties, we optically trap an endogenous vesicle embedded in the cytoplasmic-skeleton, apply an oscillatory force while measuring its displacement (Fig 1B), and calculate the shear modulus via the Generalized Stokes-Einstein relation [28]. Since vesicles serve as integrated nodes in the cytoplasmic-skeleton, they accurately reflect the mechanics and fluctuations of the network [29]. To calibrate the force on the vesicles we exploit the established observation that high-frequency fluctuations are thermal in origin [30, 24, 31]. AMR directly measures the complex modulus (G^*) characterizing the viscous and elastic resistance of the composite cytoplasmic-skeleton including any contribution from actin, intermediate filaments, microtubules, and other structures present. We find that the cytoplasmic-skeleton of oocytes has strongly viscoelastic properties similar to semiflexible biopolymer networks [32, 33], exhibiting the high-frequency power-law behavior ($G^* \propto f^\alpha$, where $\alpha \sim 0.75$). This mechanical behavior is similar to that of reconstituted networks of entangled actin filaments, but significantly stiffer (Fig 1C). Thus, the cytoplasmic-skeleton in oocytes is strongly frequency dependent, which must be accounted for when modeling its mechanical behavior.

To dissect the mechanical contributions of cytoskeletal filaments in oocytes we first perform AMR on oocytes that lack cytoplasmic actin filaments nucleated by formin-2 (Fmn -/-). We find that the mechanical properties do not change compared to WT, indicating that the actin network does not provide significant mechanical resistance in the oocyte (Fig 2A, B). This behavior is presumably because the actin network in WT oocytes is sparse (Fig 1A, right and Fig. S3) with a mesh size of $5.7 \pm 1.9 \mu\text{m}$ [17]. To check this, we examine in-vitro reconstituted actin networks with a mesh size of $\sim 200 \text{ nm}$ [34], which were found to be an order of magnitude softer than the oocyte (Fig 1C), thus supporting the result that WT oocyte mechanics is not dominated by the actin cytoskeleton. Depolymerizing the microtubules by nocodazole treatment ($1 \mu\text{M}$) does not significantly affect the mechanical properties (Fig. 2A, B). Indicating that microtubules also do not provide significant mechanical resistance in the cytoplasmic-skeleton. This result is expected since prophase I microtubules form small seeds instead of long force-bearing tubule structures [13]. These combined results suggest that there are other force-bearing structures in the cytoplasm of mouse oocytes.

While our results show that actin does not contribute significantly to the mechanical resistance, it is known that the actin-myosin-V meshwork activity plays a critical role for self-organization such as positioning of the meiotic spindle [16, 17] and nucleus centering in mouse oocytes [20]. To independently probe the activity of this network we impaired the myosin-V motor force generation by de-activating it via microinjection of a dominant negative construct (MyoV(-)) [11, 20] (see Materials and Methods). The MyoV(-) construct targets the dimerization domain of endogenous myosin-Vb, which is still able to bind vesicles and actin, but no longer allows dimerization and active force generation. When myosin-V activity is absent, the mechanical properties of the cytoplasmic-skeleton stiffens significantly as evidenced by the shift upwards in the elastic and viscous moduli (Fig 2A, B). This increased mechanical stiffness correlates with a higher density actin meshwork that is observed in the absence of myosin-V activity (Fig. S3 in SI) and could be related to increased cross-linking [12]. This result highlights how cellular activity can be used to tune mechanical properties.

The overall behavior of the cytosolic-skeleton in oocytes is strongly viscoelastic where neither the elastic or viscous components dominate by a large margin. At lower frequencies the behavior is slightly more elastic with a crossover ($\sim 10 - 20$ Hz) to more viscous at higher frequencies. However both components of the shear moduli are always within a factor of two at the observed frequencies (Fig. 2C).

2.2 Quantifying nonequilibrium mechanical activity

To quantify nonequilibrium activity we use laser-tracking to precisely measure the spontaneous motion of vesicles in the cytosolic-skeleton with high spatio-temporal resolution [35, 36, 37] (see Materials and Methods). Both the spontaneous motion and the local mechanics are measured for each individual vesicle. This allows direct comparison between the local environment experienced by the vesicle and the motor activity that is driving its motion. This is critical in order to extract information about the molecular-scale processes. In the absence of biochemical activity the motion of the vesicles would be due to purely thermal agitation, which is fully determined by the mechanical properties of the system. This basic relation is given by a fundamental theorem of statistical mechanics known as the fluctuation-dissipation theorem (FDT) [38]. The FDT relates the small fluctuating motion of the vesicles to the mechanical properties of the surrounding environment by, $\tilde{\chi}'' = \pi f \tilde{C}/k_B T$, where $\tilde{\chi}''$ is the dissipative part of the mechanical response, \tilde{C} is the power spectral density of vesicle motion, f is frequency, and $k_B T$ is thermal energy. However, in living cells the presence of biochemical activity gives rise to active forces (e.g. a nonequilibrium process) driven by energy consuming processes [21, 22, 39]. In other words, the force driving the motion of particles in a living cell (e.g. the oocyte) has two contributions: (1) a passive (purely thermal) contribution described by classical equilibrium physics; (2) an active contribution that is biochemically regulated and cannot be understood via equilibrium physics.

We quantify and explain both the passive and active contributions driving intracellular fluctuations, by independently measuring each side of the FDT. We use AMR to measure $\tilde{\chi}$ and laser-tracking to measure \tilde{C} , and use this information to check for violation of FDT [23, 21, 40], which indicates active force generation. In oocytes, at high-frequencies the mechanical response ($\tilde{\chi}''$) and the spontaneous vesicle motion ($\pi f \tilde{C}/k_B T$) are equal as expected for thermal fluctuations [30, 24] (Fig. 3A). At frequencies below ~ 300 Hz, the observed motion of vesicles is dominated by an active energy consuming process (highlighted by the pink shaded region between the two curves in Fig 3A).

To quantify the nonequilibrium activity in an active soft material it is instructive to consider the effective energy [21, 41, 42, 43], $E_{\text{eff}} = \pi f \tilde{C}/\tilde{\chi}''$, which is a measure of how far the system is from thermal equilibrium. WT oocytes exhibit the strongest departure from equilibrium due to the actin-myosin-V network activity. Accordingly, the deviation is reduced when either actin is absent (Fmn -/-) or myosin-V is inactivated (MyoV (-)) (Fig 3B). This is quantitative confirmation that the dynamic actin-myosin-V meshwork drives vesicle dynamics out-of-equilibrium in the cytosolic-skeleton of mouse oocytes [12, 20]. Additionally, this demonstrates that other sources of activity remain in the living oocyte since non-thermal activity is still evident.

To develop a more intuitive picture of the activity we quantify the forces generated in the cell by calculating the cell force spectrum (S_{cell}) [22, 24, 25, 40]. S_{cell} directly represents the total forces on vesicles from all stochastic sources (active and thermal) inside the cell. In analogy to the force on a simple spring, where the force is the stiffness \times displacement ($F = \kappa \Delta x$, where κ is stiffness and Δx is displacement), we calculate $S_{\text{cell}} \propto |G^*|^2 \tilde{C}$ where $|G^*|^2$ is the stiffness of the cytosolic-skeleton and \tilde{C} is the spontaneous displacement of the vesicle [24, 25, 44]. In our framework we separate the total force spectrum in the cell to be the sum of thermal forces and active forces ($S_{\text{cell}} = S_{\text{therm}} + S_{\text{active}}$) [45, 40]. As an illustration of this separation of thermal and active forces we show a representative trajectory of a vesicle (Fig. 3E, black). Based on our measured violation of FDT (Fig. 3A), we isolate the low-frequency vesicle motion which is due to active processes and the high-frequency motion that is dominated by thermal motion (Fig. 3E green, F respectively). The resulting force spectrum is shown in Fig 3C where at high frequencies the cell force spectrum (S_{cell}) is dominated by thermal forces (where $S_{\text{active}} \ll S_{\text{thermal}}$) as expected, but at lower frequencies ($f < 300$ Hz) active forces exist ($S_{\text{active}} \gg S_{\text{thermal}}$) which result in higher total force experienced by vesicles in the cytoplasm over thermal equilibrium (lines represent theoretical model). The cell force spectrum, S_{cell} quantifies the average stochastic force experienced by a vesicle in the cytosolic-skeleton.

2.3 Modeling active force fluctuations

Myosin-V is typically considered a cargo transport motor. However, in prophase-I mouse oocytes, myosin-V drives vesicle motion in a non-directed fashion as evidenced by its sub-linear scaling of the mean-squared-displacement (Fig. 3D, blue). Previous work has also showed that myosin-V drives random motion of vesicles (active diffusion) on longer timescales of minutes [20]. To further illustrate this point, Fig. 4A(left) shows vesicles and actin filaments embedded in the oocyte interior. The complex mechanical environment is represented by a generic continuum (gray background). When myosin-V is attached to a vesicle and applies force on an actin filament, this force is transduced through the actin filament to a neighboring vesicle where it is bound by formin-2 (e.g. black arrows in Fig. 4A, right). This process occurs frequently throughout the oocyte interior resulting in randomly distributed force-dipoles (similar to myosin-II in some systems [30, 23]). Thus, each vesicle experiences forces in random directions due to the action of myosin-V throughout the network. This is represented by many actin filaments under force as shown in magenta in Fig. 4A(right). Therefore, due to the unique network connectivity in the cytoplasmic-skeleton, myosin-V motors drive active random motion in prophase-I mouse oocytes reminiscent of cytoplasmic stirring observed previously that was driven by myosin-II [30].

To gain access to the molecular-scale kinetics of the active processes driving the polymeric interior of oocytes we developed a quantitative model describing vesicles embedded in a viscoelastic environment that are subjected to thermal and active forces. Here, the nonequilibrium processes, such as molecular motor activity, provide the active forces that reorganize the polymer cytoskeleton and drive motion of the vesicles. Our theoretical framework extends previous approaches for near-elastic networks [46, 44, 40] to include the complex mechanical properties measured experimentally (Fig 2). The model describes a vesicle that is freely fluctuating in the viscoelastic continuum due to thermal forces, experiencing a local confinement illustrated by the harmonic potential, with stiffness κ , in Fig. 4B(left) and governed by the dynamics described in equation 1. The molecular motor activity injects random forces into the network, which results in an active force f_A on the vesicle that drives it to a new equilibrium position x_0 as in Fig. 4B(right) described by equation 2. These coupled equations of motion written in the Generalized Langevin approach describe vesicle motion in the active viscoelastic environment of the cytoplasmic-skeleton,

$$\int^t dt' \gamma(t-t') \frac{dx}{dt} = -\kappa(x-x_0) + \xi \quad (1)$$

$$\int^t dt' \gamma(t-t') \frac{dx_0}{dt} = \kappa \zeta_\alpha v_A \quad (2)$$

where ξ is Gaussian colored noise representing thermal forces, κ is the local confinement, γ is the memory kernel, ζ_α is the microscopic timescale describing the mechanical properties of the cytoplasmic-skeleton, v_A is the velocity of the stochastic active force, and x is the vesicle position. To account for the mechanical behavior of the cytoplasmic-skeleton that was measured by AMR, a power-law form of the memory kernel is utilized to describe the viscoelastic properties (details in SI). This model can directly separate the passive forces that originate from the thermal fluctuations of the medium and the active forces that depend on the energy consuming processes in the active material. Note that if the active force ($f_A = \kappa \zeta_\alpha v_A$) is zero, then equation 2 is zero, and the equation of motion simplifies to the usual viscoelastic Brownian motion (equation 1). If the active force is not zero, then it originates from molecular motor activity that has step-like velocity kinetics (Fig 4B, right inset). Endogenous vesicles experience an effective force kick of average duration τ followed by a quiescent period of average duration τ_0 [44, 40]. These force kicks drive the nonequilibrium fluctuations in our model.

2.4 Extracting molecular-scale force kinetics

By combining our model and experimental measurements, we can extract the force kinetics driving nonequilibrium mechanical processes in the oocyte. The active force spectrum represents the average force experi-

enced by the vesicles due only to active processes, and can be expressed as

$$S_{\text{active}} = \underbrace{\frac{1}{(2\pi f \zeta_\alpha)^{2\alpha}}}_{\text{mechanics}} \underbrace{\frac{1}{1 + (2\pi f \tau)^2} \frac{2(F\zeta_\alpha)^2}{3(\tau + \tau_0)}}_{\text{motor activity}} \quad (3)$$

where ζ_α and α reflect the viscoelastic material properties of timescale and frequency dependence, F is the apparent active force amplitude, τ is the average time of force application, and τ_0 is the average time between force kicks (Fig. 4B, right inset). The first term in equation 3 depends on the mechanical properties of the cytoplasmic-skeleton and the second term is related to the kinetic properties of the active processes. This illustrates that the active force spectrum is dependent on the force generation by molecular motors as well as the mechanics of the environment that they must push against. The power-law scaling of the active force spectrum contains information about the underlying physics. At lower frequencies the active force spectrum scales as $f^{-2\alpha}$ reflecting the active forces pushing against the viscoelastic environment. At higher frequencies the active force spectrum provides information on the molecular kinetics of the active force generation process which scales as $f^{-(2\alpha+2)}$. Our predicted active force spectrum exhibits power-law scaling that is dependent on the mechanical properties of the system (α), in contrast to previous studies [46, 22, 47]. Previous theoretical developments predict an active force spectrum with slope of -2 that is independent of the mechanical properties [22] and a plateau (slope of 0) below a critical frequency (equation 2 in [30] and equation S1 in [24]). It is worth noting that in the near-elastic case ($\alpha \sim 0$), our model recovers the behavior observed in previous work [24, 30]. The divergence of the active force spectrum at low frequencies is consistent with our experimental measurements, and others, where a low-frequency plateau is not observed [27, 25, 48, 24, 49].

The experimental measurements for the active force spectrum ($S_{\text{active}} = S_{\text{cell}} - S_{\text{therm}}$) and theoretical model are compared in Fig 4C. The low frequency power-law behavior is clearly seen, while at higher frequencies the active forces drop off rapidly which reflects the molecular motor statistics [50]. This drop-off of the active force spectrum allows extraction of τ , the timescale of active force application. Without additional assumptions, all subsequent molecular-scale force kinetics are now constrained by our model and can be calculated, such as the apparent active force amplitude,

$$F = [3\kappa k_B T_A (\tau + \tau_0)/\zeta_\alpha]^{1/2} \quad (4)$$

where $k_B T_A$ defines the active energy scale (see SI for details). The apparent force amplitude, F , is the average active force that the endogenous vesicle feels that drives its motion. Once this force is known it is straight-forward to calculate the expected average vesicle velocity,

$$v_v = \frac{F}{\kappa \zeta_\alpha} \quad (5)$$

which is a ratio of the driving force, F , and the resistance provided by the surrounding environment, $\kappa \zeta_\alpha$. Following this argument an approximate step-size of the force kick can be computed by $\Delta x = F/\kappa$. Thus, once the timescale of the force kick (τ) is extracted from equation 3, the apparent force felt by the vesicle (F), the expected vesicle velocity (v_v), and the step-size Δx can be deduced directly.

A main result of our combined experimental and theoretical framework is access to the molecular-scale kinetics via mesoscopic measurements of the active force spectrum. In living oocytes we find that endogenous vesicles experience a force of $F \sim 0.4$ pN during a power-stroke of $\tau \sim 300$ μ s duration, with a step-size of $\Delta x \sim 20$ nm, which is strikingly similar to single molecule myosin-V kinetics measured in-vitro [51, 52, 50, 53, 54, 55, 56]. In addition, we find that the predicted average vesicle velocity due to molecular motors is $v_v \sim 320$ nm/s which is in agreement with myosin-V velocity in vitro [51, 53, 54], as well as the velocity of myosin-V driven vesicles measured in in-vivo oocytes [20, 11]. Together, our results reveal that force kinetics of myosin-V motors are remarkably similar in in-vitro single-molecule studies and in in-vivo oocytes where they drive the composite cytoplasmic-skeleton out-of-equilibrium.

The agreement between our experiments and analytic theory indicate that the model is able to capture the nonequilibrium force fluctuations of endogenous vesicles in the cytoplasmic-skeleton of living oocytes. However, this does not guarantee that it adequately describes the overall motion of the vesicles (including higher-order statistics). To further compare our experiments and theory we use the measured parameters

(mechanics, kinetics, etc.) extracted from the force spectrum to simulate vesicle dynamics via a stochastic equation of motion (see SI). These simulations of vesicle motion use exclusively values measured from experiment, without any free parameters. We find that the statistics of the simulated vesicle motion is in excellent agreement with the measured spontaneous motion of vesicles in living oocytes as is shown by their displacement correlations (Fig 4D). Measured and simulated motion of vesicles is nearly identical including the central Gaussian region and the non-Gaussian tails (shaded red in Fig 4D) at short timescales which are indicative of molecular motor activity [57]. While our analytic model describes the mean values of the experimental measurements, these simulations exploit the full range of data by capturing the entire distribution of displacement correlations. Hence, the agreement found between simulations and experiment is non-trivial and can be considered a predictive test of the model. These results show that our model of step-like active forces is able to capture the overall motion of vesicles (including higher-order statistics) embedded in the cytoplasmic-skeleton of living oocytes.

3 Discussion

3.1 The cytoplasmic-skeleton is softened by nonequilibrium fluctuations

Our mechanical measurements (AMR) indicate that myosin-V driven nonequilibrium fluctuations maintain a softer cytoplasmic-skeleton in oocytes. The mechanism of how this occurs is not yet clear but is likely related to the structural connectivity of the actin-myosin-V network. The sparsely connected network of long unbranched actin filaments connected by myosin-V positive vesicles in oocytes exhibits a unique architecture. This active actin-myosin-V network drives random nonequilibrium fluctuations of the entire composite cytoskeleton. Repeated deformation of the composite cytoskeleton may lead to breakages resulting in softening of the overall mechanical properties. In polymer physics this behavior is known as the classical Mullins effect [58], where small amplitude cyclic strain application leads to softening. This effect has been observed in actin networks with low cross-linking density [59] and motor-mediated breakage of actin filaments has been observed in-vitro [60]. Thus, it is possible that repeated deformation due to myosin-V force generation causes the observed difference in actin density between WT and MyoV(-) (Figure S3 in SI) due to rupture or breakage of filaments/cross-links [60, 61, 62]. The motor-mediated softening reported here has also been observed due to myosin-II in suspended cells in-vitro [63], which is in contrast to the stiffening reported in adherent cells [24, 64]. The origin of softening/stiffening behavior in cells is not yet understood, but may be related to adhesion with the surrounding environment.

3.2 Nonequilibrium activity dominates below 300 Hz

In mouse oocytes, nonequilibrium activity emerges at higher frequencies ($f < 300$ Hz) than observed previously in other active systems ($f < 10$ Hz)[23, 24, 30]. This observation is not surprising since the timescale of FDT violation depends on both the mechanical properties and the typical timescale of the nonequilibrium activity of the system. The cytoplasmic-skeleton in oocytes is softer than previous systems [23, 65], and thus it is expected for the crossover to thermal motion to occur at higher frequencies (Fig S2 in SI). Additionally, myosin-V kinetics are known to be faster than myosin-II [66], which was the driving force in previous experiments [23, 24, 30].

3.3 Active force spectrum reveals molecular-scale kinetics

A significant advance represented by this work is the connection between mesoscopic measurement of nonequilibrium vesicle motion and the underlying molecular-scale driving forces in a strongly viscoelastic in-vivo system. A global fit of our theoretical model to the ensemble averaged active force spectrum reveals molecular-scale kinetics in agreement for myosin-V measured in single molecule in-vitro experiments [50, 51, 52, 53, 55, 56, 54]. It is striking that our in-vivo measurements are in such close agreement with single-molecule studies given that the crowded in-vivo environment is far more complex. To capture this behavior it was necessary to extend our theoretical framework to account for strong viscoelastic memory effects. This is most clearly seen in the low-frequency power-law scaling of the active force spectrum. Previous models predict that the active force spectrum is proportional to f^{-2} [22, 46, 40] which is able to

predict measurements made in nearly elastic systems [24, 30]. However, this behavior is not consistent with our measurements in oocytes where we observe a scaling of $f^{-4/3}$ (Fig. 4B). Our model, predicts a low-frequency behavior of $S_{\text{active}} \propto f^{-2\alpha}$ which agrees with our experimental measurement $\alpha \sim 2/3$. This shows that including the strong viscoelastic memory effects of the mechanical properties is necessary to capture the nonequilibrium properties of the cytoplasmic-skeleton in mouse oocytes. This is likely the case for any cells that cannot be considered near-elastic.

Our model allows extracts the molecular-scale force kinetics directly from fitting the active force spectrum. As a result, we are able to capture the short timescale power-stroke of the active process, which is not be possible from fitting the long timescale plateau of the MSD as done previously [24, 30]. Furthermore, we predict the force, step-size, and velocity without any further model assumptions. All resulting kinetics extracted from in-vivo oocytes are in striking agreement with single-molecule kinetics measured in-vitro as summarized in Table 1. Our approach is a versatile method to access the molecular-scale force dynamics in living cells and other soft active materials.

[Table 1 about here.]

4 Conclusion

We have demonstrated the quantification of nonequilibrium properties and molecular-scale kinetics inside the cytoplasmic-skeleton of in-vivo mouse oocytes via experiments, theory, and simulation. We find that active forces can tune the mechanical properties and the nonequilibrium fluctuations of the active polymeric interior of oocytes. Through our theoretical model we access the molecular-scale force kinetics that are driving activity in the cytoplasmic-skeleton. From the material science perspective, this is a striking example of how active materials fundamentally differ from passive materials, since their microscopic dynamics are actively tuned. From a biological perspective, nonequilibrium fluctuations are important to maintain cell functionality and mesoscopic measurements provide access to molecular-scale kinetics. Our results combine concepts from equilibrium and nonequilibrium physics to reveal that myosin-V activity is remarkably similar in-vivo as in-vitro, and that their kinetics can be extracted via measurements of cytoplasmic fluctuations.

5 Materials and Methods

5.1 Oocyte Preparation

Oocytes were collected from 11 week old mice OF1, 13 week old C57BL6 (WT) or 15 week old Fmn2^{-/-} female mice as previously described [67] and maintained in Prophase I arrest in M2+BSA medium supplemented with 1 μM Milrinone [68]. Live oocytes were embedded in a collagen gel to stop movement of the overall cell during measurements. Collagen gel was made by mixing M2 medium (33.5 μL), 1X PBS (10 μL), NaOH (1M, 0.9 μL), collagen (3.6 mg/mL, 55.6 μL) to obtain 100 μL of the final collagen solution at 2 mg/mL with a pH~ 7.4. 20 μL of the collagen solution was deposited on a coverslip and live oocytes were added. The droplet was covered with another glass coverslip using Dow Corning vacuum grease to minimize evaporation. The collagen gel containing oocytes was polymerized in a humid environment at 37° C for 30 minutes.

5.2 Fmn2^{-/-} and Myosin-V dominant negative

To study the effect of the actin-myosin-V network we utilize two conditions to independently perturb the actin cytoskeleton (Fmn^{-/-}) and the myosin-V activity (MyoV⁽⁻⁾). Fmn^{-/-} mouse oocytes lack cytoplasmic actin filaments, as confirmed by several independent studies [16, 17, 69, 19]. The absence of actin filaments has also been confirmed via cytochalasin-D treated mouse oocytes which exhibit the same phenotype as Fmn^{-/-} [70]. For myosin-V dominant negative experiments (MyoV⁽⁻⁾), oocytes were injected with cRNAs using an Eppendorf Femtoject microinjector as published previously [20]. Oocytes were kept in prophase-I arrest for 1-3 hours to allow expression of fusion proteins. The myosin-Vb dominant negative construct corresponds to a portion of the coiled-coil region of the myosin-Vb that mediates dimerization of the motor [11]. We believe this construct binds to the coiled-coil region of endogenous myosin-Vb resulting in impaired motor dimerization. Thus, myosin-Vb is still able to bind to vesicles and actin filaments but cannot actively

generate force. It is specific to myosin-Vb and has been shown to stop vesicle motion in mouse oocytes as efficiently as brefeldin A (BFA), which is a general traffic inhibitor [20].

5.3 In-vitro Actin Network Preparation

A bulk solution of actin monomers 120 μM (Cytoskeleton Inc.) was stored overnight in depolymerization buffer (200 μM CaCl₂, 500 μM DTT, 2mM Tris, 200 μM ATP). It was then polymerized at a final concentration of 24 μM actin in polymerization buffer (25 mM Imidazol, 50 mM KCl, 1mM Tris, 2 mM MgCl₂, 1 mM DTT, 1 mM ATP). The actin gel was polymerized between two glass coverslips at room temperature. Polystyrene beads (1 μm) were embedded for optical tweezer measurements.

5.4 Optical Tweezer Setup

The optical tweezer system utilizes a near infrared fiber laser ($\lambda = 1064 \text{ nm}$, YLM-1-1064-LP, IPG, Germany) that passes through a pair of acousto-optical modulators (AA-Optoelectronics, France) to control the intensity and deflection of the trapping beam. The laser is coupled into the beam path via dichroic mirrors (ThorLabs) and focused into the object plane by a water immersion objective (60x, 1.2 NA, Olympus). The condenser is replaced by a long distance water immersion objective (40x, 0.9 NA, Olympus) to collect the light and imaged by a 1:4 telescope on a InGaAs quadrant photodiode (QPD) (G6849, Hamamatsu). The resulting signal is amplified by a custom built amplifier system (Oeffner Electronics, Germany) and digitized at a 500 kHz sampling rate and 16 bit using an analog input card (6353, National Instruments, Austin, TX, USA). All control of the experimental hardware is executed using LabVIEW (National Instruments). Optical trapping of endogenous vesicles was calibrated similarly as in [31, 71], where the high-frequency fluctuations ($f > 500 \text{ Hz}$) are thermal in origin [24, 30]. For direct measurement of violation of the fluctuation dissipation theorem (FDT), laser tracking interferometry is used first to measure the spontaneous fluctuations of the vesicle, followed immediately by active microrheology to measure the mechanical properties of the local environment surrounding the vesicle.

5.5 Laser Interferometry Tracking

The position of the endogenous particle is measured by back focal plane interferometry [35]. It should be noted that deformable objects (e.g., giant unilamellar vesicles 10 – 100 μm) undergo shape fluctuations that will manifest in the voltage measured by the QPD [72]. For small endogenous particles ($\sim 1 \mu\text{m}$), it has been confirmed that shape fluctuations are small and laser interferometry can be used to track their position with nanometer precision. This has been verified by several independent studies on mammalian cells [36], yeast [37], and hair bundles [21]. We also compare our QPD measurements and show that endogenous vesicles in mouse oocytes are indistinguishable from both: polystyrene beads in living cells, and in an index-matched 50:50 water:glycerol solution in the central linear region used for position measurement (see Fig. S4 in SI). Additionally, since the endogenous vesicles serve as nodes integrated in the cytoplasmic meshwork, they are accurate reporters of the network mechanics and fluctuations [29].

5.6 Data Analysis

In the active microrheology (AMR) experiments we apply a known force, F , to an endogenous vesicle and measure the resulting displacement, u . Using linear response theory, these are related to the material response by, $u(t) = \int_{-\infty}^t \chi(t-t')F(t')dt'$. In Fourier space we can directly calculate the complex response as $\tilde{\chi}(\omega) = \tilde{u}(\omega)/\tilde{F}(\omega)$. To translate the response function into a shear modulus we use the Generalized Stokes-Einstein relation, $G^* = 1/[6\pi R\tilde{\chi}(\omega)]$, to calculate the elastic and viscous shear moduli (G' , G'' respectively). For AMR measurements the laser power exiting the objective was $\sim 120 \text{ mW}$. For the spontaneous fluctuations we measure the motion, $u(t)$, of endogenous vesicles via laser interferometry (without trapping the vesicle) and calculate the power spectral density (PSD), $C(\omega) = \int \langle u(t)u(0) \rangle \exp(i\omega t) dt$, as described previously [72]. Briefly, we calculate the PSD by using MATLAB (The Mathworks, USA) to take the Fast Fourier Transform (FFT) of the vesicle position, $\tilde{u} = \text{FFT}(u)$. Then the PSD is calculated as, $PSD = \frac{\tilde{u} \times \tilde{u}^*}{p \times s}$, where $*$ denotes complex conjugate, p is the number of measurement points, and s is the sampling frequency. In systems at

thermal equilibrium the response function can be calculated from the PSD via the FDT as is done for passive microrheology (PMR) [38]. For PMR measurements the laser power exiting the objective was ~ 1 mW. Due to the particle size and linear range of the QPD measurement our PMR measurements are restricted to a range of approximately 500 nm.

6 Acknowledgements

We thank Jacques Prost and Jean-Francois Joanny for helpful discussions. We thank Melina Schuh (MRC Cambridge) for providing the MyoVb tail plasmid and Amanda Remorino for critical reading of the manuscript. WWA is a recipient of post-doctoral fellowships from La Fondation Pierre-Gilles de Gennes and Marie Curie Actions. MA is a recipient of post-doctoral fellowships from the Ligue Nationale contre le Cancer and from the Labex MemoLife. MB is a recipient of an AXA Ph.D. fellowship. NSG gratefully acknowledges funding from the ISF (grant no. 580/12). MHV gratefully acknowledges the Ligue Nationale Contre le Cancer (EL/2012/LNCC/MHV). TB was supported by the French Agence Nationale de la Recherche (ANR) Grants ANR-11-JSV5-0002, and the Deutsche Forschungsgemeinschaft (DFG), Cells-in-Motion Cluster of Excellence (EXC 1003 – CiM), University of Münster, Germany.

[Figure 1 about here.]

[Figure 2 about here.]

[Figure 3 about here.]

[Figure 4 about here.]

References

- [1] Jonathon Howard. Mechanical Signaling in Networks of Motor and Cytoskeletal Proteins. *Annual Review of Biophysics*, 38(1):217–234, jun 2009.
- [2] L Blanchoin, R Boujemaa-Paterski, C Sykes, and J Plastino. Actin dynamics, architecture, and mechanics in cell motility. *Physiol Rev*, 94:235–63, 2014.
- [3] PA Jamney and CA McCulloch. Cell mechanics: integrating cell responses to mechanical stimuli. *Annu Rev Biomed Eng*, 9:1–34, 2007.
- [4] DA Fletcher and RD Mullins. Cell mechanics and the cytoskeleton. *Nature*, 463:485–92, Jan 2010.
- [5] N Bowden, A Terfort, J Carbeck, and GM Whitesides. Self-Assembly of Mesoscale Objects into Ordered Two-Dimensional Arrays. *Science*, 276:233–5, Apr 1997.
- [6] J Palacci, S Sacanna, AP Steinberg, DJ Pine, and PM Chaikin. Living crystals of light-activated colloidal surfers. *Science*, 339:936–40, Feb 2013.
- [7] Adam J. M. Wollman, Carlos Sanchez-Cano, Helen M. J. Carstairs, Robert A. Cross, and Andrew J. Turberfield. Transport and self-organization across different length scales powered by motor proteins and programmed by DNA. *Nature Nanotech*, 9(1):44–47, nov 2013.
- [8] Y Sasai. Cytosystems dynamics in self-organization of tissue architecture. *Nature*, 493:318–26, Jan 2013.
- [9] S Wennekamp, S Mesecke, F Nédélec, and T Hiramatsu. A self-organization framework for symmetry breaking in the mammalian embryo. *Nat Rev Mol Cell Biol*, 14:452–9, 2013.
- [10] T Lecuit and PF Lenne. Cell surface mechanics and the control of cell shape, tissue patterns and morphogenesis. *Nat Rev Mol Cell Biol*, 8:633–44, 2007.
- [11] M Schuh. An actin-dependent mechanism for long-range vesicle transport. *Nat Cell Biol*, 13:1431–6, 2011.
- [12] Z Holubcová, G Howard, and M Schuh. Vesicles modulate an actin network for asymmetric spindle positioning. *Nat Cell Biol*, 15:937–47, 2013.
- [13] M Luksza, I Queguiner, MH Verlhac, and S Brunet. Rebuilding MTOCs upon centriole loss during mouse oogenesis. *Dev Biol*, 382:48–56, 2013.
- [14] V Nikolova, R Zhivkova, M Markova, T Topouzova-Hristova, A Mitkova, and S Delimitreva. Characterization of mouse oocytes and oocyte-cumulus complexes extracted for nuclear matrix and intermediate filaments (NM-IF). *Acta Morph. Anthropol*, 19:149–152, 2012.
- [15] M Almonacid, MÉ Terret, and MH Verlhac. Actin-based spindle positioning: new insights from female gametes. *J Cell Sci*, 127:477–83, 2014.
- [16] J Azoury, KW Lee, V Georget, P Rassinier, B Leader, and MH Verlhac. Spindle positioning in mouse oocytes relies on a dynamic meshwork of actin filaments. *Curr Biol*, 18:1514–9, Oct 2008.
- [17] M Schuh and J Ellenberg. A new model for asymmetric spindle positioning in mouse oocytes. *Curr Biol*, 18:1986–92, Dec 2008.
- [18] D Clift and M Schuh. Restarting life: fertilization and the transition from meiosis to mitosis. *Nat Rev Mol Cell Biol*, 14:549–62, 2013.
- [19] A Chaigne, C Campillo, NS Gov, R Voituriez, J Azoury, C Umaña-Díaz, M Almonacid, I Queguiner, P Nassoy, C Sykes, MH Verlhac, and ME Terret. A soft cortex is essential for asymmetric spindle positioning in mouse oocytes. *Nat Cell Biol*, 15:958–66, 2013.

- [20] M Almonacid, WW Ahmed, M Bussonnier, P Mailly, T Betz, R Voituriez, NS Gov, and MH Verlhac. Active diffusion positions the nucleus in mouse oocytes. *Nat Cell Biol*, 17:470–9, 2015.
- [21] P Martin, AJ Hudspeth, and F Jülicher. Comparison of a hair bundle’s spontaneous oscillations with its response to mechanical stimulation reveals the underlying active process. *Proc Natl Acad Sci U S A*, 98:14380–5, 2001.
- [22] AW Lau, BD Hoffman, A Davies, JC Crocker, and TC Lubensky. Microrheology, stress fluctuations, and active behavior of living cells. *Phys Rev Lett*, 91:198101, 2003.
- [23] D Mizuno, C Tardin, CF Schmidt, and FC Mackintosh. Nonequilibrium mechanics of active cytoskeletal networks. *Science*, 315:370–3, Jan 2007.
- [24] M Guo, AJ Ehrlicher, MH Jensen, M Renz, JR Moore, RD Goldman, J Lippincott-Schwartz, FC Mackintosh, and DA Weitz. Probing the stochastic, motor-driven properties of the cytoplasm using force spectrum microscopy. *Cell*, 158:822–32, Aug 2014.
- [25] François Gallet, Delphine Arcizet, Pierre Bohec, and Alain Richert. Power spectrum of out-of-equilibrium forces in living cells: amplitude and frequency dependence. *Soft Matter*, 5(15):2947, 2009.
- [26] P Bursac, G Lenormand, B Fabry, M Oliver, DA Weitz, V Viasnoff, JP Butler, and JJ Fredberg. Cytoskeletal remodelling and slow dynamics in the living cell. *Nat Mater*, 4:557–61, 2005.
- [27] C Wilhelm. Out-of-equilibrium microrheology inside living cells. *Phys Rev Lett*, 101:028101, Jul 2008.
- [28] D. Mizuno, D. A. Head, F. C. MacKintosh, and C. F. Schmidt. Active and Passive Microrheology in Equilibrium and Nonequilibrium Systems. *Macromolecules*, 41(19):7194–7202, oct 2008.
- [29] MT Valentine, ZE Perlman, ML Gardel, JH Shin, P Matsudaira, TJ Mitchison, and DA Weitz. Colloid surface chemistry critically affects multiple particle tracking measurements of biomaterials. *Biophys J*, 86:4004–14, Jun 2004.
- [30] N Fakhri, AD Wessel, C Willms, M Pasquali, DR Klopfenstein, FC MacKintosh, and CF Schmidt. High-resolution mapping of intracellular fluctuations using carbon nanotubes. *Science*, 344:1031–5, May 2014.
- [31] J Mas, AC Richardson, SN Reihani, LB Oddershede, and K Berg-Sørensen. Quantitative determination of optical trapping strength and viscoelastic moduli inside living cells. *Phys Biol*, 10:046006, 2013.
- [32] FC MacKintosh, J Käs, and PA Janmey. Elasticity of semiflexible biopolymer networks. *Phys Rev Lett*, 75:4425–4428, Dec 1995.
- [33] David C. Morse. Viscoelasticity of Concentrated Isotropic Solutions of Semiflexible Polymers. 2. Linear Response. *Macromolecules*, 31(20):7044–7067, oct 1998.
- [34] M. L. Gardel, M. T. Valentine, J. C. Crocker, A. R. Bausch, and D. A. Weitz. Microrheology of Entangled F-Actin Solutions. *Phys. Rev. Lett.*, 91(15), oct 2003.
- [35] F Gittes and CF Schmidt. Interference model for back-focal-plane displacement detection in optical tweezers. *Opt Lett*, 23:7–9, 1998.
- [36] S Yamada, D Wirtz, and SC Kuo. Mechanics of living cells measured by laser tracking microrheology. *Biophys J*, 78:1736–47, Apr 2000.
- [37] Iva Marija Tolić-Nørrelykke, Emilia-Laura Munteanu, Genevieve Thon, Lene Oddershede, and Kirstine Berg-Sørensen. Anomalous Diffusion in Living Yeast Cells. *Phys. Rev. Lett.*, 93(7), aug 2004.
- [38] R Kubo. The fluctuation-dissipation theorem. *Rep. Prog. Phys.*, 29(1):255–284, jan 1966.
- [39] WW Ahmed, É Fodor, and T Betz. Active cell mechanics: Measurement and theory. *Biochim Biophys Acta*, May 2015.

- [40] É. Fodor, M. Guo, N. S. Gov, P. Visco, D. A. Weitz, and F. van Wijland. Activity-driven fluctuations in living cells. *EPL*, 110(4):48005, may 2015.
- [41] T Betz, M Lenz, JF Joanny, and C Sykes. ATP-dependent mechanics of red blood cells. *Proc Natl Acad Sci U S A*, 106:15320–5, 2009.
- [42] E Ben-Isaac, Y Park, G Popescu, FL Brown, NS Gov, and Y Shokef. Effective temperature of red-blood-cell membrane fluctuations. *Phys Rev Lett*, 106:238103, Jun 2011.
- [43] J Prost, JF Joanny, and JM Parrondo. Generalized fluctuation-dissipation theorem for steady-state systems. *Phys Rev Lett*, 103:090601, Aug 2009.
- [44] É Fodor, K Kanazawa, H Hayakawa, P Visco, and Wijland F van. Energetics of active fluctuations in living cells. *Phys Rev E Stat Nonlin Soft Matter Phys*, 90:042724, 2014.
- [45] AW Lau and TC Lubensky. Fluctuating hydrodynamics and microrheology of a dilute suspension of swimming bacteria. *Phys Rev E Stat Nonlin Soft Matter Phys*, 80:011917, 2009.
- [46] FC MacKintosh and AJ Levine. Nonequilibrium mechanics and dynamics of motor-activated gels. *Phys Rev Lett*, 100:018104, Jan 2008.
- [47] Alex J. Levine and F. C. MacKintosh. The Mechanics and Fluctuation Spectrum of Active Gels †. *J. Phys. Chem. B*, 113(12):3820–3830, mar 2009.
- [48] Damien Robert, Thi-Hanh Nguyen, François Gallet, and Claire Wilhelm. In Vivo Determination of Fluctuating Forces during Endosome Trafficking Using a Combination of Active and Passive Microrheology. *PLoS ONE*, 5(4):e10046, apr 2010.
- [49] D Robert, TH Nguyen, F Gallet, and C Wilhelm. In vivo determination of fluctuating forces during endosome trafficking using a combination of active and passive microrheology. *PLoS One*, 5:e10046, 2010.
- [50] M Rief, RS Rock, AD Mehta, MS Mooseker, RE Cheney, and JA Spudich. Myosin-V stepping kinetics: a molecular model for processivity. *Proc Natl Acad Sci U S A*, 97:9482–6, Aug 2000.
- [51] AD Mehta, RS Rock, M Rief, JA Spudich, MS Mooseker, and RE Cheney. Myosin-V is a processive actin-based motor. *Nature*, 400:590–3, 1999.
- [52] G Cappello, P Pierobon, C Symonds, L Busoni, JC Gebhardt, M Rief, and J Prost. Myosin V stepping mechanism. *Proc Natl Acad Sci U S A*, 104:15328–33, Sep 2007.
- [53] C Veigel, S Schmitz, F Wang, and JR Sellers. Load-dependent kinetics of myosin-V can explain its high processivity. *Nat Cell Biol*, 7:861–9, 2005.
- [54] S Uemura, H Higuchi, AO Olivares, La Cruz EM De, and S Ishiwata. Mechanochemical coupling of two substeps in a single myosin V motor. *Nat Struct Mol Biol*, 11:877–83, 2004.
- [55] JR Sellers and C Veigel. Direct observation of the myosin-Va power stroke and its reversal. *Nat Struct Mol Biol*, 17:590–5, 2010.
- [56] C Veigel, F Wang, ML Bartoo, JR Sellers, and JE Molloy. The gated gait of the processive molecular motor, myosin V. *Nat Cell Biol*, 4:59–65, 2002.
- [57] Toshihiro Toyota, David A. Head, Christoph F. Schmidt, and Daisuke Mizuno. Non-Gaussian athermal fluctuations in active gels. *Soft Matter*, 7(7):3234, 2011.
- [58] R. W. Ogden and D. G. Roxburgh. A pseudo-elastic model for the Mullins effect in filled rubber. *Proceedings of the Royal Society A: Mathematical Physical and Engineering Sciences*, 455(1988):2861–2877, aug 1999.

- [59] KM Schmoller, P Fernández, RC Arevalo, DL Blair, and AR Bausch. Cyclic hardening in bundled actin networks. *Nat Commun*, 1:134, 2010.
- [60] MP Murrell and ML Gardel. F-actin buckling coordinates contractility and severing in a biomimetic actomyosin cortex. *Proc Natl Acad Sci U S A*, 109:20820–5, Dec 2012.
- [61] N Kikuchi, A Ehrlicher, D Koch, JA Käs, S Ramaswamy, and M Rao. Buckling, stiffening, and negative dissipation in the dynamics of a biopolymer in an active medium. *Proc Natl Acad Sci U S A*, 106:19776–9, Nov 2009.
- [62] Yali Yang, Jun Lin, Bugra Kaytanli, Omar A. Saleh, and Megan T. Valentine. Direct correlation between creep compliance and deformation in entangled and sparsely crosslinked microtubule networks. *Soft Matter*, 8(6):1776–1784, 2012.
- [63] CJ Chan, AE Ekpenyong, S Golfier, W Li, KJ Chalut, O Otto, J Elgeti, J Guck, and F Lautenschläger. Myosin II Activity Softens Cells in Suspension. *Biophys J*, 108:1856–69, Apr 2015.
- [64] WA Lam, O Chaudhuri, A Crow, KD Webster, TD Li, A Kita, J Huang, and DA Fletcher. Mechanics and contraction dynamics of single platelets and implications for clot stiffening. *Nat Mater*, 10:61–6, Jan 2011.
- [65] M Guo, AJ Ehrlicher, S Mahammad, H Fabich, MH Jensen, JR Moore, JJ Fredberg, RD Goldman, and DA Weitz. The role of vimentin intermediate filaments in cortical and cytoplasmic mechanics. *Biophys J*, 105:1562–8, 2013.
- [66] MJ Tyska and DM Warshaw. The myosin power stroke. *Cell Motil Cytoskeleton*, 51:1–15, 2002.
- [67] MH Verlhac, JZ Kubiak, HJ Clarke, and B Maro. Microtubule and chromatin behavior follow MAP kinase activity but not MPF activity during meiosis in mouse oocytes. *Development*, 120:1017–25, 1994.
- [68] A Reis, HY Chang, M Levasseur, and KT Jones. APCcdh1 activity in mouse oocytes prevents entry into the first meiotic division. *Nat Cell Biol*, 8:539–40, 2006.
- [69] S Pfender, V Kuznetsov, S Pleiser, E Kerkhoff, and M Schuh. Spire-type actin nucleators cooperate with Formin-2 to drive asymmetric oocyte division. *Curr Biol*, 21:955–60, Jun 2011.
- [70] J Dumont, K Million, K Sunderland, P Rassinier, H Lim, B Leader, and MH Verlhac. Formin-2 is required for spindle migration and for the late steps of cytokinesis in mouse oocytes. *Dev Biol*, 301:254–65, Jan 2007.
- [71] BH Blehm, TA Schroer, KM Trybus, YR Chemla, and PR Selvin. In vivo optical trapping indicates kinesin's stall force is reduced by dynein during intracellular transport. *Proc Natl Acad Sci U S A*, 110:3381–6, Feb 2013.
- [72] Timo Betz and Cécile Sykes. Time resolved membrane fluctuation spectroscopy. *Soft Matter*, 8(19):5317, 2012.

List of Figures

- Intracellular mechanics surrounding endogenous vesicles in living oocytes.** (A) Mouse oocytes are large spherical cells that have a well separated cortex and cytoplasmic-skeleton composed of biopolymer filaments (brightfield image, left)(scalebar = 20 μm). During prophase-I it contains a dynamic actin-myosin-V meshwork that drives vesicle motion (schematic shown in center and fluorescent image of actin filaments on right)(scalebar = 5 μm). Endogenous vesicles embedded in the cytoplasmic-skeleton are trapped using optical tweezers(zoomed inset). (B) Once a vesicle is trapped, the mechanical properties of the local environment can be measured by active microrheology (AMR) where a sinusoidal oscillating force is applied to the vesicle (blue) and the resulting displacement of the vesicle is measured (green). The viscoelastic shear modulus (G^*) is calculated from this force-displacement measurement via the Generalized Stokes-Einstein relation. (C) The mechanical properties surrounding vesicles in the cytoplasmic-skeleton of oocytes (blue) exhibits power-law behavior similar to reconstituted actin gels (gray) with frequency scaling $G^* \propto f^{0.75}$ except significantly stiffer. This shows that the cytoplasmic-skeleton in oocytes can be modeled as a semi-flexible polymer network.

The cytoplasmic-skeleton of mouse oocytes is viscoelastic. (A, B) Insets indicate that G' quantifies the elasticity and G'' quantifies the viscous dissipation of the cytoplasmic-skeleton. The local mechanical properties (elastic and viscous) surrounding vesicles does not change from WT (blue, \circ) when actin (red \square) or microtubules (magenta $*$) are absent. However, when myosin-V is inactivated (gray Δ), the cytoplasmic-skeleton stiffens significantly (Kolmogorov-Smirnov test, $p < 1 \times 10^{-7}$), showing that the activity driven dynamics of the actin-myosin-V meshwork maintains the soft mechanical environment surrounding vesicles in oocytes. (C) The ratio of the elastic and viscous moduli (G'/G'') in all oocytes shows that the cytoplasmic-skeleton is more elastic at lower frequencies and more viscous at higher frequencies with a crossover around $\sim 10 - 20$ Hz. This shows the highly viscoelastic nature of the oocyte cytoplasmic-skeleton. (sample size = WT: 11 cells, 32 vesicles; Fmn2: 10 cells, 33 vesicles; MyoV(-): 23 cells, 69 vesicles; Noc(1 μM): 8 cells, 52 vesicles; shaded region indicates SEM) (note: data at 10 Hz in panel A and B are presented in a different context in [20])

Active force generation by myosin-V drives the cytoplasmic-skeleton out-of-equilibrium. (A) The spontaneous motion of vesicles in oocytes (green circles) is larger than expected at thermal equilibrium (blue circles) at frequencies below 300 Hz showing that active forces are contributing to vesicle motion as highlighted by the red shaded region. This is direct evidence of nonequilibrium behavior in the cytoplasmic-skeleton (via violation of the fluctuation-dissipation theorem (FDT)). At high frequencies the observed vesicle motion resembles thermal motion indicated by the blue shaded region. (B) WT oocytes (blue) are the furthest from equilibrium as shown by their higher effective energy. In the absence of actin (red) or when myosin-V is inactivated (black) the dynamic actin-myosin-V meshwork is compromised and oocytes have lower effective energy. Solid lines are theoretical fits (equations in SI, error bars = SEM). (C) The cell force spectrum (S_{cell}) experienced by vesicles is the sum of thermal forces (S_{therm}) and active forces (S_{active}) generated by molecular motors. At high frequencies S_{cell} (green) is dominated by S_{therm} (blue) and the two spectra coincide (blue shaded region). At lower frequencies S_{cell} is larger than S_{therm} showing the existence of additional active forces. Solid lines are theoretical predictions (equations in SI), low-frequency deviation is due to simple power-law model. (D) The mean-squared-displacement (MSD) of vesicles indicates they undergo random-confined motion in the oocyte cytoplasmic-skeleton at short timescales. This behavior transitions to active diffusion at longer times [20], and is reminiscent of cytoplasmic stirring [30]. (E) When a representative trajectory (black) is filtered to remove the high-frequency thermal fluctuations the result is a smoothed trajectory (green) that represents actively driven motion. The difference between the true trajectory (gray) and the smoothed trajectory (green) recovers the high-frequency thermal fluctuations (blue) shown in (F).

- 4 **A theoretical model of active mechanics connects *in vivo* measurements to molecular force kinetics.** (A) Vesicles (dark gray) are embedded in the complex mechanical continuum (gray background) of the oocyte interior. Actin filaments emanate from the surface of vesicles creating an entangled network (green, left). Myosin-V motors generate force on actin (magenta, right) giving rise to forces throughout the network driving vesicles in random directions. (B) We model vesicles embedded in a mechanical continuum with local stiffness (κ) represented by the blue harmonic potential, viscoelastic dissipation (ζ_α, α), and thermal fluctuations (ξ) (left). Molecular motor activity generates an active force (f_A) through bursts of motion (v_A) and drive motion of vesicles (inset indicates motor kinetics). (C) The active force spectrum (S_{active}) quantifies the forces on vesicles due to only active processes. Combined with our quantitative model we find that the vesicles are subject to 0.4 pN of force, during a power-stroke of length $\Delta x \sim 20$ nm and duration $300 \mu\text{s}$, resulting in a vesicle velocity of 320 nm/s, which is strikingly similar to the kinetics measured for single molecule myosin-V in-vitro and the *in-vivo* vesicle velocity. The solid line is the theoretical fit (equation 3), and the dotted line is a $-4/3$ power-law consistent with the cytoplasmic-skeleton mechanics. (D) Simulated vesicle motion (green squares) agrees with experimental data (blue circles) for a wide range of timescales as shown by the probability distribution of displacements. This includes long timescale ($t_{\text{pdf}} = 1$ s) Gaussian behavior and short timescale ($t_{\text{pdf}} = 0.01$ s) non-Gaussian tails (indicated by red-shaded regions) that are indicative of molecular motor behavior, where t_{pdf} is the time-lag for calculation of the displacement correlations. Gaussian distributions shown in black. These results show that molecular level kinetics of active processes can be extracted from mesoscopic *in-vivo* measurements.

20

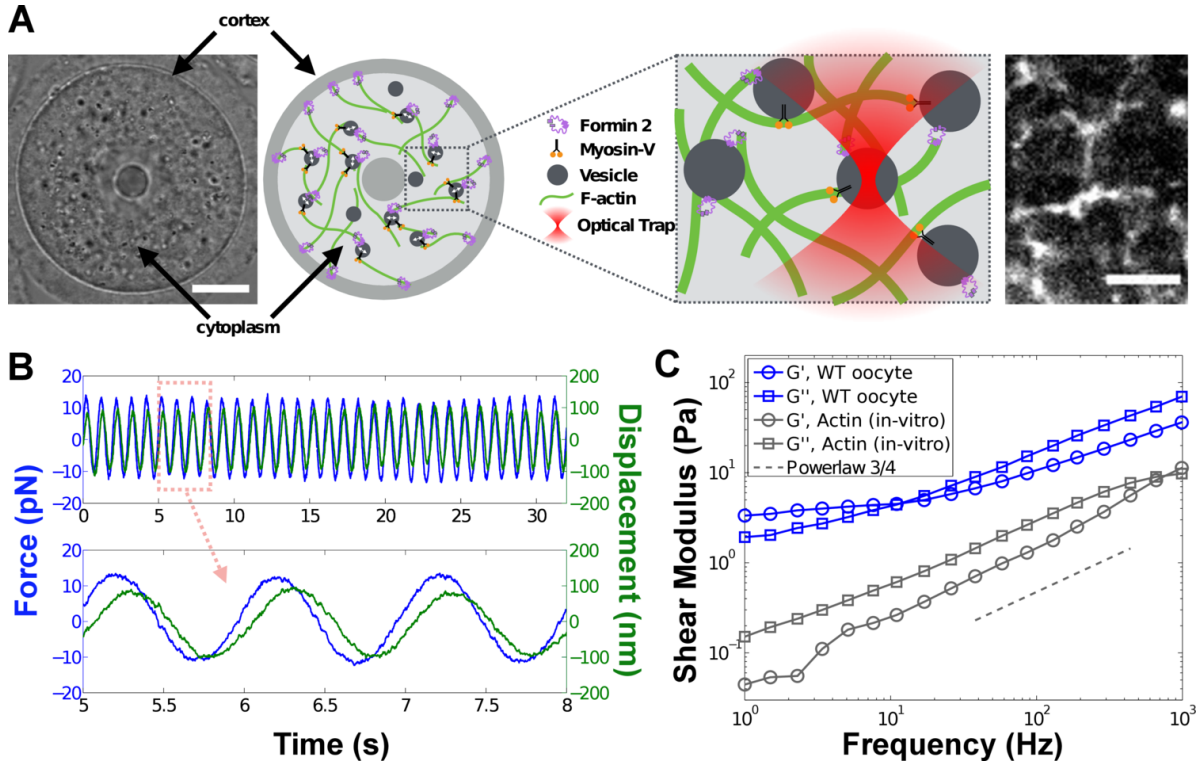


Figure 1: **Intracellular mechanics surrounding endogenous vesicles in living oocytes.** (A) Mouse oocytes are large spherical cells that have a well separated cortex and cytoplasmic-skeleton composed of biopolymer filaments (brightfield image, left)(scalebar = 20 μ m). During prophase-I it contains a dynamic actin-myosin-V meshwork that drives vesicle motion (schematic shown in center and fluorescent image of actin filaments on right)(scalebar = 5 μ m). Endogenous vesicles embedded in the cytoplasmic-skeleton are trapped using optical tweezers(zoomed inset). (B) Once a vesicle is trapped, the mechanical properties of the local environment can be measured by active microrheology (AMR) where a sinusoidal oscillating force is applied to the vesicle (blue) and the resulting displacement of the vesicle is measured (green). The viscoelastic shear modulus (G^*) is calculated from this force-displacement measurement via the Generalized Stokes-Einstein relation. (C) The mechanical properties surrounding vesicles in the cytoplasmic-skeleton of oocytes (blue) exhibits power-law behavior similar to reconstituted actin gels (gray) with frequency scaling $G^* \propto f^{0.75}$ except significantly stiffer. This shows that the cytoplasmic-skeleton in oocytes can be modeled as a semi-flexible polymer network.

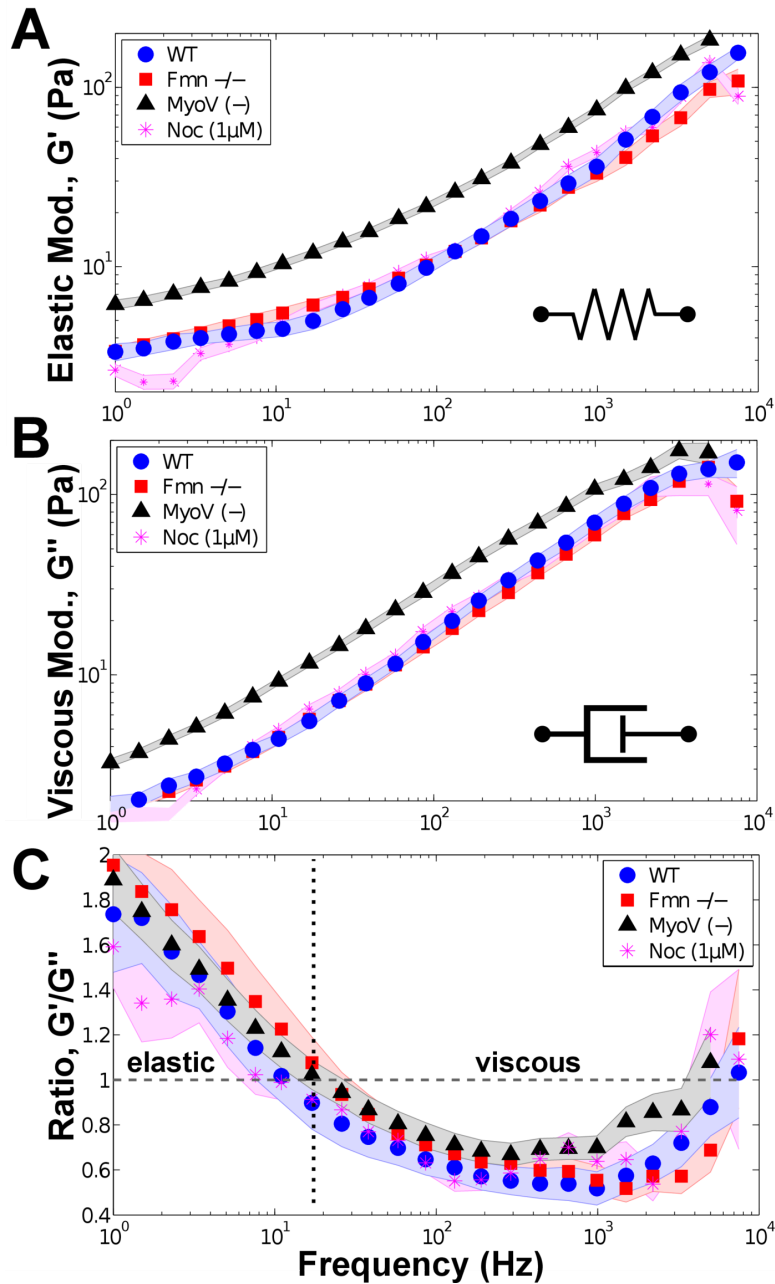


Figure 2: The cytoplasmic-skeleton of mouse oocytes is viscoelastic. (A, B) Insets indicate that G' quantifies the elasticity and G'' quantifies the viscous dissipation of the cytoplasmic-skeleton. The local mechanical properties (elastic and viscous) surrounding vesicles does not change from WT (blue, \circ) when actin (red \square) or microtubules (magenta $*$) are absent. However, when myosin-V is inactivated (gray Δ), the cytoplasmic-skeleton stiffens significantly (Kolmogorov-Smirnov test, $p < 1 \times 10^{-7}$), showing that the activity driven dynamics of the actin-myosin-V meshwork maintains the soft mechanical environment surrounding vesicles in oocytes. (C) The ratio of the elastic and viscous moduli (G'/G'') in all oocytes shows that the cytoplasmic-skeleton is more elastic at lower frequencies and more viscous at higher frequencies with a crossover around $\sim 10 - 20$ Hz. This shows the highly viscoelastic nature of the oocyte cytoplasmic-skeleton. (sample size = WT: 11 cells, 32 vesicles; Fmn2: 10 cells, 33 vesicles; MyoV(-): 23 cells, 69 vesicles; Noc(1μM): 8 cells, 52 vesicles; shaded region indicates SEM) (note: data at 10 Hz in panel A and B are presented in a different context in [20])

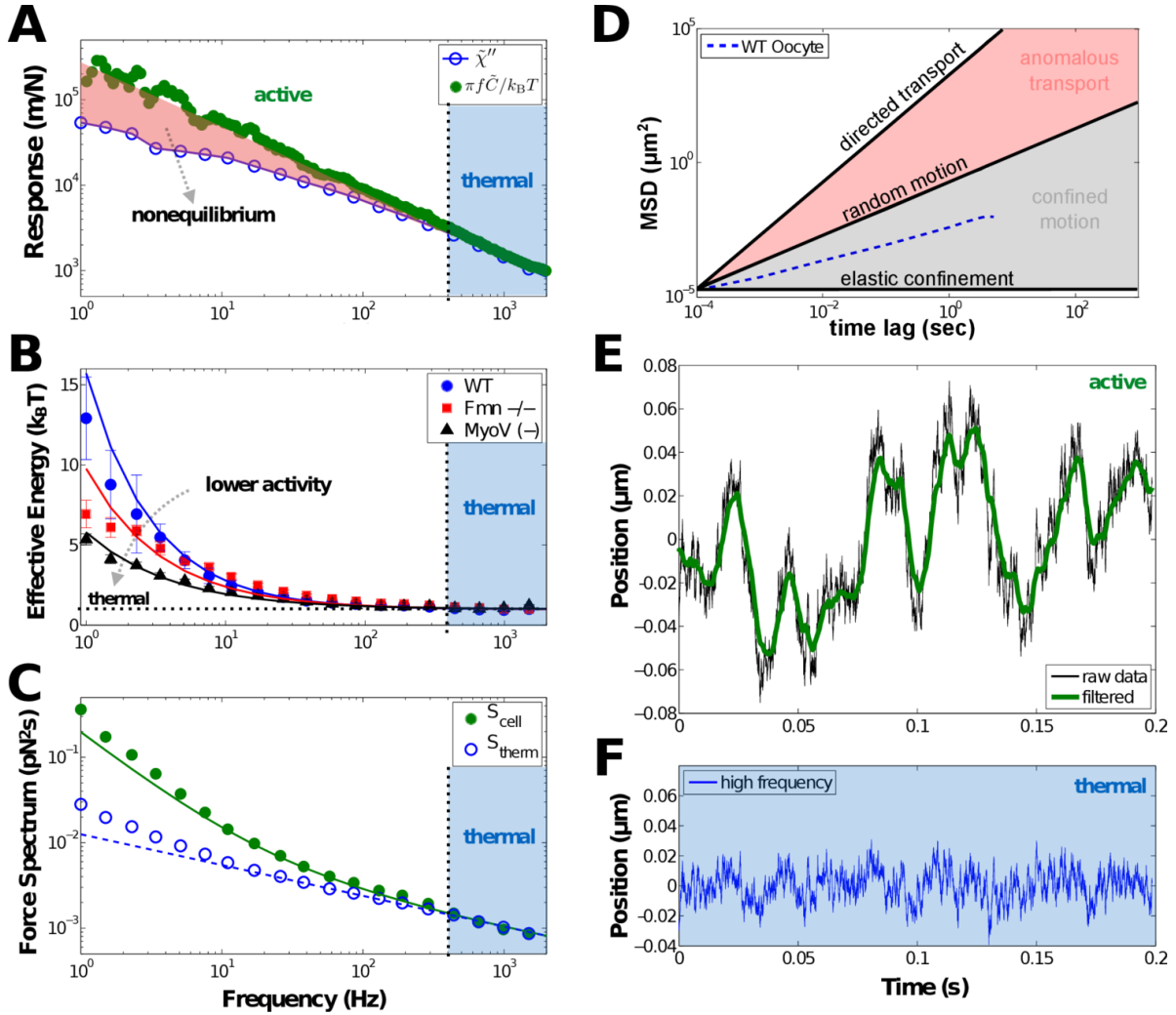


Figure 3: Active force generation by myosin-V drives the cytoplasmic-skeleton out-of-equilibrium. (A) The spontaneous motion of vesicles in oocytes (green circles) is larger than expected at thermal equilibrium (blue circles) at frequencies below 300 Hz showing that active forces are contributing to vesicle motion as highlighted by the red shaded region. This is direct evidence of nonequilibrium behavior in the cytoplasmic-skeleton (via violation of the fluctuation-dissipation theorem (FDT)). At high frequencies the observed vesicle motion resembles thermal motion indicated by the blue shaded region. (B) WT oocytes (blue) are the furthest from equilibrium as shown by their higher effective energy. In the absence of actin (red) or when myosin-V is inactivated (black) the dynamic actin-myosin-V meshwork is compromised and oocytes have lower effective energy. Solid lines are theoretical fits (equations in SI, error bars = SEM). (C) The cell force spectrum (S_{cell}) experienced by vesicles is the sum of thermal forces (S_{therm}) and active forces (S_{active}) generated by molecular motors. At high frequencies S_{cell} (green) is dominated by S_{therm} (blue) and the two spectra coincide (blue shaded region). At lower frequencies S_{cell} is larger than S_{therm} showing the existence of additional active forces. Solid lines are theoretical predictions (equations in SI), low-frequency deviation is due to simple power-law model. (D) The mean-squared-displacement (MSD) of vesicles indicates they undergo random-confined motion in the oocyte cytoplasmic-skeleton at short timescales. This behavior transitions to active diffusion at longer times [20], and is reminiscent of cytoplasmic stirring [30]. (E) When a representative trajectory (black) is filtered to remove the high-frequency thermal fluctuations the result is a smoothed trajectory (green) that represents actively driven motion. The difference between the true trajectory (gray) and the smoothed trajectory (green) recovers the high-frequency thermal fluctuations (blue) shown in (F).

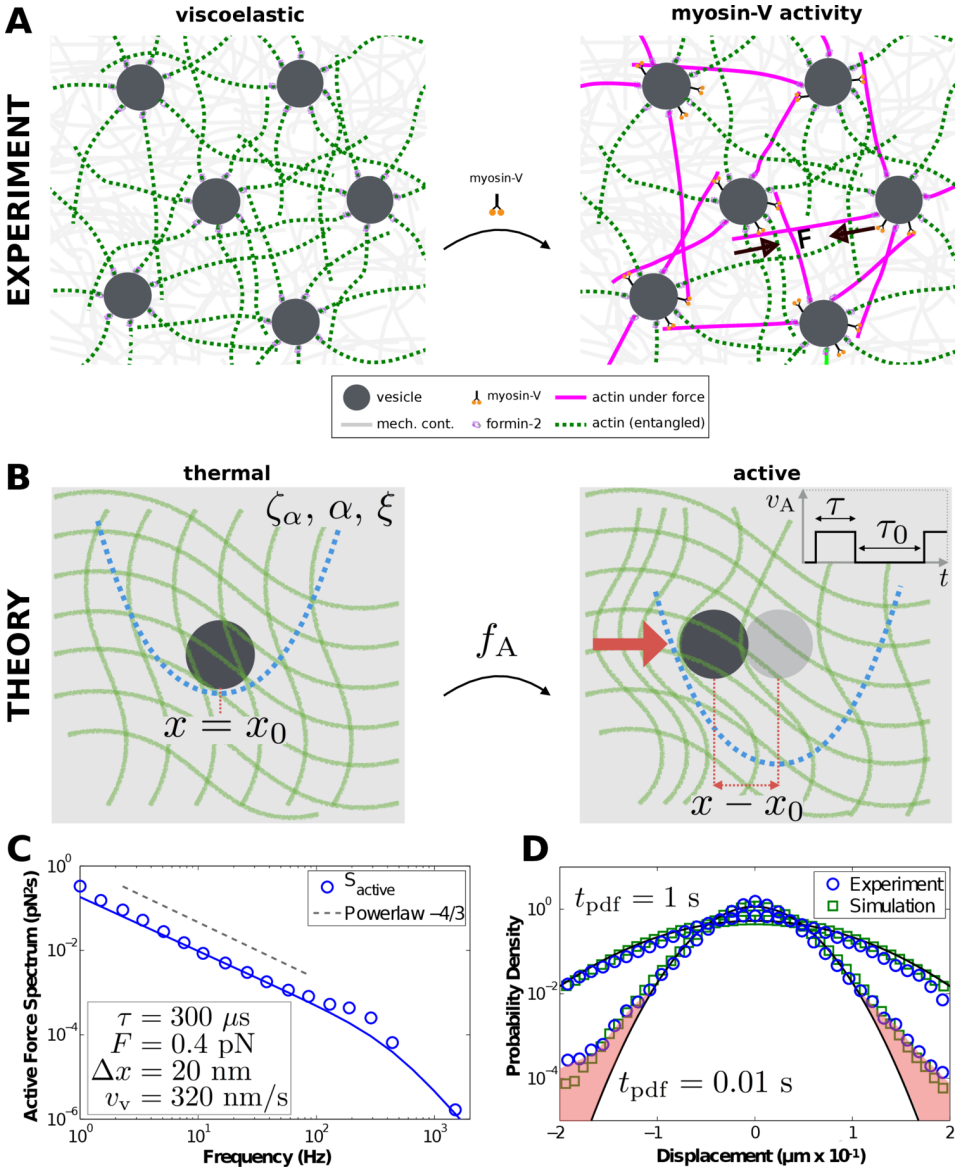


Figure 4: **A theoretical model of active mechanics connects in vivo measurements to molecular force kinetics.** (A) Vesicles (dark gray) are embedded in the complex mechanical continuum (gray background) of the oocyte interior. Actin filaments emanate from the surface of vesicles creating an entangled network (green, left). Myosin-V motors generate force on actin (magenta, right) giving rise to forces throughout the network driving vesicles in random directions. (B) We model vesicles embedded in a mechanical continuum with local stiffness (κ) represented by the blue harmonic potential, viscoelastic dissipation (ζ_α, α), and thermal fluctuations (ξ) (left). Molecular motor activity generates an active force (f_A) through bursts of motion (v_A) and drive motion of vesicles (inset indicates motor kinetics). (C) The active force spectrum (S_{active}) quantifies the forces on vesicles due to only active processes. Combined with our quantitative model we find that the vesicles are subject to 0.4 pN of force, during a power-stroke of length $\Delta x \sim 20 \text{ nm}$ and duration $300 \mu\text{s}$, resulting in a vesicle velocity of 320 nm/s, which is strikingly similar to the kinetics measured for single molecule myosin-V in-vitro and the in-vivo vesicle velocity. The solid line is the theoretical fit (equation 3), and the dotted line is a $-4/3$ power-law consistent with the cytoplasmic-skeleton mechanics. (D) Simulated vesicle motion (green squares) agrees with experimental data (blue circles) for a wide range of timescales as shown by the probability distribution of displacements. This includes long timescale ($t_{\text{pdf}} = 1 \text{ s}$) Gaussian behavior and short timescale ($t_{\text{pdf}} = 0.01 \text{ s}$) non-Gaussian tails (indicated by red-shaded regions) that are indicative of molecular motor behavior, where t_{pdf} is the time-lag for calculation of the displacement correlations. Gaussian distributions shown in black. These results show that molecular level kinetics of active processes can be extracted from mesoscopic in-vivo measurements.²⁰

List of Tables

1	Myosin-V force kinetics in-vivo and in-vitro	22
---	--	----

Table 1: Myosin-V force kinetics in-vivo and in-vitro

	in-vivo oocytes	single molecule myosin-V	reference
$F(\text{pN})$	0.4	0-4	[50, 52, 51, 53]
$\tau(\mu\text{s})$	300	160-1000	[52, 55, 54]
$\Delta x(\text{nm})$	20	15-25	[52, 56, 55, 54]
$v_v(\mu\text{m/s})$	320	270-480	[51, 53, 54]

Supporting Online Material for “Active mechanics reveal myosin-V force kinetics in living oocytes”

October 28, 2015

W. W. Ahmed*, É. Fodor*, M. Almonacid*, M. Bussonnier, M-H. Verlhac, N. S. Gov, P. Visco, F. van Wijland, T. Betz

* These authors contributed equally to this work

Theoretical Model

General: The motion of vesicles in the oocytes is modeled as tracer particles locally confined in the viscoelastic cytoplasm that is subjected to active force kicks. An active force kick is generated by a burst of motion which reorganizes the cytoskeleton and pushes the vesicle to a new position. The dynamics of the particle’s position, x , under the influence of active force kicks can be described in the overdamped Langevin framework as,

$$\int^t dt' \gamma(t-t') \frac{dx}{dt} = -\kappa(x-x_0) + \xi \quad (1)$$

$$\int^t dt' \gamma(t-t') \frac{dx_0}{dt} = \kappa \zeta_\alpha v_A \quad (2)$$

where ξ is Gaussian colored noise with correlations $\langle \xi(t)\xi(t') \rangle = k_B T \gamma(|t-t'|)$, as provided by the Fluctuation Dissipation Theorem[1], k_B is the Boltzmann constant, and T is the bath temperature of the environment. The viscoelastic material properties are described by, κ , the harmonic trap stiffness with center x_0 , and the memory kernel, $\gamma(t) = \gamma_\alpha t^{-\alpha}/\Gamma(1-\alpha)$, where Γ is the Gamma function, and $\zeta_\alpha = (\gamma_\alpha/\kappa)^{1/\alpha}$ is the microscopic timescale of the material. The active forces result from generation of the active burst velocity of molecular motors, v_A , which is a stochastic process consisting of alternating active and quiescent periods. During an active phase the active burst velocity, v_A , takes on a constant non-zero value, v , for a random exponentially distributed time of average value τ . During a quiescent phase the active burst velocity is 0 for an exponentially distributed random time τ_0 . The active burst velocity is a zero mean non-Gaussian colored noise process with correlations $\langle v_A(t)v_A(0) \rangle = k_B T_A \exp(-|t|/\tau)/(\kappa \zeta_\alpha \tau)$, where $k_B T_A = \kappa \zeta_\alpha (v\tau)^2/[3(\tau+\tau_0)]$ defines an active energy scale. Note that the dynamics of the joint process $\{x, x_0\}$ is not Markovian because of the memory kernel in the equations of motion.

From the generalized Stokes-Einstein relation, $\tilde{\gamma}(\omega) = 6\pi R \tilde{\eta}(\omega)$, where $\omega = 2\pi f$ is the frequency in radians/sec, R is the tracer’s radius, the memory kernel can be associated with a complex modulus $G^* = G' + iG''$ of the form,

$$G'(\omega) = \frac{1}{6\pi R} \left[\gamma_\alpha \omega^\alpha \cos\left(\frac{\pi\alpha}{2}\right) + \kappa \right] \quad (3)$$

$$G''(\omega) = \frac{\gamma_\alpha}{6\pi R} \omega^\alpha \sin\left(\frac{\pi\alpha}{2}\right) \quad (4)$$

where G' is the real component of the complex modulus, and G'' is the imaginary component.

The nonequilibrium properties of the motor activity are quantified by the deviation from the Fluctuation-Dissipation Theorem defined by a frequency dependent effective energy: $E_{\text{eff}}(\omega) = -\omega \tilde{C}(\omega)/(2\tilde{\chi}''(\omega))$, where

	α	ζ_α (s)	κ (pN · μm^{-1})	T_A/T	τ (ms)
WT	0.64	0.0657	20	5.5	0.30
Fmn2 -/-	0.6	0.103	18	5.0	0.15
Myo V(-)	0.57	0.163	27	3.8	0.1

Table 1: Theoretical fit parameters.

$\tilde{\chi}''$ is the imaginary part of the response Fourier Transform, and \tilde{C} is the position autocorrelation function in the Fourier Domain. We compute it in terms of the microscopic ingredients:

$$E_{\text{eff}}(\omega) = k_B T + \frac{1}{(\omega \zeta_\alpha)^{3\alpha-1} \sin(\pi \alpha/2)} \frac{k_B T_A}{1 + (\omega \tau)^2} \quad (5)$$

where $k_B T_A$ is the energy scale associated with the active process. The dynamics of the tracer can be written as: $x(t) = \int^t dt' \chi(t-t') F_{\text{cell}}(t')$, where $F_{\text{cell}} = \xi + \kappa x_0$ is the cell force which describes the thermal forces arising in the cell and the effect of the active forces via x_0 . This expression reveals one can access the cell force power spectrum S_{cell} by combining measurements of G^* and \tilde{C} : $S_{\text{cell}} = (6\pi R)^2 |G^*|^2 \tilde{C}$. Within our model, this expression can be separated into two contributions: $S_{\text{cell}} = S_{\text{therm}} + S_{\text{active}}$, where S_{therm} is the thermal force spectrum, and S_{active} is the active force spectrum. From the definition of the thermal force correlations, we deduce the thermal force spectrum: $S_{\text{therm}} = 12\pi R G'' k_B T / \omega$. We compute the explicit expression of the two contributions of the cell force spectrum:

$$S_{\text{therm}}(\omega) = 2\gamma_\alpha k_B T \omega^{\alpha-1} \sin\left(\frac{\pi\alpha}{2}\right) \quad (6)$$

$$S_{\text{active}} = \underbrace{\frac{2\kappa\zeta_\alpha}{(\omega\zeta_\alpha)^{2\alpha}}}_{\text{mechanics}} \underbrace{\frac{k_B T_A}{1 + (\omega\tau)^2}}_{\text{motor kinetics}} \quad (7)$$

If we define an apparent typical active force generated by the motor activity to be $F = \kappa v \tau$ then we can substitute this directly into the definition for the active temperature ($k_B T_A$) and rewrite the active force spectrum in a more intuitive way as,

$$S_{\text{active}} = \underbrace{\frac{1}{(\omega\zeta_\alpha)^{2\alpha}}}_{\text{mechanics}} \underbrace{\frac{1}{1 + (\omega\tau)^2} \frac{2(F\zeta_\alpha)^2}{3(\tau + \tau_0)}}_{\text{motor kinetics}} \quad (8)$$

as seen in the main text (recall that $\omega = 2\pi f$). When looking at the active force spectrum (Figure 1) the power law dependence of equation 8 becomes very clear. At low frequencies there is a power-law dependence of -4/3 consistent with the mechanics ($\alpha \approx 2/3$) and at high frequencies the power-law dependence is approximately -10/3 consistent with motor kinetics and mechanics. The crossover between these two regimes occurs at $1/\tau$ as shown approximately by the purple dotted line in Figure 1.

When applying the theoretical model to the experimental data, first the mechanical measurements from AMR was used to fit equations 3 and 4 to determine the mechanical parameters: $\alpha, \gamma_\alpha, \kappa$ from the data shown in Figure 2C, and D of the main text. Once the mechanics is determined, the remaining equations are largely constrained. The best fit of the data for effective energy (Fig 3B of main text) is used to determine $k_B T_A$ in equation 5, where the fit is independent of τ when $\tau < 10$ ms. From fitting the active force spectrum we find that $\tau = 0.3$ ms to capture the high-frequency drop-off (Figure 4B of main text). The fit parameters for the theoretical model are shown in Table 1. To summarize: $\alpha, \zeta_\alpha, \kappa$ are obtained from fitting AMR measurements of the mechanics (G', G''), T_A/T is obtained from fitting the effective energy data (E_{eff}), and τ is obtained from fitting the active force spectrum (S_{active}). Then combining the apparent typical active force, F , and the active energy scale, $k_B T_A$, we can calculate, $F = [3\kappa k_B T_A (\tau + \tau_0)/\zeta_\alpha]^{1/2}$ which is the active force felt by the vesicles due to the motor activity. Once the force, F , is known the step-size can be deduced as $\Delta x = F/\kappa$. Similarly, to estimate the velocity of a vesicle we calculate, $v_V = F/(\kappa\zeta_\alpha)$, where F is the average active force and $\kappa\zeta_\alpha$ is the resistance provided by the surrounding mechanical environment. These parameters ($F, \tau, v_V, \Delta x$) are the molecular force kinetics reported in Figure 4B of the main text.

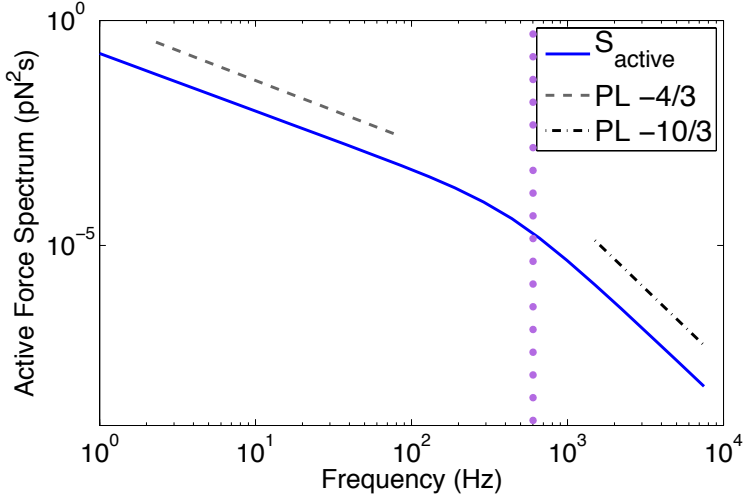


Figure 1: The active force spectrum shows two distinct power-law (PL) behaviors at low and high frequency.

Simulations To simulate the dynamics of the vesicles, we first approximate the power law memory kernel $\gamma(t) \propto t^{-\alpha}$ as a finite sum of exponential functions (Prony series): $\gamma(t) = \sum_i c_i e^{-t/\sigma_i} / \sigma_i$. Following the methods developed in [2], it is possible, with N exponential terms, to accurately approximate a power law decay over N decades. Parameters c_i and σ_i are then given by,

$$\sigma_i = \frac{10^i}{\alpha}, \quad c_i = \frac{\kappa \zeta_\alpha^\alpha}{\Gamma(1-\alpha)} \frac{10^{-i(\alpha-1)}}{\alpha \sum_j 10^{-j\alpha} e^{-\alpha/10^j}} \quad (9)$$

We approximate the power law kernel in the time window $[10^{N_-}, 10^{N_+ - 1}]$, where $N_- < 0 < N_+$, and $N = N_+ - N_- + 1$. Then, the index in the Prony series goes from $i = N_-$ to $i = N_+$.

With γ a sum of N exponential functions, it is possible to turn equations 1 and 2 into a $(2N + 2)$ -dimensional Markovian process for the variables $\{x, x_0, y_{N_-}, \dots, y_{N_+}, z_{N_-}, \dots, z_{N_+}\}$ [3]:

$$\sum_{i=N_-}^{N_+} \frac{c_i}{\sigma_i} (x - y_i) = -\kappa(x - x_0), \quad \sum_{i=N_-}^{N_+} \frac{c_i}{\sigma_i} (x_0 - z_i) = \kappa \zeta_\alpha v_A, \quad (10)$$

$$c_i \frac{dy_i}{dt} = -\frac{c_i}{\sigma_i} (y_i - x) + \xi_i, \quad \frac{dz_i}{dt} = -\frac{z_i - x_0}{\sigma_i}, \quad (11)$$

where the $\{\xi_i\}_i$ are the zero mean Gaussian noises with correlations $\langle \xi_i(t) \xi_j(t') \rangle = 2k_B T c_i \delta_{ij} \delta(t - t')$. By using Euler's methods to simulate this set of equations, the iterative equations take the following form in terms of the sampling time Δt ,

$$y_i(t + \Delta t) = y_i(t) - \frac{\Delta t}{\sigma_i} (y_i(t) - x(t)) + \sqrt{\frac{2k_B T \Delta t}{c_i}} \eta, \quad z_i(t + \Delta t) = z_i(t) - \frac{\Delta t}{\sigma_i} (z_i(t) - x_0(t)) \quad (12)$$

$$x_0(t + \Delta t) = \frac{\kappa \tau_\alpha v_A (t + \Delta t) + \sum_i c_i z_i(t + \Delta t) / \sigma_i}{\sum_i c_i / \sigma_i}, \quad x(t + \Delta t) = \frac{\kappa x_0(t + \Delta t) + \sum_i c_i y_i(t + \Delta t) / \sigma_i}{\kappa + \sum_i c_i / \sigma_i} \quad (13)$$

where η is random Gaussian variable with zero mean and variance equal to 1, and v_A is the stochastic process

described earlier, which is computed according to the following rules:

$$v_A(t + \Delta t) = \begin{cases} v_A(t) & \text{if } v_A(t) \neq 0 \text{ with Pr. } 1 - \Delta t/\tau \\ v_A(t) & \text{if } v_A(t) = 0 \text{ with Pr. } 1 - \Delta t/\tau_0 \\ 0 & \text{if } v_A(t) \neq 0 \text{ with Pr. } \Delta t/\tau \\ U_{[-v, v]} & \text{if } v_A(t) = 0 \text{ with Pr. } \Delta t/\tau_0 \end{cases} \quad (14)$$

where $U_{[-v, v]}$ is a uniform random number between $-v$ and v and $\tau_0 = \tau(1 - pon)/pon$ is the timescale over which the active burst is 0.

In order to mimic the experimental condition, we chose a sampling time $\Delta t = 10^4$ s, and we aimed to simulate our process up to 10 s. Then, we have set $\{N_-, N_+\} = \{4, -2\}$, so that the power law memory kernel is well approximated in the time window $[10^{-4}, 10]$ s, with parameter values $\{\alpha, \kappa\zeta_\alpha^\alpha, N_-, N_+\} = \{0.6, 1, -4, 2\}$

Other parameters in the simulation were chosen according to the numerical fits over experimental data, and as listed in Table 1 where $pon = 4\%$ and $v = 60\mu\text{m} \cdot \text{s}^{-1}$ where $pon = \tau/(\tau + \tau_0)$ where $(\tau + \tau_0)$ is the total myosin-V step duration [4, 5] and v is the active burst velocity of the myosin-V motor itself calculated from $v = F/(\kappa\tau)$. We also took $k_B T = 4 \times 10^{-21}$ J.

We started the simulation with all variables set to 0 and waited for thermalization by running the simulation for 10^3 time steps. We then start collecting position data x in order to build the histogram for the probability distribution function of the position. A total of approximately 10^5 samples were collected to arrive at the histogram in Fig 4 of the main text.

Crossover to thermally dominated forces

The relative balance between intracellular mechanical properties and active forces determines the frequency at which nonequilibrium activity becomes evident ($S_{\text{cell}} > S_{\text{therm}}$). To illustrate this we explore how mechanical properties change the force spectrum (equation 6 and 7). The total force spectrum is the sum of contributions from active forces and thermal forces, ($S_{\text{cell}} = S_{\text{active}} + S_{\text{therm}}$). Fig 2A shows the theoretical curves for the force spectrum measured in the present study. Here, we can observe that the magnitude of thermal and active forces is equal at 20 Hz (denoted by the purple diamond) and that thermal forces dominate the spectrum ($S_{\text{cell}} \approx S_{\text{therm}}$) at approximately 300 Hz (gray star). This also highlights that the active forces still contribute to the total force spectrum even when they are much smaller than the thermal forces. Now if the system is made softer by decreasing the coefficient of the viscoelastic memory kernel, $\gamma_\alpha = 0.2 \cdot \gamma_\alpha(\text{WT})$, we see that thermal forces do not dominate until 1000 Hz (Fig 2B). Alternatively, if the system is made stiffer ($\gamma_\alpha = 5 \cdot \gamma_\alpha(\text{WT})$) (Fig 2C), then thermal forces begin to dominate at much lower frequency (25 Hz, gray star). Therefore, by only changing the mechanical properties of the system by a small amount, the frequency at which thermal forces dominate can be changed dramatically.

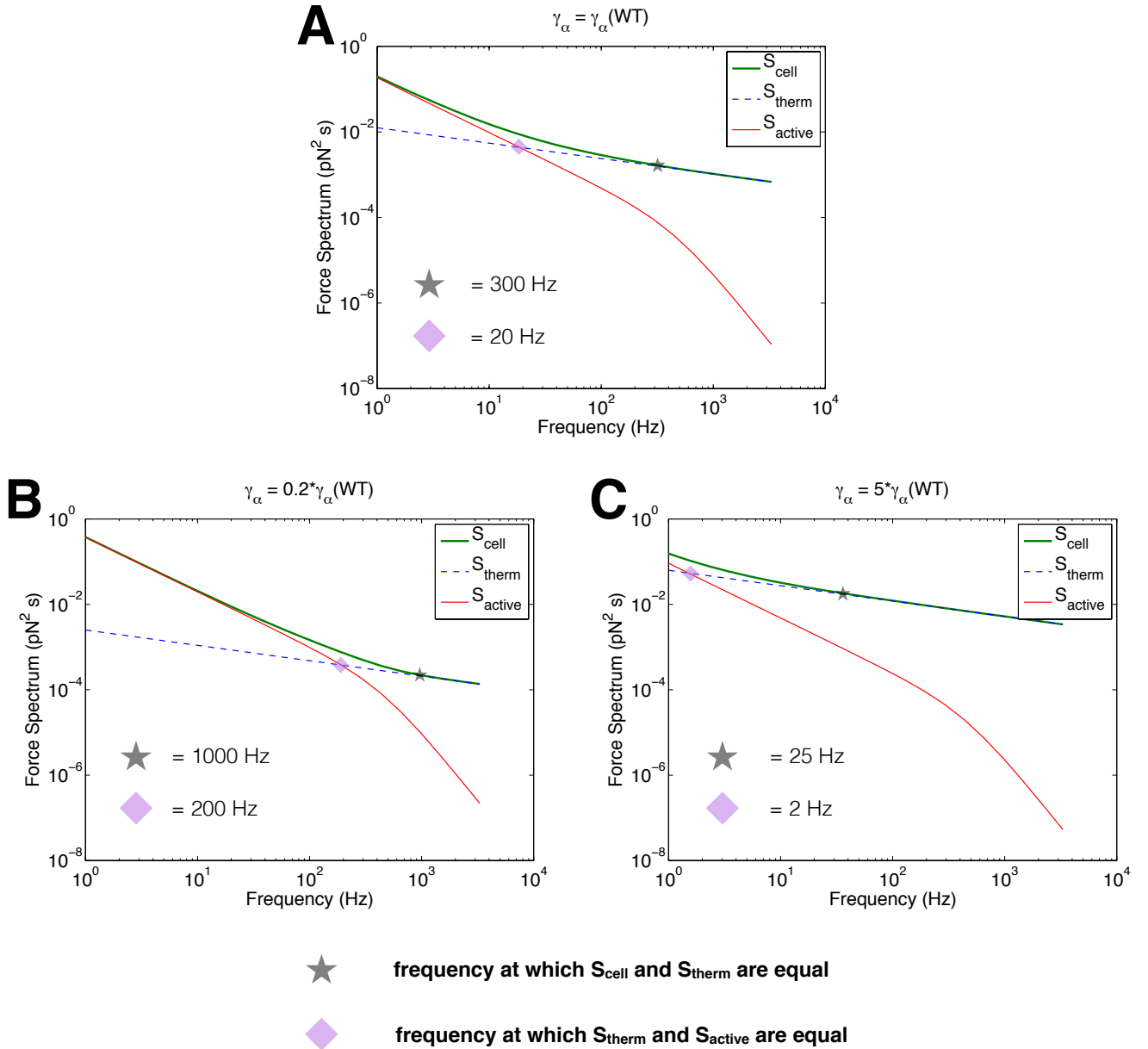


Figure 2: Force spectrum depends on the mechanical properties of the system. (A) The theoretical curves for the force spectrum measured in the experiments in this study where the coefficient of the memory kernal is $\gamma_\alpha = \gamma_\alpha(\text{WT})$ and the thermal forces dominate at around 300 Hz. (B) The mechanical properties are softened by $\gamma_\alpha = 0.2 \cdot \gamma_\alpha(\text{WT})$ and the frequency where thermal forces dominate is shifted up to 1000 Hz. (C) The mechanical properties are stiffened by $\gamma_\alpha = 5 \cdot \gamma_\alpha(\text{WT})$ and the thermal forces dominate at 25 Hz.

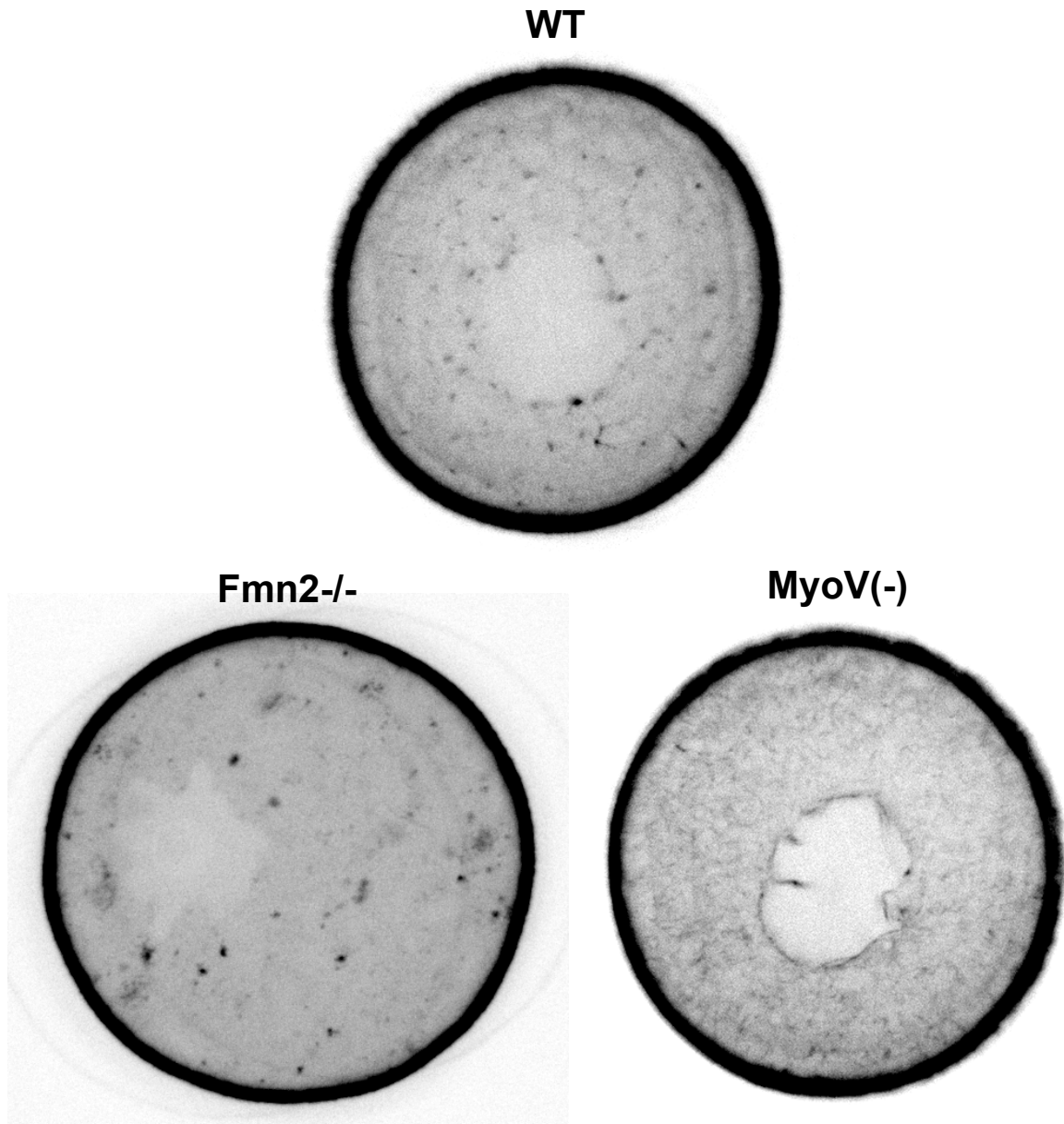


Figure 3: The actin meshwork was visualized with GFP-UtrCH to show the actin meshwork. WT oocytes exhibit a network of actin positive vesicles connected by actin filaments to create a meshwork. Fmn2 $-/-$ exhibited punctate actin but no visible meshwork. MyoV($-$) exhibit an increased density actin meshwork relative to WT. Images were captured at 37 degrees Celsius using a 40x objective (1.25NA) on a Leica DMI6000B microscope enclosed in a thermostatic chamber (Life Imaging Service) equipped with a CoolSnap HQ2/CCD-camera (Princeton Instruments) coupled to a Sutter filter wheel (Roper Scientific) and a Yokogawa CSU-X1-M1 spinning disc. (oocyte diameter is 80 μm)

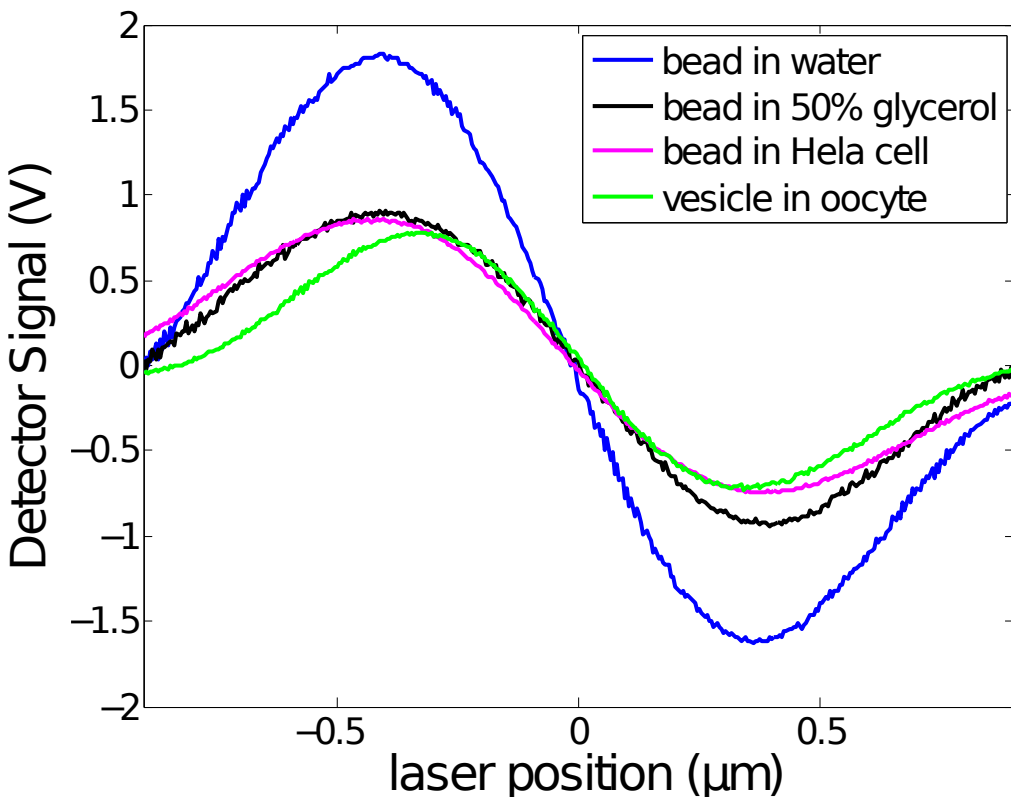


Figure 4: QPD voltage vs. laser position for various conditions. The slope of the central linear region is indistinguishable between a vesicle in an oocyte (green), a 1 micron colloidal bead in a Hela cell (magenta), and a 1 micron colloidal bead in an index matched solution of 50:50 water:glycerol. For comparison, the slope of a 1 micron colloidal bead in pure water is significantly steeper due to the higher difference in index of refraction.

References

- [1] Kubo, R. (1966) The fluctuation-dissipation theorem. *Reports on Progress in Physics* **29**, 255.
- [2] Bochud, T & Challet, D. (2007) Optimal approximations of power laws with exponentials: application to volatility models with long memory. *Quantitative Finance*.
- [3] Baczewski, A. D & Bond, S. D. (2013) Numerical integration of the extended variable generalized Langevin equation with a positive Prony representable memory kernel. *The Journal of Chemical Physics* **139**, 044107.
- [4] Cappello, G, Pierobon, P, Symonds, C, Busoni, L, Gebhardt, J. C. M, Rief, M, & Prost, J. (2007) Myosin V stepping mechanism. *Proceedings of the National Academy of Sciences of the United States of America* **104**, 15328–15333.
- [5] Uemura, S, Higuchi, H, Olivares, A. O, De La Cruz, E. M, & Ishiwata, S. (2004) Mechanochemical coupling of two substeps in a single myosin V motor. *Nature Structural & Molecular Biology* **11**, 877–883.

Nonequilibrium dissipation in living oocytes

As a first insight into the energetics of the active fluctuations with memory effects, we estimate the average power transferred from the tracer to the thermostat $\langle \dot{\mathbf{r}} \cdot (\gamma * \dot{\mathbf{r}} - \boldsymbol{\xi}) \rangle$, where $*$ denotes the convolution in time. The spectral density $I(\omega)$ of this power reads

$$I(\omega) = \frac{(\omega\tau_\alpha)^{\alpha-1} \sin(\pi\alpha/2)}{1 + 2(\omega\tau_\alpha)^\alpha \cos(\pi\alpha/2) + (\omega\tau_\alpha)^{2\alpha}} \frac{T_A}{1 + (\omega\tau)^2}. \quad (5.9)$$

It exhibits several power-law regimes with exponents depending on the mechanics via α . When integrating over the whole spectra, we deduce the average power dissipated by the tracer in the thermostat. From the best fit parameters, we estimate $\langle \dot{\mathbf{r}} \cdot (\gamma * \dot{\mathbf{r}} - \boldsymbol{\xi}) \rangle \sim 360 k_B T/s$. This is to be compared with the typical power dissipated by one myosin-V motor. Provided that one of such motors do a work of about $3 k_B T$ during a power stroke of approximately 0.3 ms, we deduce that the corresponding work is of the order of $10^4 k_B T/s$. Therefore, the power dissipated by the tracer is approximately three times smaller than the one injected by a single motor. This apparent contradiction is due to the fact that, in our phenomenological picture, the forces exerted by the motors do not act directly on the tracers, they serve to remodel the cytoskeleton network. Consequently, the power dissipated by the tracer accounts for the transmission of forces from the local rearrangement of the surrounding network into the tracer displacement, which is mediated by the dynamics of the active cage.

To provide a quantitative estimation of the efficiency of power transmission from the cage motion to the tracer motion, we compare the power of two distinct forces. As discussed in Chapter 1, the power transferred from the tracer to the thermostat reduces to the power of the active force acting directly on the tracers $\langle \dot{\mathbf{r}} \cdot \mathbf{f}_A \rangle$, where $\mathbf{f}_A = k\mathbf{r}_0$ for the active cage model. We introduce the power of the force $k\tau_\alpha \mathbf{v}_A$ which describes the active bursts driving the cage dynamics as $\langle \dot{\mathbf{r}}_0 \cdot k\tau_\alpha \mathbf{v}_A \rangle$. Taking into account the back action force and the thermal noise acting on the cage, as done in Chapter 3, this power acquires the interpretation of a balance between damping and thermal fluctuations at the level of the cage. We derive its analytic expression as

$$\langle \dot{\mathbf{r}}_0 \cdot k\tau_\alpha \mathbf{v}_A \rangle = \frac{T_A}{\tau} \left(\frac{\tau_\alpha}{\tau} \right)^{1-\alpha}. \quad (5.10)$$

It leads us to define an efficiency of power transduction as

$$\rho = \frac{\langle \dot{\mathbf{r}} \cdot \mathbf{r}_0 \rangle}{\langle \dot{\mathbf{r}}_0 \cdot \tau_\alpha \mathbf{v}_A \rangle}. \quad (5.11)$$

It only depends on the time scales τ and τ_α . Using the values extracted from the best fits of the effective temperature and the spectral density $I(\omega)$, we deduce that

the efficiency ρ is very low: $\rho \sim 10^{-3}$. This suggests that only a small proportion of the power injected by the motors in the oocytes is dedicated to displace the vesicles: the main contribution goes into the network remodeling without affecting the vesicle dynamics.

We present the details of the analytic derivations along with the data analysis in paper D reproduced below.

Nonequilibrium Dissipation in Living Oocytes

É. Fodor,^{1,*} W. W. Ahmed,^{2,*} M. Almonacid,^{3,*} M. Bussonnier,²
N. S. Gov,⁴ M.-H. Verlhac,³ T. Betz,² P. Visco,¹ and F. van Wijland^{1,5}

¹*Laboratoire Matière et Systèmes Complexes, UMR 7057 CNRS/P7, Université Paris Diderot,
10 rue Alice Domon et Léonie Duquet, 75205 Paris cedex 13, France*

²*Physico-Chimie Curie, UMR 168 CNRS/P6, Institut Curie,
11, rue Pierre et Marie Curie, 75005 Paris, France*

³*CIRB, Collège de France, CNRS-UMR7241, INSERM-U1050, 75231 Paris, Cedex 05, France*

⁴*Department of Chemical Physics, Weizmann Institute of Science, 76100 Rehovot, Israel*

⁵*Department of Chemistry, University of California, Berkeley, CA, 94720, USA*

(Dated: December 27, 2015)

Living organisms are inherently out-of-equilibrium systems. We employ new developments in stochastic energetics and rely on a minimal microscopic model to predict the amount of mechanical energy dissipated by such dynamics. Our model includes complex rheological effects and nonequilibrium stochastic forces. By performing active microrheology and tracking micron-sized vesicles in the cytoplasm of living oocytes, we provide unprecedented measurements of the spectrum of dissipated energy. We show that our model is fully consistent with the experimental data, and we use it to offer predictions for the injection and dissipation energy scales involved in active fluctuations.

PACS numbers: 05.40.-a, 05.10.Gg, 02.50.Ey, 87.10.Mn

Perrin's century old picture [1] where the Brownian motion of a colloid results from the many collisions exerted by the solvent's molecules is a cornerstone of soft-matter physics. Langevin [2] modeled the ensuing energy exchanges between the solvent and the colloidal particle in terms of a dissipation channel and energy injection kicks. The key ingredient in the success of that theory was to completely integrate out the "uninteresting" degrees of freedom of the solvent whose properties are gathered in a friction constant and a temperature. In this work we take exactly the reverse stance and ask how, by observing the motion of a tracer embedded in a living medium, one can infer the amount of energy exchange and dissipation with the surrounding medium. The main goal is to quantify the energetic properties of the medium, both injection and dissipation-wise.

This is a stimulating question because there are of course striking differences between a living cell and its equilibrium polymer gel counterpart, to which newly developed [3, 4] methods of nonequilibrium statistical mechanics apply. Beyond thermal exchanges that fall within the scope of a Langevin approach, ATP consumption fuels molecular motor activity and drives relentless rearrangement of the cytoskeleton. This chemically driven continuous injection and dissipation of energy adds a nonequilibrium channel that eludes straightforward quantitative analysis. In short, a living cell is not only a fertile playground for testing new ideas from nonequilibrium physics, but also one in which these ideas can lead to a quantitative evaluation of an otherwise ill-understood activity which is of intrinsic biophysical interest. Our work addresses both aspects by a combination of active microrheology, tracking experiments, and theoretical modeling.

One experimental way to access nonequilibrium physics

in the intracellular medium is to focus on the deviation from thermal equilibrium behavior of the tracer's position statistics: forming the ratio of the response of the tracer's position to an infinitesimal external perturbation to its unperturbed mean-square displacement leads to a quantity that only reduces to the inverse temperature when in equilibrium, by virtue of the fluctuation-dissipation theorem (FDT). Earlier tracking experiments supplemented by microrheology techniques have allowed the departure from equilibrium to be analyzed in terms of this ratio in a variety of contexts [5–10] ranging from reconstituted actin gels to single cells. However the limitations inherent to this effective temperature are well-known: it bears no universal meaning as it depends on the observable under scrutiny, thus it cannot be equated to a *bona fide* temperature, and hence it does not connect to the underlying microscopic dynamics.

Here we exploit a body of theoretical methods that have been developed over the last ten years to infer quantitative information about the nonequilibrium processes driving intracellular dynamics. Within the realm of stochastic thermodynamics [3, 4] –as it strives to extend concepts of macroscopic thermodynamics to small and highly fluctuating systems [11–13], the Harada-Sasa equality stands out as being particularly suited to our goal. Nonequilibrium systems are characterized by the dissipation of energy, which is absorbed by the surrounding thermostat *via* a transfer from the system to the bath. The Harada-Sasa equality connects the rate of dissipated energy to the spatial fluctuations in a nonequilibrium steady-state system [14, 15]. The feasibility of measuring the various ingredients in the Harada-Sasa framework was demonstrated in model systems such as a micron-sized colloidal particle in a viscous fluid [16, 17], and then later generalized to a

viscoelastic medium [18]. It has also been used to quantify the efficiency of an isolated molecular motor [19].

The systems to which we apply this equality are micron-sized vesicles that are present in the cytoplasm of mouse unfertilized eggs, known as oocytes. Their motion in the cell is mainly regulated by myosin-V motors on the actin network [20–22]. The use of such vesicles allows us to capture the intrinsic intracellular dynamics without using artificial external particles that may alter the environment. From a physics perspective, oocytes are also major assets since they constitute a rare example of a living cell that remains steady on the timescales of hours. They are spherical in shape, with typical radius of about $40 \mu\text{m}$, and their nucleus is centrally located at the end of Prophase I [23].

In this paper, we directly access nonequilibrium dissipation within the cell. We first characterize the intrinsic rheology of the medium experienced by the vesicles. Then, we present a minimal microscopic model for the dynamics of the vesicles which is driven by the nonequilibrium reorganization of the cytoskeleton by molecular motor generated forces. We use our theoretical modeling and the Harada-Sasa equality to predict and quantify the rate of nonequilibrium dissipated energy in our experimental system. Finally, we employ this new prediction to evaluate how nonequilibrium activity varies across the cell, and we offer interpretations about the role of molecular motors in vesicle motion.

Experimental setup.—Mouse oocytes are collected from 13 week old mice and embedded in a collagen gel between two glass coverslips [24, 25]. We measure the local mechanical environment surrounding vesicles in living mouse oocytes using active microrheology [5, 26]. We use an optical tweezer to trap vesicles and apply a sinusoidal oscillating force [Fig. 1]. The resulting displacement of the vesicle due to the applied force reflects the mechanical response of the system. We deduce the complex modulus of the intracellular environment surrounding the vesicle from the generalized Stokes-Einstein relation $G^* = 1/(6\pi a\tilde{\chi})$, where $\tilde{\chi}$ is the Fourier response function, and a is the vesicle's average radius.

We find that the intracellular mechanics exhibits a power law rheology at high frequencies, and levels off at lower frequencies, as seen in the real and imaginary parts of G^* , respectively denoted by G' and G'' [Fig. 1(c)]. We fit the experimental data with the function $G^*(\omega) = G_0(1 + (i\omega\tau_\alpha)^\alpha)$, where τ_α is a thermal relaxation time scale [25, 27, 28]. To experimentally quantify nonequilibrium dissipation, we must also measure the spontaneous motion of the vesicles by laser interferometry, and extract the power spectral density of the vesicles' position [29], as is done for passive microrheology [30] [Fig. 1(d)]. These spontaneous fluctuations entangle information about the thermal and nonequilibrium forces applied on vesicles in the oocyte cytoskeleton [26].

Caging model.—We propose a model for the vesicle dynamics the surrounding fluctuating actin mesh that takes the observed power law behavior of G^* into account. The

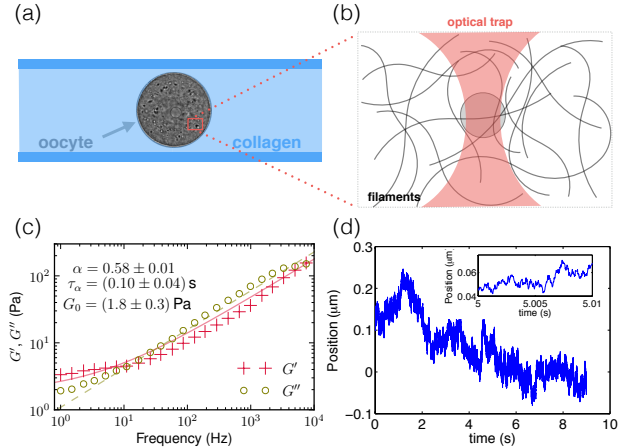


FIG. 1: (Color online) Experimental setup for measuring oocyte microrheology. (a) We embed oocytes in a collagen matrix between two glass coverslips to prevent rolling during measurement. (b) We use optical tweezers to trap intracellular vesicles and perform active microrheology to measure local mechanical properties [5]. (c) Real (G') and imaginary (G'') part of the complex modulus, measured from active microrheology. Data at 10 Hz is used in [22]. (d) We use laser tracking interferometry to track spontaneous vesicle motion with high spatiotemporal resolution (10 nm, 1 kHz) [29].

model has itself been previously introduced in [31], but it is generalized here to encompass strong memory effects [32]. The underlying physical picture is that the vesicle is caged in the cytoskeleton [Fig. 1(b)], modeled as a harmonic trap of constant k , while nonequilibrium activity induces rearrangements of the cytoskeletal network resulting in a displacement of the cage. In a medium characterized by a memory kernel ζ , we then describe the one dimensional position x of a vesicle with two coupled generalized Langevin-like equations involving the center of the cage x_0 :

$$\zeta * \frac{dx}{dt} = -k(x - x_0) + \xi, \quad \zeta * \frac{dx_0}{dt} = k\tau_\alpha v_A, \quad (1)$$

where $*$ denotes the convolution product, ξ is a zero mean Gaussian colored noise with correlations $\langle \xi(t)\xi(t') \rangle = k_b T \zeta(|t - t'|)$ as provided by the FDT [33], and T is the bath temperature.

The cage motion is given by the active burst v_A : a zero mean stochastic process representing the random vesicle motion driven by cellular activity [22, 32]. In our further analysis, we consider that this process has a single timescale τ that governs its decorrelation: $\langle v_A(t)v_A(0) \rangle = k_b T_A e^{-|t|/\tau} / (k\tau_\alpha \tau)$, where, by analogy with standard Langevin equation, we have defined an *active* temperature T_A associated to the amplitude of this process. Notice that T_A is a scalar quantity which quantifies the amplitude of the active fluctuations. We choose the memory kernel ζ to recover the observed behavior of the

measured G^* by adopting a power law decay $\zeta(t) = k(\tau_\alpha/t)^\alpha \Theta(t)/\Gamma(1-\alpha)$, where Γ is the Gamma function, Θ is the Heaviside function, and $\alpha < 1$. From the generalized Stokes-Einstein relation, we derive that $G^*(\omega) = [k + i\omega\tilde{\zeta}(\omega)]/(6\pi a)$ [34], where the superscript tilde denotes a Fourier transform [25]. This expression has exactly the same structure as the phenomenological function we use to fit G^* with $k = 6\pi a G_0$. Our approach can be extended in a straightforward manner to other kinds of rheology.

Effective temperature.—We define a frequency dependent “effective temperature” $T_{\text{eff}}(\omega) = -\omega\tilde{C}(\omega)/[2k_B\tilde{\chi}''(\omega)]$, where \tilde{C} and $\tilde{\chi}''$ are the Fourier position autocorrelation function and the imaginary part of the response function, respectively [8, 9, 35]. We compute it in terms of the microscopic parameters as [25]

$$T_{\text{eff}}(\omega) = T + \frac{1}{(\omega\tau_\alpha)^{3\alpha-1} \sin(\frac{\pi\alpha}{2})} \frac{T_A}{1 + (\omega\tau)^2}. \quad (2)$$

The high frequency value collapses to the bath temperature as for an equilibrium behaviour and constitutes a useful benchmark [8]. It also diverges at low frequency as a result of nonequilibrium activity, with a coefficient depending on both the material properties $\{\alpha, \tau_\alpha\}$ and the active temperature T_A . This interplay between mechanics and activity reflects the fact that the nonequilibrium processes operating in the system drive motion of the cytoskeletal cage, which in turn affects the vesicle dynamics.

Dissipation spectrum.—A quantification of direct physical relevance is the work done by the vesicle on the thermostat [36], which is the dissipated mechanical energy. The mean rate of energy dissipation J_{diss} is the power of the forces exerted by the vesicle on the heat bath, namely the forces opposed to the thermal forces acting on the vesicle by virtue of the action-reaction principle. The thermal forces comprise both the drag force $-\zeta * \dot{x}$ and the Gaussian noise ξ . Therefore, the dissipation rate reads $J_{\text{diss}} = \langle \dot{x}(\zeta * \dot{x} - \xi) \rangle$, where $\dot{x} = dx/dt$ is the vesicle’s velocity [36, 37]. It is proportional to the rate at which the vesicle exchanges energy with the surrounding environment [38]. In equilibrium J_{diss} would vanish, thus expressing the fact that the vesicle releases and absorbs on average the same amount of energy from the thermostat. The dissipation rate can be shown to be equal to the mean rate of entropy production times the bath temperature T [25]. Thereby, it directly characterizes the irreversible properties of the dynamics stemming from the active fluctuations.

The Harada-Sasa equality connects the spectral density I of mechanical energy dissipation to \tilde{C} and $\tilde{\chi}''$ in a viscous fluid [14, 15]. In the case of a complex rheology, we express it as $I = 2k_B(T_{\text{eff}} - T)/[1 + (G'/G'')^2]$ [25, 39]. This relation allows us to precisely identify the dissipation rate with the nonequilibrium properties of the vesicles’ dynamics, since I vanishes at equilibrium. Within our model,

the dissipation spectrum is [25]

$$I(\omega) = \frac{(\omega\tau_\alpha)^{1-\alpha} \sin(\frac{\pi\alpha}{2})}{1 + 2(\omega\tau_\alpha)^\alpha \cos(\frac{\pi\alpha}{2}) + (\omega\tau_\alpha)^{2\alpha}} \frac{2k_B T_A}{1 + (\omega\tau)^2}. \quad (3)$$

There is no nonequilibrium dissipation when $T_A = 0$ as expected, while in general it depends on both mechanics and activity as for T_{eff} . By integrating the dissipation spectrum over the whole frequency range, we can deduce the total dissipation rate $J_{\text{diss}} = \int d\omega I(\omega)/(2\pi)$. By contrast to T_{eff} , the dissipation spectrum not only quantifies the deviation from equilibrium properties, it is also related to the energy injected by the nonequilibrium processes.

In our theoretical framework, the nonequilibrium drive is embodied by the kx_0 force applied on the vesicle. The dissipation rate precisely equals the mean power of this force: $J_{\text{diss}} = \langle \dot{x}kx_0 \rangle$, reflecting the fact that the mechanical energy dissipated by the vesicle is also the energy provided by the nonequilibrium processes driving the vesicle’s motion [25]. In addition, the dissipation spectrum I equals the Fourier transform of the time symmetric correlation between the vesicle velocity \dot{x} and the driving force kx_0 [25].

Energy conversion.—The vesicle motion results from the displacement of the confining cytoskeletal cage, which is due to the active reorganization of the local environment. We denote by J_{env} the power of the random force driving the cage’s motion. This is the rate of energy injected by the nonequilibrium processes into the environment leading to the cytoskeleton rearrangement. In our model, it is given by the mean power injected by the force $k\tau_\alpha v_A$ to the cage: $J_{\text{env}} = \langle \dot{x}_0 k \tau_\alpha v_A \rangle$, where $\dot{x}_0 = dx_0/dt$. This can be computed in terms of the microscopic parameters $J_{\text{env}} = k_B T_A / \tau(\tau_\alpha/\tau)^{1-\alpha}$ [25]. Note that J_{env} can also be regarded as the work per unit time done by the cage on the thermostat [25]. This interpretation stems from the fact that our model is the limit version of one that features a reaction force of the vesicle upon the cage (for which mechanical interpretations are ambiguity-free), along with thermal fluctuations acting directly on the cage [39].

In our phenomenological picture, the energy J_{env} injected by the intracellular active processes serves to relentlessly remodel the cytoskeleton network. This energy is then transduced into the vesicles confined in such network, which is embodied by J_{diss} , thus driving their active motion. To quantify the efficiency of this energy transduction we introduce the dimensionless ratio $\rho = J_{\text{diss}}/J_{\text{env}}$ of the energy effectively dissipated through active motion of the vesicles over that injected by the nonequilibrium processes into the cage. The energetic efficiency ρ is independent of T_A , and is thus controlled by the time scales τ and τ_α . We understand such energy transduction as the conversion of the active stirring of the cytoskeleton network into the active dynamics of the intracellular components.

Quantification of the activity.—We exploit our theoretical predictions to quantify the experimental measurements of nonequilibrium dissipation inside living oocytes. We ex-

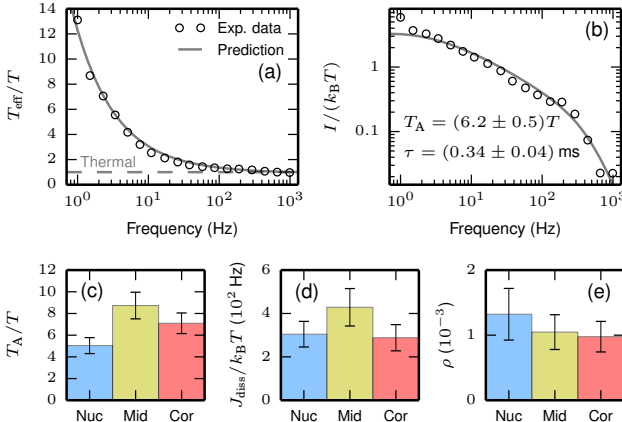


FIG. 2: (Color online) (a) Effective temperature T_{eff} and (b) dissipation spectrum I as functions of frequency (\circ), best fits in solid lines. The horizontal dashed line in (a) is the prediction for a thermal equilibrium system in the absence of activity, for which the dissipation spectrum equals zero. The experimental data is averaged over the whole oocyte. (c) Active temperature, (d) dissipation rate, and (e) power conversion rate estimated from the best fits of T_{eff} and I at three locations within the cytoplasm: near the nucleus (Nuc), near the cortex (Cor), and in the region in between (Mid).

tract the data for the effective temperature and the dissipation spectrum from a combination of active and passive microrheology. We observe that the experimental effective temperature diverges at low frequency, as a clear evidence that nonequilibrium processes drive the intracellular dynamics in this regime [Fig. 2(a)]. It reaches the equilibrium plateau at high frequency as expected. Deviation from thermal equilibrium was already reported in other living systems [7, 10, 32]. We use our analytic prediction in Eq. (3) to fit the dissipation spectrum data. As we have already quantified the viscoelastic properties, the remaining two free parameters are the ones characterizing the properties of the nonequilibrium processes, namely the active temperature T_A , and the mean persistence time τ . Our best fit is in very good agreement with the measured dissipation spectrum [Fig. 2(b)].

The extracted value of the active temperature $T_A = (6.2 \pm 0.5)T$ is larger than the bath temperature T . By contrast to T_{eff} , the active temperature is frequency independent, and it quantifies the amplitude of the active fluctuations. Hence, our estimation reveals that the fluctuations due to the nonequilibrium rearrangement of the cytoskeleton have a larger amplitude than the equilibrium thermal fluctuations dominating the short time dynamics. The time scale $\tau = (0.34 \pm 0.04) \text{ ms}$ that we obtain is of the order of the power stroke time of a single myosin-V motor [32, 40]. This teaches us that the nonequilibrium processes driving the vesicle dynamics are related to the microscopic kinetics of the molecular motors. It is consis-

tent with the fact that nonequilibrium processes are dominant at a higher frequency in our system than in others which were mainly driven by myosin-II [5, 7], for which the power stroke time is about 0.1 s [41]. Our analytic prediction for T_{eff} in Eq. (2), for which we use the parameter values $\{\alpha, \tau_\alpha, T_A, \tau\}$ extracted from the previous fits of G^* [Fig. 1(c)] and $I(\omega)$ [Fig. 2(b)], is in consistent agreement with the experimental data [Fig. 2(a)].

From the best fit parameters, we directly estimate the dissipation rate $J_{\text{diss}} = (360 \pm 110) k_B T/\text{s}$, as well as the power conversion rate $\rho = (1.7 \pm 0.8) 10^{-3}$. We find that the conversion of energy from the cytoskeletal network to the vesicle is very low. This suggests that a major proportion of the nonequilibrium injected power is dedicated to the network rearrangement, and not necessarily to vesicle dynamics *per se*. In other words, the injected energy tends to go mostly into elastic stresses, and only a small fraction ends up in kinetic energy [42].

It has been reported that a single myosin-V motor does about $3 k_B T$ of work during one power stroke [43], from which we deduce that it dissipates approximately $10^4 k_B T/\text{s}$ into the intracellular environment. This result is to be compared with our estimation of $J_{\text{env}} = (2.0 \pm 0.5) 10^5 k_B T/\text{s}$. We infer that the power injected by the nonequilibrium processes into the environment represents approximately the activity provided by 20 myosin-V motors. Assuming that the nonequilibrium processes in oocytes are indeed mainly regulated by myosin-V activity, we infer that 20 is the typical number of motors involved in the nonequilibrium reorganization of the cytoskeletal cage in the vicinity of a vesicle.

Variability across the oocyte.—One of the main advantages of our energetic approach lies in the ability to compare the same physical quantities across a large variety of living systems, or in different locations of the same system. We consider three concentric shells within the oocyte cytoplasm located near the nucleus, near the cortex, and in between these two regions. Each shell has a radial extension of about $10 \mu\text{m}$. We use our analysis to quantify T_A , J_{diss} , and ρ in the three regions [25]. Our results hint that nonequilibrium activity is increased near the middle of the cell, and slightly decreased near the nucleus, as quantified by T_A and J_{diss} [Figs. 2(c-d)]. This suggests that living oocytes locally regulate the nonequilibrium activity throughout their cytoplasm by injecting different amounts of energy. Note that the relative variation of J and T_A are similar, showing the close relation between these quantities as highlighted in Eq. (3). In comparison, the variation of ρ does not exhibit a clear trend across the oocyte [Fig. 2(e)].

Conclusion.—We quantified the amount of mechanical energy dissipated by the intracellular dynamics. Our analysis utilizes a minimal model describing the effect of the nonequilibrium stochastic forces in living systems with complex rheology. We find the predictions of our model to be in excellent agreement with the experimental results for vesicles in living mouse oocytes, thus allowing us to

quantify the main properties of the nonequilibrium dynamics: the amplitude and typical time scale of active fluctuations, the amount of dissipated energy, and the rate of energy transmitted from the cytoskeletal network to the intracellular components. The extracted parameters provide a quantitative support to the experimental picture that the nonequilibrium processes are mainly driven by myosin-V activity [20–22, 32]. The use of general principles in stochastic energetics, together with a minimal microscopic model, makes the results of our study highly relevant to a large variety of active processes in biology and soft matter.

We warmly thank Gavin Crooks for a critical reading of the manuscript and FvW acknowledges the support of the UC Berkeley Pitzer Center for Theoretical Chemistry. WWA thanks the PGG Fondation and Marie Curie Actions.

* These authors contributed equally to this work

- [1] J. Perrin, Comptes rendus hebdomadaires des séances de l'académie des sciences **147**, 530 (1908).
- [2] P. Langevin, Comptes Rendus de l'Académie des sciences **146**, 530 (1908).
- [3] K. Sekimoto, *Stochastic Energetics*, Lecture Notes in Physics (Springer, Berlin, Heidelberg, 2010).
- [4] U. Seifert, *Reports on Progress in Physics* **75**, 126001 (2012).
- [5] D. Mizuno, C. Tardin, C. F. Schmidt, and F. C. MacKintosh, *Science* **315**, 370 (2007).
- [6] P. Martin, A. J. Hudspeth, and F. Jülicher, *Proc. Natl. Acad. Sci. USA* **98**, 14380 (2001).
- [7] F. Gallet, D. Arcizet, P. Bohec, and A. Richert, *Soft Matter* **5**, 2947 (2009).
- [8] E. Ben-Isaac, Y. K. Park, G. Popescu, F. L. H. Brown, N. S. Gov, and Y. Shokef, *Phys. Rev. Lett.* **106**, 238103 (2011).
- [9] J. Prost, J.-F. Joanny, and J. M. R. Parrondo, *Phys. Rev. Lett.* **103**, 090601 (2009).
- [10] T. Betz, M. Lenz, J.-F. Joanny, and C. Sykes, *PNAS* **106**, 15320 (2009).
- [11] S. Tusch, A. Kundu, G. Verley, T. Blondel, V. Miralles, D. Démoulin, D. Lacoste, and J. Baudry, *Phys. Rev. Lett.* **112**, 180604 (2014).
- [12] S. Muy, A. Kundu, and D. Lacoste, *The Journal of Chemical Physics* **139** (2013), 10.1063/1.4821760.
- [13] S. Shinkai and Y. Togashi, *EPL* **105**, 30002 (2014).
- [14] T. Harada and S.-i. Sasa, *Phys. Rev. Lett.* **95**, 130602 (2005).
- [15] T. Harada and S.-i. Sasa, *Phys. Rev. E* **73**, 026131 (2006).
- [16] S. Toyabe, H.-R. Jiang, T. Nakamura, Y. Murayama, and M. Sano, *Phys. Rev. E* **75**, 011122 (2007).
- [17] B. Lander, J. Mehl, V. Bickle, C. Bechinger, and U. Seifert, *Phys. Rev. E* **86**, 030401 (2012).
- [18] J. M. Deutsch and O. Narayan, *Phys. Rev. E* **74**, 026112 (2006).
- [19] S. Toyabe, T. Okamoto, T. Watanabe-Nakayama, H. Take-tani, S. Kudo, and E. Muneyuki, *Phys. Rev. Lett.* **104**, 198103 (2010).
- [20] Z. Holubcová, G. Howard, and M. Schuh, *Nature cell biology* **15**, 937 (2013).
- [21] M. Schuh, *Nature cell biology* **13**, 1431 (2011).
- [22] M. Almonacid, W. W. Ahmed, M. Bussonnier, P. Mailly, T. Betz, R. Voituriez, N. S. Gov, and M.-H. Verlhac, *Nat Cell Biol* **17**, 470 (2015).
- [23] M. Łuksza, I. Queguiner, M.-H. Verlhac, and S. Brunet, *Developmental Biology* **382**, 48 (2013).
- [24] M.-H. Verlhac, J. Z. Kubiak, H. J. Clarke, and B. Maro, *Development* **120**, 1017 (1994).
- [25] See supplemental material.
- [26] W. W. Ahmed, É. Fodor, and T. Betz, *BBA - Molecular Cell Research* **1853**, 3083 (2015).
- [27] T. G. Mason, *Rheol. Acta* **39**, 371 (2000).
- [28] D. Wirtz, *Annual Review of Biophysics* **38**, 301 (2009).
- [29] F. Gittes and C. Schmidt, *Optics Letters* **23**, 7 (1998).
- [30] D. Mizuno, D. A. Head, F. MacKintosh, and C. Schmidt, *Macromolecules* **41**, 7194 (2008).
- [31] É. Fodor, M. Guo, N. S. Gov, P. Visco, D. A. Weitz, and F. van Wijland, *EPL* **110**, 48005 (2015).
- [32] W. W. Ahmed, E. Fodor, M. Almonacid, M. Bussonnier, M.-H. Verlhac, N. S. Gov, P. Visco, F. van Wijland, and T. Betz, ArXiv e-prints (2015), arXiv:1510.08299 .
- [33] R. Kubo, *Reports on Progress in Physics* **29**, 255 (1966).
- [34] T. G. Mason and D. A. Weitz, *Phys. Rev. Lett.* **74**, 1250 (1995).
- [35] L. F. Cugliandolo, J. Kurchan, and G. Parisi, *J. Phys. I France* **4**, 1641 (1994).
- [36] K. Sekimoto, *Journal of the Physical Society of Japan* **66**, 1234 (1997).
- [37] K. Sekimoto and S.-i. Sasa, *J. Phys. Soc. Jpn.* **66**, 3326 (1997).
- [38] C. Bustamante, J. Liphardt, and F. Ritort, *Physics Today* **58** (205), 10.1063/1.2012462.
- [39] É. Fodor, K. Kanazawa, H. Hayakawa, P. Visco, and F. van Wijland, *Phys. Rev. E* **90**, 042724 (2014).
- [40] G. Cappello, P. Pierobon, C. Symonds, L. Busoni, J. Christof, M. Gebhardt, M. Rief, and J. Prost, *Proc. Natl. Acad. Sci. U.S.A.* **104**, 15328 (2007).
- [41] M. J. Tyska and D. M. Warshaw, *Cell Motility and the Cytoskeleton* **51**, 1 (2002).
- [42] E. Ben-Isaac, É. Fodor, P. Visco, F. van Wijland, and N. S. Gov, *Phys. Rev. E* **92**, 012716 (2015).
- [43] K. Fujita, M. Iwaki, A. H. Iwane, L. Marcucci, and T. Yanagida, *Nature Communications* **3** (2012), 10.1038/ncomms1934.

Supplemental Material: Nonequilibrium Dissipation in Living Oocytes

É. Fodor,^{1,*} W. W. Ahmed,^{2,*} M. Almonacid,^{3,*} M. Bussonnier,²
N. S. Gov,⁴ M.-H. Verlhac,³ T. Betz,² P. Visco,¹ and F. van Wijland^{1,5}

¹Laboratoire Matière et Systèmes Complexes, UMR 7057 CNRS/P7, Université Paris Diderot,
10 rue Alice Domon et Léonie Duquet, 75205 Paris cedex 13, France

²Physico-Chimie Curie, UMR 168 CNRS/P6, Institut Curie, 11, rue Pierre et Marie Curie, 75005 Paris, France

³CIRB, Collège de France, CNRS-UMR7241, INSERM-U1050, 75231 Paris, Cedex 05, France

⁴Department of Chemical Physics, Weizmann Institute of Science, 76100 Rehovot, Israel

⁵Department of Chemistry, University of California, Berkeley, CA, 94720, USA

(Dated: July 1, 2016)

PACS numbers: 05.40.-a, 05.10.Gg, 02.50.Ey, 87.10.Mn

I. EXPERIMENTAL MATERIALS AND METHODS

Mouse oocytes are collected from 13 week old mice and maintained in Prophase 1 in M2+BSA medium [1]. Live oocytes are embedded in a collagen gel to stop movement of the overall cell during measurements. Collagen gels are made by mixing M2 medium (33.5 μ L), 1X PBS (10 μ L), NaOH (1 M, 0.9 μ L), collagen (3.6 mg/mL, 55.6 μ L) to obtain 100 μ L of the final collagen solution at 2 mg/mL with a pH about 7.4. Then, 20 μ L of the collagen solution is deposited on a coverslip and live oocytes were added. The droplet is covered with another glass coverslip using Dow Corning vacuum grease as spacers and to minimize evaporation. The collagen gel containing oocytes is polymerized in a humid environment at 37° C for 30 min. The optical tweezers setup consist of a 1064 nm laser (IPG, Germany) controlled by acousto-optic modulators (AA-Optoelectronics, France) and focused into the object plane of a water immersion objective (60x, 1.2 NA, Olympus) [2]. We calibrate the optical trap stiffness using high frequency thermal fluctuations ($\omega > 300$ Hz) [3, 4].

II. CAGING MODEL

A. Presentation

We consider the following equation for the projected vesicle dynamics in terms of the one dimensional position x

$$\zeta * \frac{dx}{dt} = -k(x - x_0) + \xi, \quad \zeta * \frac{dx_0}{dt} = k\tau_\alpha v_A, \quad (\text{S1})$$

where $*$ denotes the convolution product, ξ is a zero-mean Gaussian colored noise with correlations

$$\langle \xi(t)\xi(0) \rangle = k_B T \zeta(|t|) \equiv C_\xi(t), \quad (\text{S2})$$

as enforced by the fluctuation-dissipation theorem (FDT) [5], and T is the bath temperature. We assume that the process v_A

has a single time scale τ that governs its decorrelation:

$$\langle v_A(t)v_A(0) \rangle = k_B T_A e^{-|t|/\tau} / (k\tau_\alpha \tau) \equiv C_A(t), \quad (\text{S3})$$

where, by analogy with standard Langevin equation, we have defined an *active* temperature T_A associated to the amplitude of this process.

The generalized Stokes-Einstein relation expresses the complex modulus G^* in terms of the Fourier response function $\tilde{\chi}$ as

$$G^* \equiv 1/(6\pi a \tilde{\chi}), \quad (\text{S4})$$

where a is the average radius of the vesicles regarded as spherical particles. Our model is associated with the following complex modulus:

$$G^*(\omega) = [k + i\omega \tilde{\zeta}(\omega)] / (6\pi a). \quad (\text{S5})$$

Following the choice of the memory kernel presented in the main text

$$\zeta(t) \equiv k (\tau_\alpha/t)^\alpha \Theta(t)/\Gamma(1-\alpha), \quad (\text{S6})$$

where Γ is the Gamma function, and Θ is the Heaviside function, we deduce

$$\tilde{\zeta}(\omega) = k (i\omega \tau_\alpha)^{\alpha-1}. \quad (\text{S7})$$

As a result, we express G^* in terms of its real and imaginary parts, respectively denoted by G' and G'' , as

$$G'(\omega) = G_0 [1 + (\omega \tau_\alpha)^\alpha \cos(\pi\alpha/2)], \quad (\text{S8a})$$

$$G''(\omega) = G_0 (\omega \tau_\alpha)^\alpha \sin(\pi\alpha/2), \quad (\text{S8b})$$

where $G_0 \equiv k/(6\pi a)$.

B. Effective temperature

The effective temperature T_{eff} is defined as

$$T_{\text{eff}}(\omega) \equiv -\omega \tilde{C}(\omega) / [2k_B \tilde{\chi}''(\omega)], \quad (\text{S9})$$

* These authors contributed equally to this work

where \tilde{C} and $\tilde{\chi}''$ are the position autocorrelation function and the imaginary part of the response function in the Fourier domain, respectively. From the generalized Stokes-Einstein relation in Sec. II A, and by using Eq. (S8), we deduce

$$\tilde{\chi}''(\omega) = -\frac{(\omega\tau_\alpha)^\alpha \sin(\pi\alpha/2)/k}{1 + 2(\omega\tau_\alpha)^\alpha \cos(\pi\alpha/2) + (\omega\tau_\alpha)^{2\alpha}}. \quad (\text{S10})$$

The Fourier transform of Eq. (S1) in the body of the text gives

$$\tilde{x} = \tilde{\chi}(\tilde{\xi} + k\tilde{x}_0), \quad i\omega\tilde{\zeta}(\omega)\tilde{x}_0(\omega) = k\tau_\alpha\tilde{v}_A(\omega). \quad (\text{S11})$$

From Eqs. (S2) and (S3), we deduce

$$\tilde{C}_\xi = 2k_B T \tilde{\zeta}', \quad \tilde{C}_A(\omega) = \frac{2k_B T_A}{k\tau_\alpha [1 + (\omega\tau)^2]}, \quad (\text{S12})$$

where $\tilde{\zeta}'$ is the real part of the Fourier memory kernel. By using Eq. (S8), \tilde{C} follows as

$$\begin{aligned} \tilde{C}(\omega) &= \frac{2\tau_\alpha(\omega\tau_\alpha)^{\alpha-1}/k}{1 + 2(\omega\tau_\alpha)^\alpha \cos(\pi\alpha/2) + (\omega\tau_\alpha)^{2\alpha}} \\ &\times \left[\sin\left(\frac{\pi\alpha}{2}\right) k_B T + \frac{k_B T_A (\omega\tau_\alpha)^{1-3\alpha}}{1 + (\omega\tau)^2} \right], \end{aligned} \quad (\text{S13})$$

from which we deduce the analytic expression of T_{eff} in Eq. (2) of the body of the text.

III. DISSIPATION AND INJECTION OF ENERGY

A. Dissipation spectrum

The mean rate of energy dissipation J_{diss} is defined as

$$J_{\text{diss}} \equiv \langle \dot{x}(\zeta * \dot{x} - \xi) \rangle, \quad (\text{S14})$$

where $\dot{x} \equiv dx/dt$ is the vesicle velocity, and $*$ denotes the convolution product. From the dynamics in Eq. (S1), we deduce

$$J_{\text{diss}} = k \langle \dot{x}(x_0 - x) \rangle, \quad (\text{S15})$$

The product appearing in J_{diss} is defined in the Stratonovich sense. It follows

$$\langle \dot{x}x \rangle = \frac{1}{2} \lim_{t \rightarrow 0} [\langle \dot{x}(t)x(0) \rangle + \langle \dot{x}(0)x(t) \rangle] = 0, \quad (\text{S16})$$

leading to

$$J_{\text{diss}} = k \langle \dot{x}x_0 \rangle. \quad (\text{S17})$$

We express J_{diss} as

$$J_{\text{diss}} \equiv \int \frac{d\omega}{2\pi} I(\omega), \quad (\text{S18})$$

where the spectral density I , also referred to as the *dissipation spectrum*, is given by

$$I(\omega) = \omega^2 \tilde{C}(\omega) \tilde{\zeta}(\omega) - i\omega \tilde{C}_{x\xi}(\omega), \quad (\text{S19})$$

and

$$C_{x\xi}(t) \equiv \langle x(t)\xi(0) \rangle. \quad (\text{S20})$$

From Eqs. (S11) and (S12), and since the thermal force ξ and the process v_A are uncorrelated, we deduce

$$\tilde{C}_{x\xi} = 2k_B T \tilde{\zeta}'. \quad (\text{S21})$$

Owing to the causality of the response function χ and the memory kernel ζ , the imaginary and real parts of their Fourier transform are odd and even in ω , respectively. Since \tilde{C} is even in ω , we deduce

$$I(\omega) = [\omega \tilde{C}(\omega) - 2k_B T \tilde{\chi}''(\omega)] \omega \tilde{\zeta}'(\omega). \quad (\text{S22})$$

Finally, we use the definition of T_{eff} in Sec. II B, together with the relations

$$\tilde{\chi}'' = -G''/(6\pi a |G^*|^2), \quad \tilde{\zeta}'(\omega) = 6\pi a G''(\omega)/\omega, \quad (\text{S23})$$

to deduce the expression of I in terms of T_{eff} as provided in the body of the text.

B. Force-velocity correlation

From Eq. (S17), we express J_{diss} as

$$J_{\text{diss}} = \frac{k}{2} \lim_{t \rightarrow 0} [\langle \dot{x}(t)x_0(0) \rangle + \langle \dot{x}(0)x_0(t) \rangle]. \quad (\text{S24})$$

Moreover, we can write Eq. (S18) as

$$J_{\text{diss}} = \lim_{t \rightarrow 0} \int \frac{d\omega}{2\pi} e^{i\omega t} I(\omega), \quad (\text{S25})$$

from which we deduce

$$I(\omega) = \frac{k}{2} \int dt e^{-i\omega t} [\langle \dot{x}(t)x_0(0) \rangle + \langle \dot{x}(0)x_0(t) \rangle]. \quad (\text{S26})$$

As a result, the dissipation spectrum I exactly equals the Fourier transform of the time-symmetric correlation between the vesicle velocity \dot{x} and the active force kx_0 which is directly acting on the vesicle. It vanishes when the dynamics is invariant under a time reversal, in which case $\langle \dot{x}(t)x_0(0) \rangle = -\langle \dot{x}(0)x_0(t) \rangle$. Therefore, it can be regarded as a measurement of the time-reversal breakdown arising in the vesicle dynamics due to the nonequilibrium fluctuations powered by the active force kx_0 .

C. Entropy production rate

Provided that the thermal noise is Gaussian, the probability weight P associated with a given realization of this noise is defined as $P \propto e^{-\mathcal{A}}$, where the dynamic action \mathcal{A} reads

$$\mathcal{A} \equiv \iint \frac{du ds}{2} \Gamma(u-s) \xi(u) \xi(s). \quad (\text{S27})$$

The expression of ξ in this formula is determined by the vesicle's dynamics in Eq. (S1), and Γ is related to the thermal correlations as

$$\int dt \Gamma(u-t) \langle \xi(t) \xi(s) \rangle \equiv \delta(u-s). \quad (\text{S28})$$

Note that Γ is symmetric, as deduced from Eq. (S2). For the sake of simplicity, we consider a trajectory with initial and final times $-t$ and t , respectively, associated with a probability P expressed as

$$\mathcal{A} = \iint \frac{duds}{2} \Gamma(u-s) D(u) D(s), \quad (\text{S29})$$

where

$$D(t) \equiv k [x(t) - x_0(t)] + \int du \zeta(t-u) \dot{x}(u). \quad (\text{S30})$$

The mean rate of entropy production σ is defined in terms of the probability P for the forward trajectory $\{x\}_{-t}^t$ and the probability P^R for the backward one $\{x^R\}_t^{-t}$ as [7–9]

$$\sigma \equiv k_B \lim_{t \rightarrow \infty} \ln (P/P^R) / t = k_B \lim_{t \rightarrow \infty} (\mathcal{A}^R - \mathcal{A}) / t. \quad (\text{S31})$$

The backward trajectory consists in the reversed realization of the forward dynamics, such as

$$x^R(t) \equiv x(-t), \quad \dot{x}^R(t) \equiv -\dot{x}(-t). \quad (\text{S32})$$

We deduce

$$\mathcal{A}^R = \iint_t^{-t} \frac{duds}{2} \Gamma(u-s) D^R(u) D^R(s), \quad (\text{S33})$$

where

$$D^R(t) \equiv k [x(-t) - x_0(-t)] - \int du \zeta(t-u) \dot{x}(-u). \quad (\text{S34})$$

We perform the change of variables $\{u, s\} \rightarrow \{-u, -s\}$ in Eq. (S33), leading to

$$\mathcal{A}^R = \iint_{-t}^t dt_1 dt_2 \Gamma(t_1 - t_2) D^{RR}(t_1) D^{RR}(t_2), \quad (\text{S35})$$

where

$$D^{RR}(t) \equiv k [x(t) - x_0(t)] - \int du \zeta(u-t) \dot{x}(u). \quad (\text{S36})$$

It follows the entropy production rate can be separated in two terms $\sigma = \sigma_1 + \sigma_2$ as [7]

$$\begin{aligned} \sigma_1 &\equiv \lim_{t \rightarrow \infty} \frac{k_B}{t} \iint_{-t}^t duds \Gamma(u-s) k(x_0 - x)(u) \\ &\quad \times \int dw \zeta(|s-w|) \dot{x}(w), \end{aligned} \quad (\text{S37a})$$

$$\begin{aligned} \sigma_2 &\equiv \lim_{t \rightarrow \infty} \frac{k_B}{t} \iint_{-t}^t duds \Gamma(u-s) \iint du' ds' \dot{x}(u') \dot{x}(s') \\ &\quad \times [\zeta(u-u') \zeta(s-s') - \zeta(u'-u) \zeta(s'-s)], \end{aligned} \quad (\text{S37b})$$

where we have used $\zeta(t) + \zeta(-t) = \zeta(|t|)$, since ζ is a causal function. By using Eq. (S28), we deduce $\sigma_2 = 0$ [7], and

$$\sigma_1 = \lim_{t \rightarrow \infty} \frac{1}{t} \int_{-t}^t du k(x_0 - x)(u) \frac{\dot{x}(u)}{T} = \frac{\langle \dot{x}k(x_0 - x) \rangle}{T}, \quad (\text{S38})$$

yielding

$$\sigma = \langle \dot{x}(\zeta * \dot{x} - \xi) \rangle / T = J_{\text{diss}} / T. \quad (\text{S39})$$

The mean rate of energy dissipation is a direct measurement of the entropy production rate.

D. Rate of injected energy

From the definition of the energy rate J_{env} provided to the cage

$$J_{\text{env}} \equiv k \tau_\alpha \langle \dot{x}_0 v_A \rangle, \quad (\text{S40})$$

where $\dot{x}_0 \equiv dx_0/dt$ is the cage velocity, we deduce

$$J_{\text{env}} = \int \frac{d\omega}{2\pi} \tilde{C}_0(\omega) \tilde{\zeta}'(\omega) \omega^2, \quad (\text{S41})$$

where \tilde{C}_0 is the Fourier autocorrelation function of the cage local minimum position. This leads to

$$J_{\text{env}} = \int \frac{d\omega}{2\pi} (\omega \tau_\alpha)^{1-\alpha} \sin\left(\frac{\pi \alpha}{2}\right) \frac{2k_B T_A}{1 + (\omega \tau)^2}, \quad (\text{S42})$$

yielding

$$J_{\text{env}} = k_B T_A / \tau (\tau_\alpha / \tau)^{1-\alpha}, \quad (\text{S43})$$

as stated in the body of the text.

We now discuss the interpretation of J_{env} in terms of the work down by the cage into the thermostat. To this aim, we present an extended formulation of the model which contains a back action term in the dynamic equation for x_0 , in the same spirit as in [10]. From the action-reaction principle, a force opposed to the spring force applied on x should be exerted into x_0 . Given that the spring force accounts for the vesicle confinement by the cytoskeletal network, the characteristic cage size should be much larger than the vesicle size to avoid any escape of the vesicle. Therefore, the back action force is then necessarily small compared to the caging force acting on the vesicle. Moreover, thermal fluctuations also affects the x_0 dynamics, which amplitude should be negligible compared with the ones of thermal force applied on the x . An experimental signature of a large back action would be that the tracer's MSD would be diffusive *also* in the equilibrium limit, which is not observed within the time scale of experiment.

It follows that the dynamics can be written as

$$\zeta * \frac{dx}{dt} = -k(x - x_0) + \xi, \quad (\text{S44a})$$

$$\zeta * \frac{dx_0}{dt} = k \tau_\alpha v_A - \varepsilon k(x_0 - x) + \xi_0, \quad (\text{S44b})$$

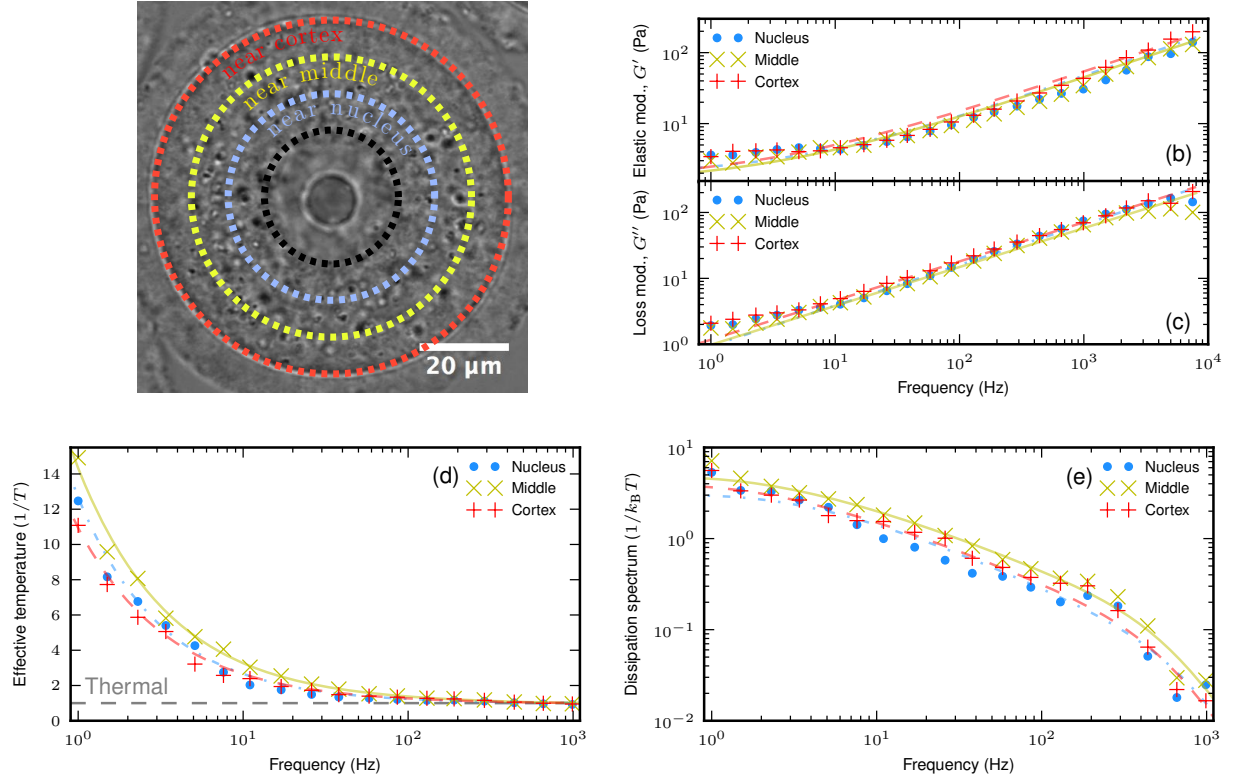


FIG. S1. (Color online) (a) We distinguish three concentric shells around the central nucleus (black) with a radial extension of about 10 μm each: near nucleus (blue), middle (yellow), and cortex (red). (b) Real and (c) imaginary parts of the complex modulus, denoted by G' and G'' respectively, as functions of frequency in three locations (symbols), and their best fitting curves [Eq. (S8)]: dot dashed, solid, and dashed lines, near nucleus, middle, and cortex, respectively. The complex modulus exhibits a power law behavior at large frequency. The low frequency curvature also hints a low frequency saturation for the real part. Data at 10 Hz is used in [6]. (d) Effective temperature and (e) dissipation spectrum as functions of frequency in three different regions (symbols) and their best fitting curves (Eqs. (2) and (3) in the body of the text).

where $\varepsilon \ll 1$ is a small parameter, and

$$\langle \xi_0(t)\xi_0(t') \rangle \equiv \varepsilon \langle \xi(t)\xi(t') \rangle. \quad (\text{S45})$$

The dynamics is not affected by ε at leading order, as was demonstrated for the case of a simple mechanics in [10]. The generalization to the rheology considered here is straightforward. In particular, the expression of I is not modified for a small ε .

Therefore, we can express J_{env} at leading order in ε as

$$J_{\text{env}} = \langle \dot{x}_0 (\zeta * \dot{x}_0 - \xi_0) \rangle, \quad (\text{S46})$$

given that it simplifies as

$$J_{\text{env}} = \langle \dot{x}_0 (k\tau_\alpha v_A - \varepsilon k(x - x_0)) \rangle = k\tau_\alpha \langle \dot{x}_0 v_A \rangle + \mathcal{O}(\varepsilon). \quad (\text{S47})$$

As a result, J_{env} has a clear mechanical interpretation, namely it is the work applied by the cage on the heat bath.

IV. DATA ANALYSIS OF THE LOCAL

NONEQUILIBRIUM PROPERTIES

To investigate how the nonequilibrium properties differ spatially in the oocyte cytoplasm, we divide it into three concentric shells around the nucleus extending to the cortex, each region having a radial extension of about 10 μm . We refer to these locations as near nucleus, near cortex, and the region in between as near middle. We perform a simultaneous fit of the rheological data, together with the effective temperature and dissipation spectrum data [Fig. S1].

We deduce the best fit values of the rheological parameters in each region:

$$\alpha = \{0.60, 0.58, 0.58\} \pm 0.07, \quad (\text{S48})$$

$$G_0 = \{1.7, 1.3, 1.5\} \pm 0.2 \text{ Pa}, \quad (\text{S49})$$

$$\tau_\alpha = \{0.09, 0.13, 0.17\} \pm 0.04 \text{ s}, \quad (\text{S50})$$

near nucleus, middle, and cortex, respectively. The best fit values of T_A , together with the corresponding values of J_{diss} and ρ , are reported in Fig. 2 of the body of the text. The extracted mean persistence times are

$$\tau = \{0.25, 0.27, 0.29\} \pm 0.07 \text{ ms}, \quad (\text{S51})$$

near nucleus, middle, and cortex, respectively.

- [1] M.-H. Verlhac, J. Z. Kubiak, H. J. Clarke, and B. Maro, *Development* **120**, 1017 (1994).
- [2] M. Bussonier, K. Carvalho, J. Lemiere, J.-F. Joanny, C. Sykes, and T. Betz, *Biophysical Journal* **In Press** (2014).
- [3] N. Fakhri, A. D. Wessel, C. Willms, M. Pasquali, D. R. Klopfenstein, F. MacKintosh, and C. Schmidt, *Science* **344**, 1031 (2014).
- [4] J. Mas, A. C. Richardson, S. N. S. Reihani, L. B. Oddershede, and K. Berg-Sørensen, *Physical Biology* **10**, 046006 (2013).
- [5] R. Kubo, *Reports on Progress in Physics* **29**, 255 (1966).
- [6] M. Almonacid, W. W. Ahmed, M. Bussonier, P. Mailly, T. Betz, R. Voituriez, N. S. Gov, and M.-H. Verlhac, *Nat Cell Biol* **17**, 470 (2015).
- [7] C. Maes, S. Safaverdi, P. Visco, and F. van Wijland, *Phys. Rev. E* **87**, 022125 (2013).
- [8] A. Crisanti, A. Puglisi, and D. Villamaina, *Phys. Rev. E* **85**, 061127 (2012).
- [9] C. Bustamante, J. Liphardt, and F. Ritort, *Physics Today* **58** (2005), 10.1063/1.2012462.
- [10] É. Fodor, K. Kanazawa, H. Hayakawa, P. Visco, and F. van Wijland, *Phys. Rev. E* **90**, 042724 (2014).

Future directions

The mechanical properties of the intracellular environment is generally characterized by power-law behaviors, with several distinct regimes depending on frequency in some cases [73]. The statistics of probes of the intracellular dynamics is also characterized by power-laws, as given by the anomalous diffusion reported in the MSD for instance [8]. In equilibrium, the exponents of the mechanics and of the tracer statistics are related, since the thermal fluctuations are dictated by the mechanics, as enforced by the FDT. Given that the motor activity is involved in the structure of the cytoskeletal network and in the force generation at the basis of nonequilibrium fluctuations, one could speculate that there would be an interplay between the mechanical properties of the cell and the spontaneous fluctuations of the tracers. As a result, the exponents of the mechanics and of the fluctuations would still be related beyond equilibrium. To assess such a relation, one would need to define an observable from the combination of response and fluctuations that would exhibit an universal power-law regime for various cell types with different rheologies and intracellular fluctuations.

For the case of living mouse oocytes presented in this Chapter, the exponent of the power-law behavior of the effective temperature at low frequency is given by $1 - 3\alpha \sim -0.8$. Such a value has also been reported for tracers injected in living cells with power-law mechanics ω^α , where α was about $0.5 - 0.6$, namely close to the one of the oocytes [77]. Besides, the divergence of the effective temperature for the tracers in living melanoma cells presented in Chapter 3 is also with exponent close to 0.8. Yet, the mechanics was nearly elastic in such a case. This is an appealing hint that the effective temperature may represent the good observable to shed light on a universal power-law scaling. It calls for a deeper test based on further investigations in various cell types.

Such an observation goes beyond the predictions of the active cage model with memory effects in its present form. To account for this, we consider a power-law decay of the active burst correlations $\langle v_A(t)v_A(0) \rangle = v_0^2(\tau/t)^\beta / \Gamma(1 - \beta)$, with exponent β related to the one of the mechanics. This type of correlations emerges when considering that the time scales of the active bursts is controlled by several processes, each one of them described by a Poisson statistics. The corresponding effective temperature would read

$$T_{\text{eff}}(\omega) = T + T_A \frac{(\omega\tau)^\beta \sin(\pi\beta/2)}{(\omega\tau_\alpha)^{3\alpha} \sin(\pi\alpha/2)}. \quad (5.12)$$

As a result, the exponent of the power-law behavior of the effective temperature at small frequencies $\beta - 3\alpha$ is a combination of the ones characterizing the mechanics and the active burst statistics. Therefore, regarding this value as constant would fix the relation between the active burst statistics and the mechanics.

Chapter 6

Vertex fluctuations in epithelial layers

In this Chapter, we investigate the dynamics of epithelial layers through the fluctuations of tricellular junctions. We shed light on the non-Gaussian features of the displacement statistics reminiscent of the ones observed for the intermittent dynamics of tracers in living cells. It leads us to analyze the vertex fluctuations on the basis of the active cage model presented in Chapter 2 to quantify key parameters of the nonequilibrium activity. On this basis, we provide a synthetic read-out to understand how inhibitors in the molecular pathway controlling the activation of motor activity affect the monolayer dynamics.

Epithelial tissues: model systems of developing embryos

Epithelial tissues consist in one or more layers of cells which are interconnected through junctions [109]. There exists several types of epithelia, whose complexity can be classified on the basis of the number of layers and the shape of the cells. They can be found in a large variety of organs in the body, ranging from the skin to the lungs and the kidney. One of the primary functions of an epithelium is to protect the underlying tissue. In that respect, the tight joining of its individual cells is a key property. Yet, these junctions being dynamic entities, they can also allow passage of substances between neighboring cells. A large number of recent studies have investigated the dramatic rearrangements occurring in the tissues of developing embryos [110–112]. The epithelial tissues undergo a series of morphological changes which lead to the formation of distinct organs: such a process is named as morphogenesis. During morphogenesis, the internal reorganization of the tissues is driven by topological transitions [113]. Two main types of such transitions are identified [Fig. 6.1]. The T1 transitions correspond to exchange of neighbors between cells, similar to the ones observed in sheared foams: two tricellular junctions merge into a single junction involving four cells, and then separate into another two tricellular junctions different from the previous ones. The T2 transitions corresponds to the merging of three or more tricellular junctions: a cell of the tissue is lost and new contacts between the cells surrounding the lost one are created. The remodeling of cell-cell contacts is made possible through dynamic intercellular adhesion. The E-cadherin molecules are known to play a major role in both the mobility and the stabilization of interfaces between cells [114, 115].

To understand the large scale reorganization occurring during the morphogenesis, minimal systems of epithelial tissues and cellular aggregates are studied *in vitro*. The mechanics of cellular aggregates has been investigated by compressing them with plates [116, 117], or alternatively via micro-pipette aspiration [118, 119]. These experiments have shed light on the possible quantification of an effective viscosity as controlled by the internal reorganization between cells. Modeling based on a continuum description of the medium relates such a viscosity to the rate of cell division and cell death occurring in the system [120]. A series of studies focused on the collective dynamics of cells in cell monolayers. Because of the dense packing of the tissue, both glassy-like behavior and jamming effects can be observed [121–123]. Interactions between neighboring cells have been modelled by a specific form of the potential energy, as controlled by the shape parameters such as the perimeter and the area of the cells. This is known as the vertex model [124]. On this basis, some works have quantified the distribution of energy barriers in tissues, which controls the migration of the cells and the transition between fluid-like and solid-like behaviors of the tissue [125, 126]. The stochastic dynamics of individual cells in the tissues has been modeled as interacting self-propelled par-

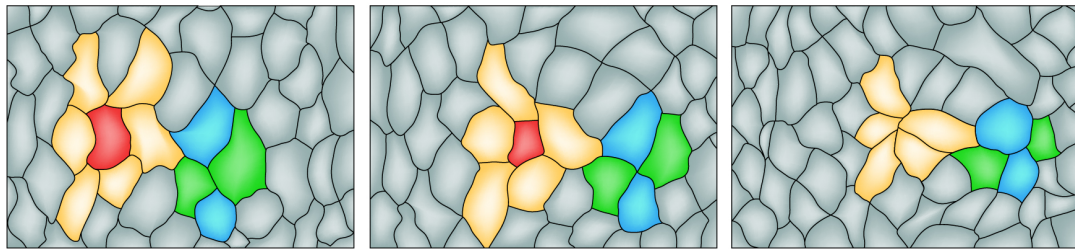


Figure 6.1 – Schematic representation of T1 (green and blue cells) and T2 (yellow and red cells) transitions. Taken from [113].

ticles, thus showing that the solid-liquid transition was only controlled by the cell motility and the cell shape independently of the density of the tissues [127].

Regulation of activity in epithelium through signaling pathway

Previous studies have investigated the role of fluctuations in the collective dynamics of tissues. Yet, the relation between the nonequilibrium fluctuations and the underlying processes which power directed forces, such as motor activity, is still lacking. It is our aim to provide a quantitative analysis of the fluctuations at the mesoscopic scale of individual cells, and to understand the regulation of these fluctuations by the molecular motors.

We consider Madin-Darby Canine Kidney (MDCK) cells for which intercellular junctions are labelled by E-cadherin fused with green fluorescent protein [128]. We focus in tricellular junctions, referred to as vertices, which we view as faithful representatives of the underlying motor activity. Typical trajectories of vertices are made of fluctuations of small amplitude in a confined volume and large displacements, as reported in Fig. 6.2. This is reminiscent of the intermittent dynamics observed for tracers in the intracellular environment. It leads us to using the phenomenological model of caging dynamics presented in Chapter 3 to analyze the vertex fluctuations. To investigate the regulation of the nonequilibrium fluctuations by the molecular motors, we use inhibitors in the molecular pathway controlling the motor activity, namely the Rho pathway. We consider inhibition of three different targets of the pathway named as Rho, Rho kinase (ROCK), and myosin-II. They build up a hierarchy in the pathway: Rho directly activates ROCK, ROCK directly activates myosin-II and also de-activates myosin-II in an indirect way. Even though this is a simplified picture of the Rho pathway, these ingredients are sufficient to understand the effect of the three different inhibitors on the activation of myosin motors. In addition, we also consider the condition where the polymerization of microtubules is inhibited, and we use untreated cells as a control.

The MSD extracted from the vertex trajectories is subdiffusive at short times

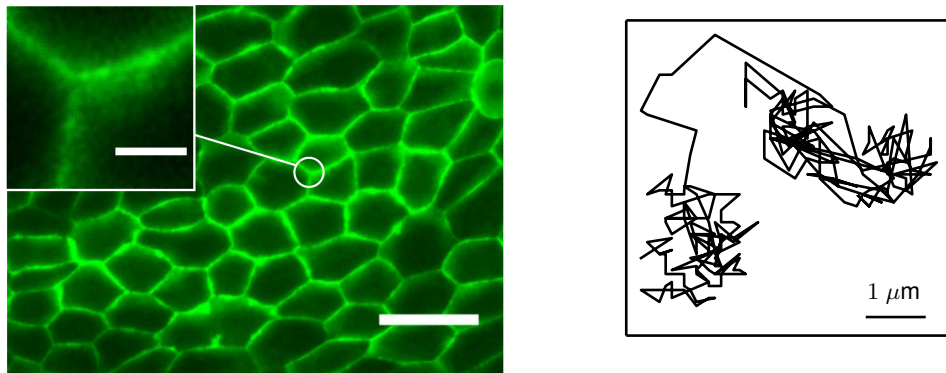


Figure 6.2 – Left: MDCK cell monolayer visualized by GFP E-cadherin. Scalebar 30 μm . (Inset) Tricellular junction named as vertex. Scalebar 4 μm . Right: Typical trajectory of a vertex. Time between two successive measurements 5 min. Taken from paper [E](#).

for all conditions. There is a transition towards superdiffusion or normal diffusion at large times depending on the conditions, except for myosin inhibitors which remains subdiffusive. We reproduce this transition with our analytic prediction. It yields a quantification of the active diffusion coefficient and the mean persistence time. Moreover, we analyze the time evolution of the whole distribution of displacement. It exhibits a central Gaussian part and exponential tails, whose extension increases with time. Besides, we demonstrate that we can reproduce the distribution measured at different times by using only one free parameter for each condition: the mean waiting time. It leads us to correlate the hierarchy in the Rho pathway to the active fluctuations of the vertices, as controlled by the active diffusion coefficient, the mean persistence time, and the mean persistence length. These parameters are increased when going upstream in the pathway. Overall, our analysis provides a synthetic read-out to quantitatively assess the effect of the molecular pathway inhibitors onto the mesoscopic fluctuations of the tissue.

The detailed analysis of the fluctuations and the interpretation of the extracted parameters are presented in paper [E](#) reproduced below.

Active fluctuations are controlled by molecular motor regulations in cell monolayer

É. Fodor,^{1,*} V. Mehandia,^{2,3,*} J. Comelles,² R. Thiagarajan,² N. S. Gov,⁴ P. Visco,¹ F. van Wijland,¹ and D. Riveline²

¹Laboratoire Matière et Systèmes Complexes, UMR 7057 CNRS/P7, Université Paris Diderot,

10 rue Alice Domon et Léonie Duquet, 75205 Paris cedex 13, France

²Laboratory of Cell Physics, ISIS/IGBMC, Université de Strasbourg and CNRS (UMR 7006),

8 allée Gaspard Monge, 67083 Strasbourg, France Development and Stem Cells Program,

IGBMC, CNRS (UMR 7104), INSERM (U964), Université de Strasbourg,

1 rue Laurent Fries, BP10142, 67400 Illkirch, France

³School of Mechanical, Materials and Energy Engineering, Indian Institute of Technology Ropar, India

⁴Department of Chemical Physics, Weizmann Institute of Science, 76100 Rehovot, Israel

(Dated: May 13, 2016)

Molecular motors power spatial fluctuations in epithelial tissues. We evaluate these fluctuations in MDCK monolayers by tracking tricellular junctions, leading us to highlight the non-Gaussian statistics of the junction displacement. Using a mesoscopic framework which separates the thermal fluctuations originating from the heat bath and the athermal ones generated by myosin-II motors, we quantify key parameters of the junction activity such as diffusion coefficient, persistence time and persistence length. When inhibiting specific targets along the molecular pathway which regulates the motors activity, we report modifications of these parameters: surprisingly, the order relation in the regulation corresponds to larger active fluctuations at vertices. Our study shows that signaling pathways regulating molecular motors have to be taken into account to capture mesoscopic dynamics in cells.

PACS numbers: 87.17.-d, 87.18.Tt, 87.18.Fx

Living and non-living matter show a variety of fluctuations at different length and timescales. Measuring these fluctuations is an effective way to study nonequilibrium systems. In living cells, the continuous supply of energy from ATP/GTP hydrolysis takes the system out-of-equilibrium. New models have been proposed to describe this nonequilibrium dynamics [1–9], yielding a proper definition of energy dissipation as related to spatial fluctuations [10–13]. One class of models exploits the similarities and differences between foams and living tissues, where cells form a connected network of straight edges and vertices [14–17]. In living tissues, the spontaneous rearrangements between vertices reveal the nonequilibrium nature of their dynamics [16, 18] involving contractile tissues during development [18–21]. The molecular origin of such nonequilibrium dynamics is associated with acto-myosin molecular motors [22, 23], which power spatial fluctuations. Yet, quantitative studies are lacking to understand their regulations. It is our aim in this paper to investigate the mechanism driving the spatial fluctuations of the cell monolayer vertices [Inset of Fig. 1(d)], using specific inhibitions of the molecular pathway controlling myosin.

In this paper, we explore the nonequilibrium active properties of epithelial monolayers by directly accessing the fluctuations of vertices. We first report the experimental methods and extraction of the data. We then present a model for the vertex dynamics, on the basis of which we characterize the vertex fluctuations in terms of time, length, and energy scales. Surprisingly, the order relation in the molecular pathway regulating the myosin motors shows an inverted relation with the active fluctuations of vertices.

Vertex tracking and inhibitors.—We use Madin-Darby

Canine Kidney (MDCK) cells stably transfected with E-cadherin fused with the Green Fluorescent Protein (GFP) as a paradigm for epithelial tissues dynamics [25]. This allows us to study live cells while interacting with each other. We seek to identify spatial points primarily involved in tissue transformations. The meeting points between three cells are involved in the exchanges between neighbouring cells, thus serving as hallmark of the tissue dynamics. We extract the vertex trajectories by tracking them as long as they are visible and in the absence of neighboring cell division, until a maximum of 8 hours [Fig. 1].

Vertex dynamics are driven by both thermal fluctuations produced by the heat bath, and the active fluctuations powered by the molecular motors. The myosin-II motors are localized in dense contractile units present in the apical surface of the tissue [22, 26] [Figs. 1(a-c)]. The Rho signalling pathway controls the acto-myosin activity inside cells (see Fig. 9 in [27]). Upstream and downstream targets install a hierarchy in the activation of myosin. To assess the relevance of the various ingredients of this pathway, we specifically inhibit different targets: Rho, Rho kinase (ROCK) and myosin-II [Fig. 1(f)]. The level of phosphorylation of the regulatory light chain (RLC) of myosin-II is a signature of myosin activity: myosin-II is active when RLC is phosphorylated, and inactive when RLC is dephosphorylated. The different layers of activation/inhibition in the Rho pathway lead to different phosphorylation levels of myosin. Moreover, we investigate the roles of microtubules (MTs) by promoting their depolymerization, and we consider untreated cells as a control [24]. Altogether, we probe five conditions on the same system.

We investigate the effect of the different inhibitors on

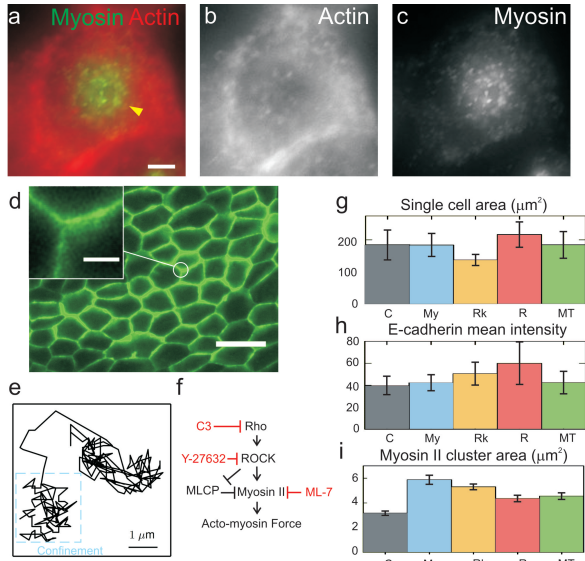


FIG. 1. (Color online) Study of vertex fluctuations. (a) Actin (red) and myosin (green) structures at the apical surface of a MDCK cell (scale bar $3 \mu\text{m}$). The myosin is concentrated in dense contractile units (yellow arrow) referred to as myosin clusters. (b) Actin structure alone. (c) Myosin structure alone. (d) We visualise MDCK cell monolayer by GFP E-cadherin (scale bar $30 \mu\text{m}$). (Inset) We identify the meeting points between three cells as the privileged point for our analysis (scale bar $4 \mu\text{m}$). (e) Extraction of a typical transition between two locally stable positions in the vertex trajectory (total time 8 hours). (f) Simplified diagram of the Rho pathway installing a order relation in myosin activation; in red the specific inhibitors and their targets. (g) Area of individual cells in each condition. C: Control; My: Myosin inhibitor; Rk: Rho kinase (ROCK) inhibitor; R: Rho inhibitor; MT: Depolymerised microtubules. (h) Mean GFP E-cadherin intensity of individual cell-cell contacts. (i) Area of myosin clusters [24].

both the architecture and the contractile forces of tissues by measuring single cell area, E-cadherin intensity and myosin cluster area in each condition. Single cell area is not strongly affected by the inhibitors, except for slightly reduced values in the Rho kinase inhibitor case, showing that the tissue architecture is barely affected by external inhibitors [Fig. 1(g)]. This is also true for the polygonicity distribution (Fig. S1 in [24]). For what concerns E-cadherin intensity, we observe an increase which supports that cell-cell adhesion is enhanced the more upstream along the Rho pathway [Fig. 1(h)]. MT depolymerization does not affect the E-cadherin intensity with respect to control.

The mean density value of myosin clusters for control is larger than in the inhibited cases (see Fig. S2(b) in [24]), suggesting a decrease in force generation for the same level of myosin per cell. In addition, the area of each myosin cluster is smaller in control than in other conditions [Fig. 1(i)]. Besides, this area decreases the more upstream

along the Rho pathway inhibition, suggesting a relaxation of the pool of myosin in the apical side, consistently with the notion that myosin force is reduced. MT depolymerization yields larger myosin cluster area compared to control. Overall, we deduce that the myosin activity is decreased the more upstream along the Rho pathway.

Because of the complexity of the processes driving tissue dynamics, anticipating the response in the vertex fluctuations to the different inhibitors is largely a challenge to physical interpretation. Our goal is to understand how the hierarchy in the Rho pathway is transferred to the cell-cell junction dynamics. We propose a synthetic read-out of this pathway captured by the vertex fluctuations extracted from the individual trajectories.

Statistics of the vertex fluctuations.—First, we compute the projected one-dimensional mean square displacement (MSD) within the five different conditions [Fig. 2(a)]. For each condition, the short time MSD exhibits a power-law behavior with exponent close to 0.7 over about one decade. The large time MSD depends on conditions and exhibits a behavior that, for simplicity, we have characterized by a power-law. The corresponding exponent is typically larger than 1, except for MT depolymerization where it is close to 1, and myosin inhibitor where it is smaller. The crossover between the two regimes appears between 20 and 60 min. The fluctuations are reduced in the myosin inhibited case, which has the lowest MSD, and they are enhanced for the Rho inhibitor, where the long time MSD is the largest.

In addition, we explore the full statistics of vertex displacement by measuring the probability distribution function (PDF) for each condition, as shown in Figs. 2(b-f). At short time the PDF is Gaussian, while it exhibits broader tails at large time. As equilibrium fluctuations are usually associated with Gaussian statistics, we interpret the non-Gaussian tails as a signature of nonequilibrium fluctuations, driven by the cellular activity. These tails reveal large displacements of the vertex, and were already observed for tracer particles in active gels [28] and living cells [3, 29, 30]. They are more pronounced in Rho inhibitor and MT depolymerization cases, as a signature of larger fluctuations possibly due to directed motion events.

Caging model.—To quantitatively discriminate between the different conditions, we test our measurements on this multicellular system with a nonequilibrium model, previously introduced in [3] to describe tracer fluctuations inside living cells. We regard the vertex as a virtual particle which dynamics is prescribed by two coupled equations: (i) an equilibrium diffusion of the vertex in a cage, modelled as a harmonic potential of stiffness k —the displacement is driven by a Gaussian white noise of variance $2\gamma k_{\text{B}}T$ with a drag force of coefficient γ ; (ii) a non-Gaussian colored diffusion equation for the center of the cage, mimicking nonequilibrium activity [24]. Inspired by the large ballistic-like displacements that we observe in experimental trajectories, we model this active noise as a two-state Poisson process: the cage has a constant velocity v in a

random uniformly sampled two-dimensional direction during a random persistence time of average τ , and it remains fixed during a random quiescence time of mean τ_0 .

We understand the confinement as an elastic mechanical stress resulting from the cells surrounding each vertex, and the nonequilibrium motion of the cage as an active stress. The effect of this active stress is to reorganize the structure of the monolayer, and therefore to spatially redistribute the elastic mechanical stress. It is worth noting that this model would be compatible with considering that each cell junction acts as a spring on the vertex [31, 32]. By adding an active stress to these junctions, one would get a similar behavior for the vertex dynamics [24].

In the absence of activity, this model predicts a short time diffusion, and then a large time plateau expressing the elastic confinement [24]. Such dynamics is entirely under the control of equilibrium thermal fluctuations. In an active system, nonequilibrium processes enhance the vertex displacement *via* the cage motion, yielding a free diffusion of the vertex with coefficient $D_A = (v\tau)^2/[2(\tau + \tau_0)]$. The large time dynamics is fully determined by the active parameters $\{v, \tau, \tau_0\}$, whereas thermal fluctuations control the short times *via* $\{k, \gamma, T\}$. A sub-diffusive transient regime appears between the two diffusions, as a crossover towards a plateau, and a super-diffusive regime can also precede the large time diffusion, as a signature of the ballistic motion involved in the active noise. In such a case thermal effects are negligible at times larger than $\tau_s = \sqrt{\tau k_B T/(k D_A)}$, a timescale quantifying the transition from the short time equilibrium-like dynamics to the large time active diffusion. Simulated trajectories exhibit clusters of similar size accounting for the transient confinement of the vertex. Occasionally large displacements of order $v\tau$ appear. The vertices do not only fluctuate around a local equilibrium position, they also undergo rapid directed jumps [compare Fig. 1(e) and Fig. 3(a)].

Active diffusion coefficient and persistence length.—We fit the MSD data to estimate the parameters characterizing nonequilibrium activity by using our analytic prediction [24]. Our fits convincingly capture the transient sub-diffusive and super-diffusive regimes [Fig. 2(a)]. We report clear quantitative variations of both the active diffusion coefficient D_A and the persistence length τ for all conditions, except for the MT depolymerization case [Figs. 3(b,c)]. It establishes that our model, based on separating the purely active fluctuations from the equilibrium thermal ones, is a reliable framework to capture the effects of our inhibitors on tissue dynamics. In that respect, D_A and τ are relevant parameters to characterize the vertex fluctuations. Therefore, our analysis indeed enables one to identify the role of each regulatory stage at a mesoscopic level.

Strikingly, D_A and τ are larger for Rho inhibitor than for Rho kinase inhibitor, and than for direct myosin inhibition [Figs. 3(b,c)]. This demonstrates that active fluctuations driving vertex dynamics are under the control of the Rho pathway: surprisingly, the more upstream the inhibi-

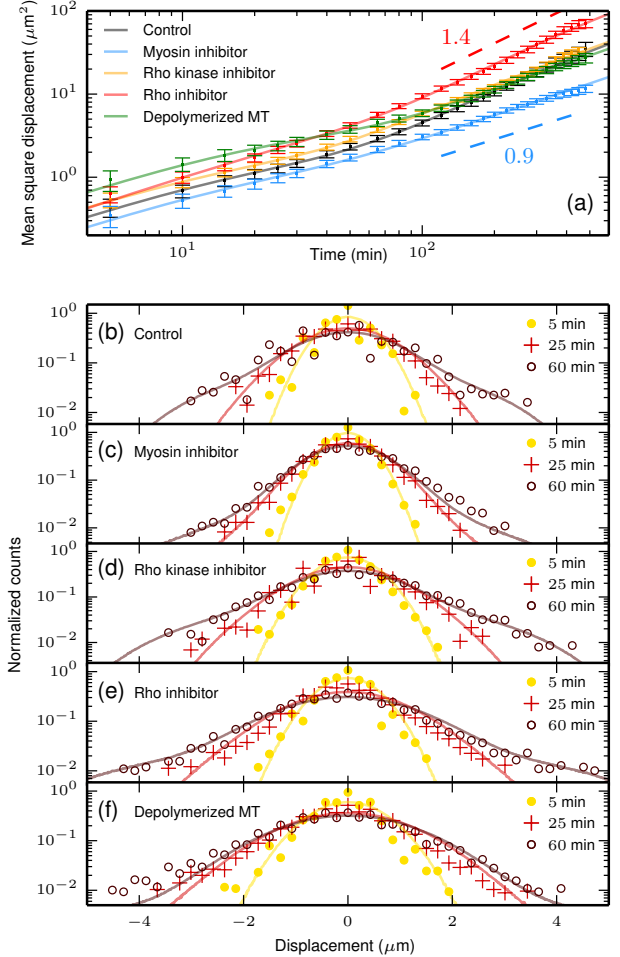


FIG. 2. (Color online) Statistics of the vertex fluctuations. (a) Mean square displacement as a function of time in five conditions: control (black), myosin inhibitor (blue), Rho kinase inhibitor (orange), Rho inhibitor (red), and microtubule depolymerization (green). The corresponding best fitting curves are in solid lines (Eq. (S5) [24]). The blue and red dashed lines report the large time behaviors. (b-f) Distribution of displacement for the five conditions at three times: 5 (●), 25 (+), and 60 min (○). Exponential tails appear at long times as a consequence of directed motion events in the vertex dynamics. Results of the simulated dynamics are in solid lines.

tion along the pathway, the larger the amplitude of fluctuations and the more persistent the ensuing displacement. The myosin inhibitor condition directly targets the myosin-II by maintaining the corresponding RLC in the dephosphorylated state [Fig. 1(f)]. It leads to the smallest D_A and τ values, showing that the mesoscopic activity of vertices is strongly affected. The Rho kinase directly activates the myosin RLC. It also inhibits the myosin light chain phosphatase (MLCP) which inhibits the myosin RLC. The net result on the phosphorylation of the myosin RLC can not *a priori* be anticipated. Our analysis shows that activity of

vertices is less affected than for the myosin inhibitor case. The corresponding value of D_A is close to the one of control, as a signature of net compensation between activation and de-activation of myosin. The MT condition illustrates the effect of a cellular scaffold on the regulation of fluctuations at a mesoscopic level. The associated values for D_A and τ are close to control, hence the effect of MT depolymerization cannot be observed from these parameters.

Eventually, our estimation of τ_s is to be compared with timescales quantifying the transition from elastic to fluid-like behavior of the material [Fig. 3(c)]. In that respect, it is of the same order as the Maxwell time reported in three-dimensional cell aggregates, *i.e.* about 40 min [33–36].

Distribution of vertex displacement.—To gain further insight into the active component of the dynamics, we compare the displacement PDF extracted from the simulated trajectories of vertex dynamics with experimental distributions [24]. The distribution at short time is Gaussian and entirely controlled by the passive parameters, as confirmed by simulations in the absence of active fluctuations where we use the passive parameters estimated from the fit of MSD data (see Fig. S6 in [24]). Including the active component of the dynamics leaves us with one remaining free parameter: the average persistence length $v\tau$ of large displacements. The short time Gaussian remains unchanged, whereas exponential tails develop at large times in the simulated PDF. The tails are more pronounced as time increases, while the central Gaussian part barely changes. We adjust the $v\tau$ value by matching the tails appearing in numerical results and experimental data.

The simulated PDFs compare very well with experiments at large times, showing that our simulations reproduce the evolution of experimental distributions at all times [Figs. 2(b-f)]. The order of magnitude of the extracted mean persistence length $v\tau$ is consistent with our measurements [Fig. 3(d)]. We report again the same order relation within the Rho pathway, *i.e.* an increase of $v\tau$ from myosin inhibitor to Rho kinase inhibitor, and from Rho kinase inhibitor to Rho inhibitor, as a signature of enhanced directed motion. The source of this enhanced motion in this latter condition could be actin polymerization, promoted by other signaling pathways such as cdc42 and Rac [37]. PDF fitting then enables us to assess a clear effect of MT depolymerization on the vertex dynamics: $v\tau$ is increased by a factor of about 2 with respect to control.

Dissipation.—The mean rate of energy dissipation is defined as the difference between the power injected by the thermostat and the one that the moving vertex gives back to the surrounding environment *via* the drag force: $J = \langle \dot{x}(\gamma \dot{x} - \sqrt{2\gamma k_B T} \xi) \rangle$, where \dot{x} is the vertex velocity, and ξ is a zero-mean Gaussian white noise [10, 11]. It vanishes for systems in a thermodynamic equilibrium state. The active nonequilibrium fluctuations lead to a non zero dissipation rate $J = kD_A/(1 + \tau k/\gamma)$ [12]. This allows us to predict the energy dissipated by the motor activity in the tissue. When computing the dissipation rate in the

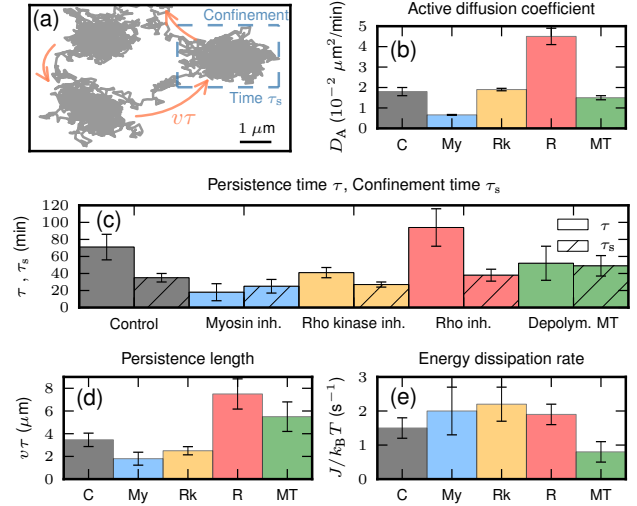


FIG. 3. (Color online) Active parameters of the vertex fluctuations. (a) Typical trajectory obtained from simulations of the vertex dynamics in control condition (scale bar 1 μm) [24]. Isotropic blobs reveal equilibrium-like transient confinement during a typical time τ_s (dashed blue box), and large displacements of order $v\tau$ occur due to nonequilibrium activity (orange arrows). (b) Best fit values of the active diffusion coefficient, (c) the persistence time and the typical confinement time, (d) the persistence length, and (e) the energy dissipation rate [24].

five conditions, it appears as approximately constant except for the depolymerized MT case [Fig. 3(e)]. This suggests that there may be an underlying coupling between mechanical properties of the tissue controlled by the passive parameters $\{\gamma, k\}$, and motor activity quantified by $\{D_A, \tau\}$. Our result supports that the same amount of energy is dissipated in such events within all the conditions, except in MT depolymerization. In this case, the lower value of J would be consistent with a reduced activity of endocytosis/exocytosis of cadherin, and with functions already reported for focal contact dynamics [38], yielding more stable cell-cell interfaces.

Discussion.—The parameters extracted from our model reveal the hierarchy in the pathway controlling the myosin activation of the vertex fluctuations: the more upstream the inhibition, the larger the active fluctuations. This approach bridges *in vivo* mechanical fluctuations to biochemical signaling pathways. We believe that our work which focuses on fluctuations localized at potential neighbor exchanges could also pave the way towards a better understanding of spontaneous topological transformations within tissues. Along this line, we have extracted the MSD from a pair of vertices undergoing a T1 transition, revealing that the transition is correlated to superdiffusive behavior (see Fig. S5 in [24], and movie 1 in [39]). It suggests that active fluctuations, powered by acto-myosin motors and experienced by vertices, may play a key role in structural rearrangements of tissues.

We thank F. Graner for helpful discussions. We acknowledge J. W. Nelson for sending the MDCK cell lines. We also thank N. Maggartou for extraction of data and lab members for discussions. This work is supported by CNRS, FRC and University of Strasbourg.

* These authors contributed equally to this work

- [1] F. Jülicher, K. Kruse, J. Prost, and J.-F. Joanny, *Physics Reports* **449**, 3 (2007).
- [2] F. C. MacKintosh and A. J. Levine, *Phys. Rev. Lett.* **100**, 018104 (2008).
- [3] É. Fodor, M. Guo, N. S. Gov, P. Visco, D. A. Weitz, and F. van Wijland, *EPL* **110**, 48005 (2015).
- [4] D. Bi, J. H. Lopez, J. M. Schwarz, and M. L. Manning, *Soft Matter* **10**, 1885 (2014).
- [5] K. Dierkes, A. Sumi, J. Solon, and G. Salbreux, *Phys. Rev. Lett.* **113**, 148102 (2014).
- [6] W. W. Ahmed, É. Fodor, and T. Betz, *BBA - Molecular Cell Research* **1853**, 3083 (2015).
- [7] E. Ben-Isaac, É. Fodor, P. Visco, F. van Wijland, and N. S. Gov, *Phys. Rev. E* **92**, 012716 (2015).
- [8] D. Bi, X. Yang, M. C. Marchetti, and M. L. Manning, ArXiv e-prints (2015), arXiv:1509.06578.
- [9] W. W. Ahmed, E. Fodor, M. Almonacid, M. Bussonnier, M.-H. Verlhac, N. S. Gov, P. Visco, F. van Wijland, and T. Betz, ArXiv e-prints (2015), arXiv:1510.08299.
- [10] K. Sekimoto and S. Sasa, *J. Phys. Soc. Jpn.* **66**, 3326 (1997).
- [11] K. Sekimoto, *J. Phys. Soc. Jpn.* **66**, 1234 (1997).
- [12] É. Fodor, K. Kanazawa, H. Hayakawa, P. Visco, and F. van Wijland, *Phys. Rev. E* **90**, 042724 (2014).
- [13] É. Fodor, W. W. Ahmed, M. Almonacid, M. Bussonnier, N. S. Gov, M.-H. Verlhac, T. Betz, P. Visco, and F. van Wijland, ArXiv e-prints (2015), arXiv:1511.00921.
- [14] R. Farhadifar, J.-C. Roper, B. Aigouy, S. Eaton, and F. Jülicher, *Curr. Bio.* **17**, 2095 (2007).
- [15] J. Käfer, T. Hayashi, A. F. M. Marée, R. W. Carthew, and F. Graner, *Proc. Natl. Acad. Sci. USA* **104**, 18549 (2007).
- [16] M. Rauzi, P. Verant, T. Lecuit, and P.-F. Lenne, *Nat Cell Biol* **10**, 1401 (2008).
- [17] D. Bi, J. H. Lopez, J. M. Schwarz, and M. L. Manning, *Nat. Physics* (2015), 10.1038/nphys3471.
- [18] C. Bertet, L. Sulak, and T. Lecuit, *Nature* **429**, 667 (2004).
- [19] A. C. Martin, M. Kaschube, and E. F. Wieschaus, *Nature* **457**, 495 (2009).
- [20] J. Solon, A. Kaya-Copur, J. Colombelli, and D. Brunner, *Cell* **137**, 1331 (2009).
- [21] C. Guillot and T. Lecuit, *Science* **340**, 1185 (2013).
- [22] M. Rauzi, P.-F. Lenne, and T. Lecuit, *Nature* **468**, 1110 (2010).
- [23] P.-L. Bardet, B. Guirao, C. Paoletti, F. Serman, V. Lopold, F. Bosveld, Y. Goya, V. Mirouse, F. Graner, and Y. Bellaïche, *Developmental Cell* **25**, 534 (2013).
- [24] See Supplemental Material at [URL will be inserted by publisher] for experimental materials and methods and for details on model, simulations, and data analysis.
- [25] C. L. Adams, Y. Chen, S. J. Smith, and W. J. Nelson, *J. Cell Biol.* **142**, 1105 (1998).
- [26] C. Klingner, A. V.Cherian, J. Fels, P. M. Diesinger, R. Aufschnaiter, N. Maghelli, T. Keil, G. Beck, I. M. Tolić-Nørrelykke, M. Bathe, and R. Wedlich-Soldner, *J. Cell Biol.* **207**, 107 (2014).
- [27] D. Riveline, E. Zamir, N. Q. Balaban, U. S. Schwarz, T. Ishizaki, S. Narumiya, Z. Kamb, B. Geiger, and A. D. Bershadsky, *J. Cell Biol.* **153**, 1175 (2001).
- [28] T. Toyota, D. A. Head, C. F. Schmidt, and D. Mizuno, *Soft Matter* **7**, 3234 (2011).
- [29] X. Trepaut, M. R. Wasserman, T. E. Angelini, E. Millet, D. A. Weitz, J. P. Butler, and J. J. Fredberg, *Nat. Physics* **5**, 426 (2009).
- [30] P. Bursac, G. Lenormand, B. Fabry, M. Oliver, D. Weitz, V. Viasnoff, J. Butler, and J. J. Fredberg, *Nat. Mater.* **4**, 557 (2005).
- [31] X. Serra-Picamal, V. Conte, R. Vincent, E. Anon, D. T. Tambe, E. Bazellieres, J. P. Butler, J. J. Fredberg, and X. Trepaut, *Nat. Physics* **8**, 628 (2012).
- [32] A. Puliafito, L. Hufnagel, P. Neveu, S. Streichan, A. Sigal, D. K. Fygenson, and B. I. Shraiman, *Proc. Natl. Acad. Sci. USA* **109**, 739 (2012).
- [33] G. Forgacs, R. A. Foty, Y. Shafrir, and M. S. Steinberg, *Biophys J* **74**, 2227 (1998).
- [34] K. Guevorkian, M.-J. Colbert, M. Durth, S. Dufour, and F. Brochard-Wyart, *Phys. Rev. Lett.* **104**, 218101 (2010).
- [35] P. Marmottant, A. Mgharbel, J. Käfer, B. Audren, J.-P. Rieu, J.-C. Vial, B. van der Sanden, A. F. M. Marée, F. Graner, and H. Delanoë-Ayari, *Proc. Natl. Acad. Sci. USA* **106**, 17271 (2009).
- [36] T. V. Stirbat, A. Mgharbel, S. Bodennec, K. Ferri, H. C. Mertani, J.-P. Rieu, and H. Delanoë-Ayari, *PLoS ONE* **8**, e52554 (2013).
- [37] S. Etienne-Manneville and A. Hall, *Nature* **420**, 629 (2002).
- [38] S. Stehbens and T. Wittmann, *J. Cell Biol.* **198**, 481 (2012).
- [39] See Supplemental Material at [URL will be inserted by publisher] for a movie of a typical T1 transition. Scale bar is 10 μm , time is in hh:mm; red and blue points record vertex trajectories.

Supplemental material: Active fluctuations are controlled by molecular motor regulations in cell monolayer

É. Fodor,^{1,*} V. Mehandia,^{2,3,*} J. Comelles,² R. Thiagarajan,² N. S. Gov,⁴ P. Visco,¹ F. van Wijland,¹ and D. Riveline²

¹*Laboratoire Matière et Systèmes Complexes, UMR 7057 CNRS/P7, Université Paris Diderot,
10 rue Alice Domon et Léonie Duquet, 75205 Paris cedex 13, France*

²*Laboratory of Cell Physics, ISIS/IGBMC, Université de Strasbourg and CNRS (UMR 7006),
8 allée Gaspard Monge, 67083 Strasbourg, France Development and Stem Cells Program,
IGBMC, CNRS (UMR 7104), INSERM (U964), Université de Strasbourg,
1 rue Laurent Fries, BP10142, 67400 Illkirch, France*

³*School of Mechanical, Materials and Energy Engineering, Indian Institute of Technology Ropar, India*

⁴*Department of Chemical Physics, Weizmann Institute of Science, 76100 Rehovot , Israel*

(Dated: May 12, 2016)

I. MATERIALS AND METHODS

A. Cell culture and tracking method

We culture cells in DMEM containing 10% Fetal Calf Serum (FCS) and antibiotics. We replate them on glass coverslips (CS) of 25 mm diameter for live cell imaging. When the cell monolayer covered 70% of the CS area, we firmly place the sample at the bottom of a custom made metallic holder. For acquisition, we change the medium to L15, 10% FCS and antibiotics. We use the following inhibitors from myosin up to Rho: inhibition of acto-myosin by ML7 (Sigma-Aldrich, 10 μ M), inhibition of Rho kinase (ROCK) by Y-27632 (Sigma-Aldrich, 10 μ M), and inhibition of Rho by C3 Transferase (Cytoskeleton, 0.04 μ M). Microtubules are depolymerised with nocodazole (Sigma-Aldrich, 10 μ M). For observation, we use a motorized inverted microscope (Nikon Eclipse Ti), equipped with a 12 bit CCD camera (Photometric CoolSNAP HQ2). The setup is temperature controlled at 37°C (Life Imaging Services). We check with fluorescent beads (4 μ m, TetraSpeck) grafted on CS surface that no drift appears during 24 hours of live imaging after 2 hour stabilization. We take pictures of the monolayer every 5 min during the next 8 hours with multiple z-stacks 1 μ m apart. They span 3 μ m depth of the cell monolayer. We merge the z-stacks into one image by using the maximum intensity projection. We then extract the vertex positions from the sequence of merged images by manually clicking in each frame as long as they are visible. For each condition, we check that the average cell area was always about $180 \pm 15 \mu\text{m}^2$, and we consider more than 20 vertices for at least 3 biological repeats.

B. Myosin cluster area and mean intensity

The immunostaining for actin and myosin was performed on wild type MDCK monolayers. The monolayer was incubated with respective cytoskeletal inhibitor drug for 2 hours and fixed with 3% paraformaldehyde (PFA). After fixation,

the cells were permeabilized with 0.5% Triton in blocking solution (5% BSA solution). The permeabilized samples were treated with 50 mM ammonium chloride solution for 10 minutes at room temperature to quench the auto-fluorescence of PFA. For myosin staining, the samples were incubated in rabbit myosin IIA non-muscle antibody (Sigma-Aldrich M8064) (1:1000 diluted in blocking solution) for 1 hour. For co-staining actin, the samples were then incubated in a cocktail of Alexa fluor 488 labelled goat anti-rabbit antibody (Molecular Probes A-11034) and Alexa fluor 546 labelled phalloidin (Molecular Probes A-22283) for 1h. Finally the samples were mounted on microscope slide with glycerol-PBS (1:1) mixture for imaging. Fluorescence images of actin and myosin were acquired through z-stacks by using a CoolSnap HQ2 camera mounted on a Nikon Ti epifluorescence microscope with a x60 oil objective. Apical myosin structures were identified, their area and mean intensity were measured using Image J. Values were normalized to the mean cluster intensity of control condition from each biological repeat. Statistics (N: number of experiments, n: number of clusters): (i) control N=2, n=312; (ii) Myosin inhibitor N=2, n=186; (iii) Rho kinase inhibitor N=2, n=197; (iv) Rho inhibitor N=2, n=257; (v) Depolymerized microtubules N=2, n=111.

C. Cell area measurement and E-cadherin intensity

Cell boundaries were identified and cell area was measured. A polygon was assigned to the area and the boundary of each cell using Packing Analyzer software [1–4]. Statistics (N: number of experiments, n: number of cells): (i) control N=4, n=235; (ii) Myosin inhibitor N=4, n=246; (iii) Rho kinase inhibitor N=3, n=249; (iv) Rho inhibitor N=3, n=148; (v) Depolymerized microtubules N=4, n=243. Afterwards, the segmented images identifying cell boundaries were used as mask for E-cadherin intensity. The boundaries were dilated up to 7 pixels using Image J. The resulting image was applied as mask on the original GFP-E-cadherin image. Statistics (N: number of experiments, n: number of contacts): (i) control N=4, n=311; (ii) Myosin inhibitor N=4, n=566; (iii) Rho kinase inhibitor N=4, n=555; (iv) Rho inhibitor N=2, n=339; (v) Depolymerized microtubules N=4, n=357.

* These authors contributed equally to this work

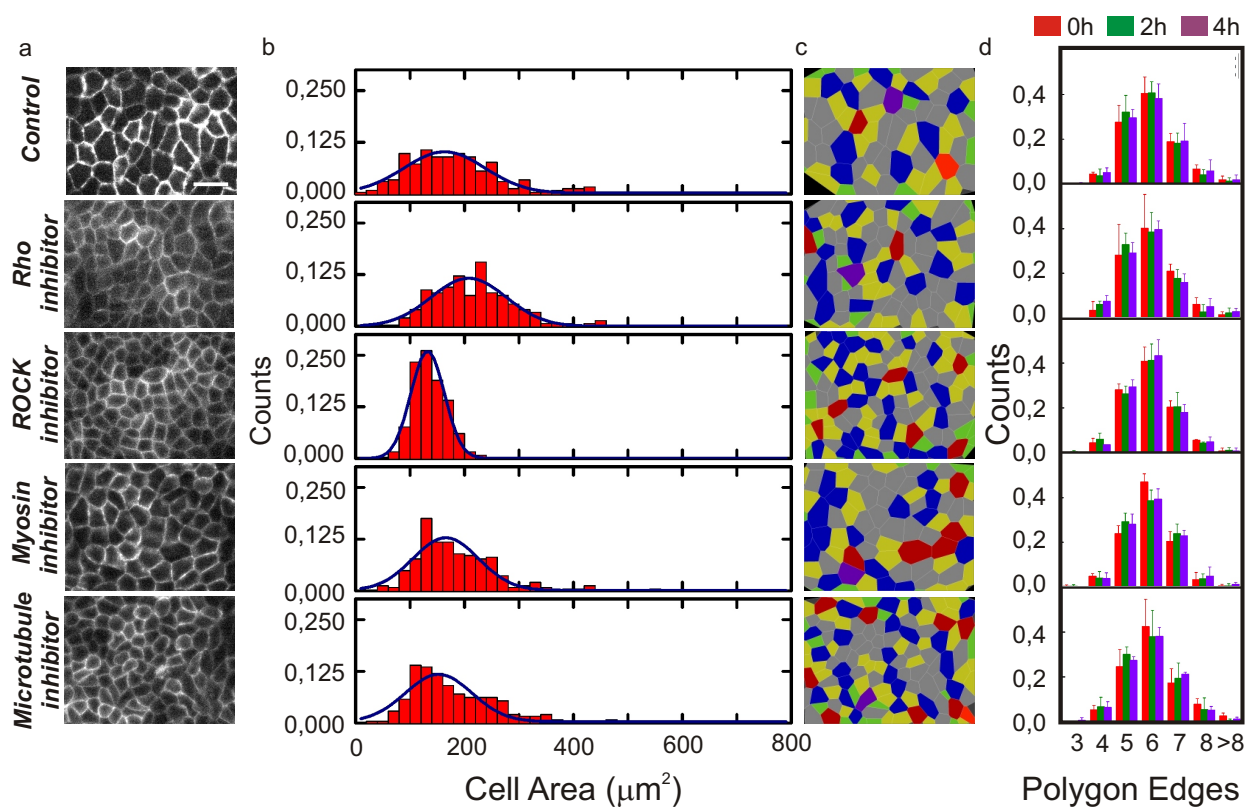


FIG. S1. (Color online) Monolayer architecture. (a) Snapshots of cell-cell contacts (GFP-E-cadherin) for each condition after 4 hours. Scale bar 20 μ m. (b) Histograms of single cell area after 4 hours for each condition. (c) Polygon approximation of (a). (d) Distribution of polygons at 0, 2 and 4 hours.

D. Statistical Analysis

The results presented in the main text are the mean value and the standard error of the mean of data sets from at least three independent experiments. Analysis of Variance (1-way ANOVA) tests were performed on Cell Area, E-cadherin intensity, Myosin Cluster Area and Myosin Cluster Intensity. Normality (Kolmogorov-Smirnov) and Bimodality (Hartigans Dip Statistic) tests were performed on Myosin Cluster Intensity results. Finally, t-test was used to determine the significance for the fitting parameters: Active Diffusion Coefficient, Persistence time, Confinement time, Persistence length, and Energy Disipation rate with significance levels p below 0.05 (not significant above). All the tests were performed using MATLAB (The MathWorks, Natick, MAA).

II. CAGING MODEL

A. Presentation

We consider the following set of equations for the two-dimensional positions of the vertex \mathbf{r} and the cage center \mathbf{r}_0

$$\gamma \frac{d\mathbf{r}}{dt} = -k(\mathbf{r} - \mathbf{r}_0) + \sqrt{2\gamma k_B T} \xi, \quad \frac{d\mathbf{r}_0}{dt} = \mathbf{v}_A, \quad (\text{S1})$$

where ξ is a zero mean isotropic Gaussian white noise, and \mathbf{v}_A is a stochastic process consisting in alternating active phases with quiescent periods. The bath temperature is denoted by T , and γ is the friction coefficient. In the active phase, \mathbf{v}_A has a constant value v over a random direction uniformly sampled in the two-dimensional space during an exponentially distributed time of average τ . In the quiescent phase, $\mathbf{v}_A = \mathbf{0}$ during an exponentially distributed time of mean value τ_0 .

The projection of the process \mathbf{v}_A on one dimension defines the process v_A . We denote P_{2D} and P_{1D} the distributions of a two-dimensional unit vector $\hat{\mathbf{n}}$, and of $n_x = \hat{\mathbf{n}} \cdot \hat{\mathbf{x}}$ in the x -axis, respectively. They are related as $P_{2D}(\theta) |d\theta| = P_{1D}(n_x) |dn_x|$, where $\hat{\mathbf{n}} = (\cos \theta, \sin \theta)$ in the (x, y) basis. Given $P_{2D} = 1/(2\pi)$ is uniform and $n_x = \cos \theta$, we deduce $P_{1D} = |\mathrm{d}\arccos(n_x)/dn_x|/(2\pi)$. It follows that the active phase of v_A is now characterized by a random velocity in the interval $[-v, v]$ distributed as

$$P(v_A) = \frac{1}{\pi v \sqrt{1 - (v_A/v)^2}}. \quad (\text{S2})$$

The time distribution of each phase remains unchanged in the projected process. From this result, we arrive at the equations for the projected positions x and x_0

$$\gamma \frac{dx}{dt} = -k(x - x_0) + \sqrt{2\gamma k_B T} \xi, \quad \frac{dx_0}{dt} = v_A, \quad (\text{S3})$$

where ξ is still a zero mean Gaussian noise such as $\langle \xi(t)\xi(t') \rangle = \delta(t - t')$, and now v_A is the random process depicted in Fig. S3. It is a zero mean non-Gaussian colored noise with correlations $\langle v_A(t)v_A(t') \rangle = D_A e^{-|t-t'|/\tau}/\tau$, where $D_A = (v\tau)^2/[2(\tau + \tau_0)]$ defines an active diffusion coefficient in terms of the active parameters.

B. Analogy with active cell-cell junctions

We consider that a cell-cell junction acts as a spring on the vertex. We treat the fluctuations of these junctions with an active noise regulating the dynamics of the rest length of the associated spring. We account for the interaction with the surrounding bath by means of a white noise term and a damping force, and we discard inertial effects. It follows that the dynamics of the vertex position \mathbf{r} obeys

$$\gamma \frac{d\mathbf{r}}{dt} = -k(3\mathbf{r} - \mathbf{r}_1 - \mathbf{r}_2 - \mathbf{r}_3) + \xi, \quad \frac{d\mathbf{r}_i}{dt} = \mathbf{v}_{Ai}, \quad (\text{S4})$$

where \mathbf{r}_i denotes the position of each neighboring vertex and where each noise term \mathbf{v}_{Ai} has the same properties as \mathbf{v}_A defined above, with zero cross-correlations. By projecting Eq. (S4) on one dimension, we end up with a dynamics similar to Eq. (S3), where the correlations of the noise term v_A exhibit the same exponential decay.

C. Mean square displacement

From the Fourier transform of Eq. (S3), we compute the position autocorrelation function $C(t) = \langle x(t)x(0) \rangle$, and then deduce the one-dimensional mean square displacement (MSD) as $\langle \Delta x^2 \rangle(t) = 2(C(0) - C(t))$. We denote the thermal contribution to the MSD by $\langle \Delta x_T^2 \rangle$, and the MSD when the particle is only subjected to motor activity by $\langle \Delta x_A^2 \rangle$, so that: $\langle \Delta x^2 \rangle = \langle \Delta x_T^2 \rangle + \langle \Delta x_A^2 \rangle$. The thermal MSD is the same as for an Ornstein-Uhlenbeck process, and we compute the active contribution in terms of the parameters characterizing the active force

$$\langle \Delta x_T^2 \rangle(t) = 2D_T \tau_r \left(1 - e^{-t/\tau_r}\right), \quad (\text{S5a})$$

$$\begin{aligned} \langle \Delta x_A^2 \rangle(t) = & \frac{2D_A \tau_r}{1 - (\tau/\tau_r)^2} \left[\left(\frac{\tau}{\tau_r}\right)^3 \left(1 - e^{-t/\tau} - \frac{t}{\tau}\right) \right. \\ & \left. + e^{-t/\tau_r} + \frac{t}{\tau_r} - 1 \right], \end{aligned} \quad (\text{S5b})$$

where $D_T = k_B T / \gamma$ is the thermal diffusion coefficient, and $\tau_r = \gamma/k$ is a microscopic relaxation time scale. It appears the MSD depends on four independent parameters, two of them characterizing active fluctuations $\{D_A, \tau\}$, and the two others being associated with equilibrium thermal properties $\{D_T, \tau_r\}$.

III. DATA ANALYSIS

A. Mean square displacement

We extract the experimental MSD from individual trajectories in each condition. We compute the value of the MSD at each time t by performing a sliding time average on every trajectory, and an ensemble average over the different trajec-

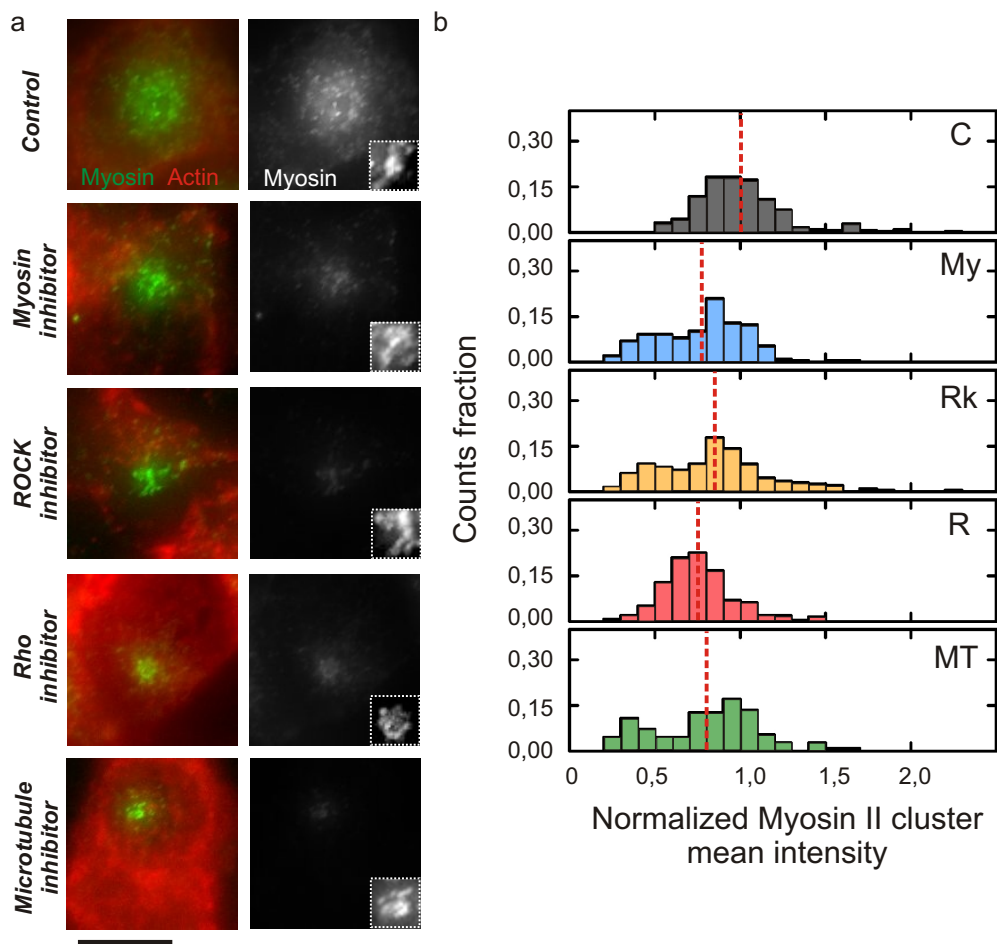


FIG. S2. (Color online) Acto-myosin cytoskeleton. (a) Actin (red) and myosin (green) structures (left), and myosin structure alone at the apical surface of MDCK cells for the different experimental conditions (right). Scale bar is $5 \mu\text{m}$. The Lookup Table (LUT) were unaltered to show the differences in actin and myosin intensities. Insets in (right) show zooms on typical myosin clusters with increased contrast for clarity. (b) Distributions of myosin clusters mean intensity for each condition after 2 hours of the beginning of the experiment. Values were normalized to the mean cluster intensity of control condition from each biological repeat. The dashed red lines indicate the mean value.

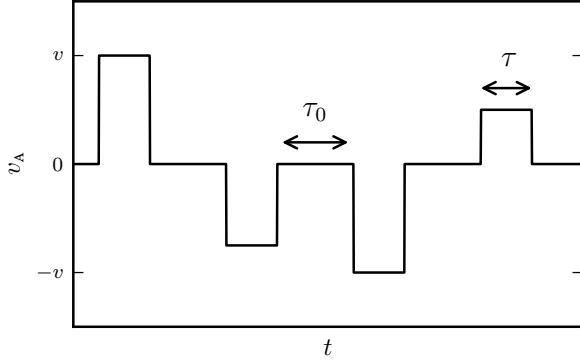


FIG. S3. Example trajectory of the active burst projection v_A . It equals zero over a random duration of average τ_0 , and is a random value between $-v$ and v during a random time of order τ .

tories

$$\text{MSD}(t) = \frac{\Delta t}{N(t_m - t)} \sum_{j=1}^N \sum_{i=1}^{\frac{t_m-t}{\Delta t}} [x_j(t + i\Delta t) - x_j(i\Delta t)]^2, \quad (\text{S6})$$

where N is the number of experimental trajectories, $t_m = 8$ hours is the longest measurement time, and $\Delta t = 5$ min is the experimental sampling time. The error bars for the estimated active parameters shown in Fig. 2 of the main text account for the standard error of the experimental points. These errors are used as weights associated with each point in the average MSD when fitting the experimental data. Moreover, we report a systematic error due to the spatial resolution, which we estimate as $0.2 \mu\text{m}$.

We present in Fig. S4 the MSD data for the five conditions along with the best fit curves for which we have extended the time window with respect to Fig. 2(a) in the main text, thus highlighting the predicted large time diffusive regime.

B. T1 transition

We analyse a vertex trajectory which contains a T1 transition, that is for which two neighbouring vertices merge during the trajectory (Fig. S5). To provide a quantitative probe of the merging event, we compute the vertex interdistance as a function of time. We identify the time interval of the T1 transition as the time needed for the two vertices to gather and then separate. In that respect, we assume that the transition ends when the vertex interdistance increases again. The interdistance fluctuates around $15 \mu\text{m}$ until about 300 min when it starts to drop off, and it increases again at ~ 600 min.

We extract the MSD of the trajectory by performing an ensemble average only over the neighbouring vertices. The MSD exponent is close to 1 at short and large times, that is before and after the transition. During the transition, the exponent first increases rapidly, and then decreases to reach a

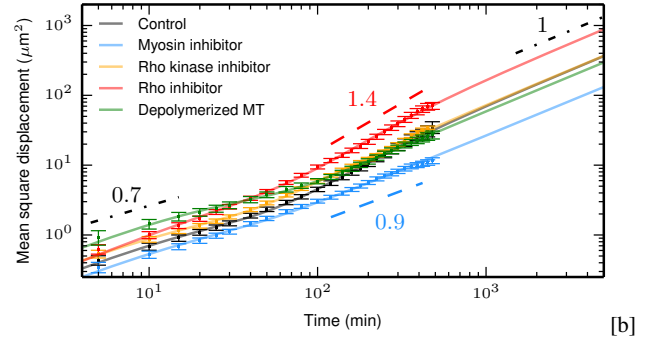


FIG. S4. (Color online) Mean square displacement as a function of time in five conditions: control (black), myosin inhibitor (blue), Rho kinase inhibitor (orange), Rho inhibitor (red), and microtubule depolymerization (green). The corresponding best fitting curves are in solid lines. The best fit curves are extended beyond the experimental time window to highlight the predicted large time diffusive regime.

ballistic regime until the end of the transition. This behavior supports the hypothesis that T1 transitions correspond to superdiffusive events in the vertex trajectory, which are triggered by active fluctuations within our model.

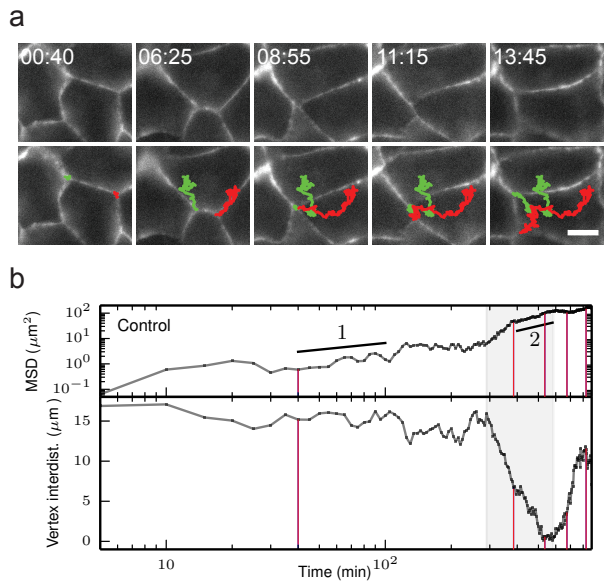


FIG. S5. (Color online) (a) Snapshots of a vertex undergoing a T1 transition, visualized by GFP-E-Cadherin. Red and green lines describe the trajectories of triple points during a T1 transition. Time in hh:mm. Scale bar $10 \mu\text{m}$ (see movie 1 in [5]). (b) Plot of the evolution of the mean square displacement (MSD) and vertex interdistance for the T1 transition shown in (a). Black lines are guides to eyes for the diffusive and superdiffusive regimes. Vertical red lines correspond to the time points of snapshots in (a).

IV. NUMERICAL SIMULATIONS

A. Methods

We use Euler's method to simulate Eq. (S3). The iterative equations take the following form in terms of the sampling time Δt

$$x(t + \Delta t) = x(t) - \frac{\Delta t}{\tau_r} (x(t) - x_0(t)) + \sqrt{2D_r \Delta t} \eta, \quad (\text{S7a})$$

$$x_0(t + \Delta t) = x_0(t) + v_a(t) \Delta t, \quad (\text{S7b})$$

where η is a random Gaussian variable with zero mean and variance 1. The iterative equation for the active burst v_a obeys

$$v_a(t + \Delta t) = \begin{cases} v_a(t) & \text{if } v_a(t) \neq 0 \quad \text{prob. } 1 - \Delta t/\tau_r, \\ v_a(t) & \text{if } v_a(t) = 0 \quad \text{prob. } 1 - \Delta t/\tau_0, \\ 0 & \text{if } v_a(t) \neq 0 \quad \text{prob. } \Delta t/\tau_r, \\ \chi_{[-v, v]} & \text{if } v_a(t) = 0 \quad \text{prob. } \Delta t/\tau_0, \end{cases} \quad (\text{S8})$$

where $\chi_{[-v, v]}$ is a random number between $-v$ and v with probability given by Eq. (S2).

B. Results: Short-time dynamics

We extract the probability distribution function (PDF) of displacement from the simulated trajectories, to be compared

with the experimental distributions. The short time dynamics is Gaussian and entirely controlled by the passive parameters $\{D_r, \tau_r\}$. First, we run simulations with the best values estimated from the fit of the experimental MSD, as reported in Tab. I, without any active noise, namely $v_a = 0$. The corresponding PDFs reproduce the experimental data, as shown in Fig. S6(a-e). Then, we include the active nonequilibrium fluctuations. The short time PDF is still Gaussian as expected, and we adjust the value of $v\tau$ by matching the exponential tails between numerical results and experimental data (Fig. 2(b-f) of the main text). We present in Fig. S6(f) the comparison between the analytic MSD in Eq. (S5) and the MSD extracted from simulated trajectories, showing a good agreement. This confirms that there is a well defined time scale which separates equilibrium fluctuations from active nonequilibrium fluctuations.

TABLE I. Best fit value of D_r and τ_r estimated from the fit of the experimental MSD presented in Fig. 2(a) of the main text.

	$D_r (10^{-2} \mu\text{m}^2/\text{min})$	$\tau_r (\text{min})$
Control	2.4 ± 0.2	13 ± 2
Myosin inh.	1.8 ± 0.1	13 ± 3
Rho kinase inh.	3.2 ± 0.2	10 ± 1
Rho inh.	2.8 ± 0.2	24 ± 6
Depolym. MT	4.6 ± 0.7	15 ± 4

-
- [1] M. C. Gibson, A. B. Patel, R. Nagpal, and N. Perrimon, *Nature* **442**, 1038 (2006).
 - [2] R. Farhadifar, J.-C. Röper, B. Aigouy, S. Eaton, and F. Jülicher, *Current Biology* **17**, 2095 (2007).
 - [3] B. Aigouy, R. Farhadifar, D. B. Staple, A. Sagner, J.-C. Röper, F. Jülicher, and S. Eaton, *Cell* **142**, 773 (2010).
 - [4] D. Staple, R. Farhadifar, J.-C. Röper, B. Aigouy, S. Eaton, and F. Jülicher, *EPJE* **33**, 117 (2010).
 - [5] See Supplemental Material at [URL will be inserted by publisher] for a movie of a typical T1 transition. Scale bar is $10 \mu\text{m}$, time is in hh:mm; red and blue points record vertex trajectories.

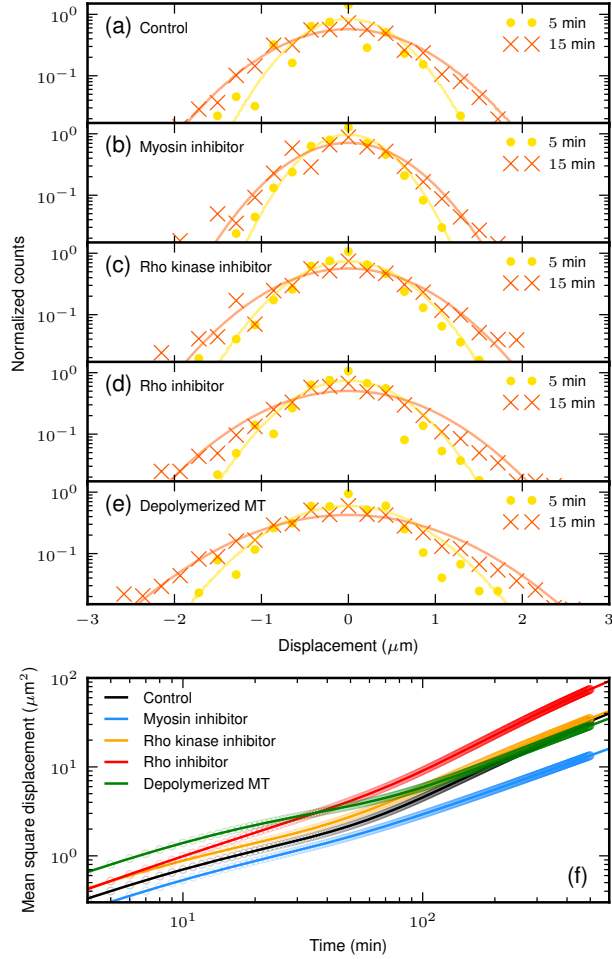


FIG. S6. (Color online) (a-e) Probability distribution function of displacement for the five conditions at two times: 5 (yellow ●), and 15 min (orange ×). We present the results of simulations without active noise of the vertex dynamics in solid lines. (f) Mean square displacement as a function of time in five conditions: control (black), myosin inhibitor (blue), Rho kinase inhibitor (orange), Rho inhibitor (red), and microtubule depolymerization (green). Results of simulations with active noise are shown in ○, and the corresponding analytic curves are in solid lines.

Future directions

As discussed in paper E, it would be interesting to investigate the connection between nonequilibrium fluctuations and topological transition, such as T1 transitions, in epithelial tissues. Indeed, it has been reported that fluctuations of vertices facilitate such transitions [110]. For instance, one could relate the directed motion periods in the vertex trajectory to the merging events starting a T1 transition to demonstrate that fluctuations of large amplitude are able to trigger topological transitions. Moreover, the insight that we provide into the time scales involved in these fluctuations could motivate the possibility to trigger topological transitions from an external perturbation. One could investigate if applying an oscillatory shear, either to the whole tissue or at a given location inside it, with a well tuned frequency would activate such transitions. Eventually, measuring the response from an external perturbation, to be compared with the spontaneous fluctuations, would provide a better insight into the nonequilibrium component of the dynamics, as a crucial test for the robustness of our minimal description.

Chapter 7

Nonequilibrium properties of persistent self-propelled particles

This Chapter, unlike the previous ones, addresses collective effects stemming from interactions between a large number of self-propelled particles. We first present the phenomenology of such systems. Then, we motivate the study of a specific dynamics for which the self-propulsion stems from a noise term with persistent correlations. We discuss the success and limitations of previous approximation schemes used to describe such dynamics. We determine the steady state for the many-body distribution within a controlled and systematic perturbation theory. Moreover, we quantify the breakdown of the irreversibility of the dynamics to shed light on the existence of an effective equilibrium regime. Eventually, we derive the collective modes of the dynamics.

7.1 Self-propelled particles as an active matter system

Phenomenology of active matter

A widely studied class of active matter systems is given by interacting self-propelled particles. In such systems, energy is injected at the level of the individual particles to power self-propelled motion, thus producing a microscopic energy flux. By contrast with systems driven far from equilibrium by an external field, no large scale current is observed. Self-propelled particles can undergo a phase separation even when interactions are purely repulsive. This phenomenon is known as the motility-induced phase separation (MIPS) [13, 14]. The formation of clusters has been reported experimentally, using Janus particles in a solution of hydrogen peroxide for instance [11, 129, 130], as shown in Fig. 7.1. These particles are made of two sides with physical properties associated with different chemical reactions. As a result, chemical gradients develop and power the motion of the particles. In such experimental systems, the details of the interactions are neither well understood nor well controlled in general. To gain a better understanding of the role of interactions in the emerging collective physics, numerical simulations of active particles have been performed for minimal models of self-propulsion [131–134]. They have studied in detail the phase diagram, the structure of the dense phase, as well as the kinetics of the phase separation. Another characteristic of active particles is the accumulation at the boundaries of an external potential [135–140]. The unexpected density profiles under confinement is the signature of a non-Boltzmann stationary distribution, which is sometimes regarded as the hallmark of nonequilibrium in active systems. The sedimentation of active particles has also been described theoretically in line with experimental results [141, 142]. Other numerical studies have explored the shift of the usual glass transition in dense systems of self-propelled particles [143–147].

Existing models of self-propulsion

The theoretical investigations of interacting active particles rely on minimal models of self-propulsion. Among the many descriptions of self-propulsion, two of them have received special attention: run-and-tumble particles (RTPs), and active Brownian particles (ABPs). The motion of RTPs is made of periods with constant speed whose direction varies instantaneously in a random manner. This model has been used to describe the erratic motion of bacteria such as *Escherichia coli* [13, 148]. Concerning ABPs, the velocity of self-propulsion has also a fixed norm, yet the direction now varies through angular diffusion [Fig. 7.2]. The dynamics of these two models can be cast in the following form. Provided that inertial effects

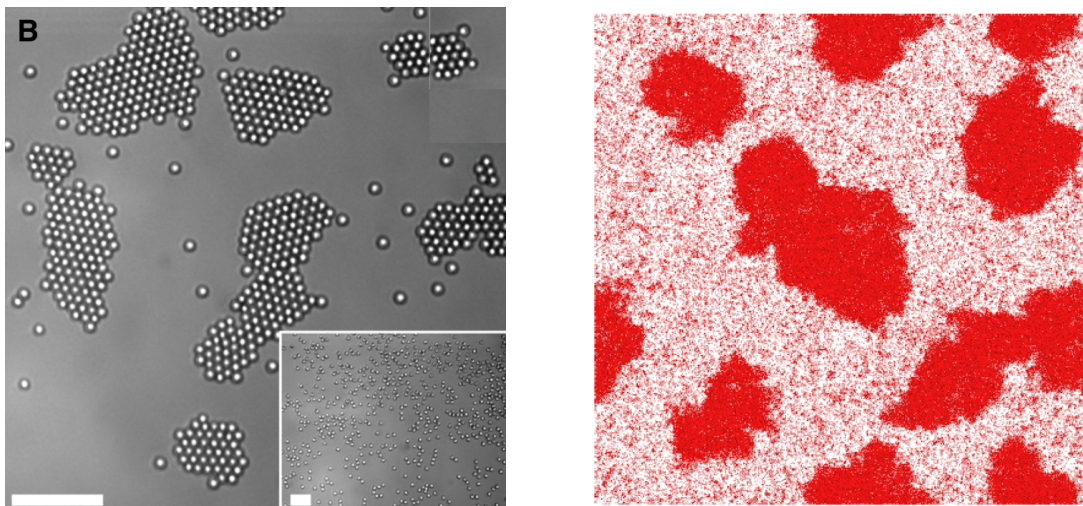


Figure 7.1 – Clusters of photoactivated colloidal particles (left, taken from [11]), and simulated active particles (right, taken from [132]).

are negligible, the velocity $\dot{\mathbf{r}}_i$ of the particle i is given by the sum of a deterministic and a stochastic contribution as

$$\dot{\mathbf{r}}_i = -\nabla_i \Phi + \mathbf{v}_i, \quad (7.1)$$

where we have set the friction coefficient to one, and we have introduced the potential Φ . This potential can account for interactions between the particles as well as the effect of an external force field. The self-propulsion \mathbf{v}_i is a noise term which is uncorrelated between the particles. In the case of RTPs, it corresponds to the active burst process presented in Chapter 3 in the limit of vanishing waiting time. Therefore, it is both a colored and non-Gaussian noise. In the case of ABPs, the self-propulsion noise term is also colored and non-Gaussian, though it has been shown that non-Gaussian effects can be neglected for some regimes in three dimensions [149]. Considering free particles, the large time and large scale dynamics is purely diffusive for both ABPs and RTPs. The diffusion coefficient is defined in terms of the amplitude of the velocity, as well as the rate of directional variation and the rotational diffusion coefficient, for ABPs and RTPs respectively [14].

Questions of interest

Recent developments have strived to build a unified description of interacting self-propelled particles based on what can be saved of thermodynamics concepts. They are led by the search for an equation of state by analogy with equilibrium [150]. In that respect, a crucial issue is to extend the definition of temperature [140, 151–154] and pressure [155, 156] beyond equilibrium. Another

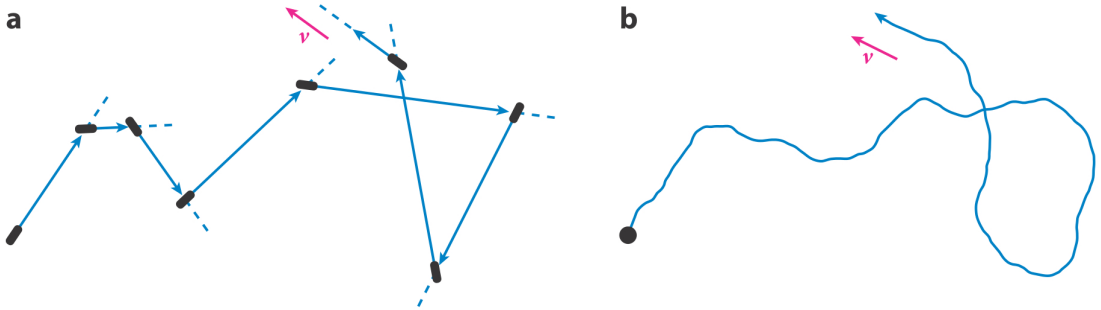


Figure 7.2 – Typical trajectories of (a) run-and-tumble particles, and (b) active Brownian particles. Taken from [14].

important question concerns the emergence of MIPS. This phenomenon has been studied through hydrodynamic coarse graining of the dynamics [130, 131, 134, 157–159], yielding mean-field descriptions of the phase separation in terms of a free energy density functional. A related question is whether this unexpected phase separation can be understood at the microscopic level as stemming from an effective interaction between the particles. Following this route, it may be possible to anticipate the phase diagram from the stationary distribution of the interacting particles, as suggested by recent studies [149, 160]. Eventually, understanding how the structural relaxation of a dense suspension of colloids is affected by the self-propulsion is an open issue, though recent methods based on extending mode-coupling approximations have been proposed to capture results from numerical simulations [161–163].

7.2 Interacting particles under persistent fluctuations

Previous models, such as ABPs and RTPs, have encoded the self-propulsion in a fluctuating noise term with exponential correlations and non-Gaussian statistics. Yet, the non-Gaussian properties may not be crucial in the description of ABPs in three dimensions [149]. Based on this observation, our aim is to provide an extensive description of the dynamics of active particles for which the self-propulsion reduces to a Gaussian noise. Building on the case of ABPs and RTPs, we consider that the correlations are exponentially decaying as

$$\langle v_{i\alpha}(t)v_{j\beta}(0) \rangle = T\delta_{ij}\delta_{\alpha\beta} \frac{e^{-|t|/\tau}}{\tau}, \quad (7.2)$$

where T is a temperature controlling the amplitude of the noise, and τ is a persistence time. By contrast to ABPs and RTPs, the self-propulsion no longer has a fixed norm. Such dynamics have been shown to successfully reproduce the behavior of passive tracers in an active bath of bacteria [164]. Within this formulation, the self-propulsion is an Ornstein-Uhlenbeck process, whose dynamics can be written in terms of a Gaussian white noise ξ_i , with correlations $\langle \xi_{i\alpha}(t)\xi_{j\beta}(0) \rangle = \delta_{ij}\delta_{\alpha\beta}\delta(t)$, as

$$\tau\dot{\mathbf{v}}_i = -\mathbf{v}_i + (2T)^{1/2}\xi_i. \quad (7.3)$$

If we were to describe equilibrium dynamics, the drag force in the dynamics (7.1) would contain a memory kernel related to the noise correlations, as discussed in Chapter 1. The relation between the noise correlations and the drag force being different from the thermal one, the fluctuations of the internal self-propulsion drive the dynamics out-of-equilibrium. One recovers equilibrium dynamics in the limit of vanishing τ for which the self-propulsion reduces to a Gaussian white noise. The dynamics given by Eqs. (7.1) and (7.3) can be written in terms of the particle velocity, denoted by \mathbf{p}_i , as

$$\tau\dot{\mathbf{p}}_i = -\mathbf{p}_i - (1 + \tau\mathbf{p}_k \cdot \nabla_k)\nabla_i\Phi + (2T)^{1/2}\xi_i. \quad (7.4)$$

The effect of the self-propulsion leads us to expressing the dynamics in an under-damped form for which the damping force is affected by the potential.

Approximate dynamics

Two different approximate treatments of the dynamics (7.4) have been proposed based on extending previous approximation schemes to interacting particles. Considering non-interacting particles, they are referred to as the unified colored-noise approximation (UCNA) [165, 166] and the Fox theory [167, 168]. Such approximations were first motivated by the description of the fluctuations of the radiation in the dye laser [166, 169]. They have led to provide results for the stationary distribution and for mean first-passage times [170–172].

The UCNA consists in neglecting the left-hand side in Eq. (7.4):

$$\mathbb{M}_{i\alpha,j\beta}\dot{r}_{j\beta} = -\partial_{i\alpha}\Phi + (2T)^{1/2}\xi_{i\alpha}. \quad (7.5)$$

where $\partial_{i\alpha} = \partial/\partial r_{i\alpha}$, and we have introduced the tensor $\mathbb{M}_{i\alpha,j\beta} = \delta_{ij}\delta_{\alpha\beta} + \tau\partial_{i\alpha,j\beta}^2\Phi$. As a result, the dynamics is now Markovian for the particle positions. The product appearing in the left-hand side of Eq. (7.5) is to be understood with the Stratonovitch convention, since we have used the common rules of differential calculus to obtain it. It follows that the associated Fokker-Planck equation for the set of positions $P(\{\mathbf{r}_i\}, t)$ reads

$$\partial_t P = \partial_{i\alpha} \left(P \mathbb{M}_{i\alpha,j\beta}^{-1} \partial_{j\beta} \Phi \right) + T \partial_{i\alpha} \left[\mathbb{M}_{i\alpha,j\beta}^{-1} \partial_{k\gamma} \left(\mathbb{M}_{k\gamma,j\beta}^{-1} P \right) \right], \quad (7.6)$$

where \mathbb{M}^{-1} denotes the inverse of \mathbb{M} . The corresponding stationary measure can be exactly determined

$$P_s \sim \exp \left[-\frac{\Phi}{T} - \frac{\tau (\nabla_i \Phi)^2}{2T} \right] |\det \mathbb{M}|. \quad (7.7)$$

This is a straightforward generalization of the one-dimensional case presented in [173]. As a result, the stationary distribution differs from the equilibrium Boltzmann distribution $e^{-\Phi/T}$. The equilibrium distribution is recovered in the limit of vanishing persistence time, as it should. Numerical results have been tested against this prediction in the case of a one-dimensional system for two interacting particles. They support the validity of the UCNA in the small τ regime, as shown in Fig. 7.3. In such a regime, the distribution can be simplified as

$$P_s \sim \exp \left[-\frac{\Phi}{T} - \frac{\tau (\nabla_i \Phi)^2}{2T} + \tau \nabla_i^2 \Phi + \mathcal{O}(\tau^2) \right]. \quad (7.8)$$

One can identify an effective potential $\Phi_{\text{eff}} = -T \ln P_s$ from this expression by analogy with the Boltzmann distribution. In the case where the bare potential Φ is an external confining potential, minimizing Φ_{eff} provides information about the favored particle positions under confinement, which may differ from the ones for the original potential. The correction term $\tau (\nabla_i \Phi)^2/2$ is always positive, thus driving the system away from regions of large forces. The second correction term $-\tau \nabla_i^2 \Phi$ is dominant for large values of T , and it can take both signs. It selects local extrema of Φ , whether minima or maxima when being negative or positive, respectively. Considering that the bare potential describes pair-wise interactions, the corresponding effective potential contains three-body interactions stemming from the term $\tau (\nabla_i \Phi)^2/2$. Moreover, when Φ corresponds to repulsive interactions only, the associated Φ_{eff} combines repulsive and attractive interactions. This may explain why the self-propulsion produces attractive effects from a genuine repulsion, as reported experimentally in clustering colloidal systems [11, 129, 130]. Furthermore, the form of the first order correction of the effective potential appears in a different context. The quantum mapping of the dynamics of Brownian particles displays an effective potential which is related to the bare potential in the same way as the first order correction of Φ_{eff} [174–176].

The Fox theory uses functional calculus applied on the weight of a given time realization of the particle trajectories to propose an approximate Fokker-Planck equation. It has been generalized to interacting particles in [149], yet this derivation is erroneous. We demonstrate in Appendix A that the correct Fokker-Planck equation takes the following form:

$$\partial_t P = \partial_{i\alpha} (P \partial_{i\alpha} \Phi) + T \partial_{i\alpha, j\beta}^2 \left(\mathbb{M}_{i\alpha, j\beta}^{-1} P \right). \quad (7.9)$$

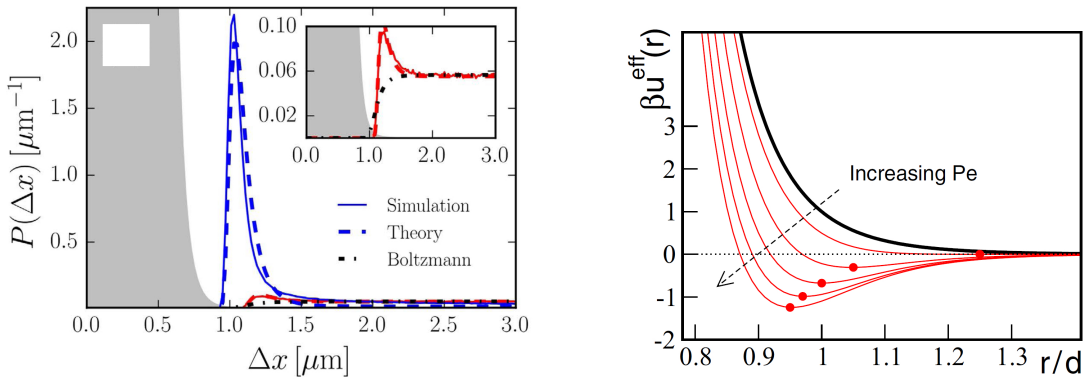


Figure 7.3 – Left: Stationary distribution for two self-propelled particles interacting via a potential r^{-12} . Taken from [173]. Right: Effective pair potential (red) deduced from a bare repulsive potential of the form r^{-12} (black) for different values of the Péclet number, as a function of the inter-particle distance scaled by the typical particle size. The Péclet number is proportional to the amplitude of the self-propulsion. Taken from [149].

Comparing this result with the one for the UCNA in Eq. (7.6), it appears that the probability currents of UCNA and the Fox theory are proportional to each other with coefficient given by M^{-1} . It follows that the Fox theory shares the same stationary distribution as the UCNA. This result is different from the one presented in [149], yet the stationary distribution of [149] coincides in the small τ regime with ours in Eq. (7.8). This is supported by the good comparison between numerical simulations and analytic predictions of [149] in this regime. From this stationary distribution, one can explicitly predict the form of the attractive part in the effective potential, when considering a pair-wise bare potential, by retaining only the two-body part in the effective potential. For a bare repulsion of the form r^{-12} , the effective potential exhibits a minimum as a balance between attractive and repulsive effects, the depth of which increases with the amplitude of the self-propulsion, as shown in Fig. 7.3.

Stationary distribution in position-velocity space: perturbative treatment

The two approximation schemes presented above yield some Markovian dynamics for the particle positions. In that respect, they both lead to discard the inertia-like effects inherent to the original dynamics. In particular, they do not provide any prediction about the distribution of velocity in the steady state. It has been shown recently that the conditional distribution of velocity $P_s(\{\mathbf{r}_i\} | \{\mathbf{p}_i\})$ associated with the UCNA position distribution has a Gaussian form [177]. Yet, such a distribution can not account for the existence of a particle current in a ratchet

experiment, namely when the particles are put in a potential made of asymmetric energy barriers [178]. Therefore, an approximate form of the position-velocity distribution able to predict such effect is still lacking.

Our goal is to perturbatively determine the steady state of the dynamics (7.4) in the limit of small persistence time. Previous attempts to obtain the steady state are neither based on a systematic scheme, nor well controlled. We will account for the effect of the self-propulsion in both the inertia-like term and the modified damping term. To this aim, we scale time as $t \rightarrow \tau^{1/2}t$ and we use the scaled velocities as $\mathbf{p}_i \rightarrow \tau^{-1/2}\mathbf{p}_i$, following [165, 179]. As a result, the stationary distribution satisfies $\mathcal{L}P_s(\{\mathbf{r}_i, \mathbf{p}_i\}) = 0$, where the operator \mathcal{L} reads

$$\mathcal{L} = -p_{i\alpha} \frac{\partial}{\partial r_{i\alpha}} + \tau^{-1/2} \frac{\partial}{\partial p_{i\alpha}} \left(\mathbb{M}_{i\alpha,j\beta} p_{j\beta} + \tau^{1/2} \partial_{i\alpha} \Phi + T \frac{\partial}{\partial p_{i\alpha}} \right). \quad (7.10)$$

The equation $\mathcal{L}P_s = 0$ is invariant under the transformation $\{\tau, \mathbf{p}_i\} \rightarrow -\{\tau, \mathbf{p}_i\}$. It follows that the stationary distribution displays the same symmetry. We use the following ansatz:

$$P_s \sim \exp \left[-\frac{\Phi}{T} - \frac{\mathbf{p}_i^2}{2T} + \sum_{n=2}^{\infty} \tau^{n/2} \psi_n(\{\mathbf{r}_i, \mathbf{p}_i\}) \right]. \quad (7.11)$$

Substituting this ansatz in the equation $\mathcal{L}P_s = 0$, we obtain a set of recursive equations for the ψ_n to every order in $\tau^{1/2}$. They all take the following form:

$$\left(p_{i\alpha} \frac{\partial}{\partial p_{i\alpha}} - T \frac{\partial^2}{\partial p_{i\alpha} \partial p_{i\alpha}} \right) \psi_n = f_n(\{\mathbf{r}_i, \mathbf{p}_i\}). \quad (7.12)$$

It follows that each ψ_n is solved up to a function $g_n(\{\mathbf{r}_i\})$ which only depends on the particle positions. Using the symmetry of the evolution operator, we deduce that the functions ψ_n have the same parity in n and \mathbf{p}_i . It follows that g_n is zero for odd n . At leading order, the first equation to be solved reads

$$f_2 = \left[\nabla_i^2 - \frac{1}{T} (\mathbf{p}_i \cdot \nabla_i)^2 \right] \Phi, \quad (7.13)$$

yielding

$$\psi_2 = -\frac{1}{2T} (\mathbf{p}_i \cdot \nabla_i)^2 \Phi + g_2. \quad (7.14)$$

In order to determine the expression for g_2 , we need to solve the higher orders of the expansion. to the next order, we obtain

$$f_3 = \frac{1}{2T} \left[(\mathbf{p}_i \cdot \nabla_i)^3 \Phi - (\mathbf{p}_i \cdot \nabla_i)(\nabla_j \Phi)^2 \right] - \mathbf{p}_i \cdot \nabla_i g_2, \quad (7.15)$$

from which we deduce ψ_3 as

$$\psi_3 = \frac{1}{2T} \left\{ \left[\frac{1}{3}(\mathbf{p}_i \cdot \nabla_i)^3 + T(\mathbf{p}_i \cdot \nabla_i)\nabla_j^2 \right] \Phi - (\mathbf{p}_i \cdot \nabla_i)(\nabla_j \Phi)^2 \right\} - \mathbf{p}_i \cdot \nabla_i g_2. \quad (7.16)$$

This solution does not enforce any condition on g_2 , leading us to go to the next order:

$$\begin{aligned} f_4 = & -(\mathbf{p}_i \cdot \nabla_i)^2 \left[\nabla_j^2 + \frac{1}{6T}(\mathbf{p}_j \cdot \nabla_j)^2 \right] \Phi + \frac{1}{2T}(\mathbf{p}_i \cdot \nabla_i)^2 \Phi \left[\frac{1}{T}(\mathbf{p}_j \cdot \nabla_j)^2 - \nabla_j^2 \right] \Phi \\ & + \nabla_i \Phi \cdot \nabla_i \left[\nabla_j^2 + \frac{3}{2T}(\mathbf{p}_j \cdot \nabla_j)^2 \right] \Phi - \frac{1}{T}(\nabla_i \Phi \cdot \nabla_i)^2 \Phi \\ & + g_2 \left[\nabla_i^2 - \frac{1}{T}(\mathbf{p}_i \cdot \nabla_i)^2 \right] \Phi + \left[(\mathbf{p}_i \cdot \nabla_i)^2 - \nabla_i \Phi \cdot \nabla_i \right] g_2. \end{aligned} \quad (7.17)$$

When solving the corresponding equation for ψ_4 , the normalization condition enforces the expression of g_2 :

$$g_2 = \frac{3}{2}\nabla_i^2 \Phi - \frac{(\nabla_i \Phi)^2}{2T}. \quad (7.18)$$

Eventually, the full solution at order $\tau^{3/2}$ can be cast in the form

$$\begin{aligned} P_S \sim & e^{-\frac{\Phi+\mathbf{p}_i^2/2}{T}} \left\{ 1 - \frac{\tau}{2T} \left\{ (\nabla_i \Phi)^2 + \left[(\mathbf{p}_i \cdot \nabla_i)^2 - 3T\nabla_i^2 \right] \Phi \right\} \right. \\ & \left. + \frac{\tau^{3/2}}{6T}(\mathbf{p}_i \cdot \nabla_i) \left[(\mathbf{p}_j \cdot \nabla_j)^2 - 3T\nabla_j^2 \right] \Phi + \mathcal{O}(\tau^2) \right\}. \end{aligned} \quad (7.19)$$

The velocity distribution obtained by integrating over the particle position is Gaussian at first order in τ , with the same variance as in [177]. Yet, the order $\tau^{3/2}$ shows that the distribution is non-Gaussian, which was not captured in [177]. An important feature of the full distribution is the coupling between position and velocity, in contrast with equilibrium for which it can be split into kinetic and potential parts. In particular, it leads to a modified equipartition theorem:

$$\langle p_{i\alpha}^2 \rangle = T - \tau \langle (\nabla_i \Phi)^2 \rangle_B + \mathcal{O}(\tau^2), \quad (7.20)$$

where $\langle \dots \rangle_B$ denotes the average with respect to the Boltzmann distribution $e^{-\Phi/T}$. Moreover, we can also obtain the probability current in position space \mathbf{J}_i from the full distribution. It is defined by $\partial_t P(\{\mathbf{r}_i\}, t) = -\nabla_i \cdot \mathbf{J}_i$. From the expression of the operator \mathcal{L} , we deduce $\mathbf{J}_i = \tau^{-1/2} \langle \mathbf{p}_i \rangle$, where the velocity is expressed in scaled units whereas the current is in the original ones. By using the stationary distribution in position and velocity, we estimate that the average velocity is at least of order $\tau^{5/2}$, since the order τ^2 of the distribution is even in velocity. It

follows that the current is at least of order τ^2 , in line with previous works which highlighted that the increase of the current with the persistence time was faster than linear for a ratchet [180, 181]. Integrating the full distribution over the velocities yields the position distribution at order τ . It coincides with the UCNA and Fox predictions to this order, as was already confirmed by the good agreement with numerical simulations in the small τ regime [149, 173].

7.3 Effective equilibrium regime

Breakdown of the time reversal

To explore the nonequilibrium properties of the dynamics (7.4), we focus on the time irreversibility of this dynamics. As introduced in Chapter 1, the breakdown of the time reversal invariance is quantified by the entropy production rate. It is defined in terms of the weights for a given time realization of the forward and backward processes. It vanishes for the two approximate dynamics presented above, showing that they are unable to capture any of the genuine nonequilibrium feature of the original dynamics. Introducing the reversed dynamics as $\mathbf{r}_i^R(t) = \mathbf{r}_i(-t)$ and $\mathbf{p}_i^R(t) = -\mathbf{p}_i(-t)$, we demonstrate that the entropy production rate reads

$$\sigma = \frac{\tau^{1/2}}{2T} \left\langle (\mathbf{p}_i \cdot \nabla_i)^3 \Phi \right\rangle, \quad (7.21)$$

where the velocities are expressed in scaled unit, as discussed above. When comparing this expression with Eq. (1.22) in Chapter 1, it seems that there entropy production no longer coincides with the power of an active force. This because the nonequilibrium nature of the dynamics now stems from the mismatch between the noise correlations and the memory kernel. To provide a deeper insight into the physics associated with the entropy production (7.21), we introduce the kernel \mathcal{K} defined in terms of the self-propulsion correlations as

$$\int \mathcal{K}(t-u) \langle v_{i\alpha}(s)v_{j\beta}(u) \rangle du = \delta(t-s)\delta_{ij}\delta_{\alpha\beta}. \quad (7.22)$$

Multiplying the left and right hand sides of the dynamics (7.1), we get an equivalent dynamics written as

$$\int \mathcal{K}(t-s) \dot{\mathbf{r}}_i(s) ds = \boldsymbol{\eta}_i - \int \mathcal{K}(t-s) \nabla_i \Phi(\{\mathbf{r}_i(s)\}) ds, \quad (7.23)$$

where the noise term $\boldsymbol{\eta}_i$ is Gaussian with correlations $\langle \eta_{i\alpha}(t)\eta_{j\beta}(0) \rangle = \delta_{ij}\delta_{\alpha\beta}\mathcal{K}(t)$. The correlations of the noise term now coincide with the memory kernel as for an equilibrium thermal bath. Within this formulation, it appears that the dynamics

of self-propelled particles with a viscous drag can be mapped into the one of Brownian particles in contact with a viscoelastic equilibrium bath and subjected to a nonequilibrium forcing $\mathbf{f}_A = -\mathcal{K} * \nabla_i \Phi$, where $*$ denotes the convolution product. Therefore, using Eq. (1.22), the entropy production rate is readily deduced as

$$\sigma = \frac{\langle \mathbf{p}_i \cdot \mathcal{K} * \nabla_i \Phi \rangle}{T}. \quad (7.24)$$

This result is independent of the specific form of the self-propulsion correlations, encoded in the kernel \mathcal{K} . In the case where the correlations of self-propulsion are exponentially decaying, the kernel reads $\mathcal{K}(t) = [1 - \tau^2(d/dt)^2] \delta(t)$, from which we recover the first expression of the entropy production rate in Eq. (7.21). Moreover, we can use the full stationary distribution in position-velocity space to estimate the correlation function appearing in the entropy production rate. Given that this correlation is odd in the velocities, the leading order in the entropy production rate comes from the second order correction in the steady state, yielding

$$\sigma = \frac{T\tau^2}{2} \langle (\nabla_i \nabla_j \nabla_k \Phi)^2 \rangle_B + \mathcal{O}(\tau^3). \quad (7.25)$$

An important feature of this result is that it is independent of the first order correction in the stationary measure. Therefore, we claim that there exists a regime where the self-propulsion affects the steady state, yet it provides a negligible contribution to the entropy production rate. We refer to such a regime as an effective equilibrium regime, distinct from the thermal equilibrium regime for a vanishing τ which is associated with a Boltzmann steady state.

Fluctuation-dissipation relation

To probe the existence of the effective equilibrium regime, we propose a protocol based on a new fluctuation-dissipation relation (FDR). We consider that an external operator perturbs the dynamics with a force \mathbf{f}_j applied on the particle j :

$$\dot{\mathbf{r}}_i = -\nabla_i \Phi + \delta_{ij} \mathbf{f}_j + \mathbf{v}_i. \quad (7.26)$$

Such a perturbed dynamics can be written in the underdamped version as

$$\tau \dot{\mathbf{p}}_i = -\mathbf{p}_i - (1 + \tau \mathbf{p}_k \cdot \nabla_k) \nabla_i \Phi + \delta_{ij} (\mathbf{f}_j + \tau \dot{\mathbf{f}}_j) + (2T)^{1/2} \boldsymbol{\xi}_i. \quad (7.27)$$

Perturbing the original dynamics does not simply result in adding the same perturbation force in the corresponding underdamped formulation. We introduce the response as

$$R_{i\alpha,j\beta}(t) = \left. \frac{\delta \langle r_{i\alpha}(t) \rangle}{\delta f_{j\beta}(0)} \right|_{f=0}. \quad (7.28)$$

In the regime where time reversal holds, we demonstrate that it can be written as

$$R_{i\alpha,j\beta}(t) = -\frac{1}{T} \frac{d}{dt} \left\langle r_{i\alpha}(t)r_{j\beta}(0) + \tau^2 p_{i\alpha}(t)p_{j\beta}(0) \right\rangle, \quad (7.29)$$

where the velocities are expressed in real units. This result is different from the one for the UCNA and the Fox theory, as discussed in Appendix A. The FDR now involves the position autocorrelation function as in the FDT, along with the velocity autocorrelation function, by contrast to equilibrium. Yet, this additional correlation function is independent of the potential Φ , similarly to the equilibrium case. This property is robust with respect to any form of the self-propulsion correlations. Considering an arbitrary perturbation by modifying the potential as $\Phi \rightarrow \Phi - h(t)B(\{\mathbf{r}_i, \mathbf{p}_i\})$, we express the generalized response R_G introduced in Chapter 1 in the effective equilibrium regime as

$$R_G(t) = -\frac{1}{T} \frac{d}{dt} \langle A(t)B(0) \rangle - \frac{\tau^2}{T} \langle A(t) [(\ddot{\mathbf{p}}_i \cdot \nabla_i)B](0) \rangle. \quad (7.30)$$

In contrast with thermal equilibrium, the correlation functions of the right hand side can not be written as a total time derivative. The FDT is often used to assess the existence of several temperatures associated with different time scales in models of sheared fluids [28, 182], self-propelled particles [151, 183, 184], and biological systems [185]. Our result suggests that, in the effective equilibrium regime, one can define a single temperature at all times from the response-correlation diagram when considering the appropriate correlation function.

The results described above are presented and discussed in details in paper F reproduced below.



How Far from Equilibrium Is Active Matter?

Étienne Fodor,¹ Cesare Nardini,^{2,3} Michael E. Cates,^{2,3} Julien Tailleur,¹ Paolo Visco,¹ and Frédéric van Wijland¹

¹Université Paris Diderot, Sorbonne Paris Cité, MSC, UMR 7057 CNRS, 75205 Paris, France

²SUPA, School of Physics and Astronomy, University of Edinburgh, Edinburgh EH9 3FD, United Kingdom

³DAMTP, Centre for Mathematical Sciences, University of Cambridge, Wilberforce Road, Cambridge CB3 0WA, United Kingdom

(Received 18 April 2016; revised manuscript received 31 May 2016; published 13 July 2016)

Active matter systems are driven out of thermal equilibrium by a lack of generalized Stokes-Einstein relation between injection and dissipation of energy at the microscopic scale. We consider such a system of interacting particles, propelled by persistent noises, and show that, at small but finite persistence time, their dynamics still satisfy a time-reversal symmetry. To do so, we compute perturbatively their steady-state measure and show that, for short persistent times, the entropy production rate vanishes. This endows such systems with an effective fluctuation-dissipation theorem akin to that of thermal equilibrium systems. Last, we show how interacting particle systems with viscous drags and correlated noises can be seen as in equilibrium with a viscoelastic bath but driven out of equilibrium by nonconservative forces, hence providing energetic insight into the departure of active systems from equilibrium.

DOI: 10.1103/PhysRevLett.117.038103

Active matter systems comprise large assemblies of individual units that dissipate energy, often stored in the environment, to produce mechanical work [1]. From the collective motion of self-propelled particles [2,3] to the existence of a liquid phase in the absence of attractive forces [4–6], many intriguing phenomena have generated a continuously growing interest for active matter over the past decades [1]. Since active systems break detailed balance at the microscopic scale, they cannot be described by equilibrium statistical mechanics. However, it is often difficult to pinpoint precisely the signature of nonequilibrium physics in their emerging properties. For instance, motility-induced phase separation (MIPS), which leads to the liquid-gas coexistence of repulsive self-propelled particles, is not associated to the emergence of steady-state mass currents. A number of works have actually proposed that its large scale physics can be captured by an equilibrium theory [4,7–9], the limits of which are heavily debated [10–12]. Even for systems where steady currents arise, the connection to equilibrium physics can sometimes be maintained, as for the transition to collective motion which amounts, for simple systems, to a liquid-gas phase transition [13,14]. More and more approaches to active matter thus partly rely on the intuition built for equilibrium systems [4,7,8,12,15–18].

Building a thermodynamic approach for active matter thus first requires understanding how active systems depart from thermal equilibrium. Insight into this question was gained by studying how the fluctuation dissipation theorem (FDT) breaks down in active matter [19–22]. At short time and space scales, the persistent motion of active particles typically precludes the existence of effective temperatures, while at larger scales, FDTs can sometimes be recovered. In living systems, the violation of FDT is used to characterize

the forces generated by intracellular active processes [23–28]. The information extracted from violations of the FDT is however rather limited and nonequilibrium statistical mechanics offers more elaborate tools to quantify the departure from equilibrium. In particular, the entropy production rate quantifies the breakdown of time-reversal symmetry, whence probing the irreversibility of the particle trajectories [29]. Hard to compute, and even harder to measure experimentally, it has been little studied in active systems [30,31], hence the need for “simple but not simpler” systems which offer a natural way to establish theoretical frameworks.

In this Letter, we study a model system of active matter which has recently attracted lots of interest [9,32–34]. It comprises overdamped “self-propelled” particles evolving as

$$\dot{\mathbf{r}}_i = -\mu \nabla_i \Phi + \mathbf{v}_i, \quad (1)$$

where i refers to the particle label, μ to their mobility, and Φ is an interaction potential. The self-propulsion velocities \mathbf{v}_i , rather than having fixed norms as in models of active Brownian particles [5] (ABPs) or run-and-tumble particles [35] (RTPs), are zero-mean persistent Gaussian noises of correlations $\langle v_{i\alpha}(t)v_{j\beta}(0) \rangle = \delta_{ij}\delta_{\alpha\beta}\Gamma(t)$, with greek indices corresponding to spatial components. In the simplest of cases, the \mathbf{v}_i 's are Ornstein-Uhlenbeck processes, solutions of $\tau \dot{\mathbf{v}}_i = -\mathbf{v}_i + \sqrt{2D}\boldsymbol{\eta}_i$, with $\boldsymbol{\eta}_i$'s zero-mean unit-variance Gaussian white noises, so that $\Gamma(t) = De^{-|t|/\tau}/\tau$. Here, D controls the amplitude of the noise and τ its persistence time.

Since the temporal correlations of the noise are not matched by similar correlations for the drag, this system

does not satisfy the standard generalization of the Stokes-Einstein relation to systems with memory [36]. Consequently, the system is out of thermal equilibrium, and its stationary measure is not the Boltzmann weight $P_B \equiv Z^{-1} \exp(-\beta\Phi)$. This model, to which we refer in the following as active-Ornstein-Uhlenbeck particles (AOUPs), shares the essential features of active systems: it correctly reproduces the behavior of passive tracers in bacterial baths [32,37], leads to the standard accumulation of active particles close to confining walls [33], and shows a shifted onset of the glass transition [34]. As for many other self-propelled particles [21,38], the limit of vanishing persistence time of AOUPs correspond to an equilibrium Brownian dynamics, since \mathbf{v}_i reduces to a Gaussian white noise.

In the following, we characterize how the AOUPs depart from thermal equilibrium. First, we compute perturbatively their steady state at small but finite persistence time τ . Surprisingly, we show that the small τ limit yields a non-Boltzmann distribution with which the particle dynamics *still respects detailed balance*: the entropy production, which we compute, can indeed be shown to vanish at order τ . In this regime, to which we refer as *effective equilibrium*, we also show that AOUPs satisfy a generalized FDT. Finally, we close this Letter by providing an energetic interpretation of the breakdown of detailed balance for AOUPs.

We consider N particles, propelled by Ornstein-Uhlenbeck processes, interacting through a potential Φ . For illustration purposes, we use pairwise repulsive forces in 2D

$$\Phi = \frac{1}{2} \sum_{i,j} V(\mathbf{r}_i - \mathbf{r}_j), \quad V(\mathbf{r}) = A \exp\left[-\frac{1}{1 - (r/a)^2}\right], \quad (2)$$

for which Fig. 1 shows that AOUPs exhibit motility-induced phase separation [4,6], extending this phenomenon

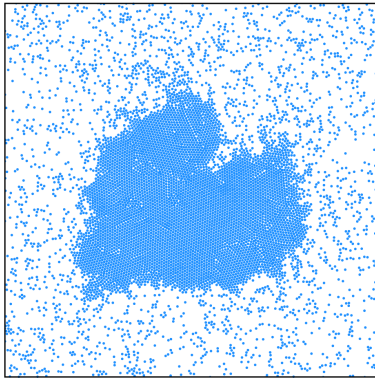


FIG. 1. AOUPs interacting via the potential (2) exhibit MIPS in a 2D box of size L with periodic boundary conditions. Parameters: $A = 100$, $a = 2$, $N = 10000$, $L = 250$, $D = 100$, $\tau = 20$.

beyond the reported cases of RTPs [4,22] and ABPs [5,9,39]. Our analytical results, however, are valid beyond this example and hold for general potentials and dimensions. Introducing the velocities $\mathbf{p}_i = \dot{\mathbf{r}}_i$ and taking the time derivative of (1) yields

$$\tau \dot{\mathbf{p}}_i = -\mathbf{p}_i - (1 + \tau \mathbf{p}_k \cdot \nabla_k) \nabla_i \Phi - \sqrt{2T} \mathbf{\eta}_i, \quad (3)$$

where the mobility μ is set to one. Here and in what follows, repeated indices are implicitly summed over.

We have introduced $T \equiv D/\mu$ so that taking $\tau = 0$ in Eq. (3) directly maps the dynamics onto an equilibrium overdamped Langevin equation at temperature T . Surprisingly, there exist other *equilibrium* approximations of Eq. (3). First, taking $\tau = 0$ in the rhs maps AOUPs onto an underdamped Kramers-Langevin equation. Conversely, taking $\tau = 0$ in the lhs corresponds to the unified colored noise approximation [33,40] which has been shown to satisfy detailed balance [33]. Here, we propose to determine perturbatively the steady state of AOUPs in the small τ limit, retaining both contributions of τ in Eq. (3). Rescaling time as $t = \sqrt{\tau}t$ and introducing the rescaled velocities $\tilde{\mathbf{p}}_i = \sqrt{\tau}\mathbf{p}_i$, the probability distribution satisfies the Fokker-Planck equation $\dot{P}(\{\mathbf{r}_i, \tilde{\mathbf{p}}_i\}) = \mathcal{L}P(\{\mathbf{r}_i, \tilde{\mathbf{p}}_i\})$, where the operator \mathcal{L} reads

$$\begin{aligned} \mathcal{L} = & -\tilde{p}_{ia} \frac{\partial}{\partial r_{ia}} + \frac{1}{\sqrt{\tau} \partial \tilde{p}_{ia}} \left[\tilde{p}_{ia} + \tau \frac{\partial^2 \Phi}{\partial r_{ia} \partial r_{jb}} \tilde{p}_{jb} \right] \\ & + \frac{\partial}{\partial \tilde{p}_{ia}} \frac{\partial \Phi}{\partial r_{ia}} + \frac{T}{\sqrt{\tau}} \frac{\partial^2}{\partial \tilde{p}_{ia}^2}. \end{aligned} \quad (4)$$

In steady state, we propose the following ansatz for small τ :

$$P \propto \exp\left[-\frac{\Phi}{T} - \frac{\tilde{\mathbf{p}}_i^2}{2T} + \sum_{n=2}^{\infty} \tau^{n/2} \psi_n(\{\mathbf{r}_i, \tilde{\mathbf{p}}_i\})\right]. \quad (5)$$

Solving for $\mathcal{L}P = 0$ then leads to a consistent set of equations at every order in $\sqrt{\tau}$, which recursively yield

$$\begin{aligned} P \propto & e^{-[(\Phi + \tilde{\mathbf{p}}_i^2/2)/T]} \left\{ 1 - \frac{\tau}{2T} [(\nabla_i \Phi)^2 + (\tilde{\mathbf{p}}_i \cdot \nabla_i)^2 \Phi - 3T \nabla_i^2 \Phi] \right. \\ & \left. + \frac{\tau^{3/2}}{6T} (\tilde{\mathbf{p}}_i \cdot \nabla_i)^3 \Phi - \frac{\tau^{3/2}}{2} (\tilde{\mathbf{p}}_i \cdot \nabla_i) \nabla_j^2 \Phi + \mathcal{O}(\tau^2) \right\}. \end{aligned} \quad (6)$$

The distribution of positions can then be deduced by integrating (6) over velocities; this leads to a Boltzmann-like measure, $P(\{\mathbf{r}_i\}) \propto \exp(-\tilde{\Phi}/T)$, with an effective potential,

$$\tilde{\Phi} \equiv \Phi + \tau[(\nabla_i \Phi)^2/2 - T \nabla_i^2 \Phi] + \mathcal{O}(\tau^2). \quad (7)$$

In the limit of vanishing τ , one recovers the standard Maxwell-Boltzmann distribution. The joint distribution of

position and velocities (6) beyond this regime is our first important result. First, it shows how, for finite τ , positions and velocities are correlated, in agreement with the UCNA approximation [41] but at contrast to thermal equilibrium where the energy can be separated between kinetic and potential parts. In particular, this leads to a modified equipartition theorem,

$$\langle \tilde{\mathbf{p}}_{ia}^2 \rangle = T - \tau \langle (\nabla_i \Phi)^2 \rangle_B + \mathcal{O}(\tau^2), \quad (8)$$

where the average $\langle \dots \rangle_B$ is taken with respect to the Boltzmann weight P_B . Second, the effective potential $\tilde{\Phi}$ predicts that repulsive pairwise potentials lead to effective attractive interactions, consistently with other approximation schemes [9,33]. This explains why purely repulsive interactions can trigger MIPS. Note also how a pairwise potential leads to effective three-body interactions through the term $(\nabla_i \Phi)^2$. At this stage, our controlled expansion allows us to describe the static properties of AOUPs in terms of an effective Boltzmann weight (7). Interestingly, for the evolution operator (4), the asymmetry in $\tilde{\mathbf{p}}_i$ of the steady-state measure (4) implies that the dynamics is out of equilibrium [42]. This asymmetry is not captured by the UCNA approximation [41] which cannot describe the nonequilibrium properties of AOUPs.

To better measure the degree of irreversibility of the dynamics, we derive its entropy production rate σ [29]. It is obtained by comparing the probability weights associated with a given trajectory $\mathbf{r}_i(t)$ and its time-reversed counterpart, respectively, denoted by \mathcal{P} and \mathcal{P}^R ,

$$\sigma \equiv \lim_{t \rightarrow \infty} \frac{1}{t} \ln \frac{\mathcal{P}}{\mathcal{P}^R}. \quad (9)$$

To keep the scaling in τ explicit, we work for now with the rescaled variables \tilde{t} and $\tilde{\mathbf{p}}_i$ and use the fact that σ is intensive in time. Using standard path-integral formalism [43], the trajectory weight can be written as $\mathcal{P}[\{\mathbf{r}_i(\tilde{t})\}] \sim \exp(-\mathcal{S}[\{\mathbf{r}_i(\tilde{t})\}])$ with

$$\mathcal{S} = \frac{\sqrt{\tau}}{4T} \int_0^{\tilde{t}} du \left[\dot{\tilde{\mathbf{p}}}_i + \frac{\tilde{\mathbf{p}}_i}{\sqrt{\tau}} + (1 + \sqrt{\tau} \tilde{\mathbf{p}}_k \cdot \nabla_k) \nabla_i \Phi \right]^2. \quad (10)$$

The time-reversed trajectories are then given by $t^R = -t$, $\mathbf{r}_i^R(t) \equiv \mathbf{r}_i(-t)$. For $\mathbf{r}_i^R(t)$ to be a solution of the equation of motion (1), one then needs $\mathbf{p}_i^R(t) = -\mathbf{p}_i(-t)$. The probability \mathcal{P}^R is then simply obtained by injecting these expressions into (10). The entropy production rate is thus given by $\sigma \sim \delta\mathcal{S}/t$, where $\delta\mathcal{S}$ is the difference between the forward and backward actions [44]. All in all, the entropy production rate reads

$$\begin{aligned} \sigma &= -\lim_{\tilde{t} \rightarrow \infty} \frac{\sqrt{\tau}}{T\tilde{t}} \int_0^{\tilde{t}} du (\dot{\tilde{\mathbf{p}}}_i \cdot \nabla_i)(\tilde{\mathbf{p}}_j \cdot \nabla_j) \Phi \\ &= \frac{\sqrt{\tau}}{2T} \langle (\tilde{\mathbf{p}}_i \cdot \nabla_i)^3 \Phi \rangle, \end{aligned} \quad (11)$$

where the last equality follows from integrating by parts [45] and using the equality between time and ensemble averages in steady state [46]. Interestingly, the entropy production rate exactly vanishes when Φ is quadratic in the particle displacements, hence showing that AOUPs are in this case an equilibrium model. Their steady state is however not the Boltzmann measure P_B , which explains the difficulty of defining a temperature in this case [21]. As a result, the anharmonicity of the potential acts as a control parameter for the nonequilibrium nature of AOUPs.

The entropy production rate can also be computed in the small τ limit, using the stationary distribution (6) to evaluate the correlation function appearing in Eq. (11). Going back to the initial variables, the entropy production rate is given by

$$\sigma = \frac{T\tau^2}{2} \langle (\nabla_i \nabla_j \nabla_k \Phi)^2 \rangle_B + \mathcal{O}(\tau^3). \quad (12)$$

The first nonvanishing contribution to σ comes from the $\tau^{3/2}$ correction in the steady state measure (6). At order τ , we thus have a non-Boltzmann steady state given by the first line of (6), or equivalently by (7) in position space, with a vanishing entropy production rate. In such a regime, the AOUPs are effectively a nonthermal *equilibrium* model, which is the central result of this Letter.

Let us now discuss the practical consequences of this effective equilibrium dynamics. Oscillatory shear experiments have become an increasingly standard procedure to sample the microrheology of active systems [23,24,47,48]. In this context, the violation of the equilibrium FDT has proven a natural measure of the distance to equilibrium [19,20,49]. Let us consider that an external operator perturbs the dynamics by applying a small constant force \mathbf{f}_j on the particle j , hence modifying the potential Φ as $\Phi \rightarrow \Phi - \mathbf{f}_j \cdot \mathbf{r}_i$. We define the response function R as

$$R_{i\alpha j\beta}(t, s) \equiv \left. \frac{\delta \langle r_{i\alpha}(t) \rangle}{\delta f_{j\beta}(s)} \right|_{\mathbf{f}=0}. \quad (13)$$

Following standard procedures [50], we can use the dynamic action formalism and the fact that $\delta\mathcal{P} = -\delta\mathcal{S}\mathcal{P}$ to rewrite the response as

$$R_{i\alpha j\beta}(t, s) = - \left\langle r_{i\alpha}(t) \left. \frac{\delta \mathcal{S}}{\delta f_{j\beta}(s)} \right|_{\mathbf{f}=0} \right\rangle. \quad (14)$$

The perturbed dynamics of the AOUPs is readily given by

$$\tau \dot{\mathbf{p}}_i = -\mathbf{p}_i - (1 + \tau \mathbf{p}_k \cdot \nabla_k) \nabla_i \Phi + \mathbf{f}_i + \tau \dot{\mathbf{f}}_i - \sqrt{2T} \mathbf{n}_i, \quad (15)$$

so that the dynamical action \mathcal{S} becomes

$$\mathcal{S} = \frac{1}{4T} \int_0^t du \left[\left(1 + \tau \frac{d}{du} \right) (\mathbf{p}_i + \nabla_i \Phi - \mathbf{f}_i) \right]^2. \quad (16)$$

The response function is then given by

$$R_{i\alpha j\beta}(t, s) = \left(1 - \tau^2 \frac{d^2}{dt^2} \right) \left[-\frac{1}{T} \frac{d}{dt} \langle r_{i\alpha}(t) r_{j\beta}(s) \rangle + \frac{1}{2T} (\langle r_{i\alpha}(t) \nabla_{j\beta} \Phi |_{t=s} \rangle - \langle r_{i\alpha}(s) \nabla_{j\beta} \Phi |_t \rangle) \right]. \quad (17)$$

In the effective equilibrium regime, the vanishing entropy production tells us that the dynamics is symmetric under time reversal so that the second line of Eq. (17) vanishes and the response function finally reads

$$R_{i\alpha j\beta}(t, s) = -\frac{1}{T} \frac{d}{dt} \langle r_{i\alpha}(t) r_{j\beta}(s) + \tau^2 p_{i\alpha}(t) p_{j\beta}(s) \rangle. \quad (18)$$

We have thus derived a generalized FDT, which holds in the small τ limit where the AOUPs are effectively in equilibrium, though not with respect to the Boltzmann measure P_B . This explains the atypical form of the correlation function entering, which involves the position autocorrelation function, as in thermal equilibrium, along with the velocity autocorrelation function. Note that, as in equilibrium, this FDT is completely independent of the interaction potential Φ , so that it should be measurable without knowledge of the intimate details of particle interactions.

To test whether a finite τ regime exists where our generalized FDT can indeed be measured, we consider a perturbation $\Phi \rightarrow \Phi - f \varepsilon_i x_i$, where ε_i is a random variable equal to ± 1 with equal probability [49]. We measure the susceptibility $\chi(t) \equiv \int_0^t ds R_{ixix}(t, s)/N$ in simulations of AOUPs interacting with the repulsive potential (2). Our modified FDT predicts that

$$NT\chi(t) = \langle [x_i(0) - x_i(t)] x_i(t) \rangle + \tau^2 \langle [\dot{x}_i(0) - \dot{x}_i(t)] \dot{x}_i(t) \rangle, \quad (19)$$

which is shown to be valid at small τ in Fig. 2(a). (See [51] for simulation details).

Note that an entropy production rate σ of order τ^2 means that trajectories of length $\propto \tau^{-2}$ lead to an overall entropy production of order one. Since we are working in the small- τ -but-finite- D limit, diffusive equilibration times ℓ^2/D remain of order one, which legitimates the claim of an effective equilibrium regime. Nevertheless, we expect our FDT to break down in the long time limit. The connection between σ and the breakdown of the FDT can be

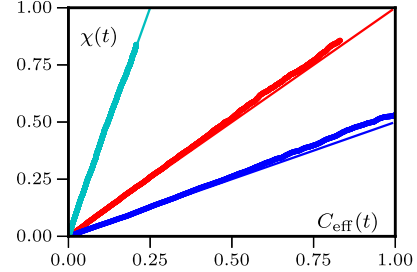


FIG. 2. Parametric plot between the susceptibility $\chi(t)$ and the correlation function $C_{\text{eff}}(t) = \langle x_i(t)[x_i(t) - x_i(0)] + \tau^2 \dot{x}_i(t)[\dot{x}_i(t) - \dot{x}_i(0)] \rangle$ for N AOUPs interacting via the potential (2). The particles experience a stiff harmonic potential when they try to exit a box of linear size L . Parameters: $L = 30$, $N = 720$, $\tau = 0.01$, $A = 20$. Blue, red, and cyan dots correspond to $T = 2, 1, 0.25$ and the solid line corresponds to the theoretical prediction (19).

rationalized through a simple generalization of the Harada-Sasa relation [53,54]

$$\sigma = \frac{1}{T} \int \frac{d\omega}{2\pi} \frac{\omega}{\mu} [2TR''_{i\alpha i\alpha}(\omega) + \omega C(\omega)K(\omega)], \quad (20)$$

where $R''(\omega)$ is the imaginary part of the response in Fourier space, $K(\omega) \equiv 1 + (\omega\tau)^2$ is the inverse of the noise correlator $\Gamma(t)$ in Fourier space and $C(t) \equiv \langle \mathbf{r}_i(t) \cdot \mathbf{r}_i(0) \rangle$. Interestingly, the measurement of σ through (20) no longer requires the knowledge of the interaction potential Φ , at variance with the use of Eq. (11).

To get more physical insight into our effective equilibrium regime and its breakdown as τ increases, let us now discuss the energetics of AOUPs. Active matter is traditionally regarded as a nonequilibrium medium because injection and dissipation of energy are uncorrelated. Indeed the former stems from the conversion of some form of stored energy while the latter results from the friction with the surrounding medium. Consequently, fluctuations and dissipations are not constrained by any form of Stokes-Einstein relations. For driven Langevin processes, the nonequilibrium nature of the dynamics can be measured as a mean heat transfer between particles and thermostat [55,56]. This leads to a standard definition of dissipation J as the imbalance between the power injected by the thermal noise and the one dissipated *via* the drag force. This definition furthermore provides an energetic interpretation of the entropy production since $J = T\sigma$ [56]. A naive generalization of this reasoning to AOUPs would lead to the definition of dissipation through

$$J = \mu^{-1} \langle \mathbf{p}_i \cdot (\mathbf{p}_i - \mathbf{v}_i) \rangle. \quad (21)$$

It is however straightforward to see that $J = \langle \mathbf{p}_i \cdot \nabla_i \Phi \rangle = d\langle \Phi \rangle/dt$, which necessarily vanishes in steady state.

The breakdown of detailed balance for AOUPs is indeed not linked to a mean heat flux extracted from an equilibrated bath but from the apparent lack of generalized FDT between damping and fluctuations in (1). To get more insight on the entropy production rate σ , we remark that this dynamics is equivalent to

$$K * \dot{\mathbf{r}}_i = \xi_i - \mu K * \nabla_i \Phi, \quad (22)$$

where $K(t) = [1 - \tau^2(d/dt)^2]\delta(t)$, $*$ denotes time convolution, and we have introduced the noise term $\xi_i \equiv K * \mathbf{v}_i$. The lhs of (22) corresponds to the damping of a viscoelastic fluid with memory kernel K . The first term on the rhs is a fluctuating force whose variance is

$$\langle \xi_{ia}(t)\xi_{jb}(0) \rangle = \delta_{ij}\delta_{ab}K(t), \quad (23)$$

since by definition $(K * \Gamma)(t) = \delta(t)$. The damping and fluctuating forces appearing in (22) thus satisfy a generalized Stokes-Einstein relation [36]. They correspond to the connection of particles with an *equilibrated* viscoelastic bath, for which the standard definition of the dissipation applies

$$\mathcal{J} = \mu^{-1} \langle \mathbf{p}_i \cdot (K * \mathbf{p}_i - \xi_i) \rangle. \quad (24)$$

From there, simple algebra shows that $\mathcal{J} = T\sigma$, which yields a physical interpretation to σ as the dissipation in an equilibrated bath for the dynamics (22).

Interestingly, this shows that the breakdown of detailed balance in AOUPs can be seen equivalently as resulting from a lack of generalized Stokes-Einstein relation between damping and fluctuations or from the fact that $K * \nabla_i \Phi$ is not a conservative force. In this second interpretation, the entropy production rate now has a standard energetic interpretation. The existence of an effective equilibrium regime for small τ is then due to the fact that $K * \nabla_i \Phi$ behaves as a conservative force $\nabla_i \tilde{\Phi}$ in this limit. The dynamics (22) with $K * \nabla_i \Phi$ replaced by $\nabla_i \tilde{\Phi}$ can be regarded as a dynamical equilibrium approximation of AOUPs; one indeed checks, for instance, that $\langle \tilde{\Phi} \rangle - \langle K * \Phi \rangle = \mathcal{O}(\tau^2)$ or that our generalized FDT corresponds to perturbing this equilibrium dynamics as $\tilde{\Phi} \rightarrow \tilde{\Phi} - \mathbf{r}_i \cdot (K * \mathbf{f}_i)$.

In this Letter, we have thus shown that, as their persistence time increases, active Ornstein-Uhlenbeck particles do not immediately leave the realm of equilibrium physics. At short persistent time, they behave as an equilibrated viscoelastic medium with effective Boltzmann weight $P \propto \exp(-\tilde{\Phi}/T)$ which differs from the thermal equilibrium $P_B \propto \exp(-\Phi/T)$. In this regime, the fact that repulsive forces lead to effective attractive interactions can directly be read in $\tilde{\Phi}$. Beyond this static result, the existence of an effective equilibrium regime

enforces a generalized fluctuation dissipation theorem, akin to its thermal counterpart though different correlators are involved. The breakdown of this FDT for larger persistence times can be linked to a nonzero entropy production rate whose expression we have computed analytically. Last, we have shown how to extend the notion of dissipation to understand the breakdown of detailed balance in AOUPs.

Most of the results presented in this Letter have been derived for the particular choice of noise correlator $\Gamma(t) = De^{-|t|/\tau}/\tau$. Many of our results, such as Eq. (20) or the discussion on dissipation, however extends to more general correlators. Furthermore, it has recently been shown that static approximations derived for the steady state of AOUPs capture very well the physics of ABPs [9]. It would thus be very interesting to know whether our effective equilibrium regime also extends to this system. More generally, our study suggests that when systems are driven out of thermal equilibrium by the conversion of some form of stored energy, an effective equilibrium regime may remain when the drive is moderate. This would be a first step towards a thermodynamics of active matter.

We thank M. Baiesi, J. L. Barrat, E. Bertin, O. Grossein, C. Maggi, R. di Leonardo, G. Szamel for interesting discussions. J. T. was supported by ANR project Bactterns. C. N. was supported by EPSRC Grant No. Nr. EP/J007404.

- [1] M. Marchetti, J. Joanny, S. Ramaswamy, T. Liverpool, J. Prost, M. Rao, and R. A. Simha, *Rev. Mod. Phys.* **85**, 1143 (2013).
- [2] T. Vicsek, A. Czirók, E. Ben-Jacob, I. Cohen, and O. Shochet, *Phys. Rev. Lett.* **75**, 1226 (1995).
- [3] T. Vicsek and A. Zafeiris, *Phys. Rep.* **517**, 71 (2012).
- [4] J. Tailleur and M. E. Cates, *Phys. Rev. Lett.* **100**, 218103 (2008).
- [5] Y. Fily and M. C. Marchetti, *Phys. Rev. Lett.* **108**, 235702 (2012).
- [6] M. E. Cates and J. Tailleur, *Annu. Rev. Condens. Matter Phys.* **6**, 219 (2015).
- [7] T. Speck, J. Bialké, A. M. Menzel, and H. Löwen, *Phys. Rev. Lett.* **112**, 218304 (2014).
- [8] S. C. Takatori, W. Yan, and J. F. Brady, *Phys. Rev. Lett.* **113**, 028103 (2014).
- [9] T. F. F. Farage, P. Krininger, and J. M. Brader, *Phys. Rev. E* **91**, 042310 (2015).
- [10] R. Wittkowski, A. Tiribocchi, J. Stenhammar, R. J. Allen, D. Marenduzzo, and M. E. Cates, *Nat. Commun.* **5**, 4351 (2014).
- [11] A. P. Solon, J. Stenhammar, R. Wittkowski, M. Kardar, Y. Kafri, M. E. Cates, and J. Tailleur, *Phys. Rev. Lett.* **114**, 198301 (2015).
- [12] J. Bialké, J. T. Siebert, H. Löwen, and T. Speck, *Phys. Rev. Lett.* **115**, 098301 (2015).
- [13] A. P. Solon and J. Tailleur, *Phys. Rev. Lett.* **111**, 078101 (2013).

- [14] A. P. Solon, H. Chaté, and J. Tailleur, *Phys. Rev. Lett.* **114**, 068101 (2015).
- [15] S. A. Mallory, A. Šarić, C. Valeriani, and A. Cacciuto, *Phys. Rev. E* **89**, 052303 (2014).
- [16] X. Yang, M. L. Manning, and M. C. Marchetti, *Soft Matter* **10**, 6477 (2014).
- [17] S. C. Takatori and J. F. Brady, *Phys. Rev. E* **91**, 032117 (2015).
- [18] F. Ginot, I. Theurkauff, D. Levis, C. Ybert, L. Bocquet, L. Berthier, and C. Cottin-Bizonne, *Phys. Rev. X* **5**, 011004 (2015).
- [19] D. Loi, S. Mossa, and L. F. Cugliandolo, *Phys. Rev. E* **77**, 051111 (2008).
- [20] D. Loi, S. Mossa, and L. F. Cugliandolo, *Soft Matter* **7**, 3726 (2011).
- [21] G. Szamel, *Phys. Rev. E* **90**, 012111 (2014).
- [22] A. Solon, M. Cates, and J. Tailleur, *Eur. Phys. J. Spec. Top.* **224**, 1231 (2015).
- [23] D. Mizuno, C. Tardin, C. F. Schmidt, and F. C. MacKintosh, *Science* **315**, 370 (2007).
- [24] C. Wilhelm, *Phys. Rev. Lett.* **101**, 028101 (2008).
- [25] F. Gallet, D. Arcizet, P. Bohec, and A. Richert, *Soft Matter* **5**, 2947 (2009).
- [26] E. Ben-Isaac, Y. K. Park, G. Popescu, F. L. H. Brown, N. S. Gov, and Y. Shokef, *Phys. Rev. Lett.* **106**, 238103 (2011).
- [27] É. Fodor, M. Guo, N. S. Gov, P. Visco, D. A. Weitz, and F. van Wijland, *Europhys. Lett.* **110**, 48005 (2015).
- [28] W. W. Ahmed, E. Fodor, M. Almonacid, M. Bussonnier, M.-H. Verlhac, N. S. Gov, P. Visco, F. van Wijland, and T. Betz, [arXiv:1510.08299](https://arxiv.org/abs/1510.08299).
- [29] J. L. Lebowitz and H. Spohn, *J. Stat. Phys.* **95**, 333 (1999).
- [30] C. Ganguly and D. Chaudhuri, *Phys. Rev. E* **88**, 032102 (2013).
- [31] D. Chaudhuri, *Phys. Rev. E* **90**, 022131 (2014).
- [32] N. Koumakis, C. Maggi, and R. Di Leonardo, *Soft Matter* **10**, 5695 (2014).
- [33] U. Marini Bettolo Marconi and C. Maggi, *Soft Matter* **11**, 8768 (2015).
- [34] G. Szamel, E. Flener, and L. Berthier, *Phys. Rev. E* **91**, 062304 (2015).
- [35] M. J. Schnitzer, *Phys. Rev. E* **48**, 2553 (1993).
- [36] R. Kubo, *Rep. Prog. Phys.* **29**, 255 (1966).
- [37] C. Maggi, M. Paoluzzi, N. Pellicciotta, A. Lepore, L. Angelani, and R. Di Leonardo, *Phys. Rev. Lett.* **113**, 238303 (2014).
- [38] J. Tailleur and M. Cates, *Europhys. Lett.* **86**, 60002 (2009).
- [39] G. S. Redner, M. F. Hagan, and A. Baskaran, *Phys. Rev. Lett.* **110**, 055701 (2013).
- [40] P. Jung and P. Hänggi, *Phys. Rev. A* **35**, 4464 (1987).
- [41] U. M. B. Marconi, N. Gnan, M. Paoluzzi, C. Maggi, and R. Di Leonardo, *Sci. Rep.* **6**, 23297 (2016).
- [42] C. W. Gardiner *et al.*, *Handbook of Stochastic Methods*, Vol. 3 (Springer-Verlag, Berlin, 1985).
- [43] L. Onsager and S. Machlup, *Phys. Rev.* **91**, 1505 (1953).
- [44] Note that we did not carefully specify the time-discretization of the Langevin equation (3) since it does not affect σ .
- [45] Note that temporal boundary terms, appearing for instance after integration by parts, do not contribute to σ thanks to the $1/t$ prefactor.
- [46] We assume that this standard result valid for the equilibrium Kramers operator extends to its slightly modified version (4).
- [47] D. Robert, T.-H. Nguyen, F. Gallet, and C. Wilhelm, *PLoS One* **5**, e10046 (2010).
- [48] W. W. Ahmed, É. Fodor, and T. Betz, *Biochimica et Biophysica Acta (BBA) - Molecular Cell Research* **1853**, 3083 (2015).
- [49] D. Levis and L. Berthier, *Europhys. Lett.* **111**, 60006 (2015).
- [50] L. F. Cugliandolo, *J. Phys. A* **44**, 483001 (2011).
- [51] See Supplemental Material at <http://link.aps.org/supplemental/10.1103/PhysRevLett.117.038103> for simulation details, which includes Ref. [52].
- [52] D. Villamaina, A. Puglisi, and A. Vulpiani, *J. Stat. Mech.* (2008) L10001.
- [53] T. Harada and S.-i. Sasa, *Phys. Rev. E* **73**, 026131 (2006).
- [54] The result (20) is related to, but distinct from, a recent extension of the Harada-Sasa relation to continuous active field theories; E. Fodor *et al.* (to be published).
- [55] K. Sekimoto and S.-i. Sasa, *J. Phys. Soc. Jpn.* **66**, 3326 (1997).
- [56] K. Sekimoto, *J. Phys. Soc. Jpn.* **66**, 1234 (1997).

How far from equilibrium is active matter?

Étienne Fodor,¹ Cesare Nardini,^{2,3} Michael E. Cates,^{2,3} Julien Tailleur,¹ Paolo Visco,¹ and Frédéric van Wijland¹

¹*Université Paris Diderot, Sorbonne Paris Cité, MSC, UMR 7057 CNRS, 75205 Paris, France*

²*SUPA, School of Physics and Astronomy, University of Edinburgh, Edinburgh EH9 3FD, United Kingdom*

³*DAMTP, Centre for Mathematical Sciences, University of Cambridge, Wilberforce Road, Cambridge CB3 0WA, United Kingdom*

(Dated: May 27, 2016)

NUMERICAL SIMULATIONS

We use Euler time-stepping to simulate the dynamics of AOUPs:

$$\dot{\mathbf{r}}_i = -\mu \nabla_i \Phi + \mathbf{v}_i; \quad \tau \dot{\mathbf{v}}_i = -\mathbf{v}_i + \sqrt{2D} \boldsymbol{\eta}_i \quad (1)$$

To observe the MIPS reported in Fig. 1 of the main text, we use periodic boundary conditions and the repulsive potential given by Eq.(2) of the main text. The figure is obtained by starting from a random homogenous configuration, integrating the dynamics (1) with a time-step $dt = 10^{-3}$ and taking a snapshot of the particle positions after a time $t = 10^4$.

To test the validity of our modified FDT, we consider AOUPs in \mathbb{R}^2 , confined by a harmonic potential

$$\begin{aligned} V_W(x, y) = & \frac{\lambda}{2} \theta(x - L)(x - L)^2 + \frac{\lambda}{2} \theta(-x)x^2 \\ & + \frac{\lambda}{2} \theta(-y)y^2 + \frac{\lambda}{2} \theta(y - L)(y - L)^2, \end{aligned} \quad (2)$$

where $\theta(u)$ is the Heaviside function. In the simulations reported on Fig. 2 of the main text, we use $\lambda = 10$. We integrate the dynamics of AOUPs using $dt = 5 \cdot 10^{-4}$. We first let the system relax to its steady-state by simulating its dynamics for a time 50.

To measure the correlation function $C_{\text{eff}}(t)$, we choose a given value of t_0 and store $x_i(t_0)$ and $\dot{x}_i(t_0)$. We then compute $[x_i(t_0) - x_i(t_0 + t)]x_i(t_0 + t)$ and $[\dot{x}_i(t_0) - \dot{x}_i(t_0 + t)]\dot{x}_i(t_0 + t)$ for $t \in [0, 2]$. We finally average over 20 000 values of t_0 to obtain the correlation function plotted in Fig. 2 of the main text.

To measure the susceptibility $\chi(t)$, we create a copy of the system at a given time t_0 . This copy evolves with a perturbed dynamics in which $\Phi \rightarrow \Phi - f\epsilon_i x_i$ where the ϵ_i are chosen at random in $\{-1, 1\}$. The original system evolves with the unperturbed dynamics and we use the *same noise realisations* $\boldsymbol{\eta}_i$ for the two systems [1]. We then deduce the susceptibility as

$$\chi(t) = \sum_i \epsilon_i \frac{x_i^c(t + t_0) - x_i(t + t_0)}{f}. \quad (3)$$

for $t \in [0, 2]$, where x_i^c are the abscissa of the perturbed system. We finally average over 20 000 values of t_0 to obtain $\chi(t)$.

[1] D. Villamaina, A. Puglisi, and A. Vulpiani, *J. Stat. Mech.* **2008**, L10001 (2008).

7.4 Collective modes

To gain insight into the collective modes of the interacting self-propelled particles, we investigate the dynamics of the densities of position and velocity. They are fluctuating quantities, respectively denoted by ρ and \mathbf{g} , and defined as

$$\rho(\mathbf{r}, t) = \sum_{i=1}^N \delta[\mathbf{r} - \mathbf{r}_i(t)], \quad g_\alpha(\mathbf{r}, t) = \sum_{i=1}^N p_{i\alpha} \delta[\mathbf{r} - \mathbf{r}_i(t)]. \quad (7.31)$$

In the case of Brownian particles with pair-wise interactions, it has been shown that an exact closed dynamics could be obtained for the position density, referred to as the Dean-Kawasaki equation [186, 187]. It is written as a multiplicative Langevin equation with a collective mobility depending on the density. Such dynamics are consistent with the definition of a free-energy density functional split into an entropic and interaction parts. Concerning inertial Brownian particles, no closed form can be obtained for the fluctuating densities of position and velocity. Several closure have been proposed, some of them on the basis of a local steady state assumption [188–191]. A recent attempt has been made to close the dynamics by only relying on a discernibility condition: no particles can share the same position at the same time [192]. All these closures lead to a coupled dynamics for ρ and \mathbf{g} , which we refer to as the fluctuating hydrodynamics.

Fluctuating hydrodynamics

We first derive the set of equations ruling the coupled dynamics of ρ and \mathbf{g} . The time derivative of the position density reads

$$\partial_t \rho(\mathbf{r}, t) = -\partial_\alpha \sum_{i=1}^N \dot{r}_{i\alpha} \delta[\mathbf{r} - \mathbf{r}_i(t)] = -\partial_\alpha g_\alpha(\mathbf{r}, t). \quad (7.32)$$

This is the conservation law for the number of particles. The time derivative of the velocity density is given by

$$\partial_t g_\alpha(\mathbf{r}, t) = -\partial_\beta \sum_{i=1}^N p_{i\alpha} p_{i\beta} \delta[\mathbf{r} - \mathbf{r}_i(t)] + \sum_{i=1}^N \dot{p}_{i\alpha} \delta[\mathbf{r} - \mathbf{r}_i(t)]. \quad (7.33)$$

To proceed further, we assume that the particle interact through pair-wise interactions only:

$$\Phi = \frac{1}{2} \sum_{\{i,j\}=1}^N V(\mathbf{r}_i - \mathbf{r}_j). \quad (7.34)$$

When substituting the microscopic dynamics (7.4) in the expression for the time derivative of \mathbf{g} , a term of the following form appears:

$$\begin{aligned} \sum_{\{i,j\}=1}^N p_{j\beta} \partial_{i\alpha} \partial_{j\beta} \Phi \delta [\mathbf{r} - \mathbf{r}_i(t)] &= \sum_{\{i,j,k\}=1}^N p_{j\beta} \partial_{i\alpha} \partial_{j\beta} V(\mathbf{r}_i - \mathbf{r}_k) \delta [\mathbf{r} - \mathbf{r}_i(t)] \\ &= \sum_{\{i,k\}=1}^N (p_{i\beta} \partial_{i\beta} + p_{k\beta} \partial_{k\beta}) \partial_{i\alpha} V(\mathbf{r}_i - \mathbf{r}_k) \delta [\mathbf{r} - \mathbf{r}_i(t)] \\ &= [g_\beta \partial_{\alpha\beta}^2 (V_* \rho) - \rho \partial_{\alpha\beta}^2 (V_* g_\beta)] (\mathbf{r}, t). \end{aligned} \quad (7.35)$$

Following standard procedures [187], the dynamic equation for the density of velocity follows as

$$\tau \partial_t g_\alpha + \partial_\beta \kappa_{\alpha\beta} = -g_\alpha - \tau [g_\beta \partial_{\alpha\beta}^2 (V_* \rho) + \rho \partial_{\alpha\beta}^2 (V_* g_\beta)] - \rho \partial_\alpha (V_* \rho) + (2T\rho)^{1/2} \Lambda_\alpha, \quad (7.36)$$

where $*$ now denotes a convolution in space. The noise term Λ_α is Gaussian with correlations $\langle \Lambda_\alpha(\mathbf{r}, t) \Lambda_\beta(\mathbf{x}, s) \rangle = \delta_{\alpha\beta} \delta(t-s) \delta(\mathbf{r}-\mathbf{x})$, and we have introduced the fluctuating density of kinetic-like energy κ defined as

$$\kappa_{\alpha\beta}(\mathbf{r}, t) = \tau \sum_{i=1}^N p_{i\alpha} p_{i\beta} \delta [\mathbf{r} - \mathbf{r}_i(t)]. \quad (7.37)$$

It can be also written in terms of the fluctuating density of position and velocity $\Psi(\mathbf{r}, \mathbf{p}, t) = \sum_i \delta[\mathbf{r} - \mathbf{r}_i(t)] \delta[\mathbf{p} - \mathbf{p}_i(t)]$ as $\kappa_{\alpha\beta}(\mathbf{r}, t) = \tau \int p_\alpha p_\beta \Psi(\mathbf{r}, \mathbf{p}, t) d\mathbf{p}$. To close the dynamical equations, we propose an estimation for the density of kinetic-like energy based on a local steady state approximation. Following [177], we assume that Ψ can be approximated by a Gaussian distribution, whose variance is affected by the interactions:

$$\Psi_{\text{lss}}(\mathbf{p} | \rho, \mathbf{g}) \sim \rho \exp \left\{ -\frac{\tau}{2T} [\delta_{\alpha\beta} + \tau \partial_{\alpha\beta}^2 (V_* \rho)] \left(\mathbf{p} - \frac{\mathbf{g}}{\rho} \right)_\alpha \left(\mathbf{p} - \frac{\mathbf{g}}{\rho} \right)_\beta \right\}, \quad (7.38)$$

yielding

$$\kappa_{\alpha\beta} = \tau \frac{g_\alpha g_\beta}{\rho} + T \rho [\delta_{\alpha\beta} + \tau \partial_{\alpha\beta}^2 (V_* \rho)]^{-1}. \quad (7.39)$$

As a result, the fluctuating hydrodynamics reads

$$\begin{aligned} \tau \left[\partial_t g_\alpha + \partial_\beta \left(\frac{g_\alpha g_\beta}{\rho} \right) \right] &= -g_\alpha^{\text{eff}} - \rho \partial_\alpha (V_* \rho) + (2T\rho)^{1/2} \Lambda_\alpha \\ &\quad - T \partial_\beta \left\{ \rho [\delta_{\alpha\beta} + \tau \partial_{\alpha\beta}^2 (V_* \rho)]^{-1} \right\}, \end{aligned} \quad (7.40)$$

where the effective damping term g_α^{eff} is given by

$$g_\alpha^{\text{eff}} = g_\alpha + \tau \left[g_\beta \partial_{\alpha\beta}^2 (V_* \rho) - \rho \partial_{\alpha\beta}^2 (V_* g_\beta) \right]. \quad (7.41)$$

Concerning inertial Brownian particles, a similar closure can be used: the local steady state approximation amounts to considering a form similar to the Maxwell-Boltzmann distribution for Ψ_{lss} . As a result, the damping term reduces to g_α , and the last term in Eq. (7.40), which controls the diffusion of the density, is simply given by $-T\partial_\alpha\rho$ [191]. We detail below the practical consequences of these differences.

To investigate the propagation of density waves in the fluid, we consider a perturbation around the homogeneous steady position density as $\rho(\mathbf{r}, t) = \rho_0 + \delta\rho(\mathbf{r}, t)$, and $g_\alpha(\mathbf{r}, t) = \delta g_\alpha(\mathbf{r}, t)$. The linearized dynamics for the velocity density reads

$$\begin{aligned} \tau\partial_t\delta g_\alpha &= -T\partial_\alpha \left[\delta\rho + \tau\rho_0\partial_{\beta\beta}^2 (V_*\delta\rho) \right] - \delta g_\alpha + \tau\rho_0\partial_{\alpha\beta}^2 (V_*\delta g_\beta) - \rho_0\partial_\alpha (V_*\delta\rho) \\ &\quad + (2T\rho_0)^{1/2} \Lambda_\alpha. \end{aligned} \quad (7.42)$$

By using the conservation law $\partial_t\delta\rho = -\partial_\alpha\delta g_\alpha$, we obtain a closed equation for the linearized position density. The time evolution of the mode k of density, defined as $\delta\rho_k(t) = \int e^{ik_\alpha r_\alpha} \delta\rho(\mathbf{r}, t) d\mathbf{r}$, is given by

$$\begin{aligned} \tau\partial_{tt}^2\delta\rho_k &= - \left(1 + \tau\rho_0 k_\alpha^2 V_k \right) \partial_t\delta\rho_k - k_\alpha^2 \left[\rho_0 V_k + T \left(1 + \tau\rho_0 k_\beta^2 V_k \right) \right] \delta\rho_k \\ &\quad + i(2T\rho_0)^{1/2} k_\alpha \Lambda_k^\alpha. \end{aligned} \quad (7.43)$$

To shed light on the equilibrium nature of this dynamics, we write it as

$$\partial_t\delta\rho_k(t) = -k_\alpha^2 \left[\rho_0 V_k + T \left(1 + \tau\rho_0 k_\beta^2 V_k \right) \right] \int_0^t \mathcal{K}_k(t-s) \delta\rho_k(s) ds + i(2T\rho_0)^{1/2} k_\alpha \zeta_k^\alpha(t), \quad (7.44)$$

where the memory kernel \mathcal{K}_k is given by

$$\mathcal{K}_k(t) = \frac{1}{\tau} e^{-t(1+\tau\rho_0 k_\alpha^2 V_k)/\tau}, \quad (7.45)$$

and the noise term ζ_k^α is Gaussian with correlations $\langle \zeta_k^\alpha(t) \zeta_q^\beta(s) \rangle = (2\pi)^d \delta_{\alpha\beta} \delta(\mathbf{k} + \mathbf{q}) \mathcal{K}_k(|t-s|)$. This relation is the same as the one enforced by the FDT, as discussed in Chapter 1, thus showing that the linearized dynamics is in equilibrium. Yet, the linearized dynamics is different from the one of inertial Brownian particles. First, the factor multiplying the kernel in Eq. (7.44) now depends on the persistence time, which can be viewed as a modification of the interactions due to the self-propulsion. Second, the correlation time of the kernel is renormalized by the interactions for self-propelled particles, which is the main qualitative difference with respect to inertial Brownian particles. Formally, it stems from the fact

that the damping term in the fluctuating hydrodynamics (7.40) depends on these interactions. We consider a density wave of the form $\delta\rho(\mathbf{r}, t) = \varepsilon e^{i(q_\alpha r_\alpha + \omega t)}$, where $|\mathbf{q}| = k + i\lambda^{-1}$, and the amplitude ε is small compared with the bulk density ρ_0 . The speed of density waves is given by $c = \omega/k$, and λ is the attenuation length. Substituting this expression in Eq. (7.43), and equating real and imaginary parts, we obtain

$$c^2 = \frac{1}{\tau} [\rho_0 V_k + T (1 + \tau \rho_0 k^2 V_k)], \quad \lambda = \frac{2\omega}{k} \frac{\tau}{1 + \tau \rho_0 k^2 V_k}, \quad (7.46)$$

where we have assumed $k\lambda \gg 1$. Comparing with the case of inertial Brownian particles, the modification of the interactions only affect the wave speed, whereas the renormalization of correlation time has only an effect on the attenuation length. The speed of sound corresponds to the long wavelength limit: $c^2 = \tau^{-1} (\rho_0 V_0 + T)$, and it is the same as for inertial Brownian particles [188].

Dean-Kawasaki equation

We want now to obtain a closed dynamics for the position density. To this aim, we regard the velocity density as a fast variable which we eliminate adiabatically in the limit of small persistence. We then deduce the corresponding Dean-Kawasaki equation at first order in τ . Introducing a collective drift velocity ν_α and a collective diffusivity matrix $\mathcal{D}_{\alpha\beta}$ as

$$\begin{aligned} \nu_\alpha &= -\partial_\beta (V_* \rho) [\delta_{\alpha\beta} - \tau \partial_{\alpha\beta}^2 (V_* \rho)] - \tau \partial_{\alpha\beta}^2 [V_* \rho \partial_\beta (V_* \rho)], \\ \mathcal{D}_{\alpha\beta} &= T [\delta_{\alpha\beta} - 2\tau \partial_{\alpha\beta}^2 (V_* \rho)], \end{aligned} \quad (7.47)$$

we demonstrate in Appendix B that the dynamics for ρ can be written as

$$\partial_t \rho = \partial_\alpha (-\rho \nu_\alpha + \mathcal{D}_{\alpha\beta} \partial_\beta \rho + \Gamma_\alpha). \quad (7.48)$$

The noise term Γ_α is Gaussian with correlations

$$\begin{aligned} \langle \Gamma_\alpha(\mathbf{r}, t) \Gamma_\beta(\mathbf{x}, s) \rangle &= 2\delta(t-s) (\mathcal{D}_{\alpha\beta} \rho)(\mathbf{r}, t) \delta(\mathbf{r} - \mathbf{x}) \\ &\quad + 4T\tau \delta(t-s) \rho(\mathbf{r}, t) \rho(\mathbf{x}, s) \partial_{r_\alpha r_\beta}^2 V(\mathbf{r} - \mathbf{x}). \end{aligned} \quad (7.49)$$

Comparing with the coarse grained dynamics for the position density of ABPs and RTPs, the main qualitative difference is that the correlations of the noise term now contains a non-local contribution [134, 140]. In the case of ABPs, the coarse graining procedures are based in a expansion in terms of the moments and the gradients of the full distribution of position and self-propulsion angular direction [131, 157, 193]. A major consequence of the unusual noise correlations for the collective dynamics of persistent self-propelled particles is that one can not

directly identify a free-energy density functional from the deterministic part of the Dean-Kawasaki equation. Yet, it is possible to deduce the form of the free-energy at the level of the functional Fokker-Planck equation, as discussed below.

Recent attempts have strived to infer the expression of the free-energy density functional from the many-body stationary distribution [160, 194, 195]. They consider the distribution (7.7) obtained from the two approximate microscopic dynamics, which coincides with our prediction at first order in the persistence time, as a starting point. Yet, these approaches are at best limited to the simple case of two interacting particles, the main difficulty lying in the analytic treatment of the determinant appearing in the distribution. To go beyond these studies, we propose an explicit expression of the free-energy at the first order in the persistence time inspired by the corresponding many-body distribution (7.8):

$$\begin{aligned}\mathcal{F} = & T \int \rho (\ln \rho - 1) d\mathbf{r} + \frac{1}{2} \int \rho(\mathbf{r}) \rho(\mathbf{x}) \left(1 - 2T\tau \partial_{r_\alpha r_\alpha}^2 \right) V(\mathbf{r} - \mathbf{x}) d\mathbf{r} d\mathbf{x} \\ & + \frac{\tau}{2} \int \rho(\mathbf{r}) \rho(\mathbf{x}) \rho(\mathbf{y}) \partial_{r_\alpha} V(\mathbf{r} - \mathbf{x}) \partial_{r_\alpha} V(\mathbf{r} - \mathbf{y}) d\mathbf{r} d\mathbf{x} d\mathbf{y}.\end{aligned}\quad (7.50)$$

The first term corresponds to the entropic part, which is already present in the absence of interactions. We want to show that such a specific form is consistent with the dynamic (7.48) for the position density. The functional Fokker-Planck equation for the distribution of density $\mathcal{P}([\rho], t)$ associated with this dynamics reads

$$\begin{aligned}\partial_t \mathcal{P} = & \int \frac{\delta}{\delta \rho} \left\{ \partial_\alpha \left[-\rho \nu_\alpha + \mathcal{D}_{\alpha\beta} \left(\partial_\beta \rho + \rho \partial_\beta \frac{\delta}{\delta \rho} \right) \right] \mathcal{P} \right\} d\mathbf{r} \\ & - 2T\tau \int \frac{\delta}{\delta \rho(\mathbf{r})} \left\{ \partial_{r_\alpha} \left[\rho(\mathbf{r}) \rho(\mathbf{x}) \partial_{r_\alpha x_\beta}^2 V(\mathbf{r} - \mathbf{x}) \right] \partial_{x_\beta} \frac{\delta \mathcal{P}}{\delta \rho(\mathbf{x})} \right\} d\mathbf{r} d\mathbf{x}.\end{aligned}\quad (7.51)$$

To demonstrate that $\mathcal{P}_s \sim e^{-\mathcal{F}/T}$ is a stationary solution at first order in the persistence time, it is sufficient to show that the corresponding steady probability current vanishes at this order. We split the steady current into two contributions: $\mathcal{J}_\alpha = \mathcal{J}_\alpha^{(a)} + \mathcal{J}_\alpha^{(b)}$, such as

$$\begin{aligned}\mathcal{J}_\alpha^{(a)}(\mathbf{r}) = & \left[\rho \nu_\alpha - \mathcal{D}_{\alpha\beta} \left(\partial_\beta \rho + \rho \partial_\beta \frac{\delta}{\delta \rho} \right) \right] (\mathbf{r}) \mathcal{P}_s [\rho(\mathbf{r})], \\ \mathcal{J}_\alpha^{(b)}(\mathbf{r}) = & 2T\tau \rho(\mathbf{r}) \partial_{r_\alpha} \int \rho(\mathbf{x}) \partial_{x_\beta} V(\mathbf{r} - \mathbf{x}) \partial_{x_\beta} \frac{\delta \mathcal{P}_s}{\delta \rho(\mathbf{x})} d\mathbf{x}.\end{aligned}\quad (7.52)$$

From the expression of the free-energy in Eq. (7.50), we deduce

$$-T \frac{\delta \ln \mathcal{P}_s}{\delta \rho} = T \ln \rho + \left(1 - 2T\tau \partial_{\alpha\alpha}^2 \right) (V_* \rho) + \frac{\tau}{2} (V_* \rho)^2 - \tau \partial_\alpha [V_* \rho \partial_\alpha (V_* \rho)], \quad (7.53)$$

yielding

$$\begin{aligned} -\rho \mathcal{D}_{\alpha\beta} \partial_\beta \frac{\delta \ln \mathcal{P}_s}{\delta \rho} = & \mathcal{D}_{\alpha\beta} \partial_\beta \rho + \rho \partial_\alpha \left(1 - 2T\tau \partial_{\beta\beta}^2 \right) (V_* \rho) - \tau \rho \partial_\beta (V_* \rho) \partial_{\alpha\beta}^2 (V_* \rho) \\ & - \tau \rho \partial_{\alpha\beta}^2 [V_* \rho \partial_\alpha (V_* \rho)] + \mathcal{O}(\tau^2). \end{aligned} \quad (7.54)$$

The current $\mathcal{J}_\alpha^{(a)}$ follows as

$$\mathcal{J}_\alpha^{(a)} = -2\tau\rho \mathcal{P}_s \left\{ T \partial_{\alpha\beta\beta}^3 (V_* \rho) + \partial_{\alpha\beta}^2 [V_* \rho \partial_\beta (V_* \rho)] \right\} + \mathcal{O}(\tau^2). \quad (7.55)$$

To obtain the current $\mathcal{J}_\alpha^{(b)}$, we note that

$$\begin{aligned} T \int_{\mathbf{x}} \rho(\mathbf{x}) \partial_{x_\beta} V(\mathbf{r} - \mathbf{x}) \partial_{x_\beta} \frac{\delta \ln \mathcal{P}_s}{\delta \rho(\mathbf{x})} \\ = - \int [T \partial_{x_\beta} \rho + \rho \partial_{x_\beta} (V_* \rho)] (\mathbf{x}) \partial_{x_\beta} V(\mathbf{r} - \mathbf{x}) d\mathbf{x} + \mathcal{O}(\tau) \\ = T \partial_{\beta\beta}^2 (V_* \rho) (\mathbf{r}) + \partial_\beta [V_* \rho \partial_\beta (V_* \rho)] (\mathbf{r}) + \mathcal{O}(\tau), \end{aligned} \quad (7.56)$$

where we have integrated by part the first term to get the second line. We directly deduce $\mathcal{J}_\alpha^{(b)} = -\mathcal{J}_\alpha^{(a)}$. As a consequence, the free-energy (7.50) can be regarded as a sound basis to develop a density dynamic functional theory for the persistent self-propelled particles. In particular, it could provide a better insight into the phase separation observed numerically, as reported in paper F. Following this route, the main difficulty would rely in developing an appropriate treatment of the three-body interactions arising from the self-propulsion.

Future directions

Rheological properties of a bath made of interacting Brownian particles have been recently investigated, both in the overdamped and underdamped cases [191, 196]. For inertial Brownian particles, the existence of a shear thickening regime controlled by the inertial time has emerged. Since self-propelled particles also exhibit inertia-like effects, it would be interesting to determine whether such a shear thickening also exists, even in the overdamped regime. From a broader perspective, these studies offer an explicit form of the Langevin dynamics of a passive tracer immersed in the bath. The noise and damping terms hold the signature of the interactions with the constituents of the bath. It would be interesting to extend this approach to the case of a bath made of persistent self-propelled particles. In particular, one would expect that the equilibrium relation between the noise correlations and the damping kernel would no longer be valid. As a result, the usual FDT would no longer hold. Predicting the new relation between response and correlations could provide an explicit way to access the microscopic nonequilibrium features of the bath from the dynamics of a passive tracer.

Main results and outlook

Present day imaging techniques allow for particle tracking in living cells with unprecedented statistics. They can be coupled to active microrheology experiments to measure the response in such systems. Accessing the characteristics of the motion, either free or driven, is exploited in a variety of experimental living media, ranging from isolated cells to cell aggregates. While the experimental data are now of very high statistical quality and abundant, the original motivation, namely quantitatively understanding the role of active processes in shaping fluctuations in these living media, has remained an elusive goal. To address the frustrating contrast, to our taste, between experimental progress and physical understanding of the intracellular environment, we have proposed in Chapter 3 a minimal phenomenological model for the dynamics of tracers embedded in living cells. It is based on a confining potential, describing the interaction with the surrounding cytoskeletal network, which undergoes random hops as a result of the intracellular activity. Our modeling has successfully been tested against a series of data extracted from three different living systems.

First, we have quantified an active temperature inside living melanoma cells which controls both the statistics of the tracers at large times and the amplitude of the fluctuations powered by the nonequilibrium processes. We have shown that it is smaller than the bath temperature by three orders of magnitude, which does not contradict the major role of active fluctuations in large scale intracellular transport within our phenomenological picture (Chapter 4). Second, we have investigated the fluctuations in living mouse oocytes as probed by vesicles already present in the cytoplasm. We have generalized our model to account for a more complex rheology. We have estimated force and time scales associated with the active fluctuations which are comparable with the one reported from single motor experiments. Moreover, we have shown that the transduction of energy from the cytoskeletal remodeling to the tracer dynamics operates with a very low efficiency (Chapter 5). Third, we have demonstrated that our picture can also be regarded as a fruitful approach to describe the dynamics of dense multicellular

systems. By analyzing the fluctuations of tricellular junctions in epithelial tissues, we have established a correlation between the hierarchy in the molecular pathway regulating motor activity and the features of nonequilibrium fluctuations at a mesoscopic scale (Chapter 6).

Eventually, we have investigated in Chapter 7 the nonequilibrium properties of interacting self-propelled systems. Over the past decades, a large number of studies have strived to determine to which extent such systems differ from equilibrium ones, showing that intuition gained from equilibrium can still be useful in some cases. Inspired by existing minimal models, we have focused on a specific dynamics for which the self-propulsion stems from persistent fluctuations. First, we have used a systematic scheme to determine perturbatively the steady state. Second, we have quantified the breakdown of the time reversal, as the hallmark of genuine nonequilibrium. It has led us to reveal the existence of an effective equilibrium regime distinct from thermal equilibrium. Our insight into this regime is based on the analysis of the fluctuation and response. Last, we have derived the collective modes of the dynamics using a coarse graining procedure.

Whether the protocols that we have offered in paper A can be used either in living cells or reconstituted *in vitro* systems is an open question. While we have built our protocols on the basis of existing and available microrheology techniques, the implementation of these within an actual experimental system still remains a challenge. From a general standpoint, we believe that the ability to extract work from a single source of fluctuations, provided that its statistics is non-Gaussian, can be regarded as a stimulating perspective for future experimental realizations. It would stand out as a decisive asset with respect to equilibrium, with a view to crafting active materials with unprecedented properties.

The canonical dynamics of active matter comprise fluctuations which are non-Gaussian with temporal correlations. We have investigated in Chapter 7 such dynamics when fluctuations are Gaussian with temporal correlations. The natural complement of this approach consists in exploring whether the active phenomenology is maintained when considering non-Gaussian fluctuations without any time correlations. Recent studies have shown that non-Gaussian fluctuations are of paramount importance when the dissipation and injection of energy are mediated by two different heat baths [101, 197]. They have also shown the possibility to infer the statistics of a non-Gaussian bath from the dynamics of a passive tracer [198]. Moreover, the collective modes of the active particles could be investigated by extending standard coarse graining procedures to non-Gaussian fluctuations [186, 187, 199].

Another broader research axis that could be explored is to derive from a first principle standpoint the emergence of an active thermostat, that is a heat bath

which does not fulfil the common equilibrium requirements. Systematic projection methods developed by Zwanzig and Mori have been successful in describing the relaxation in an equilibrium bath [22]. An interesting route would be to extend these methods for a bath made of active particles. Starting from the microscopic dynamics of the individual components, one could derive an exact dynamics for the tracer containing a damping force and a fluctuating term. This is motivated by several experimental studies of tracer dynamics in suspensions of bacteria and swimming microrganisms [60, 200–202].

Appendix A

Persistent self-propelled particles: approximate dynamics

We present in this Appendix two approximate forms of the dynamics of interacting persistent self-propelled particles. They are inspired by approximation schemes which were originally proposed for non-interacting particles: the unified colored-noise approximation [165, 166], and the Fox theory [167, 168].

Unified colored-noise approximation

We derive the stationary distribution of the unified colored-noise approximation (UCNA). To this aim, we turn the multiplicative Langevin equation, written with the Stratonovich convention in Eq. (7.5), into an additive one by introducing the following change of variables:

$$q_{i\alpha} = \int \mathbb{M}_{i\alpha,j\beta} dr_{j\beta}, \quad (\text{A.1})$$

so that the Jacobian between \mathbf{q}_i and \mathbf{r}_i is given by $|\det \mathbb{M}|$. The corresponding Langevin equation reads

$$\dot{q}_{i\alpha} = -\frac{\partial \Phi}{\partial r_{i\alpha}} + (2T)^{1/2} \xi_{i\alpha}. \quad (\text{A.2})$$

It is straightforward to write the corresponding Fokker-Planck equation, from which we deduce the stationary distribution as

$$P_s(\{\mathbf{q}_i\}) \sim \exp \left(-\frac{1}{T} \int \frac{\partial \Phi}{\partial r_{i\alpha}} dq_{i\alpha} \right), \quad (\text{A.3})$$

leading to

$$P_s(\{\mathbf{r}_i\}) \sim \exp \left(-\frac{1}{T} \int \frac{\partial \Phi}{\partial r_{i\alpha}} \mathbb{M}_{i\alpha,j\beta} dr_{j\beta} \right) |\det \mathbb{M}|. \quad (\text{A.4})$$

Using $\mathbb{M}_{i\alpha,j\beta} = \delta_{ij}\delta_{\alpha\beta} + \tau\partial_{i\alpha,j\beta}^2\Phi$, the explicit expression of the stationary distribution (7.7) follows directly.

The dynamics for the unified colored-noise approximation (UCNA) is written in the Itô convention as:

$$\dot{r}_{i\alpha} = \mathbb{M}_{i\alpha,j\beta}^{-1} \left[-\partial_{j\beta}\Phi + (2T)^{1/2}\xi_{j\beta} \right] + T\mathbb{M}_{j\beta,k\gamma}^{-1}\partial_{j\beta}\mathbb{M}_{i\alpha,k\gamma}^{-1}. \quad (\text{A.5})$$

We use the dynamics in the Itô convention to derive the corresponding dynamic action, since the Jacobian between realizations of the noise terms and the particle trajectories does not give any contribution in this convention [203, 204]:

$$\begin{aligned} \mathcal{A} = & \frac{1}{4T} \int_0^t \mathbb{M}_{i\alpha,j\beta}^2 \left(\dot{r}_{i\alpha} + \mathbb{M}_{i\alpha,k\gamma}^{-1}\partial_{k\gamma}\Phi - T\mathbb{M}_{l\lambda,k\gamma}^{-1}\partial_{l\lambda}\mathbb{M}_{i\alpha,k\gamma}^{-1} \right) \\ & \times \left(\dot{r}_{j\beta} + \mathbb{M}_{j\beta,k\gamma}^{-1}\partial_{k\gamma}\Phi - T\mathbb{M}_{l\lambda,k\gamma}^{-1}\partial_{l\lambda}\mathbb{M}_{j\beta,k\gamma}^{-1} \right) du. \end{aligned} \quad (\text{A.6})$$

To obtain the response for UCNA, we start from the following perturbed dynamics:

$$\dot{r}_{i\alpha} = \mathbb{M}_{i\alpha,j\beta}^{-1} \left[-\partial_{j\beta}\Phi + f_{j\beta} + (2T)^{1/2}\xi_{j\beta} \right] + T\mathbb{M}_{j\beta,k\gamma}^{-1}\partial_{j\beta}\mathbb{M}_{i\alpha,k\gamma}^{-1}. \quad (\text{A.7})$$

The variation of the weight for a given time realization of the dynamics induced by the perturbation can be written as $\delta\mathcal{P} = -\mathcal{P}\cdot\delta\mathcal{A}$, so that the response is be expressed in terms of the variation of the dynamic action as

$$R_{i\alpha,j\beta}(t) = - \left\langle r_{i\alpha}(t) \left. \frac{\delta\mathcal{A}}{\delta f_{j\beta}(0)} \right|_{f=0} \right\rangle. \quad (\text{A.8})$$

It follows that we only need to compute the dynamic action at linear order in the perturbation to determine the response:

$$\begin{aligned} \delta\mathcal{A} = & -\frac{1}{2T} \int_0^t \mathbb{M}_{i\alpha,j\beta}^2 \mathbb{M}_{j\beta,m\mu}^{-1} f_{m\mu} \left(\dot{r}_{i\alpha} + \mathbb{M}_{i\alpha,k\gamma}^{-1}\partial_{k\gamma}\Phi - T\mathbb{M}_{l\lambda,k\gamma}^{-1}\partial_{l\lambda}\mathbb{M}_{i\alpha,k\gamma}^{-1} \right) du + \mathcal{O}(f^2) \\ = & -\frac{1}{2T} \int_0^t f_{m\mu} \left(\mathbb{M}_{i\alpha,m\mu} \dot{r}_{i\alpha} + \partial_{m\mu}\Phi - T\mathbb{M}_{i\alpha,m\mu} \mathbb{M}_{l\lambda,k\gamma}^{-1}\partial_{l\lambda}\mathbb{M}_{i\alpha,k\gamma}^{-1} \right) du + \mathcal{O}(f^2). \end{aligned} \quad (\text{A.9})$$

The response follows as

$$R_{i\alpha,j\beta}(t) = \frac{1}{2T} \left\langle r_{i\alpha}(t) \left(\mathbb{M}_{j\beta,m\mu} \dot{r}_{m\mu} + \partial_{j\beta}\Phi - T\mathbb{M}_{j\beta,m\mu} \mathbb{M}_{l\lambda,k\gamma}^{-1}\partial_{l\lambda}\mathbb{M}_{m\mu,k\gamma}^{-1} \right) (0) \right\rangle. \quad (\text{A.10})$$

To express the response in terms of the time derivative of a correlation function, we consider the time antisymmetric form of the response $R(t) - R(-t)$. It contains

time antisymmetric correlation functions. The dynamics is invariant under a time reversal, since the entropy production rate vanishes. From this property, we deduce

$$\begin{aligned} & \left\langle r_{i\alpha}(t) \left(\partial_{j\beta} \Phi - T \mathbb{M}_{j\beta, m\mu} \mathbb{M}_{l\lambda, k\gamma}^{-1} \partial_{l\lambda} \mathbb{M}_{m\mu, k\gamma}^{-1} \right)(0) \right\rangle \\ &= \left\langle r_{i\alpha}(0) \left(\partial_{j\beta} \Phi - T \mathbb{M}_{j\beta, m\mu} \mathbb{M}_{l\lambda, k\gamma}^{-1} \partial_{l\lambda} \mathbb{M}_{m\mu, k\gamma}^{-1} \right)(t) \right\rangle, \\ & \langle r_{i\alpha}(t) (\mathbb{M}_{j\beta, m\mu} \dot{r}_{m\mu})(0) \rangle = - \langle r_{i\alpha}(0) (\mathbb{M}_{j\beta, m\mu} \dot{r}_{m\mu})(t) \rangle. \end{aligned} \quad (\text{A.11})$$

Causality provides that $R(-t) = 0$ for $t > 0$, yielding

$$R_{i\alpha, j\beta}(t) = -\frac{1}{T} \frac{d}{dt} \langle r_{i\alpha}(t) (r_{j\beta} + \tau \partial_{j\beta} \Phi)(0) \rangle. \quad (\text{A.12})$$

This fluctuation-dissipation relation is different from both the FDT and the one for the original dynamics in the effective equilibrium regime.

Fox theory

Another approximate dynamics can be derived by using functional calculus on the weight \mathcal{P} of a given time realization of the noises. Introducing the kernel \mathcal{K} defined in terms of the self-propulsion correlations as

$$\int \mathcal{K}(t-u) \langle v_{i\alpha}(s) v_{j\beta}(u) \rangle du = \delta(t-s) \delta_{ij} \delta_{\alpha\beta}, \quad (\text{A.13})$$

we write the probability weight \mathcal{P} as

$$\mathcal{P} = \exp \left[-\frac{1}{2} \iint_0^t \mathcal{K}(u-s) v_{i\alpha}(u) v_{i\alpha}(s) du ds \right]. \quad (\text{A.14})$$

The distribution of position at given t can be expressed in terms of this probability weight as

$$P(\{\mathbf{r}_i\}, t) = \int \mathcal{P} \prod_{k=1}^N \delta[\mathbf{r}_k - \mathbf{q}_k(t)] \mathcal{D}\mathbf{v}_k, \quad (\text{A.15})$$

where the positions \mathbf{q}_k satisfy the dynamics $\dot{\mathbf{q}}_k = -\nabla_k \Phi + \mathbf{v}_k$. It follows that the time derivative of this distribution reads

$$\begin{aligned} \partial_t P &= \nabla_i \cdot \left\{ \int \mathcal{P} [\nabla_i \Phi - \mathbf{v}_i] \prod_{k=1}^N \delta[\mathbf{r}_k - \mathbf{q}_k(t)] \mathcal{D}\mathbf{v}_k \right\} \\ &= \nabla_i \cdot (P \nabla_i \Phi) - \nabla_i \cdot \left\{ \int \mathcal{P} \mathbf{v}_i \prod_{k=1}^N \delta[\mathbf{r}_k - \mathbf{q}_k(t)] \mathcal{D}\mathbf{v}_k \right\}. \end{aligned} \quad (\text{A.16})$$

To proceed further, we note that

$$v_{i\alpha}(t) \mathcal{P} = \mathcal{P} \int \delta(t-s) v_{i\alpha}(s) ds = - \int_0^t \langle v_{i\alpha}(t) v_{i\alpha}(s) \rangle \frac{\delta \mathcal{P}}{\delta v_{i\alpha}(s)} ds, \quad (\text{A.17})$$

where we have used Eqs. (A.13) and (A.14). It leads to

$$\begin{aligned} & \int \mathcal{P} v_{i\alpha} \prod_{k=1}^N \delta [\mathbf{r}_k - \mathbf{q}_k(t)] \mathcal{D}\mathbf{v}_k \\ &= - \int_0^t \langle v_{i\alpha}(s) v_{i\alpha}(t) \rangle ds \int \frac{\delta \mathcal{P}}{\delta v_{i\alpha}(s)} \prod_{k=1}^N \delta [\mathbf{r}_k - \mathbf{q}_k(t)] \mathcal{D}\mathbf{v}_k \\ &= -\nabla_j \cdot \left\{ \int_0^t \langle v_{i\alpha}(s) v_{i\alpha}(t) \rangle ds \int \mathcal{P} \frac{\delta \mathbf{q}_j(t)}{\delta v_{i\alpha}(s)} \prod_{k=1}^N \delta [\mathbf{r}_k - \mathbf{q}_k(t)] \mathcal{D}\mathbf{v}_k \right\}, \end{aligned} \quad (\text{A.18})$$

where we have integrated by parts with respect to $v_{i\alpha}$ to get the second line. From the dynamics $\dot{\mathbf{q}}_i = -\nabla_i \Phi + \mathbf{v}_i$, we obtain the following identity

$$\frac{d}{dt} \frac{\delta q_{j\beta}(t)}{\delta v_{i\alpha}(s)} = -\frac{\delta q_{j\beta}(t)}{\delta v_{i\alpha}(s)} \frac{\partial^2 \Phi}{\partial q_{i\alpha} q_{j\beta}} + \delta_{ij} \delta_{\alpha\beta} \delta(t-s). \quad (\text{A.19})$$

This equation contains a sum which was omitted in [149]. Introducing the Hessian \mathbb{H} with elements $\mathbb{H}_{i\alpha,j\beta} = \partial^2 \Phi / \partial q_{i\alpha} q_{j\beta}$, the solution can be written for $t > s$ as

$$\frac{\delta q_{j\beta}(t)}{\delta v_{i\alpha}(s)} = \left[e^{-\int_s^t \mathbb{H}(w) dw} \right]_{i\alpha,j\beta}. \quad (\text{A.20})$$

Substituting this result in Eq. (A.18) and using $\langle v_{i\alpha}(t) v_{i\alpha}(s) \rangle = T e^{-|t-s|}/\tau$, we get

$$\begin{aligned} & \int \mathcal{P} v_{i\alpha} \prod_{k=1}^N \delta [\mathbf{r}_k - \mathbf{q}_k(t)] \mathcal{D}\mathbf{v}_k \\ &= \frac{T}{\tau} \partial_{j\beta} \left\{ \int \mathcal{P} \int_0^t e^{-(t-s)/\tau} \left[e^{-\int_s^t \mathbb{H}(w) dw} \right]_{i\alpha,j\beta} ds \prod_{k=1}^N \delta [\mathbf{r}_k - \mathbf{q}_k(t)] \mathcal{D}\mathbf{v}_k \right\} \\ &= T \partial_{j\beta} (P \mathbb{D}_{i\alpha,j\beta}), \end{aligned} \quad (\text{A.21})$$

where we have introduced the diffusion tensor \mathbb{D} as

$$\mathbb{D}(t) = \int_0^t e^{-(t-s)/\tau} e^{-\int_s^t \mathbb{H}(w) dw} ds = \int_0^t e^{-u/\tau} e^{-\int_{t-u}^t \mathbb{H}(w) dw} du. \quad (\text{A.22})$$

This is valid for all values of τ , since we have not used any approximation at this stage of the derivation. To get rid of the kernel in \mathbb{D} , we assume that \mathbb{H} varies slowly in time, in the same spirit as the original Fox theory [167, 168]:

$$\int_{t-u}^t \mathbb{H}(w) dw \sim u \mathbb{H}(t), \quad (\text{A.23})$$

yielding

$$\mathbb{D}(t) \sim \int_0^t e^{-u/\tau} e^{-u \mathbb{H}(t)} du = \int_0^t e^{-u \mathbb{M}(t)/\tau} du, \quad (\text{A.24})$$

where we have used the definition of \mathbb{M} as $\mathbb{M}_{i\alpha,j\beta} = \delta_{ij}\delta_{\alpha\beta} + \tau\mathbb{H}_{i\alpha,j\beta}$. Integrating and performing the same approximation as Fox gives

$$\mathbb{D}(t) \sim \tau\mathbb{M}^{-1}(t) [1 - e^{-t\mathbb{M}(t)/\tau}] \sim \tau\mathbb{M}^{-1}(t). \quad (\text{A.25})$$

The Fokker-Planck equation (7.9) follows directly.

The corresponding set of Langevin equations is written in the Itô convention as

$$\dot{r}_{i\alpha} = -\partial_{i\alpha}\Phi + (2T)^{1/2}\mathbb{N}_{i\alpha,j\beta}^{-1}\xi_{j\beta}, \quad (\text{A.26})$$

where we have introduced the tensor \mathbb{N} defined by $\mathbb{N}^2 = \mathbb{M}$. The Fox theory amounts to proposing an approximate Markovian form for the noise term, yet the deterministic part is unchanged. The corresponding dynamic action reads

$$\mathcal{A} = \frac{1}{4T} \int_0^t \mathbb{M}_{i\alpha,j\beta} (\dot{r}_{i\alpha} + \partial_{i\alpha}\Phi) (\dot{r}_{j\beta} + \partial_{j\beta}\Phi) du. \quad (\text{A.27})$$

We consider the perturbed dynamics as

$$\dot{r}_{i\alpha} = -\partial_{i\alpha}\Phi + \delta_{ij}f_{j\alpha} + (2T)^{1/2}\mathbb{N}_{i\alpha,j\beta}^{-1}\xi_{j\beta}. \quad (\text{A.28})$$

The corresponding dynamic action is written at linear order in the perturbation as

$$\delta\mathcal{A} = -\frac{1}{2T} \int_0^t f_{i\alpha}\mathbb{M}_{i\alpha,j\beta} (\dot{r}_{j\beta} + \partial_{j\beta}\Phi) du + \mathcal{O}(f^2), \quad (\text{A.29})$$

from which we deduce the response, following the same procedure as the one used for UCNA, as

$$R_{i\alpha,j\beta}(t) = -\frac{1}{T} \frac{d}{dt} \langle r_{i\alpha}(t) (r_{j\beta} + \tau\partial_{j\beta}\Phi)(0) \rangle. \quad (\text{A.30})$$

This is the same relation as for the UCNA.

Appendix B

Persistent self-propelled particles: Dean-Kawasaki equation

In this Appendix, we present the derivation of the closed dynamics for the position density of interacting persistent self-propelled particles. It is based on the discernibility condition previously introduced in [192]. We assume that two particles can not share the same position at the same time:

$$\delta [\mathbf{r} - \mathbf{r}_i(t)] \delta [\mathbf{r} - \mathbf{r}_j(t)] = \delta_{ij} \delta [\mathbf{r} - \mathbf{r}_i(t)] \delta [\mathbf{r} - \mathbf{r}_j(t)]. \quad (\text{B.1})$$

It amounts to considering that one can detect the particle positions with an infinite precision to be able to distinguish each one of them at every time. This becomes relevant when considering soft-core interactions between the particles, for which they can overlap with a finite cost of energy, in contrast with hard-core interactions. As a consequence, the density of kinetic-like energy is simplified

$$\begin{aligned} \kappa_{\alpha\beta}(\mathbf{r}, t) &= \sum_{\{i,j\}=1}^N p_{i\alpha} p_{j\beta} \delta [\mathbf{r} - \mathbf{r}_i(t)] \delta [\mathbf{r} - \mathbf{r}_j(t)] \left\{ \sum_{k=1}^N \delta [\mathbf{r} - \mathbf{r}_k(t)] \right\}^{-1} \\ &= \left(\frac{g_\alpha g_\beta}{\rho} \right) (\mathbf{r}, t). \end{aligned} \quad (\text{B.2})$$

It follows that the dynamics for the velocity density is written as

$$\begin{aligned} \tau \left[\partial_t g_\alpha + \partial_\beta \left(\frac{g_\alpha g_\beta}{\rho} \right) \right] &= -g_\alpha - \tau \left[g_\beta \partial_{\alpha\beta}^2 (V_* \rho) - \rho \partial_{\alpha\beta}^2 (V_* g_\beta) \right] - \rho \partial_\alpha (V_* \rho) \\ &\quad + (2T\rho)^{1/2} \Lambda_\alpha. \end{aligned} \quad (\text{B.3})$$

This result is formally distinct from the fluctuating hydrodynamics (7.40). We understand this difference as follows. The local steady state approximation used to obtain Eq. (7.40) can be regarded as a coarse graining of the dynamics. The fluctuating fields \mathbf{g} and ρ appearing in these equations are smoothed functions: they result from an average over the positions and the velocities of the local microscopic particles. Consequently, the discernibility condition is no longer valid, since the details of the particle coordinates are lost by the coarse graining. In contrast, the densities of position and velocity appearing in Eq. (B.3) still contain the microscopic information about the self-propelled particles, in which case the discernibility remains valid.

To obtain a closed dynamics for the position density at first order in the persistence time, we eliminate the velocity density in the small τ regime. First, we note that the position density can be expressed as

$$\partial_t \rho(\mathbf{r}, t) = -\partial_\alpha \lim_{\Delta t \rightarrow 0} \frac{1}{\Delta t} \int_t^{t+\Delta t} g_\alpha(\mathbf{r}, s) ds. \quad (\text{B.4})$$

Therefore, we need to evaluate the integral only at first order in Δt to obtain the dynamics for ρ . From Eq. (B.3), we split the expression of the velocity density into four contributions

$$g_\alpha = \Upsilon_\alpha + \Xi_\alpha + \Pi_\alpha + \Sigma_\alpha, \quad (\text{B.5})$$

where

$$\begin{aligned} \Upsilon_\alpha(\mathbf{r}, t) &= - \int_0^t \chi_{\alpha\beta}(\mathbf{r}, t-s) \rho \partial_\beta (V_* \rho)(\mathbf{r}, s) ds, \\ \Xi_\alpha(\mathbf{r}, t) &= \int_0^t \chi_{\alpha\beta}(\mathbf{r}, t-s) (2T\rho)^{1/2} \Lambda_\beta(\mathbf{r}, s) ds, \\ \Pi_\alpha(\mathbf{r}, t) &= -\tau \int_0^t \chi_{\alpha\beta}(\mathbf{r}, t-s) \partial_\gamma \left(\frac{g_\beta g_\gamma}{\rho} \right) (\mathbf{r}, s) ds, \\ \Sigma_\alpha(\mathbf{r}, t) &= \tau \int_0^t \chi_{\alpha\beta}(\mathbf{r}, t-s) [\rho \partial_{\beta\gamma}^2 (V_* g_\gamma)] (\mathbf{r}, s) ds. \end{aligned} \quad (\text{B.6})$$

The response matrix $\chi_{\alpha\beta}$ reads

$$\chi_{\alpha\beta}(\mathbf{r}, t) = \frac{1}{\tau} [e^{-t\mathbb{L}(\mathbf{r}, t)/\tau}]_{\alpha\beta}, \quad (\text{B.7})$$

where $\mathbb{L}_{\alpha\beta} = \delta_{\alpha\beta} + \tau \partial_{\alpha\beta}^2 (V_* \rho)$. In what follows, we use the property

$$\int_0^t \chi_{\alpha\beta}(\mathbf{r}, t-s) A_\beta(\mathbf{r}, s) ds = A_\beta(\mathbf{r}, t) [\delta_{\alpha\beta} - \tau \partial_{\alpha\beta}^2 (V_* \rho)] (\mathbf{r}, t) + \mathcal{O}(\tau^2). \quad (\text{B.8})$$

We deduce the contribution from Υ_α and Ξ_α as

$$\begin{aligned} \lim_{\Delta t \rightarrow 0} \int_t^{t+\Delta t} (\Upsilon_\alpha + \Xi_\alpha)(\mathbf{r}, s) ds \\ = [\delta_{\alpha\beta} - \tau \partial_{\alpha\beta}^2 (V_* \rho)] [-\rho \partial_\beta (V_* \rho) + (2T\rho)^{1/2} \Lambda_\beta] (\mathbf{r}, t) + \mathcal{O}(\tau^2). \end{aligned} \quad (\text{B.9})$$

In the limit of small τ , one should recover the Dean-Kawasaki equation for Brownian particles:

$$g_\alpha = -\rho \partial_\alpha (V_* \rho) - T \partial_\alpha \rho + (2T\rho)^{1/2} \Lambda_\alpha + \mathcal{O}(\tau). \quad (\text{B.10})$$

The contribution from Σ_α follows as

$$\begin{aligned} \lim_{\Delta t \rightarrow 0} \int_t^{t+\Delta t} \Sigma_\alpha(\mathbf{r}, s) ds \\ = \tau \rho \partial_{\alpha\beta}^2 \left\{ V_* \left[-\rho \partial_\beta (V_* \rho) - T \partial_\beta \rho + (2T\rho)^{1/2} \Lambda_\beta \right] \right\} (\mathbf{r}, t) + \mathcal{O}(\tau^2). \end{aligned} \quad (\text{B.11})$$

Following [192], we express the contribution from Π_α as

$$\int_t^{t+\Delta t} \Pi_\alpha(\mathbf{r}, s) ds = -\tau \int_t^{t+\Delta t} ds \int_0^s \chi_{\alpha\beta}(\mathbf{r}, s-u) \partial_\gamma \left(\frac{\Xi_\beta \Xi_\gamma}{\rho} \right) (\mathbf{r}, u) du + \mathcal{O}(\Delta t^2). \quad (\text{B.12})$$

To compute explicitly this contribution, we need to estimate the following product:

$$\begin{aligned} (\Xi_\beta \Xi_\gamma)(\mathbf{r}, u) &= 2T \iint_{w_1, w_2=0}^u \chi_{\beta\mu}(\mathbf{r}, u-w_1) \chi_{\gamma\nu}(\mathbf{r}, u-w_2) \\ &\quad \times \rho^{1/2}(\mathbf{r}, w_1) \rho^{1/2}(\mathbf{r}, w_2) d\Lambda_\mu(\mathbf{r}, w_1) d\Lambda_\nu(\mathbf{r}, w_2). \end{aligned} \quad (\text{B.13})$$

Given that Λ_α is a Gaussian noise delta correlated in space and time, we use Itô's rule to obtain $d\Lambda_\mu(\mathbf{r}, w_1) d\Lambda_\nu(\mathbf{r}, w_2) = \delta_{\mu\nu} \delta(w_1 - w_2) dw_1 \delta(\mathbf{r} - \mathbf{r})$. Moreover, the discernibility condition (B.1) provides the identity $\delta(\mathbf{r} - \mathbf{r}) \rho(\mathbf{r}, w) = \rho^2(\mathbf{r}, w)$. The product $\Xi_\beta \Xi_\gamma$ follows as

$$\begin{aligned} (\Xi_\beta \Xi_\gamma)(\mathbf{r}, u) &= 2T \int_0^u \chi_{\beta\gamma}^2(\mathbf{r}, u-w) \rho^2(\mathbf{r}, w) dw \\ &= \frac{T}{\tau} \left[\delta_{\beta\gamma} - \tau \partial_{\beta\gamma}^2 (V_* \rho) (\mathbf{r}, u) \right] \rho^2(\mathbf{r}, u) + \mathcal{O}(\tau), \end{aligned} \quad (\text{B.14})$$

yielding

$$\partial_\gamma \left(\frac{\Xi_\beta \Xi_\gamma}{\rho} \right) = \frac{T}{\tau} \left[\delta_{\beta\gamma} - \tau \partial_{\beta\gamma}^2 (V_* \rho) \right] \partial_\gamma \rho - T \rho \partial_{\beta\gamma\gamma}^3 (V_* \rho) + \mathcal{O}(\tau). \quad (\text{B.15})$$

Substituting this expression in Eq. (B.12), we deduce

$$\begin{aligned} \lim_{\Delta t \rightarrow 0} \int_t^{t+\Delta t} \Pi_\alpha(\mathbf{r}, s) ds \\ = \left\{ T \tau \rho \partial_{\alpha\beta\beta}^3 (V_* \rho) - T \left[\delta_{\alpha\beta} - 2\tau \partial_{\alpha\beta}^2 (V_* \rho) \right] \partial_\beta \rho \right\} (\mathbf{r}, t) + \mathcal{O}(\tau^2). \end{aligned} \quad (\text{B.16})$$

Finally, substituting Eqs. (B.9), (B.11) and (B.16) in Eq. (B.4), we obtain the Dean-Kawasaki equation (7.48) to first order in τ .

The noise term Γ_α can be split into two contributions: $\Gamma_\alpha = \Gamma_\alpha^{(0)} + \tau\Gamma_\alpha^{(1)}$, where

$$\Gamma_\alpha^{(0)} = (2T\rho)^{1/2} \Lambda_\alpha, \quad \Gamma_\alpha^{(1)} = \rho\partial_{\alpha\beta}^2 [V_*(2T\rho)^{1/2}\Lambda_\beta] - (2T\rho)^{1/2} \Lambda_\beta\partial_{\alpha\beta}^2 (V_*\rho). \quad (\text{B.17})$$

The noise term is Gaussian, since it is a linear combination of Gaussian variables, with correlations

$$\begin{aligned} \langle \Gamma_\alpha(\mathbf{r}, t)\Gamma_\beta(\mathbf{x}, s) \rangle &= \left\langle \Gamma_\alpha^{(0)}(\mathbf{r}, t)\Gamma_\beta^{(0)}(\mathbf{x}, s) \right\rangle \\ &\quad + \tau \left[\left\langle \Gamma_\alpha^{(1)}(\mathbf{r}, t)\Gamma_\beta^{(0)}(\mathbf{x}, s) \right\rangle + \left\langle \Gamma_\alpha^{(0)}(\mathbf{r}, t)\Gamma_\beta^{(1)}(\mathbf{x}, s) \right\rangle \right] + \mathcal{O}(\tau^2). \end{aligned} \quad (\text{B.18})$$

From the correlations $\langle \Lambda_\alpha(\mathbf{r}, t)\Lambda_\alpha(\mathbf{x}, s) \rangle = \delta_{\alpha\beta}\delta(t-s)\delta(\mathbf{r}-\mathbf{x})$, we deduce

$$\begin{aligned} \left\langle \Gamma_\alpha^{(0)}(\mathbf{r}, t)\Gamma_\beta^{(0)}(\mathbf{x}, s) \right\rangle &= 2T\rho(\mathbf{r}, t)\delta_{\alpha\beta}\delta(t-s)\delta(\mathbf{r}-\mathbf{x}), \\ \left\langle \Gamma_\alpha^{(1)}(\mathbf{r}, t)\Gamma_\beta^{(0)}(\mathbf{x}, s) \right\rangle &= 2T\delta(t-s)\rho(\mathbf{r}, t)\rho(\mathbf{x}, s)\partial_{r_\alpha r_\beta}^2 V(\mathbf{r}-\mathbf{x}) \\ &\quad - 2T\delta(t-s) [\rho\partial_{\alpha\beta}^2 (V_*\rho)](\mathbf{r}, t)\delta(\mathbf{r}-\mathbf{x}). \end{aligned} \quad (\text{B.19})$$

The noise correlations (7.49) follow directly.



Contents lists available at ScienceDirect

Physica A

journal homepage: www.elsevier.com/locate/physa

Generalized Langevin equation with hydrodynamic backflow: Equilibrium properties



Étienne Fodor^a, Denis S. Grebenkov^b, Paolo Visco^a, Frédéric van Wijland^{a,c,*}

^a Laboratoire Matière et Systèmes Complexes, CNRS UMR 7057, Université Paris Diderot, 10 rue Alice Domon et Léonie Duquet, 75205 Paris cedex 13, France

^b Laboratoire de Physique de la Matière Condensée (UMR 7643), CNRS – École Polytechnique, 91128 Palaiseau, France

^c Department of Chemistry, University of California, Berkeley, CA, 94720, USA

ARTICLE INFO

Article history:

Received 10 September 2014

Received in revised form 26 November 2014

Available online 17 December 2014

Keywords:

Generalized Langevin equation

Fluctuation-dissipation theorem

Basset force

Hydrodynamics

Subdiffusion

Optical tweezers

ABSTRACT

We review equilibrium properties for the dynamics of a single particle evolving in a viscoelastic medium under the effect of hydrodynamic backflow which includes added mass and Basset force. Arbitrary equilibrium forces acting upon the particle are also included. We discuss the derivation of the explicit expression for the thermal noise correlation function that is consistent with the fluctuation-dissipation theorem. We rely on general time-reversal arguments that apply irrespective of the external potential acting on the particle, but also allow one to retrieve existing results derived for free particles and particles in a harmonic trap. Some consequences for the analysis and interpretation of single-particle tracking experiments are briefly discussed.

© 2014 Elsevier B.V. All rights reserved.

1. Introduction

Single-particle tracking experiments can access dynamical, structural and microrheological properties of complex viscoelastic media such as polymer gels or living cells [1,2]. Random displacements of a tracer are often analyzed with the help of a generalized Langevin equation which incorporates all relevant interactions of the tracer, e.g., viscous or visco-elastic Stokes force, inertial and hydrodynamic effects, active pulling by motor proteins, and eventual optical trapping [3–10]. Since several different mechanisms interplay in a complex medium, the correct formulation of the underlying phenomenological model can be sophisticated. For instance, the correlation function of the thermal noise has to be related, at equilibrium, to the memory kernels of the generalized Stokes and Basset forces according to the fluctuation-dissipation theorem. A recent experiment by Kheifets et al. [11] tracking micrometer-sized glass beads in water or acetone reveals that equipartition is broken in equilibrium by a contribution involving the mass of the displaced fluid. This raises the question of which ingredients relating to the surrounding fluid will appear in other manifestations of equilibrium, such as the fluctuation-dissipation theorem.

In this paper, we investigate the equilibrium properties of a generalized Langevin equation with hydrodynamic interactions and we provide the correct noise correlation function, consistent with the fluctuation-dissipation theorem. The role of the acceleration of the displaced fluid is sorted out, thus justifying the assumption made in Ref. [12] and amending that of Refs. [9,10]. Our analysis goes along the lines of that of Baiesi et al. [13]. Some consequences for the analysis and interpretation of single-particle tracking experiments are briefly discussed.

* Corresponding author at: Laboratoire Matière et Systèmes Complexes, CNRS UMR 7057, Université Paris Diderot, 10 rue Alice Domon et Léonie Duquet, 75205 Paris cedex 13, France.

E-mail addresses: etienne.fodor@univ-paris-diderot.fr (É. Fodor), denis.grebenkov@polytechnique.edu (D.S. Grebenkov), pao.lo.visco@univ-paris-diderot.fr (P. Visco), fvw@univ-paris-diderot.fr (F. van Wijland).

2. Model

We are interested in the short time-scale motion of a tracer with mass m the displacement of which takes place in a complex visco-elastic medium, such as a gel. For simplicity, we restrict here to the one dimensional case, although generalization to two and three dimensions is straightforward. We denote by $x(t)$ the tracer's position, and we assume the tracer is subjected to an external force F_{ext} and we further allow ourselves the possibility to apply a small perturbation force f_p . Newton's equation for the tracer reads

$$m\ddot{x} = F_S + F_B + F_{\text{ext}} + f_p + \xi, \quad (1)$$

where \ddot{x} is the tracer's acceleration. In Eq. (1), in addition to the deterministic forces F_{ext} and f_p , we have included a Gaussian colored noise $\xi(t)$ accounting for the interaction of the tracer with the heat bath. We have also included a generalized Stokes force F_S , which expresses the viscous friction exerted by the fluid on the tracer. The latter force, when coarse-graining out the degrees of freedom of the surrounding medium, can be cast in the form [14,15]

$$F_S(t) = - \int_{t_0}^{\infty} dt' \gamma(t-t') \dot{x}(t'), \quad (2)$$

where the memory kernel $\gamma(\tau)$ is causal (i.e., $\gamma(\tau) = 0$ for $\tau < 0$), and the starting time t_0 is typically set either to $-\infty$ or to 0. A number of experiments [16–19] in living cells or in synthetic polymer solutions point to γ being accurately described by a power law [4,6], thereby expressing that a hierarchy of time-scales is involved in viscous friction for these complex media. Much less studied in a visco-elastic medium is the Basset force F_B which we have also included in Eq. (1) following Refs. [9,10]. As much as the usual inertia contribution $m\ddot{x}$, the Basset force is usually negligible at the macroscopic observation time scales considered in standard tracking experiments, but its effects have been shown to be prominent at short time-scales in Refs. [20,21,7–10]. This force is related to the inertia of the boundary layer surrounding the tracer. While the initial derivation for the expression of the Basset force in terms of the tracer's position dates back to Boussinesq for Newtonian fluids, Zwanzig and Bixon [22,23] provided a derivation of that force for a visco-elastic fluid characterized by a memory kernel γ as in Eq. (2). The generalized Basset force then reads

$$F_B(t) = -\frac{m_f}{2} \ddot{x}(t) - \int_{t_0}^{\infty} dt' \zeta_B(t-t') \ddot{x}(t'), \quad (3)$$

where m_f is the mass of the fluid displaced by the tracer. The memory kernel ζ_B is causal as well, and can be argued to be related to γ in the following fashion:

$$\hat{\zeta}_B(\omega) = 3\sqrt{\frac{m_f \hat{\gamma}(\omega)}{2i\omega}}, \quad \tilde{\zeta}_B(s) = 3\sqrt{\frac{m_f \tilde{\gamma}(s)}{2s}} \quad (4)$$

where the hat and the tilde stand for the Fourier and the Laplace transforms, respectively. In order to arrive at Eq. (4), the argument put forward in Ref. [22] goes as follows: for a Newtonian fluid, one has $\hat{\zeta}_B(\omega) = 6\pi a^2 \sqrt{\frac{\rho \eta}{i\omega}}$, where a is the tracer's radius. For a visco-elastic medium, the viscosity is to be replaced with its frequency-dependent expression $\hat{\eta}(\omega)$, thus leading to $\hat{\zeta}_B(\omega) = 6\pi a^2 \sqrt{\frac{\rho \hat{\eta}}{i\omega}}$. Finally, with the generalized Stokes law $\hat{\gamma} = 6\pi \hat{\eta} a$ for spherical tracers, we obtain Eq. (4). Note that the following derivation does not rely on relation (4) between memory kernels $\gamma(t)$ and $\zeta_B(t)$, and it is thus valid in a more general situation.

The question we now ask regards to thermal noise correlations $\sigma(t-t') = \langle \xi(t)\xi(t') \rangle$ that we must impose to ensure that in the absence of a perturbing force ($f_p = 0$) and for a conservative external force F_{ext} that derives from a potential, the tracer undergoes equilibrium and reversible dynamics, in agreement with, e.g., the fluctuation-dissipation theorem. In the absence of the Basset force, this issue has been settled in the seminal paper by Kubo [24] and further discussed in the nice reviews by Mainardi et al. [25] or by Hänggi [26]. We begin by recalling the expression of the fluctuation-dissipation theorem.

3. Stating the fluctuation-dissipation theorem

The response of a position-dependent observable A to an infinitesimal external perturbation $f_p(t')$ is denoted by χ and it is defined by

$$\chi(t, t') = \left. \frac{\delta \langle A(t) \rangle}{\delta f_p(t')} \right|_{f_p=0}. \quad (5)$$

Equilibrium first requires stationarity, namely time-translation invariance, so that $\chi(t, t') = \chi(t-t')$ in the regime of interest. Causality ensures the response function vanishes if the measurement is performed before the perturbation, when $t \leq t'$. The fluctuation-dissipation theorem (FDT) states that in equilibrium the response is related to the correlation between the observable and the perturbation as [27]:

$$\chi(t-t') = \beta \frac{\partial \langle A(t) \chi(t') \rangle}{\partial t'} \Theta(t-t'), \quad (6)$$

where $\beta = 1/(k_B T)$, T is the bath temperature, and Θ denotes the Heaviside function. Stationarity also leads to $\langle A(t)x(t') \rangle = \langle A(t-t')x(0) \rangle$. The FDT can be written without enforcing explicit causality as

$$\chi(\tau) - \chi(-\tau) = -\beta \frac{d \langle x(\tau)A(0) \rangle}{d\tau}. \quad (7)$$

In single-particle tracking experiments the observable A is the tracer's position $x(t)$ and $\langle A(t)x(t') \rangle = \langle x(t)x(t') \rangle = C_x(t, t')$ is the position auto-correlation function, which, in equilibrium, is a function of $t - t'$ only, $C_x(t, t') = C_x(t - t')$. The FDT in Eq. (7) has the equivalent Fourier formulation

$$k_B T = \frac{-\omega \hat{C}_x(\omega)}{2 \hat{\chi}''(\omega)}, \quad (8)$$

where $\hat{\chi}''$ denotes the imaginary part of the response Fourier transform (and where our convention for the Fourier transform is $\hat{f}(\omega) = \int_{-\infty}^{\infty} dt e^{-i\omega t} f(t)$). Alternatively, the FDT can be stated in the Laplace domain in terms of the mean square displacement (MSD) $\langle \Delta x^2 \rangle(t) = 2(C_x(0) - C_x(t))$ as:

$$k_B T = \frac{s \langle \Delta \tilde{x}^2 \rangle(s)}{2 \tilde{\chi}(s)} \quad (9)$$

where the Laplace transform is defined by $\tilde{f}(s) = \int_0^{\infty} dt e^{-st} f(t)$.

In systems with a very small Reynolds number such as living cells, that is when inertial effects are negligible – which includes the Basset force – the response function is simply related to the Stokes memory kernel in the Laplace domain by $\tilde{\chi}(s) = 1/(s\tilde{\eta}(s))$. The FDT is then usually stated in terms of the complex modulus $\mathcal{G}^*(s) = s\tilde{\eta}(s)$ as [28–30]:

$$\langle \Delta \tilde{x}^2 \rangle(s) = \frac{k_B T}{3\pi a s \mathcal{G}^*(s)}. \quad (10)$$

4. Noise correlations in equilibrium

Our goal is now to explicitly derive the expression of the thermal noise correlations $\langle \xi(t)\xi(t') \rangle = \sigma(t - t')$, as imposed by the FDT in the presence of inertial effects. By definition, the function σ is even, $\sigma(t) = \sigma(-t)$. Here we follow the approach presented in Refs. [31,32]. Since the thermal noise has Gaussian statistics, the probability weight \mathcal{P} associated with a given realization of the thermal noise is $\mathcal{P}[\xi] \propto e^{-\delta[\xi]}$, where $\delta[\xi] = \frac{1}{2} \iint_{t_0}^{\infty} dt_1 dt_2 \xi(t_1) \Gamma(t_1 - t_2) \xi(t_2)$. The expression of ξ in this formula is determined by the tracer's dynamics in Eq. (1), and the symmetric function Γ is related to the thermal noise correlations by $\int_{t_0}^{\infty} dt_1 \sigma(t - t_1) \Gamma(t_1 - t') = \delta(t - t')$. The application of the external perturbation f_p results in a variation $\delta\delta$ of δ , so that the response function is expressed as:

$$\chi(t, t') = - \left\langle A(t) \left. \frac{\delta\delta}{\delta f_p(t')} \right|_{f_p=0} \right\rangle. \quad (11)$$

Substituting ξ from Eq. (1) into $\delta[\xi]$ and calculating the functional derivative in Eq. (11) yields the expression of the response function $\chi = \chi_{\text{in}} + \chi_{\text{ext}} + \chi_S + \chi_B$, with four contributions:

$$\chi_{\text{in}}(t, t') = m^* \int_{t_0}^{\infty} dt_1 \Gamma(t_1 - t') \langle \ddot{x}(t_1) A(t) \rangle, \quad (12a)$$

$$\chi_{\text{ext}}(t, t') = - \int_{t_0}^{\infty} dt_1 \Gamma(t_1 - t') \langle F_{\text{ext}}(t_1) A(t) \rangle, \quad (12b)$$

$$\chi_S(t, t') = \iint_{t_0}^{\infty} dt_1 dt_2 \Gamma(t_1 - t') \gamma(t_1 - t_2) \langle \dot{x}(t_2) A(t) \rangle, \quad (12c)$$

$$\chi_B(t, t') = \iint_{t_0}^{\infty} dt_1 dt_2 \Gamma(t_1 - t') \zeta_B(t_1 - t_2) \langle \ddot{x}(t_2) A(t) \rangle, \quad (12d)$$

where $m^* = m + m_f/2$. In order to compare this prediction with the FDT, we focus on the regime where the system reaches an equilibrium state, namely when the dynamics does no longer depend on initial conditions, by setting $t_0 \rightarrow -\infty$. In this regime, the correlation functions are time-translational invariant, and the response functions depends only on the time lag $\tau = t - t'$. We split the difference $\chi(\tau) - \chi(-\tau)$ into four contributions corresponding to the functions defined in Eq. (12). The first contribution is expressed as:

$$\chi_{\text{in}}(\tau) - \chi_{\text{in}}(-\tau) = m^* \int_{-\infty}^{\infty} dt_1 [\Gamma(t_1 - \tau) \langle \ddot{x}(t_1) A(0) \rangle - \Gamma(t_1 + \tau) \langle \ddot{x}(t_1) A(0) \rangle]. \quad (13)$$

We perform the change of variable $t_1 \rightarrow -t_1$ in the second integral. The key trademark of equilibrium that we now make use of is time reversibility, which implies, $\langle \ddot{x}(t_1)A(0) \rangle = \langle \ddot{x}(-t_1)A(t) \rangle$. Given that Γ is even, it follows $\chi_{\text{in}}(\tau) = \chi_{\text{in}}(-\tau)$, and we show similarly that $\chi_{\text{ext}}(\tau) = \chi_{\text{ext}}(-\tau)$. We perform the changes of variable $t_1 \rightarrow -t_1$ and $t_2 \rightarrow -t_2$ in the expression of χ_S and χ_B , and given the parity of the observables in the correlation functions of Eqs. (12c) and (12d), we deduce:

$$\chi_S(\tau) - \chi_S(-\tau) = \iint_{-\infty}^{\infty} dt_1 dt_2 \Gamma(t_1 - \tau) \langle \dot{x}(t_2)A(0) \rangle (\gamma(t_1 - t_2) + \gamma(t_2 - t_1)), \quad (14a)$$

$$\chi_B(\tau) - \chi_B(-\tau) = \iint_{-\infty}^{\infty} dt_1 dt_2 \Gamma(t_1 - \tau) \langle \ddot{x}(t_2)A(0) \rangle (\zeta_B(t_1 - t_2) - \zeta_B(t_2 - t_1)). \quad (14b)$$

As a result, we finally obtain the expression of the difference $\chi(\tau) - \chi(-\tau)$ in terms of the kernels appearing in the generalized Stokes force and the Basset force. For an equilibrium process, this expression should be identical to the prediction of the FDT in Eq. (7), which enforces that

$$\begin{aligned} \beta \langle \dot{x}(\tau)A(0) \rangle &= \iint_{-\infty}^{\infty} dt_1 dt_2 \Gamma(t_1 - \tau) [(\gamma(t_1 - t_2) + \gamma(t_2 - t_1)) \langle \dot{x}(t_2)A(0) \rangle \\ &\quad + (\zeta_B(t_1 - t_2) - \zeta_B(t_2 - t_1)) \langle \ddot{x}(t_2)A(0) \rangle]. \end{aligned} \quad (15)$$

This relation is independent of the parity of the observable we consider for the response function. In the case where a more general perturbation force $f_p(x) = -a_p(t)U'(x(t))$ is applied to the tracer, it is also possible to define the response function with respect to the parameter a_p :

$$\chi_U(t, t') = \frac{\delta \langle A(t) \rangle}{\delta a_p(t')} \Big|_{a_p=0}. \quad (16)$$

We then recover the standard FDT (analogous to Eq. (6)):

$$\chi_U(t - t') = \beta \frac{\partial \langle A(t)U(x(t')) \rangle}{\partial t'} \Theta(t - t'). \quad (17)$$

In the Fourier domain, and since the Fourier transform of thermal correlations is related to $\hat{\Gamma}$ as: $\hat{\sigma}(\omega) = 1/\hat{\Gamma}(\omega)$, we obtain from Eq. (15)

$$\hat{\sigma}(\omega) = 2k_B T \left(\hat{\gamma}'(\omega) - \omega \hat{\zeta}_B''(\omega) \right), \quad (18)$$

where $\hat{\gamma}'$ and $\hat{\zeta}_B''$ denote the real part of the γ Fourier transform and the imaginary part of the ζ_B Fourier transform, respectively. Hence, we deduce the thermal noise correlations read:

$$\langle \tilde{\xi}(t)\tilde{\xi}(t') \rangle = k_B T \left[\gamma(|t - t'|) + \frac{d\zeta_B}{dt}(|t - t'|) \right]. \quad (19)$$

This result can be decoded as an effective visco-elastic memory kernel $\gamma^* = \gamma + d\zeta_B/dt$, which could have been guessed by integrating by parts the Basset memory term. In that case however integration by parts involves a $\zeta_B(0)$ term which at best is not well defined, while our derivation encompasses this problem by using an anti-symmetric function $\zeta_B(t) - \zeta_B(-t)$. Note that m_f does not appear in this expression, so that only the terms with memory kernels in the Basset force and the generalized Stokes force contribute to the dissipation of the tracer with the heat bath as expressed by the FDT. This is in fully consistent with the free-particle situation considered by Fellerhof [33] (his Eq. (2.10)) or by Indei et al. [8] (their Eqs. (64) and (65)). In the Laplace domain, the thermal correlation function is expressed as:

$$\langle \tilde{\xi}(s)\tilde{\xi}(s') \rangle = k_B T \left[\frac{\tilde{\gamma}(s) + \tilde{\gamma}(s')}{s + s'} + \frac{s\tilde{\zeta}_B(s) + s'\tilde{\zeta}_B(s')}{s + s'} \right]. \quad (20)$$

The equipartition theorem represents an alternative method to characterize equilibrium properties. It relates the initial value of the velocity autocorrelation function $C_v(t - t') = \langle \dot{x}(t)\dot{x}(t') \rangle$ to the bath temperature as: $C_v(0) = k_B T/m$. By using the FDT prediction in Eq. (9), and given the velocity autocorrelation function is simply related to the MSD in the Laplace domain as: $\tilde{C}_v(s) = \frac{1}{2}s^2 \langle \Delta \tilde{x}^2 \rangle(s)$, we deduce: $\tilde{C}_v(s) = k_B T s \tilde{G}(s)$, where G denotes the “usual” response function [4,6]. Considering the dynamics described by Eq. (1) with an external force $F_{\text{ext}} = -kx$, we compute the response function in the Laplace domain, and we use Eq. (4) to obtain:

$$\tilde{G}(s) = \frac{1}{s^2 m^* + 3s^{3/2} \sqrt{m_f \tilde{\gamma}(s)/2} + s\tilde{\gamma}(s) + k}. \quad (21)$$

From the initial value theorem, we finally deduce:

$$\frac{C_v(0)}{k_B T} = \lim_{s \rightarrow \infty} \frac{1}{m^* + 3\sqrt{m_f \tilde{\gamma}(s)/(2s)} + \tilde{\gamma}(s)/s + k/s^2}. \quad (22)$$

As discussed in Section 2, the Laplace transform of the Stokes memory kernel in the high frequency regime behaves like $s^{\alpha-1}$, where $\alpha < 2$, so that: $\tilde{\gamma}(s)/s \xrightarrow[s \rightarrow \infty]{} 0$. It follows that the initial value of the velocity autocorrelation function $\langle \dot{x}^2 \rangle = k_B T/m^*$ is different from the “usual” equipartition theorem prediction, as already noticed in Ref. [12]. Earlier works on this subject, like those of Widom [34] or Case [35] used to determine correlation functions by assuming the “usual” equipartition, leading to slightly wrong results. Here we show that using the FDT as starting point avoids such issues. We also note that this result remains the same if we consider a constant value for the viscosity coefficient in the expression of the Basset force memory kernel. When an arbitrary external force F_{ext} is applied to the tracer, the initial value of the velocity autocorrelation function satisfies Eq. (22) under the modification $k \rightarrow k(s) = -\tilde{C}_{\text{ext}}(s)/\tilde{C}_x(s)$, where $C_{\text{ext}}(t) = \langle x(t)F_{\text{ext}}(0) \rangle$. This roughly means that in the $s \rightarrow \infty$ limit k can be replaced by $-\langle xF_{\text{ext}} \rangle_{\text{eq}} / \langle x^2 \rangle_{\text{eq}} = k_B T / \langle x^2 \rangle_{\text{eq}}$. Given the process defined in Eq. (1) has a Gaussian statistics, an experimental method to verify the validity of this result lies in measuring the stationary distribution of the tracer's velocity [11], for which the variance should equal the initial value of the velocity autocorrelation function. For an overdamped system in the absence of external force, the condition $\langle \Delta x^2 \rangle(0) = 0$ associated with the FDT prediction in Eq. (9) imposes α is positive, meaning the Stokes kernel necessarily diverges in the short time limit for such a system.

In summary, we have revised some equilibrium properties of generalized Langevin equation with hydrodynamic interactions. Under the fluctuation-dissipation theorem, the memory kernels $\gamma(t)$ and $\zeta_B(t)$ of generalized Stokes and Basset forces have been related to the noise correlation function $\langle \xi(t)\xi(t') \rangle$ according to Eq. (19). The derivation is valid in both Fourier and Laplace domains. This relation allows one to refine phenomenological models that are used for the analysis and interpretation of single-particle tracking experiments in complex visco-elastic media, notably in living cells. In particular, we showed that the noise correlation function in Refs. [9,10] should not contain the term $m_f s/2$ which came from a naive extension of the fluctuation-dissipation theorem to the Basset force (since this term could alter tracer's dynamics only at very short time scales, its presence does not affect the results reported in Refs. [9,10]). Note also that relation (4) between the memory kernels of the generalized Stokes and Basset forces allows one to reduce the number of model parameters in Refs. [9,10] yielding potentially more robust fits. Future optical tweezers single-particle tracking experiments at short time scales can further clarify hydrodynamic interactions between the tracer, the solvent, and semi-flexible polymers such as, e.g., actin filaments.

References

- [1] A. Rohrbach, C. Tischer, D. Neumayer, E.-L. Florin, E.H.K. Stelzer, Trapping and tracking a local probe with a photonic force microscope, Rev. Sci. Instrum. 75 (2004) 2197. URL: <http://dx.doi.org/10.1063/1.1753097>.
- [2] D. Wirtz, Particle-tracking microrheology of living cells: principles and applications, Annu. Rev. Biophys. 38 (2009) 301–326. URL: <http://www.annualreviews.org/doi/pdf/10.1146/annurev.biophys.050708.133724>.
- [3] H.J.H. Clercx, P.P.J.M. Schram, Brownian particles in shear flow and harmonic potentials: a study of long-time tails, Phys. Rev. A 46 (1992) 1942. URL: <http://journals.aps.org/pra/abstract/10.1103/PhysRevA.46.1942>.
- [4] M.A. Despósito, A.D. Viñales, Subdiffusive behavior in a trapping potential: mean square displacement and velocity autocorrelation function, Phys. Rev. E 80 (2009) 021111. URL: <http://link.aps.org/doi/10.1103/PhysRevE.80.021111>.
- [5] L. Bruno, V. Levi, M. Brunstein, M.A. Despósito, Transition to superdiffusive behavior in intracellular actin-based transport mediated by molecular motors, Phys. Rev. E 80 (2009) 011912. URL: <http://journals.aps.org/pre/abstract/10.1103/PhysRevE.80.011912>.
- [6] D.S. Grebenkov, Time-averaged quadratic functionals of a Gaussian process, Phys. Rev. E 83 (2011) 061117. URL: <http://link.aps.org/doi/10.1103/PhysRevE.83.061117>.
- [7] T. Indei, J.D. Schieber, A. Córdoba, Competing effects of particle and medium inertia on particle diffusion in viscoelastic materials, and their ramifications for passive microrheology, Phys. Rev. E 85 (2012) 041504. URL: <http://dx.doi.org/10.1103/PhysRevE.85.041504>.
- [8] T. Indei, J.D. Schieber, A. Córdoba, E. Pilyugina, Treating inertia in passive microbead rheology, Phys. Rev. E 85 (2012) 021504. URL: <http://dx.doi.org/10.1103/PhysRevE.85.021504>.
- [9] D.S. Grebenkov, M. Vahabi, E. Bertseva, L. Forró, S. Jeney, Hydrodynamic and subdiffusive motion of tracers in a viscoelastic medium, Phys. Rev. E 88 (2013) 040701R. URL: <http://journals.aps.org/pre/abstract/10.1103/PhysRevE.88.040701>.
- [10] D.S. Grebenkov, M. Vahabi, Analytical solution of the generalized Langevin equation with hydrodynamic interactions: subdiffusion of heavy tracers, Phys. Rev. E 89 (2014) 012130. URL: <http://link.aps.org/doi/10.1103/PhysRevE.89.012130>.
- [11] S. Kheifets, A. Simha, K. Melin, T. Li, M.G. Raizen, Observation of Brownian motion in liquids at short times: instantaneous velocity and memory loss, Science 343 (6178) (2014) 1493–1496. URL: <http://dx.doi.org/10.1126/science.1248091>.
- [12] K. Seki, S. Komura, Brownian dynamics in a thin sheet with momentum decay, Phys. Rev. E 47 (1993) 2377–2383. URL: <http://link.aps.org/doi/10.1103/PhysRevE.47.2377>.
- [13] M. Baiesi, C. Maes, B. Wynants, Nonequilibrium linear response for Markov dynamics, I: jump processes and overdamped diffusions, J. Stat. Phys. 137 (5–6) (2009) 1094–1116. URL: <http://dx.doi.org/10.1007/s10955-009-9852-8>.
- [14] H. Mori, Transport, collective motion, and Brownian motion, Progr. Theoret. Phys. 33 (1965) 423. URL: <http://ptp.oxfordjournals.org/content/33/3/423.short>.
- [15] W. Hess, R. Klein, Generalized hydrodynamics of systems of Brownian particles, Adv. Phys. 32 (1983) 173–283. URL: <http://www.tandfonline.com/doi/abs/10.1080/00018738300101551#.VJX5OAAE>.
- [16] C. Wilhelm, Out-of-equilibrium microrheology inside living cells, Phys. Rev. Lett. 101 (2008) 028101. URL: <http://link.aps.org/doi/10.1103/PhysRevLett.101.028101>.
- [17] F. Gallet, D. Arcizet, P. Bohec, A. Richert, Power spectrum of out-of-equilibrium forces in living cells: amplitude and frequency dependence, Soft Matter 5 (2009) 2947–2953. URL: <http://dx.doi.org/10.1039/B901311C>.
- [18] M. Balland, N. Desprat, D. Icard, S. Féreol, A. Asnacios, J. Browaeys, S. Hénon, F. Gallet, Power laws in microrheology experiments on living cells: comparative analysis and modeling, Phys. Rev. E 74 (2006) 021911. URL: <http://link.aps.org/doi/10.1103/PhysRevE.74.021911>.

- [19] E. Bertseva, D. Grebenkov, P. Schmidhauser, S. Gribkova, S. Jeney, L. Forró, Optical trapping microrheology in cultured human cells, *Eur. Phys. J. E* 35 (7) (2012) 1–8. URL: <http://dx.doi.org/10.1140/epje/i2012-12063-4>.
- [20] T. Franosch, M. Grimm, M. Belushkin, F.M. Mor, G. Foffi, L. Forró, S. Jeney, Resonances arising from hydrodynamic memory in Brownian motion, *Nature* 478 (2011) 85–88. URL: <http://dx.doi.org/10.1038/nature10498>.
- [21] R. Huang, I. Chavez, K.M. Taute, B. Lukic, S. Jeney, M.G. Raizen, E.-L. Florin, Direct observation of the full transition from ballistic to diffusive Brownian motion in a liquid, *Nat. Phys.* 7 (2011) 576–580. URL: <http://dx.doi.org/10.1038/NPHYS1953>.
- [22] R. Zwanzig, M. Bixon, Hydrodynamic theory of the velocity correlation function, *Phys. Rev. A* 2 (1970) 2005–2012. URL: <http://link.aps.org/doi/10.1103/PhysRevA.2.2005>.
- [23] J.D. Schieber, A. Córdoba, T. Indei, The analytic solution of Stokes for time-dependent creeping flow around a sphere: application to linear viscoelasticity as an ingredient for the generalized Stokes–Einstein relation and microrheology analysis, *J. Non-Newton. Fluid Mech.* 200 (2013) 3–8. URL: <http://dx.doi.org/10.1016/j.jnnfm.2012.08.002>.
- [24] R. Kubo, The fluctuation–dissipation theorem, *Rep. Progr. Phys.* 29 (1) (1966) 255. URL: <http://dx.doi.org/10.1088/0034-4885/29/1/306>.
- [25] F. Mainardi, A. Mura, F. Tampieri, Brownian motion and anomalous diffusion revisited via a fractional Langevin equation, *Mod. Probl. Stat. Phys.* 8 (2009) 3–23. URL: <http://mptalam.org/200901.pdf>.
- [26] P. Hänggi, Generalized Langevin equations: a useful tool for the perplexed modeller of nonequilibrium fluctuations? in: L. Schimansky-Geier, T. Pöschel (Eds.), *Stochastic Dynamics*, in: *Lecture Notes in Physics*, vol. 484, Springer, Berlin, Heidelberg, 1997, pp. 15–22. URL: <http://dx.doi.org/10.1007/BFb0105595>.
- [27] H.B. Callen, T.A. Welton, Irreversibility and generalized noise, *Phys. Rev.* 83 (1951) 34–40. URL: <http://link.aps.org/doi/10.1103/PhysRev.83.34>.
- [28] A.W.C. Lau, B.D. Hoffman, A. Davies, J.C. Crocker, T.C. Lubensky, Microrheology, stress fluctuations, and active behavior of living cells, *Phys. Rev. Lett.* 91 (2003) 198101. URL: <http://link.aps.org/doi/10.1103/PhysRevLett.91.198101>.
- [29] T.G. Mason, Estimating the viscoelastic moduli of complex fluids using the generalized Stokes–Einstein equation, *Rheol. Acta* 39 (4) (2000) 371–378. URL: <http://dx.doi.org/10.1007/s003970000094>.
- [30] T.G. Mason, D.A. Weitz, Optical measurements of frequency-dependent linear viscoelastic moduli of complex fluids, *Phys. Rev. Lett.* 74 (1995) 1250–1253. URL: <http://link.aps.org/doi/10.1103/PhysRevLett.74.1250>.
- [31] C. Maes, S. Safaverdi, P. Visco, F. van Wijland, Fluctuation-response relations for nonequilibrium diffusions with memory, *Phys. Rev. E* 87 (2013) 022125. URL: <http://link.aps.org/doi/10.1103/PhysRevE.87.022125>.
- [32] P. Bohec, F. Gallet, C. Maes, S. Safaverdi, P. Visco, F. van Wijland, Probing active forces via a fluctuation–dissipation relation: application to living cells, *Europhys. Lett.* 102 (5) (2013) 50005. URL: <http://stacks.iop.org/0295-5075/102/i=5/a=50005>.
- [33] B.U. Felderhof, Estimating the viscoelastic moduli of a complex fluid from observation of Brownian motion, *J. Chem. Phys.* 131 (16) (2009) URL: <http://scitation.aip.org/content/aip/journal/jcp/131/16/10.1063/1.3258343>.
- [34] A. Widom, Velocity fluctuations of a hard-core Brownian particle, *Phys. Rev. A* 3 (1971) 1394–1396. URL: <http://link.aps.org/doi/10.1103/PhysRevA.3.1394>.
- [35] K.M. Case, Velocity fluctuations of a body in a fluid, *Phys. Fluids* (1958–1988) 14 (10) (1971) 2091–2095. URL: <http://scitation.aip.org/content/aip/journal/pof1/14/10/10.1063/1.1693298>.



Contents lists available at ScienceDirect

Biochimica et Biophysica Acta

journal homepage: www.elsevier.com/locate/bbamcr

Review

Active cell mechanics: Measurement and theory[☆]Wylie W. Ahmed ^{a,b,c,*}, Étienne Fodor ^d, Timo Betz ^{a,b,c}^a Institut Curie, Centre de recherche, 11, rue Pierre et Marie Curie, 75005 Paris, France^b Sorbonne Universités, Université Pierre et Marie Curie, Paris, France^c Centre National de la Recherche Scientifique, UMR168, Paris, France^d Laboratoire Matière et Systèmes Complexes, UMR7057, Université Paris Diderot, 75013 Paris, France

ARTICLE INFO

Article history:

Received 2 March 2015

Received in revised form 16 May 2015

Accepted 21 May 2015

Available online 27 May 2015

Keywords:

Cell mechanics

Nonequilibrium biophysics

Force measurement

Generalized Langevin Equation

ABSTRACT

Living cells are active mechanical systems that are able to generate forces. Their structure and shape are primarily determined by biopolymer filaments and molecular motors that form the cytoskeleton. Active force generation requires constant consumption of energy to maintain the nonequilibrium activity to drive organization and transport processes necessary for their function. To understand this activity it is necessary to develop new approaches to probe the underlying physical processes. Active cell mechanics incorporates active molecular-scale force generation into the traditional framework of mechanics of materials. This review highlights recent experimental and theoretical developments towards understanding active cell mechanics. We focus primarily on intracellular mechanical measurements and theoretical advances utilizing the Langevin framework. These developing approaches allow a quantitative understanding of nonequilibrium mechanical activity in living cells. This article is part of a Special Issue entitled: Mechanobiology.

© 2015 The Authors. Published by Elsevier B.V. This is an open access article under the CC BY-NC-ND license (<http://creativecommons.org/licenses/by-nc-nd/4.0/>).

1. Introduction

Living cells are complex machines that constantly consume energy to maintain their spatial and temporal organization [1,2]. This energy consumption is required to overcome the tendency to maximize entropic disorder, and is used to self-organize the cell. From the statistical mechanics point of view, a cell represents a system far away from thermodynamic equilibrium. This non-equilibrium behavior allows the organization and operation of complex mechanical processes at the molecular scale. The current interest in building nanoscale machines can greatly profit from such strategies as typical engineering methods break down at the small scale where thermal fluctuations dominate over directed and controlled movement. Furthermore, the study of working principles used by living cells provides interesting insight on how active mechanical forces can modify or even control the mechanical properties of a polymer network [3–5]. An interesting example is provided by strain stiffening [5], where the active contraction of molecular motors can increase the mechanical stiffness of a material by more than an order of magnitude.

The effect of active forces on self organization and material properties is a highly active research field [6–10]. Typical experimental approaches combine active mechanical measurements, with detailed

analysis of the intracellular movement [4,11,131,132,134]. Furthermore, in recent years active gel theories have been successfully applied to describe and quantify flows and deformation within cells [10,12,13–16]. These active gel models have been recently reviewed [9,17]. Here we focus on experimental and theoretical approaches that allow local measurement and modeling of active systems. We define the term 'active mechanics' that integrates active components in the mechanical description of a material. A main part of this article describes Langevin-equation based approaches to derive the experimentally accessible quantities such as effective energy and force spectra using molecular properties of the underlying processes. This approach separates the contributions from thermal fluctuations and active forces to provide a framework to interpret and analyze activity measurements. Additionally, this approach does not rely on a hydrodynamic analysis as typically done in active gel theories. These active gel theories are optimal to describe active behavior on long timescales, where most biological material is considered fluid. In contrast, both the experimental and theoretical aspects of this work focus on a description of processes at intermediate and short timescales, where the viscoelastic material properties are dominant.

2. Experimental approaches

2.1. Principle of measurement

Advanced methods are used in materials science to determine the mechanical properties of a material, well known under the keyword

[☆] This article is part of a Special Issue entitled: Mechanobiology.

* Corresponding author at: Institut Curie, Centre de recherche, 11, rue Pierre et Marie Curie, 75005 Paris, France.

E-mail address: wylie.ahmed@gmail.com (W.W. Ahmed).

rheology [18,19]. Rheology exploits the constitutive relation between stress (force per unit area) and strain (relative deformation) which is commonly known as Hooke's law, illustrated in Fig. 1a. The simplest form of this law ($F = kx$) describes how a force F , applied to an object with elastic constant k leads to a deformation x . This simplified law applies for 1D objects such as springs or rubber bands. To capture the geometric parameters of a 3D object the general form of Hooke's law $\sigma = E \times u$ is commonly used. Here the stress $\sigma = F/A$ is defined as the force F acting on a unit area A of the material. The strain $u = x/x_0$ corresponds to the relative deformation (Fig. 1a). Since the force direction with respect to the surface can be decomposed into normal or parallel components, the resulting deformation is found to be a tensile or shear deformation respectively. Depending on the type of deformation the mechanical properties are described by the Young's modulus E (normal deformation), the shear modulus G (shear deformation), or the bulk modulus K (uniform compression), as illustrated in Fig. 1a. In the case of linear elasticity, these different moduli are simple scalar numbers, related to each other by the Poisson's ratio ν , that quantifies compressibility [20]. As we describe later, these moduli can become time, or frequency dependent to describe biological materials that are typically viscoelastic. In the more complex case of anisotropic materials, the introduced constitutive equation requires tensors, where the mechanical modulus becomes a fourth order tensor. In the following we only consider the case of isotropic material for simplicity, however, the described reasoning can be directly extended to a tensor notation.

In the context of living cells, the actual mechanical properties depend on the timescale of force application, and hence are described within the framework of viscoelastic materials. Here, the mechanical properties are decomposed into an elastic and a dissipative (viscous) component, where both may depend on the timescale investigated. The extreme case of pure elastic or purely viscous material is illustrated in Fig. 1b. The viscoelastic moduli are not scalars as in the pure elastic case, but functions of time or frequency. There are two main experimental strategies to determine the viscoelastic properties, namely the application of a step stress/strain, and the application of periodic stress/strain. A typical example of the first strategy is a creep experiment, where a step stress is applied resulting in a deformation of the material over time. Similarly, stress relaxation experiments can be used to apply a step deformation while measuring the stress in the system. The corresponding constitutive equation is $\sigma(t) = \int_{-\infty}^t E(t-t') \times \frac{du}{dt'} dt'$. Here, the time dependent viscoelastic modulus $E(t)$ is replacing the scalar Young's modulus. If a step deformation is applied, the strain rate becomes a delta

function that annihilates the integral, thus directly giving the viscoelastic properties as illustrated in Fig. 1c. While giving direct access to all timescales in one single experiment, practically this approach suffers from a low signal to noise ratio.

Modern rheometers avoid this problem by applying an oscillating stress and measuring the resulting time dependent strain. This results in a complex elastic modulus $G^*(\omega) = G'(\omega) + iG''(\omega)$ where the real part $G'(\omega)$ corresponds to the elastic energy stored in the material at timescales corresponding to the frequency ω (hence storage modulus) and the imaginary part $G''(\omega)$ corresponds to the energy dissipated by the viscous deformation (hence loss modulus) [18].

For measurement on the micron-scale, as relevant for living cells, typically a known force $F(t)$ is applied and the resulting absolute deformation $x(t)$ is monitored as a function of time [21–23]. Such experimental approaches, called active micro-rheology (AMR), give direct access to the mechanical response function χ that links an applied time dependent force to the resulting deformation via: $x(t) = \int_{-\infty}^t \chi(t-t') \times F(t') dt'$. This is equivalent to a convolution of the force with the time dependent response function. In the frequency domain it can hence be expressed as a multiplication of the Fourier transforms: $\tilde{x}(\omega) = \tilde{\chi}(\omega) \times \tilde{F}(\omega)$, where the tilde denotes for the Fourier transform of the corresponding variable. The transition from the response function to the shear modulus is provided by the Generalized Stokes–Einstein relation [21]: $G(\omega) = 1/(6\pi R \tilde{\chi}(\omega))$, where R is the radius of the probe particle. This last step assumes a homogenous and isotropic environment, which was already used when omitting the tensor notation.

The AMR methods directly probe the mechanical properties of the material. In contrast, passive microrheology approaches use the thermally driven particle fluctuations to access the dissipative part of the response function using the fluctuation dissipation theorem (FDT) $\tilde{C}(\omega) = \frac{2k_B T}{\omega} \tilde{\chi}''(\omega)$. Here $\tilde{C}(\omega)$ is the power spectral density that is calculated based on the particle trajectories by taking the square of the absolute value of the Fourier transform. Implicitly, this method assumes that the particle movement is driven purely by thermal movement and that the system is in thermodynamic equilibrium [24,25]. This assumption is known to be wrong in active systems such as living cells that are constantly consuming energy and are therefore non-equilibrium systems. For this reason, passive microrheology should only be used with care in living cells. Typically, in the high frequency regions fluctuations do not exhibit violation of the FDT [4,11]. Experimentally, 100 ms has been shown to be a typical timescale at

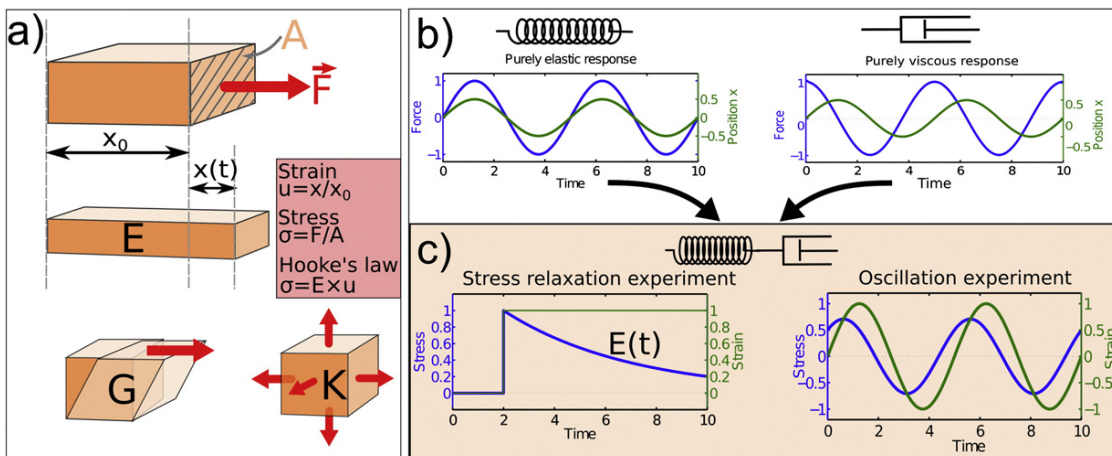


Fig. 1. Introduction of the mechanical principles to determine mechanics. (a) A force acting on a material applies a stress that will then create a strain. Depending on the deformation, the mechanical properties are described by a Young's modulus E , a shear modulus G or a bulk modulus K . (b) For viscoelastic materials the response can be separated into a purely elastic deformation that is in phase with an applied sinusoidal force, or a purely viscous deformation that has a 90° phase shift with the applied force. (c) Both combined give the information necessary to describe a viscoelastic material. The time dependent elastic moduli can be measured using step stress or strain experiments, as well as oscillating force application that gives information about the mechanics at the frequency of the applied force.

which active contributions emerge, both in reconstituted [4] and living systems [11]. However, this characteristic timescale should indeed depend on the cycling time of the active mechanical process, and might also be a function of the mechanical properties of the cell. On the other hand testing the validity of the FDT by comparing the directly measured response from AMR with the expected response calculated from spontaneous fluctuations is an elegant and direct way to determine the regimes of active and passive movements. For the study of active cell mechanics, the ideal experimental access is by a simultaneous measurement of both, the material properties such as the response function and/or the shear modulus by stress-strain measurements as well as the free particle motion via particle tracking. In the following we will briefly review the main techniques used for both of these measurements, with a special focus on the experimental setups that allow easy access to both the material properties and the free fluctuations.

2.2. Active measurement of mechanical properties

The direct measurement of the mechanical material properties requires both, a well defined force application and a precise measurement of the resulting deformation. On the cell level, the most common techniques providing this information are optical tweezers, magnetic tweezers and atomic force microscopy. Each of these methods has their technical advantages and limitations.

2.2.1. Optical tweezers (OT)

Optical tweezers use the gradient forces that act on polarizable materials in the center of a highly focused laser beam [26] (Fig. 2a). Typically, a high numerical aperture objective is used for both imaging and focusing of the laser. To provide stable 3D trapping a high numerical aperture objective is necessary to create sufficient axial gradient forces, which is required to balance scattering forces that push the particle out of the trap in the axial direction. To create a sufficient gradient force, high numerical apertures are required, and hence typically either oil or water immersion objectives with numerical apertures ($NA > 1$) are used [27]. While oil immersion objectives can provide higher NAs, and hence better 3D trapping they suffer from spherical aberration effects

when the tweezers are used more than $10 \mu\text{m}$ away from the glass surface. These effects can be compensated in some objectives. Water immersion objectives do not have this inherent problem as long as the buffer solution in the experiment has a refractive index close to water. Therefore water immersion objectives allow optical tweezing up to working distances of hundreds of μm ; however, with a slightly reduced trap stiffness due to the lower NA. When the experiment is done in close proximity to the coverslip, oil immersion objectives offer more advantages, while experiments in bulk should be performed using water immersion objectives. An interesting alternative is a double OT, where two counter-propagating lasers are focused on the same spot in 3D [28]. In such setups, the scattering force compensates and a small numerical aperture is sufficient for stable trapping. In consequence, long working distances up to mm can be realized [29].

Optical tweezers must be calibrated to determine the trap stiffness to calculate the force acting on the trapped particle as a function of the distance from the trap center. Calibration methods use the power spectral density of free particle fluctuations via the fluctuation dissipation theorem [30,31], the drag force method using the known viscosity of the medium [32] or Boltzmann distribution approach where the variance of the average particle position is associated to the trap stiffness of the tweezers [33]. These methods have been reviewed elsewhere [34]. A further elegant method is to directly infer the force by measuring the asymmetry of the scattered photons to directly determine the force using the conservation of momentum. This method, however, requires that all photons are collected after interaction with the sample which is achieved using a condenser with a higher NA than the objective [35].

To perform mechanical measurements either the laser focus or the sample itself must be displaced. To move the laser, piezo controlled mirrors [36] or acousto optical deflectors (AOD) [37,38] are commonly used. The mirrors have the advantage that the transverse laser mode is not influenced and the laser focus is continuously moving. The disadvantage of current piezo mirrors is their limited speed with maximal movements in the order of 1 kHz, and a limited angular travel of 1–10 mrad. Acousto optical deflectors exploit photon-phonon scattering, where both the intensity and the deflection angle can be controlled by

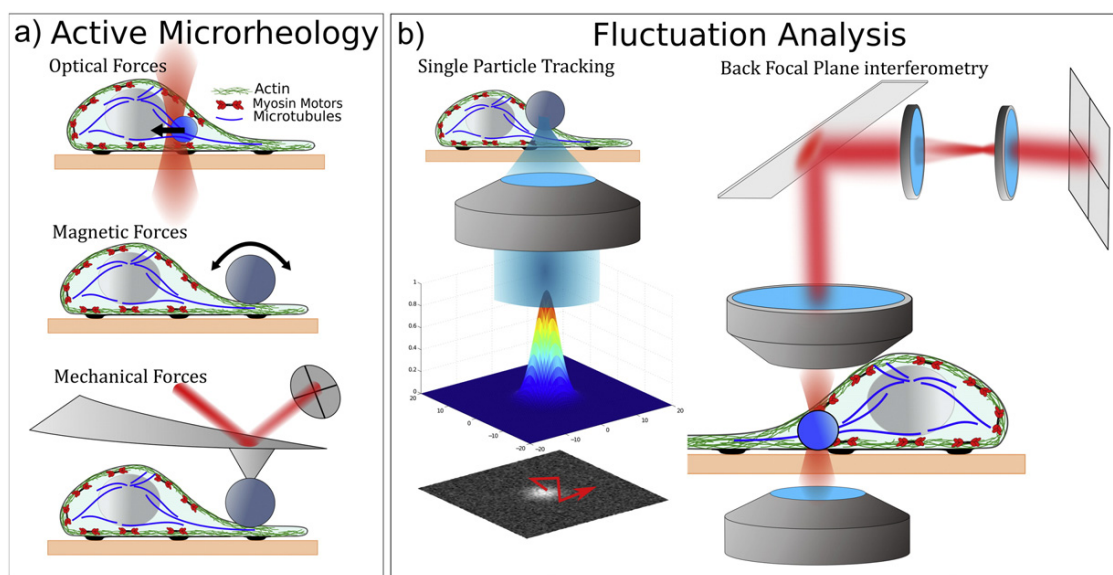


Fig. 2. Overview of the commonly used experimental methods to determine the local cell mechanics and the spontaneous particle movements. (a) Active microrheology methods provide detailed and local viscoelastic material properties. Commonly optical tweezers, magnetic tweezers, and optical magnetic twisting cytometry are used to assess intracellular and surface properties, while AFM typically measures the mechanics on the cell surface. (b) To determine the position of beads or organelles within cells, single particle methods image the fluorescence or bright field image, and then fit the expected intensity distribution to the image. This allows spatial precision down to several nm, with a time resolution depending on the image acquisition rate. Alternatively, back focal plane interferometry images the back focal plane of the condenser on a detector. After calibrating the detector response to the bead position, this can be used to gain sub-nm precision and high-speed (up to several hundred kHz) position information.

the intensity and frequency of a HF wave in a special birefringent crystal. AODs allow the trap to jump to arbitrary positions within a couple of μs , hence allowing for high speed measurements. The speed of the AODs is physically only limited by the time the acoustic wave needs to cross the laser beam size in the AOD. This high speed can be used to create multiple traps by rapid switching between multiple positions. If the switching frequency is an order of magnitude faster than the corner frequency of the power spectral density of the particle motion in the trap, it can be considered to be permanent for the particle despite the temporary absence. Downsides of the AODs are that during the switching, the laser focus is not well defined. Furthermore, if operating multiple tweezers via time-sharing, the actual calibration has to be done carefully in the same conditions as the final experiments are performed. Alternatively to switching, multiple traps can also be generated by superimposing several acoustic frequencies in the AOD. In optical tweezers, bead position is either detected using video microscopy or position sensitive detectors [39,40].

The response function can be measured by applying either an oscillating or a step force to intracellular particles such as endogenous vesicles or beads [11,41]. A step force protocol rapidly moves the laser or the stage and records the movement of the bead relaxing back into the laser focus. Step displacements probe the temporal dependence of the response function that can be translated to the frequency domain by a Fourier transform. In an oscillating force protocol, either the laser or the stage is moved with a sinusoidal function. The amplitude of this movement depends on the actual system, however, it has to be ensured that the applied movement is not exceeding the linear regime of the trap, which is determined by the bead size and the laser focus. To access different timescales, the same protocol is repeated for a series of frequencies. By observing the bead movement relative to the laser trap, both the applied forces, and the bead movement in the reference frame of the cell are determined. Dividing the Fourier transforms of the force and the displacement gives direct access to the real and imaginary part of the frequency dependent response function. The advantage of the oscillating force protocol is that by modulating a sine function with a well defined frequency, experimental and measurement noise can be filtered out by using lock-in amplifiers [4], or during post-processing of the data. The resulting response functions are very precise and the accuracy can be even increased by including more oscillations in the measurement. In contrast, the advantage of the step function is that the experiment does in parallel access all the different timescales, hence the experimental time is largely reduced, at the price of increased noise in the measurements.

2.2.2. Magnetic tweezers (MT) and optical magnetic twisting cytometry (OMTC)

An alternative method to apply well defined local forces is the magnetic tweezers [42,43]. Here either magnetic gradient forces create a well defined force on a paramagnetic particle [44], or oscillating magnetic fields create a torque on magnetic particles that are typically attached to the surface of a cell [43] (Fig. 2a). Magnetic tweezers and OMTC have the advantage of higher forces (up to 100 nN, [45]) and the absence of interaction between the magnetic field and the cell. The setup requires a strong magnetic gradient that can be generated by a variety of coil alignments [46]. Depending on the actual coil design, open cell culture dishes are often necessary to achieve high forces [45].

In the case of OMTC, ferromagnetic beads are incubated with the cells and attached to the surface either by specific receptors or by unspecific binding. A short, strong field ($<1 \text{ s}, >0.1 \text{ T}$) induces a horizontal magnetization in the beads. This is followed by a probe field that is applied vertically to the cells, hence applying a torque on the beads. This vertical field is typically weaker than the magnetization field ($<0.01 \text{ T}$) and can be varied with a sinusoidal function, or a step force. With OMTC, high frequencies ($>1 \text{ kHz}$) can be measured by controlling the applied oscillation frequency. The analysis of the frequency

dependent measurements follows the same signal processing methods as described for the optical tweezers [47].

In both magnetic techniques, the bead movement is typically detected using video microscopy, where a precise trigger of the force application and the frame acquisition is important. Using single particle tracking algorithms, the position sensitivity of the bead motion measurement can be in the order of several nm. While the analysis of the response function and the shear modulus for magnetic tweezers is similar to optical tweezers, OMTC requires a model that connects the magnetic torque driven rotational movement to the elasticity of the underlying substrate. In this model the actual attachment area is an important parameter that is either taken from literature or is assessed via finite element modeling [48]. Errors in this factor will influence the absolute results, but not the relative comparisons.

Magnetic tweezers and OMTC have the advantage that they allow higher forces, and parallel application for forces on multiple particles, thus improving the possible applications and the throughput of the measurements.

2.2.3. Atomic force microscopy (AFM)

A third, commonly used method to locally measure the mechanical properties of living cells is atomic force microscopy. A flexible cantilever is used to indent the cell or object of interest [49–51]. The deflection of the cantilever is measured using a laser that is reflected off the surface of the cantilever tip and illuminates a quadrant photodiode as illustrated in Fig. 2a. To measure the mechanical properties of cells, the cantilever tip is typically spherical. This allows to use an analysis model such as the Hertz [52] or the Sneddon [53] model that describes the force as a function of indentation depth, using the mechanical properties of the substrate. These models are more complex compared to intracellular particles as the interaction area increases while the cantilever indents the cell. To assess the viscoelastic properties of the cells, a slow approach protocol can be added to a well defined oscillation. Using lock-in amplifiers this was demonstrated to access the localized frequency dependent viscoelastic properties of living cells [54,55]. Big advantages of the AFM are the large range of accessible forces, well developed commercial microscopes, and a large range of possible cantilever geometries. On the other hand, AFM measurements typically probe the cellular surface and not intracellular properties. It is possible to infer bulk properties with large indentation depths, however, interpretation is more difficult. Also, as cell chambers are open to allow cantilever access, special care for the correct conditions of the cells such as pH, temperature and osmolarity must be taken. Finally, AFMs do not allow parallel data acquisition. Still, AFMs are a main method to determine the mechanical properties of cells.

2.3. Measuring spontaneous fluctuations

In the absence of active mechanical forces, passive techniques have been used to successfully determine the mechanical properties of viscoelastic materials [21,56,57,133]. These techniques rely on precise measurement of the particle position, ideally in 3D. The trajectories of single particles are then used to either determine the mean square displacement (MSD), the autocorrelation, or the power spectral density, that are used to calculate the mechanical response function using equilibrium thermodynamic assumptions, such as the FDT. This method has been recently reviewed in detail [58].

In the presence of active forces, the measurement of spontaneous fluctuations provides information about both, the mechanical properties of the material but also the active forces that move the particle. In the absence of any additional access to the mechanical properties, however, it remains complicated to distinguish between the fluctuations that are due to the thermal agitation of the particle and the active forces [23]. This is especially true when the active forces act in an uncorrelated and isotropic way [59], hence showing statistical properties similar to thermal movement. The measurement of particle fluctuations is

typically done using either of the two main techniques: single particle tracking and laser interferometry (Fig. 2b).

2.3.1. Single particle tracking

Single particle tracking is a well established technique that has been introduced to determine diffusion coefficients from videomicroscopy [60–62]. This image based technique requires the acquisition of images either in bright field [63], or fluorescence microscopy, where the advantage of fluorescence microscopy is a high signal-to-noise ratio that allows for a better position measurement [64,65]. A downside of the fluorescence acquisition is that the sample often bleaches, thus limiting the total acquisition time. Bright field images are typically used if the particle to be tracked provides a strong contrast, such as optically trapped beads or magnetic beads, but can also be used on intracellular particles [63]. The tracking can be done by a number of open source programs, that vary in complexity, and which have been recently critically compared [39]. For the highest positional detection, modern algorithms fit the predicted function using the microscope specific point spread function to obtain subpixel resolution down to several nm. The big advantage of single particle tracking methods is the possibility to obtain simultaneously several particle traces. However, the particle tracking may require time intensive image processing and the temporal resolution depends on the image acquisition rate. This method is typically used in combination with magnetic tweezers, but also in many cases for optical tweezers [11,66].

2.3.2. Laser interferometry

An alternative tracking method uses a laser that is focused on the particle to be tracked [67–71]. After interacting with the particle, the scattered light and unscattered light create an interference pattern in the Fourier plane of the laser focus. This plane is imaged on either a position sensitive detector or a quadrant photodiode, that directly determines any asymmetry in the light illuminating the detector. These detectors then convert the photocurrent to a voltage that is measured using modern data acquisition boards. This voltage measures the illumination asymmetry in Δx and Δy , as well as the sum signal that corresponds to the total amount of light detected. After recording a calibration curve that maps the voltage difference to the distance of the particle from the laser focus, the movement of the particle can be followed with very high spatial ($<nm$) and temporal ($<10\ \mu s$) resolutions [37]. This technique is directly compatible with an optical tweezers setup, where the laser power is simply reduced to the μW range to prevent an influence of the particle due to optical trapping effects [72]. Using the sum signal or an additional detector, 3D tracking is also possible [73]. However, in case the particle moves out of the linear regime of the calibration curve the laser or the particle needs to be recentered in the laser focus. This limits the method to shorter tracks, typically of length smaller 400 nm, unless an automated repositioning is used. The advantage of this method is that it gives directly the 3D coordinates of the tracked particle with high spatial-temporal resolution while avoiding complex post-processing or data analysis. The laser tracking method is commonly used in optical tweezers as the setup requires only the addition of a position detector in the Fourier plane of the laser focus. Recently, laser tracking has even been used to track the complex shape fluctuations of helical bacteria [74].

2.4. Quantifying active mechanics

To get direct experimental access to the active contribution in the movement of an intracellular particle, detailed knowledge about the local mechanical properties is indispensable. Hence, the currently used methods to quantify the active mechanics in living cells measure both, the viscoelastic properties as well as the spontaneous fluctuations. It is important that these measurements are done on the same probe particle and without large time delay, as cellular systems vary both in time and space. In principle, the mechanics measurement itself might

change the mechanical properties as it may trigger mechanosensing pathways that result in a restructuring of the cytoskeleton or an activation of motor proteins [75–77].

3. Theoretical models

3.1. Purpose and types of models

To get a deeper understanding of this nonequilibrium activity it is necessary to develop models to interpret the experimental measurements. For active cell mechanics, we focus on models that seek to understand what is happening at the level of the cytoskeleton and molecular motors. Hydrodynamic theories have made significant progress towards our understanding of active matter systems. These theories are based mainly on symmetries and do not involve specific microscopic details, and thus are applicable to a wide range of systems over varying scales. For extensive reviews of these approaches see [9,13,17,78]. These frameworks build on traditional hydrodynamics [79] by adding non-equilibrium forces and are primarily used for systems that are viscous at long time-scales. Recent theoretical advancements of active matter built upon previous theories have been applied to systems ranging from bacterial swarms [80,81] to large groups of organisms [82–85]. In this review, we focus on the Langevin framework for models of active mechanics which describes the motion of particles via a stochastic differential equation. We use this approach because it provides intuitive access to the model components. The Langevin approach introduces the activity via the active nonthermal noise which requires a microscopic description of the active process. Thus this approach is not generic like the hydrodynamic approach, but it offers straightforward coupling to molecular models. The purpose of this section is to do a simple walkthrough of the Langevin framework to provide a basis for readers unfamiliar with this topic to understand and develop their own simple models.

3.2. Langevin approach

The Langevin approach is the application of Newton's second law to a Brownian particle. It was the first example of a stochastic differential equation leading to the development of new fields in mathematics and physics [86]. Let's begin by describing Brownian motion in a purely viscous liquid using the Langevin framework. If we apply Newton's law ($F = ma$) to a Brownian particle we have the following equation of motion,

$$m\ddot{x} = -\gamma \dot{x} + \xi(t) \quad (1)$$

where m is the mass of the particle, $x(t)$ is its position and \dot{x} , \ddot{x} represents the first and second time derivatives respectively, γ is the constant coefficient of friction, and $\xi(t)$ is the stochastic force that comes from thermal motion. In biological systems at the cell and molecular level the inertia is typically negligible (we can ignore the mass of the particle) and we have the overdamped form of the Langevin equation,

$$\gamma \dot{x} = \xi(t) \quad (2)$$

If we solve this equation for the particle trajectory,

$$x(t) = \frac{1}{\gamma} \int_0^t \xi(t') dt' + x_0 \quad (3)$$

we see that the position of the particle, $x(t)$, depends on the entire history of the stochastic force, $\xi(t)$. This means that each time you solve Eq. (3) for the position of the particle it will be different depending on the specific realization of the stochastic force, $\xi(t)$, giving rise to the variation in trajectories of Brownian particles (Fig. 3a). For pure Brownian motion of a particle in a viscous liquid the stochastic force has the properties of

Gaussian white noise where the average force is zero, $\langle \xi(t) \rangle = 0$, and the forces are uncorrelated in time, $\langle \xi(t)\xi(t') \rangle = A\delta(t-t')$, where A is the amplitude of the thermal forces, and δ is the Dirac delta function. Now that we have the properties of the stochastic force, we can derive some properties of particle motion. First let's calculate the mean position of the particle over several realizations of the stochastic force,

$$\langle x(t) \rangle = \frac{1}{\gamma} \int_0^t \langle \xi(t') \rangle dt' + x_0 \quad (4)$$

$$= x_0 \quad (5)$$

because $\langle \xi(t) \rangle = 0$. Thus, on average a particle stays at its original starting point when averaged over many realizations of the stochastic force (as expected). This is not very exciting. A more exciting metric is the mean squared displacement (MSD) of the particle which should resemble perfect diffusion in a purely viscous liquid. To calculate the MSD let us first take the square of the position in Eq. (3) to get,

$$x(t)^2 = \frac{1}{\gamma^2} \int_0^t \int_0^t \xi(t_1)\xi(t_2) dt_1 dt_2 + x_0^2 + \frac{2}{\gamma} x_0 \int_0^t \xi(t') dt' \quad (6)$$

and by taking the properties of the stochastic force we have,

$$\langle x(t)^2 \rangle - x_0^2 = \frac{1}{\gamma^2} \int_0^t A dt_1 \quad (7)$$

$$= \frac{A}{\gamma^2} t \quad (8)$$

which is the familiar result that the MSD is proportional to time for a particle undergoing thermal diffusion in a purely viscous liquid. We can compare this to the original result derived by Einstein [87] that $\langle x(t)^2 \rangle = 2Dt$ where $D = \frac{k_B T}{\gamma}$ is the diffusion coefficient. This comparison also allows us to equate the amplitude of thermal force to the diffusion coefficient to find the fluctuation-dissipation theorem of the second kind,

$$A = 2\gamma k_B T \quad (9)$$

showing that the amplitude of the thermal forces is directly related to the friction coefficient and the temperature. This example shows how the Langevin framework can be used in a straight-forward fashion to describe stochastic motion in an intuitive way.

3.3. Models of mechanics

Once the equation of motion, $x(t)$, is known it is possible to derive the mechanical behavior of medium in thermal equilibrium in two steps. First we apply linear-response theory (LRT), $x(t) = \int_{-\infty}^t \chi(t-t')F(t')dt'$, to calculate the response of the system $x(t)$ to a force, $F(t)$. Second, we apply the Generalized Stokes–Einstein (GSE) equation [88,89] to calculate the complex shear modulus which represents the mechanical behavior of the system.

Let's first describe the mechanics of the purely viscous liquid described in the previous section. Often times in mechanics it is more intuitive (and mathematically tractable) to work in the frequency domain. Eq. (2) written in the Fourier domain is,

$$i\omega\gamma\tilde{x} = \tilde{\xi} \quad (10)$$

Now if we apply linear response theory, $\tilde{x} = \tilde{\chi}\tilde{F}$, where we know that the force acting on the particle is the thermal force ($\tilde{F}_{\text{thermal}} = \tilde{\xi}$) then we can deduce the response function,

$$\tilde{\chi} = \frac{1}{i\omega\gamma} \quad (11)$$

To get the complex shear modulus we use the GSE, $G^* = \frac{1}{6\pi R\tilde{\chi}}$ to find

$$G_{\text{liquid}}^* = \frac{i\omega\gamma}{6\pi R} \quad (12)$$

where R is the radius of the particle. Notice if we separate the complex modulus into its elastic (G') and viscous (G'') components then we have,

$$G_{\text{liquid}}' = 0 \quad (13)$$

$$G_{\text{liquid}}'' = \frac{\omega\gamma}{6\pi R} \quad (14)$$

and we can see that a purely viscous liquid provides no elastic resistance and its viscous resistance scales linearly with frequency as shown by the open circles in Fig. 3b.

The complex shear modulus of a purely elastic solid can be derived similarly as above. If we represent the elasticity of the material using a simple harmonic potential ($E = \frac{1}{2}\kappa x^2$) then the equation of motion is,

$$\kappa\tilde{x} = \tilde{\xi} \quad (15)$$

where κ is the stiffness of the harmonic potential. Applying LRT and GSE we have,

$$G_{\text{solid}}' = \frac{\kappa}{6\pi R} \quad (16)$$

$$G_{\text{solid}}'' = 0 \quad (17)$$

where for a simple harmonic spring the shear modulus is not dependent on frequency (see Fig. 3b, closed circles). This result is consistent with the sketched representation as shown in Fig. 1, where purely elastic response is fully in phase of an oscillating force, while a purely viscous response is out-of phase.

Since most biological materials are not purely viscous or purely elastic it is typically necessary to describe them as viscoelastic. Incorporating both of these effects leads to an equation of motion for a particle that contains both viscous and elastic terms,

$$i\omega\tilde{\gamma}\tilde{x} = -\kappa\tilde{x} + \tilde{\xi} \quad (18)$$

These terms ($\tilde{\gamma}, \kappa$) can take on various forms to describe different viscoelastic systems. The cytoskeleton is often described as a semi-flexible polymer network which exhibits power-law rheology at high frequencies with a low frequency elastic plateau [90–92]. A simple way to describe this is to adopt a power-law memory kernel for $\gamma(t) = \frac{\kappa(\tau_\alpha/t)^\alpha}{\Gamma(1-\alpha)}$, where $0 < \alpha < 1$ is the power-law scaling, τ_α is the viscoelastic time constant, and Γ is the Gamma function. Taking the Fourier transform yields $\tilde{\gamma} = \kappa\tau_\alpha(i\omega\tau_\alpha)^{\alpha-1}$. Following the same procedure as before and applying LRT and GSE gives us,

$$G_{\text{viscoelastic}}' = \frac{1}{6\pi R} [\kappa\tau_\alpha^\alpha \omega^\alpha \cos(\pi\alpha/2) + \kappa] \quad (19)$$

$$G_{\text{viscoelastic}}'' = \frac{1}{6\pi R} [\kappa\tau_\alpha^\alpha \omega^\alpha \sin(\pi\alpha/2)] \quad (20)$$

as shown in Fig. 3b (squares).

3.4. Models of activity

Now that we have derived the mechanical response of the system in the Langevin framework, we can turn to the purpose of this review which is adding nonequilibrium forces. In the previous section on mechanics, notice that the only stochastic force involved is thermal in nature because the systems are in thermal equilibrium. This is because

material properties are typically defined for materials in thermal equilibrium. For systems that are out-of-equilibrium, such as biological systems, there are additional forces coming from processes occurring inside the cell (e.g. molecular motors and polymerization). The advantage of the Langevin framework is that additional forces can be intuitively incorporated into the equation of motion of the particle [131]. As an example, let us add a stochastic force that is non-thermal in origin to the right side of the equation of motion for a viscoelastic material. Thus we have,

$$i\omega\tilde{\gamma}\ddot{x} = -\kappa\ddot{x} + \xi + \tilde{f}_A \quad (21)$$

where f_A is the stochastic active force. The active force can be modeled in many ways to account for different physical systems. Using this approach, a molecular scale model of the active force can be developed and incorporated into the Langevin framework. Additionally, if the form of the active force is too complex to be solved analytically, it can straightforwardly be explored via simulations. Thus predictions for the average dynamics of objects inside the cell can be calculated, allowing close comparison between experiments and theory. As an example, we will present a simple minimal model for the active force, f_A , that has been described previously [93,94] and is illustrated in Fig. 4a. This model describes the force contribution from molecular motors that actively kick the particle and cause it to move around randomly. The force due to this motion can be expressed as, $f_A = \kappa \int v_A(t') dt'$ where v_A is the active velocity described by a random process that equals 0 for an average duration of τ_0 and is a uniform random value over $[-v, v]$ for an average duration of τ . The statistics of v_A reflect molecular motor statistics and are a zero mean non-Gaussian process with correlations: $\langle v_A(t)v_A(t') \rangle = k_B T_A \exp(-|t-t'|/\tau)/(\tau\gamma)$ where $k_B T_A = \frac{\gamma(v\tau)^2}{3(\tau+\tau_0)}$ is the effective active energy scale [93,94]. A representative realization of the motor force kinetics is shown in Fig. 4b.

Now that we have the equation of motion for a particle in a viscoelastic material subjected to an active stochastic force we can explore some of the system properties. A common way to quantify the nonequilibrium properties of a system is to calculate its effective energy, which quantifies deviation from equilibrium. This requires combining information from the mechanical response, $\tilde{\chi}''(\omega)$, and the spontaneous fluctuations, $\tilde{C}(\omega)$, of the particle motion where $\tilde{C}(\omega) = \langle \dot{x}(t)x(0) \rangle \exp(i\omega t) dt$ is the power spectral density of position fluctuations. The effective energy is basically the ratio of these two, $E_{\text{eff}} = \frac{\omega\tilde{C}(\omega)}{2\tilde{\chi}''(\omega)}$, in units of $k_B T$. In the experimental measurements the response

is calculated from active rheology and the spontaneous fluctuations are from particle tracking. For our example theoretical model this can be calculated as,

$$E_{\text{eff}}(\omega) = k_B T + \frac{1}{(\omega\tau_r)^2} \frac{k_B T_A}{1 + (\omega\tau)^2} \quad (22)$$

where $\tau_r = \gamma/\kappa$ is the relaxation time of the surrounding material, and it is clear if T_A is zero the system is in thermal equilibrium (Fig. 4c). While the effective energy provides a way to quantify the deviation from equilibrium, it does not directly provide insight into the active forces generated in the system. To gain insight into the active mechanics we must look at the force correlations. First, let us note that the total force driving the system is the sum of the active force and thermal force, $\tilde{F}_{\text{tot}} = \tilde{f}_A + \xi$. Following the derivation above we can find that the mechanical properties of the system are, $G^* = \frac{1}{6\pi R}(\kappa + i\omega\gamma)$, where κ and γ are constants for simplicity that are related to the elastic and viscous properties of the system. This framework now allows direct access to the active force spectrum that is generated exclusively from nonequilibrium sources. To look at the active forces we calculate its power spectrum (i.e. the Fourier transform of the time correlation function $\langle f_A(0)f_A(t') \rangle$),

$$S_{\text{active}}(\omega) = \frac{1}{(\omega\tau_r)^2} \frac{2\gamma k_B T_A}{1 + (\omega\tau)^2} \quad (23)$$

as is shown in Fig. 4d [93]. Thus it is clear that the mechanical properties of the surrounding material also contribute to the active forces. Again, notice that if the system is in equilibrium, $T_A = 0$, then the active force spectrum would be zero. The analytical expression of the active force spectrum can be fitted to the experimental measurements to extract the characteristic timescale, τ , of the molecular process driving the non-equilibrium behavior. This provides a connection between the observable motion of a tracer particle and the underlying stochastic driving forces.

Recent developments in stochastic thermodynamics leverage the Langevin framework to allow quantification of the rate of energy dissipation [95]. Energy dissipation is a fundamental property that characterizes non-equilibrium steady-state systems and allows comparison between different model systems. The Harada–Sasa equality relates the violation of the FDT to the amount of energy dissipated in the system. Therefore, if violation of FDT can be measured and modeled, the energy dissipation can be directly calculated and related to a

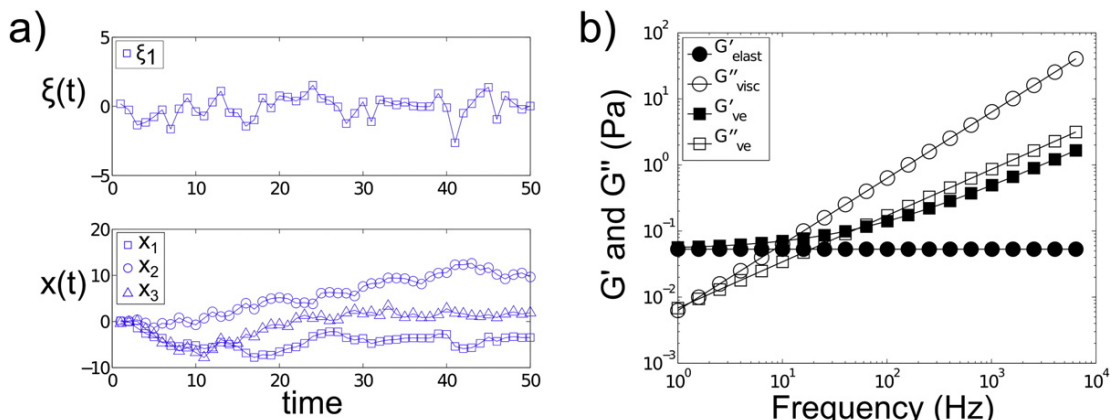


Fig. 3. (a) One realization of the stochastic thermal force is shown to illustrate the time course of a zero-mean Gaussian process (ξ_1 , top panel). The trajectory of a particle, $x(t)$, is found by integrating the random thermal force, $\xi(t)$, over time as shown in 3 separate realizations (lower panel). (b) The complex shear modulus is shown for three different models of mechanics. A purely viscous liquid has dissipative modulus, G'' , that scales linearly with frequency (open circles). A purely elastic solid has an elastic modulus, G' , that is frequency independent (closed circles). A viscoelastic material exhibits intermediate behavior with frequency dependent elastic and dissipative moduli.

molecular scale model. In this framework the dissipation in the system is the work done by the particle on the surrounding environment. The mean rate of energy dissipation is,

$$J_{\text{diss}} = \langle \dot{x} (\gamma \dot{x} - \xi) \rangle \quad (24)$$

where \dot{x} is the particle velocity. J_{diss} can be thought of as the difference between the power dissipated by the particle drag force ($\gamma \dot{x}$) and the power injected by the thermal force (ξ). In an equilibrium process, these two powers are equal as a consequence of FDT, and thus J_{diss} would be zero. Harada and Sasa showed that the dissipated power in a nonequilibrium steady state system can be calculated from the correlation and response functions [95],

$$J_{\text{diss}} = \gamma \int d\omega [\omega \tilde{C}(\omega) + 2T \tilde{\chi}''(\omega)] \omega / 2\pi \quad (25)$$

where $\tilde{C}(\omega)$ is the power spectral density of the position fluctuations and $\tilde{\chi}''(\omega)$ is the imaginary part of the response function. Since all the terms in the Harada–Sasa relation can be measured experimentally and modeled theoretically, it provides a direct way to compare experimental and theoretical results of local power dissipation in nonequilibrium steady-state systems. Since power dissipation is a fundamental thermodynamic quantity it is possible to relate these measurements to the mechanical efficiency of a process.

4. Nonequilibrium biopolymer mechanics

The theoretical tools in the previous section provide a useful framework to understand the complex mechanics of nonequilibrium biopolymers and reconstituted in-vitro networks provide a simple experimental system to probe their behavior. It is known that external stress/stain applied to reconstituted biopolymer gels can lead to both softening and stiffening. Complex interactions at the local molecular scale can give rise to bulk changes in behavior even without active forces. Stress-softening has been attributed to local buckling of actin filaments [96], force induced rupture of cross-links [97], and nonlinear force response and filament turnover [98]. Stress stiffening has been shown to be due to network structure [99,100], dynamic re-binding of cross-links [101,102], and cyclic-loading [103].

4.1. Softening

An entangled polymer solution naturally exhibits viscoelastic mechanical behavior. If molecular motors are added to the entangled polymer, its properties can be actively modulated. Myosin-II motor activity in a solution of entangled actin filaments will significantly shorten the stress relaxation time leading to fluidization of the material [3] (Fig. 5a). Myosin-II motors interact with the actin and allow filaments to slide longitudinally past each other leading to bulk fluidization. A theoretical model shows that the active forces generate directed reptation of the polymers leading to fluidization [104]. Together, these studies indicate a way that internally generated active forces can tune the bulk mechanical properties of the material without physically changing its building blocks. A similar study showed that adding cross-linking can increase the energy dissipation in active actin networks at short timescales while still allowing fluidization at longer times [105]. This points to the high sensitivity of biopolymer network mechanics to motor activity and cross-linking which can provide a way to tune the material properties [106]. In addition to tuning material properties, myosin-II motors have been shown to buckle, fragment, and depolymerize actin filaments, directly changing the network and leading to stress relaxation [107–109]. These controlled in-vitro studies show possible mechanisms that living cells could utilize to tune their mechanical behavior. In living cells it has been reported that force application fluidizes the cell mechanical properties [110] as measured by

magnetic twisting cytometry. Direct measurement in living cells is sparse, however some studies have shown that applied deformation may also lead to decreased cytoplasmic resistance [111,112]. And metabolic activity was shown to fluidize the cytoplasm and facilitate motion of larger components in bacteria cells [113]. Another recent study has used several different measurement techniques to show that myosin-II activity softens cells in suspension [114]. Further measurements and theories are necessary to understand these processes at the molecular level.

4.2. Stiffening

Stiffening due to motor activity is also a common observation. A landmark study of nonequilibrium mechanics in active actin–myosin gels showed that cross-linked networks stiffen (by up to 100×) due to the action of molecular motors [4] (Fig. 5b). A theoretical model showed that even small forces generated by molecular motors in a semi-flexible gel (exhibiting nonlinear elasticity) lead to a strong stiffening of the network [115,116]. It has been suggested that cells operate in this highly sensitive nonlinear regime such that small changes in motor activity allow them to modulate their mechanical response greatly [5]. Interestingly, a recent study created an active gel using noncytoskeletal components (DNA and FtsK50C) and found similar results, highlighting that the observed behavior is not specific to actin and myosin [118]. Similar behavior has been observed indirectly in living cells. Single platelet cells increase their bulk stiffness when allowed to contract between two rigid surfaces [119]. In living oocytes the stiffness of the cortex is maintained by myosin-II activity, and it dramatically softens if these motors are excluded [120]. And in the cytoplasm of cultured cells the stiffness has also been shown to decrease when myosin-II motors are deactivated via blebbistatin [11]. It is important to mention that the studies discussed here in living cells make direct force measurements, which allow direct access to the mechanical properties. Generally, it should be noted that studies in living cells must be interpreted carefully since their response to pharmacological treatment and genetic tools is often highly sensitive to dosage and recovery time.

4.3. Active organization

In addition to nonequilibrium mechanics, an interesting property of active matter is its ability to dynamically self-organize. High-density motility assays of actin filaments, myosin-II motors, and cross-linking proteins have shown a wide range of self-organization phenomena ranging from large-scale polar structures to contracting networks [121]. Collective motion emerges from the random molecular motor activity on polar actin filaments leading to coherent moving structures with clusters, swirls, and interconnected bands due to hydrodynamic coupling between filaments [122,123]. These complex interactions also give rise to frozen steady-states and giant fluctuations in density [124,125]. Beyond these dynamic moving structures, active actin–gel networks can also form quasi-static heterogeneous structures in the form of clusters of different sizes [126]. Interestingly, studies of active matter consisting of microtubules and kinesin also show active organization that is quite different from actin–myosin gels. Bundles of microtubules containing hundreds of kinesin motors spontaneously synchronize their motion and generate large-scale oscillations [127], suggesting that only two-components are sufficient to create cilia-like beating. When the microtubule–kinesin network is assembled inside an emulsion droplet, it exhibits internally driven chaotic flows leading to fractures and self-healing of microtubules and also drives autonomous motility of the droplet [128]. To mimic cellular structures the microtubule–kinesin network was encapsulated in a lipid vesicle where it exhibited periodically oscillating active nematic defects and shape-changing dynamics with filopodia-like

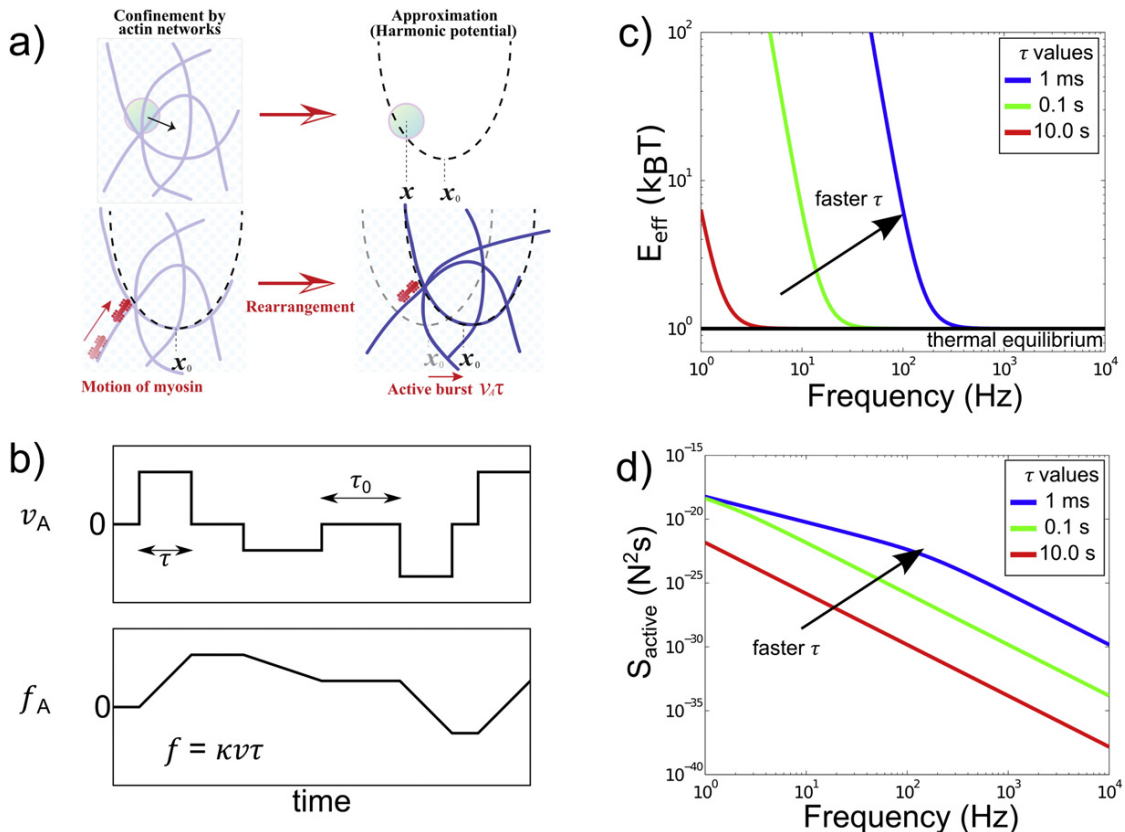


Fig. 4. (a) A schematic diagram of the viscoelastic material with motor-driven activity. The surrounding medium provides local confinement of particles modeled as a harmonic potential. Particles embedded in the material undergo thermal fluctuations with a mean position of x_0 . In addition, molecular motors inject nonequilibrium activity into the system and push the particle further from the equilibrium position giving rise to additional forces that are nonthermal in origin. (b) Molecular motor statistics are modeled as an active burst where they have a velocity v_A , which is a random value between $-v$ and v for a random duration of order τ followed by a velocity of 0 for average duration τ_0 (top panel). The example realization of active burst activity results in the active forces shown in the lower panel. (c) The effective energy quantifies how far the system is from equilibrium at higher frequencies. (d) The active force spectrum quantifies the forces generated by the motor-driven activity. In the presented model faster motor kinetics, τ , result in higher active forces.

(b) Reprinted with permission from [94] Copyright (2014) by the American Physical Society.

protrusions [129]. These reconstituted active matter systems bring us closer to understanding how cells utilize activity to organize their functional structures. A recent example was observed in living oocytes where coordinated molecular motor activity generates a gradient force to center the nucleus at the cell center [130].

5. Outlook

Nonequilibrium activity is required for the maintenance of life. Without it, all systems decay to their lowest energy state corresponding to maximum disorder. For living cells to maintain their

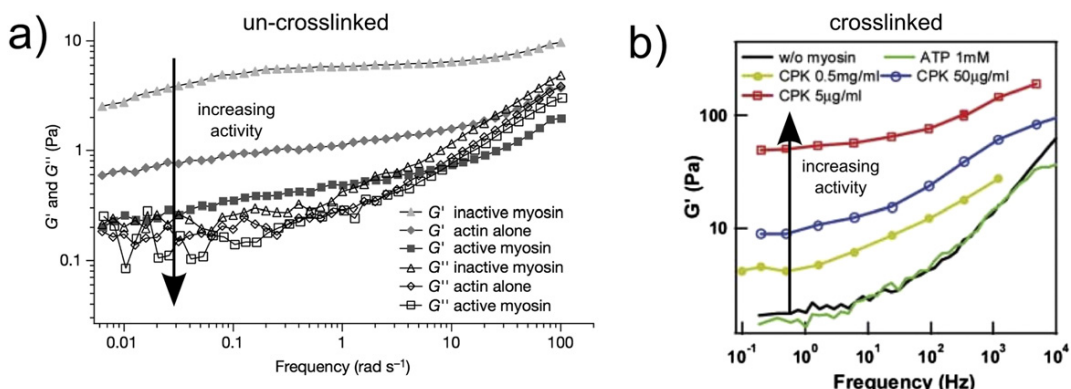


Fig. 5. (a) Un-crosslinked actin-myosin networks exhibit significantly smaller shear moduli when myosin is active. This is an example of activity-induced softening of an active material. (b) Conversely, cross-linked actin-myosin networks exhibit significantly larger shear moduli when myosin is active, an example of activity-induced stiffening. (a) Adapted by permission from Macmillan Publishers Ltd: [3], Copyright (2002). (b) From reference [4]. Reprinted with permission from AAAS.

cytoskeletal structure, organization, and dynamic behavior they must constantly consume and dissipate energy. By understanding how this nonequilibrium activity drives self-organization we will gain a deeper understanding of biophysical processes at the molecular scale. The emerging experimental and theoretical frameworks to probe nonequilibrium mechanics will allow direct quantification of activity in living cells and allow us to dissect the complex underlying processes. These same techniques can also be applied to synthetic or reconstituted systems to understand fundamental processes in non-equilibrium physics. This interface between living cells and synthetic systems will undoubtedly lead to the design and engineering of new bio-inspired materials with advanced functionalities.

Acknowledgements

We thank Paolo Visco and Frédéric van Wijland for their helpful discussions. WWA is a recipient of post-doctoral fellowships from La Fondation Pierre-Gilles de Gennes and Marie Curie Actions. TB was supported by the French Agence Nationale de la Recherche (ANR) grant ANR-11-JSV5-0002 and LabEx CelTisPhyBio grant No. ANR-10-LBX-0038.

References

- [1] A.S. Mikhailov, B. Hess, Self-Organization in Living Cells: Networks of Protein Machines and Nonequilibrium Soft Matter, *J. Biol. Phys.* 28 (4) (December 2002) 655–672.
- [2] F.C. MacKintosh, C.F. Schmidt, Active cellular materials, *Curr. Opin. Cell Biol.* 22 (1) (February 2010) 29–35.
- [3] D. Humphrey, C. Duggan, D. Saha, D. Smith, J. Kas, Active fluidization of polymer networks through molecular motors, *Nature* 416 (6879) (March 2002) 413–416.
- [4] D. Mizuno, C. Tardin, C.F. Schmidt, F.C. MacKintosh, Nonequilibrium mechanics of active cytoskeletal networks, *Science* 315 (5810) (January 2007) 370–373.
- [5] G.H. Koenderink, Z. Dogic, F. Nakamura, P.M. Bendix, F.C. MacKintosh, J.H. Hartwig, T.P. Stossel, D.A. Weitz, An active biopolymer network controlled by molecular motors, *Proc. Natl. Acad. Sci.* 106 (36) (September 2009) 15192–15197.
- [6] S. Wang, P.G. Wolynes, Active contractility in actomyosin networks, *Proc. Natl. Acad. Sci. U. S. A.* 109 (17) (April 2012) 6446–6451.
- [7] R. Levayer, T. Lecuit, Biomechanical regulation of contractility: spatial control and dynamics, *Trends Cell Biol.* 22 (2) (February 2012) 61–81.
- [8] M. Soares e Silva, M. Depken, B. Stührmann, M. Korsten, F.C. MacKintosh, G.H. Koenderink, Active multistage coarsening of actin networks driven by myosin motors, *Proc. Natl. Acad. Sci.* 108 (23) (June 2011) 9408–9413.
- [9] J. Prost, F. Jülicher, J.-F. Joanny, Active gel physics, *Nat. Phys.* 11 (2) (February 2015) 111–117.
- [10] K. Kruse, J.F. Joanny, F. Jülicher, J. Prost, K. Sekimoto, Aster, Vortices, and Rotating Spirals in Active Gels of Polar Filaments, *Phys. Rev. Lett.* 92 (7) (February 2004) 078101.
- [11] M. Guo, A.J. Ehrlicher, M.H. Jensen, M. Renz, J.R. Moore, R.D. Goldman, J. Lippincott-Schwartz, F.C. MacKintosh, D.A. Weitz, Probing the stochastic, motor-driven properties of the cytoplasm using force spectrum microscopy, *Cell Camb. MA* 158 (4) (August 2014) 822–832.
- [12] H. Turlier, B. Audoly, J. Prost, J.F. Joanny, Furrow constriction in animal cell cytokinesis, *Biophys. J.* 106 (1) (January 2014) 114–123.
- [13] J.F. Joanny, J. Prost, Active gels as a description of the actin myosin cytoskeleton, *HFSP J.* 3 (2) (2009) 94–104.
- [14] K. Kruse, J.F. Joanny, F. Jülicher, J. Prost, K. Sekimoto, Generic theory of active polar gels: a paradigm for cytoskeletal dynamics, *Eur. Phys. J. E* 16 (1) (January 2005) 5–16.
- [15] S. Ramaswamy, M. Rao, Active-filament hydrodynamics: instabilities, boundary conditions and rheology, *New J. Phys.* 9 (11) (November 2007) 423.
- [16] A.J. Levine, F.C. MacKintosh, The Mechanics and Fluctuation Spectrum of Active Gels, *J. Phys. Chem. B* 113 (12) (March 2009) 3820–3830.
- [17] M.C. Marchetti, J.F. Joanny, S. Ramaswamy, T.B. Liverpool, J. Prost, M. Rao, R. Aditi Simha, Hydrodynamics of soft active matter, *Rev. Mod. Phys.* 85 (3) (July 2013) 1143–1189.
- [18] R.S. Lakes, *Viscoelastic Solids*, CRC Press, October 1998.
- [19] F.A. Morrison, *Understanding Rheology*, Oxford University Press, New York, January 2001.
- [20] G.N. Greaves, A.L. Greer, R.S. Lakes, T. Rouxel, Poisson's ratio and modern materials, *Nat. Mater.* 10 (11) (November 2011) 823–837.
- [21] A.J. Levine, T.C. Lubensky, One- and Two-Particle Microrheology, *Phys. Rev. Lett.* 85 (8) (August 2000) 1774–1777.
- [22] A.R. Bausch, F. Ziemann, A.A. Boulbitch, K. Jacobson, E. Sackmann, Local measurements of viscoelastic parameters of adherent cell surfaces by magnetic bead microrheometry, *Biophys. J.* 75 (4) (October 1998) 2038–2049.
- [23] D. Mizuno, D.A. Head, F.C. MacKintosh, C.F. Schmidt, Active and Passive Microrheology in Equilibrium and Nonequilibrium Systems, *Macromolecules* 41 (19) (October 2008) 7194–7202.
- [24] H.B. Callen, T.A. Welton, Irreversibility and Generalized Noise, *Phys. Rev.* 83 (1) (July 1951) 34–40.
- [25] R. Kubo, The fluctuation-dissipation theorem, *Rep. Prog. Phys.* 29 (1) (January 1966) 255.
- [26] A. Ashkin, J.M. Dziedzic, E. Bjorkholm, S. Chu, Observation of a single-beam gradient force optical trap for dielectric particles, *Opt. Lett.* 11 (5) (May 1986) 288–290.
- [27] S. Nader, S. Reihani, L.B. Oddershede, Improving optical trapping in the axial direction and a continuous change of the optimal trapping depth, *Proc. SPIE* 6644, Optical Trapping and Optical Manipulation IV 2007, p. 664421.
- [28] S.B. Smith, Y. Cui, C. Bustamante, Optical-trap force transducer that operates by direct measurement of light momentum, *Methods Enzymol.* 361 (2003) 134–162.
- [29] Z. Bryant, M.D. Stone, J. Gore, S.B. Smith, N.R. Cozzarelli, C. Bustamante, Structural transitions and elasticity from torque measurements on DNA, *Nature* 424 (6946) (July 2003) 338–341.
- [30] K. Berg-Sørensen, H. Flyvbjerg, Power spectrum analysis for optical tweezers, *Rev. Sci. Instrum.* 75 (3) (March 2004) 594–612.
- [31] P.M. Hansen, I. Marija Tolic-Nørrellykke, H. Flyvbjerg, K. Berg-Sørensen, tweezercalib 2.1: Faster version of MatLab package for precise calibration of optical tweezers, *Comput. Phys. Commun.* 175 (8) (October 2006) 572–573.
- [32] R.M. Simmons, J.T. Finer, S. Chu, J.A. Spudich, Quantitative measurements of force and displacement using an optical trap, *Biophys. J.* 70 (4) (April 1996) 1813–1822.
- [33] E.-L. Florin, A. Pralle, E.H.K. Stelzer, J.K.H. Horber, Photonic force microscope calibration by thermal noise analysis, *Appl. Phys. A Mater. Sci. Process.* 66 (7) (1998) S75–S78.
- [34] K.C. Neuman, S.M. Block, Optical trapping, *Rev. Sci. Instrum.* 75 (9) (2004) 2787–2809.
- [35] A. Farré, M. Montes-Usategui, A force detection technique for single-beam optical traps based on direct measurement of light momentum changes, *Opt. Express* 18 (11) (May 2010) 11955–11968.
- [36] M. Mahamdeh, E. Schäffer, Optical tweezers with millikelvin precision of temperature-controlled objectives and base-pair resolution, *Opt. Express* 17 (19) (September 2009) 17190–17199.
- [37] M. Bussonnier, K. Carvalho, J. Lemière, J.-F. Joanny, C. Sykes, T. Betz, Mechanical Detection of Long-Range Actin Network Emanating from a Biomimetic Cortex, *Biophys. J.* 107 (4) (August 2014) 854–862.
- [38] J. Peukes, T. Betz, Direct measurement of the cortical tension during the growth of membrane blebs, *Biophys. J.* 107 (8) (October 2014) 1810–1820.
- [39] N. Chenouard, I. Smal, F. de Chaumont, M. Maška, I.F. Sbalzarini, Y. Gong, J. Cardinale, C. Cartheil, S. Coraluppi, M. Winter, A.R. Cohen, W.J. Godinez, K. Rohr, Y. Kalaidzidis, L. Liang, J. Duncan, H. Shen, Y. Xu, K.E.G. Magnusson, J. Jaldén, H.M. Blau, P. Paul-Gilloteaux, P. Roudot, C. Kervrann, F. Waharte, J.-Y. Tinevez, S.L. Shorte, J. Willemse, K. Celler, G.P. van Wezel, H.-W. Dan, Y.-S. Tsai, C. Ortiz de Solórzano, J.-C. Olivo-Marin, E. Meijering, Objective comparison of particle tracking methods, *Nat. Methods* 11 (3) (March 2014) 281–289.
- [40] S.F. Tolic-Nørrellykke, E. Schäffer, J. Howard, F.S. Pavone, F. Jülicher, H. Flyvbjerg, Calibration of optical tweezers with positional detection in the back focal plane, *Rev. Sci. Instrum.* 77 (10) (2006) 103101–103101–11.
- [41] J. Mas, A.C. Richardson, S. Nader, S. Reihani, L.B. Oddershede, K. Berg-Sørensen, Quantitative determination of optical trapping strength and viscoelastic moduli inside living cells, *Phys. Biol.* 10 (4) (August 2013) 046006.
- [42] A.R. Bausch, W. Möller, E. Sackmann, Measurement of local viscoelasticity and forces in living cells by magnetic tweezers, *Biophys. J.* 76 (1 Pt 1) (1999) 573–579.
- [43] M. Puig-de Morales-Marinkovic, M. Grubulosa, J. Alcaraz, J. Mullol, G.N. Maksym, J.J. Fredberg, D. Navajas, Measurement of cell microrheology by magnetic twisting cytometry with frequency domain demodulation, *J. Appl. Physiol.* 91 (3) (September 2001) 1152–1159.
- [44] F. Amblard, B. Yurke, A. Pargellis, S. Leibler, A magnetic manipulator for studying local rheology and micromechanical properties of biological systems, *Rev. Sci. Instrum.* 67 (3) (March 1996) 818–827.
- [45] P. Kollmannsberger, B. Fabry, High-force magnetic tweezers with force feedback for biological applications, *Rev. Sci. Instrum.* 78 (11) (2007) 114301.
- [46] I. De Vlaminck, C. Dekker, Recent Advances in Magnetic Tweezers, *Annu. Rev. Biophys.* 41 (1) (2012) 453–472.
- [47] N. Wang, J.P. Butler, D.E. Ingber, Mechanotransduction across the cell surface and through the cytoskeleton, *Science* 260 (5111) (May 1993) 1124–1127.
- [48] S.M. Mijaïlović, M. Kojic, M. Živković, B. Fabry, J.J. Fredberg, A finite element model of cell deformation during magnetic bead twisting, *J. Appl. Physiol.* 93 (4) (October 2002) 1429–1436.
- [49] M. Radmacher, R.W. Tillmann, M. Fritz, H.E. Gaub, From molecules to cells: imaging soft samples with the atomic force microscope, *Science* 257 (5078) (September 1992) 1900–1905.
- [50] M. Radmacher, R.W. Tillmann, H.E. Gaub, Imaging viscoelasticity by force modulation with the atomic force microscope, *Biophys. J.* 64 (3) (March 1993) 735–742.
- [51] M. Radmacher, Studying the mechanics of cellular processes by atomic force microscopy, *Methods Cell Biol.* 83 (2007) 347–372.
- [52] H. Hertz, Über die Berührung Fester Elastischer Körper (on the contact of elastic solids), *J. Reine Angew. Math.* 92 (1881) 156–171.
- [53] I.N. Sneddon, The relation between load and penetration in the axisymmetric boussinesq problem for a punch of arbitrary profile, *Int. J. Eng. Sci.* 3 (1) (May 1965) 47–57.
- [54] R.E. Mahaffy, C.K. Shih, F.C. MacKintosh, J. Kas, Scanning probe-based frequency-dependent microrheology of polymer gels and biological cells, *Phys. Rev. Lett.* 85 (4) (July 2000) 880–883.

- [55] R.E. Mahaffy, S. Park, E. Gerde, J. Kas, C.K. Shih, Quantitative analysis of the viscoelastic properties of thin regions of fibroblasts using atomic force microscopy, *Biophys. J.* 86 (3) (March 2004) 1777–1793.
- [56] T.G. Mason, D.A. Weitz, Optical Measurements of Frequency-Dependent Linear Viscoelastic Moduli of Complex Fluids, *Phys. Rev. Lett.* 74 (7) (February 1995) 1250–1253.
- [57] J.C. Crocker, M.T. Valentine, E.R. Weeks, T. Gisler, P.D. Kaplan, A.G. Yodh, D.A. Weitz, Two-point microrheology of inhomogeneous soft materials, *Phys. Rev. Lett.* 85 (4) (July 2000) 888–891.
- [58] T.M. Squires, T.G. Mason, Fluid Mechanics of Microrheology, *Annu. Rev. Fluid Mech.* 42 (1) (2010) 413–438.
- [59] N. Fakhri, A.D. Wessel, C. Willms, M. Pasquali, D.R. Klopfenstein, F.C. MacKintosh, C.F. Schmidt, High-resolution mapping of intracellular fluctuations using carbon nanotubes, *Science* 344 (6187) (May 2014) 1031–1035.
- [60] M.J. Saxton, K. Jacobson, Single-particle tracking: applications to membrane dynamics, *Annu. Rev. Biophys. Biomol. Struct.* 26 (1997) 373–399.
- [61] J.M. Saxton, Single-particle tracking: the distribution of diffusion coefficients, *Biophys. J.* 72 (4) (1997) 1744–1753.
- [62] H. Qian, M.P. Sheetz, E.L. Elson, Single particle tracking. Analysis of diffusion and flow in two-dimensional systems, *Biophys. J.* 60 (4) (October 1991) 910–921.
- [63] S.S. Rogers, T.A. Waigh, X. Zhao, J.R. Lu, Precise particle tracking against a complicated background: polynomial fitting with Gaussian weight, *Phys. Biol.* 4 (3) (September 2007) 220.
- [64] T. Savin, P.S. Doyle, Static and dynamic errors in particle tracking microrheology, *Biophys. J.* 88 (1) (January 2005) 623–638.
- [65] T. Savin, P.S. Doyle, Role of a finite exposure time on measuring an elastic modulus using microrheology, *Phys. Rev. E* 71 (4) (2005) 041106.
- [66] P. Bursac, B. Fabry, X. Trepaut, G. Lenormand, J.P. Butler, N. Wang, J.J. Fredberg, Steven S. An, Cytoskeleton dynamics: fluctuations within the network, *Biochem. Biophys. Res. Commun.* 355 (2) (April 2007) 324–330.
- [67] W. Denk, W.W. Webb, Optical measurement of picometer displacements of transparent microscopic objects, *Appl. Opt.* 29 (16) (1990) 2382–2391.
- [68] F. Gittes, C.F. Schmidt, Interference model for back-focal-plane displacement detection in optical tweezers, *Opt. Lett.* 23 (1) (January 1998) 7–9.
- [69] F. Gittes, C.F. Schmidt, Signals and noise in micromechanical measurements, *Methods Cell Biol.* 55 (1997) 129–156.
- [70] A. Pralle, M. Prummer, E.L. Florin, E.H. Stelzer, J.K. Hörber, Three-dimensional high-resolution particle tracking for optical tweezers by forward scattered light, *Microsc. Res. Tech.* 44 (5) (March 1999) 378–386.
- [71] K.C. Vermeulen, J. van Mameren, G.J.M. Stienen, E.J.G. Peterman, G.J.L. Wuite, C.F. Schmidt, Calibrating bead displacements in optical tweezers using acousto-optic deflectors, *Rev. Sci. Instrum.* 77 (1) (2006) (013704–013704–6).
- [72] T. Betz, M. Lenz, J.-F. Joanny, C. Sykes, ATP-dependent mechanics of red blood cells, *Proc. Natl. Acad. Sci. U. S. A.* 106 (36) (2009) 15320–15325.
- [73] M. Speidel, L. Friedrich, A. Rohrbach, Interferometric 3D tracking of several particles in a scanning laser focus, *Opt. Express* 17 (2) (January 2009) 1003–1015.
- [74] M. Koch, A. Rohrbach, Object-adapted optical trapping and shape-tracking of energy-switching helical bacteria, *Nat. Photonics* 6 (10) (2012) 680–686.
- [75] T. Luo, K. Mohan, P.A. Iglesias, D.N. Robinson, Molecular mechanisms of cellular mechanosensing, *Nat. Mater.* 12 (11) (November 2013) 1064–1071.
- [76] B.D. Hoffman, J.C. Crocker, Cell mechanics: dissecting the physical responses of cells to force, *Annu. Rev. Biomed. Eng.* 11 (2009) 259–288.
- [77] J. Etienne, J. Fouchard, D. Mitrosilis, N. Bufl, P. Durand-Smet, A. Asnacios, Cells as liquid motors: Mechanosensitivity emerges from collective dynamics of actomyosin cortex, *Proc. Natl. Acad. Sci.* 112 (9) (March 2015) 2740–2745.
- [78] S. Ramaswamy, The Mechanics and Statistics of Active Matter, *Annu. Rev. Condens. Matter Phys.* 1 (9) (April 2010) 1–23.
- [79] A. Okubo, Dynamical aspects of animal grouping: swarms, schools, flocks, and herds, *Adv. Biophys.* 22 (1986) 1–94.
- [80] G. de Magistris, D. Marenduzzo, An introduction to the physics of active matter, *Physica A: Statistical Mechanics and its Applications* 418 (2015) 65–77.
- [81] S.C. Takatori, W. Yan, J.F. Brady, Swim Pressure: Stress Generation in Active Matter, *Phys. Rev. Lett.* (2014).
- [82] A. Cavagna, L. Del Castello, I. Giardina, T. Grigera, A. Jelic', S. Melillo, T. Mora, L. Parisi, E. Silvestri, M. Viale, Flocking and turning: a new model for self-organized collective motion, *J. Stat. Phys.* 158 (3) (2014) 601–627.
- [83] A. Attanasi, A. Cavagna, L. Del Castello, I. Giardina, Information transfer and behavioural inertia in starling flocks, *Nat. Phys.* 10 (9) (2014) 691–696.
- [84] N. Kumar, H. Soni, S. Ramaswamy, A.K. Sood, Flocking at a distance in active granular matter, *Nat. Commun.* 5 (4688) (2014).
- [85] W. Bialek, A. Cavagna, I. Giardina, T. Mora, E. Silvestri, M. Viale, A.M. Walczak, Statistical mechanics for natural flocks of birds, *Proc. Natl. Acad. Sci.* 109 (13) (March 2012) 4786–4791.
- [86] D.S. Lemons, A. Gythiel, Paul Langevin's 1908 paper "On the Theory of Brownian Motion" "Sur la théorie du mouvement brownien," *CR Acad. Sci. (Paris)* [bold 146], 530–533 (1908), *Am. J. Phys.* 65 (1079) (1997).
- [87] A. Einstein, On the theory of the Brownian movement, *Ann. Phys.* 4 (19) (1906) 371–378.
- [88] T.G. Mason, Estimating the viscoelastic moduli of complex fluids using the generalized Stokes-Einstein equation, *Rheol. Acta* 39 (4) (2000) 371–378.
- [89] F. Gittes, B. Schnurr, P.D. Olmsted, F.C. MacKintosh, C.F. Schmidt, Microscopic viscoelasticity: shear moduli of soft materials determined from thermal fluctuations, *Phys. Rev. Lett.* 79 (17) (1997) 3286.
- [90] F.C. MacKintosh, J. Kas, P.A. Janmey, Elasticity of semiflexible biopolymer networks, *Phys. Rev. Lett.* 75 (24) (December 1995) 4425–4428.
- [91] D.C. Morse, Viscoelasticity of concentrated isotropic solutions of semiflexible polymers. 1. Model and stress tensor, *Macromolecules* 31 (20) (1998) 7030–7043.
- [92] D.C. Morse, Viscoelasticity of concentrated isotropic solutions of semiflexible polymers. 2. Linear response, *Macromolecules* 31 (20) (1998) 7044–7067.
- [93] É. Fodor, M. Guo, N. Gov, P. Visco, D. Weitz, F. van Wijland, Activity Driven Fluctuations in Living Cells, May 2015 (arXiv:1505.06489).
- [94] É. Fodor, K. Kanazawa, H. Hayakawa, P. Visco, F. van Wijland, Energetics of active fluctuations in living cells, *Phys. Rev. E* 90 (4) (October 2014) 042724.
- [95] T. Harada, S.-i. Sasa, Equality connecting energy dissipation with a violation of the fluctuation-response relation, *Phys. Rev. Lett.* 95 (13) (September 2005) 130602.
- [96] O. Chaudhuri, S.H. Parekh, D.A. Fletcher, Reversible stress softening of actin networks, *Nature* 445 (7125) (January 2007) 295–298.
- [97] H. Lee, J. Ferrer, M. Lang, R. Kamm, Molecular origin of strain softening in cross-linked F-actin networks, *Phys. Rev. E* (2010).
- [98] T. Kim, M.L. Gardel, Ed. Munro, Determinants of fluidlike behavior and effective viscosity in cross-linked actin networks, *Biophys. J.* 106 (3) (February 2014) 526–534.
- [99] C. Storm, J.J. Pastore, F.C. MacKintosh, T.C. Lubensky, P.A. Janmey, Nonlinear elasticity in biological gels, *Nature* 435 (7039) (May 2005) 191–194.
- [100] H. Kang, Qi Wen, P.A. Janmey, J.X. Tang, E. Conti, F.C. Mackintosh, Nonlinear elasticity of stiff filament networks: strain stiffening, negative normal stress, and filament alignment in fibrin gels, *J. Phys. Chem. B* 113 (12) (March 2009) 3799–3805.
- [101] T. Kim, W. Hwang, R.D. Kamm, Dynamic role of cross-linking proteins in actin rheology, *Biophys. J.* 101 (7) (October 2011) 1597–1603.
- [102] Y. Yang, M. Bai, W.S. Klug, A.J. Levine, M.T. Valentine, Microrheology of highly crosslinked microtubule networks is dominated by force-induced crosslinker unbinding, *Soft Matter* 9 (2) (January 2013) 383–393.
- [103] K.M. Schmoller, P. Fernandez, R.C. Arevalo, D.L. Blair, A.R. Bausch, Cyclic hardening in bundled actin networks, *Nat. Commun.* 1 (134) (2010).
- [104] T. Liverpool, A. Maggs, A. Ajdari, Viscoelasticity of Solutions of Motile Polymers, *Phys. Rev. Lett.* 86 (18) (April 2001) 4171–4174.
- [105] M. Keller, R. Thermann, M.A. Dichtl, A.R. Bausch, E. Sackmann, Slow filament dynamics and viscoelasticity in entangled and active actin networks, *Philos. Trans. R. Soc. A Math. Phys. Eng. Sci.* 361 (1805) (April 2003) 699–711 (discussion 711–2).
- [106] D. Smith, F. Ziebert, D. Humphrey, C. Duggan, M. Steinbeck, W. Zimmermann, J. Kas, Molecular motor-induced instabilities and cross linkers determine biopolymer organization, *Biophys. J.* 93 (12) (December 2007) 4445–4452.
- [107] S.K. Vogel, Z. Petrasek, F. Heinemann, P. Schwille, Myosin motors fragment and compact membrane-bound actin filaments, *eLife Sci.* 2 (2013).
- [108] L. Haviv, D. Gillo, F. Backouche, A. Bernheim-Grosbäss, A cytoskeletal demolition worker: myosin II acts as an actin depolymerization agent, *J. Mol. Biol.* 375 (2) (January 2008) 325–330.
- [109] T.S. Matsui, R. Kaunas, M. Kanazaki, M. Sato, S. Deguchi, Non-muscle myosin II induces disassembly of actin stress fibres independently of myosin light chain phosphorylation, *Interface Focus* 1 (5) (October 2011) 754–766.
- [110] X. Trepaut, L. Deng, S.S. An, D. Navajas, D.J. Tschumperlin, W.T. Gerthoffer, J.P. Butler, J.J. Fredberg, Universal physical responses to stretch in the living cell, *Nature* 447 (7144) (May 2007) 592–595.
- [111] R. Krishnan, C. Young Park, Y.-C. Lin, J. Mead, R.T. Jaspers, X. Trepaut, G. Lenormand, D. Tambe, A.V. Smolensky, A.H. Knoll, J.P. Butler, J.J. Fredberg, Reinforcement versus fluidization in cytoskeletal mechanoresponsiveness, *PLoS ONE* 4 (5) (2009) e5486.
- [112] W.W. Ahmed, T.A. Saif, Active transport of vesicles in neurons is modulated by mechanical tension, *Sci. Rep.* 4 (4481) (March 2014).
- [113] B.R. Parry, I.V. Surovtsev, M.T. Cabeen, C.S. O'Hern, E.R. Dufresne, C. Jacobs-Wagner, The Bacterial Cytoplasm Has Glass-like Properties and Is Fluidized by Metabolic Activity, *Cell Camb.* MA 156 (1–2) (January 2014) 183–194.
- [114] C.J. Chan, A.E. Ekpenyong, S. Golifer, W. Li, K.J. Chalut, O. Otto, J. Elgeti, J. Guck, F. Lautenschläger, Myosin II Activity Softens Cells in Suspension, *Biophysj.* 108 (8) (April 2015) 1856–1869.
- [115] F.C. MacKintosh, A.J. Levine, Nonequilibrium mechanics and dynamics of motor-activated gels, *Phys. Rev. Lett.* 100 (1) (2008) 18104.
- [116] C.P. Broedersz, F.C. MacKintosh, Molecular motors stiffen non-affine semiflexible polymer networks, *Soft Matter* 7 (7) (2011) 3186.
- [117] O.J.N. Bertrand, D. Kuchnir Fygenson, O.A. Saleh, Active, motor-driven mechanics in a DNA gel, *Proc. Natl. Acad. Sci.* 109 (43) (October 2012) 17342–17347.
- [118] W.A. Lam, O. Chaudhuri, A. Crow, K.D. Webster, T.-D. Li, A. Kita, J. Huang, D.A. Fletcher, Mechanics and contraction dynamics of single platelets and implications for clot stiffening, *Nat. Mater.* 10 (1) (December 2010) 61–66.
- [119] A. Chaigne, C. Campillo, N.S. Gov, R. Voituriez, J. Azoury, C. Umaña-Díaz, M. Almonacid, I. Queguiner, P. Nassoy, C. Sykes, M.-H. Verlhac, M.-E. Terret, A soft cortex is essential for asymmetric spindle positioning in mouse oocytes, *Nat. Cell Biol.* 15 (8) (August 2013) 958–966.
- [120] V. Schaller, K.M. Schmoller, E. Karaköse, B. Hammerich, M. Maier, A.R. Bausch, Crosslinking proteins modulate the self-organization of driven systems, *Soft Matter* 9 (30) (2013) 7229.
- [121] V. Schaller, C. Weber, C. Semmrich, E. Frey, A.R. Bausch, Polar patterns of driven filaments, *Nature* 467 (7311) (September 2010) 73–77.
- [122] V. Schaller, C. Weber, E. Frey, A.R. Bausch, Polar pattern formation: hydrodynamic coupling of driven filaments, *Soft Matter* 7 (7) (2011) 3213–3218.
- [123] V. Schaller, C. Weber, B. Hammerich, E. Frey, A.R. Bausch, Frozen steady states in active systems, *Proc. Natl. Acad. Sci. U. S. A.* 108 (48) (2011) 19183–19188.
- [124] V. Schaller, A.R. Bausch, Topological defects and density fluctuations in collectively moving systems, *Proc. Natl. Acad. Sci. U. S. A.* (2013).

- [126] S. Köhler, V. Schaller, A.R. Bausch, Structure formation in active networks, *Nat. Mater.* 10 (6) (June 2011) 462–468.
- [127] T. Sanchez, D. Welch, D. Nicastro, Z. Dogic, Cilia-like beating of active microtubule bundles, *Science* 333 (6041) (July 2011) 456–459.
- [128] T. Sanchez, D.T.N. Chen, S.J. DeCamp, M. Heymann, Z. Dogic, Spontaneous motion in hierarchically assembled active matter, *Nature* 491 (7424) (November 2012) 431–434.
- [129] F.C. Keber, E. Loiseau, T. Sanchez, S.J. DeCamp, L. Giomi, M.J. Bowick, M. Cristina Marchetti, Z. Dogic, A.R. Bausch, Topology and dynamics of active nematic vesicles, *Science* 345 (6201) (September 2014) 1135–1139.
- [130] M. Almonacid, W.W. Ahmed, W.W. Bussonnier, M. Mailly, T. Betz, R. Voituriez, M.H. Verlhac, Active diffusion positions the nucleus in mouse oocytes, *Nature cell biology* (2015).
- [131] A.W. Lau, B.D. Hoffman, A. Davies, J.C. Crocker, T.C. Lubensky, Microrheology, stress fluctuations, and active behavior of living cells, *Phys. Rev. Lett.* 91 (19) (2003) 198101.
- [132] C. Wilhelm, Out-of-equilibrium microrheology inside living cells, *Physical review letters* 101.2 (2008) 028101.
- [133] B.D. Hoffman, G. Massiera, K.M. Van Citters, J.C. Crocker, The consensus mechanics of cultured mammalian cells, *Proc. Natl. Acad. Sci. U.S.A.* 103 (27) (2006) 10259–10264.
- [134] P. Martin, A.J. Hudspeth, F. Jülicher, Comparison of a hair bundle's spontaneous oscillations with its response to mechanical stimulation reveals the underlying active process, *Proc. Natl. Acad. Sci.* 98 (25) (2001) 14380–14385.

Modeling the dynamics of a tracer particle in an elastic active gel

E. Ben-Isaac,¹ É. Fodor,² P. Visco,² F. van Wijland,² and Nir S. Gov¹

¹Department of Chemical Physics, Weizmann Institute of Science, Rehovot 76100, Israel

²Laboratoire Matière et Systèmes Complexes, UMR 7057 CNRS/P7, Université Paris Diderot, 10 rue Alice Domon et Léonie Duquet, 75205 Paris cedex 13, France

(Received 18 November 2014; published 22 July 2015)

The internal dynamics of active gels both in artificial (*in vitro*) model systems and inside the cytoskeleton of living cells has been extensively studied with experiments of recent years. These dynamics are probed using tracer particles embedded in the network of biopolymers together with molecular motors, and distinct nonthermal behavior is observed. We present a theoretical model of the dynamics of a trapped active particle, which allows us to quantify the deviations from equilibrium behavior, using both analytic and numerical calculations. We map the different regimes of dynamics in this system and highlight the different manifestations of activity: breakdown of the virial theorem and equipartition, different elasticity-dependent “effective temperatures,” and distinct non-Gaussian distributions. Our results shed light on puzzling observations in active gel experiments and provide physical interpretation of existing observations, as well as predictions for future studies.

DOI: 10.1103/PhysRevE.92.012716

PACS number(s): 87.10.Ca, 05.40.-a, 87.10.Mn

I. INTRODUCTION

In vitro experiments have probed the nonthermal (active) fluctuations in an “active gel,” which is most commonly realized as a network composed of cross-linked filaments (such as actin) and molecular motors (such as myosin-II) [1–4]. The fluctuations inside the active gel were measured using the tracking of individual tracer particles and used to demonstrate the active (nonequilibrium) nature of these systems through the breaking of the Fluctuation-Dissipation theorem (FDT) [2]. In these active gels, myosin-II molecular motors generate relative motion between the actin filaments, through consumption of ATP, and thus drive the athermal random motion of the probe particles dispersed throughout the network. This tracking technique was also implemented in living cells [5–7]. The motion of these tracers in cells was also shown to deviate from simple thermal Brownian diffusion.

There are several puzzling observations of the dynamics of the tracer particles inside the active gels, for example, the distinct non-Gaussianity of the displacement correlations and their time dependence [1,4,8]. We propose here a simple model for the random active motion of a tracer particle within a (linearly) elastic active gel, and we use our model to resolve their distinct nonequilibrium dynamics. On long time scales the tracer particles are observed to perform hopping-like diffusion, which is beyond the regime of the present model and will be treated in following work, as will be the introduction of nonlinear elasticity [9]. The activity is modeled through colored shot noise [10,11], and the elastic gel is described by a confining harmonic potential. We use the model to derive expressions directly related to the experimentally accessible observations, such as the position and velocity distributions and their deviations from the thermal Gaussian form. Our model allows us to offer a physical interpretation to existing experiments, to characterize the microscopic active processes in the active gel, and to make specific predictions for future exploration of the limits of the active forces and elasticity. The simplicity of this model makes this model applicable to a wide range of systems and allows us to gain analytic solutions, intuition, and understanding of the dynamics, which is usually

lacking in out-of-equilibrium systems. This would be more difficult to obtain with a more complex description of the gel, such as visco-elastic that has more intrinsic time scales.

II. MODEL

Our model treats a particle in a harmonic potential, kicked randomly by thermal and active forces (active noise) [11]. The corresponding Langevin equation for the particle velocity v (in one dimension or one component in higher dimensions, with the mass set to $m = 1$) is

$$\dot{v} = -\lambda v + f_a + f_T - \frac{\partial U(x)}{\partial x}, \quad (1)$$

where λ is the effective friction coefficient and the harmonic potential is $U(x) = kx^2/2$, with k proportional to the bulk modulus of the gel (related to the gel density, cross-linker density, and other structural factors). The thermal force f_T is an uncorrelated Gaussian white noise: $\langle f_T(t)f_T(t') \rangle = 2\lambda T\delta(t - t')$, with T the ambient temperature, and Boltzmann’s constant set to $k_B = 1$.

We model the active force f_a as arising from the independent action of N_m molecular motors, each motor producing pulses of a given fixed force $\pm f_0$, for a duration $\Delta\tau$ (either a constant or drawn from a Poissonian process with an average value $\Delta\tau$, i.e., shot noise), with a random direction (sign). The active pulses turn on randomly as a Poisson process with an average waiting time τ (during which the active force is zero), which determines the “duty ratio” of the motor (the probability to be turned “on”): $p_{on} = \Delta\tau/(\tau + \Delta\tau)$.

III. RESULTS: MEAN KINETIC AND POTENTIAL ENERGIES

The mean-square velocity and position fluctuations of the trapped particle, essentially the mean kinetic ($T_v = \langle v^2 \rangle$) and potential ($T_x = k\langle x^2 \rangle$) energies, can be calculated for the case of shot noise force correlations [details given in the Appendices, Eqs. (A1a)–(C4), and Figs. 3–4]. Note that the mean $\langle \cdot \rangle$ is over many realizations of the system or over a long

time. In the limit of vanishing trapping potential the position fluctuations $\langle x^2 \rangle$ diverge, but the potential energy approaches a constant: $T_x|_{k \rightarrow 0} \rightarrow f_0^2 \Delta\tau / \lambda$. The kinetic energy approaches the constant value for a free particle [11]: $T_v|_{k \rightarrow 0} \rightarrow T_v/(1 + \lambda\Delta\tau)$. We therefore find that the virial theorem is in general not satisfied in this active system, which in a harmonic potential gives $T_v|_{eq} = T_x|_{eq}$, even in the limit of weak trapping. The virial theorem, and equipartition, breaks down due to the strong correlations between the particle position and the applied active force: In the limit of perfect correlations, the particle is stationary at $x = \pm x_0$ when the force is turned on (the stationary position in the trap where the potential balances the active force: $x_0 = f_0/k$), and at $x = 0$ when it is off. In this extreme case the potential energy is finite while the kinetic energy is zero.

In the limit of strong trapping $k \rightarrow \infty, k/\lambda^2 \gg 1$, the potential energy behaves as $T_x \propto k^{-1}$ [Eqs. (B6) and (B9)], while the kinetic energy decays faster as $T_v \propto k^{-3/2}$ [Eq. (D2)]. One can understand this limit as follows: When the trapping is very strong, the shortest time scale in the problem is the natural oscillation frequency in the trap, $\omega_k \sim \sqrt{k}$. In this regime of $k\Delta\tau^2 \gg 1$ we find that during the active pulse $\Delta\tau$, the particle reaches x_0 , and the mean potential energy is therefore proportional to $T_x \sim kx_0^2 \propto 1/k$. The kinetic energy in this limit decays faster, since the fraction of time that the particle is moving is only during the acceleration phase determined by the time scale $\omega_k^{-1} \sim \sqrt{k}$. We therefore find that in the presence of strong elastic restoring forces the potential energy will be much larger than the kinetic energy, in an active system ($T_x \gg T_v$). This was recently found in the study of active semiflexible polymers [12].

Note that in a real active gel the different parameters may be coupled: larger local density of the network filaments increases the local value of the elastic stiffness parameter k but may also increase locally the density of motors and their ability to exert an effective force, thereby increasing N_m and f_0 . The tracer bead behavior as expressed by T_v and T_x can therefore be a complex function of the local network parameters.

IV. RESULTS: VELOCITY AND POSITION DISTRIBUTIONS

The distributions of the velocity and position in the different regimes are shown in Fig. 1 for the case of a single active motor. The simulations of the model were carried out using explicit Euler integration of Eq. (1) (see also the Appendices for details). We study this case in order to highlight the deviations from Gaussian (equilibrium-like) behavior, which is restored by many simultaneous motors [11]. In an infinite gel, with a constant density of motors, we may therefore treat the distant (and numerous) motors as giving rise to an additional thermal-like contribution to the tracer dynamics [Eqs. (D1) and (D2)], while the nonequilibrium behavior is dominated by a single proximal motor [1].

In the limit of weak damping, $\lambda\Delta\tau \ll 1$, both the position and velocity distributions are very close to Gaussian, with the width of the Gaussian distributions given by T_v and T_x [Figs. 1(b) and 1(d), Eqs. (B4) and (C1)]: $P(v) \propto \exp[-v^2/(2T_v)]$, $P(x) \propto \exp[-kx^2/(2T_x)]$.

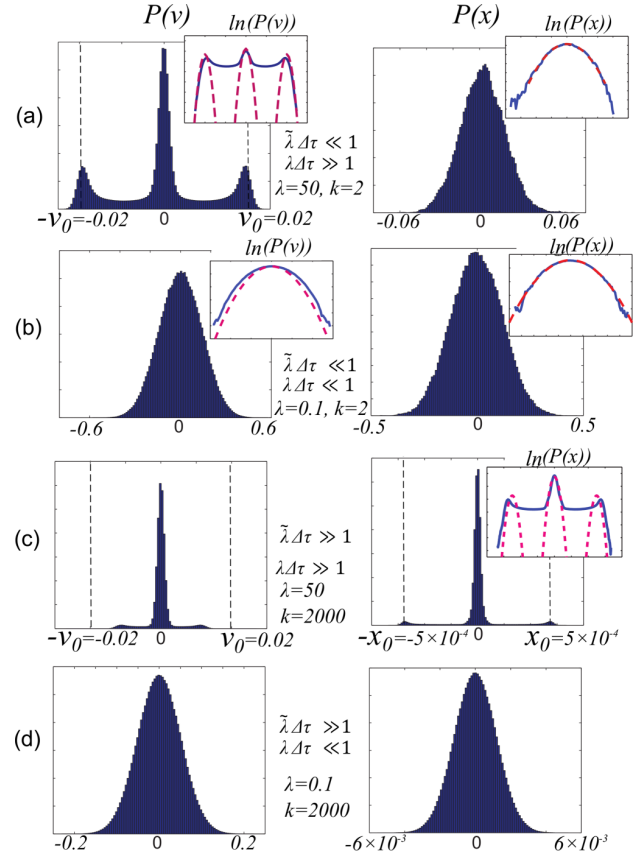


FIG. 1. (Color online) Distribution of position and velocity for particle trapped within a harmonic trap of various stiffness ($k = 1, 1000$ for a, b and c, d, respectively) and for different regimes of friction ($\lambda = 50, 0.1$ for a, c and b, d, respectively). The time scale of the active bursts is $\Delta\tau = 0.1$, the amplitude of the active force $f_0 = 1$, and the waiting time $\tau = 1$ (so that $p_{on} \approx 0.1$). For simplicity we plot the behavior for the case of a single motor with a constant burst duration. The insets compare the simulated distribution (blue line) to the analytic approximation (red dashed line), in log-linear scale, as simple Gaussians or as a sum of shifted thermal Gaussians.

In the highly damped limit, $\lambda\Delta\tau \gg 1$, the distributions become highly non-Gaussian [Figs. 1(a) and 1(c)]. We can make a useful approximation in this limit, by neglecting the inertial term in Eq. (1) and get the following equation for the particle position x inside the potential well:

$$\lambda v = -kx + f_a + f_T \quad (2)$$

$$\Rightarrow \dot{x} = -\tilde{\lambda}x + \frac{f_a + f_T}{\lambda}, \quad (3)$$

where $\tilde{\lambda} = k/\lambda$. This equation is now analogous to the equation for the velocity v of a free particle [Eq. (1) when $U(x) = 0$]. Due to this analogy we can use the analytic solutions for the free particle [11] to describe the particle position in the well. For weak trapping [Fig. 1(a)], we therefore expect the position distribution to be roughly Gaussian, since we are in the limit of $\tilde{\lambda}\Delta\tau \ll 1$ of Eq. (3), with a width given by [from

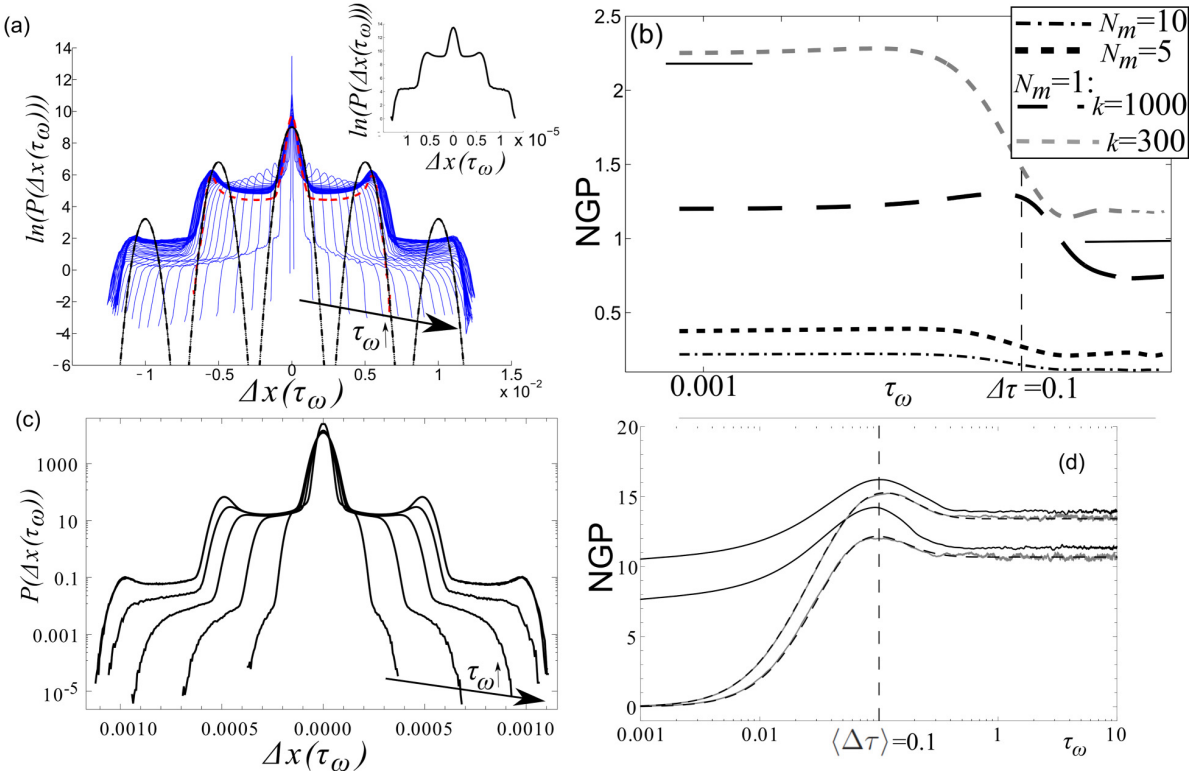


FIG. 2. (Color online) (a) Distribution of particle displacements $P[\Delta x(\tau_\omega)]$, for various lag time duration τ_ω (blue lines), for a single motor and constant burst duration. The traces correspond to increasing time lag durations (black arrow), in the range $1 > \tau_\omega > 5 \times 10^{-4}$. The red dashed line denotes the spatial distribution $P(x)$, and the black dashed lines denote $P[\Delta x(\infty)]$ [Eq. (6)] for the approximation of $P(x)$ as a sum of three Gaussians. Inset shows the displacement distribution for very short lag times τ_ω . Parameters as in Fig. 1(c). (b) Calculated NGP for the $P[\Delta x(\tau_\omega)]$, for various number of motors (N_m), and confinement strength. The short horizontal black lines denote (left) the NGP of $P(x)$, and (right) of $P[\Delta x(\infty)]$ [Eq. (6)], for the $k = 1000, N_m = 1$ case. (c) Displacement distributions [as in (a)] for a calculation without the inertia term [Eq. (2)], using $k = 1000$, Poissonian $\langle \Delta\tau \rangle = 0.1$, and increasing lag time indicated by the arrow $\tau_\omega = 10^{-3}, 2.5 \times 10^{-3}, 5 \times 10^{-3}, 10^{-2}, 1$, and (d) the corresponding NGP, comparing the simulation (solid gray lines) to the analytical result (see Appendix for details), for $k = 300, 1000$ (top, bottom). The NGP with inertia is given by the solid black lines.

Eq. (3) and (B6)]

$$T'_x = \frac{p_{on} N_m \lambda (\tilde{\lambda} \Delta\tau + e^{-\tilde{\lambda} \Delta\tau} - 1)}{k^2 \Delta\tau} f_0^2, \quad (4)$$

$$T_x = 2 \frac{p_{on} N_m \langle \Delta\tau \rangle}{\lambda (1 + \tilde{\lambda} \langle \Delta\tau \rangle)} f_0^2, \quad (5)$$

where T'_x describes the case of a constant $\Delta\tau$ and T_x the case of a Poissonian burst distribution and fits well the calculated distribution [inset of Fig. 1(a)]. In the limit of weak confinement we expect the velocity distribution to approach the behavior of the free damped particle [11], which is well approximated as a sum of thermal Gaussians, centered at $v = 0, \pm v_0$ ($v_0 = F_0/\lambda$). This is indeed a good approximation, as shown in the inset of Fig. 1(a).

For strong potentials [$\tilde{\lambda} \Delta\tau \gg 1$, Fig. 1(c)] we expect from the analogy given in Eq. (3) that the spatial distribution is now well described by the sum of shifted thermal Gaussians [Fig. 1(c)] [11], centered at $x = 0, \pm x_0$. The velocity distribution in this regime is also non-Gaussian: the maximal active velocity is of order v_0 at the origin of the potential, but since the particle immediately slows due to the confinement (up to a

complete stop at $\pm x_0$), the peaks of the distribution are located at roughly $\pm v_0/2$.

V. RESULTS: NON-GAUSSIANITY OF THE DISPLACEMENT DISTRIBUTION

The distribution of relative particle displacements (Van Hove correlation function) $P[\Delta x(\tau_\omega)]$, where $\Delta x(\tau_\omega) = x(t + \tau_\omega) - x(t)$ (τ_ω is the lag-time duration), is a useful measure for the particle dynamics. We plot it in Fig. 2(a) for the interesting regime of strong confinement and damping and compared to the distribution of particle positions $P(x)$ [Fig. 1(c)]. We see that $P[\Delta x(\tau_\omega)]$ has double the number of peaks of $P(x)$ and is distinctly non-Gaussian for all τ_ω . In Fig. 2(c) we show that the same qualitative behavior is obtained for Poissonian burst duration.

The deviations from Gaussianity are quantified in Fig. 2(b) using the Non-Gaussianity Parameter (NGP) of the displacement distributions: $\kappa = \langle \Delta x^4 \rangle / 3 \langle \Delta x^2 \rangle^2 - 1$. This deviation of the kurtosis from the value for a Gaussian is an established measure for studying distributions [13]. We find that the NGP has a finite value for $\tau_\omega \rightarrow 0$. This is as a consequence of the periods during which the particle is accelerated by the active

force, and the result is a finite probability for displacements of the order of $\Delta x \simeq v_0 \tau_\omega$ [inset of Fig. 2(a)]. With increasing τ_ω the NGP reaches a maximum, at lag times that are of order $\Delta\tau$, where the full effect of the active bursts is observed.

We find that the maximal value of the NGP for $P[\Delta x(\tau_\omega)]$ is close to the NGP of $P(x)$ [Fig. 2(b)], which is a function for which we have a good analytic approximation [11] [Eqs. (F1) and (F2)]. In the limit of $\tau_\omega \rightarrow \infty$ the calculated NGP remains finite and can be calculated analytically since the displacement distribution becomes

$$P[\Delta x(\infty)] = \int_{-\infty}^{\infty} P(x)P(x + \Delta x) dx, \quad (6)$$

and the $P(x)$ in this regime is well approximated by the sum of shifted thermal Gaussians [inset of Fig. 1(c)]. This calculation fits well the simulated result [Fig. 2(b)]. For a larger number of motors, the distribution $P[\Delta x(\tau_\omega)]$ approach a Gaussian [Figs. 2(b) and 6].

In the limit where we discard inertia from the equations of motion [Eq. (2)], we can calculate the NGP analytically (see details in the Appendices). In Fig. 2(c) we plot the displacement distributions for this case, and in Fig. 2(d) we show that indeed the analytical calculation describes exactly the simulation results. We find that this treatment captures correctly the qualitative features of the full system, such as the position of the peak, followed by a constant value at long lag times. The large discrepancy is in the limit of $\tau_\omega \rightarrow 0$, where the inertial effects of the oscillations inside the trap are missing from Eq. (2).

VI. RESULTS: FDT

An alternative method to characterize the nonequilibrium dynamics is through the deviations from the FDT [2]. We can quantify these deviations by defining an effective temperature, using the Fourier transform of the position fluctuations [$S_{xx}(\omega)$] and linear response [susceptibility of the position to an external force $\chi(\omega)$] of the system. We can calculate both for our trapped particle position using Eq. (3) for the $\tilde{\lambda}\Delta\tau \gg 1$ limit, to get [for Poissonian burst duration $\Delta\tau$, see details in Appendix G, Eqs. (G1)–(G3)]

$$T_{FDT}(\omega) = \frac{\omega S_{xx}(\omega)}{2\text{Im}[\chi(\omega)]} = \frac{N_m p_{on} f_0^2 \langle \Delta\tau \rangle}{\lambda[1 + (\omega \langle \Delta\tau \rangle)^2]} + T. \quad (7)$$

Note that $T_{FDT}(\omega)$ is independent of the shape of the harmonic potential (k) and is identical to the result for a free active particle [11]. This result highlights the fact that while different “effective temperatures” in an active system [T_v and T_x , Eqs. (4) and (5)] give a measure of the activity, they can have very different properties.

VII. DISCUSSION

We now use our results to interpret several experiments on active gels *in vitro* and extract the values that characterize these active systems. In Ref. [2] the breakdown of the FDT was measured. Comparing to our T_{FDT} [Eq. (G3)] we find that the onset of the deviation from equilibrium occurs for frequencies $\omega \leq \Delta\tau^{-1}$, from which we find that $\Delta\tau \approx 100$ ms, which is the scale of the release time of the myosin-II-induced stress [2] in this system. The measured deviation from

the FDT was found to increase with decreasing frequency [2] and at the lowest measured frequencies the ratio was found to be $T_{FDT}(\omega \rightarrow 0)/T \approx 20\text{--}100$. This number fixes for us the combination of the parameters given in Eq. (G3).

Recent experiments shed more detail on the active motion in this system [1], and it was found that the tracer particle performs random confined motion interspersed by periods of large excursions. The confined motion part can be directly related to the mean-square displacement in our model T_x [Eq. (5)] and is observed to be a factor of $T_x/T \approx 10\text{--}50$ larger than in the inert system (not containing myosins) [1]. These values are in general agreement with the values extracted above for T_{FDT} from Ref. [2], and note that we predict [Eqs. (5) and (G3)]: $T_{FDT}(\omega \rightarrow 0)/T_x = 1 + \tilde{\lambda}\langle \Delta\tau \rangle > 1$.

Furthermore, in these experiments [1] it was observed that the distribution of relative particle displacements $P[\Delta x(\tau_\omega)]$ is highly non-Gaussian. Comparing this to Fig. 2(b) we note that both the experiments and in our calculations the NGP has a finite value for $\tau_\omega \rightarrow 0$. With increasing τ_ω the NGP reaches a maximum, both in the experiments and in our calculations [Figs. 2(b) and 2(d)]. By comparing to our model we expect the peak to appear at $\tau_\omega \approx \Delta\tau$, so the observations [1] suggest the burst duration is of order $\Delta\tau \approx 1\text{--}10$, in agreement with similar studies [4,8]. Note that very similar NGP time scales were observed in living cells [14,15]. Our model predicts that the maximal value of the NGP is a nonmonotonic function of p_{on} , and this may be explored by varying the concentration of ATP in the system. Furthermore, from our model we predict that the NGP decrease with decreasing active force, and increasing stiffness of the confining network [Figs. 2(b) and 2(d), Eq. (F2)]. These predictions can be related to the observed activity dependence of the NGP in cells [15] and the decay of the NGP during the aging and coarsening of an active gel [4].

The large observed deviations from Gaussianity indicate that the particle is in the strong confinement regime: $\tilde{\lambda}\langle \Delta\tau \rangle > 1$. The maximal value of the observed NGP $\approx 2\text{--}4$ can be used to get an estimate of T_x , by taking it to be equal to NGP_{\max} [Eq. (F2)]. This gives us $T_x \approx 10\text{--}30k_B T$ and $p_{on} \approx 2\%\text{--}3\%$. This value of T_x is in good agreement with the estimate made above. The value of p_{on} is in agreement with the observation that the waiting-time between bursts is much longer than the burst duration [2], and with the measured duty ratio of myosin-II [16].

In the limit of $\tau_\omega \rightarrow \infty$ the observed NGP of the displacement distribution $P[\Delta x(\tau_\omega)]$ decays to zero [1], while for the calculated confined particle the NGP remains finite [Figs. 2(b) and 2(d)]. At long times ($\gtrsim 10$ s) the observed trajectory has large excursions [1], which we interpret as the escape of the particle from the confining potential. The ensuing hopping-type diffusion causes the NGP to vanish, as for free diffusion [17]. Within our model we therefore interpret the observed time scale of the vanishing of the NGP, $\tau_\omega \approx 10\text{--}100$ s, as the time scale, which corresponds to the mean trapping time of the bead within the confining actin gel. Beyond this time scale the bead has a large chance to escape the confinement, and hop to a new trapping site, which corresponds to a reorganization of the actin network. The real actin-myosin gel undergoes irreversible processes that make its properties time-dependent and render it inhomogeneous [4,18–20]. Such effects make the comparison to the model

much more challenging. Large deviations from Gaussianity were also observed for the Van Hove correlations in other forms of active gels [21].

VIII. CONCLUSION

We investigated here the dynamics of a trapped active particle, with several interesting results: (i) The activity leads to strong deviations from equilibrium, such as the breakdown of the virial theorem and equipartition. We find that in the presence of elastic restoring forces the activity is mostly “stored” in the potential energy of the system. (ii) Different “effective temperatures” give a measure of the activity, and some are dependent on the stiffness of the elastic confinement. (iii) The displacement, position, and velocity distributions of the particle are highly non-Gaussian in the regime of strong elastic confinement and small number of dominant motors. These distributions can be used, together with our simple model, to extract information about the microscopic properties of the active motors. Note that in our model the activity affects the motion and position distributions of the trapped particle, which is complementary to models where the activity drives only the large-scale reorganization that moves the particle between trapping sites [22,23] or leads to network collapse [24]. The results of this model are in good agreement with observations of the dynamics of tracer beads inside active gels, and the simplicity of the model may make it applicable for a wide range of systems. More complex viscoelastic relations can be used in place of the simple elasticity presented here to describe the dynamics inside living cells [25,26], as well as nonlinear elasticity [9]. Note that in most current experiments on actin-myosin gels, the myosin-driven activity is strong enough to lead to large-scale reorganization of the actin network, eventually leading to the network collapse [4,18–20]. In order to observe the active motion for the elastically trapped tracer in the intact network, which we have calculated, much weaker active forces will be needed. Our work can therefore give motivation for such future studied.

ACKNOWLEDGMENTS

N.S.G. would like to thank ISF Grant No. 580/12 for support. This research is made possible in part by the historic generosity of the Harold Perlman Family.

APPENDIX A: NUMERICAL SIMULATIONS

The simulations of the dynamics of the particle inside the one-dimensional harmonic potential were carried out using explicit Euler integration of Eq. (1). We were careful to use a small time step Δt , such that it was always an order of magnitude smaller than the smallest time scale in the problem. The time scales in the problem are $\tau, \Delta\tau$ and $\sqrt{2/k}$, where the last time scale is that of the oscillation frequency of the particle inside the harmonic potential.

The iterative equations take the following form in terms of the sampling time Δt :

$$v(t + \Delta t) = v(t) + [-\lambda v(t) - kx(t) + f_a(t)]\Delta t + \sqrt{2\lambda T \Delta t} \eta, \quad (\text{A1a})$$

$$x(t + \Delta t) = x(t) + v(t)\Delta t, \quad (\text{A1b})$$

where η is a random Gaussian variable with zero mean and variance 1. Considering that both the waiting time and the persistence time are exponentially distributed with mean values τ and $\Delta\tau$, respectively, the iterative equation for the active force f_a obeys

$$f_a(t + \Delta t) = \begin{cases} f_a(t) & \text{if } f_a(t) \neq 0 \text{ prob. } 1 - \Delta t/\Delta\tau, \\ f_a(t) & \text{if } f_a(t) = 0 \text{ prob. } 1 - \Delta t/\tau, \\ 0 & \text{if } f_a(t) \neq 0 \text{ prob. } \Delta t/\Delta\tau, \\ \epsilon_{\{-f, f\}} & \text{if } f_a(t) = 0 \text{ prob. } \Delta t/\tau, \end{cases} \quad (\text{A2})$$

where $\epsilon_{\{-f, f\}} = \{f, -f\}$ with same probability.

APPENDIX B: POSITION FLUCTUATIONS OF A TRAPPED PARTICLE

From the model equations of motion [Eq. (1)], we can calculate the mean-square fluctuations in the particle position for a shot noise force correlations with average burst duration $\Delta\tau$. We begin by Fourier transforming Eq. (1) to get

$$-\omega^2 \tilde{x} = i\omega\lambda\tilde{x} + \tilde{f}_a + \tilde{f}_T - k\tilde{x}, \quad (\text{B1})$$

where the $\tilde{\cdot}$ denotes the FT. From Eq. (B1) we get

$$\tilde{x}(\omega) = \frac{\tilde{f}_a(\omega) + \tilde{f}_T(\omega)}{-\omega^2 - i\omega\lambda + k}. \quad (\text{B2})$$

The fluctuations (correlations) are therefore

$$\langle x^2 \rangle(\omega) = \langle \tilde{x}(\omega)\tilde{x}^*(\omega) \rangle = \frac{\langle \tilde{f}_a^2 \rangle(\omega) + \langle \tilde{f}_T^2 \rangle(\omega)}{(k - \omega^2)^2 + (\omega\lambda)^2}, \quad (\text{B3})$$

where we have $\langle \tilde{f}_a^2 \rangle(\omega) = N_m p_{on} f_0^2 \frac{\Delta\tau}{1 + (\omega\Delta\tau)^2}$ (Poissonian shot noise with mean burst length $\Delta\tau$), and $\langle \tilde{f}_T^2 \rangle(\omega) = 2\lambda T$ (thermal white noise) [11].

For the active part alone, we get

$$\langle x^2 \rangle = \frac{N_m p_{on} f_0^2}{2\pi} \int_0^\infty \frac{1}{(\omega^2 - k)^2 + (\omega\lambda)^2} \frac{\Delta\tau}{1 + (\omega\Delta\tau)^2} d\omega. \quad (\text{B4})$$

The solution for this integral is quite lengthy. In the limit of weak trapping, $k \rightarrow 0$, we get that the mean-square displacement diverges,

$$\langle x^2 \rangle \rightarrow 2 \frac{N_m p_{on} f_0^2 \Delta\tau}{k(k\Delta\tau + \lambda)}, \quad (\text{B5})$$

such that the mean potential energy in this limit approaches a constant value

$$T'_x \simeq k \langle x^2 \rangle \rightarrow 2 \frac{N_m p_{on} f_0^2 \Delta\tau}{(k\Delta\tau + \lambda)}. \quad (\text{B6})$$

In the limit of large k , we can expand the integrand of Eq. (B4) in powers of k^{-1} to get the integral

$$\langle x^2 \rangle = \frac{2N_m p_{on} f_0^2}{\pi} \int_0^{\sqrt{k}} \frac{\Delta\tau}{k^2[1 + (\omega\Delta\tau)^2]} d\omega, \quad (\text{B7})$$

which is also bound with a maximal frequency corresponding to the natural frequency of the harmonic trap. This integral gives a simple expression, which gives a good fit description

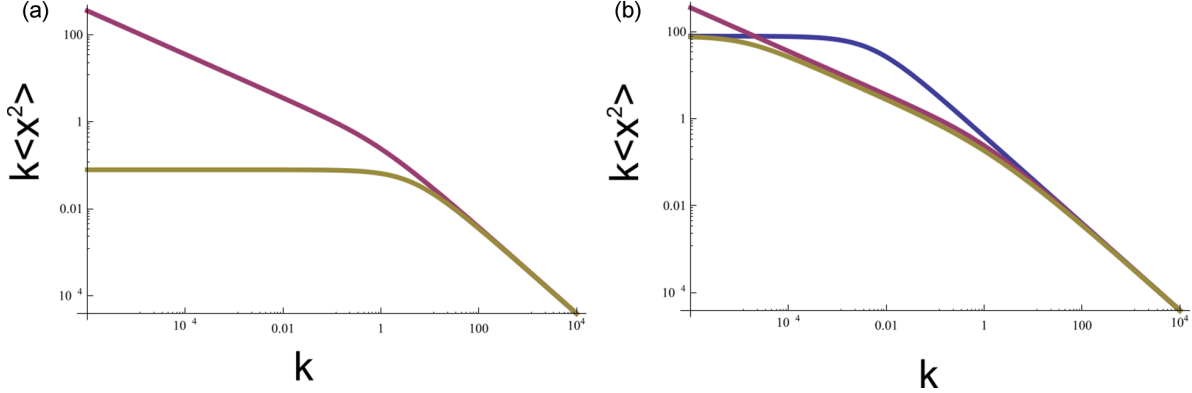


FIG. 3. (Color online) Calculated mean-square position fluctuations (plotted as a mean potential energy) for the trapped particle: Brown line, full solution; purple line, approximate solution [Eq. (B8)]; blue line, approximate expression T'_x for the limit $\lambda\Delta\tau \gg 1$ [Eq. (B9)]. In both panels we used $\Delta\tau = 1$, and (a) $\lambda = 10$, (b) $\lambda = 0.01$. In (a) the blue line agrees perfectly with the full solution, while in (b) it has a discrepancy at intermediate confinements.

as long as $k \gg \lambda^2$ (Fig. 3):

$$\langle x^2 \rangle_k = \frac{2N_m p_{on} f_0^2}{\pi k^2} \arctan [\sqrt{k/2}\Delta\tau]. \quad (\text{B8})$$

Finding the value of k for which the scaling changes from $\langle x^2 \rangle \sim k^{-3/2}$ to $\langle x^2 \rangle \sim k^{-2}$, is simply by equating the large and small k limits of $\langle x^2 \rangle_k$ [Eq. (B8)].

In the limit of $\lambda\Delta\tau \gg 1$ we find the simple approximate expression (Fig. 3)

$$T'_x \simeq k \langle x^2 \rangle \simeq \frac{\Delta\tau N_m p_{on} f_0^2}{8\lambda^2(k\Delta\tau/2\lambda + 1)}. \quad (\text{B9})$$

The numerical simulations, in the highly damped limit ($\lambda\Delta\tau \gg 1$) indicate the k^{-1} and k^{-2} limits [Fig. 4(a)].

APPENDIX C: VELOCITY FLUCTUATIONS OF A TRAPPED PARTICLE

Similar to the procedure for the position fluctuations described above, we can calculate the velocity fluctuations. The mean-square fluctuations in the particle velocity are given

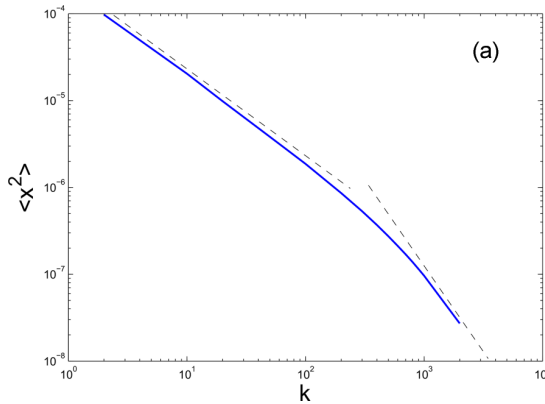


FIG. 4. (Color online) Simulated mean-square particle displacements (a) and velocity (b) in the limit of $\lambda\Delta\tau \gg 1$, using $\Delta\tau = 1$, $\lambda = 50$, $f_0 = 1$, $p_{on} = 0.1$. The dashed lines indicate the power laws with exponents -1 , -2 in (a) and $-3/2$ in (b).

simply from Eq. (B4) by

$$\langle v^2 \rangle = \frac{N_m p_{on} f_0^2}{2\pi} \int_0^\infty \frac{\omega^2}{(\omega^2 - k)^2 + (\omega\lambda)^2} \frac{\Delta\tau}{1 + (\omega\Delta\tau)^2} d\omega. \quad (\text{C1})$$

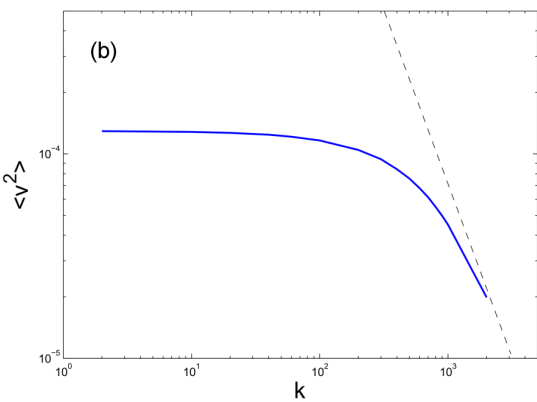
The solution for this integral is again quite lengthy. As for the position distribution, we can find an approximation for the large k limit, using

$$\langle v^2 \rangle = \frac{2N_m p_{on} f_0^2}{\pi} \int_0^{\sqrt{k}} \frac{\omega^2 \Delta\tau}{k^2[1 + (\omega\Delta\tau)^2]} d\omega, \quad (\text{C2})$$

which is also bound with a maximal frequency corresponding to the natural frequency of the harmonic trap. This integral gives a simple expression, which gives a good fit description as long as $k \gg \lambda^2$:

$$\langle v^2 \rangle_k = \frac{2N_m p_{on} f_0^2}{\pi k^2 \Delta\tau^2} (\sqrt{k/2}\Delta\tau - \arctan [\sqrt{k/2}\Delta\tau]). \quad (\text{C3})$$

The scaling of $\langle v^2 \rangle_k$ changes from $\langle v^2 \rangle \sim k^{-0.5}$ to $\langle v^2 \rangle \sim k^{-3/2}$ as k increases [Fig. 5(b)].



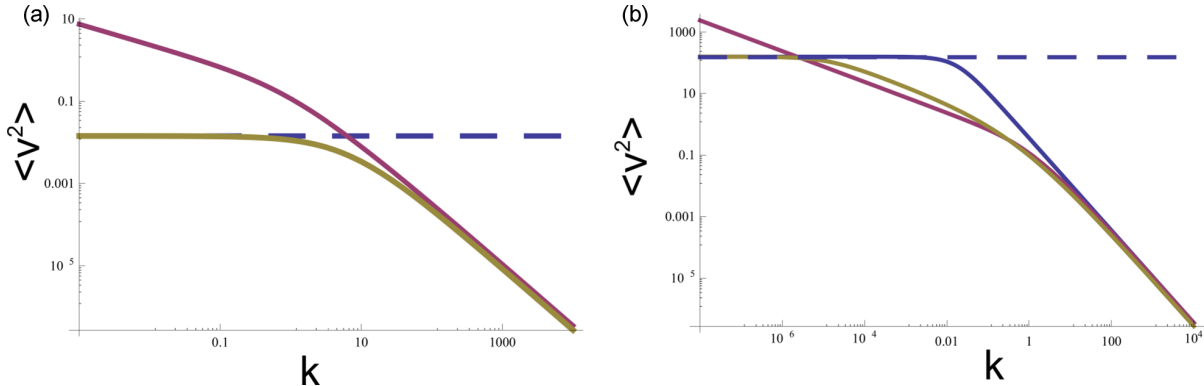


FIG. 5. (Color online) Calculated mean-square velocity fluctuations for the trapped particle: brown line, full solution; purple line, approximate solution [Eq. (C3)]; blue line, highly damped limit [Eq. (C4)]; and the dashed blue line is the free-particle value [11]. In both panels we used $\Delta\tau = 1$ and (a) $\lambda = 10$, (b) $\lambda = 0.01$.

In the limit of $\lambda\Delta\tau \gg 1$ we have the simple approximate expression

$$\langle v^2 \rangle \simeq \frac{\Delta\tau N_m p_{on} f_0^2}{4[\lambda(1 + \Delta\tau\lambda) + \pi\Delta\tau^2\sqrt{k^3/8}]}, \quad (\text{C4})$$

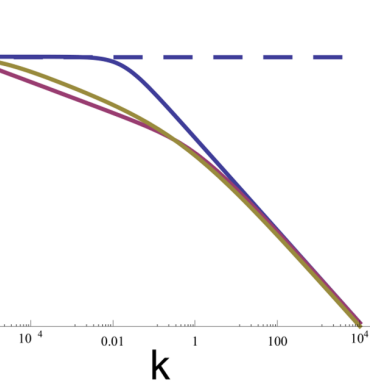
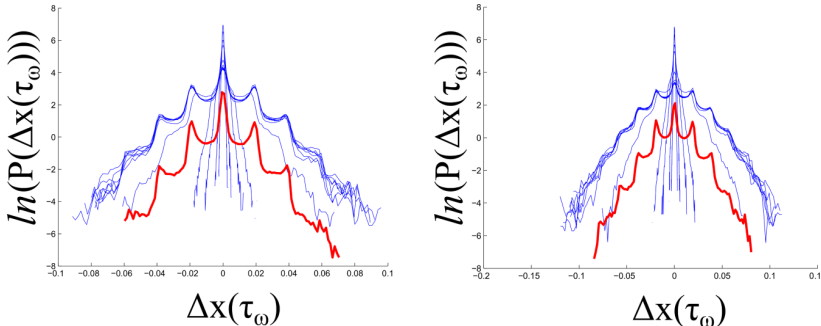
which fits quite well the full expression in Fig. 5(a).

The numerical simulations, in the highly damped limit ($\lambda\Delta\tau \gg 1$) indicate the k^0 and $k^{-3/2}$ limits [Fig. 4(b)].

APPENDIX D: EFFECTIVE TEMPERATURE DUE TO FORCES FROM DISTANT (AND NUMEROUS) MOTORS

In a linear elastic medium, the displacements and stresses decay from a point source (at least) as $1/r^2$. Since there are numerous distant motors affecting the bead, their cumulative random forces are most likely to give rise to Gaussian distribution of position and velocities for the trapped particle. Each shell (of thickness dr) at radius r from the tracer beads has $N_m(r) = 4\pi r^2 \rho dr$ motors (at constant density ρ), and therefore they contribute to the mean-square velocity the following contribution [in the limit of $\lambda\Delta\tau \gg 1$, using Eq. (C4)]:

$$\begin{aligned} \langle v^2 \rangle &\simeq N_m(r) \left(N_m p_{on} f_0 \frac{a^2}{r^2} \right)^2 \frac{\Delta\tau}{4[\lambda(1 + \Delta\tau\lambda) + \pi\Delta\tau^2\sqrt{k^3}]} \\ &\propto \frac{1}{r^2}, \end{aligned} \quad (\text{D1})$$



where we isolated the number of motors and the r dependence of the active forces and introduced a length scale a beyond which the far-field calculation holds. Integrating this expression we get

$$\langle v^2 \rangle_{far} \simeq \langle v^2 \rangle_0 (4\pi\rho a^3), \quad (\text{D2})$$

where $\langle v^2 \rangle_0$ is the value for the single proximal motor given in Eq. (C4). We find that the far-field contribution of the distant motors is proportional to their density ρ .

APPENDIX E: DISPLACEMENT DISTRIBUTION FOR NUMEROUS MOTORS

As the number of motors kicking the particle (N_m) increases, we find that the distribution of the particle position becomes more Gaussian, even in the limit of larger damping $\lambda\Delta\tau \gg 1$ and strong confinement $\tilde{\lambda}\Delta\tau \gg 1$. We demonstrate this in Fig. 6, which shows that the position distributions $P(x)$ and the displacement distributions $P[\Delta x(\tau_\omega)]$ approach a Gaussian for N_m larger than ~ 10 .

APPENDIX F: NGP FOR THE HIGHLY DAMPED LIMIT

We find that the maximal value of the NGP for $P[\Delta x(\tau_\omega)]$ is close to the NGP of $P(x)$ [Fig. 2(b)], which is a function for which we have a good analytic approximation [11], given by

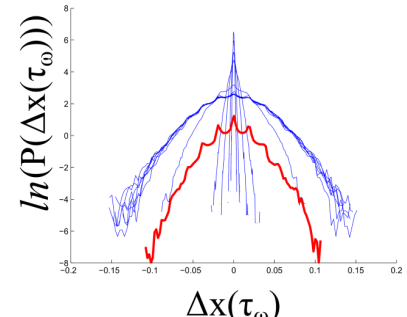


FIG. 6. (Color online) Simulated particle position distribution $P(x)$ (red lines) and displacement distributions $P[\Delta x(\tau_\omega)]$ (blue lines), for increasing number of motors: $N_m = 5, 10, 20$ (left to right), using $\Delta\tau = 1$, $\lambda = 50$, $f_0 = 1$, $p_{on} = 0.1$.

(for a single motor)

$$NGP(N_m = 1) = \frac{4(1 - 3p_{on})p_{on}^3 T_{x,1}^2}{3(1 + 2p_{on}^2 T_{x,1})^2}, \quad (\text{F1})$$

where $T_{x,1}$ is the effective temperature of the spatial distribution [Eqs. (4) and (5)] for $p_{on} = 1$. The maximal value of the NGP for a single motor, as a function of p_{on} is obtained from Eq. (F1) at $p_{on} = \alpha/(2 + 6\alpha)$ and is given by

$$NGP_{\max} = \frac{(1 + 3\alpha)^2}{3\alpha(2 + 3\alpha)} - 1, \quad (\text{F2})$$

where $\alpha = k_B T / T_{x,1}$. This is a monotonously decreasing function of the stiffness k , due to the decrease in $T_{x,1}$ in stiffer gels [Eqs. (4) and (5)].

APPENDIX G: EFFECTIVE TEMPERATURE FROM THE FDT, T_{FDT}

Following Ref. [11], and using Eq. (3), we can write for the $\tilde{\lambda}\Delta\tau \gg 1$ limit (when $T = 0$)

$$\text{Response : } \chi_{xx}(\omega) = \frac{1}{\gamma(i\omega - \tilde{\lambda})}, \quad (\text{G1})$$

$$\text{Fluctuations : } S_{xx}(\omega) = \frac{f_0^2}{\lambda(\tilde{\lambda}^2 + \omega^2)} \frac{\langle \Delta\tau \rangle}{1 + (\omega\langle \Delta\tau \rangle)^2}, \quad (\text{G2})$$

$$\Rightarrow T_{FDT}(\omega) = \frac{\omega S_{xx}(\omega)}{2\text{Im}[\chi(\omega)]} = \frac{N_m p_{on} f_0^2 \langle \Delta\tau \rangle}{\lambda[1 + (\omega\langle \Delta\tau \rangle)^2]}, \quad (\text{G3})$$

resulting in Eq. (G3).

APPENDIX H: ANALYTIC CALCULATION OF THE NGP WITHOUT INERTIAS

To compute the expression of the NGP, we derive the mean quartic displacement (MQD) $\langle \Delta x^4 \rangle$ in the regime where it is

$$\langle \Delta x_{A,a}^4 \rangle(t) = T_A^2 \frac{3\tau_r^4 (2\tau_0 + \tau_r)(\tau_0 + \tau) e^{-\frac{4t}{\tau_r}} (e^{t/\tau_r} - 1)^4}{\lambda^2 (\tau_r + \tau)(\tau_r + 3\tau)[\tau_r(\tau_0 + \tau) + 2\tau_0\tau]}, \quad (\text{H4a})$$

$$\langle \Delta x_{A,a}^3 \Delta x_{A,b} \rangle(t) = T_A^2 \frac{3\tau_r^4 \tau (2\tau_0 + \tau_r)(\tau_0 + \tau) e^{-\frac{4t}{\tau_r}} (e^{t/\tau_r} - 1)^3 (e^{t(\frac{1}{\tau_r} - \frac{1}{\tau})} - 1)}{\lambda^2 (\tau_r - \tau)(\tau_r + \tau)(\tau_r + 3\tau)[\tau_r(\tau_0 + \tau) + 2\tau_0\tau]}, \quad (\text{H4b})$$

$$\begin{aligned} \langle \Delta x_{A,a}^2 \Delta x_{A,b}^2 \rangle(t) &= T_A^2 \frac{\tau_r^4 (e^{t/\tau_r} - 1)^2 e^{-\frac{4t}{\tau_r} - \frac{t}{\tau}}}{\lambda^2 (\tau_r - \tau_0)(\tau - \tau_r)(\tau_r + \tau)^2 [\tau_r(\tau_0 + \tau) - 2\tau_0\tau][\tau_r(\tau_0 + \tau) + 2\tau_0\tau]} \\ &\times \{4\tau_0^4 (\tau - \tau_r)(\tau_r + \tau) e^{\frac{2t}{\tau_r} - \frac{t}{\tau_0}} + (\tau_r - \tau_0)(\tau - \tau_r)[\tau_r^2(\tau_0 + \tau)^2 - 4\tau_0^2\tau^2] e^{t(\frac{2}{\tau_r} + \frac{1}{\tau})} \\ &+ (\tau_0 - \tau_r)(\tau_0 + \tau)(\tau_r + \tau) e^{t/\tau} [4\tau_0^2\tau - \tau_r^2(\tau_0 + \tau)] \\ &- 2(\tau_0 + \tau) e^{t/\tau_r} [2\tau_0^2\tau_r + \tau(\tau_0 - \tau_r)(2\tau_0 + \tau_r)][2\tau_0\tau - \tau_r(\tau_0 + \tau)]\}, \end{aligned} \quad (\text{H4c})$$

$$\begin{aligned} \langle \Delta x_{A,a} \Delta x_{A,b}^3 \rangle(t) &= -T_A^2 \frac{3\tau_r^4 e^{-\frac{4t}{\tau_r}} (e^{t/\tau_r} - 1)}{\lambda^2 \tau (\tau_r + \tau)} \left\{ \frac{\tau^2 (2\tau_0 - \tau_r)(\tau_0 + \tau)}{(\tau_r - 3\tau)(\tau_r - \tau)[\tau_0(\tau_r - 2\tau) + \tau_r\tau]} + \frac{2\tau_0^4 e^{-t(\frac{1}{\tau_0} - \frac{2}{\tau_r} + \frac{1}{\tau})}}{(\tau_0 - \tau_r)(\tau_0 + \tau_r)[\tau_r(\tau_0 + \tau) - 2\tau_0\tau]} \right. \\ &\left. + \frac{(\tau_0 + \tau)[\tau_0(\tau_r + \tau) - \tau_r\tau] e^{t(\frac{1}{\tau_r} - \frac{1}{\tau})}}{(\tau_r - \tau_0)(\tau_r^2 - \tau^2)} + \frac{(\tau_0 + \tau)[\tau(\tau_0 + \tau_r) - \tau_0\tau_r] e^{\frac{3t}{\tau_r} - \frac{t}{\tau}}}{(\tau_0 + \tau_r)(\tau_r^2 - 4\tau_r\tau + 3\tau^2)} + \frac{\tau^2 e^{\frac{2t}{\tau_r}}}{\tau_r^2 - \tau^2} \right\}, \end{aligned} \quad (\text{H4d})$$

time translational invariant:

$$\langle \Delta x^4 \rangle = \langle \Delta x_T^4 \rangle + \langle \Delta x_A^4 \rangle + 6\langle \Delta x_T^2 \rangle \langle \Delta x_A^2 \rangle, \quad (\text{H1})$$

where the subscripts T and A refer, respectively, to the thermal and active contributions. The expression of the MSD is given by

$$\begin{aligned} \langle \Delta x_T^2 \rangle(t) &= \frac{2k_B T}{k} (1 - e^{-t/\tau_r}), \\ \langle \Delta x_A^2 \rangle(t) &= \frac{2k_B T_A/k}{(\tau/\tau_r)^2 - 1} \left[\frac{\tau}{\tau_r} (1 - e^{-t/\tau}) + e^{-t/\tau_r} - 1 \right], \end{aligned} \quad (\text{H2})$$

where $\tau_r = \lambda/k$ is a thermal relaxation time scale. The MQD under purely thermal conditions is related to the thermal MSD since the thermal process is Gaussian $\langle \Delta x_T^4 \rangle = 3\langle \Delta x_T^2 \rangle^2$. To compute the active MQD, we separate the position displacement $\Delta x_A(t_f, t_i) = x_A(t_f) - x_A(t_i)$ in several contributions, such that $\langle \Delta x_A^4 \rangle$ is a power law combination of these contributions. We compute each term using the active force statistics and take the limit of large t_i at fixed t corresponding to the time translational regime. The advantage of the separation we propose is that each term of the active MQD converges in such limit. The appropriate separation is

$$\Delta x_{A,a}(t_f, t_i) = (e^{-t/\tau_r} - 1) \int_{t_i}^{t_f} dt' \chi(t_i - t') f_A(t'), \quad (\text{H3a})$$

$$\Delta x_{A,b}(t_f, t_i) = \int_{t_i}^t dt' \chi(t - t') f_A(t_i + t'), \quad (\text{H3b})$$

where $\chi(t) = e^{-t/\tau_r}/\lambda$ is the noncausal response function, and $t = t_f - t_i$ is the time lag. In the time translational regime, we compute

$$\langle \Delta x_{A,b}^4 \rangle(t) = T_A^2 \frac{3\tau_r^4 e^{-\frac{4t}{\tau_r}}}{\lambda^2 \tau (\tau_r + \tau)} \left\{ -\frac{\tau(2\tau_0 - \tau_r)(\tau_0 + \tau)(\tau_r + \tau)}{(\tau_r - 3\tau)(\tau_r - \tau)[\tau_0(\tau_r - 2\tau) + \tau_r \tau]} \right. \\ \left. + \frac{8\tau_0^5(\tau_r + \tau)e^{t(-\frac{1}{\tau_0} + \frac{2}{\tau_r} - \frac{1}{\tau})}}{(\tau_r - \tau_0)(\tau_0 + \tau_r)[\tau_r(\tau_0 + \tau) - 2\tau_0 \tau] \tau_r(\tau_0 + \tau) + 2\tau_0 \tau} - \frac{4(\tau_0 + \tau)[\tau(\tau_0 + \tau_r) - \tau_0 \tau_r]e^{\frac{3t}{\tau_r} - \frac{t}{\tau}}}{(\tau_0 + \tau_r)(\tau_r^2 - 4\tau_r \tau + 3\tau^2)} \right. \\ \left. + \frac{4(\tau_0 + \tau)[\tau_0(\tau_r + \tau) - \tau_r \tau]e^{t(\frac{1}{\tau_r} - \frac{1}{\tau})}}{(\tau_0 - \tau_r)(\tau_r - \tau)(\tau_r + 3\tau)} + \frac{\tau(2\tau_0 + \tau_r)(\tau_0 + \tau)e^{\frac{4t}{\tau_r}}}{(\tau_r + 3\tau)[\tau_r(\tau_0 + \tau) + 2\tau_0 \tau]} + \frac{2\tau e^{\frac{2t}{\tau_r}}}{\tau - \tau_r} \right\}, \quad (H4e)$$

from which we deduce

$$\langle \Delta x_A^4 \rangle = \langle \Delta x_{A,a}^4 \rangle + 3\langle \Delta x_{A,a}^4 \Delta x_{A,b} \rangle + 6\langle \Delta x_{A,a}^2 \Delta x_{A,b}^2 \rangle + 3\langle \Delta x_{A,a} \Delta x_{A,b}^3 \rangle + \langle \Delta x_{A,b}^4 \rangle. \quad (H5)$$

- [1] T. Toyota *et al.*, *Soft Matter* **7**, 3234 (2011).
- [2] D. Mizuno, C. Tardin, C. F. Schmidt, and F. C. MacKintosh, *Science* **315**, 370 (2007).
- [3] N. Fakhri, A. D. Wessel, C. Willms, M. Pasquali, D. R. Klopfenstein, F. C. MacKintosh, and C. F. Schmidt, *Science* **344**, 1031 (2014).
- [4] B. Stuhrmann, M. Soares e Silva, M. Depken, F. C. MacKintosh, and G. H. Koenderink, *Phys. Rev. E* **86**, 020901(R) (2012).
- [5] A. Caspi, R. Granek, and M. Elbaum, *Phys. Rev. E* **66**, 011916 (2002).
- [6] P. Bursac *et al.*, *Biochem. Biophys. Res. Comm.* **355**, 324 (2007).
- [7] W. W. Ahmed, É. Fodor, and T. Betz, *Biochimica et Biophysica Acta (BBA)-Molecular Cell Research* (2015), doi: 10.1016/j.bbamer.2015.05.022.
- [8] M. Soares e Silva, B. Stuhrmann, T. Betz, and G. H. Koenderink, *New J. Phys.* **16**, 075010 (2014).
- [9] C. Storm, J. J. Pastore, F. C. MacKintosh, T. C. Lubensky, and P. A. Janmey, *Nature (London)* **435**, 191 (2005).
- [10] M. Annunziato, *Phys Rev E* **65**, 021113 (2002).
- [11] E. Ben-Isaac, YongKeun Park, G. Popescu, F. L. H. Brown, N. S. Gov, and Y. Shokef, *Phys. Rev. Lett.* **106**, 238103 (2011).
- [12] A. Ghosh and N. S. Gov, *Biophys. J.* **107**, 1065 (2014).
- [13] A. Rahman, *Phys. Rev.* **136**, A405 (1964).
- [14] P. Bursac, G. Lenormand, B. Fabry, M. Oliver, D. A. Weitz, V. Viasnoff, J. P. Butler, and J. J. Fredberg, *Nature Materials* **4**, 557 (2005).
- [15] N. Gal, D. Lechtman-Goldstein, and D. Weihs, *Rheologica Acta* **52**, 425 (2013).
- [16] J. Howard, *Mechanics of Motor Proteins and the Cytoskeleton* (Sinauer Associates, Sunderland, MA, 2001).
- [17] D. Bi, J. H. Lopez, J. M. Schwarz, and M. L. Manning, *Soft Matter* **10**, 1885 (2014).
- [18] F. Backouche, L. Haviv, D. Groszwasser, and A. Bernheim-Groszwasser, *Phys. Biol.* **3**, 264 (2006).
- [19] S. Khler, V. Schaller, and A. R. Bausch, *Nature Materials* **10**, 462 (2011).
- [20] M. Soares e Silva, M. Depken, B. Stuhrmann, M. Korsten, F. C. MacKintosh, and G. H. Koenderink, *Proc. Natl. Acad. Sci. USA* **108**, 9408 (2011).
- [21] O. J. N. Bertrand, D. K. Fygenson, and O. A. Saleh, *Proc. Natl. Acad. Sci. USA* **109**, 17342 (2012).
- [22] É. Fodor *et al.*, *Europhys. Lett.* **110**, 48005 (2015).
- [23] É. Fodor, K. Kanazawa, H. Hayakawa, P. Visco, and F. van Wijland, *Phys. Rev. E* **90**, 042724 (2014).
- [24] M. Sheinman, A. Sharma, J. Alvarado, G. H. Koenderink, and F. C. MacKintosh, *Phys. Rev. Lett.* **114**, 098104 (2015).
- [25] C. Wilhelm, *Phys. Rev. Lett.* **101**, 028101 (2008).
- [26] F. Gallet, D. Arcizet, P. Bohec, and A. Richert, *Soft Matter* **5**, 2947 (2009).

Active cage model of glassy dynamics

Étienne Fodor,¹ Hisao Hayakawa,² Paolo Visco,¹ and Frédéric van Wijland^{1,2}

¹Laboratoire Matière et Systèmes Complexes, UMR 7057 CNRS/P7, Université Paris Diderot,
10 rue Alice Domon et Léonie Duquet, 75205 Paris cedex 13, France

²Yukawa Institute for Theoretical Physics, Kyoto University, Kitashirakawa-oiwake cho, Sakyo-ku, Kyoto 606-8502, Japan
(Received 8 February 2016; revised manuscript received 5 May 2016; published 12 July 2016)

We build up a phenomenological picture in terms of the effective dynamics of a tracer confined in a cage experiencing random hops to capture some characteristics of glassy systems. This minimal description exhibits scale invariance properties for the small-displacement distribution that echo experimental observations. We predict the existence of exponential tails as a crossover between two Gaussian regimes. Moreover, we demonstrate that the onset of glassy behavior is controlled only by two dimensionless numbers: the number of hops occurring during the relaxation of the particle within a local cage and the ratio of the hopping length to the cage size.

DOI: 10.1103/PhysRevE.94.012610

I. INTRODUCTION

Time-dependent density correlations in an atomic or colloidal glass former exhibit, as temperature is decreased (or as density is increased), a two-step relaxation. The short-time β relaxation is associated with localized motion of the particles while the longer-time α relaxation is associated with cooperatively rearranging regions (CRR). This behavior of the dynamic structure factor is well accounted for [1], at sufficiently high temperatures, by the mode-coupling theory (MCT) [2]. MCT being an approximate theory it does have its share of pitfalls, but these are well-documented, and it is fair to say that they are not fully understood, let alone on intuitive grounds. One such prediction is the existence of a critical temperature below which the α -relaxation stage extends to arbitrary large times. This is often connected to the difficulty of capturing the dynamics of the CRRs, which is built from rare and intermittent events. One recent research direction has been to brute-force improve the theoretical basis of the MCT, and recent promising results [3] seem to indicate that this may pay off to eliminate some of its unpleasant features. Regarding the dynamics (diffusive versus arrested) of an individual tracer [4,5], similar efforts are being made at looking beyond the existing MCT. The most recent experiments, instead of focusing on the relaxation of collective density modes, are based on the observation of individual tracers. Tracking experiments have been conducted by many different groups, both in actual colloidal systems [6–11] as well as *in silico* [12,13]. The increasing accuracy of these methods allows one to measure the probability distribution function of the tracer displacement with unprecedented statistics [14].

To analyze and interpret tracking experiments, minimal phenomenological models have been developed. By using a continuous-time random walk (CTRW) description, glassy systems have been studied numerically [15,16], and exact analytic results have been obtained for the Van Hove correlation function [13]. The CTRW considers instantaneous transitions between locally stable positions, thus decoupling the diffusion in a confined environment from the cage jumps [17]. Some model variations include the existence of a multiplicity of timescales in the cage dynamics [18–21], whereas others, which include a single waiting timescale, successfully reproduce many features of the dynamics of tracers in glassy

systems [13,22]. Despite the success of these minimal models, the existence of a scale invariant regime for the displacement distribution, as observed experimentally [6,8,10], is still an open issue. The main purpose of this work is to show that this scale invariance feature can emerge from a phenomenological description.

Note that systems other than glasses fall within the scope of our study, such as sheared fluids [23–26] or interacting self-propelled particles [27–31]. For these systems glassy behavior is generally investigated through the self-intermediate scattering function (SISF). In the case of self-propelled particles it has been observed that the onset of glassy behavior is progressively shifted when self-propulsion increases. Even though a direct extension of MCT is enough to account for this phenomenon [32–34], an effective one-body dynamics that clearly determines how self propulsion affects the glassy behavior is still missing. We present here a minimal model that describes such one-body dynamics. By investigating the displacement distribution, we show that it displays scale invariance for small displacement, and we determine how the onset of glassy behavior is linked to self propulsion. Finally, we introduce an effective mean-field potential to bridge over back to a system of interacting particles.

II. MODEL

Our model is based on a common picture that has emerged for glassy and granular systems connecting the slowing down of the dynamics to the cage effect [13,18,20,36,37]. The escape of the particle from the local confinement stems from structural rearrangements of the system. The activation of such sudden and irreversible reorganization can be of three types: spontaneous thermal fluctuations, external shear, or internal self-propulsion. In what follows, we refer to such a process as a directed event, by contrast to the passive diffusion of the particle within the cage, whose precise structure is given by collective many-body effects of the global system.

We consider a particle confined within a harmonic cage of typical size σ . We introduce the timescale τ_R quantifying the time needed by the particle to explore the cage. The fluctuations of the particle in the cage are driven by a noise of amplitude $D = \sigma^2/\tau_R$. To account for structural

rearrangements, we assume that the central position of the cage is subjected to random shifts. This is to mimic the modification of the metastable state explored by the particle. The cage hops instantaneously by a random distance, which is exponentially distributed with a characteristic hopping length ε . The time between two consecutive hops is also exponentially distributed, with a mean value τ_0 . After a cage rearrangement, the particle relaxes toward the new cage position. We regard such relaxation as an equilibrium process. The fluctuation-dissipation theorem enforces that the relaxation time should equal the typical time of exploration τ_R . We end up describing the one-dimensional dynamics of the particle position x as

$$\frac{dx}{dt} = -\frac{x(t) - x_0(t)}{\tau_R} + \xi_G(t), \quad \frac{dx_0}{dt} = \xi_{NG}(t), \quad (1)$$

where ξ_G is a zero-mean Gaussian white noise with correlations $\langle \xi_G(t) \xi_G(t') \rangle = 2D\delta(t-t')$. More realistic higher-dimensional generalizations do not induce any physical difference with the one-dimensional modeling we adopt here.

Our motivations for the explicit form of the noise ξ_{NG} acting on the cage are twofold. One the one hand, we expect the rare intermittent events behind the α relaxation to be unable to build up uncorrelated Gaussian statistics. On the other hand, we choose a specific form that has the advantage of allowing for a closed-form analytic solution that will ease the subsequent analysis. It leads us to consider a zero-mean non-Gaussian white noise with cumulants,

$$\langle \xi_{NG}(t_1) \dots \xi_{NG}(t_{2n}) \rangle_C = (2n)! \frac{\varepsilon^{2n}}{\tau_0} \delta_{2n}(t_1, \dots, t_{2n}). \quad (2)$$

We decouple caging and hopping dynamics, so that ξ_G and ξ_{NG} are uncorrelated processes. For symmetry reasons, only the $2n$ -time correlation functions of ξ_{NG} are nonzero. Additional arguments on the robustness of our results with a generic-time symmetric non-Gaussian white noise is given in Appendix A. We will explicitly demonstrate that the scale invariance of the small-displacement distribution is indeed insensitive to the specifics of the hop distribution, but the exponential crossover regime to a Gaussian rests on a typical exponential distribution of cage hops.

We distinguish the passive and active fluctuations of the particle. The former are associated with the confined motion of the particle in a steady cage, as measured by D . The latter are induced by the cage hops, thus describing the motion in a nonconfined environment characterized by the diffusion coefficient $D_A = \varepsilon^2/\tau_0$. The coexistence of both Gaussian and non-Gaussian noises is crucially important to enhance non-Gaussian nature [38].

III. STATISTICS OF DISPLACEMENT

A. Fourier distribution of displacement

We are interested in the fluctuations of the displacement $\Delta x(t, t_i) = x(t + t_i) - x(t_i)$, which no longer depends on the initial time of measurement t_i in the limit $t_i \rightarrow \infty$. We define the probability distribution of displacement in the Fourier domain as

$$\tilde{P}(q, t) = \lim_{t_i \rightarrow \infty} \langle e^{iq\Delta x(t, t_i)} \rangle. \quad (3)$$

Since the passive and active processes are uncorrelated, we separate the displacement distribution as $\tilde{P} = \tilde{P}_P \tilde{P}_A$, where the subscripts P and A refer, respectively, to passive and active contributions. The passive distribution is Gaussian, thus being entirely determined by the passive mean-square displacement,

$$\tilde{P}_P(q, t) = e^{-(q\sigma)^2 f_t}, \quad (4)$$

where $f_t = 1 - e^{-t/\tau_R}$. We express the active distribution as

$$\tilde{P}_A(q, t) = \lim_{t_i \rightarrow \infty} \left\langle \exp \left[iq \int_0^\infty ds h(s) \xi_{NG}(s) \right] \right\rangle, \quad (5)$$

where

$$h(s) = [1 - e^{-(t_i + t - s)/\tau_R}] \Theta(t_i + t - s) \Theta(s - t_i) + e^{-(t_i - s)/\tau_R} [1 - e^{-t/\tau_R}] \Theta(t_i - s), \quad (6)$$

with Θ being the Heaviside step function. We evaluate the average in Eq. (5) with the expression of the characteristic functional of the white non-Gaussian noise ξ_{NG} [39–41],

$$\tilde{P}_A(q, t) = \lim_{t_i \rightarrow \infty} \exp \left\{ \sum_{n=1}^{\infty} \frac{(iq\varepsilon)^{2n}}{\tau_0} \int_0^\infty ds [h(s)]^{2n} \right\} \quad (7)$$

$$= \lim_{t_i \rightarrow \infty} \exp \left\{ -\frac{1}{\tau_0} \int_0^\infty ds \frac{[q\varepsilon h(s)]^2}{1 + [q\varepsilon h(s)]^2} \right\}, \quad (8)$$

where we have used the explicit form of the noise cumulants in Eq. (2). We compute the integral in Eq. (8) by using the explicit expression of h in Eq. (6), and we take the limit of large t_i after the integration. From this, we arrive at the result:

$$\begin{aligned} \tilde{P}(q, t) &= \exp \left\{ -\frac{\tau_R q \varepsilon / \tau_0}{1 + (q\varepsilon)^2} \left[\frac{q\varepsilon t}{\tau_R} - \arctan(q\varepsilon f_t) \right] \right\} \\ &\times [1 + (q\varepsilon f_t)^2]^{-\frac{\tau_R}{2\tau_0} \frac{(q\varepsilon)^2}{1+(q\varepsilon)^2}} e^{-(q\sigma)^2 f_t}. \end{aligned} \quad (9)$$

This result contains all the statistical information related to the displacement $\Delta x(t)$. In particular, all the moments are defined as

$$\langle \Delta x^n(t) \rangle = \lim_{t_i \rightarrow \infty} \langle \Delta x^n(t, t_i) \rangle = \left. \frac{\partial^n \tilde{P}}{\partial (iq)^n} \right|_{q=0}. \quad (10)$$

B. Mean-square displacement and non-Gaussianity

As a first insight into the dynamics of our model, we study the time evolution of the second moment $\langle \Delta x^2(t) \rangle$, i.e., the mean-square displacement (MSD). Its expression can be computed from Eq. (10):

$$\text{MSD} = 2(D - D_A)\tau_R f_t + 2D_A t, \quad (11)$$

The behavior of the MSD is controlled by three independent parameters $\{D, D_A, \tau_R\}$. It is diffusive at short and long times with diffusion coefficients D and D_A , respectively [Fig. 1(a)]. The predictions for a steady and a hopping cage coincide at times shorter than $t^* = \tau_R D/D_A = \tau_0(\sigma/\varepsilon)^2$, referred to as the passive regime. This shows that the effect of the active fluctuations is hidden as long as the typical distance covered by the cage $\varepsilon\sqrt{t/\tau_0}$ is smaller than the cage size σ . Between the two diffusions, a plateau regime appears when $D_A \ll D$, as an evidence of the cage effect, and we observe a transient superdiffusion if $D_A \gg D$. The time when the MSD deviates

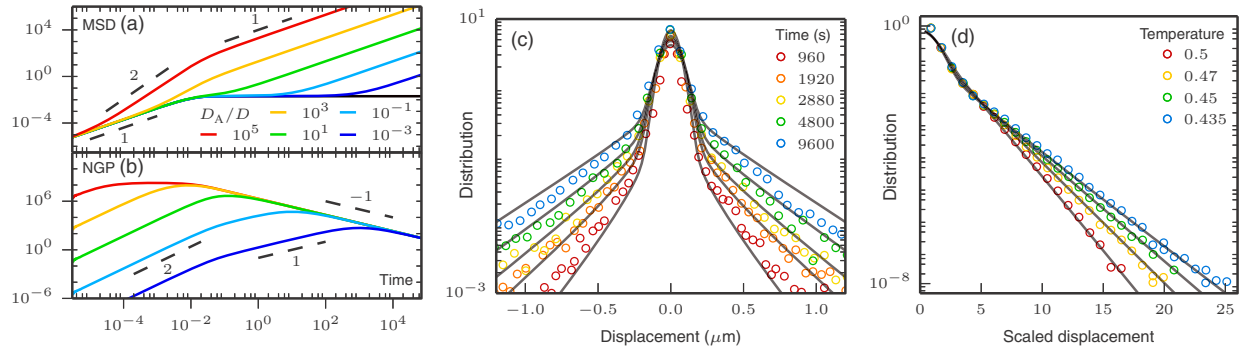


FIG. 1. Time-evolution of (a) the mean-square displacement (MSD), and (b) the non-Gaussian parameter (NGP). The MSD saturates for a steady cage (solid black line), corresponding to a vanishing NGP. (c) Comparison of the theoretical prediction of the distribution of displacement with that of colloidal particles at density $\varphi = 0.429$ taken from Ref. [10]. (d) Theoretical distribution of displacement scaled by the standard deviation of the central Gaussian part corresponding to a binary Lennard-Jones glass-forming mixture for different temperatures at the α relaxation time [35]. See the details in Appendix B.

from the plateau, equal to t^* , can be shifted to an arbitrary large value. Conversely, the time when superdiffusion arises, also equal to t^* , can be arbitrarily short [30]. Our model contains the existence of ballistic directed events, as assessed by the superdiffusion, even if there is no persistence time in its formulation. The asymptotic behaviors of the MSD are summarized in Table I.

Beyond MSD, the fourth moment is generally investigated to identify non-Gaussian features of the displacement statistics. More precisely, the deviation of the displacement distribution from Gaussian is quantified by the non-Gaussian parameter:

$$\text{NGP} = \frac{\langle \Delta x^4 \rangle}{3\langle \Delta x^2 \rangle^2} - 1. \quad (12)$$

In our model, deviations from Gaussian behavior are governed by atypical events in which rare but important excursions occur. In that respect, the NGP characterizes the amount of directed events in the particle trajectory, probing the structural rearrangements of the system. Again using Eq. (10), its calculation is straightforward:

$$\text{NGP} = \frac{\tau_0}{3\tau_R} \frac{2e^{-\frac{3t}{\tau_R}} - 9e^{-\frac{2t}{\tau_R}} + 18e^{-\frac{t}{\tau_R}} - 11 + \frac{6t}{\tau_R}}{[(D/D_A - 1)f_t + t/\tau_R]^2}. \quad (13)$$

Its evolution is determined by $\{D_A/D, \tau_R, \tau_0\}$, where τ_0 only affects the amplitude. The NGP vanishes at short and long time, corresponding to the passive and active Gaussian regimes,

TABLE I. Different regimes in the time evolution of the MSD and the NGP.

$D_A \ll D$	$t \ll \tau_R$	$\tau_R \ll t \ll \tau_R \sqrt{D/D_A}$	$\tau_R D/D_A \ll t$
MSD	$2Dt$	$2D\tau_R$	$2D_A t$
NGP	$\frac{\tau_0}{2\tau_R} \left(\frac{D_A t}{D\tau_R}\right)^2$	$2t\tau_0 \left(\frac{D_A}{D\tau_R}\right)^2$	$\frac{2\tau_0}{t}$
$D_A \gg D$	$t \ll \tau_R D/D_A$	$\tau_R D/D_A \ll t \ll \tau_R$	$\tau_R \ll t$
MSD	$2Dt$	$\frac{2D_A t^2}{\tau_R}$	$2D_A t$
NGP	$\frac{\tau_0}{2\tau_R} \left(\frac{D_A t}{D\tau_R}\right)^2$	$\frac{2\tau_0}{\tau_R}$	$\frac{2\tau_0}{t}$

respectively. It takes positive values in the transient regime, for which the distribution is broader than Gaussian [Fig. 1(b)]. When $D_A \ll D$, the peak time equals t^* , namely the time when the MSD deviates from the transient plateau, as observed in colloidal systems [6,8,10,42,43], and the peak value reads $(\varepsilon/\sigma)^2/2$. When $D_A \gg D$, there is a plateau regime around the peak value, equal to $2\tau_0/\tau_R$. In both cases, the NGP starts to decrease when the long-time diffusive regime sets in. These asymptotic behaviors are also summarized in Table I.

C. Distribution of displacement

To characterize further the non-Gaussian behavior of the displacement fluctuations, we have to deal with the complete form of the spatial Fourier transform Eq. (9). Even though a complete Fourier inversion is not possible analytically, we can deduce several useful informations by looking at limiting cases, where approximations make calculations easier.

First, we observe that the active part of distribution in Eq. (9) can be simplified in the small and large q limits:

$$\tilde{P}_A(q,t) \underset{q\varepsilon \ll 1}{\sim} \exp \left[-(q\varepsilon)^2 \frac{\tau_R}{\tau_0} \left(\frac{t}{\tau_R} - f_t \right) \right], \quad (14)$$

$$\tilde{P}_A(q,t) \underset{q\varepsilon \gg 1}{\sim} e^{-t/\tau_0} (|q|\varepsilon f_t)^{-\tau_R/\tau_0}. \quad (15)$$

Taking $q = 1/\sigma$, it follows that the total distribution \tilde{P} is Gaussian at all times when $\varepsilon \ll \sigma$, whereas the non-Gaussian features affect the large-time relaxation when $\varepsilon \gtrsim \sigma$, as reported in Table II.

TABLE II. Different regimes in the time evolution of the Fourier-displacement distribution at $q = 1/\sigma$. It is always Gaussian at times shorter than the terminal relaxation time $t^* = \tau_R D/D_A$, and some non-Gaussian features appear at later times if $\varepsilon \gtrsim \sigma$.

$\tilde{P}(1/\sigma, t)$	$\varepsilon \ll \sigma$	$\varepsilon \gtrsim \sigma$
$t \ll t^*$	$e^{-(q\sigma)^2 f_t}$	$e^{-(q\sigma)^2 f_t}$
$t \gg t^*$	$e^{-q^2 D_A t}$	$e^{-(q\sigma)^2 f_t - t/\tau_0} (q \varepsilon f_t)^{-\tau_R/\tau_0}$

The displacement distribution is also always Gaussian at asymptotically short and long times, corresponding, respectively, to the passive and active diffusions. In the intermediate transient regime, it is Gaussian for small and large displacements, with a non-Gaussian crossover in between.

The active distribution P_A has a Gaussian behavior for large displacements and large times, as a signature of the central limit theorem. It behaves like a power law for small displacements with an exponential cutoff of the form $e^{-|\Delta x|/(\varepsilon f_t)}$. Mathematically, the exponential tails are due from the pole in the last term of Eq. (9). Therefore, the total distribution \tilde{P} is Gaussian at short and large displacement with exponential tails in between. The power-law behavior is only observed in the deviation from the central Gaussian part, as discussed below. To determine the deviation from the large Gaussian part, we expand $\ln \tilde{P}$ for small q as

$$\begin{aligned} \ln \tilde{P}(q,t) = & -\frac{\langle \Delta x^2(t) \rangle}{2} q^2 + \frac{\langle \Delta x^4(t) \rangle - 3\langle \Delta x^2(t) \rangle^2}{4} q^4 \\ & + \mathcal{O}(q^6). \end{aligned} \quad (16)$$

It follows that the transition between the large Gaussian part and non-Gaussian features appears at $\Delta x \sim [(\langle \Delta x^4(t) \rangle / \langle \Delta x^2(t) \rangle - 3\langle \Delta x^2(t) \rangle)/2]^{1/2}$.

The accessible range of displacements for experimental and simulated systems does not always allow one to observe the large Gaussian part of the distribution (they can clearly be seen, though, in Ref. [10]). The existence of directed events is quantified through the deviation from the central Gaussian, that is via the crossover between the two Gaussian parts. Within our model, it is given by exponential tails, as commonly reported in glassy systems [13], of the form $e^{-|\Delta x|/(\varepsilon f_t)}$. To quantitatively test the predictions of our model with experiments and computer simulations, we have compared our results with existing data for a dense suspension of colloidal particles [10] and a binary Lennard-Jones mixture [13,35]. Our model perfectly fits these results, as shown in Figs. 1(c) and 1(d). For the colloidal system, we reproduce the time evolution of the distribution with parameters $\{\tau_0/\tau_R, \varepsilon/\sigma\} = \{25, 6\}$ [Fig. 1(c)]. In the Lennard-Jones mixture, the measurements are taken for four temperatures at the α relaxation time, corresponding to t^* within our model (see below). The central Gaussian part barely varies, whereas the tails decrease with temperature. We identify the temperature with the diffusion coefficient D of the confined motion, and we adjust the corresponding exponential tails with $\varepsilon = \{0.2, 0.25, 0.29, 0.33\}$ from left to right in Fig. 1(d). Available data supporting our choice of an exponential cage-hop distribution, however, extend over a single decade, and it is likely that other choices of distribution could fit the data. More detail on the analysis on the experimental and numerical data is provided in Appendix B.

To further characterize the departure from the central Gaussian, we investigate the transition between the central Gaussian part and the tails by looking at the intermediate-displacement part of the distribution P_{int} , which does not include the exponential tails. We focus on the case $\tau_0 > \tau_R$, namely when the time needed for the particle to relax within the cage is shorter than two successive cage hops. We start considering the Fourier distribution of displacement at large wave number. From Eqs. (4) and (15), we deduce the

expression of this distribution in the limit $q\varepsilon \gg 1$:

$$\tilde{P}(q,t) \underset{q\varepsilon \gg 1}{\sim} e^{-(q\sigma)^2 f_t t / \tau_0} (|q| \varepsilon f_t)^{-\tau_R / \tau_0}. \quad (17)$$

We perform the inverse Fourier transform of Eq. (17) to obtain

$$P(x,t) \underset{x \ll \varepsilon}{\sim} {}_1F_1\left[\frac{\tau_0 - \tau_R}{2\tau_0}, \frac{1}{2}; -\frac{(x/\sigma)^2}{4f_t}\right] \equiv P_{\text{int}}(x,t), \quad (18)$$

where ${}_1F_1$ is the confluent hypergeometric function of the first kind. It depends on the hopping statistics only via the typical waiting time τ_0 between two successive cage hops, thus being independent of the hopping length ε . Besides, this result remains unchanged for any hopping distribution. This suggests that the intermediate-displacement distribution is an appropriate probe to reveal universal behavior in glassy systems.

The asymptotic behaviors of P_{int} are given by

$$P_{\text{int}}(x,t) \underset{x \rightarrow 0}{\sim} e^{-(1 - \frac{\tau_R}{\tau_0}) \frac{(x/\sigma)^2}{4f_t}}, \quad (19)$$

$$P_{\text{int}}(x,t) \underset{x \rightarrow \infty}{\sim} \left[\left(1 - \frac{\tau_R}{\tau_0}\right) \frac{(x/\sigma)^2}{4f_t} \right]^{\frac{\tau_R - \tau_0}{2\tau_0}} g_{\tau_0/\tau_R}, \quad (20)$$

where

$$g_u = \frac{1}{\sqrt{\pi}} \Gamma\left(1 - \frac{1}{2u}\right) \sin\left(\frac{\pi}{2u}\right). \quad (21)$$

Therefore, the central part is Gaussian with standard deviation $\sigma \sqrt{2f_t/(1 - \tau_R/\tau_0)}$, and the departure from this Gaussian is given by power-law tails with exponent $\tau_R/\tau_0 - 1$ [Fig. 2]. Note that P_{int} only characterizes the deviation from the central Gaussian part, so that it does contain the exponential tails appearing for larger displacement. The typical length scale X of the crossover between the Gaussian central part of this distribution and the power-law tails can be obtained by considering the small-displacement distribution for displacements scaled by $x^*(t) = \sigma \sqrt{2f_t/(1 - \tau_R/\tau_0)}$. From Eqs. (19) and (20), we

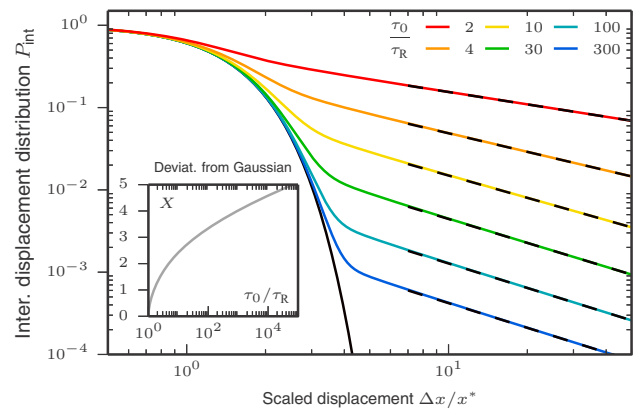


FIG. 2. Distribution of small displacement scaled by $x^*(t) = \sigma \sqrt{2f_t/(1 - \tau_R/\tau_0)}$ in Eq. (18). The central part is Gaussian (solid black line) with power-law tails (dashed lines). (Inset) Crossover value X between the central Gaussian part and the tails of the distribution as a function of τ_0/τ_R .

determine its expression as

$$X(u) = \sqrt{\frac{1-u}{u}} W\left[-2(g_u)^{\frac{2u}{u-1}}\right], \quad (22)$$

where W is the principal branch of the Lambert W function defined by

$$z = W(z)e^{W(z)}. \quad (23)$$

We plot X as a function of τ_0/τ_R in the inset of Fig. 2.

IV. SCATTERING FUNCTION

The comparison with glassy dynamics can be extended further by investigating the time evolution of the Fourier-displacement distribution $\tilde{P}(q,t)$ at some fixed wave number, yet to be determined. To this end, we can regard $\tilde{P}(q,t)$ as an approximation for the sISF in a N -body system,

$$F_S(q,t) = \frac{1}{N} \sum_{i=1}^N \langle e^{iq[x_i(t)-x_i(0)]} \rangle. \quad (24)$$

In that case, the relevant choice for q would be the value at the first peak of the structure factor, which corresponds to the inverse of the typical interparticle distance. Provided that caging stems from the steric hindrance, the typical distance between particles should be encoded in the cage size. This leads us to choose $1/\sigma$ as the appropriate wave number.

There is a transition from a single to a two-step relaxation of the sISF as D_A/D decreases [Fig. 3]. This is typical

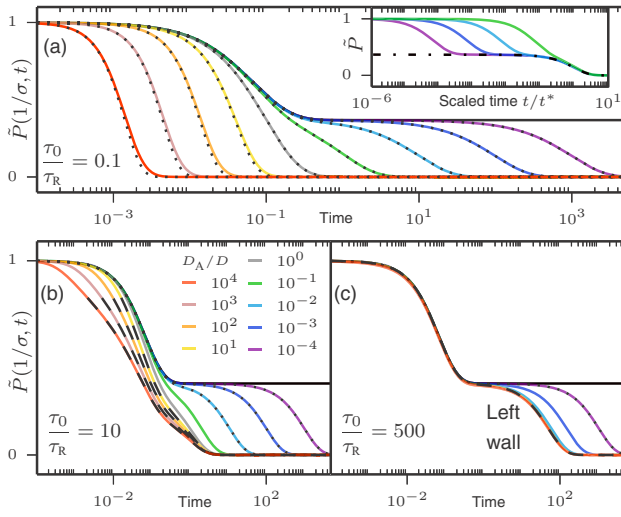


FIG. 3. Flow curves of the Fourier-displacement distribution at $q = 1/\sigma$. (a) The transition from a single to a two-step relaxation as D_A/D decreases is the hallmark of glassy systems. There is no terminal relaxation for a steady cage (solid black line). The curves are Gaussian at all times when $\varepsilon \ll \sigma$ (dotted lines). (Inset) For the two-step dynamics, we scale the time by the terminal relaxation time to reveal an exponential master curve (dot-dashed line). (b) The non-Gaussian statistics affects the relaxation when $\varepsilon \gtrsim \sigma$ (dashed lines). (c) The curves such as $\varepsilon \gtrsim \sigma$ fall into the left wall $e^{-t/\tau_0 + f_t}$ (dashed line), reflecting the dynamical slowing down as the cage hops become less frequent.

of the behavior observed in glasses, the two-step dynamics being reminiscent of the β and α relaxations. The sISF for a steady cage relaxes within a time τ_R to a nonzero value, equal to the transient plateau value of the sISF for a hopping cage. Such behavior is similar to the kinetic arrest reported in glasses, when the particle evolves in a metastable state for an infinite long time. The plateau value reads $e^{-(q\sigma)^2}$ for an arbitrary wave number. Cage rearrangements occur in the active case; then the particle overcomes the local confinement. The terminal relaxation for single and two-step dynamics starts at time t^* , namely when the passive regime ends. For a two-step dynamics, the terminal relaxation occurs when the NGP reaches its peak value [10,43–47], and it can be shifted to an arbitrary long time [27].

The sISF is Gaussian at all times when $\varepsilon \ll \sigma$, the structural relaxation thus being entirely determined by the MSD. In such a case, the long-time behavior is independent of D_A when scaling the time by t^* . For a two-step relaxation, the corresponding master curve $e^{-(1+t/t^*)}$ is exponential [Inset of Fig. 3(a)]. A stretched exponential is usually reported, with an exponent close to one [24,25]. Our result suggests that one would clearly observe exponential behavior when the terminal relaxation time t^* is large compared with the time τ_R of the first relaxation. The non-Gaussian fluctuations play a role in the dynamics if $\varepsilon \gtrsim \sigma$, the higher-order statistics of the displacement thereby affecting the relaxation of the system [Fig. 3(b)].

A left wall appears in the flow curves if $\tau_R \ll \tau_0$, namely all the flow curves such that $\varepsilon \gtrsim \sigma$ fall onto a master curve [Fig. 3(c)]. The expression of the left wall reads $e^{-t/\tau_0 - f_t}$, the associated terminal relaxation time being τ_0 . The existence of a left wall is reminiscent of the dynamics for *in silico* shear glasses [26]. The sheared region close to the left wall reflects the slowing down of the relaxation as the cage hops become less frequent, that is when τ_0 increases. On the opposite, the particle does not relax toward the center of the cage between two successive hops when $\tau_R \gtrsim \tau_0$, in which case there is no left wall because the transient caging does not lead to any dynamical slowing down.

V. RELATION WITH MANY-BODY SYSTEMS

We now try to understand how our one-body approach can be connected with multicomponent systems. Using the expression of the Fourier-displacement distribution in Eq. (9), we can deduce its time evolution:

$$\partial_t \tilde{P}(q,t) = -q^2 \left[D e^{-t/\tau_R} + \frac{D_A f_t}{1 + (q\varepsilon f_t)^2} \right] \tilde{P}(q,t). \quad (25)$$

It follows that the displacement distribution obeys the following master equation:

$$\begin{aligned} \partial_t P(x,t) = & \frac{\rho_{\text{ref}}}{\zeta} \partial_{xx}^2 \int dy V_{\text{eff}}(x-y,t) P(y,t) \\ & + D_{\text{eff}}(t) \partial_{xx}^2 P(x,t), \end{aligned} \quad (26)$$

where for later convenience we have introduced a reference density ρ_{ref} and a friction coefficient ζ . The time-dependent

diffusion coefficient D_{eff} and effective potential V_{eff} read

$$D_{\text{eff}}(t) = D e^{-t/\tau_R}, \quad (27)$$

$$V_{\text{eff}}(x, t) = \frac{\zeta \varepsilon}{2\rho_{\text{ref}} \tau_0} \exp\left(-\frac{|x|}{\varepsilon f_t}\right). \quad (28)$$

Our aim is to establish that the one-body problem can be mapped into a system of N particles with diffusion coefficient D_{eff} and interaction potential V_{eff} , which are time-dependent. The corresponding dynamics of a particle i reads

$$\frac{dx_i}{dt} = -\frac{1}{\zeta} \sum_{j=1}^N \partial_{x_j} V_{\text{eff}}(x_i - x_j(t), t) + \sqrt{2D_{\text{eff}}(t)} \xi_i(t), \quad (29)$$

where ξ_i is a zero-mean Gaussian noise with correlations $\langle \xi_i(t) \xi_j(t') \rangle = \delta_{ij} \delta(t - t')$. Note that Eq. (29) describes a nonequilibrium dynamics since the correlations of the noise are different from the prediction of the fluctuation-dissipation theorem. The self-intermediate scattering function $F_S(q, t)$ is defined as

$$F_S(q, t) = \frac{1}{N} \sum_{i=1}^N \langle e^{iq(x_i(t) - x_i(0))} \rangle. \quad (30)$$

The inverse Fourier transform of $F_S(q, t)$ is the self-part of the Van Hove correlation function $G_S(x, t)$

$$G_S(x, t) = \frac{1}{N} \sum_{i=1}^N \langle \delta[x + x_i(0) - x_i(t)] \rangle. \quad (31)$$

The n -body correlation functions of the density are generally connected via a hierarchy of equations. The simplest closure scheme, referred to as the random phase approximation (RPA), consists in truncating this hierarchy at the Gaussian order,

$$\begin{aligned} \partial_t G_S(x, t) &= \frac{\rho_0}{\zeta} \partial_{xx}^2 \int dy V_{\text{eff}}(x - y, t) G_S(y, t) \\ &\quad + D_{\text{eff}}(t) \partial_{xx}^2 G_S(x, t), \end{aligned} \quad (32)$$

where $\rho_0 = N/L$ is defined in terms of the system size L . We identify the density of particle ρ_0 with the reference density ρ_{ref} introduced earlier, and we choose D_{eff} and V_{eff} to obey Eqs. (27) and (28), respectively. It follows that Eqs. (32) and (A5) describe the same dynamics, from which we deduce that the distribution of displacement for the one-body dynamics equals the Van Hove correlation function for interacting particles within the RPA. Likely, the Fourier-displacement distribution corresponds to the self-intermediate scattering function. The effective potential arising from the non-Gaussian statistics of the cage's dynamics can be regarded as a mean-field potential resulting from the interaction between many particles. Such potential describes repulsive interactions with a very soft core, thus allowing the overlap of the particles with a finite cost of energy [48]. The range of interaction increases with time as f_t , namely it saturates within a time τ_R to ε . Therefore, there is a transition between: (i) a diffusive dynamics with very short interaction, (ii) a dynamics with a very small diffusion coefficient and a larger interaction range, corresponding, respectively, to times shorter and longer than τ_R . The existence of interactions is a direct consequence of the cage rearrangements within our model. The explicit form

of the potential is determined by the statistics of the cage hops, which are exponentially distributed in the present case. This suggests that the non-Gaussian properties of the particle dynamics hold information about the details of interaction between the particles.

VI. DISCUSSION

We have presented a minimal model of a particle immersed in a glassy system, based on an active cage with non-Gaussian dynamics. By focusing on a single particle we are able to decouple complex phenomena that arise from collective effects from the sole dynamics of the particle. Of course, this approach is not intended in understanding how collective phenomena emerge but rather to provide a vivid picture explaining experiments on glassy systems. Despite the simplicity of this model, we have demonstrated that its dynamics encompasses the complex behaviors arising in glassy systems and that the onset of glassy behavior is shifted by the active component of the dynamics, in line with numerical evidence [27,28,30,31]. Moreover, we have highlighted the scale invariance of the small-displacement distribution. The dynamics of tracers in living systems shares common features with the glassy dynamics [49,50]. The tracers can be either attached or embedded in a network of filaments, whose rearrangement is induced by nonequilibrium processes, thus monitoring transitions between locally stable configurations [51,52]. The minimal approach of intermittent dynamics that we offer in the present paper should also be relevant for a large variety of biological systems [53–60], as a useful tool to understand the existence of a scale-invariant regime in the tracer displacement [49,61,62].

ACKNOWLEDGMENTS

The authors acknowledge useful discussions with Kiyoshi Kanazawa and Daisuke Mizuno. É.F. and F.v.W. acknowledge the support of the YITP and SoftActive program, as well as of the JSPS core-to-core program “Non-equilibrium dynamics of soft matter and information.” This work was partially supported by JSPS KAKENHI Grants No. 25287098 and No. 16H04025.

APPENDIX A: GENERALIZATION TO AN ARBITRARY HOPPING DISTRIBUTION

We introduce the distribution \mathcal{W} , which prescribes the distance of the instantaneous hops experienced by the cage. We assume that the waiting time between two consecutive jumps remains exponentially distributed with mean value τ_0 . Hence, the cumulants of ξ_{NG} read

$$\langle \xi_{\text{NG}}(t_1) \dots \xi_{\text{NG}}(t_n) \rangle_C = K_n \delta_n(t_1, \dots, t_n), \quad (\text{A1})$$

where

$$K_n = \frac{1}{\tau_0} \int dx_0 \mathcal{W}(x_0) x_0^n. \quad (\text{A2})$$

Note that we recover Eq. (2) for an exponential distribution $\mathcal{W}(x_0) = e^{-|x_0|/\varepsilon}/\varepsilon$, as expected. We express the active

distribution in terms of the cumulant coefficients K_n as

$$\tilde{P}_A(q,t) = \exp \left[\sum_{n=1}^{\infty} \frac{(iq)^n K_n}{n!} \left(\frac{f_t^n}{n} + \int_0^t ds f_{t-s}^n \right) \right]. \quad (\text{A3})$$

We deduce the time-derivative of the total distribution,

$$\begin{aligned} \partial_t \tilde{P}(q,t) &= -q^2 D_{\text{eff}}(t) \tilde{P}(q,t) + \sum_{n=1}^{\infty} \frac{(iq)^n K_n}{n!} \frac{d}{dt} \\ &\quad \times \left(\frac{f_t^n}{n} + \int_0^t ds f_{t-s}^n \right) \tilde{P}(q,t), \end{aligned} \quad (\text{A4})$$

where

$$\frac{d}{dt} \left(\frac{f_t^n}{n} + \int_0^t ds f_{t-s}^n \right) = e^{-t/\tau_R} f_t^{n-1} + f_t^n = f_t^{n-1}. \quad (\text{A5})$$

By using Eqs. (A2) and (A5), we write the second term in the righthand side of Eq. (A4) in terms of the hopping distribution \mathcal{W} as

$$[\partial_t + q^2 D_{\text{eff}}] \tilde{P} = \frac{1}{\tau_0 f_t} \int dx_0 \mathcal{W}(x_0) \sum_{n=1}^{\infty} \frac{(iq x_0)^n}{n!} f_t^n \tilde{P} \quad (\text{A6})$$

$$= \frac{1}{\tau_0 f_t} \int dx_0 \mathcal{W}(x_0) [e^{iq x_0 f_t} - 1] \tilde{P} \quad (\text{A7})$$

$$= \frac{1}{\tau_0 f_t} [\tilde{\mathcal{W}}(q f_t) - 1] \tilde{P}, \quad (\text{A8})$$

where we have used $\int dx_0 \mathcal{W}(x_0) = 1$. Our aim lies in deriving the distribution for small displacements. To this end, we consider Eq. (A8) in the large- q limit. Provided that the hopping distribution \mathcal{W} is not a δ function, its Fourier transform should decay to zero for wave numbers sufficiently large compared with the inverse typical hopping length $1/\varepsilon$.

In this limit, we express Eq. (A8) as

$$\partial_t \tilde{P}(q,t) \underset{q\varepsilon \gg 1}{\sim} - \left[q^2 D_{\text{eff}}(t) + \frac{1}{\tau_0 f_t} \right] \tilde{P}(q,t). \quad (\text{A9})$$

The solution of the above equation is consistent with Eq. (17). However, the power-law prefactor in q in Eq. (17) can only be obtained after a careful analysis of the asymptotics of $\tilde{\mathcal{W}}(q f_t)$ (and it shows up only if \mathcal{W} decays exponentially or slower at large distances).

APPENDIX B: DATA ANALYSIS

We present in this appendix the analysis of the distribution of displacement obtained from two different systems: (i) a binary Lennard-Jones glass-forming mixture [13,35] and (ii) a dense suspension of colloid particles [10]. In the two systems, we can reproduce both the central Gaussian part and the exponential tails as reported in Figs. 1(c) and 1(d).

For the Lennard-Jones mixture, we scale the displacement distribution by the standard deviation of the Gaussian central part. The measurements are taken for four temperatures at the α relaxation time, corresponding to $t^* = \tau_R D / D_A$ within our model. We identify the temperature with the diffusion coefficient D of the confined motion, leaving us with three free parameters $\{\tau_R, \tau_0, \varepsilon\}$. The timescales $\{\tau_R, \tau_0\} = \{0.05, 1.05\}$ are taken as the same for all temperatures, and we adjust the corresponding exponential tails with ε .

For the colloidal system, the measurements are taken at five different times. We fix the ratio τ_R/τ_0 from the deviation of the central Gaussian part, and we determine $\{\sigma, \tau_R, \tau_0\} = \{0.05 \mu\text{m}, 10^3 \text{s}, 25 \times 10^3 \text{s}\}$ by fitting the central Gaussian parts of the distribution. Eventually, we adjust the exponential tails with $\varepsilon = 0.3 \mu\text{m}$. The time evolution of the distribution is reproduced with the same set of parameters.

-
- [1] L. Berthier and G. Biroli, *Rev. Mod. Phys.* **83**, 587 (2011).
 - [2] W. Götze, *Complex Dynamics of Glass-Forming Liquids, a Mode-Coupling Theory* (Oxford University Press, Oxford, 2009).
 - [3] L. M. C. Janssen and D. R. Reichman, *Phys. Rev. Lett.* **115**, 205701 (2015).
 - [4] M. Priya, N. Bidhoodi, and S. P. Das, *Phys. Rev. E* **92**, 062308 (2015).
 - [5] N. Bidhoodi and S. P. Das, *Physica A* **449**, 357 (2016).
 - [6] E. R. Weeks, J. C. Crocker, A. C. Levitt, A. Schofield, and D. A. Weitz, *Science* **287**, 627 (2000).
 - [7] W. K. Kegel and A. van Blaaderen, *Science* **287**, 290 (2000).
 - [8] E. R. Weeks and D. A. Weitz, *Phys. Rev. Lett.* **89**, 095704 (2002).
 - [9] Y. Gao and M. L. Kilfoil, *Phys. Rev. Lett.* **99**, 078301 (2007).
 - [10] Y. Gao and M. L. Kilfoil, *Phys. Rev. E* **79**, 051406 (2009).
 - [11] T. A. Caswell, Z. Zhang, M. L. Gardel, and S. R. Nagel, *Phys. Rev. E* **87**, 012303 (2013).
 - [12] D. A. Stariolo and G. Fabricius, *J. Chem. Phys.* **125**, 064505 (2006).
 - [13] P. Chaudhuri, L. Berthier, and W. Kob, *Phys. Rev. Lett.* **99**, 060604 (2007).
 - [14] Y. Gao and M. L. Kilfoil, *Opt. Express* **17**, 4685 (2009).
 - [15] J. Helfferich, F. Ziebert, S. Frey, H. Meyer, J. Farago, A. Blumen, and J. Baschnagel, *Phys. Rev. E* **89**, 042603 (2014).
 - [16] J. Helfferich, F. Ziebert, S. Frey, H. Meyer, J. Farago, A. Blumen, and J. Baschnagel, *Phys. Rev. E* **89**, 042604 (2014).
 - [17] L. O. Hedges, L. Maibaum, D. Chandler, and J. P. Garrahan, *J. Chem. Phys.* **127**, 211101 (2007).
 - [18] R. Pastore, A. Coniglio, and M. Pica Ciamarra, *Soft Matter* **10**, 5724 (2014).
 - [19] R. Pastore, A. Coniglio, and M. Pica Ciamarra, *Sci. Rep.* **5**, 11770 (2014).
 - [20] R. Pastore, M. Pica Ciamarra, G. Pesce, and A. Sasso, *Soft Matter* **11**, 622 (2015).
 - [21] J. Helfferich, *Eur. Phys. J. E* **37**, 73 (2014).
 - [22] P. Chaudhuri, Y. Gao, L. Berthier, M. Kilfoil, and W. Kob, *J. Phys.: Condens. Matter* **20**, 244126 (2008).
 - [23] L. Berthier, J.-L. Barrat, and J. Kurchan, *Phys. Rev. E* **61**, 5464 (2000).

- [24] L. Berthier and J.-L. Barrat, *Phys. Rev. Lett.* **89**, 095702 (2002).
- [25] L. Berthier and J.-L. Barrat, *J. Chem. Phys.* **116**, 6228 (2002).
- [26] F. Varnik, L. Bocquet, J.-L. Barrat, and L. Berthier, *Phys. Rev. Lett.* **90**, 095702 (2003).
- [27] R. Ni, M. A. C. Stuart, and M. Dijkstra, *Nat. Commun.* **4**, 2704 (2013).
- [28] L. Berthier, *Phys. Rev. Lett.* **112**, 220602 (2014).
- [29] D. Levis and L. Berthier, *Phys. Rev. E* **89**, 062301 (2014).
- [30] R. Mandal, P. J. Bhuyan, M. Rao, and C. Dasgupta, *Soft Matter* (2016), doi:10.1039/C5SM02950C.
- [31] A. Wysocki, R. G. Winkler, and G. Gompper, *Europhys. Lett.* **105**, 48004 (2014).
- [32] L. Berthier and J. Kurchan, *Nat. Phys.* **9**, 310 (2013).
- [33] G. Szamel, E. Flenner, and L. Berthier, *Phys. Rev. E* **91**, 062304 (2015).
- [34] T. F. F. Farage and J. M. Brader, arXiv:1403.0928.
- [35] L. Berthier and W. Kob, *J. Phys.: Cond. Mat.* **19**, 205130 (2007).
- [36] C. Scalliet, A. Gnoli, A. Puglisi, and A. Vulpiani, *Phys. Rev. Lett.* **114**, 198001 (2015).
- [37] A. Lasanta and A. Puglisi, *J. Chem. Phys.* **143**, 064511 (2015).
- [38] K. Kanazawa, T. G. Sano, T. Sagawa, and H. Hayakawa, *Phys. Rev. Lett.* **114**, 090601 (2015).
- [39] M. O. Cáceres and A. A. Budini, *J. Phys. A* **30**, 8427 (1997).
- [40] A. Baule and E. G. D. Cohen, *Phys. Rev. E* **79**, 030103 (2009).
- [41] A. Baule and E. G. D. Cohen, *Phys. Rev. E* **80**, 011110 (2009).
- [42] E. R. Weeks, J. C. Crocker, and D. A. Weitz, *J. Phys.: Condens. Matter* **19**, 205131 (2007).
- [43] S. V. Franklin and E. R. Weeks, arXiv:1406.5782.
- [44] W. Kob, C. Donati, S. J. Plimpton, P. H. Poole, and S. C. Glotzer, *Phys. Rev. Lett.* **79**, 2827 (1997).
- [45] T. Narumi, S. V. Franklin, K. W. Desmond, M. Tokuyama, and E. R. Weeks, *Soft Matter* **7**, 1472 (2011).
- [46] P. Charbonneau, A. Ikeda, G. Parisi, and F. Zamponi, *Proc. Natl. Acad. Sci. USA* **109**, 13939 (2012).
- [47] M. Vogel and S. C. Glotzer, *Phys. Rev. E* **70**, 061504 (2004).
- [48] A. K. Bacher, T. B. Schrøder, and J. C. Dyre, *Nat. Commun.* **5**, 5424 (2013).
- [49] P. Bursac, G. Lenormand, B. F. M. Oliver, D. A. Weitz, V. Viasnoff, J. P. Butler, and J. J. Fredberg, *Nat. Mat.* **4**, 557 (2005).
- [50] T. E. Angelini, E. Hannezo, X. Trepat, M. Marquez, J. J. Fredberg, and D. A. Weitz, *Proc. Natl. Acad. Sci. USA* **108**, 4714 (2011).
- [51] C. P. Brangwynne, G. H. Koenderink, F. C. MacKintosh, and D. A. Weitz, *Trends Cell Biol.* **19**, 423 (2009).
- [52] W. W. Ahmed, É. Fodor, and T. Betz, *BBA-Mol. Cell Res.* **1853**, 3083 (2015).
- [53] I. Zaid, H. L. Ayade, and D. Mizuno, *Biophys. J.* **106**, 171a (2014).
- [54] M. Aridome, T. Kurihara, H. Ayade, I. Zaid, and D. Mizuno, *Biophys. J.* **106**, 580a (2014).
- [55] É. Fodor, K. Kanazawa, H. Hayakawa, P. Visco, and F. van Wijland, *Phys. Rev. E* **90**, 042724 (2014).
- [56] É. Fodor, M. Guo, N. S. Gov, P. Visco, D. A. Weitz, and F. van Wijland, *Europhys. Lett.* **110**, 48005 (2015).
- [57] E. Ben-Isaac, É. Fodor, P. Visco, F. van Wijland, and N. S. Gov, *Phys. Rev. E* **92**, 012716 (2015).
- [58] É. Fodor, V. Mehandia, J. Comelles, R. Thiagarajan, N. S. Gov, P. Visco, F. van Wijland, and D. Riveline, arXiv:1512.01476.
- [59] W. W. Ahmed, E. Fodor, M. Almonacid, M. Bussonnier, M.-H. Verlhac, N. S. Gov, P. Visco, F. van Wijland, and T. Betz, arXiv:1510.08299.
- [60] É. Fodor, W. W. Ahmed, M. Almonacid, M. Bussonnier, N. S. Gov, M.-H. Verlhac, T. Betz, P. Visco, and F. van Wijland, arXiv:1511.00921.
- [61] N. Gal, D. Lechtman-Goldstein, and D. Weihs, *Rheol. Acta* **52**, 425 (2013).
- [62] B. Wang, S. M. Anthony, S. C. Bae, and S. Granick, *Proc. Natl. Acad. Sci. USA* **106**, 15160 (2009).

Bibliography

- [1] M. C. Marchetti, J. F. Joanny, S. Ramaswamy, T. B. Liverpool, J. Prost, M. Rao, and R. A. Simha. “Hydrodynamics of soft active matter”. *Rev. Mod. Phys.* 85 (2013), pp. 1143–1189. DOI: [10.1103/RevModPhys.85.1143](https://doi.org/10.1103/RevModPhys.85.1143).
- [2] C. Jarzynski. “Equalities and Inequalities: Irreversibility and the Second Law of Thermodynamics at the Nanoscale”. *Annu. Rev. CMP* 2 (2015), pp. 329–351. DOI: [10.1146/annurev-conmatphys-062910-140506](https://doi.org/10.1146/annurev-conmatphys-062910-140506).
- [3] U. Seifert. “Stochastic thermodynamics, fluctuation theorems and molecular machines”. *Rep. Prog. Phys.* 75.12 (2012), p. 126001. DOI: [10.1088/0034-4885/75/12/126001](https://doi.org/10.1088/0034-4885/75/12/126001).
- [4] C. P. Brangwynne, G. H. Koenderink, F. C. MacKintosh, and D. A. Weitz. “Cytoplasmic diffusion: molecular motors mix it up”. *J. Cell Biol.* 183.4 (2008), pp. 583–587. DOI: [10.1083/jcb.200806149](https://doi.org/10.1083/jcb.200806149).
- [5] F. C. MacKintosh and C. F. Schmidt. “Active cellular materials”. *Current Opinion in Cell Biology* 22.1 (2010). Cell structure and dynamics, pp. 29–35. DOI: [10.1016/j.ceb.2010.01.002](https://doi.org/10.1016/j.ceb.2010.01.002).
- [6] B. D. Hoffman, G. Massiera, K. M. Van Citters, and J. C. Crocker. “The consensus mechanics of cultured mammalian cells”. *Proc. Natl. Acad. Sci. USA* 103.27 (2006), pp. 10259–10264. DOI: [10.1073/pnas.0510348103](https://doi.org/10.1073/pnas.0510348103).
- [7] D. Wirtz. “Particle-tracking microrheology of living cells: principles and applications”. *Annu. Rev. Biophys.* 38 (2009), pp. 301–326. DOI: [10.1146/annurev.biophys.050708.133724](https://doi.org/10.1146/annurev.biophys.050708.133724).
- [8] N. Gal, D. Lechtman-Goldstein, and D. Weihs. “Particle tracking in living cells: a review of the mean square displacement method and beyond”. *Rheol. Acta* 52.5 (2013), pp. 425–443. DOI: [10.1007/s00397-013-0694-6](https://doi.org/10.1007/s00397-013-0694-6).
- [9] L. F. Cugliandolo. “The effective temperature”. *J. Phys. A: Math. Theor.* 44.48 (2011), p. 483001. DOI: [10.1088/1751-8113/44/48/483001](https://doi.org/10.1088/1751-8113/44/48/483001).

- [10] A. Sokolov, I. S. Aranson, J. O. Kessler, and R. E. Goldstein. “Concentration Dependence of the Collective Dynamics of Swimming Bacteria”. *Phys. Rev. Lett.* 98 (2007), p. 158102. DOI: [10.1103/PhysRevLett.98.158102](https://doi.org/10.1103/PhysRevLett.98.158102).
- [11] J. Palacci, S. Sacanna, A. P. Steinberg, D. J. Pine, and P. M. Chaikin. “Living Crystals of Light-Activated Colloidal Surfers”. *Science* 339.6122 (2013), pp. 936–940. DOI: [10.1126/science.1230020](https://doi.org/10.1126/science.1230020).
- [12] T. Vicsek, A. Czirók, E. Ben-Jacob, I. Cohen, and O. Shochet. “Novel Type of Phase Transition in a System of Self-Driven Particles”. *Phys. Rev. Lett.* 75 (1995), pp. 1226–1229. DOI: [10.1103/PhysRevLett.75.1226](https://doi.org/10.1103/PhysRevLett.75.1226).
- [13] J. Tailleur and M. E. Cates. “Statistical Mechanics of Interacting Run-and-Tumble Bacteria”. *Phys. Rev. Lett.* 100 (2008), p. 218103. DOI: [10.1103/PhysRevLett.100.218103](https://doi.org/10.1103/PhysRevLett.100.218103).
- [14] M. E. Cates and J. Tailleur. “Motility-Induced Phase Separation”. *Annu. Rev. CMP* 6.1 (2015), pp. 219–244. DOI: [10.1146/annurev-conmatphys-031214-014710](https://doi.org/10.1146/annurev-conmatphys-031214-014710).
- [15] A. P. Solon and J. Tailleur. “Revisiting the Flocking Transition Using Active Spins”. *Phys. Rev. Lett.* 111 (2013), p. 078101. DOI: [10.1103/PhysRevLett.111.078101](https://doi.org/10.1103/PhysRevLett.111.078101).
- [16] A. P. Solon, H. Chaté, and J. Tailleur. “From Phase to Microphase Separation in Flocking Models: The Essential Role of Nonequilibrium Fluctuations”. *Phys. Rev. Lett.* 114 (2015), p. 068101. DOI: [10.1103/PhysRevLett.114.068101](https://doi.org/10.1103/PhysRevLett.114.068101).
- [17] J. Perrin. “L’agitation moléculaire et le mouvement brownien”. *Comptes rendus hebdomadaires des séances de l’Académie des sciences* 146 (1908), pp. 967–970.
- [18] P. Langevin. “Sur la théorie du mouvement brownien”. *Comptes rendus hebdomadaires des séances de l’Académie des sciences* 146 (1908), pp. 530–533.
- [19] N. G. Van Kampen. *Stochastic Processes in Physics and Chemistry*. Elsevier Science, 2007.
- [20] U. M. B. Marconi, A. Puglisi, L. Rondoni, and A. Vulpiani. “Fluctuation–dissipation: response theory in statistical physics”. *Phys. Rep.* 461.4 (2008), pp. 111–195. DOI: [10.1016/j.physrep.2008.02.002](https://doi.org/10.1016/j.physrep.2008.02.002).
- [21] S. Kheifets, A. Simha, K. Melin, T. Li, and M. G. Raizen. “Observation of Brownian Motion in Liquids at Short Times: Instantaneous Velocity and Memory Loss”. *Science* 343.6178 (2014), pp. 1493–1496. DOI: [10.1126/science.1248091](https://doi.org/10.1126/science.1248091).

- [22] R. Zwanzig. *Non-equilibrium statistical mechanics*. Oxford University Press, 2001.
- [23] R. Kubo. “The fluctuation-dissipation theorem”. *Rep. Prog. Phys.* 29.1 (1966), p. 255. DOI: [10.1088/0034-4885/29/1/306](https://doi.org/10.1088/0034-4885/29/1/306).
- [24] R. Zwanzig and M. Bixon. “Hydrodynamic Theory of the Velocity Correlation Function”. *Phys. Rev. A* 2 (1970), pp. 2005–2012. DOI: [10.1103/PhysRevA.2.2005](https://doi.org/10.1103/PhysRevA.2.2005).
- [25] D. Panja. “Generalized Langevin equation formulation for anomalous polymer dynamics”. *J. Stat. Mech.* 2010.02 (2010), p. L02001. DOI: [10.1088/1742-5468/2010/02/L02001](https://doi.org/10.1088/1742-5468/2010/02/L02001).
- [26] D. Panja. “Anomalous polymer dynamics is non-Markovian: memory effects and the generalized Langevin equation formulation”. *J. Stat. Mech.* 2010.06 (2010), P06011. DOI: [10.1088/1742-5468/2010/06/P06011](https://doi.org/10.1088/1742-5468/2010/06/P06011).
- [27] L. Berthier, J.-L. Barrat, and J. Kurchan. “A two-time-scale, two-temperature scenario for nonlinear rheology”. *Phys. Rev. E* 61 (5 2000), pp. 5464–5472. DOI: [10.1103/PhysRevE.61.5464](https://doi.org/10.1103/PhysRevE.61.5464).
- [28] L. Berthier and J.-L. Barrat. “Nonequilibrium dynamics and fluctuation-dissipation relation in a sheared fluid”. *J. Chem. Phys.* 116.14 (2002), pp. 6228–6242. DOI: [10.1063/1.1460862](https://doi.org/10.1063/1.1460862).
- [29] M. Baiesi, C. Maes, and B. Wynants. “Fluctuations and Response of Nonequilibrium States”. *Phys. Rev. Lett.* 103 (2009), p. 010602. DOI: [10.1103/PhysRevLett.103.010602](https://doi.org/10.1103/PhysRevLett.103.010602).
- [30] M. Baiesi and C. Maes. “An update on the nonequilibrium linear response”. *New J. Phys.* 15.1 (2013), p. 013004. DOI: [10.1088/1367-2630/15/1/013004](https://doi.org/10.1088/1367-2630/15/1/013004).
- [31] P. Bohec, F. Gallet, C. Maes, S. Safaverdi, P. Visco, and F. van Wijland. “Probing active forces via a fluctuation-dissipation relation: Application to living cells”. *EPL* 102.5 (2013), p. 50005. DOI: [10.1209/0295-5075/102/50005](https://doi.org/10.1209/0295-5075/102/50005).
- [32] C. Maes, S. Safaverdi, P. Visco, and F. van Wijland. “Fluctuation-response relations for nonequilibrium diffusions with memory”. *Phys. Rev. E* 87 (2013), p. 022125. DOI: [10.1103/PhysRevE.87.022125](https://doi.org/10.1103/PhysRevE.87.022125).
- [33] J. L. Lebowitz and H. Spohn. “A Gallavotti–Cohen-Type Symmetry in the Large Deviation Functional for Stochastic Dynamics”. *J. Stat. Phys.* 95.1-2 (1999), pp. 333–365. DOI: [10.1023/A:1004589714161](https://doi.org/10.1023/A:1004589714161).
- [34] L. Onsager and S. Machlup. “Fluctuations and Irreversible Processes”. *Phys. Rev.* 91 (1953), pp. 1505–1512. DOI: [10.1103/PhysRev.91.1505](https://doi.org/10.1103/PhysRev.91.1505).

- [35] T. Harada and S.-i. Sasa. “Equality Connecting Energy Dissipation with a Violation of the Fluctuation-Response Relation”. *Phys. Rev. Lett.* 95 (2005), p. 130602. DOI: [10.1103/PhysRevLett.95.130602](https://doi.org/10.1103/PhysRevLett.95.130602).
- [36] T. Harada and S.-i. Sasa. “Energy dissipation and violation of the fluctuation-response relation in nonequilibrium Langevin systems”. *Phys. Rev. E* 73 (2006), p. 026131. DOI: [10.1103/PhysRevE.73.026131](https://doi.org/10.1103/PhysRevE.73.026131).
- [37] J. M. Deutsch and O. Narayan. “Energy dissipation and fluctuation response for particles in fluids”. *Phys. Rev. E* 74 (2006), p. 026112. DOI: [10.1103/PhysRevE.74.026112](https://doi.org/10.1103/PhysRevE.74.026112).
- [38] K. Sekimoto. “Kinetic Characterization of Heat Bath and the Energetics of Thermal Ratchet Models”. *J. Phys. Soc. Jpn.* 66.5 (1997), pp. 1234–1237. DOI: [10.1143/JPSJ.66.1234](https://doi.org/10.1143/JPSJ.66.1234).
- [39] K. Sekimoto and S.-i. Sasa. “Complementarity Relation for Irreversible Process Derived from Stochastic Energetics”. *J. Phys. Soc. Jpn.* 66.11 (1997), pp. 3326–3328. DOI: [10.1143/JPSJ.66.3326](https://doi.org/10.1143/JPSJ.66.3326).
- [40] U. Seifert. “Stochastic thermodynamics: principles and perspectives”. *Eur. Phys. J. B* 64.3 (2008), pp. 423–431. DOI: [10.1140/epjb/e2008-00001-9](https://doi.org/10.1140/epjb/e2008-00001-9).
- [41] A. Bruce, B. Dennis, K. Hopkin, A. Johnson, J. Lewis, M. Raff, K. Roberts, and P. Walter. *Essential Cell Biology*. Garland Science, 2009.
- [42] T. Toyota, D. A. Head, C. F. Schmidt, and D. Mizuno. “Non-Gaussian athermal fluctuations in active gels”. *Soft Matter* 7 (2011), pp. 3234–3239. DOI: [10.1039/C0SM00925C](https://doi.org/10.1039/C0SM00925C).
- [43] J. Apgar, Y. Tseng, E. Fedorov, M. B. Herwig, S. C. Almo, and D. Wirtz. “Multiple-Particle Tracking Measurements of Heterogeneities in Solutions of Actin Filaments and Actin Bundles”. *Biophys. J.* 79.2 (2000), pp. 1095–1106. DOI: [10.1016/S0006-3495\(00\)76363-6](https://doi.org/10.1016/S0006-3495(00)76363-6).
- [44] M. L. Gardel, J. H. Shin, F. C. MacKintosh, L. Mahadevan, P. A. Matsudaira, and D. A. Weitz. “Scaling of F-Actin Network Rheology to Probe Single Filament Elasticity and Dynamics”. *Phys. Rev. Lett.* 93 (2004), p. 188102. DOI: [10.1103/PhysRevLett.93.188102](https://doi.org/10.1103/PhysRevLett.93.188102).
- [45] M. L. Gardel, J. H. Shin, F. C. MacKintosh, L. Mahadevan, P. Matsudaira, and D. A. Weitz. “Elastic Behavior of Cross-Linked and Bundled Actin Networks”. *Science* 304.5675 (2004), pp. 1301–1305. DOI: [10.1126/science.1095087](https://doi.org/10.1126/science.1095087).

- [46] M. Soares e Silva, M. Depken, B. Stuhrmann, M. Korsten, F. C. MacKintosh, and G. H. Koenderink. “Active multistage coarsening of actin networks driven by myosin motors”. *Proc. Natl. Acad. Sci. USA* 108.23 (2011), pp. 9408–9413. DOI: [10.1073/pnas.1016616108](https://doi.org/10.1073/pnas.1016616108).
- [47] M. Sheinman, A. Sharma, J. Alvarado, G. H. Koenderink, and F. C. MacKintosh. “Inherently unstable networks collapse to a critical point”. *Phys. Rev. E* 92 (2015), p. 012710. DOI: [10.1103/PhysRevE.92.012710](https://doi.org/10.1103/PhysRevE.92.012710).
- [48] J. Alvarado, M. Sheinman, A. Sharma, F. C. MacKintosh, and G. H. Koenderink. “Molecular motors robustly drive active gels to a critically connected state”. *Nat. Phys.* 9.9 (2013), pp. 591–597. DOI: [10.1038/nphys2715](https://doi.org/10.1038/nphys2715).
- [49] M. Sheinman, A. Sharma, J. Alvarado, G. H. Koenderink, and F. C. MacKintosh. “Anomalous Discontinuity at the Percolation Critical Point of Active Gels”. *Phys. Rev. Lett.* 114 (2015), p. 098104. DOI: [10.1103/PhysRevLett.114.098104](https://doi.org/10.1103/PhysRevLett.114.098104).
- [50] E. H. Zhou et al. “Universal behavior of the osmotically compressed cell and its analogy to the colloidal glass transition”. *Proc. Natl. Acad. Sci. USA* 106.26 (2009), pp. 10632–10637. DOI: [10.1073/pnas.0901462106](https://doi.org/10.1073/pnas.0901462106).
- [51] M. Guo et al. “Probing the Stochastic, Motor-Driven Properties of the Cytoplasm Using Force Spectrum Microscopy”. *Cell* 158 (2014), pp. 822–832. DOI: [10.1016/j.cell.2014.06.051](https://doi.org/10.1016/j.cell.2014.06.051).
- [52] L. Deng, X. Trepaut, J. P. Butler, E. Millet, K. G. Morgan, D. A. Weitz, and J. J. Fredberg. “Fast and slow dynamics of the cytoskeleton”. *Nat. Mat.* 5.8 (2006), pp. 636–640.
- [53] P. Bursac, G. Lenormand, B. F. M. Oliver, D. A. Weitz, V. Viasnoff, J. P. Butler, and J. J. Fredberg. “Cytoskeletal remodelling and slow dynamics in the living cell”. *Nat. Mat.* 4 (2005), pp. 557–561. DOI: [10.1038/nmat1404](https://doi.org/10.1038/nmat1404).
- [54] F. Gallet, D. Arcizet, P. Bohec, and A. Richert. “Power spectrum of out-of-equilibrium forces in living cells: amplitude and frequency dependence”. *Soft Matter* 5 (2009), pp. 2947–2953. DOI: [10.1039/B901311C](https://doi.org/10.1039/B901311C).
- [55] A. Caspi, R. Granek, and M. Elbaum. “Enhanced Diffusion in Active Intracellular Transport”. *Phys. Rev. Lett.* 85 (2000), pp. 5655–5658. DOI: [10.1103/PhysRevLett.85.5655](https://doi.org/10.1103/PhysRevLett.85.5655).
- [56] A. Caspi, R. Granek, and M. Elbaum. “Diffusion and directed motion in cellular transport”. *Phys. Rev. E* 66 (2002), p. 011916. DOI: [10.1103/PhysRevE.66.011916](https://doi.org/10.1103/PhysRevE.66.011916).

- [57] N. Gal and D. Weihs. “Intracellular Mechanics and Activity of Breast Cancer Cells Correlate with Metastatic Potential”. *Cell Biochemistry and Biophysics* 63.3 (2012), pp. 199–209. DOI: [10.1007/s12013-012-9356-z](https://doi.org/10.1007/s12013-012-9356-z).
- [58] B. Stuhrmann, M. Soares e Silva, M. Depken, F. C. MacKintosh, and G. H. Koenderink. “Nonequilibrium fluctuations of a remodeling *in vitro* cytoskeleton”. *Phys. Rev. E* 86 (2012), p. 020901. DOI: [10.1103/PhysRevE.86.020901](https://doi.org/10.1103/PhysRevE.86.020901).
- [59] M. S. e Silva, B. Stuhrmann, T. Betz, and G. H. Koenderink. “Time-resolved microrheology of actively remodeling actomyosin networks”. *New J. Phys.* 16.7 (2014), p. 075010. DOI: [10.1088/1367-2630/16/7/075010](https://doi.org/10.1088/1367-2630/16/7/075010).
- [60] K. C. Leptos, J. S. Guasto, J. P. Gollub, A. I. Pesci, and R. E. Goldstein. “Dynamics of Enhanced Tracer Diffusion in Suspensions of Swimming Eukaryotic Microorganisms”. *Phys. Rev. Lett.* 103 (2009), p. 198103. DOI: [10.1103/PhysRevLett.103.198103](https://doi.org/10.1103/PhysRevLett.103.198103).
- [61] A. Rahman. “Correlations in the Motion of Atoms in Liquid Argon”. *Phys. Rev.* 136 (1964), A405–A411. DOI: [10.1103/PhysRev.136.A405](https://doi.org/10.1103/PhysRev.136.A405).
- [62] N. Desprat, A. Richert, J. Simeon, and A. Asnacios. “Creep Function of a Single Living Cell”. *Biophys. J.* 88 (2003), pp. 2224–2233. DOI: [10.1529/biophysj.104.050278](https://doi.org/10.1529/biophysj.104.050278).
- [63] T. Betz, M. Lenz, J.-F. Joanny, and C. Sykes. “ATP-dependent mechanics of red blood cells”. *Proc. Natl. Acad. Sci. USA* 106.36 (2009), pp. 15320–15325. DOI: [10.1073/pnas.0904614106](https://doi.org/10.1073/pnas.0904614106).
- [64] H. Turlier et al. “Equilibrium physics breakdown reveals the active nature of red blood cell flickering”. *Nat. Phys.* (2016). DOI: [10.1038/nphys3621](https://doi.org/10.1038/nphys3621).
- [65] A. R. Bausch, W. Möller, and E. Sackmann. “Measurement of Local Viscoelasticity and Forces in Living Cells by Magnetic Tweezers”. *Biophys. J.* 76.1 (1999), pp. 573–579. DOI: [http://dx.doi.org/10.1016/S0006-3495\(99\)77225-5](http://dx.doi.org/10.1016/S0006-3495(99)77225-5).
- [66] J.-F. Berret. “Local viscoelasticity of living cells measured by rotational magnetic spectroscopy”. *Nat. Com.* 7 (2016). DOI: [10.1038/ncomms10134](https://doi.org/10.1038/ncomms10134).
- [67] B. Fabry, G. N. Maksym, J. P. Butler, M. Glogauer, D. Navajas, and J. J. Fredberg. “Scaling the Microrheology of Living Cells”. *Phys. Rev. Lett.* 87 (2001), p. 148102. DOI: [10.1103/PhysRevLett.87.148102](https://doi.org/10.1103/PhysRevLett.87.148102).
- [68] P. Fernández, P. A. Pullarkat, and A. Ott. “A master relation defines the nonlinear viscoelasticity of single fibroblasts”. *Biophys. J.* 90.10 (2006), pp. 3796–3805. DOI: [10.1529/biophysj.105.072215](https://doi.org/10.1529/biophysj.105.072215).

- [69] P. Kollmannsberger and B. Fabry. “Linear and nonlinear rheology of living cells”. *Annu. Rev. Mat. Res.* 41 (2011), pp. 75–97. DOI: [10.1146/annurev-matsci-062910-100351](https://doi.org/10.1146/annurev-matsci-062910-100351).
- [70] D. Robert, K. Aubertin, J.-C. Bacri, and C. Wilhelm. “Magnetic nanomanipulations inside living cells compared with passive tracking of nanoprobes to get consensus for intracellular mechanics”. *Phys. Rev. E* 85 (2012), p. 011905. DOI: [10.1103/PhysRevE.85.011905](https://doi.org/10.1103/PhysRevE.85.011905).
- [71] T. Gisler and D. A. Weitz. “Scaling of the Microrheology of Semidilute F-Actin Solutions”. *Phys. Rev. Lett.* 82 (1999), pp. 1606–1609. DOI: [10.1103/PhysRevLett.82.1606](https://doi.org/10.1103/PhysRevLett.82.1606).
- [72] J. Liu, M. L. Gardel, K. Kroy, E. Frey, B. D. Hoffman, J. C. Crocker, A. R. Bausch, and D. A. Weitz. “Microrheology Probes Length Scale Dependent Rheology”. *Phys. Rev. Lett.* 96 (2006), p. 118104. DOI: [10.1103/PhysRevLett.96.118104](https://doi.org/10.1103/PhysRevLett.96.118104).
- [73] D. Humphrey, C. Duggan, D. Saha, D. Smith, and J. Käs. “Active fluidization of polymer networks through molecular motors”. *Nature* 416.6879 (2002), pp. 413–416. DOI: [10.1038/416413a](https://doi.org/10.1038/416413a).
- [74] D. Mizuno, C. Tardin, C. F. Schmidt, and F. C. MacKintosh. “Nonequilibrium Mechanics of Active Cytoskeletal Networks”. *Science* 315.5810 (2007), pp. 370–373. DOI: [10.1126/science.1134404](https://doi.org/10.1126/science.1134404).
- [75] G. H. Koenderink, Z. Dogic, F. Nakamura, P. M. Bendix, F. C. MacKintosh, J. H. Hartwig, T. P. Stossel, and D. A. Weitz. “An active biopolymer network controlled by molecular motors”. *Proc. Natl. Acad. Sci. USA* 106.36 (2009), pp. 15192–15197. DOI: [10.1073/pnas.0903974106](https://doi.org/10.1073/pnas.0903974106).
- [76] P. Martin, A. J. Hudspeth, and F. Jülicher. “Comparison of a hair bundle’s spontaneous oscillations with its response to mechanical stimulation reveals the underlying active process”. *Proc. Natl. Acad. Sci. USA* 98 (2001), pp. 14380–14385. DOI: [10.1073/pnas.251530598](https://doi.org/10.1073/pnas.251530598).
- [77] C. Wilhelm. “Out-of-Equilibrium Microrheology inside Living Cells”. *Phys. Rev. Lett.* 101 (2008), p. 028101. DOI: [10.1103/PhysRevLett.101.028101](https://doi.org/10.1103/PhysRevLett.101.028101).
- [78] F. C. MacKintosh and A. J. Levine. “Nonequilibrium Mechanics and Dynamics of Motor-Activated Gels”. *Phys. Rev. Lett.* 100 (2008), p. 018104. DOI: [10.1103/PhysRevLett.100.018104](https://doi.org/10.1103/PhysRevLett.100.018104).
- [79] A. J. Levine and F. C. MacKintosh. “The Mechanics and Fluctuation Spectrum of Active Gels†”. *J. Phys. Chem. B* 113.12 (2009), pp. 3820–3830. DOI: [10.1021/jp808192w](https://doi.org/10.1021/jp808192w).

- [80] T. B. Liverpool. “Anomalous fluctuations of active polar filaments”. *Phys. Rev. E* 67 (2003), p. 031909. DOI: [10.1103/PhysRevE.67.031909](https://doi.org/10.1103/PhysRevE.67.031909).
- [81] N. Gov. “Membrane Undulations Driven by Force Fluctuations of Active Proteins”. *Phys. Rev. Lett.* 93 (2004), p. 268104. DOI: [10.1103/PhysRevLett.93.268104](https://doi.org/10.1103/PhysRevLett.93.268104).
- [82] K. I. Morozov and L. M. Pismen. “Motor-driven effective temperature and viscoelastic response of active matter”. *Phys. Rev. E* 81 (2010), p. 061922. DOI: [10.1103/PhysRevE.81.061922](https://doi.org/10.1103/PhysRevE.81.061922).
- [83] E. Ben-Isaac, Y. Park, G. Popescu, F. L. H. Brown, N. S. Gov, and Y. Shokef. “Effective Temperature of Red-Blood-Cell Membrane Fluctuations”. *Phys. Rev. Lett.* 106 (2011), p. 238103. DOI: [10.1103/PhysRevLett.106.238103](https://doi.org/10.1103/PhysRevLett.106.238103).
- [84] C. P. Broedersz and F. C. MacKintosh. “Modeling semiflexible polymer networks”. *Rev. Mod. Phys.* 86 (2014), pp. 995–1036. DOI: [10.1103/RevModPhys.86.995](https://doi.org/10.1103/RevModPhys.86.995).
- [85] P. Ronceray and M. Lenz. “Connecting local active forces to macroscopic stress in elastic media”. *Soft matter* 11.8 (2015), pp. 1597–1605. DOI: [10.1039/C4SM02526A](https://doi.org/10.1039/C4SM02526A).
- [86] P. Ronceray, C. P. Broedersz, and M. Lenz. “Fiber networks amplify active stress”. *Proc. Natl. Acad. Sci. USA* 113.11 (2016), pp. 2827–2832. DOI: [10.1073/pnas.1514208113](https://doi.org/10.1073/pnas.1514208113).
- [87] F. Jülicher, K. Kruse, J. Prost, and J.-F. Joanny. “Active behavior of the Cytoskeleton”. *Physics Reports* 449.1–3 (2007). Nonequilibrium physics: From complex fluids to biological systems III. Living systems, pp. 3–28. DOI: [10.1016/j.physrep.2007.02.018](https://doi.org/10.1016/j.physrep.2007.02.018).
- [88] J.-F. Joanny and J. Prost. “Active gels as a description of the actin-myosin cytoskeleton”. *HFSP J.* 3.2 (2009), pp. 94–104.
- [89] J. Prost, F. Jülicher, and J. Joanny. “Active gel physics”. *Nat. Phys.* 11.2 (2015), pp. 111–117. DOI: [10.1038/NPHYS3224](https://doi.org/10.1038/NPHYS3224).
- [90] R. Voituriez, J. F. Joanny, and J. Prost. “Spontaneous flow transition in active polar gels”. *EPL (Europhysics Letters)* 70.3 (2005), p. 404. DOI: [10.1209/epl/i2004-10501-2](https://doi.org/10.1209/epl/i2004-10501-2).
- [91] R. Voituriez, J. F. Joanny, and J. Prost. “Generic Phase Diagram of Active Polar Films”. *Phys. Rev. Lett.* 96 (2006), p. 028102. DOI: [10.1103/PhysRevLett.96.028102](https://doi.org/10.1103/PhysRevLett.96.028102).

- [92] H. Turlier, B. Audoly, J. Prost, and J.-F. Joanny. “Furrow Constriction in Animal Cell Cytokinesis”. *Biophys. J.* 106.1 (2014), pp. 114–123. DOI: [10.1016/j.bpj.2013.11.014](https://doi.org/10.1016/j.bpj.2013.11.014).
- [93] A. W. C. Lau, B. D. Hoffman, A. Davies, J. C. Crocker, and T. C. Lubensky. “Microrheology, Stress Fluctuations, and Active Behavior of Living Cells”. *Phys. Rev. Lett.* 91 (2003), p. 198101. DOI: [10.1103/PhysRevLett.91.198101](https://doi.org/10.1103/PhysRevLett.91.198101).
- [94] C. Raupach, D. P. Zitterbart, C. T. Mierke, C. Metzner, F. A. Müller, and B. Fabry. “Stress fluctuations and motion of cytoskeletal-bound markers”. *Phys. Rev. E* 76 (2007), p. 011918. DOI: [10.1103/PhysRevE.76.011918](https://doi.org/10.1103/PhysRevE.76.011918).
- [95] C. Metzner, C. Raupach, D. Paranhos Zitterbart, and B. Fabry. “Simple model of cytoskeletal fluctuations”. *Phys. Rev. E* 76 (2007), p. 021925. DOI: [10.1103/PhysRevE.76.021925](https://doi.org/10.1103/PhysRevE.76.021925).
- [96] C. Metzner, C. Raupach, C. T. Mierke, and B. Fabry. “Fluctuations of cytoskeleton-bound microbeads—the effect of bead–receptor binding dynamics”. *J. Phys.: Condens. Matter* 22.19 (2010), p. 194105. DOI: [10.1088/0953-8984/22/19/194105](https://doi.org/10.1088/0953-8984/22/19/194105).
- [97] T. G. Mason and D. A. Weitz. “Optical Measurements of Frequency-Dependent Linear Viscoelastic Moduli of Complex Fluids”. *Phys. Rev. Lett.* 74 (1995), pp. 1250–1253. DOI: [10.1103/PhysRevLett.74.1250](https://doi.org/10.1103/PhysRevLett.74.1250).
- [98] T. G. Mason. “Estimating the viscoelastic moduli of complex fluids using the generalized Stokes–Einstein equation”. *Rheol. Acta* 39.4 (2000), pp. 371–378. DOI: [10.1007/s003970000094](https://doi.org/10.1007/s003970000094).
- [99] C. P. Brangwynne, G. H. Koenderink, F. C. MacKintosh, and D. A. Weitz. “Intracellular transport by active diffusion”. *Trends Cell Biol.* 19.9 (2009), pp. 423–427. DOI: dx.doi.org/10.1016/j.tcb.2009.04.004.
- [100] A. Bérut, A. Arakelyan, A. Petrosyan, S. Ciliberto, R. Dillenschneider, and E. Lutz. “Experimental verification of Landauer’s principle linking information and thermodynamics”. *Nature* 483 (Mar. 2012), pp. 187–189. DOI: [10.1038/nature10872](https://doi.org/10.1038/nature10872).
- [101] K. Kanazawa, T. Sagawa, and H. Hayakawa. “Energy pumping in electrical circuits under avalanche noise”. *Phys. Rev. E* 90 (1 2014), p. 012115. DOI: [10.1103/PhysRevE.90.012115](https://doi.org/10.1103/PhysRevE.90.012115).
- [102] L. Chevry, N. K. Sampathkumar, A. Cebers, and J.-F. Berret. “Magnetic wire-based sensors for the microrheology of complex fluids”. *Phys. Rev. E* 88 (2013), p. 062306. DOI: [10.1103/PhysRevE.88.062306](https://doi.org/10.1103/PhysRevE.88.062306).

- [103] R. Colin, L. Chevry, J.-F. Berret, and B. Abou. “Rotational microrheology of Maxwell fluids using micron-sized wires”. *Soft Matter* 10 (2014), pp. 1167–1173. DOI: [10.1039/C3SM52726C](https://doi.org/10.1039/C3SM52726C).
- [104] L. Chevry, R. Colin, B. Abou, and J.-F. Berret. “Intracellular micro-rheology probed by micron-sized wires”. *Biomaterials* 34.27 (2013), pp. 6299–6305. DOI: <http://dx.doi.org/10.1016/j.biomaterials.2013.05.002>.
- [105] M. Schuh. “An actin-dependent mechanism for long-range vesicle transport”. *Nat. Cell Biol.* 13 (2011), pp. 1431–1436. DOI: [10.1038/ncb2353](https://doi.org/10.1038/ncb2353).
- [106] Z. Holubcová, G. Howard, and M. Schuh. “Vesicles modulate an actin network for asymmetric spindle positioning”. *Nat. Cell Biol.* 15 (2013), pp. 937–947. DOI: [10.1038/ncb2802](https://doi.org/10.1038/ncb2802).
- [107] A. Chaigne, C. Campillo, N. Gov, R. Voituriez, C. Sykes, M. Verlhac, and M. Terret. “A narrow window of cortical tension guides asymmetric spindle positioning in the mouse oocyte”. *Nat. Com.* 6 (2015). DOI: [10.1038/ncomms7027](https://doi.org/10.1038/ncomms7027).
- [108] M. Almonacid, W. W. Ahmed, M. Bussonnier, P. Mailly, T. Betz, R. Voituriez, N. S. Gov, and M.-H. Verlhac. “Active diffusion positions the nucleus in mouse oocytes”. *Nat. Cell Biol.* 17.1 (4 2015), pp. 470–479. DOI: [10.1038/ncb3131](https://doi.org/10.1038/ncb3131).
- [109] A. T. L. Van Lommel. *From Cells to Organs: A Histology Textbook and Atlas*. Springer US, 2003.
- [110] M. Rauzi, P. Verant, T. Lecuit, and P.-F. Lenne. “Nature and anisotropy of cortical forces orienting Drosophila tissue morphogenesis”. *Nat. Cell Biol.* 10.12 (2008), pp. 1401–1410. DOI: [10.1038/ncb1798](https://doi.org/10.1038/ncb1798).
- [111] M. Rauzi, P.-F. Lenne, and T. Lecuit. “Planar polarized actomyosin contractile flows control epithelial junction remodelling”. *Nature* 468 (2010), pp. 1110–1114. DOI: [10.1038/nature09566](https://doi.org/10.1038/nature09566).
- [112] C. Guillot and T. Lecuit. “Mechanics of Epithelial Tissue Homeostasis and Morphogenesis”. *Science* 340.6137 (2013), pp. 1185–1189. DOI: [10.1126/science.1235249](https://doi.org/10.1126/science.1235249).
- [113] A. C. Oates, N. Gorfinkel, M. Gonzalez-Gaitan, and C.-P. Heisenberg. “Quantitative approaches in developmental biology”. *Nat. Rev. Gen.* 10.8 (2009), pp. 517–530. DOI: [10.1038/nrg2548](https://doi.org/10.1038/nrg2548).
- [114] E. Knust and O. Bossinger. “Composition and formation of intercellular junctions in epithelial cells”. *Science* 298.5600 (2002), pp. 1955–1959. DOI: [10.1126/science.1072161](https://doi.org/10.1126/science.1072161).

- [115] M. Cavey, M. Rauzi, P.-F. Lenne, and T. Lecuit. “A two-tiered mechanism for stabilization and immobilization of E-cadherin”. *Nature* 453 (2008), pp. 751–756. DOI: [10.1038/nature06953](https://doi.org/10.1038/nature06953).
- [116] P. Marmottant et al. “The role of fluctuations and stress on the effective viscosity of cell aggregates”. *Proc. Natl. Acad. Sci. USA* 106.41 (2009), pp. 17271–17275. DOI: [10.1073/pnas.0902085106](https://doi.org/10.1073/pnas.0902085106).
- [117] T. V. Stirbat, A. Mgharbel, S. Bodennec, K. Ferri, H. C. Mertani, J.-P. Rieu, and H. Delanoë-Ayari. “Fine Tuning of Tissues’ Viscosity and Surface Tension through Contractility Suggests a New Role for -Catenin”. *PLoS ONE* 8.2 (Feb. 2013), e52554. DOI: [10.1371/journal.pone.0052554](https://doi.org/10.1371/journal.pone.0052554).
- [118] K. Guevorkian, M.-J. Colbert, M. Durth, S. Dufour, and F. Brochard-Wyart. “Aspiration of Biological Viscoelastic Drops”. *Phys. Rev. Lett.* 104 (2010), p. 218101. DOI: [10.1103/PhysRevLett.104.218101](https://doi.org/10.1103/PhysRevLett.104.218101).
- [119] J. Brugués, B. Maugis, J. Casademunt, P. Nassoy, F. Amblard, and P. Sens. “Dynamical organization of the cytoskeletal cortex probed by micropipette aspiration”. *Proc. Natl. Acad. Sci. USA* 107.35 (2010), pp. 15415–15420. DOI: [10.1073/pnas.0913669107](https://doi.org/10.1073/pnas.0913669107).
- [120] J. Ranft, M. Basan, J. Elgeti, J.-F. Joanny, J. Prost, and F. Jülicher. “Fluidization of tissues by cell division and apoptosis”. *Proc. Natl. Acad. Sci. USA* 107.49 (2010), pp. 20863–20868. DOI: [10.1073/pnas.1011086107](https://doi.org/10.1073/pnas.1011086107).
- [121] T. E. Angelini, E. Hannezo, X. Trepat, M. Marquez, J. J. Fredberg, and D. A. Weitz. “Glass-like dynamics of collective cell migration”. *Proc. Natl. Acad. Sci. USA* 108.12 (2011), pp. 4714–4719. DOI: [10.1073/pnas.1010059108](https://doi.org/10.1073/pnas.1010059108).
- [122] E. M. Schöltz, M. Larcos, J. A. Talbot, and M. L. Manning. “Glassy dynamics in three-dimensional embryonic tissues”. *J. R. Soc. Interface* 10 (89 2013), pp. 1885–1890. DOI: [10.1098/rspa.2013.0726](https://doi.org/10.1098/rspa.2013.0726).
- [123] S. Garcia, E. Hannezo, J. Elgeti, J.-F. Joanny, P. Silberzan, and N. S. Gov. “Physics of active jamming during collective cellular motion in a monolayer”. *Proc. Natl. Acad. Sci. USA* 112.50 (2015), pp. 15314–15319. DOI: [10.1073/pnas.1510973112](https://doi.org/10.1073/pnas.1510973112).
- [124] R. Farhadifar, J.-C. Röper, B. Aigouy, S. Eaton, and F. Jülicher. “The Influence of Cell Mechanics, Cell-Cell Interactions, and Proliferation on Epithelial Packing”. *Curr. Biol.* 17 (2007), pp. 2095–2104. DOI: [10.1016/j.cub.2007.11.049](https://doi.org/10.1016/j.cub.2007.11.049).
- [125] D. Bi, J. H. Lopez, J. M. Schwarz, and M. L. Manning. “Energy barriers and cell migration in densely packed tissues”. *Soft Matter* 10 (2014), pp. 1885–1890. DOI: [10.1039/C3SM52893F](https://doi.org/10.1039/C3SM52893F).

- [126] D. Bi, J. H. Lopez, J. M. Schwarz, and M. L. Manning. “A density-independent rigidity transition in biological tissues”. *Nat. Phys.* (2015). DOI: [10.1038/nphys3471](https://doi.org/10.1038/nphys3471).
- [127] D. Bi, X. Yang, M. C. Marchetti, and M. L. Manning. “Motility-Driven Glass and Jamming Transitions in Biological Tissues”. *Phys. Rev. X* 6 (2016), p. 021011. DOI: [10.1103/PhysRevX.6.021011](https://doi.org/10.1103/PhysRevX.6.021011).
- [128] C. L. Adams, Y.-T. Chen, S. J. Smith, and W. James Nelson. “Mechanisms of Epithelial Cell–Cell Adhesion and Cell Compaction Revealed by High-resolution Tracking of E-Cadherin–Green Fluorescent Protein”. *J. Cell Biol.* 142.4 (1998), pp. 1105–1119. DOI: [10.1083/jcb.142.4.1105](https://doi.org/10.1083/jcb.142.4.1105).
- [129] I. Theurkauff, C. Cottin-Bizonne, J. Palacci, C. Ybert, and L. Bocquet. “Dynamic Clustering in Active Colloidal Suspensions with Chemical Signaling”. *Phys. Rev. Lett.* 108 (2012), p. 268303. DOI: [10.1103/PhysRevLett.108.268303](https://doi.org/10.1103/PhysRevLett.108.268303).
- [130] I. Buttinoni, J. Bialké, F. Kümmel, H. Löwen, C. Bechinger, and T. Speck. “Dynamical Clustering and Phase Separation in Suspensions of Self-Propelled Colloidal Particles”. *Phys. Rev. Lett.* 110 (2013), p. 238301. DOI: [10.1103/PhysRevLett.110.238301](https://doi.org/10.1103/PhysRevLett.110.238301).
- [131] Y. Fily and M. C. Marchetti. “Athermal Phase Separation of Self-Propelled Particles with No Alignment”. *Phys. Rev. Lett.* 108 (2012), p. 235702. DOI: [10.1103/PhysRevLett.108.235702](https://doi.org/10.1103/PhysRevLett.108.235702).
- [132] G. S. Redner, M. F. Hagan, and A. Baskaran. “Structure and Dynamics of a Phase-Separating Active Colloidal Fluid”. *Phys. Rev. Lett.* 110 (2013), p. 055701. DOI: [10.1103/PhysRevLett.110.055701](https://doi.org/10.1103/PhysRevLett.110.055701).
- [133] J. Stenhammar, A. Tiribocchi, R. J. Allen, D. Marenduzzo, and M. E. Cates. “Continuum Theory of Phase Separation Kinetics for Active Brownian Particles”. *Phys. Rev. Lett.* 111 (2013), p. 145702. DOI: [10.1103/PhysRevLett.111.145702](https://doi.org/10.1103/PhysRevLett.111.145702).
- [134] M. E. Cates and J. Tailleur. “When are active Brownian particles and run-and-tumble particles equivalent? Consequences for motility-induced phase separation”. *EPL* 101.2 (2013), p. 20010. DOI: [10.1209/0295-5075/101/20010](https://doi.org/10.1209/0295-5075/101/20010).
- [135] J. Tailleur and M. E. Cates. “Sedimentation, trapping, and rectification of dilute bacteria”. *EPL* 86.6 (2009), p. 60002. DOI: [10.1209/0295-5075/86/60002](https://doi.org/10.1209/0295-5075/86/60002).
- [136] J. Elgeti and G. Gompper. “Self-propelled rods near surfaces”. *EPL* 85.3 (2009), p. 38002. DOI: [10.1209/0295-5075/85/38002](https://doi.org/10.1209/0295-5075/85/38002).

- [137] Y. Fily, A. Baskaran, and M. F. Hagan. “Dynamics of self-propelled particles under strong confinement”. *Soft Matter* 10 (30 2014), pp. 5609–5617. DOI: [10.1039/C4SM00975D](https://doi.org/10.1039/C4SM00975D).
- [138] X. Yang, M. L. Manning, and M. C. Marchetti. “Aggregation and segregation of confined active particles”. *Soft Matter* 10 (34 2014), pp. 6477–6484. DOI: [10.1039/C4SM00927D](https://doi.org/10.1039/C4SM00927D).
- [139] Y. Fily, A. Baskaran, and M. F. Hagan. “Dynamics and density distribution of strongly confined noninteracting nonaligning self-propelled particles in a nonconvex boundary”. *Phys. Rev. E* 91 (1 2015), p. 012125. DOI: [10.1103/PhysRevE.91.012125](https://doi.org/10.1103/PhysRevE.91.012125).
- [140] A. Solon, M. Cates, and J. Tailleur. “Active brownian particles and run-and-tumble particles: A comparative study”. English. *EPJST* 224.7 (2015), pp. 1231–1262. ISSN: 1951-6355. DOI: [10.1140/epjst/e2015-02457-0](https://doi.org/10.1140/epjst/e2015-02457-0).
- [141] M. Enculescu and H. Stark. “Active Colloidal Suspensions Exhibit Polar Order under Gravity”. *Phys. Rev. Lett.* 107 (5 2011), p. 058301. DOI: [10.1103/PhysRevLett.107.058301](https://doi.org/10.1103/PhysRevLett.107.058301).
- [142] F. Ginot, I. Theurkauff, D. Levis, C. Ybert, L. Bocquet, L. Berthier, and C. Cottin-Bizonne. “Nonequilibrium Equation of State in Suspensions of Active Colloids”. *Phys. Rev. X* 5 (2015), p. 011004. DOI: [10.1103/PhysRevX.5.011004](https://doi.org/10.1103/PhysRevX.5.011004).
- [143] R. Ni, M. A. C. Stuart, and M. Dijkstra. “Pushing the glass transition towards random close packing using self-propelled hard spheres”. *Nat. Com.* 4 (2013), p. 2704. DOI: [10.1038/ncomms3704](https://doi.org/10.1038/ncomms3704).
- [144] R. Mandal, P. Jyoti Bhuyan, M. Rao, and C. Dasgupta. “Active fluidization in dense glassy systems”. *ArXiv e-prints* (2014). arXiv: [1412.1631](https://arxiv.org/abs/1412.1631).
- [145] A. Wysocki, R. G. Winkler, and G. Gompper. “Cooperative motion of active Brownian spheres in three-dimensional dense suspensions”. *EPL* 105.4 (2014), p. 48004. DOI: [10.1209/0295-5075/105/48004](https://doi.org/10.1209/0295-5075/105/48004).
- [146] D. Levis and L. Berthier. “Clustering and heterogeneous dynamics in a kinetic Monte Carlo model of self-propelled hard disks”. *Phys. Rev. E* 89 (6 2014), p. 062301. DOI: [10.1103/PhysRevE.89.062301](https://doi.org/10.1103/PhysRevE.89.062301).
- [147] L. Berthier. “Nonequilibrium Glassy Dynamics of Self-Propelled Hard Disks”. *Phys. Rev. Lett.* 112 (22 2014), p. 220602. DOI: [10.1103/PhysRevLett.112.220602](https://doi.org/10.1103/PhysRevLett.112.220602).
- [148] M. J. Schnitzer. “Theory of continuum random walks and application to chemotaxis”. *Phys. Rev. E* 48 (1993), pp. 2553–2568. DOI: [10.1103/PhysRevE.48.2553](https://doi.org/10.1103/PhysRevE.48.2553).

- [149] T. F. F. Farage, P. Krinninger, and J. M. Brader. “Effective interactions in active Brownian suspensions”. *Phys. Rev. E* 91 (2015), p. 042310.
- [150] A. P. Solon, J. Stenhammar, R. Wittkowski, M. Kardar, Y. Kafri, M. E. Cates, and J. Tailleur. “Pressure and Phase Equilibria in Interacting Active Brownian Spheres”. *Phys. Rev. Lett.* 114 (2015), p. 198301. DOI: [10.1103/PhysRevLett.114.198301](https://doi.org/10.1103/PhysRevLett.114.198301).
- [151] D. Loi, S. Mossa, and L. F. Cugliandolo. “Effective temperature of active matter”. *Phys. Rev. E* 77 (May 2008), p. 051111. DOI: [10.1103/PhysRevE.77.051111](https://doi.org/10.1103/PhysRevE.77.051111).
- [152] D. Loi, S. Mossa, and L. F. Cugliandolo. “Effective temperature of active complex matter”. *Soft Matter* 7 (8 2011), pp. 3726–3729. DOI: [10.1039/COSM01484B](https://doi.org/10.1039/COSM01484B).
- [153] D. Loi, S. Mossa, and L. F. Cugliandolo. “Non-conservative forces and effective temperatures in active polymers”. *Soft Matter* 7 (21 2011), pp. 10193–10209. DOI: [10.1039/C1SM05819C](https://doi.org/10.1039/C1SM05819C).
- [154] G. Szamel. “Self-propelled particle in an external potential: Existence of an effective temperature”. *Phys. Rev. E* 90 (2014), p. 012111. DOI: [10.1103/PhysRevE.90.012111](https://doi.org/10.1103/PhysRevE.90.012111).
- [155] S. A. Mallory, A. Šarić, C. Valeriani, and A. Cacciuto. “Anomalous thermomechanical properties of a self-propelled colloidal fluid”. *Phys. Rev. E* 89 (2014), p. 052303. DOI: [10.1103/PhysRevE.89.052303](https://doi.org/10.1103/PhysRevE.89.052303).
- [156] A. P. Solon, Y. Fily, A. Baskaran, M. E. Cates, Y. Kafri, M. Kardar, and J. Tailleur. “Pressure is not a state function for generic active fluids”. *Nat. Phys.* 11 (2015), pp. 1745–2473. DOI: [10.1038/nphys3377](https://doi.org/10.1038/nphys3377).
- [157] Y. Fily, S. Henkes, and M. C. Marchetti. “Freezing and phase separation of self-propelled disks”. *Soft Matter* 10 (2014), pp. 2132–2140. DOI: [10.1039/C3SM52469H](https://doi.org/10.1039/C3SM52469H).
- [158] T. Speck, J. Bialké, A. M. Menzel, and H. Löwen. “Effective Cahn-Hilliard Equation for the Phase Separation of Active Brownian Particles”. *Phys. Rev. Lett.* 112 (2014), p. 218304. DOI: [10.1103/PhysRevLett.112.218304](https://doi.org/10.1103/PhysRevLett.112.218304).
- [159] T. Speck, A. M. Menzel, J. Bialké, and H. Löwen. “Dynamical mean-field theory and weakly non-linear analysis for the phase separation of active Brownian particles”. *J. Chem. Phys.* 142.22 (2015). DOI: [10.1063/1.4922324](https://doi.org/10.1063/1.4922324).
- [160] U. M. B. Marconi, M. Paoluzzi, and C. Maggi. “Effective potential method for active particles”. *Molecular Physics* (), pp. 1–11. DOI: [10.1080/00268976.2016.1155777](https://doi.org/10.1080/00268976.2016.1155777).

- [161] T. F. Farage and J. M. Brader. “Dynamics and rheology of active glasses”. *ArXiv e-prints* (2014). arXiv: [1403.0928](#).
- [162] G. Szamel, E. Flenner, and L. Berthier. “Glassy dynamics of athermal self-propelled particles: Computer simulations and a nonequilibrium microscopic theory”. *Phys. Rev. E* 91 (2015), p. 062304. DOI: [10.1103/PhysRevE.91.062304](#).
- [163] G. Szamel. “Theory for the dynamics of dense systems of athermal self-propelled particles”. *Phys. Rev. E* 93 (2016), p. 012603. DOI: [10.1103/PhysRevE.93.012603](#).
- [164] C. Maggi, M. Paoluzzi, N. Pellicciotta, A. Lepore, L. Angelani, and R. Di Leonardo. “Generalized Energy Equipartition in Harmonic Oscillators Driven by Active Baths”. *Phys. Rev. Lett.* 113 (2014), p. 238303. DOI: [10.1103/PhysRevLett.113.238303](#).
- [165] P. Jung and P. Hänggi. “Dynamical systems: A unified colored-noise approximation”. *Phys. Rev. A* 35 (1987), pp. 4464–4466. DOI: [10.1103/PhysRevA.35.4464](#).
- [166] L. Cao, D.-j. Wu, and X.-l. Luo. “Effects of saturation in the transient process of a dye laser. III. The case of colored noise with large and small correlation time”. *Phys. Rev. A* 47 (1 1993), pp. 57–70. DOI: [10.1103/PhysRevA.47.57](#).
- [167] R. F. Fox. “Functional-calculus approach to stochastic differential equations”. *Phys. Rev. A* 33 (1 1986), pp. 467–476. DOI: [10.1103/PhysRevA.33.467](#).
- [168] R. F. Fox. “Uniform convergence to an effective Fokker-Planck equation for weakly colored noise”. *Phys. Rev. A* 34 (5 1986), pp. 4525–4527. DOI: [10.1103/PhysRevA.34.4525](#).
- [169] P. Jung and P. Hänggi. “Optical instabilities: new theories for colored-noise-driven laser instabilities”. *JOSA B* 5.5 (1988), pp. 979–986. DOI: [10.1364/JOSAB.5.000979](#).
- [170] R. F. Fox. “Mean first-passage times and colored noise”. *Phys. Rev. A* 37 (1988), pp. 911–917. DOI: [10.1103/PhysRevA.37.911](#).
- [171] A. J. Bray and A. J. McKane. “Instanton Calculation of the Escape Rate for Activation over a Potential Barrier Driven by Colored Noise”. *Phys. Rev. Lett.* 62 (1989), pp. 493–496. DOI: [10.1103/PhysRevLett.62.493](#).
- [172] P. Hanggi and P. Jung. “Colored noise in dynamical systems”. *Advances in chemical physics* 89 (1995), pp. 239–326. DOI: [10.1002/9780470141489.ch4](#).

- [173] C. Maggi, U. Marini Bettolo Marconi, N. Gnan, and R. Di Leonardo. “Multidimensional stationary probability distribution for interacting active particles”. *Sci. Rep.* 5 (2015). DOI: [10.1038/srep10742](https://doi.org/10.1038/srep10742).
- [174] P. Faccioli, M. Sega, F. Pederiva, and H. Orland. “Dominant Pathways in Protein Folding”. *Phys. Rev. Lett.* 97 (2006), p. 108101. DOI: [10.1103/PhysRevLett.97.108101](https://doi.org/10.1103/PhysRevLett.97.108101).
- [175] M. Sega, P. Faccioli, F. Pederiva, G. Garberoglio, and H. Orland. “Quantitative Protein Dynamics from Dominant Folding Pathways”. *Phys. Rev. Lett.* 99 (2007), p. 118102. DOI: [10.1103/PhysRevLett.99.118102](https://doi.org/10.1103/PhysRevLett.99.118102).
- [176] E. Autieri, P. Faccioli, M. Sega, F. Pederiva, and H. Orland. “Dominant reaction pathways in high-dimensional systems”. *J. Chem. Phys.* 130.6 (2009). DOI: [10.1063/1.3074271](https://doi.org/10.1063/1.3074271).
- [177] U. Marini Bettolo Marconi, N. Gnan, C. Maggi, and R. Di Leonardo. “Velocity distribution in active particles systems”. *Sci. Rep.* 6 (2015). DOI: [10.1038/srep23297](https://doi.org/10.1038/srep23297).
- [178] N. Koumakis, C. Maggi, and R. Di Leonardo. “Directed transport of active particles over asymmetric energy barriers”. *Soft Matter* 10 (31 2014), pp. 5695–5701. DOI: [10.1039/C4SM00665H](https://doi.org/10.1039/C4SM00665H).
- [179] C. R. Doering, P. S. Hagan, and C. D. Levermore. “Bistability driven by weakly colored Gaussian noise: The Fokker-Planck boundary layer and mean first-passage times”. *Phys. Rev. Lett.* 59 (1987), pp. 2129–2132. DOI: [10.1103/PhysRevLett.59.2129](https://doi.org/10.1103/PhysRevLett.59.2129).
- [180] M. M. Millonas and M. I. Dykman. “Transport and current reversal in stochastically driven ratchets”. *Phys. Lett. A* 185.1 (1994), pp. 65–69. DOI: [10.1016/0375-9601\(94\)90989-X](https://doi.org/10.1016/0375-9601(94)90989-X).
- [181] C. R. Doering, W. Horsthemke, and J. Riordan. “Nonequilibrium fluctuation-induced transport”. *Phys. Rev. Lett.* 72 (1994), pp. 2984–2987. DOI: [10.1103/PhysRevLett.72.2984](https://doi.org/10.1103/PhysRevLett.72.2984).
- [182] L. Berthier and J.-L. Barrat. “Shearing a Glassy Material: Numerical Tests of Nonequilibrium Mode-Coupling Approaches and Experimental Proposals”. *Phys. Rev. Lett.* 89 (2002), p. 095702. DOI: [10.1103/PhysRevLett.89.095702](https://doi.org/10.1103/PhysRevLett.89.095702).
- [183] L. Berthier and J. Kurchan. “Non-equilibrium glass transitions in driven and active matter”. *Nat. Phys.* 9 (2013), pp. 310–314. DOI: [10.1038/nphys2592](https://doi.org/10.1038/nphys2592).

- [184] D. Levis and L. Berthier. “From single-particle to collective effective temperatures in an active fluid of self-propelled particles”. *EPL* 111.6 (2015), p. 60006. DOI: [10.1209/0295-5075/111/60006](https://doi.org/10.1209/0295-5075/111/60006).
- [185] E. Dieterich, J. Camunas-Soler, M. Ribezzi-Crivellari, U. Seifert, and F. Ritort. “Single-molecule measurement of the effective temperature in non-equilibrium steady states”. *Nat. Phys.* 11 (2015), pp. 971–977. DOI: [10.1038/nphys3435](https://doi.org/10.1038/nphys3435).
- [186] K. Kawasaki. “Stochastic model of slow dynamics in supercooled liquids and dense colloidal suspensions”. *Physica A* 208.1 (1994), pp. 35–64. ISSN: 0378-4371. DOI: [10.1016/0378-4371\(94\)90533-9](https://doi.org/10.1016/0378-4371(94)90533-9).
- [187] D. S. Dean. “Langevin equation for the density of a system of interacting Langevin processes”. *J. Phys. A* 29.24 (1996), p. L613. DOI: [10.1088/0305-4470/29/24/001](https://doi.org/10.1088/0305-4470/29/24/001).
- [188] A. J. Archer. “Dynamical density functional theory for dense atomic liquids”. *J. Phys.: Condens. Matter* 18.24 (2006), p. 5617. DOI: [10.1088/0953-8984/18/24/004](https://doi.org/10.1088/0953-8984/18/24/004).
- [189] A. J. Archer. “Dynamical density functional theory for molecular and colloidal fluids: A microscopic approach to fluid mechanics”. *J. Chem. Phys.* 130.1 (2009). DOI: [10.1063/1.3054633](https://doi.org/10.1063/1.3054633).
- [190] S. P. Das and A. Yoshimori. “Coarse-grained forms for equations describing the microscopic motion of particles in a fluid”. *Phys. Rev. E* 88 (2013), p. 043008. DOI: [10.1103/PhysRevE.88.043008](https://doi.org/10.1103/PhysRevE.88.043008).
- [191] V. Démery. “Mean-field microrheology of a very soft colloidal suspension: Inertia induces shear thickening”. *Phys. Rev. E* 91 (2015), p. 062301. DOI: [10.1103/PhysRevE.91.062301](https://doi.org/10.1103/PhysRevE.91.062301).
- [192] T. Nakamura and A. Yoshimori. “Derivation of the nonlinear fluctuating hydrodynamic equation from the underdamped Langevin equation”. *J. Phys. A: Math. Theor.* 42.6 (2009), p. 065001. DOI: [10.1088/1751-8113/42/6/065001](https://doi.org/10.1088/1751-8113/42/6/065001).
- [193] F. D. C. Farrell, M. C. Marchetti, D. Marenduzzo, and J. Tailleur. “Pattern Formation in Self-Propelled Particles with Density-Dependent Motility”. *Phys. Rev. Lett.* 108 (2012), p. 248101. DOI: [10.1103/PhysRevLett.108.248101](https://doi.org/10.1103/PhysRevLett.108.248101).
- [194] U. Marini Bettolo Marconi and C. Maggi. “Towards a statistical mechanical theory of active fluids”. *Soft Matter* 11 (2015), pp. 8768–8781. DOI: [10.1039/C5SM01718A](https://doi.org/10.1039/C5SM01718A).

- [195] U. Marini Bettolo Marconi, C. Maggi, and S. Melchionna. “Pressure and surface tension of an active simple liquid: a comparison between kinetic, mechanical and free-energy based approaches”. *ArXiv e-prints* (2016). arXiv: [1603.05291](https://arxiv.org/abs/1603.05291).
- [196] V. Démery, O. Bénichou, and H. Jacquin. “Generalized Langevin equations for a driven tracer in dense soft colloids: construction and applications”. *New J. Phys.* 16.5 (2014), p. 053032. DOI: [10.1088/1367-2630/16/5/053032](https://doi.org/10.1088/1367-2630/16/5/053032).
- [197] K. Kanazawa, T. G. Sano, T. Sagawa, and H. Hayakawa. “Asymptotic Derivation of Langevin-like Equation with Non-Gaussian Noise and Its Analytical Solution”. *J. Stat. Phys.* 160.5 (2015), pp. 1294–1335. DOI: [10.1007/s10955-015-1286-x](https://doi.org/10.1007/s10955-015-1286-x).
- [198] T. G. Sano, K. Kanazawa, and H. Hayakawa. “Granular rotor as a probe for a non-equilibrium bath”. *ArXiv e-prints* (2015). arXiv: [1511.08594](https://arxiv.org/abs/1511.08594).
- [199] K. Kanazawa, T. Sagawa, and H. Hayakawa. “Stochastic Energetics for Non-Gaussian Processes”. *Phys. Rev. Lett.* 108 (2012), p. 210601. DOI: [10.1103/PhysRevLett.108.210601](https://doi.org/10.1103/PhysRevLett.108.210601).
- [200] X.-L. Wu and A. Libchaber. “Particle Diffusion in a Quasi-Two-Dimensional Bacterial Bath”. *Phys. Rev. Lett.* 84 (2000), pp. 3017–3020. DOI: [10.1103/PhysRevLett.84.3017](https://doi.org/10.1103/PhysRevLett.84.3017).
- [201] D. T. N. Chen, A. W. C. Lau, L. A. Hough, M. F. Islam, M. Goulian, T. C. Lubensky, and A. G. Yodh. “Fluctuations and Rheology in Active Bacterial Suspensions”. *Phys. Rev. Lett.* 99 (2007), p. 148302. DOI: [10.1103/PhysRevLett.99.148302](https://doi.org/10.1103/PhysRevLett.99.148302).
- [202] G. Miño et al. “Enhanced Diffusion due to Active Swimmers at a Solid Surface”. *Phys. Rev. Lett.* 106 (2011), p. 048102. DOI: [10.1103/PhysRevLett.106.048102](https://doi.org/10.1103/PhysRevLett.106.048102).
- [203] A. W. C. Lau and T. C. Lubensky. “State-dependent diffusion: Thermo-dynamic consistency and its path integral formulation”. *Phys. Rev. E* 76 (2007), p. 011123. DOI: [10.1103/PhysRevE.76.011123](https://doi.org/10.1103/PhysRevE.76.011123).
- [204] C. Aron, G. Biroli, and L. F. Cugliandolo. “Symmetries of generating functionals of Langevin processes with colored multiplicative noise”. *J. Stat. Mech.* 2010.11 (2010), P11018. DOI: [10.1088/1742-5468/2010/11/P11018](https://doi.org/10.1088/1742-5468/2010/11/P11018).

Papers

P10 É. Fodor, C. Nardini, M. E. Cates, J. Tailleur, P. Visco, and F. van Wijland
“How far from equilibrium is active matter?”

Physical Review Letters **117**, 038103 (2016), [arXiv:1604.00953](https://arxiv.org/abs/1604.00953)
Selected as Editor’s Suggestion, highlighted in Physics (2016)

P9 É. Fodor, H. Hayakawa, P. Visco, and F. van Wijland

“Active cage model of glassy dynamics”
Physical Review E **94**, 012610 (2016), [arXiv:1601.06613](https://arxiv.org/abs/1601.06613)

P8 É. Fodor*, V. Mehandia*, J. Comelles, R. Thiagarajan, N. S. Gov, P. Visco,
F. van Wijland, and D. Riveline

“Active fluctuations are controlled by molecular motor regulations in cell
monolayer”
[arXiv:1512.01476](https://arxiv.org/abs/1512.01476)

P7 É. Fodor*, W. W. Ahmed*, M. Almonacid*, M. Bussonnier, N. S. Gov, M.-H.
Verlhac, T. Betz, P. Visco, and F. van Wijland

“Nonequilibrium dissipation in living oocytes”
[arXiv:1511.00921](https://arxiv.org/abs/1511.00921)

P6 W. W. Ahmed*, É. Fodor*, M. Almonacid*, M. Bussonnier, N. S. Gov, M.-H.
Verlhac, P. Visco, F. van Wijland, and T. Betz

“Active mechanics in living oocytes reveals myosin-V force kinetics in vivo”
[arXiv:1510.08299](https://arxiv.org/abs/1510.08299)

P5 E. Ben Isaac, É. Fodor, P. Visco, F. van Wijland, and N. S. Gov

“Modeling the dynamics of a tracer particle in an elastic active gel”
Physical Review E **92**, 012716 (2015), [arXiv:1507.00917](https://arxiv.org/abs/1507.00917)

- P4** W. W. Ahmed, É. Fodor, and T. Betz
“Active cell mechanics: Measurement and theory”
Biochimica et Biophysica Acta (BBA) - Molecular Cell Research **1853**, 3083
(2015)
- P3** É. Fodor*, M. Guo*, N. S. Gov, P. Visco, D. A. Weitz, and F. van Wijland
“Activity-driven fluctuations in living cell”
Europhysics Letters **110**, 48005 (2015), [arXiv:1505.06489](https://arxiv.org/abs/1505.06489)
Selected as editor’s choice, highlighted in Europhysics News 46/5 (2015)
- P2** É. Fodor, D. S. Grebenkov, P. Visco, and F. van Wijland
“Generalized Langevin equation with hydrodynamic backflow: equilibrium properties”
Physica A: Statistical Mechanics and its Applications **422**, 107 (2015),
[arXiv:1412.3235](https://arxiv.org/abs/1412.3235)
- P1** É. Fodor, K. Kanazawa, H. Hayakawa, P. Visco, and F. van Wijland
“Energetics of active fluctuations in living cells”
Physical Review E **90**, 042724 (2014), [arXiv:1406.1732](https://arxiv.org/abs/1406.1732)

* Equal contribution of these authors to this work

Résumé

Les systèmes vivants évoluent hors de l'équilibre par l'injection permanente d'énergie fournie par l'ATP. La dynamique des composants intracellulaires, tels que les protéines, organelles et filaments du cytosquelette, est contrôlée par des fluctuations thermiques d'équilibre ainsi que des forces actives aléatoires produites par les moteurs moléculaires. Des traceurs sont injectés dans les cellules pour étudier ces fluctuations. Pour distinguer les fluctuations hors de l'équilibre des effets purement thermiques, des mesures de fluctuations spontanées et de réponse sont combinées. Nous récapitulons théoriquement les fluctuations observées à l'aide d'un modèle phénoménologique. Cela nous permet de quantifier les échelles de temps, de longueur, et d'énergie des fluctuations actives dans trois systèmes expérimentaux : des mélanomes, des ovocytes de souris, et des tissus épithéliaux.

Les particules auto-propulsées extraient de l'énergie de leur environnement pour effectuer un mouvement dirigé. Une telle dynamique conduit à une riche phénoménologie qui ne peut être capturée par la physique d'équilibre. Un exemple frappant est la possibilité pour des particules répulsives de subir une séparation de phase. Pour un modèle spécifique d'auto-propulsion, nous explorons à quelle distance de l'équilibre opère la dynamique. Nous quantifions la rupture du renversement temporel, et nous délimitons un régime d'équilibre effectif. L'identification de ce régime est basée sur l'analyse des fluctuations et réponse des particules.

Abstract

Living systems operate far from equilibrium due to the continuous injection of energy provided by ATP supply. The dynamics of the intracellular components, such as proteins, organelles and cytoskeletal filaments, are driven by both thermal equilibrium fluctuations, and active stochastic forces generated by the molecular motors. Tracer particles are injected in living cells to study these fluctuations. To sort out genuine nonequilibrium fluctuations from purely thermal effects, measurements of spontaneous tracer fluctuations and of response are combined. We theoretically rationalize the observed fluctuations with a phenomenological model. This model, in turn, allows us to quantify the time, length and energy scales of the active fluctuations in three different experimental systems: living melanoma cells, living mouse oocytes and epithelial tissues.

Self-propelled particles are able to extract energy from their environment to perform a directed motion. Such a dynamics lead to a rich phenomenology that cannot be accounted for by equilibrium physics arguments. A striking example is the possibility for repulsive particles to undergo a phase separation, as reported in both experimental and numerical realizations. On a specific model of self-propulsion, we explore how far from equilibrium the dynamics operate. We quantify the breakdown of the irreversibility of the dynamics, and we delineate a bona fide effective equilibrium regime. Our insight into this regime is based on the analysis of fluctuations and response of the particles.